DEFENCE ACADEMY
OF THE UNITED KINGDOM
Cranfield UNIVERSITY
Defence College of Management and Technology

CRANFIELD UNIVERSITY

COLIN MORISON

THE RESISTANCE OF LAMINATED GLASS TO BLAST PRESSURE LOADING AND THE COEFFICIENTS FOR SINGLE DEGREE OF FREEDOM ANALYSIS OF LAMINATED GLASS.

DEFENCE COLLEGE OF MANAGEMENT AND TECHNOLOGY

PhD THESIS

CRANFIELD UNIVERSITY

DEFENCE COLLEGE OF MANAGEMENT AND TECHNOLOGY

ENGINEERING SYSTEMS DEPARTMENT

PhD THESIS

Academic Year 2006-2007

Colin Morison

The resistance of laminated glass to blast pressure loading and the coefficients for single degree of freedom analysis of laminated glass.

Supervisor: Dr P D Smith

May 2007

© Cranfield University 2007. All rights reserved. No part of this publication may be reproduced without the written permission of the copyright owner

Abstract

For terrorist explosions or accidental explosions in urban areas, the greatest threat of death and serious injury comes from the effects of glass fragments.

Laminated glazing has been proven by trials and experience of actual events to eliminate the risk of significant fragment injury to people behind the glazing, and also to provide substantial protection from blast injury effects, provided that after cracking it remains as a continuous membrane substantially attached to the supporting frame. However, design of laminated glazing is currently based on extrapolation from testing, with limited understanding of the material behaviour that underlies the behaviour under blast loading.

This thesis presents an investigation into the application of a simplified method of dynamic analysis for laminated glass, the development of parameters derived from the properties of the materials in laminated glass and the behaviour of laminated glass systems that can be applied to the design of laminated glazing to resist blast loading.

The development of the single degree of freedom method for analysis of dynamic response is reviewed from its inception use for analysis of glazing, through its adaptation for reinforced concrete analysis, to its modern use for analysis of glazing. Although the principles of the method are widely applicable, some procedures established for elastic-plastic reinforced concrete analysis in the 1950s are not appropriate for glazing, and should be treated with care. Coefficients for analysis of reinforced concrete date from approximate analyses in the 1950s and 60s and are not accurate. New calculations using advanced yield line models and finite element analysis have been used to provide alternative coefficients for rectangular panels supported on four edges.

The elastic analyses for reinforced concrete are linear because they are based on small-deflection theory. Deflections of most uncracked glass panes exceed the limits of this theory. The development of practical non-linear large-deflection analyses in the 1980s was dependent on numerical methods and computer analysis, but they have previously only been applied to resistance and cracking. New non-linear finite element analyses refine the existing resistance data, and data from the same calculations has been used to derive large deflection single degree of freedom parameters for dynamic analysis and to assess the reaction distribution.

The cracking of glass arises from small flaws in its surface, and can be very variable in its onset. In addition, the strength is sensitive to the loading rate. Statistical approaches have been based on quasi-static tests, either assuming a normal distribution, or using a more complex Weibull distribution. However, statistical refinement gains little, as strengths then need to be increased for the faster loading under blast. Back-analysis of extensive blast tests had been used to establish deterministic lower bound design cracking strengths for different types of glass. These have been applied in this thesis for design, and back-analysis of blast trials indicates that the design cracking strengths are lower bound.

Formulae for a monolithic pane with equivalent behaviour to a laminated glass pane are proposed that would allow the large deflection analysis to be applied to laminated

glass up to cracking of the final ply. The results of some blast trials of uncracked laminated glass are reported which are consistent with an equivalent monolithic analysis. They indicate that laminated glass under blast can be taken as fully composite to temperatures approaching 20ºC, but that it is not fully composite at 29ºC or above. Unfortunately, there is currently no data to indicate the performance in the critical temperature range between.

After laminated glass cracks, the resistance is provided by an interlayer of the viscoelastic polymer, Polyvinyl Butyral. Though research is ongoing, non-linear viscoelastic material models for finite element analyses have not yet been developed to the point that they can reproduce the full range of behaviour observed in the tensile tests over the range of temperatures and elongation rates which are reported in the thesis. Instead, the results of the tensile tests are fitted to a simple bilinear material model by back-analysis of the tensile tests to give three stiffness and strength parameters that vary with temperature and strain rate.

Non-linear finite element analyses of PVB membranes corresponding to two series of laminated glass blast trials are used to produce single degree of freedom parameters for membrane response. The blast trials are reported, and back-analysis of the deflection histories is used to estimate the ratio of the PVB material strain rates and the observed laminated glass strain rates for the best-fit calculated response. This ratio, found to have a mean value of 3.8, is expected to reflect the stiffening of PVB by attached glass fragments, together with other factors. However, the scatter in the data is large, so the reliability of this figure should be viewed with this in mind.

Laminated glass providing blast protection is normally maintained close to room temperature, so a design based on a room temperature of 23ºC is proposed, using single degree of freedom data that is a composite of the uncracked data up to cracking and the membrane data after that point. For normal laminated glazing where the observed strain rate is expected to be about 10 /s, design membrane properties based on a PVB strain rate of 40 /s are proposed, but this may need to be modified for other cases.

Typical design cases for marginal behaviour are analysed on this basis, and also for material properties at temperatures 6ºC higher and lower than 23ºC, to assess the sensitivity of the design to likely temperature variations. These indicate that a margin of 16-21% may be needed on deflection limits to allow for temperature increases, but that the calculated deflections would still be below the maximum deflections observed in the trials without PVB failure. The analyses indicate that the peak reactions are unlikely to be sensitive to temperature. However, they indicate that a margin of safety of 2.4 will need to be incorporated in the design anchorage strength to resist in-plane tension in the PVB membrane at reduced temperature.

The thesis develops an improved design method under blast loading for laminated glass and double glazing incorporating laminated glass, although some of the values used in the method should be considered tentative. The thesis also indicates a level of anchorage strength sensitivity to temperature reductions that needs to be taken into account in practical glazing designs.

Acknowledgements

My hearfelt thanks go to Dr Peter Smith, my academic supervisor for this research and the writing of this thesis, for his unstinting support throughout the six year gestation period, and for his assistance in so many different ways – Thank you Peter.

My sincere thanks also go to Dr Michael Iremonger and Dr Tim Rose, the other members of my thesis committee for their regular help and guidance.

I cannot acknowledge too highly the contribution to this research made by Permasteelisa, and particularly by Marc Zobec, their chief engineer and research and development director, who has funded commercial research into laminated glass curtain-walling, involved me in that research and given me permission to use the results of that research in this thesis. This thesis would be a poorer (and thinner) document without my access to that research.

Others at Permasteelisa who have actively helped with the research include Luca de Bertoli and Alberto Franceschet.

I would like to acknowledge the role of the Home Office Scientific Development Branch and its predecessors in forwarding the research into blast resistance of glazing in the UK, and disseminating their results to those active in the counter-terrorist design field. They, more than anyone, have provided the state of the art on which I have been trying to improve by this research. I would particularly wish to thank Nick Johnson for his guidance and advice over the years, and Kevin Claber and Bob Sheldon for providing data from their tests.

I would like to acknowledge my managers at TPS over this period, Steve Harvey and Chris Bowes, who allowed me to use valuable software and the extensive library of explosives-related documents for my own purposes, and my colleagues in the Explosion Effects division, Darius Aibara, David Brettell, Malcolm Connell, Carson Holmes, Ken Holt and Paul Jackson for their tolerance of 'brain picking', book borrowing and ideas being bounced off them.

Particular individuals that I would like to thank for material assistance or information include:

Kevin Webster of Romag Ltd, who donated the PVB tested at Shrivenham.

Malcolm Connell who introduced me to the wealth of World War II research on the effects of blast on glazing.

Dr Tim Rose, who provided one paper that opened up to me the field of viscoelasticity in PVB.

Mike Crossley, who provided the key words 'Griffith flaws' that gave me the connection between glazing and fracture mechanics, and who provided a number of useful references from his library on glazing.

John Williams of HSBC, who provided additional information and photographs of the HSBC building in Istanbul.

I would like to thank the scientists, engineers, technicians and support staff that run the test facilities and specialist test equipment, and without whom there would be no test data. Specifically:

Paul Cronin, Ian Graham, and the Advantica staff and contractors at Spadeadam for the arena trials,

Mike Lowak, JR Montoya, and their team at BakerRisk for the Shock tube trials,

Celia Watson and Prof Ian Horsfall for the Shrivenham PVB tensile tests,

Hugh McGillivary for the PVB tensile tests at Imperial College, London.

Last, but not least, I would like to thank the librarians that have helped me to find how to find references in their systems and on their shelves, and have found them for me when my limited skills proved inadequate. In particular I would like to thank those at:

Cranfield University, Defence College of Management and Technology, Shrivenham,

The Institution of Civil Engineers, Westmister,

The British Library, St Pancras,

The National Archive, Kew.

Contents

List of Tables

List of Figures

Notation

a	span of panel in direction x (generally long span)
a_T	time shift parameter in generalised Maxwell series
A	initial amplitude of blast loading
AS	axial stiffness
b	span of panel in direction y (generally short span)
B	risk function in Weibull distribution
c	damping coefficient per unit area
c_A	damping at standard atmospheric conditions
$c_P(t)$	damping history for pressure history
$c(x,y)$	Weibull biaxial stress correction factor
C, $C(t)$	total damping coefficient
C_r	pressure reflection coefficient
C_e	equivalent lumped damping coefficient
d	non-dimensional glass plate deflection
$d`$	non-dimensional membrane deflection
D	stiffness coefficient = $EI/(1-\nu^2)$
D_C	depth of cavity
E	Young's modulus
E_e	equivalent Young's modulus
E_g	Young's modulus for glass
E_p	Young's modulus for PVB
f	loading
$f(t)$	dynamic loading history
$f_e(t)$	equivalent lumped dynamic loading history
$f_x(x)$	function defining deflected shape of span
F	loading
F_1-F_5	equivalence thickness factors 1-5
$F(t)$	equivalent static loading
FS	flexural stiffness
$G(t)$	viscoelastic shear relaxation modulus
G_i	shear modulus of ith Maxwell component
G_0	instantaneous shear modulus
G_∞	long term shear stiffness
h	thickness
h_1, h_2	strain hardening parameters
h_e	equivalent thickness
h_g	glass thickness
h_t	total thickness
H	height, hardening modulus
i_c	corner support fixity
i_l	long side support fixity
i_s	specific side-on impulse, short side support fixity
I	second moment of area
I_r	reflected impulse of blast load
J_1, J_2	material constants for temperature time shift of generalised Maxwell series
k	stiffness, Weibull surface strength parameter
ke	elastic stiffness

K bulk modulus, material consistency
K_L load transformation factor
$K_L(z)$ load transformation factor function with deflection
K_{LM} load-mass transformation factor = K_M / K_L
K_M mass transformation factor
$K_M(z)$ mass transformation function with deflection
K_R resistance transformation factor
L length of span
L_{ND} non-dimensional load
m distributed mass, orthotropic bending moment capacity, term number in Fourier series, Weibull surface strength parameter, strain hardening coefficient
m_F bending moment capacity at fixed support
m_{FA} long span bending moment capacity at fixed support
m_{FB} short span bending moment capacity at fixed support
m_{SA} long span bending moment capacity in span
m_{SB} short span bending moment capacity in span
M mass
M_e equivalent mass
n term number in Fourier series
p pressure
p_0 atmospheric pressure
p_{max} maximum overpressure
p_r peak reflected overpressure
p_s peak side-on overpressure
Δp_{min} peak underpressure
P_{ND} non-dimensional pressure
P_{ND}` non-dimensional pressure on membranes
$\overline{P}$ total pressure
$P(t)$ blast pressure history
P_A atmospheric pressure
$P_e(t)$ equivalent loading history
P_f Weibull cumulative probability of failure
P_p equivalent static pressure
P_s equivalent static suction
q resistance, laminated stress distribution parameter
q_e yield resistance
r yield line fan radius
R range from charge centre, Resistance
$R(z)$ resistance function with deflection
Re elastic resistance limit
$R_e(z)$ equivalent lumped resistance function with deflection
Ru plastic resistance
S membrane tension force
S_{ND} non-dimensional in-planemembrane tension
t, t` time
t_0 duration of total blast wave (positive and negative phases)
t_e time to elastic deflection limit z_e
t_{max} time of maximum deflection
t_r triangular duration of reflected blast impulse

t_s arrival time of blast wave front
T temperature
T_0 reference temperature
T_n natural period
T_s positive phase duration
U pressure wave velocity (sound speed)
V_{FL} loading reaction coefficient for long span
V_{FS} loading reaction coefficient for short span
V_L maximum total reaction on long side
V_{LD} maximum mean distributed reaction on long side
V_{LP} maximum peak reaction on long side
$V_L(t)$ total reaction history of long side
V_{RL} resistance reaction coefficient for long span
V_{RS} resistance reaction coefficient for short span
V_S maximum total reaction on short side
V_{SD} maximum mean distributed reaction on short side
V_{SP} maximum peak reaction on short side
$V_S(t)$ total reaction history of short side
w transverse deflection, viscoelastic parameter, distributed load on beams
w_n weighting factor on node n
W mass of spherical TNT charge
W_C cubic resistance coefficient from WINGARD
x position on span or panel
X control location on span
X_e elastic deflection limit
X_{ep} elastoplastic deflection limit
y position on panel
z deflection
z_a deflected shape
z_{centre} deflection at central node of panel
z_e elastic deflection limit, equivalent deflection
z_{max} maximum deflection
z_n deflection of node n
Z scaled distance, plastic modulus
α yield line variable
β viscoelastic time constant, yield line variable, thermal dependency coefficient, ratio of negative to positive loading impulse
γ adiabatic constant (7/5 in air), yield line variable
δ yield line variable
ε strain
$\dot{\varepsilon}$ strain rate
$\dot{\varepsilon}_{ij}$ viscoelastic deviatoric strain rate
ε_E engineering strain
ε_T true strain
ε_x, ε_y strain in the x and y directions
θ angle
θ_1, θ_2 yield line fan angles
η_i damping of ith Maxwell component
λ aspect ratio
λ` aspect ratio of affine orthotropic panel

v	Poisson's ratio, ratio of negative to positive loading phase duration,
ρ	density
ρ_A	atmospheric density
σ	stress
σ_E	engineering stress
σ_f	modulus of rupture
σ_{max}	maximum stress
$\overline{\sigma}_{max}$	maximum positive principal stress
σ_T	true stress
$\sigma(t)$	viscoelastic stress
$\sigma_{ij}(t)$	viscoelastic deviatoric stress component
$\sigma_u(t)$	viscoelastic uniaxial tensile stress
σ_{ND}	non-dimensional stress
σ_w	Weibull effective stress
σ_y	yield stress
σ_0	Weibull median failure strength
τ	time
τ_i	time constant of *i*th Maxwell component
χ	position on span
ω	angular frequency

Abbreviations

ACI	American Concrete Institute
A&W	Ammann and Whitney
AR	aspect ratio
ASCE	American Society of Civil Engineers
ASTM	American Society for Testing and Measurement
C of V	coefficient of variance
DLF	dynamic load factor
DR	deflection ratio
FAWG	Forcible Attack Working Group
FE	finite element
FEA	finite element analysis
HOSDB	Home Office Scientific Development Branch
HME	home made explosives
HSBC	Hongkong and Shanghai Banking Corporation
IOD	improvised explosives device
MIT	Massachusetts Institute of Technology
MSc	Master of Science
ND	non-dimensional

NDRC	National Defence Research Committee
PhD	Doctor of Philosophy
PSA	Property Services Agency
PSADS	Protective Structures Automated Design System
PVB	polyvinyl butyral
RC	reinforced concrete
SDOF	single degree of freedom
SFE	Security Facilities Executive
SR	strain rate
TNT	trinitrotoluene
UK	United Kingdom
UPVC	unplasticised polyvinyl chloride
US	United States (of America)
USACE	United States Army Corps of Engineers
USAF	United States Air Force
WDR	work done ratio
2DOF	two degree of freedom

Glossary

Adiabatic. An adiabatic process is one in which no heat is transferred to or from a working fluid. Because blast phenomena occur very quickly there is generally little time for heat transfer, so most blast phenomena can be treated as adiabatic.

Adiabatic constant. In ideal gases under adiabatic conditions the relationship between pressure P and specific volume V is defined as PV^{γ} =constant, where the adiabatic constant γ is defined as the ratio of the specific heats at constant pressure and constant volume. It can also be defined as $(1+\alpha)/\alpha$, where α is the number of degrees of freedom divided by 2 (5/2 for diatomic gases). As air is composed primarily of diatomic gases, γ in air can be taken as 7/5.

Aeroelastic damping. Damping of the motion of a solid through air due to interaction of the surfaces of the solid with the surrounding air generating restoring forces proportional to the velocity of the solid, in a direction to reduce the velocity. The specific damping coefficient at each surface is equal to the impedence (density times soundspeed) of the air in contact with the surface. When a solid moves through still air there is a dynamic pressure created in front and a dynamic suction behind, both opposing the motion. When a solid moves away from a reflecting blast wave, the effect of the motion of the surface is to reduce the reflected blast pressures.

Affinity Theorem. Theorem in yield line analysis where an orthotropic panel is mapped to an isotropic panel (with known solutions) by an affine transformation i.e. one which preserves collinearity and ratios.

Anticlastic surface. A deformed surface shape with principal curvatures of opposite sign, resulting in a negative Gaussian curvature. This often results in a "saddle" shape.

Cauchy Stress. Stress defined at any state of deformation by the current force divided by the current cross-sectional area. Useful for large strains.

Cauchy-Green deformation tensors. Strain tensors that combine with a rotation tensor to define a deformation gradient. They come in right hand and left hand versions depending on the order of multiplication with the rotation tensors. The individual terms are products of the stretches and the stretch eigenvectors. Suitable for the treatment of large strains, deformations and rotations when used with a logarithmic strain definition.

Blast. A shock pressure wave transmitted through a gas, with a characteristic shape due to non-linear gas properties.

Clearing. A phenomenon in blast reflection from a face of finite size, when release waves propagate across the reflection face from the free edges, causing a reduction in the pressure acting at a point on the face once the reflection wave reaches that point. The net effect is a reduced reflected impulse from the blast, with a greater reduction near the edges of the face,

Drucker Prager Yield Model. Pressure sensitive material model for bi-axial and tri-axial yield that takes both normal and shear stresses into account. Frequently used to model plastic yielding of soils and failure of concrete.

Engineer's Strain. Uniaxial strain defined at any stage of elongation by the elongation divided by the original length. This can be easily calculated from tensile tests, but will distort the real material behaviour at large deformation. The three dimensional equivalent is the Kirchoff strain tensor.

Engineer's Stress. Uniaxial stress defined at any stage of elongation by the force divided by the original area. This can be easily calculated from tensile tests, but will distort the real material behaviour at large deformation. The three dimensional equivalent is the first Piola-Kirchoff stress tensor.

Friedlander curve. A mathematical representation of an idealised blast wave pressure-time history.

Glass. A transparent fused solid of oxides with a non-crystalline matrix. Most window glass is soda lime silicate glass. Strong in compression, but brittle and relatively weak in tension due to the presence of Griffith flaws in the surface.

Generalised Maxwell series. A model of viscoelastic material behaviour comprising a parallel set of Maxwell components with different time constants. A Maxwell component comprises a spring & a dashpot in series.

Green's strain. Tensile strain based on a differential formulation. In three dimensions this becomes the Green-Lagrange strain tensor. Suitable for evaluation of large deflections, but only small strains.

Griffith flaws. Sub-microscopic but very sharp flaws in the surface of glass, hypothesised by A A Griffith as the cause of the low and variable tensile strength of glass. They have been observed only indirectly, but can explain much glass strength behaviour on the basis of the thermodynamics of fracture mechanics.

High Hazard. Fragment hazard classification for fragments likely to cause severe and potentially fatal injuries. Based on a classification system developed in the UK and adopted internationally with minor variations.

Hourglassing. An effect in continuum finite element analyses in which a zero-energy deformation is incorporated in the solution, producing an oscillation in the stresses between lines of nodes, and a distortion that results in pairs of rectangular elements forming an 'hourglass' distorted shape in some types of analysis.

Jaumann formulation. Material constituitive model based on the Jaumann derivative of the stress tensor, a time derivative of the components of the tensor as measured with respect to a rigid coordinate system which translates and rotates with the material, in terms of a spin tensor. This is used to separate the time dependent elastic (viscoelastic) terms from the inelastic terms in co-rotational equations of state for non-linear viscoelastic and viscoplastic solids and fluids.

Laminated glass. A layered system of glass plies bonded to one or more plastic interlayers. The most common interlayer material is polyvinyl butyral (PVB).

Mach reflection. Blast phenomenon where the reflected wave from an oblique reflection interacts with the wave incident on the next section of the reflection surface. As this travels along the reflection surface it generates a composite wave perpendicular to the surface (the Mach stem) with a pressure and impulse higher than a normal blast reflection.

Ogden material model. A hyperelastic material law used to model the nonlinear behaviour of rubber materials. Higher order versions with more parameters will be more accurate over larger ranges of extension, but will require substantially more testing to calculate values for the parameters.

Second Piola Kirchoff stress tensor. Three dimensional stress definition that relates forces in the reference configuration to areas in the reference configuration. It has limited physical meaning, but is suitable for evaluation of large deformations, being independent of material orientation. It is energy conjugate with Green's strain.

Rayleigh method. A method for calculating deflections of a continuous member or system, by assuming a deflected shape, and calculating the deflection necessary to equate the work done by the loading with the internal strain energy.

Semiloof shell finite element. A thin, doubly curved (quadratic) shell element. The displacements and rotations are considered independent, with three displacement degrees of freedom at eight corner and mid-side nodes, and a single rotation degree of freedom, perpendicular to the edge only, at eight 'loof nodes', two on each edge of the element.

Shear-locking. A phenomenon of simple linear 2D or 3D elements which cannot accurately model curvature within the element, leading to exaggerated stiffness in coarse meshes. Can be eliminated by the use of enhanced strain formulations in some types of linear element to improve modelling of curvature or by the use of quadratic elements with mid-side nodes, or can be mitigated by the use of finer meshes.

Single Degree-of-Freedom Analysis. Simplified dynamic analysis in which the equation of motion is reduced to one displacement variable and its derivatives with respect to time.

Shocking-up. A phenomenon in blast reflection where multiple reflected blast waves at a re-entrant corner interact with each other to produce an increased peak pressure and impulse against the reflecting surfaces in the immediate vicinity of the corner.

Static fatigue. A reduction in cracking strength of glass over time, under sustained or increasing static loading.

Stress corrosion. In glass, the mechanism by which atmospheric water vapour weakens the chemical bonds at the tip of the Griffith flaws, reducing crack toughness over time, and resulting in the observed phenomenon of static fatigue.

Tensor. Mathematical description of amplitude and direction(s) in a matrix form. The order of the tensor indicates the number of directions described. Stress and strain tensors are tensors of order 2, with three dimensional stresses or strains expressed as a 3 x 3 matrix with direct stress or strain components on the leading diagonal and shear stress or strain components off the diagonal.

Thick shell finite element. Linear (four-node) or quadratic (eight-node) shell element with three translation degrees of freedom and two or three rotational degrees of freedom at each node. The formulation includes shear stiffness and the output includes transverse shear forces.

True strain. Uniaxial strain defined at any stage of elongation by the elongation divided by the current length. One three dimensional equivalent is logarithmic strain.

True stress. Uniaxial stress defined at any stage of elongation by the current force divided by the current area. The three dimensional equivalent is the Cauchy stress tensor.

von-Mises Yield Model. Material model to relate bi-axial and tri-axial yield behaviour to a uniaxial yield stress which is similar for tension and compression, based on a constant distortion energy at yield. Frequently used to model yielding of metals.

1 Introduction

1.1 Explosions and glazing

Outsides the hazards of wartime, explosions in built-up areas can occur because of accidents, or deliberately, as a result of terrorist action.

Large quantities of hazardous materials that can cause explosions in oil and gas depots, oil refineries, munitions manufacturing and storage facilities and the like, tend to be located in dedicated facilities. These are usually separated from ordinary buildings by safety zones to prevent a significant blast hazard reaching occupied buildings.

Smaller quantities of hazardous materials can give rise to an accidental explosion hazard throughout built-up areas. Where the hazardous materials cannot be eliminated, this hazard is best controlled by reducing the risk of an explosion occurring.

Of growing significance over the last thirty years, however, has been the threat of terrorist explosions.

Some specific buildings such as embassies, government offices and army barracks have been favoured targets because of their function and occupants. However, a major terrorist aim has been disruption of society, and this has led to targeting of transportation in the form of stations, airports and bridges, and the targeting of commercial and retail centres.

With the advent of fanatical bombers, there is a trend to deliberately target large numbers of vulnerable civilians, wherever they may be assembled. This has resulted in attacks on crowded trains and buses, bars and night-clubs. Theatres and sports stadiums have, allegedly, been considered as targets and must also be considered at risk.

Although some attacks may involve suicide bombers carrying explosives into buildings, the larger attacks involve the detonation of a larger charge in a vehicle, usually located outside a target building. The hazards of bomb attack will not just apply to potential target buildings or structures, but to all the buildings in the vicinity of such an attack.

For military anti-personnel munitions and for some small terrorist devices such as pipe bombs and nail bombs, the high velocity fragments from the explosive device (primary fragments) may be a greater hazard than the blast. For accidental explosions and terrorist vehicle bombs the dominant hazard results from the blast wave caused by the explosion.

In built-up areas, the main consequence of a blast wave is the breaking of windows and the creation of large quantities of hazardous secondary fragments of glass. Although they will have relatively low velocities compared to primary fragments, they are created throughout the zone around the explosion, wherever windows are broken, and so may completely permeate the blast-affected area. A lorry bomb may break windows up to 400 m away, and so may affect a zone of approximately half a square kilometre.

At particular risk are occupants of rooms facing the explosion, where sharp glass fragments can be blown across the room. However, closer to the explosion, windows facing in other directions may also be blown in, while glass debris falling from buildings will also be a hazard to passers-by in the street.

The other effects of blast are to injure or kill by damaging lungs, bursting eardrums and by knocking people over. These effects have a high probability of injuring people (who will also be vulnerable to glass fragments) in a small area close to the explosion. However, the maximum range of these effects is much shorter than for window breakage, and so the areas of vulnerable are only a few percent of the overall affected zone.

Similarly, damage to other façade materials and structural collapse that could threaten health and safety will generally only occur at shorter ranges.

The highest risk of death and injury from an explosion in a built-up area comes from flying glass fragments from ordinary windows. The introduction of enhanced glazing in building facades to reduce the risk of people being struck by hazardous glass fragments can substantially reduce the consequences of terrorist or accidental explosions.

1.2 The role of laminated glass in blast resistant glazing

Laminated glass, in which two or more plies of glass are bonded to ductile plastic interlayers, was first developed for the motor industry to reduce accident injuries from windscreens. Architectural laminated glass was adopted as a safety glass [1] in building glazing as it offers reduced hazards from human impact and protection of an opening even after the glass is cracked. A variety of materials have been used for the interlayer, of which polyvinyl butyral (PVB) is the most common.

PVB sheet is manufactured in 0.015″ (0.38mm) thickness, and is laminated by compression and heating between the glass plies in an autoclave. Normally, the interlayer may be formed of up to four layers (1.52mm) of PVB sheet, although greater thicknesses have been used for special applications.

Early research into the consequences of glass breakage [2] showed that a ductile film bonded to a glass pane would substantially reduce flying fragments of glass, even though it did not prevent or delay cracking. Laminated glass provides a bonded film in the PVB interlayer that does not affect the visual properties of the glazing and is protected from damage or degradation by the glass. This provides a bonded film that will last the life of the glazing, unlike externally applied films.

Blast testing of various laminated glass configurations [3] showed that thinner PVB membranes of single (0.38mm thick) or double sheets of PVB tend to fail prematurely by cutting at the supports once the glass has cracked. However, laminates with triple or quadruple thick PVB interlayers, adequately anchored at the supports, were shown to have a substantially enhanced resistance to blast loading due to the stretching of the PVB interlayer as an anchored membrane following the cracking of the glass.

This was illustrated in the effect of the Bishopsgate lorry bomb on 24 April 1993 on three adjacent properties about 70m from the detonation. In the first property the glazing was of annealed glass. This shattered, as shown in Fig. 1, and jagged fragments were thrown to the back of the rooms, while blast entry caused further damage to room contents and false ceilings. If the attack had not occurred on a Saturday there could have been serious injuries or even fatalities inside the building.

Figure 1. Damage to annealed glass windows in Bishopsgate

Adhesive anti-shatter film had been applied to the inner face of the glazing in the second property. This broke away from the supports once the glass cracked, but most fragments remained attached to the film, and the inwards velocity was sufficiently low that some were caught by the Venetian blinds, as seen in Fig. 2, and the rest flopped inwards a short distance only.

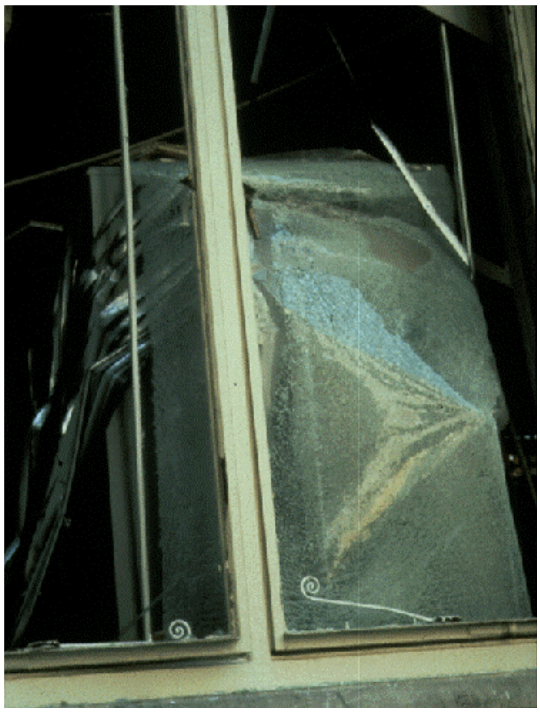

Figure 2. Damage to annealed glass window with anti-shatter film in Bishopsgate

The windows in the third property had been replaced by new glazing with laminated glass anchored in aluminium frames. The glass cracked but remained in place, with the perimeter of the glazing anchored to the frame and the rest retained by the PVB membrane, as seen in Fig. 3. This would have completely protected the interior and occupants, and even remained weathertight, if the infill panel above the main window had been built to the same standard, rather than being annealed glass.

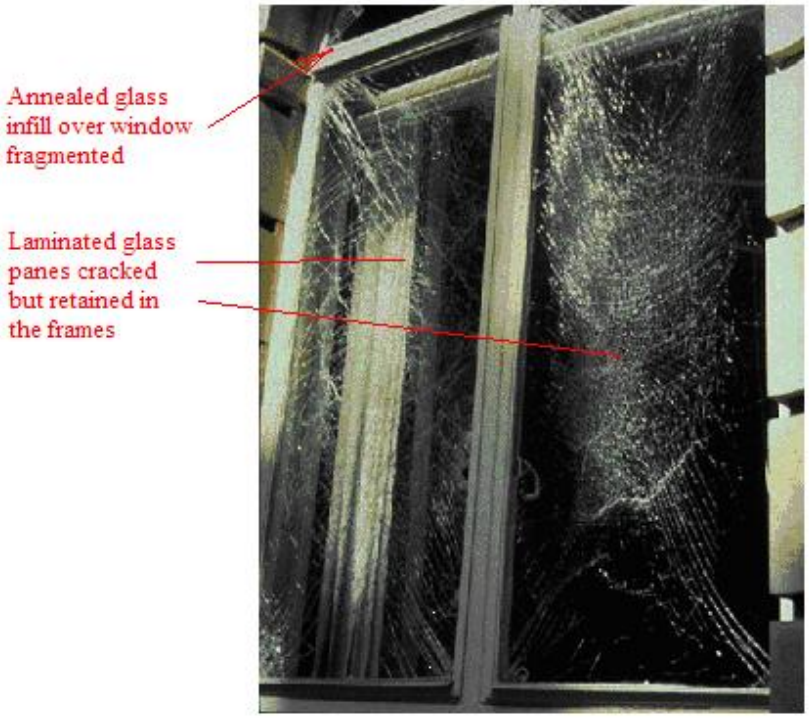

Figure 3. Damage to laminated glass window in Bishopsgate

Even when loaded beyond failure of the membrane or support, well-designed PVB laminated glass glazing in robust frames tends to leave most of the glass debris bonded to the PVB and often anchored to one or more supports rather than flying freely. Hence it gives rise to a lower hazard to people behind the glazing in the event of an explosion than for other types of glazing. When loaded within the capacity of the anchored membrane, the risk to people behind the glazing of fatality or severe injury is very low.

This was illustrated in the attack on the 15 storey HSBC bank building in Istanbul on 20 November 2003. Fig. 4 shows the aftermath, with many laminated glass panes in the lower part of the building blown in after failure of the support, and spandrel cladding panels remaining attached or rebounding. However, even with this destruction of the façade, the glazing resisted sufficiently long to provide substantial protection; there were only three occupants of the office building killed, one seriously injured and 43 others injured [4,5]. The fatalities occurred in the ground floor entrance lobby, most exposed to the blast. The great majority of the fatalities from the attack occurred in the adjacent shopping centre and the street.

Figure 4. HSBC bank Istanbul, after the 2003 bomb blast

Testing [3] provided guidance on the capacity of glazing panels of several sizes and types trialled over a range of blast threats. However, this did not provide a practical method of applying this data to the full range of panel sizes, shapes and make-ups that are possible for glazing, and provided little reliable information on the reactions acting on the frames, connections and supports. Although laminated glazing, or double glazing with an inner leaf of laminated glass, was shown to be the most practical and economic way of providing blast protection to conventional buildings, expensive blast testing of prototypes is still the only practical means of demonstrating the suitability of particular designs.

In his MSc dissertation, the Author [6] presented a method for single degree of freedom (SDOF) analysis of rectangular panes of laminated glass, and its incorporation into multi degree of freedom analyses of glazing systems. This allowed any size and proportion of rectangular panel to be analysed, and was checked by analysis of blast tested panels.

This SDOF method primarily used already existing analytical or numerical solutions for various stages of deformation of laminated glass to define a resistance function, and to calculate SDOF parameters. However, there were gaps in the information: no reliable stiffness or SDOF coefficients for elastic membranes were available; some analytical solutions were used beyond their proven range; high rate-of-strain PVB material properties were extrapolated from low rate-of-strain tests.

In addition, some of the long-standing coefficients for SDOF analysis given in many military manuals and text books for simply supported elastic spans, presently used for all types of panel, including glazing, were found to be inaccurate. These were found to be derived from only two analyses. This led to more general concern about the reliability of all of the SDOF data from the same sources. More broadly, it demonstrated the risk in relying on adapting standard solutions beyond their original context, and in relying on "received wisdom" without periodic review.

It was perceived that a fundamental re-assessment of the SDOF analysis approach for glazing response would be timely.

1.3 The aim of this research

The aim of this research is to develop a better method of analysis of laminated glass under blast loading which can be used to reproduce the response of actual glazing panels in blast trials. With suitable design values for material properties, this method can be used to design glazing with appropriate levels of conservatism.

1.4 The objectives of this research

The principal objective of the research undertaken for this thesis was to derive formulae and values to define the lateral resistance at high rates of strain of rectangular panels of PVB laminated glass with various aspect ratios up to at least four. This was expected to be calculated piecewise by combining the effects from various different phases of the deformation of laminated glass.

Associated with this was a second objective: the derivation of equivalent SDOF coefficients for mass, loading and damping, and reaction and reaction distribution coefficients for the supports of the rectangular glazing panes. These were expected to vary with the phases and with the non-linear response within phases.

It was intended that the resistance and SDOF coefficients so developed should be appropriate for the calculation of SDOF and multi-degree of freedom response of laminated glazing systems under blast loading.

1.5 Methodology and scope

The deformation of laminated glass is expected to cover various phases:

- Linear bending for small deflection
- Non-linear bending to first crack
- Non-linear bending to second crack
- Elastic stretching of the interlayer
- 'Plastic' stretching of the interlayer
- Recovery from 'plastic' stretching of the interlayer.

A range of finite element analyses have been undertaken using models that can represent rectangular panels in the various phases (with the exception of the recovery phase, which will be represented by an analytical model). The SDOF resistance function for each phase has been calculated from the plot of the loading applied to each model against the deflection of the point representing the centre of the panel at successive increments of loading. A resistance curve for laminated glass can then be plotted as a piecewise combination of the models between transition deflections which are calculated from a plot of the maximum stresses in the models against the central deflections.

The various equivalent SDOF coefficients for each phase are calculated from the deflection fields and stress fields at each increment of the analysis, and plotted as a curve. These can be combined into curves of these coefficients for laminated glass by combining the analysis curves piecewise between the same transition deflections.

The glass material properties for design have been based on current UK practice, and are considered to be appropriate lower bound design properties at high strain rates. The cracking strength of glass is variable and, in back analysis of trials, an attempt has been made to identify the cracking strength of individual trial panels from measured deflection histories.

Small deflection analyses give elastic, elasto-plastic and plastic bending phases for reinforced concrete, which have been compared with existing methodology. A variant of the elastic analysis with appropriate material properties applies to small deflection of glass panes. A non-linear elastic large deflection flexural analysis of glass plates has then been used to represent the non-linear bending behaviour of laminated glass to first and second crack transition events. Some blast trials are used to illustrate the sensitivity of the composite behaviour of uncracked laminated glass to temperature.

High rate of strain tensile testing of PVB specimens has been undertaken to establish material properties for the elastic and 'plastic' phases of interlayer stretching. These have then been combined into a single membrane model, which includes the gradual transition from elastic to 'plastic' membrane behaviour. The use of a 'plastic' phase is a simplification of the nonlinear viscoelastic behaviour of PVB, and the sensitivity of the material parameters to temperature and strain rate needs to be taken into account. Back analysis of a number of blast trials has been used to quantify the difference between membranes of bare PVB and cracked laminated glass.

2 Review of literature – Blast and the effects on structures

The seeds were sown for the analysis of blast effects on structures in the nineteenth century, with the development of the gas equations and the Rankine-Hugoniot equations [7]. However, the study of the effect of blast on structures has been closely associated with aerial bombing.

The most long-established approach to blast quantification developed in the First World War was Hopkinson's cube-root scaling law [8]. It seems significant that this was first documented in a proposal for modelling the effect of aerial bombs on structures.

In the Second World War, bombing of both industrial capacity and civilian populations involved extensive attacks on built-up areas using general-purpose high explosives bombs. In addition, precision attacks on hardened facilities such as U-boat pens took place. These both encouraged research into blast and offered many opportunities to study blast damage to conventional and hardened buildings.

Systematic study of blast and other weapons effects were undertaken immediately prior to and through the Second World War by the Research and Experimental Department of the UK Ministry of Home Security, with assistance from the Building Research Station and the Road Research Laboratory. These studies included theoretical analysis, experimental work and systematic reviews of damage from bombs initially in the UK, and subsequently in Western Europe.

The work of this extensive research programme was generally classified at the time, and not released for thirty years. Several papers related to work of the Research & Experimental Department were published by the Institution of Civil Engineers in 1948. However, they were related to the review of bomb damage of existing structures rather than to blast analysis, and only one paper by Thomas [9] makes even passing reference to glass damage. The full range of work was not publicly documented until Walley [10] in 1994 highlighted the documents available at that time in the Public Records Office (now the National Archive).

The main conclusions about blast analysis drawn at the time were described in Christopherson's 1945 paper "Structural Defence" [11]. Although book length and unclassified, this remains a typewritten document with manuscript equations, and was given only limited circulation. Christopherson's declared intent was to make available to engineers information on the structural effect of air attack and the means of improving resistance to bombing. In practice, it appears to have been very influential with researchers and specialists in military engineering, but not to have been more widely known. The paper was not a guide for structural design, but did present some methods of analysis that are reviewed in more detail in Chapter 3 of this thesis, and practical considerations for structures and glazing.

Some structural design guides were developed in the UK from this research data, most notably by the Ministry of Works [12], but they were "recipe" type guides, giving

specific solutions for specific aerial bomb threats based on analysis of damage, rather than developing more general methods of analysis. The design guides were classified documents developed for internal use by a UK Government department and were closely held. The most public outcomes of the UK wartime and post-war research were the explosives quantity-distances developed for safety reasons by the Explosives Safety and Transportation Committee [13], which were applied to civilian storage of explosives as well as to the military.

The United States also undertook experimental work on weapon effects in the Second World War, coordinated by the National Defence Research Committee (NDRC), but involving the National Academy of Sciences as well as the War and Navy Departments. They cooperated with the UK and shared research data.

After the Second World War, the US Department of the Army published an engineering manual "Fundamentals of Protective Design (Non-nuclear)" in 1946. This was reprinted as TM 5-855-1 in 1965 [14], and was not formally revised until 1986. The purpose of this manual was to provide a guide for engineers in the planning and design of protective structures, and it referred to the US and UK Second World War research as its source of information. The method of analysis of members for response to blast is reviewed in more detail in Section 3.3 of Chapter 3.

In the 1950s and 1960s an attack with atomic weapons was of greatest concern, and much of the blast research and design manuals arising from it were focused on the effect of atomic weapons. In 1957 the US Army Corps of Engineers (USACE) introduced an engineering manual "Design of Structures to Resist the Effects of Atomic Weapons", which included volumes on analysis of a range of structural members for blast loading [15,16]. These are reviewed in Section 3.5 of Chapter 3, with a detailed review of the parameter values in Chapter 5.

In 1969 these manuals were joined by a third, "Structures to Resist the Effects of Accidental Explosions" [17], which included data on analysis of structural members under internal or external blast loading from the detonation of high explosives.

These manuals indicate several significant differences between UK and US practice at the time. The manuals were printed in book form, and were unclassified. The US government permitted distribution not only to allied governments, but to US consultants working for the government and to consultants working for allied governments. The US government also involved academics and consultants in the preparation of the manuals, with Ammann & Whitney credited with development and preparation for References 15-17.

The US Army was not alone in the preparation of manuals. The US Air Force produced its own guides on the effect of nuclear weapons [18] and conventional weapons [19] with involvement from consultants Newmark, Hansen & Associates and Mechanics Research Inc. The US Navy and the Defence Special Weapons Agency also produced manuals. Many of the manuals on design of protective structures were upgraded or replaced one or more times [20-22] before being superseded by a single multi-service electronic manual, the "Protective Structures Automated Design System" [23] in 1998. The USACE manual on accidental explosions was also updated in 1990 [24], and is still current.

A US consultant-led manual on the effect of nuclear weapons was also produced by the American Society of Civil Engineers in 1961 [25], amended in 1964 and revised in 1985 [26].

The sharing of research within a broad defence community including academics and consultants, together with the friendly competition in the production of design manuals, and the cold war pressures that ensured demand and funding, resulted in development of several practical tools for analysis of blast response by hand, and a sifting process to identify the most suitable, which is reviewed in Chapter 3.

3 Review of literature - Analysis of blast response

3.1 Blast loading of structures

3.1.1 Explosives

Blast waves are initiated in a gaseous atmosphere when there is a sudden and substantial local change in pressure. The causes of this pressure change may be physical, e.g. by the bursting of a compressed gas container, nuclear (with a sudden release of energy due to fission or fusion of nuclei), or chemical [27].

A chemical explosion involves the rapid oxidation of fuel elements (primarily carbon and hydrogen atoms) forming part of an explosive compound or mixture, a process generally described as combustion. There are two types of "runaway" chemical reaction that can result in an explosion, distinguished by the speed of combustion.

Where the speed of the combustion reaction through the explosive material exceeds the speed of sound in the material, the process is known as detonation, and a detonation wave front propagates through the explosive material. The spread of the detonation wave front from the initiating stimulus is accompanied by large pressure and temperature gradients. When combustion is complete, the explosive material has been converted to a high pressure and temperature gas in the initial volume. It is the violent expansion of this gas that causes the surrounding air to "shock-up" and form a blast wave which propagates into the surrounding atmosphere. Explosive materials that detonate are known as high explosives.

Where the speed of the combustion reaction through the material is significantly lower than the sound speed the process is known as deflagration, or rapid burning. Deflagration is propagated by the liberated heat of reaction. The pressures can dissipate as the combustion occurs, so peak pressures during deflagation are much lower. Explosives such as gunpowder and gun cotton that tend to deflagrate rather than detonate are commonly used as propellants, as they impose lower forces on the gun and projectile. These materials can still cause a blast wave, but it tends to arise from physical phenomena such as bursting of a container or the release of pressure when a projectile clears a gun barrel. Deflagration is common in mixtures such as gunpowder and in fuel/ air mixtures with vapour or powder fuels such as flour or sawdust, where the oxygen is not so intimately mixed with the fuel.

Detonation and deflagration are not mutually exclusive. The speed of petrochemical vapour explosions can increase and undergo transition from deflagration to detonation if partial confinement causes pressure waves to reflect through the explosive mixture, or if flow at obstructions leads to turbulent mixing. The detonation products from oxygen-poor high explosives like Trinitrotoluene (TNT) burn with oxygen in the surrounding air as they mix in a process known as afterburn. This does not increase the blast, but adds to the gas pressure from confined explosions, which can substantially increase the loading on confining structures.

Most high explosives are condensed (solid or liquid) materials containing the oxygen required for the detonation. Many are compounds containing all the reactive elements

in a single unstable molecule, which decomposes during detonation. Primary high explosives can be initiated by spark, flame or impact. Secondary high explosives are detonated less easily, and often require a shock wave from a primary explosive or other detonator to initiate. Military high explosives tend to be secondary explosives with a long shelf life.

Some chemical mixtures of an oxidiser and a fuel can also be high explosives, particularly in large quantities. These are often used by terrorist organisations with limited access to military explosives because they can be manufactured from readily available materials such as fertiliser and diesel fuel or weed-killer and sugar. These can have a short shelf life, being unstable or susceptible to contamination by atmospheric moisture, can require a strong shock from a booster charge of another high explosive for reliable initiation, and may vary in performance depending on the mixing and preparation.

3.1.2 Blast waves

When a condensed high explosive is detonated in the atmosphere, the explosion reaction generates hot gases at pressures from 10 up to 30 GPa at temperatures around 3000-4000ºC [27]. These gases then expand violently, forcing the surrounding atmosphere away from the expanding volume. As a consequence, a zone of compressed air, the blast wave, forms in front of the gases, containing most of the detonation energy of the explosive.

This compressed zone propagates away from the explosion site at the pressure wave velocity of the most highly compressed air in the wave. Because the pressure wave velocity increases with pressure, the peak of the wave will always be the fastest moving part. The leading edge of the blast wave will be a shock front, rising from the ambient atmospheric pressure instantaneously to the peak. The trailing edge will decay gradually, and will become elongated as the blast wave travels with the velocity of the trailing edge always less than that of the peak. As the blast wave travels, it expands spherically from the source, spreading the energy over a larger blast wave-front surface. The elongation and the increased wave-front area both contribute to a reduction of the peak pressure over time.

The explosive gases expand behind the blast wave, cooling and reducing in pressure. The momentum of the gas molecules results in the gas “over-expanding” and the pressure reducing below the ambient atmospheric for a period, until a reverse flow towards the source allows the pressure to return to ambient. The result of this is a period of under-pressure that forms the ‘negative phase’ of the blast wave. The total gas pressure cannot be less than zero (pure vacuum), so the magnitude of the negative phase pressure can never be numerically greater than the ambient atmospheric pressure. As the blast wave expands the negative phase amplitude grows less intense. As the blast wave progresses to the point where the peak positive pressure has dropped below 1 GPa, the negative pressure is typically of the order 10% of the peak pressure, but the duration is of the order ten times the duration of the positive phase. A typical idealised pressure-time curve of a blast wave approaching this stage is shown in Fig. 5.

The cube root scaling law [7]:

$$Z = R / W^{1/3} \tag{1}$$

allows the parameters of the blast wave caused by a charge of mass W at a particular range R to be related to the blast wave from a unit charge at scaled range Z. In addition, the effects of different types of explosives are related to that of TNT by a TNT equivalence value. This is often based on the ratio of detonation energies [24]. Using these factors, all detonations can be related to a unit charge of TNT.

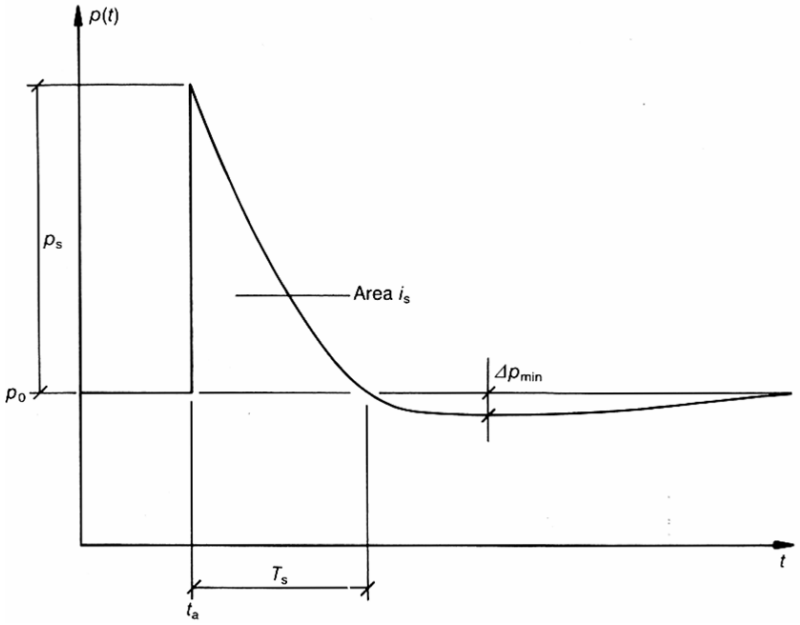

Figure 5. Typical idealised incident blast pressure history [26]

The TNT equivalence of terrorist home-made explosives (HME) is difficult to define because of the variability of its formulation and quality of manufacture, but can vary between about 0.4 for some formulations to over 1.0 for others. In practice, design threats for improvised explosive devices (IED) tend to be quoted in TNT equivalent mass, based on intelligence on the capability of the terrorist group responsible for the material's manufacture, and back-analysis of previous devices from the damage caused.

Various empirical equations for blast parameters with scaled range have been derived from testing. For example, Ref. 27 cites Brode for peak pressure (in bar) as:

$$p_s = \frac{0.975}{Z} + \frac{1.455}{Z^2} + \frac{5.85}{Z^3} - 0.019 \qquad (0.1<p_s<10 \text{ bar}) \tag{2}$$

The equations and charts for positive phase loading parameters in current use in US military manuals [23,24] are mostly taken from the comprehensive analysis of blast trials by Kingery & Bulmash [28]. Numerical blast analysis tends to converge closely to most of these parameters. Charts are also provided in the military manuals giving parameters for the negative phase of loading.

In both blast measurements and numerical analysis of the detonation of condensed explosives, a small second blast wave occurs, as a result of partial reflection at the boundary between the detonation gases and the air as the blast wave passes through the boundary. Initially it appears as a blip on the trailing edge of the main pressure pulse with a peak lower and later than the main peak. This gradually falls behind the main blast pulse, so at moderate ranges it distorts the negative phase pressures, sometimes giving a small excursion into positive pressure. This can significantly complicate analytical modelling of negative phase blast and comparison with test measurements. A typical pressure history calculated numerically is shown in Figure 6, where the second shock wave is clearly shown.

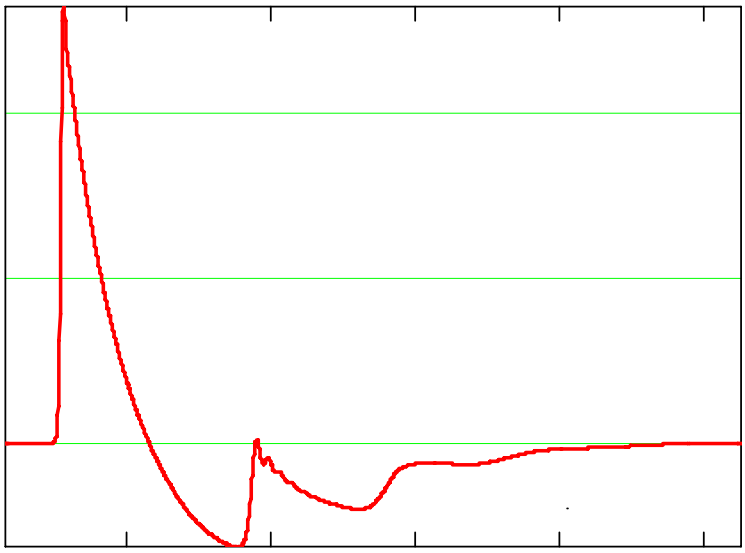

Figure 6. Typical calculated incident pressure history [6]

When the blast wave passes a surface side-on to the direction of travel of the wave, the incident pressure in the blast wave acts to load the surface, so the incident pressure is also known as the side-on pressure.

Reflection of the blast wave from a surface face-on to the direction of travel gives a pressure history amplified over the incident pressure. The pressure reflection coefficient C_r can be calculated from the equations of Rankine and Hugoniot [7]:

$$C_r = \frac{p_r}{p_s} = \left[1 + \frac{p_0 + p_s}{p_0 + \frac{\gamma - 1}{2 \cdot \gamma} p_s} \right] = 2 \left[\frac{7 p_0 + 4 p_s}{7 p_0 + p_s} \right] \qquad (3)$$

where, for air, the adiabatic constant γ is taken as 7/5, and p_0 and p_s are as shown in Fig. 5. For high blast pressures, the peak pressure reflection coefficient can approach a value of four, except at very short range where gas dissociation effects increase the reflected pressure further [26], and approaches 2.0 when the incident pressure is much smaller than atmospheric.

Equation 3 also applies to the pressures after the initial peak. The area under the positive phase of the incident pressure curve is called the positive impulse, shown as i_s

in Figure 5. The reflection coefficient for the positive impulse will be greater than 2.0, but less than the reflection factor for the peak pressure. Similarly, the reflection factor for the negative pressure will be between 2.0 for small amplitudes, down to 1.0 for pure vacuum, with the reflection factor for the negative impulse higher than that for the peak negative pressure.

Detonations close to the ground will also involve reflection of the blast wave from the ground surface. The limiting case is for a hemispherical charge on the ground surface. For perfect reflection from the ground, this would correspond to a spherical charge of twice the charge size. However, some of the blast energy goes into the ground to form a crater and propagate as ground-shock waves, so trial data indicates a blast corresponding to around 180% of an air burst charge is appropriate for design [6].

Equations and charts in current manuals [23,24] cover reflected wave parameters as well as incident, and both ground and air bursts, based on a range of test configurations. Depending on the position of the detonation and the orientation of the building, the loading on a building façade could be represented by any of these cases for simple building and threat geometry.

More complex reflecting geometry can modify the pressure histories from these cases. Blast waves reflecting off oblique facades can interact with the incident wave to produce a combined wave running across the face with an enhanced reflection factor, an effect called Mach reflection. Reflection surfaces of finite size have pressure relief waves that are initiated at the edges and travel across the face, reducing the reflected impulse in an effect known as clearing. Re-entrant corners generate multiple reflections, increasing the reflected impulse on both faces, and the peak reflected pressure close to the corner, a phenomenon known as shocking-up.

Although the military manuals [23,24] contain guidance on some of these effects, such guidance is not always accurate or complete, and does not allow for combinations of these effects. For more complex geometries, numerical analysis of blast phenomena using hydrodynamic software that models blast effects from first principles can give the most reliable pressure histories to use as loading on a façade.

The initial development of methods of analysis of the response of structures to blast loading was closely associated with the early measurement of blast pressure histories, as described below.

3.2 Early analysis methods for response to blast loading

3.2.1 Equivalent static load method

Through the Second World War, UK researchers considered a method of analysing structural response called the equivalent static load method, based upon an elastic single-degree-of-freedom (SDOF) analysis. This was developed by Fox & Harris in 1939 [29,30]. The method was reviewed by Christopherson in 1945 [11] in the light of additional research.

The analytical single degree of freedom deflection z of a lumped mass-spring system at any time t due to a dynamic load $f(t)$, is given by the solution of the equation of motion:

$$\frac{d^2z}{dt^2} \cdot M + k \cdot z = f(t) \tag{4}$$

where M is the mass and k the stiffness. This deflection is equated to that produced by a static force F, such that an equivalent static blast $F(t)$ can be defined:

$$F(t) = \omega \int_0^t f(\tau) \cdot \sin \omega(t-\tau) d\tau \tag{5}$$

where $F(t)$ is the force which, if acting as a static force, would give a deflection to the system equal to the value of the dynamic deflection z at the instant t.

Definition in this form eliminates the mass and stiffness except from the definition of the angular frequency: $\omega = \sqrt{k/M}$, and even then they do not need to be known explicitly if ω for real systems can be measured or calculated by other methods.

The equivalent static blast involves an integral term that incorporates the load history $f(t)$, so an analytical solution requires an analytical formula for the blast pressure history. Fox and Harris looked at three types of loading:

- Positive phases of various shapes in isolation
- Positive phases followed by a similar negative phase
- Positive phases followed by dissimilar negative phases

Analytical formulae were derived for the first two types and for a damped continuous sine wave. Numerical values were calculated from these formulae for combinations of dissimilar positive phase and negative phase loadings. The form selected to represent a blast wave was a triangular positive phase of initial amplitude A, followed by a negative phase in the form of a damped half sine wave, as shown in figure 7. The equivalent static blast at any time could be calculated by summing the values at that time from three analytical curves with offset starting times.

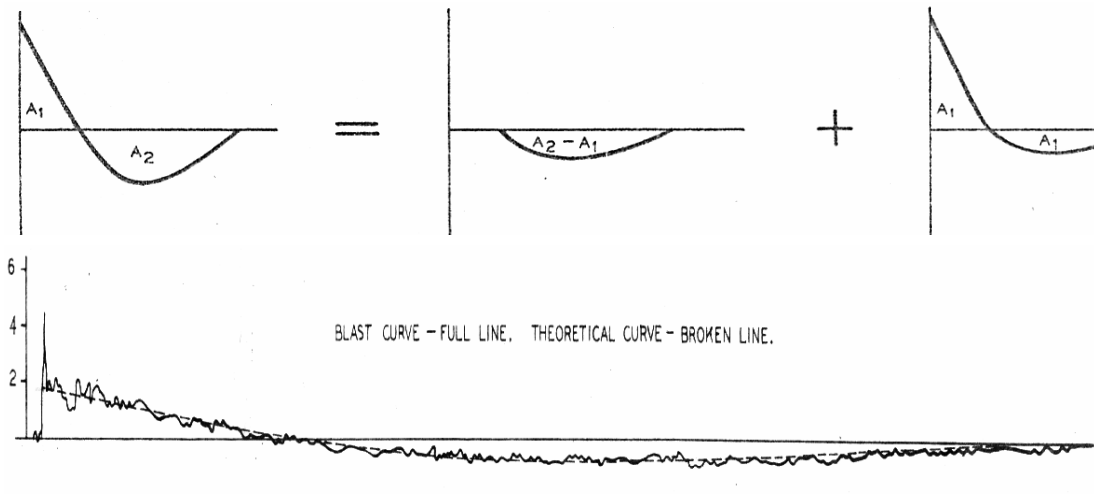

Figure 7. Representation of blast waves and comparison with measurements [29,30]

Non-dimensional charts were prepared of $P_p/\omega A$ and $P_s/\omega A$ against t_0/T_n where equivalent static pressure P_p and equivalent static suction P_s are defined as the peak positive and negative values of the equivalent static blast $F(t)$ calculated in Equation 5, t_0 is the combined duration of the two phases of the blast wave and T_n is the natural period of the system $= 2\pi/\omega$. Curves were plotted for combinations of two ratios: the negative to positive phase durations ν and the negative to positive impulses β. These are shown in Fig. 8.

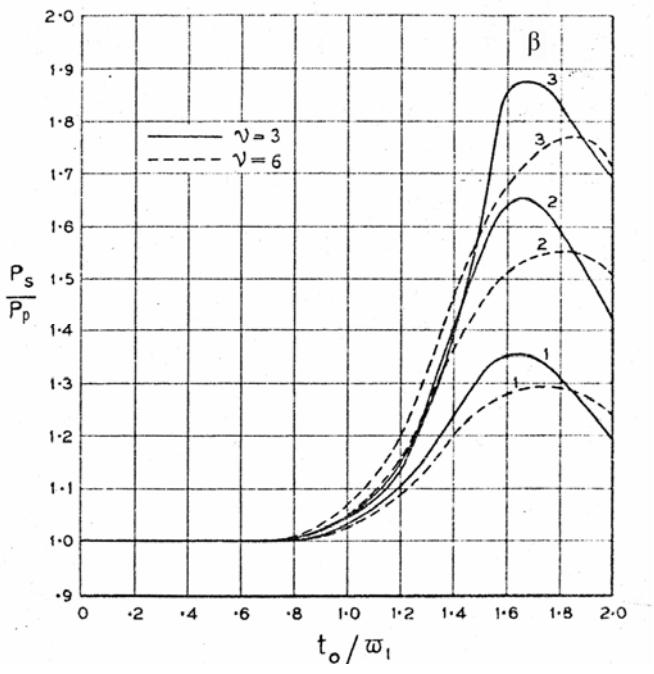

Figure 8. Chart of SDOF peak response for a range of blast parameters [29]

These charts showed that, for blast load durations less than about 0.8 of the natural period, the peak responses are equal, but for blast loads from 0.8 to greater than 2 times the natural period, the value of P_s/P_p was greater than 1 for a wide range of ν

and β. Not charted, but discussed in the paper, for very long duration blast waves or systems with high frequencies the value of P_p could be up to twice the value of the maximum pressure while P_s could be equal to the sum of the maximum pressure and the maximum suction, which would be less, so P_s/P_p would be less than 1.

Fox and Harris [30] used four pressure traces from experimental measurements described in Ref. 29 to derive values of t_0, A, ν and β, and to graph values of P_p and P_s against natural frequency for 500lb bombs at 50ft and 100ft range, as shown in Fig. 9. Measured values of ν ranged from 3 to 6, while measured values of β ranged from 1.2 to 2.5. The damping factor in the negative phase was selected to give a good fit to the shape of the experimental curves. In a 1945 review of blast research [31], Philip states that these were the first blast pressure histories measured in the UK. These curves, and additional curves based on subsequent blast trials, were used in subsequent research [32].

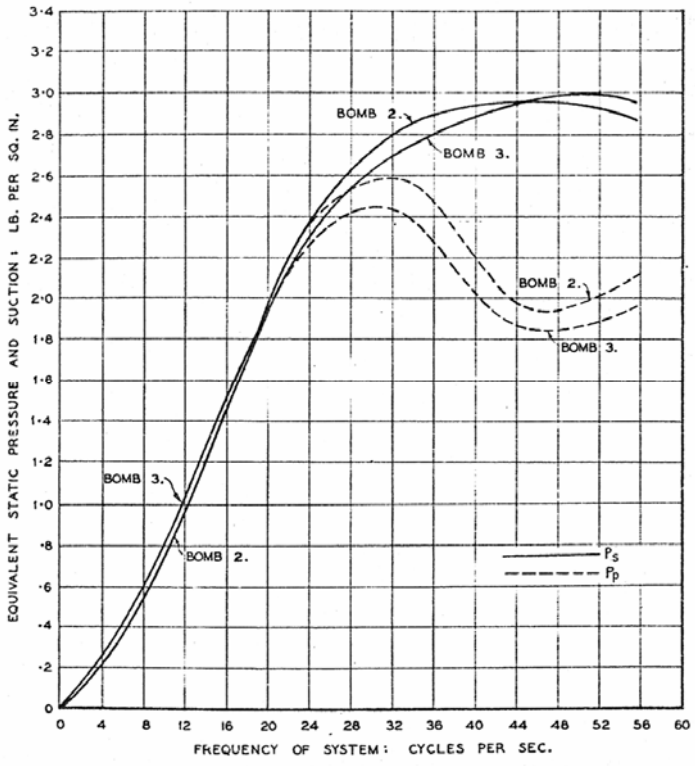

Figure 9. Chart of SDOF peak response for 500 lb bombs [30]

Although the analysis was for a simple lumped mass-spring system, Fox and Harris [30] briefly described some preliminary analysis of beams and plates supported in various manners to have multiple modes of vibration. They concluded that if the fundamental period is of the same order or less than the duration of the blast, then the fundamental wave will predominate when loaded by the blast, and the structure may be treated as a simple system with a frequency equal to the fundamental frequency. Various subsequent research papers covered calculation or measurement of fundamental frequencies, particularly of glass panes.

For systems with the fundamental period much longer than the duration of the blast, other modes may be excited more than the fundamental. A tentative approximation of the effects of the harmonic modes on P_p and P_s was proposed in Ref. 30 making these values proportional to frequency in this range.

In his review of this method in 1945, Christopherson [11] considered a simpler negative phase as an undamped half sine wave, and gave an analytical solution for the equivalent static blast, now referred to as the equivalent static load. However, he conceded that the ordinary method of finding maxima by differentiation gives multiple solutions, and that it would be necessary to use numerical solutions for which "the computations are likely to be lengthy."

Similarly, Christopherson computed the contribution of higher modes of a simple beam as a Fourier series, but conceded that "the equation is clearly intractable in the general case" because it is not sufficient to calculate the peaks for each term and sum them, as the maxima of the different terms do not occur at the same time. He supported the earlier conclusion that if the duration of the blast is not much less than the fundamental period of the beam, it is sufficient to regard the system as having only a single degree of freedom.

For shorter duration loading, Christopherson included a later hypothesis by Fox that the effect of the higher modes will be to prevent the combined equivalent static pressure from reducing below the maximum from the fundamental mode as the duration becomes very short. According to this hypothesis, for total loading duration less than the maximum displacement the probability of damage will be correlated directly with the blast impulse.

Although not explicitly stated by Fox and Harris [30] or Christopherson [11], the way in which the analysis is used is by comparing the maximum of the Equivalent Static Pressure or Suction with the maximum static load capacity determined from the bending stress at failure, to identify whether the elastic member survives or fails.

Christopherson [11] identified a major limitation of this approach in that it is based on elastic theory. He considered that this limited the method to the "relatively trivial problem of the breaking of window panes". For analysis of reinforced concrete, an alternative approach, the 'impulse method' was advocated, as described below.

3.2.2 Impulse method

For the transient load imposed by bombing, a structure may be considered to fail only if it collapses instantaneously or (for some structures) if it is damaged beyond repair. For ductile materials, or quasi-ductile masonry, distortions far beyond the elastic limit can occur without loss of load-bearing capacity. For these plastic materials Christopherson [11] proposed a 'constant yield load' hypothesis, i.e. a rigid-plastic model.

In considering the deflected form of a plastic member subjected to a uniformly distributed blast pressure, Christopherson uses angular acceleration of the different parts of the member to calculate a 'virtual mass' that depends on the deflected shape.

He considered 4 different deflected shapes including ‘yield line’ patterns of two-way spanning slabs and a first mode elastic deflected shape. Because he found that the value for a two-way span is rather variable depending on the deformed shape assumed, he proposed as a general approximation that a virtual mass of 2/3 of the total mass be used, as derived for a uniformly loaded one-way span.

Christopherson used energy calculations to derive a formula for the deflection of this model in the impulsive regime, where the load is of high intensity and short duration, and the result is not sensitive to the shape of the pressure curve.

3.3 Early US methods

3.3.1 Vibration of rectangular plates

A paper by Wise at Princeton University for the NDRC [33] used an elastic method to analyse glass panes, applying Rayleigh's theorem, i.e. the energy method for an assumed deflected shape.

A deformed shape of the fundamental mode was assumed for a particular edge support condition and the equations for the strain energy and kinetic energy were calculated for free vibration in that shape. Both of these equations gave the energy as proportional to the square of the maximum deflection.

An equation for the angular frequency of the fundamental mode of vibration of a rectangular pane ω was calculated by equating the peak strain energy and peak kinetic energy. The natural frequency so calculated was independent of amplitude.

The energy method was then used to define an equation for the work done by a static pressure force, which was proportional to the maximum deflection and the pressure. By equating this with the strain energy equation, an equation was defined for the maximum static deflection under a given pressure, or for the spring stiffness k of the pane.

The tensile and compressive stress were defined in terms of differentials of the deflected shape, and for an identified location, an equation for the maximum stress was developed in terms of static loads if the maximum deflection formula as derived above is substituted.

For this analysis the air blast was approximated by a so called "Friedlander curve", as shown in Figure 10:

$$p(t) = p_s(1-\frac{t}{T_s})\cdot e^{-t/T_s} \qquad (6)$$

where T_s is the duration of the positive phase, and $p(t)$ the pressure at time t.

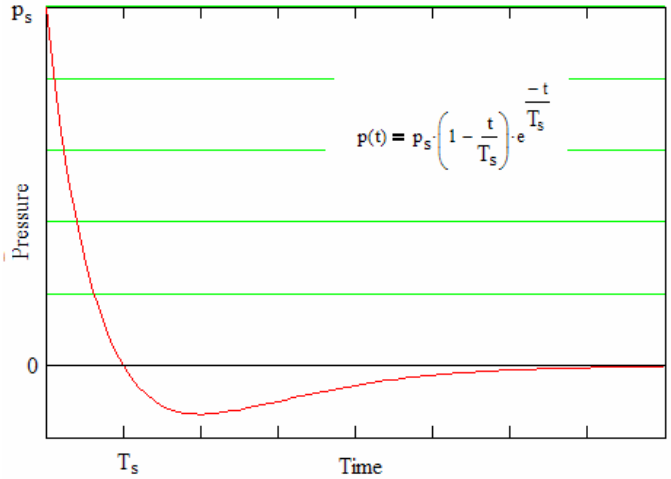

Figure 10. Friedlander loading curve used by Wise [32]

This was applied to a single degree of freedom motion calculation, with ω and k used to eliminate the mass. An equation for the deflection was derived in terms of p_s/k, ω, T_s and t. Differentiation to give an equation for velocity and setting this to zero was used to calculate the time of maximum deflection t_{max}, and hence the maximum deflection itself. In practice only the first root was considered, and this equation was solved for a range of values of ωT_s from 0.25 to 10 to plot non-dimensional values ωt_{max} and the maximum deflection was converted to an equivalent static load $P_p = kz_{max}$ and plotted non-dimensionally as P_p / p_s, as shown in Fig. 11.

This non-dimensional chart allows an equivalent static pressure to be calculated for a particular combination of panel size and shock wave amplitude and duration, and to be applied to calculate the maximum stress. This could then be compared with the modulus of rupture of the material to identify panes that break or survive.

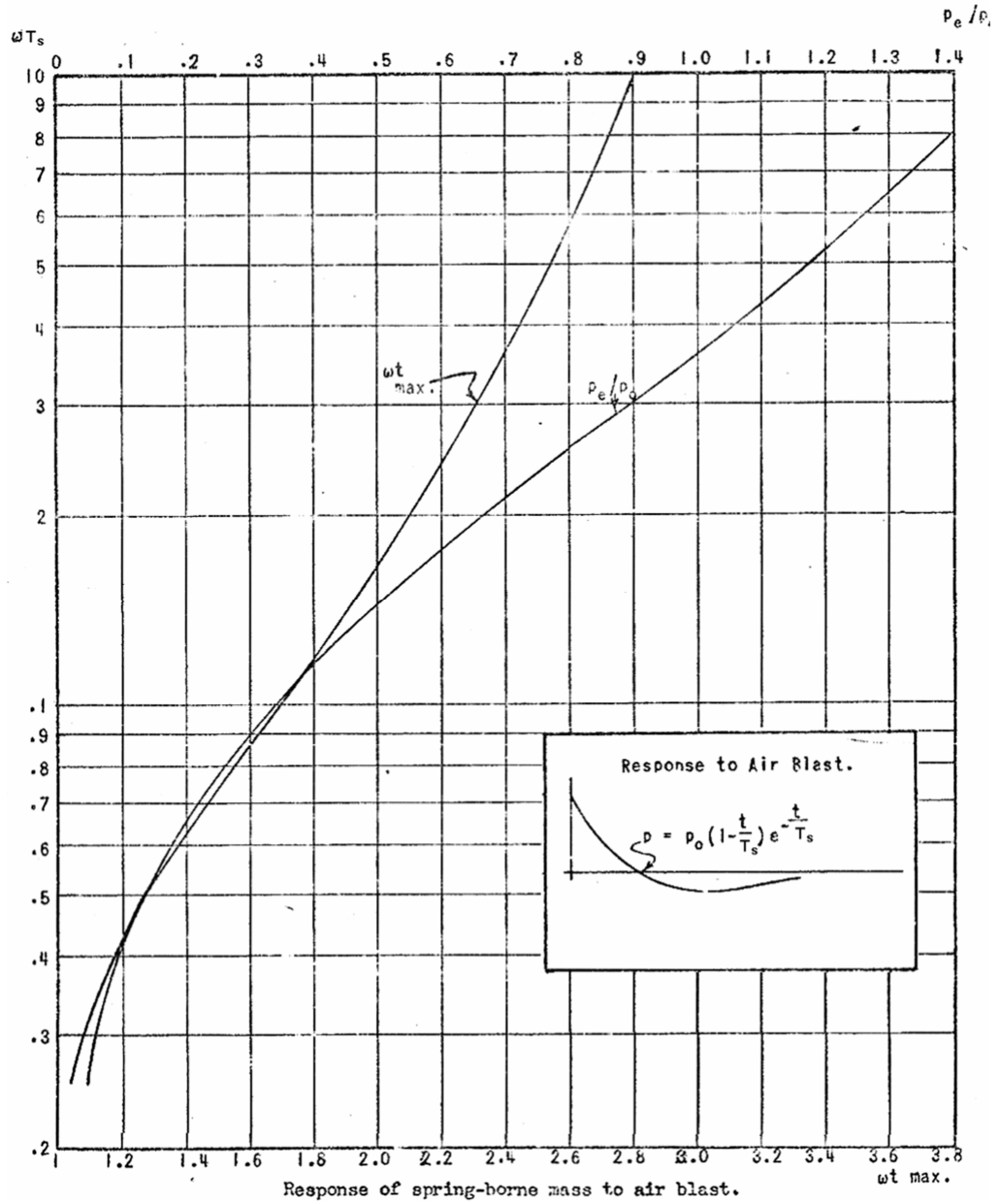

Figure 11. Wise's response chart [32]

The initial approach in this method is different from that used in the UK (i.e. calculating the properties ω and k from energy equations for an assumed modal shape), but the dynamic application uses the Equivalent Static Load method. This is not surprising, as half of the references cited are from the UK wartime research. However, the use of a single simplified loading curve, and the SDOF chart suitable for a range of threats are significant developments in the presentation of the method.

3.3.2 The load factor method

The 1946 US Army manual "Fundamentals of Protective Design (Non-Nuclear)" [14] contained the first proposed method of applying a single degree of freedom analysis to reinforced concrete structural members.

The single degree of freedom calculation was based upon the elastic modal approach of the equivalent static load method, but the loading considered was simplified to two differently shaped positive phase pulses, a rectangular pulse for air blast or a half sine wave pulse for ground shock. Dynamic load factors (DLF), defined in this document as the ratio of the peak equivalent static load to the impulsive load, were plotted against the ratio of the duration of the pulse T_s over the natural period T_n, as shown in Figure 12. With only a positive pulse considered, the positive DLF was always greater than or equal to the negative DLF, and both varied from 0 to 2 for different time ratios.

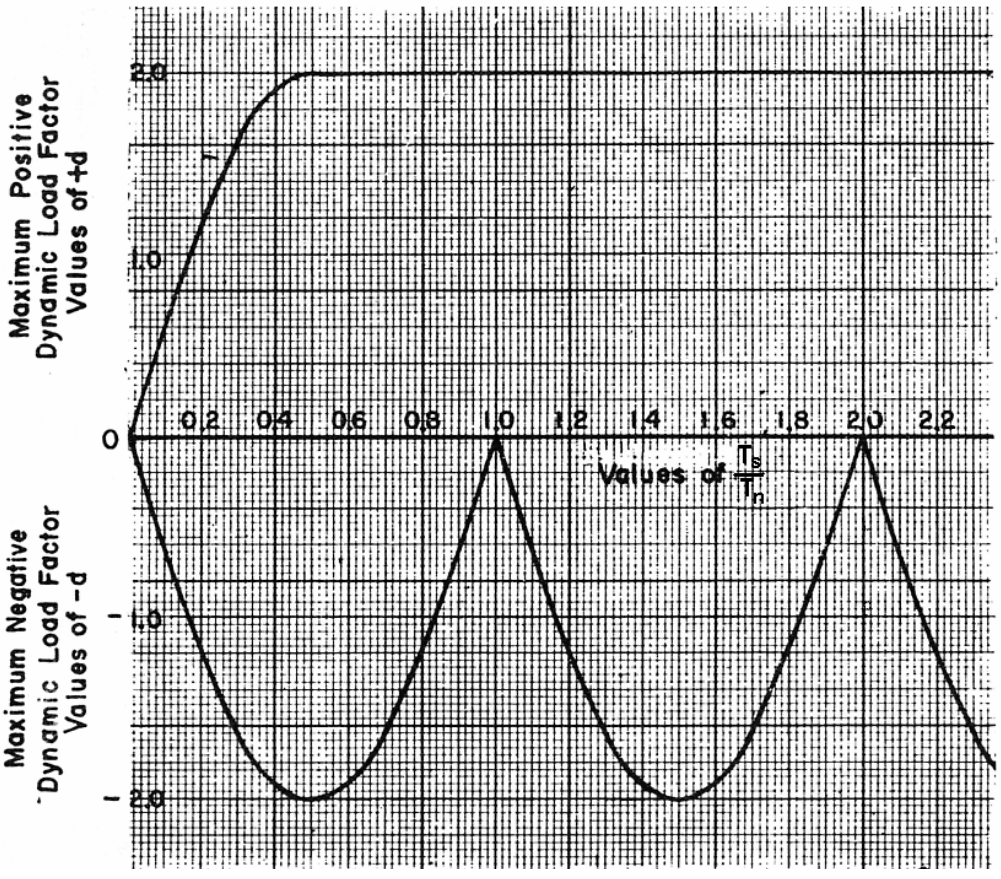

Figure 12. Maximum positive and negative dynamic load factors [13]

Formulae and nomograms were provided for the calculation of side-on and reflected peak pressures and impulses from air blast using cube root scaling laws. The duration of the loading pulse was derived from these by taking a triangular pulse shape. The logic for applying a DLF based on a rectangular pulse shape to a triangular loading pulse (if any) was not given.

Three formulae were provided for natural periods applicable to fortified structures:

- A simple beam, to be used for all bending members impulsively loaded over their whole span
- A lumped mass-spring, to be used for all members like columns subject to concentric axial impulsive loading
- A compound pendulum, to be used for a rigid body free to rotate when subject to eccentric impulsive loading

Although it was conceded that formulae for various structures were available in text books, the proposition was made that, in terms of energy absorption, there was no advantage in fixed ends, and so it seemed probable that the limiting impulse of a fixed-end beam would not differ greatly from the same beam simply-supported. Because of this proposition and the easier analysis of simply-supported members the manual proposed that, in analysis, continuous beams and slabs would be treated as simply-supported. The effect that the substantial difference between assumed and real natural frequencies might have on the calculation of DLF seems not to have been considered.

The manual acknowledged that the application of this impulsive elastic analysis to a plastic material such as reinforced concrete was artificial and produced fictitious stresses in the extreme fibres. However, a study had been undertaken relating these fictitious stresses to flexural impact tests of reinforced concrete beams. This concluded that the fictitious elastic stresses at failure for reinforcement in tension, concrete in compression and shear and bond between reinforcement and concrete were all about 10 times the usual static ultimate values. It also showed that the failure energy was comparable whether calculated on either the enhanced elastic or plastic basis.

The simplification of the loading to a positive phase only made a simple design method for any blast threat practicable at the expense of omitting a proper assessment of an elastic rebound response. However, as this was being applied on an equivalent energy basis to an elastic-plastic response where the rebound would not be significant, this omission was justified for the application of the load factor method to elastic-plastic design.

3.4 Development of elastic-plastic modal methods

The early single degree of freedom analysis methods described so far are all elastic modal methods. During the 1950s, effort was concentrated on assessing structural survival under the effects of atomic weapons, the major threat in the Cold War. This required consideration of long duration positive phase pressures, which had not been analysed in any depth in the Second World War, and of plastic response.

A major part in the development of elastic-plastic dynamic analysis was played by Newmark. As a professor at the University of Illinois he published papers on the subject, and was in the forefront of developing new techniques, including early use of computer methods for structural dynamics. However, his bibliographies show that in addition he was writing both unclassified and classified reports for the United States Air Force (USAF) and the Department of Defence from 1949. As a member of the American Society of Civil Engineers (ASCE) committee and as principal of Newmark Hanson Associates he was a major author of ASCE and USAF manuals on design to resist atomic weapons in the late 1950s and early 1960s.

The method of elastic-plastic SDOF analysis developed by Newmark is presented in his paper "An Engineering Approach to Blast Resistant Design" [34]. He first demonstrated that the blast loading on structures could conveniently be approximated by a triangular pressure history with an instantaneous rise to peak pressure p_{max}, and then a linear decay to zero at time T_s. In the context of an atomic blast and a plastic response, he states "For most structures it is convenient and not inaccurate to neglect the negative phase of the blast".

He then demonstrated that any plastic resistance could be approximated by an elastic-pure plastic resistance typified by a plastic resistance q and an elastic deflection limit z_e. More complex plastic resistances such as work-hardening and unstable resistance could be represented by equivalent uniform resistance giving curves of similar area. Structures with fixed supports giving an elasto-plastic phase could be modelled with an equivalent elastic limit and a modified elastic stiffness.

Equations for the solution of the equation of motion can be derived by consideration of an acceleration-time plot for the applied load divided by mass and the deceleration versus time plot of the resistance divided by mass, both plotted as positive, as shown in Fig. 13. This is all formed by straight lines except for the deceleration due to elastic resistance, which is a complex curve formed by double integrating the net acceleration up to the time t_e when the elastic deflection z_e is reached. The area to the left of the two curves represents the maximum velocity, and an equal area to the right will indicate the time to maximum deflection t_{max}, as the net velocity at this time will be zero. The moment of the couple formed by these equal areas is equal to the maximum displacement z_{max}.

In practice, the SDOF mass M is eliminated from the equations by substituting the natural period T_n defined as:

$$T_n = 2\pi\sqrt{\frac{M \cdot z_e}{q_e}} \tag{7}$$

where q_e is the yield resistance.

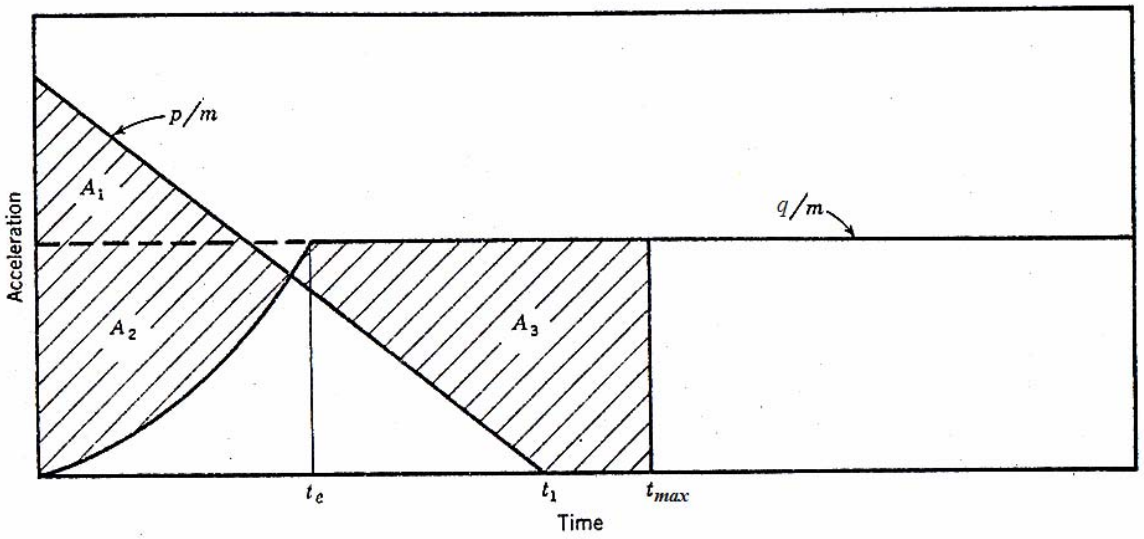

Figure 13. Acceleration – time plot for calculating t_{max} and z_{max} [33]

In Ref. 34, Newmark uses simplified approximations to estimate values of the ratios t_{max}/T_n and p_{max}/q_e for known values of T_n/T_s and ductility ratio z_{max}/z_e. He also used the ENIAC computer at Illinois University and his research on numerical integration algorithms to undertake accurate numerical solutions and to plot curves of t_{max}/T_n and q_e/p_{max} on a log-log graph with axes of T_s/T_n and z_{max}/z_e, Fig. 14. The graph can be used in design to select a resistance strength to achieve a given ductility ratio, or in analysis to calculate the maximum deflection of a given structural member.

The graph shown in the paper is clear, but too coarse to be of much practical use. A more detailed version was published in a 1959 USAF manual for the design of protective structures to resist the effects of nuclear weapons, produced with the assistance of Newmark Hanson Associates [18]. It should be noted that Newmark's graphs started from a ductility ratio of 1, and therefore only covered SDOF responses that extended into the plastic phase of response. This was consistent with the simplification of ignoring the negative loading phase and the possibility of a larger elastic response on rebound.

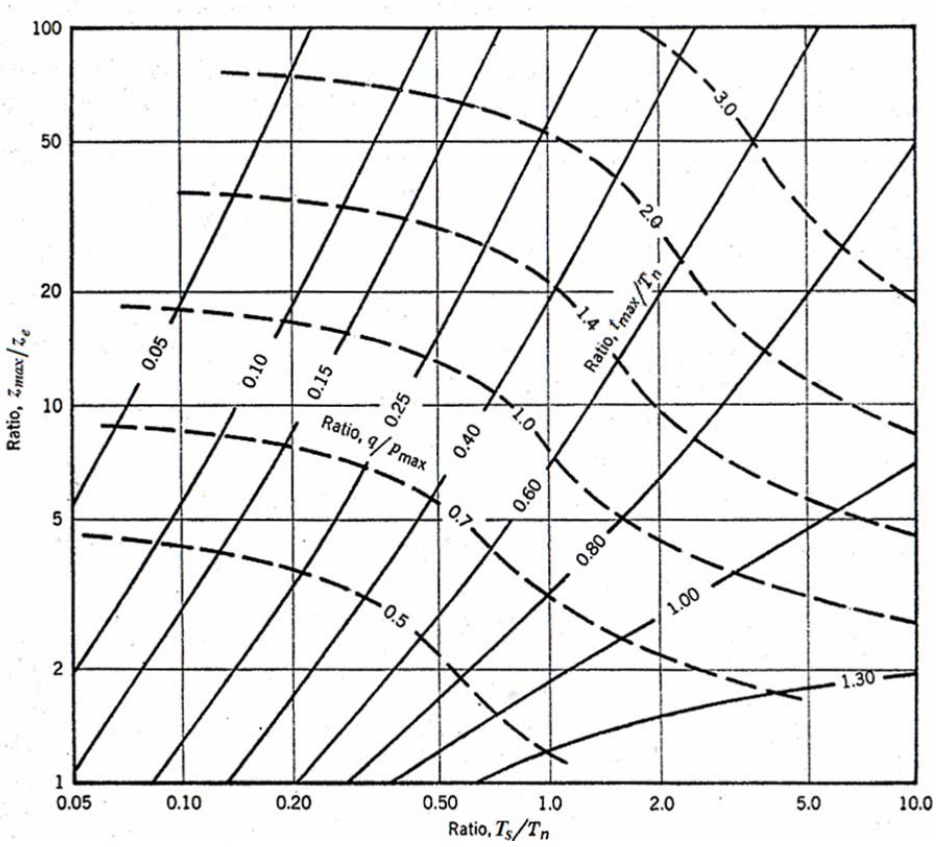

Figure 14. Newmark's chart for analysis of elasic-plastic SDOF response [34]

Although Ref. 34 does not discuss the derivation of the natural period T_n in any detail, Ref. 18 contains formulae for 6 configurations of reinforced concrete beam, 6 configurations of steel beams, several two-way spanning slabs, arches and domes, together with adjustments for columns and for soil surcharge, and references for additional methods of calculating natural frequency. When combined with the corresponding equations for strength and elastic stiffness they could be substituted into Eqn. 7 to assess the "virtual mass" in the various SDOF calculations.

The same method of analysis was included in the 1961 ASCE manual for the design of structures to resist nuclear weapons effects [25]. The formulae for natural period were consolidated into:

- Three beam formulae, incorporating both lumped and distributed mass and steel or cracked concrete stiffness, for three different support fixities.
- A formula for flat slabs.

In an introduction to the principles of SDOF analysis, Ref 18 identifies that, for an ideal correspondence between an actual structural system deforming in an assumed pattern and the SDOF system model, the following will be true:

- The displacement, velocity and acceleration of the model are at all times equal to the displacement, first time derivative and second time derivative of the governing dimension of the actual structure.

- The kinetic energy, strain energy and work done by external loads for the model are equivalent at all times to the corresponding total energies for the actual structural system.

Ref. 18 states that equivalence factors for mass, stiffness and loading of the structural system can be calculated for use in the equations for the SDOF model. However, for an actual system vibrating without load in a particular mode shape and a SDOF model in free vibration, the effect of these equivalences can be obtained by adjusting the factors to obtain the same natural period for the SDOF model as for that mode of the actual structural system, usually the fundamental mode.

This means that the modal SDOF methods considered up to this point are a particular application of a more general method of applying SDOF analysis techniques to actual structural systems, called the Equivalent SDOF method, which is discussed below.

3.5 The Equivalent SDOF method

3.5.1 Introduction to the Equivalent SDOF method

The Equivalent SDOF method was first presented fully in the USACE 1957 manual "Design of Structures to Resist the Effects of Atomic Weapons". This was a 9-volume manual, of which two volumes covered the Equivalent SDOF method, Volume 5, EM1110-345-415 "Principals of Dynamic Analysis and Design" [15] and Volume 6, EM1110-345-416 "Structural Elements Subjected to Dynamic Loads" [16]. The firm of Amman and Whitney (A&W) were credited with much of the basic analytical work and the Massachusetts Institute of Technology (MIT) for further study and development of design material, and for the compilation, both under contract to the USACE. References cited included a 1949 MIT report on structural elements under impulsive loads, and a 1952 A&W interim design manual for protective construction.

The principles of the Equivalent SDOF method are only briefly touched on in Ref 15, with the bulk of the volume describing the way that SDOF methods can be used for analysis and design, not just of elements such as beams and slabs, but for multi-storey buildings subject to lateral loading.

The solution of any dynamic structural system is based on the use of two equations, Newton's Equation of motion (Eqn. 4), defining dynamic equilibrium of forces, and the principle of Conservation of Energy, stated as:

$$\text{Work Done} = \text{Kinetic Energy} + \text{Strain Energy} \tag{8}$$

Three approaches were presented for analysing a basic dynamic system:

- Fictitious Maximum Work Done, where the Work Done Ratio (WDR) is the ratio of the actual maximum work done as calculated in Eqn. 8 to the fictitious work calculated from the loading impulse. This is a SDOF equivalent to the Impulse Method in Section 3.2.2, and ideal for systems with pure plastic resistance, although also suitable for elastic-plastic systems.

- Dynamic Load Factor (DLF), applied to elastic systems, which is the same as the Equivalent Static Load Method in Section 3.2.1, used for elastic systems.

- Deflection Ratio (DR), defined as the ratio of the maximum deflection to the elastic deflection, also known as the ductility ratio. This can be solved either by rigorous analytical integration of the differential equations, or by numerical methods, which is equivalent to the approach by Newmark, in Section 3.4.

Ref. 15 showed that the Dynamic Load Factor was a special case of the displacement calculation used for the Deflection Ratio. Thus, there were two basic methods, using either the energy equation or the equation of motion to derive a solution. Although both were used in the document, sensitivity studies of percentage increment ratios for

a variety of factors and simplifications indicated that there was no real increase in accuracy in using the energy method.

Both methods could be used to calculate dimensionless charts using simplified loading and resistance functions. However, dimensional analysis showed that, for three dimensionless ratios presented on a single chart, only four independent variables could be used to define the loading and resistance. If two were used to define an elastic-plastic resistance, then the loading definition was limited to two variables, one for amplitude and one for time. This limits charts to loadings like a triangular pulse, a rectangular pulse and a step load with a finite rise time. However even this required solutions from up to eight different differential equations to find the peak deflection, so in practice the rigorous solution was limited to pre-solved simplified charts for preliminary design.

For the three loading types, charts were provided of DLF and peak time for elastic resistance, of WDR and peak time for plastic resistance, and DR, WDR and peak time for elastic-plastic resistance. Unlike the Newmark [34] chart , the DR ratio extended down to 0.1, with elastic deflections shown with deflection ratios less than 1, as shown in Fig. 15 for a triangular load. However it should be noted that the simplified loading curves only included positive phases, so the simplified charts do not model critical elastic rebound deflection from blast loading that includes a negative loading phase.

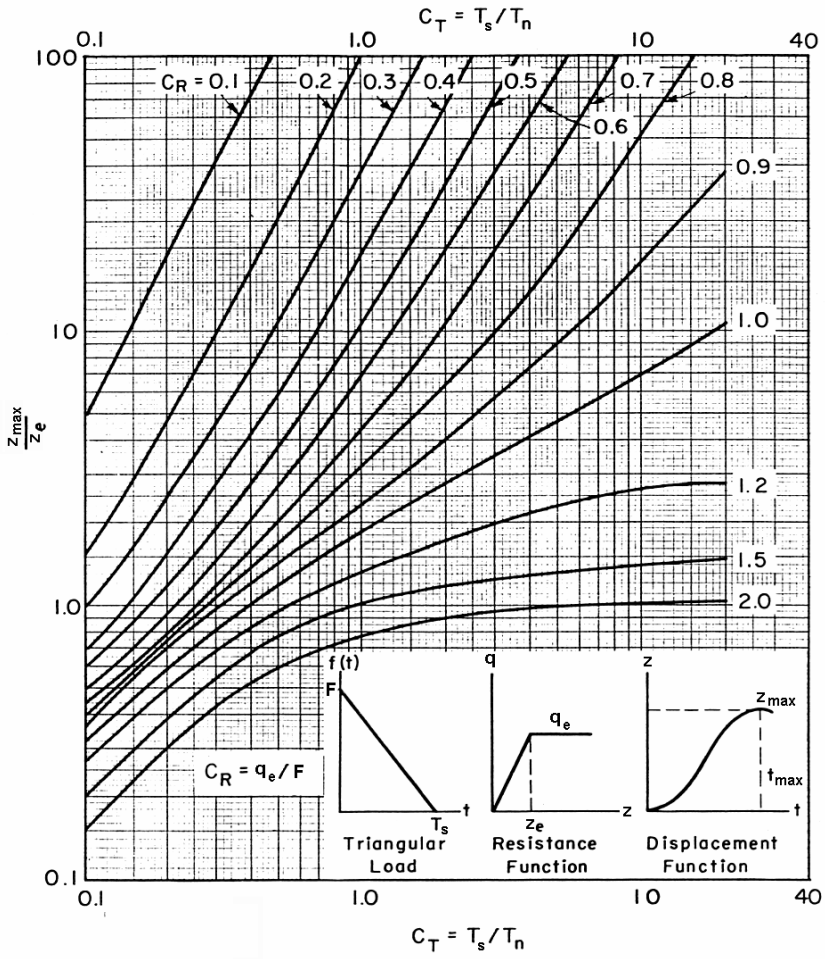

Figure 15. DR chart for elastic-plastic resistance with a triangular load [15]

Ref. 15 included two methods of numerical integration, citing work by Newmark on numerical methods. The Linear Acceleration Extrapolation Method is more accurate, but required iteration to find the deflection in the elastic range. The Acceleration Impulse Extrapolation Method is less accurate for the same timestep, but required no iterations. These methods are potentially more flexible than charts based on rigorous analysis, as simplification of loading or resistance functions is not required. Ref 15 recommends using the charts with simplified functions for initial design, and then performing a numerical analysis without the simplifications.

3.5.2 The principles of the Equivalent SDOF method

Ref. 15 states that in order to simplify a structural dynamic problem, a given structure is replaced by a dynamically equivalent system. The distributed masses of the given structure are lumped together into a number of concentrated masses. The strain energy is assumed to be stored in a number of weightless springs which do not have to behave elastically. Similarly the distributed load is replaced by a number of concentrated loads acting on the concentrated mass and varying with time.

The reduction of a given distributed structure to an equivalent dynamic system involves the principle of dynamic similarity, which is the requirement that the work done, strain energy and kinetic energy of the equivalent system must be identical with the respective property of the given structure.

The simplest dynamic system consists of a single concentrated mass supported by a single spring acting in one direction and subjected to a single concentrated load in that direction, i.e. a system with a single degree of freedom (SDOF).

Ref. 16 covers the derivation of the transformation factors for mass, loading and resistance that need to be applied to the properties of distributed structures, be they beams, slabs or whole buildings, to derive the equivalent mass, loading and resistance of the equivalent SDOF system. This is a function of the deflected shape of the distributed structure. The deflected shape is a function of both time and position, but it is assumed that these functions are separable into separate functions in time and position:

$$z_a = f(x,t) = f_x(x) \cdot f(t) \tag{9}$$

where $f_x(x)$ is a function describing the deflected shape through the structure, and *f(t)* is a function describing the variation of the loading with time.

Taking the equivalent deflection equal to the deflection at a selected control location *X*:

$$z_e = z_{aX} = f_x(X) \cdot f(t) \tag{10}$$

Ref. 15 derives the load transformation factor K_L for a uniformly distributed load *p(t)* over a span *L* by considering the work done, to give:

$$K_L = \frac{P_e(t)}{p(t) \cdot L} = \frac{\int_0^L f_x(x) \cdot dx}{L \cdot f_x(X)} \tag{11}$$

and derives the mass transformation factor K_M for a uniformly distributed mass m over a span L by considering the kinetic energy, to give:

$$K_M = \frac{M_e}{m \cdot L} = \frac{\int_0^L f_x(x)^2 \cdot dx}{L \cdot f_x(X)^2} \tag{12}$$

In these solutions, equal terms of the temporal distribution of velocity, $d(f(t))/dt$, appear on both top and bottom of the equations, and cancel out.

Ref. 16 states that comparison shows the resistance factor K_R, found by consideration of strain energy, will always be equal to K_L, and demonstrates this for both elastic and plastic strain.

The dynamic reaction transmitted to the supports of the lumped mass SDOF system is equal to the resistance. However, the dynamic reaction for the actual structure cannot be obtained from the resistance alone. An approximate, but reasonably simple, approach to obtaining dynamic reactions was presented in Ref 16, in which the rotational dynamic equilibrium of sections of the structure between supports and lines of zero shear is used to define the reaction in terms of resistance and loading. Inertial forces of varying magnitude will also be present, but if the equilibrium is calculated about the centroid of the inertial forces they will be eliminated from the calculation. This is illustrated in Figure 16 for a uniformly distributed load and an assumed deflected shape equal to the elastic static deflected shape under uniform loading.

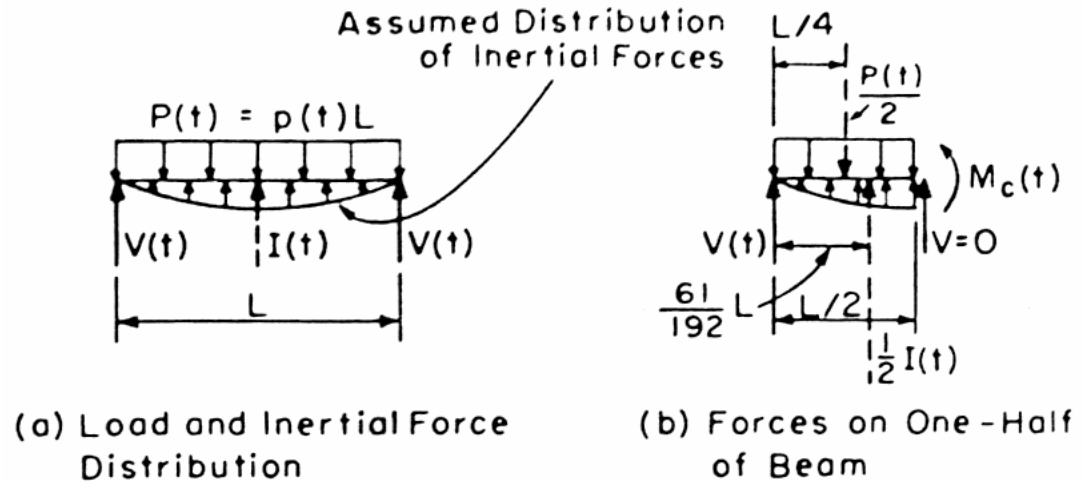

Figure 16. Equilibrium diagram for reaction from simply supported one-way span [16]

For a uniformly distributed mass, the distribution of inertial forces is the same as the distribution of acceleration, $d^2 z_a / dt^2$. Given the separation of time and position functions assumed in Eqn. 9, the distribution of the acceleration is the same as the distribution of deflection, $f_x(x)$, and the centroid position can be calculated from this.

If the true deflected shape throughout the response were described by the deflection function $f_x(x)$, then the dynamic response of the equivalent SDOF system would exactly model the response of the control location *X* on the structure, and the reactions will be exact. However, the true deflected shape cannot be known ahead of analysis, and, in any case, is likely to vary with time. In practice, the equivalent SDOF method is used as an approximate method with assumed deflected shapes.

For elastic analysis, common assumed deflected shapes are the shape of the fundamental mode of vibration with the same mass distribution, and the static deflected shape with the same load distribution. However, different deflected shapes can be used for different phases of the response, such as the plastic phase and the elasto-plastic phase for fixed supports. The mode shape is irrelevant for plastic phases, but the approach using static deflected shape can be applied throughout. This is the approach that has been used in Ref. 16 to calculate transformation factors and reaction coefficients for a range of structures.

3.5.3 Further developments of the Equivalent SDOF principles

Although clearer explanation of the principles of the Equivalent SDOF method have been provided in a number of subsequent manuals and text books, developments of the principles beyond those presented in 1957 are limited.

One important development is presented by Biggs in 1964 [35]. In a non-linear response with elastic, elastic-plastic and plastic phases, the characteristic deflected shapes used to represent the velocity and acceleration shapes, and hence to calculate the transformation factors and the distribution of the inertia forces, are those of the incremental distortions, not the total distortions. However, the force diagram used to calculate the reactions is the total force diagram. This becomes significant in asymmetric structures such as a propped cantilever, where elastic shears have to be incorporated in the dynamic reactions for elastic-plastic and plastic phases.

Biggs [35] also presented the formulae for the transformation factors in more general terms than Eqns. 11 and 12, which included non-uniform load or mass distribution and concentrated loads and masses on a span.

Damping has never been a significant factor in the response of reinforced concrete structures to air blast, and damping terms have generally been omitted from the equations of motion used for blast analysis. Since soil-structure interaction (impedance damping) was recognised to significantly affect ground shock response, there have been attempts to incorporate damping into SDOF analyses in subsequent manuals [22,23]. This has been confused by the non-linear nature of soil impedance when tension cracks open in the soil, and attempts have been made to model soil-structure interaction as additional loading terms.

Aeroelastic damping is a recognised phenomenon in wind vibration calculations, and the transformation factor for damping has been calculated in that context. Buchholdt [36] equated distributed and equivalent virtual work to show that the formula for a damping transformation factor is the same as that for the mass transformation factor in Eqn. 12, for the same distribution of mass and damping. However, it should be noted that structural damping defined as a percentage of critical damping is already an equivalent system damping property, and requires no transformation.

With constant shape factors for each phase, the assumed separation of the deflection into separate shape and time functions is valid except when there is a change between phases. The error at the discontinuity is brief and does not have a significant effect on the deflection calculations. However this is not necessarily the case when there is a continuous variation in the shape. Recently, Zobec & De Bertoli [37] have used partial differential equations to assess the transformation factors using a varying deformation without the assumed separation in Eqn. 9. They have shown that the transformed mass has two terms:

$$M_e \cdot \frac{d^2 z}{dt^2} = M \cdot \left(K_M \cdot \frac{d^2 z}{dt^2} + \frac{dK_M}{dz} \cdot \left(\frac{dz}{dt} \right)^2 \right) \tag{13}$$

Where K_M is the normal definition of the mass factor, as Equation 12.

3.5.4 Initial calculation of SDOF parameters

Ref. 16 contains tables of transformation factors, resistance functions and reaction coefficients that have been calculated for a range of structures. These include:

- Beams and one way spans in elastic, plastic and, where appropriate, elasto-plastic phases for simple, fixed and mixed supports with distributed and a range of concentrated load cases
- Two-way slabs in elastic, plastic and, where appropriate, elasto-plastic phases for distributed loading over a range of aspect ratios and simple and fixed supports on all edges, and for fixed and pinned on alternate edges
- Square flat slabs in the elastic and plastic phases
- Elastic, plastic and elasto-plastic Tee beams with uniform and triangular distributions of load and/or mass and fixity at one or both ends
- Elastic deep beams
- Trusses in the elastic range and with plastic yielding at either the mid-span or the end bay of the truss.

The manual also contains worked examples demonstrating how the parameters were derived, or references for values taken from elsewhere.

It is the first two categories that are of enduring interest, and which are considered further in this thesis.

3.5.4.1 One-way spans

The static deflected shapes for elastic one-way spans are well known, and can be derived by repeated integration of the load distribution, and the elastic stiffness and maximum elastic resistance can be derived from the same calculation.

The familiarity of the formulae was a source of error in one case, as the elastic spring constant for the propped-cantilever case with distributed loading was based on the familiar formula for maximum deflection, rather than the deflection at the central reference point, as shown in Fig. 17.

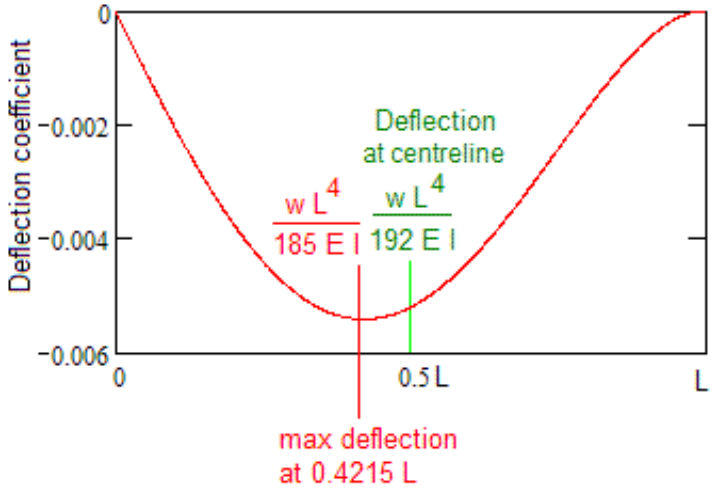

Figure 17. Deflections in an elastic propped cantilever under distributed loading

With hinges having formed at fixed supports, the elasto-plastic deflected shapes were based on the deflected shape of the simply supported span. This is appropriate for the incremental deflected shape, as described by Biggs [35]. However, the force and moment diagrams were taken as the incremental diagrams also, which is not correct. The difference between incremental and total moment distribution is shown in Fig. 18. This makes no difference for symmetric spans, but resulted in a number of errors in the factors for propped cantilever spans, and would also affect asymmetrically loaded spans.

The plastic deflected shapes were based on straight-line deflections between plastic hinges, again appropriate for the incremental deflected shape. However, the hinge positions should be based upon the total bending moment diagram, as shown in Fig. 18, not the incremental moments. This resulted in an incorrect deflected shape being used for some of the propped cantilever calculations, where the hinge will not occur on the centreline.

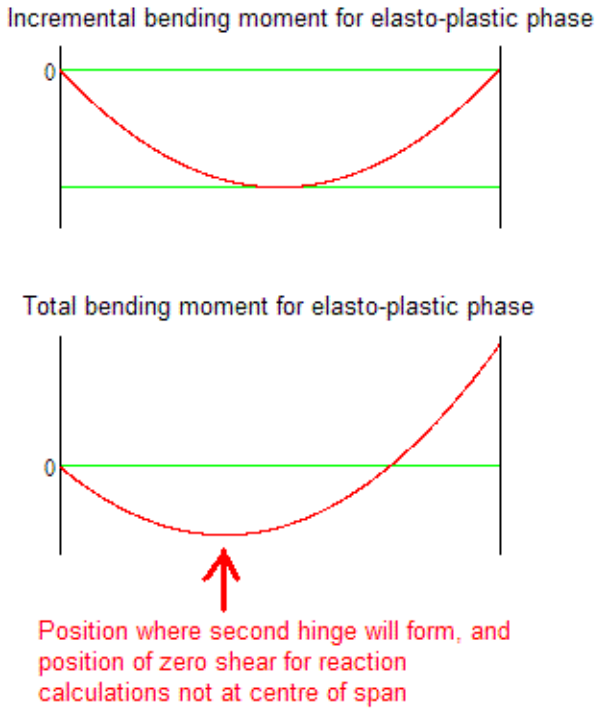

Figure 18. Bending moment distribution for an elasto-plastic propped cantilever under uniformly distributed loading

The principle for calculation of the centroid of inertia as described in section 3.5.2 was followed throughout, resulting in the same dynamic reaction coefficients for distributed or lumped mass. This was incorrect, and the error lies in the original statement of principle, which was only correct for uniformly distributed mass; the true distribution of inertia forces is the product of the distribution of mass and the distribution of acceleration, not the distribution of the acceleration alone. This will give different dynamic reaction coefficients for lumped masses, as the centroid of the inertia forces will be in line with the lumped masses, as shown in Fig. 19.

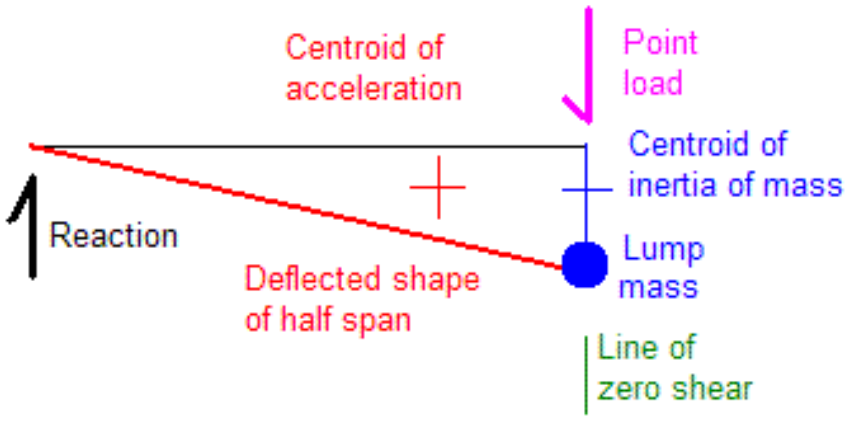

Figure 19. Centroids of acceleration and inertia for a half-span with concentrated load and mass

As the elasto-plastic and plastic analysis of propped cantilever spans and analysis of lumped mass structures do not have a direct bearing on the objective of this thesis, these topics are not explored further. However, these do illustrate the flaws that can still exist even in "tried and tested" methods.

3.5.4.2 Two-way spans

The plastic analysis of two-way spans was stated in Ref. 15 to be based on yield line analysis, but, as implemented, was actually based on a mixture of methods, including a simplified yield line approach. The plastic deflected shape was assumed to be a classic yield line pattern with a fixed diagonal yield line angle of 45º, as shown in Fig. 20.

The assumption of a fixed angle allowed interpolation from the square panel, at an aspect ratio of one, to a one-way panel, at an aspect ratio of zero. In fact, only two two-way plastic calculations were undertaken, of square panels, one with all edges pinned and a similar panel with all edges fixed, and then values for aspect ratios down to a value of 0.5 were tabulated by interpolation. The approximations and implications arising from the assumptions are described later in this thesis.

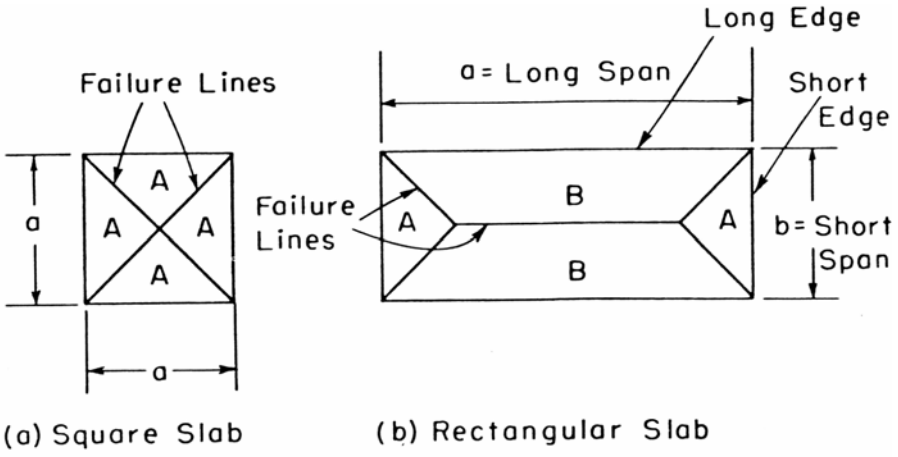

Figure 20. 45 degree failure line pattern assumed [16]

The reaction coefficients were based on there being no shear forces across the assumed yield lines, which is a common assumption, but is not always true. The reaction coefficients for each edge were calculated from the equilibrium of the triangular and trapezoidal sections at each edge, but again the fixed angles allowed an interpolation, with the trapezoid being treated as the combination of a 45º triangle and a one-way span.

The elastic deflected shape was a very rough approximation, produced by applying the one-way span elastic deflected shape to the triangles and trapezoids of the plastic deflected shape. Again, only square panels with all pinned supports and with all fixed supports were calculated, and the other aspect ratios calculated by interpolation. For panels with mixed fixed and pinned supports, the deflected shapes assumed triangles of one one-way shape and trapezoids of the other, as shown in Fig. 21, which did not even meet correctly at the corners for a kinematically possible deflected shape, but which allowed interpolation to be used.

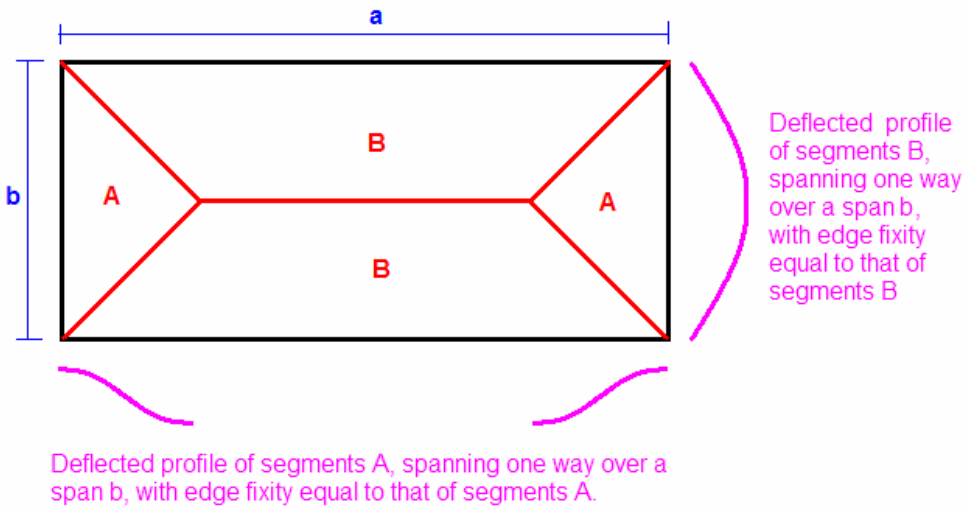

Figure 21. Assumed elastic deflected shape in Ref. 16 for mixed support conditions

As for the plastic analysis, the elastic shear coefficients again were calculated on the basis of there being no shear forces across the 45º lines, as shown in Fig. 22, an assumption for which there is no basis in elastic theory except for the square panel.

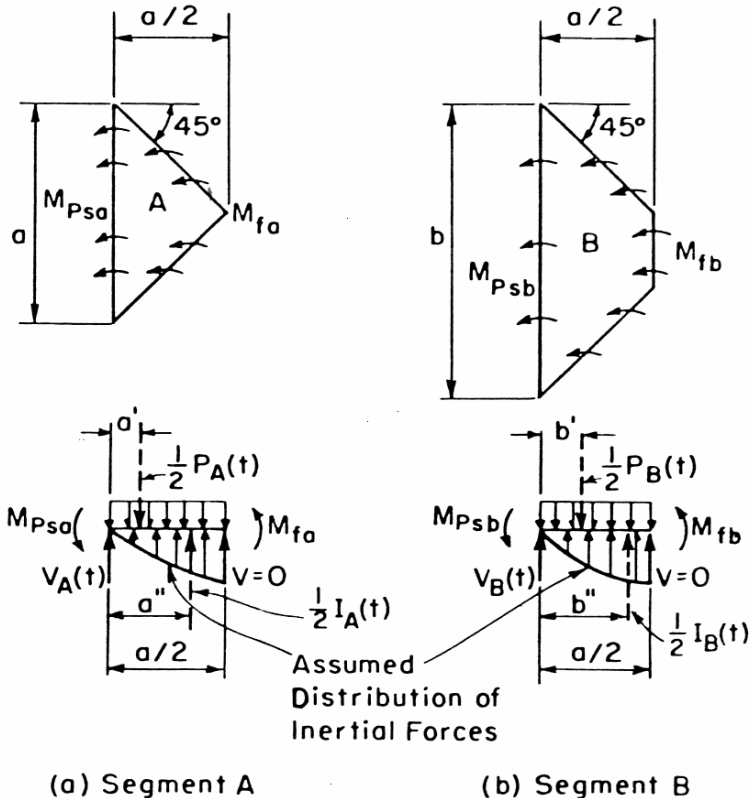

Figure 22. Method of calculation of two-way shear coefficients [16] (note different use of *a* and *b* in this figure)

The coefficients for the maximum resistance cannot be calculated by interpolation, but were not based on yield line analyses. Instead Ref. 16 cited an American Concrete Institute publication, ACI 318-51. The values given are higher than those produced by

classic yield line analysis even when a 45º angle is assumed, which is already an upper-bound approach.

To complete the resistance functions, the elastic stiffness values were taken from Timoshenko's "Theory of plates and shells" [38], even though the Poisson's ratio for the calculated values was suitable for steel rather than reinforced concrete.

The approximations adopted for the two-way slabs were attributed principally to methods presented in the 1952 Ammann & Whitney manual. Ref. 16 stated that "the approximate nature of the methods of design and analysis and of the basic data used therein do not warrant the development of exact relationships for determining the behaviour of two-way slabs subjected to impulsive loads". However the reviews against more exact methods were limited to one-way spans, and it seems probable that the authors did not realise that some of the two-way approximations introduced errors significantly greater than any in the one-way spans, as described later in this thesis.

Although the principles of the equivalent SDOF method were generally sound, some of the initial application misinterpreted them, and some of the calculations involved approximations introducing significant errors, primarily to reduce the burden of calculation in preparing the data in Ref. 16.

3.5.5 Alternative calculation of SDOF parameters

3.5.5.1 Biggs

In his 1964 book, Biggs [35] identified and corrected for the lack of elastic shear in one-way spanning propped cantilevers. However, he did not identify the error in the point of zero shear that this introduced, so his revised reaction coefficients solved only part of the problem in Ref. 16 due to the use of incremental forces rather than total forces in the plastic calculations. He only included the two-way span tables for fully fixed and fully pinned panels in his book, so he did not identify the missing elastic shear in elasto-plastic and plastic two-way panels with mixed support fixity.

Biggs [35] also corrected the elastic stiffness for Poisson's ratio in reinforced concrete, provided alternative and more realistic values for the elastic resistance limit of the fixed-edge panel, and corrected anomalies between the pinned elastic and fixed elasto-plastic transformation factors, but did not challenge or question the assumptions and simplifications used in Ref 16.

One great benefit of the book was Biggs' clear presentation of worked examples of numerical integrations.

3.5.5.2 TM5-1300

In 1969, a new analysis of Equivalent SDOF parameters was published in TM 5-1300 [17]. This used the equilibrium method for calculating the position of the yield lines in a classic yield line mechanism, and used this to derive the plastic resistance and the plastic K_{LM} transformation factor, the ratio of K_M and K_L, for panels with all four edges supported, and for panels with one or two free edges.

In the calculation of plastic resistance, a reduction in moment resistance in yield lines near the corners was introduced to account for more complex corner stiffness. This reduced the resistance for all edge fixities by between 11% and 17%, but was not a standard yield line approach.

The equilibrium method formulae included the correct yield line treatment for orthotropic reinforcement, but did not include terms for nodal forces at free edges, a requirement by then well-established in the equilibrium method of yield line analysis [39].

A method was given for calculating elastic and elasto-plastic resistances and stiffnesses, with different parts going plastic in turn. However, the transitions were calculated from elastic charts at the position of maximum bending, and so tended to underestimate the true transition resistances.

The elastic K_{LM} transformation factors given for square panels with full fixity and no fixity were consistent with true elastic deflected shapes. Thereafter, interpolation had been applied, with the factor varying linearly between these for 1, 2 or 3 sides fixed, and then varying linearly to one-way spanning at an aspect ratio of 0.5 or 2. This treatment was in spite of the elastic stiffness charts in the manual that showed that the elastic moments and deflections did not converge on the one-way span until an aspect ratio of about 0.25.

The treatment of elastic panels with a free edge was even less accurate. Interpolation was between a one-way span at an aspect ratio of 0.5 and a cantilever at an aspect ratio of 2, without ever going through a two-way spanning stage, even though the two-way spanning action would actually be at its greatest around an aspect ratio of 2.

Ref. 17 did not provide calculation of reaction coefficients. It acknowledged that the reactions are a function of both loading and resistance, but proposed that peak shear calculations be based on a quasi-static analysis of the peak resistance only, because the Equivalent SDOF coefficients could produce an exaggerated early peak reaction and shear. Unfortunately, this prevented calculation of a reaction history that could be used as dynamic loading on supporting members.

In part, this consideration of the peak values rather than the whole response was a result of the concentration in Ref. 17 on the use of charts rather than numerical methods. The document demonstrated the truth of the dimensional limit of charts described in Ref. 15 (see section 3.5.1) by trying to break the limit. Charting bi-linear loading in combination with an elastic-plastic resistance added two extra variables and required 212 pages of charts, as opposed to the single page for the triangular loading. Both would be equally easily solved by numerical analysis for a particular case.

3.5.5.3 Mayor & Flanders

In the 1990 Theory Manual for the computer program BLAST [40] that calculated blast resistance of walls and windows, Mayor & Flanders reported calculations of elastic transformation factors by Finite Element methods, and checked by the Navier solution from Timoshenko [38].

To derive transformation factors for masonry walls with openings, they used a plate finite element model with 16 elements a side to calculate elastic deflections for fixed and pinned supports over a range of aspect ratios and a range of opening sizes, including cases without openings.

The K_L factor was calculated by the numerical integration of the deflections at each node, and the K_M factor by the numerical integration of the square of the deflections at each node.

The K_L factors were checked by calculating the integral of the first 30 terms of the Navier double-Fourier equation for the deflection of the simply supported panels without openings. This showed that, even with the coarse finite element mesh used, the K_L values were within 1% of the analytical solution.

This appears to have been the first occasion when an analysis of elastic transformation factors was reported over a range of aspect ratios, and therefore the first check on the interpolation assumptions in the calculations in Refs. 16 and 17. However, the connection does not appear to have been made at that time, or the divergence from the values in these manuals noted.

3.5.5.4 PSADS

The Protective Structures Automated Design System (PSADS)[23], the current design manual for buildings protected against military threats, incorporates the current version of TM5-855-1 and a collection of computer applications, including a SDOF analysis program SpanW, which will undertake a numerical analysis up to the first peak of deflection. PSADS uses resistance and SDOF parameters based on Ref. 16, but it does recognise that there are alternatives, and has the SDOF parameters from Ref. 17 included as an appendix, without giving any indication as to why they differ or what action to take given the differences.

The parameters in the main body of the report and in SpanW include the case of a fixed edge panel with one free edge, as for Ref. 17, but based on 45 degree yield lines in accordance with Ref. 16. The other parameters incorporate some of Biggs' [35] revisions, but not all.

One difference is a reduction of 10% in the resistance of panels with fixed edges, to account for the reduced resistance of advanced yield line mechanisms. This would be almost correct for the fully fixed case if the resistances had actually come from a classic yield line analysis, rather than the source cited in Ref. 16. In practice, Ref. 23 will over-estimate the resistance of fully fixed and simply-supported panels, and under-estimate the resistance of mixed fixity panels, but it is closer to advanced yield line analysis results than previous manuals.

Ref. 23 contains SDOF reaction coefficients, which can be used to calculate loading on supports, but proposes the use of the maximum resistance calculation for shear design as in Ref. 17, because of the exaggeration of reaction that can occur in the initial loading pulse.

Ironically, Ref. 23 seems to have lost touch with its roots, and does not even reference Ref. 16, where the assumptions and approximations behind the tabulated values are described. One example is that the table of SDOF factors is headed as being for a Poisson's ratio of 0.3, while they are independent of Poisson's ratio, and the elastic stiffnesses, which are now in a different table, follow Biggs [35] and are based on a Poisson's ratio of 0.15.

3.5.5.5 Previous work by the Author

In his MSc dissertation, the Author [6] compared the coefficients for simply supported elastic panels presented in Refs. 35, 17 and 40. The K_{LM} value was not presented by Mayor & Flanders [40], but has been calculated from the ratio of their numerical values of K_L and K_M. The results are shown in Table 1.

Source		Aspect Ratio					
	Coefficient	1.0	0.9	0.8	0.7	0.6	0.5
Biggs [35]	K_L	0.46	0.47	0.49	0.51	0.53	0.55
	K_M	0.31	0.33	0.35	0.37	0.39	0.41
	K_{LM}	**0.67**	**0.70**	**0.71**	**0.73**	**0.74**	**0.75**
	V_{FS}	0.07	0.06	0.06	0.05	0.04	0.04
	V_{RS}	0.18	0.16	0.14	0.13	0.11	0.09
	V_{FL}	0.07	0.08	0.08	0.08	0.09	0.09
	V_{RL}	0.18	0.20	0.22	0.24	0.26	0.28
TM 5-1300 [17]	K_{LM}	**0.63**	**0.63**	**0.67**	**0.70**	**0.74**	**0.79**
Mayor & Flanders [40]	$K_{L\ (Analysis)}$	0.419	0.419	0.420	0.423	0.427	0.435
	$K_{L\ (Numerical)}$	0.416	0.416	0.417	0.419	0.423	0.431
	$K_{M\ (Numerical)}$	0.257	0.257	0.258	0.260	0.264	0.271
	$K_{LM\ (Numerical)}$	**0.618**	**0.618**	**0.619**	**0.621**	**0.624**	**0.629**

Table 1. Simply supported elastic SDOF parameters from Refs. 35, 17 and 39.

The author also undertook fresh calculations using the double Fourier equation for deflection *w* at any point *(x,y)* of a rectangular panel *a* long by *b* wide, developed by Navier, and presented by Timoshenko [38] and Donnell [41]:

$$w(x,y) = \frac{16a^4 p}{\pi^6 D} \cdot \sum_m \sum_n \frac{\sin\frac{m\pi x}{a} \sin\frac{n\pi y}{b}}{mn(m^2 + \frac{a^2}{b^2} \cdot n^2)} \tag{14}$$

with *p* the pressure and *D* the stiffness coefficient, which defines an infinite series in *n* and *m* where *n* and *m* are odd integers, together with the corresponding stress equations. The results are shown in Table 2.

Source		Aspect Ratio					
	Coefficient	1.0	1.3 (0.77)	1.5 (0.67)	2.0 (0.5)	3.0	4.0
Analysis based on Navier equations, from Refs. 38 and 41	K_L	0.419	0.421	0.424	0.435	0.465	0.495
	K_M	0.262	0.264	0.267	0.277	0.307	0.339
	K_{LM}	**0.626**	**0.627**	**0.629**	**0.637**	**0.661**	**0.685**
	V_{FS}	0.099	0.097	0.096	0.091	0.081	0.071
	V_{RS}	0.151	0.105	0.082	0.044	0.001	-0.003
	V_{FL}	0.099	0.100	0.100	0.101	0.102	0.102
	V_{RL}	0.151	0.198	0.222	0.264	0.308	0.330

Table 2. Simply supported elastic SDOF parameters by the Author [6]

The deflections converge fairly quickly, so that better than 3 significant figures were obtained with no more than 28 terms in the series (4 x 7), but the reactions at the supports converge very slowly, so that up to 40,000 terms (200 x 200) were required for similar accuracy in reaction coefficients.

An alternative algorithm was used to calculate the reaction coefficients in accordance with the same principals of rotational dynamic equilibrium. This is illustrated in Fig. 23. Zero shear was taken at the lines of symmetry, so that equilibrium was calculated for a quadrant. Simultaneous equations for rotational equilibrium in the long axis and short axis directions were solved to derive the reaction coefficients on both supported edges. This required the shear distribution along the edges of the panel to identify the position of the centre of the reaction. The concentrated reverse reaction at simply supported corners was taken as being divided evenly between the two sides.

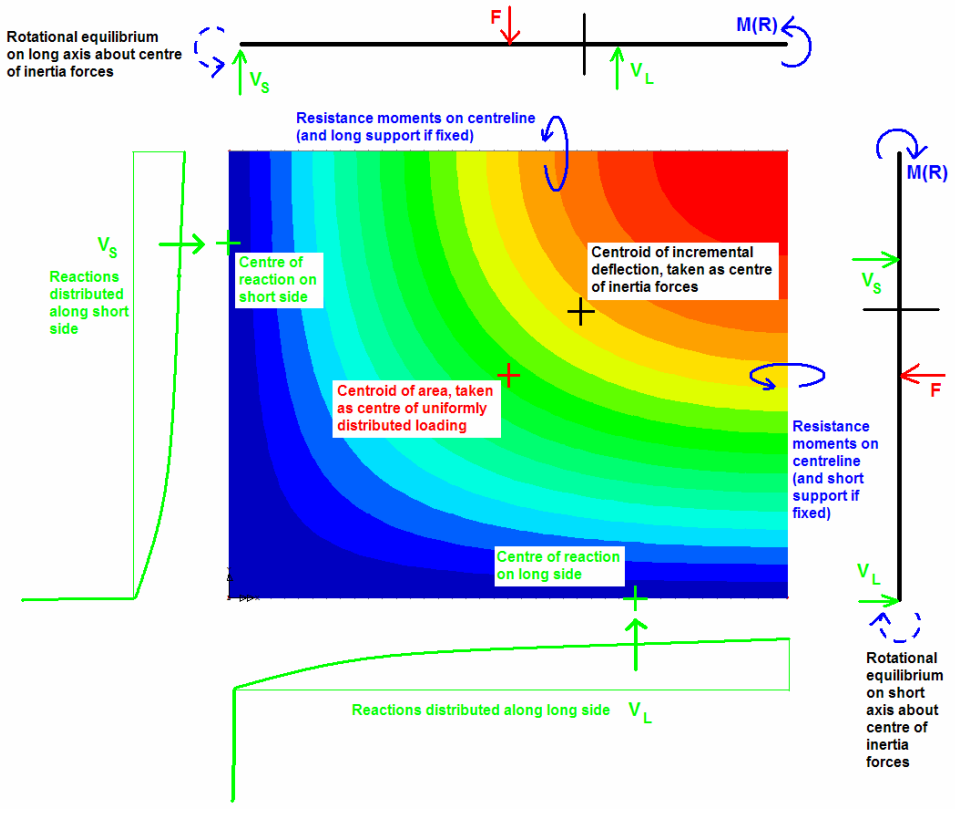

Figure 23. Rotational equilibrium of forces in a quadrant, as used in [6]

The versatility of the Equivalent SDOF method was demonstrated by the calculation of parameters for a different resistance mechanism: plastic membrane tension. This was based on the deflection formula for "soap bubble" membranes 2*a* by 2*b*, given by Timoshenko and Goodier [42]:

$$z(x,y) = \frac{16 \cdot p \cdot a^2}{S \cdot \pi^3} \cdot \sum_{n=1,3,5\ldots}^{\infty} \frac{1}{n^3} \cdot (-1)^{(n-1)/2} \left[1 - \frac{\cosh(n \cdot \pi \cdot y / 2a}{\cosh(n \cdot \pi \cdot b / 2a} \right] \cdot \cos \frac{n \cdot \pi \cdot x}{2a} \qquad (15)$$

where S is the membrane tension force, equal to $\sigma_y \cdot h$, and p is the loading pressure. These membranes had attracted considerable detailed study in engineering because of the mathematical equivalence to shear.

For small deflections (when $\sin(z/a) \approx z/a$) the SDOF parameters are as given in Table 3, but for larger deflections the reaction distribution changes due to the geometry, and reaction coefficients and non-linear resistance were calculated over a range of deflections expected from a PVB membrane, and tabulated in an appendix in Ref. 6.

Source		Aspect Ratio					
	Coefficient	1.0	1.3 (0.77)	1.5 (0.67)	2.0 (0.5)	3.0	4.0
Analysis based on Soap bubble membrane, from Ref 41	K_L	0.477	0.481	0.486	0.502	0.537	0.564
	K_M	0.314	0.317	0.322	0.340	0.378	0.409
	K_{LM}	0.658	0.660	0.664	0.677	0.704	0.725
	V_{FS}	0.090	0.092	0.093	0.095	0.096	0.097
	V_{RS}	0.160	0.110	0.084	0.040	-0.006	-0.029
	V_{FL}	0.090	0.087	0.084	0.078	0.065	0.065
	V_{RL}	0.160	0.211	0.258	0.287	0.345	0.378

Table 3. Plastic membrane SDOF parameters derived by the Author [6]

3.6 Overview of methods of analysis for response to blast

3.6.1 Virtual mass and transformation factors

It is interesting to note that although Christopherson [11] considered two classic plastic yield line deflected shapes in assessing the 'virtual mass' for the impulse method in 1945, he did not identify the appropriate critical plastic deflected shape. Although the seminal work on yield line theory by Johansen which is described in Ref. 39 was not available to him at the time, earlier UK work by Ingerslev [43] in 1922 had covered "classic" yield line patterns and ultimate resistance in rectangular RC slabs supported on all edges. Although the concept foreshadowed the transformation factor from the Equivalent SDOF method, a factor based on a plastic one-way span was proposed for general use in plastic impulse analysis. The method is still commonly used for impulsive loading, but the "virtual mass" is now calculated from the plastic Equivalent SDOF transformation factor K_{LM}.

Although the dynamics approach used by Wise [33] does not explicitly use a "virtual mass", this is implicit in the use of ω and k to eliminate mass from the equation of motion. The equations for these properties could have been used to calculate the virtual mass factor implicit in the method. It would have been sensitive to the assumed deflected shape, and, depending on the shape assumed, might also have been sensitive to aspect ratio.

By implication, the Equivalent Static Load method of analysis [29, 30] also implied a "virtual mass" by the use of natural frequency and stiffness, although this was made less obvious by the use of measured natural frequencies in much of the research, so only a numerical estimation of the "virtual mass" would have been possible.

The use of these elastic properties to define the virtual mass made the development of elastic-plastic methods difficult. Newmark [34] achieved this by using the elastic "virtual mass" even in the plastic zone. When his charts were subsequently used with transformation factors from the Equivalent SDOF method, a designer was required to choose a single average transformation factor to calculate an equivalent natural period [17].

The transformation factor K_{LM} from the Equivalent SDOF method provided a means of calculating the "virtual mass" that was not based upon elastic properties, and could be calculated for a range of deflected shapes representing different forms and stages of bending response, or different forms of resistance. In combination with numerical analysis it greatly extended the capability of SDOF analysis, and the Equivalent SDOF method justifiably became the dominant method used in design manuals.

3.6.2 Maximum rebound deflection

The initial analyses by Fox and Harris [29,30] showed that for elastic response to bomb blast loading the maximum response at some frequencies was in the rebound, giving a larger equivalent suction than an equivalent pressure. The blast analyses that this was based on gave negative to positive impulse ratios that are high compared to

modern values for bare charges. This could be because part of the positive impulse was converted into fragment impulse, or because the early pressure gauges could not accurately measure the rapid pressure changes in the positive blast pressure phase.

The use of the first root of the velocity equation by Wise [33] to define the time of maximum deflection limited the method to the initial inwards response. The subsequent peaks were assumed to be smaller due to damping. This assumption was not justified, as the UK research showed analytically that the first rebound will be more critical at some frequencies. The Friedlander loading curve used by Wise has equal positive and negative impulse, but Fox & Harris [29] had shown that, even for equal impulse (i.e. a β value of 1 in Fig. 8), the equivalent suction could be of the order 30% greater than the equivalent pressure at some frequencies due to the different durations of the two impulses.

The practice of considering only a simplified positive phase loading and ignoring the negative phase loading was introduced in Ref. 14, and has been followed in all of the subsequent military manuals.

This was justified in its original context of designing reinforced concrete subject to large plastic deformation, as the rebound deflections will be small or non-existent if the inward plastic deflections are significant. The elastic-plastic charts produced by Newmark [34] did not cover ductility ratios less than 1, i.e. elastic response of reinforced concrete.

However, in subsequent manuals the limitation of this approximation has been lost, and this simplified loading has been used for elastic design charts and for charts of rebound reactions after inwards plastic deformation, even though this may significantly underestimate the worst case.

In the revised TM5-1300 [24] it was proposed that charts based on a positive triangular load should be used to calculate the breakage of glazing. This would fail to account for the cases where glass fails to break inwards, but breaks outwards on rebound, although this behaviour has been well documented in reports of explosions and trials from the Second World War to the present.

Even using numerical methods of SDOF analysis, many computer programs based on methods presented by Biggs [35] only ran until the first inwards peak deflection had been identified. Such methods are inadequate for calculation of elastic response. For elastic analysis that may involve rebound, a numerical analysis incorporating the negative phase loading will be required.

3.6.3 Accuracy of published SDOF parameters

The maximum plastic resistance values adopted in Ref. 16 are more upper-bound than the upper-bound yield line method. This will result in an exaggerated resistance which will be non-conservative for deflection and deflection ratio. Classic yield line solutions for rectangular panels have been available since 1922 [43], so the claim that the plastic analysis is based on yield line methods is at best only partially true, and the resistances used are upper bound.

The result of the 45º yield line constraint is to introduce error into the other SDOF parameters. This approximation is commonly used in static design, where the only parameter required is the resistance. The error in resistance is small because the critical resistance occurs at a turning point, where a moderate error in the yield line angle will produce a small error in the resistance. This is not the case for other parameters. A moderate error in the angle will produce a moderate error in the transformation factors, which are not at a turning point, while a moderate error in angle may produce a large error in reaction coefficients because it invalidates the assumption of no shear transfer across the yield line, and because the calculation can involve small differences between larger numbers. The effects of this are reviewed in Chapter 5.

Ref. 17 introduced calculation of plastic resistance by the Equilibrium Yield Line method to identify the critical location of the yield lines. For the classic patterns used, the method employed is correct, except for panels with a free edge, where nodal forces to represent shear and torsion across yield lines are required, according to yield line text books [39]. However, instead of using a more complex yield line pattern such as corner levers or fans to reduce the conservatism of the upper-bound calculation, a yield line strength reduction has been introduced indiscriminately. The effect of this has been to reduce the resistance in most panels more than can be justified.

The smaller and more selective reduction in resistance used in Ref. 23 is closer to the true resistance, as is shown in Chapter 5, where some advanced yield line analyses are presented. However, it does not modify the deflected shape for calculating other parameters.

Given the crude approximations of elastic deflected shape used in Ref. 16, the citation of Timoshenko [38] for elastic stiffness is rather ironic, as the values are calculated using the Levy method described in Ref. 38, which would have been suitable for deriving all the correct elastic deflected shapes.

The approximation of the deflected shape and the assumption of no shear on 45º lines in the elastic cases were apparently introduced to minimise the calculation required in the preparation of the manual, but have introduced possibly significant errors into the many calculations that have used the data since. The scale of the differences between Refs 35, 17 and 40 and subsequently the differences found between Refs 35 and 6, indicated the need for a ‘root and branch’ review of all the slab parameters, as has been undertaken in Chapter 5.

The more accurate transformation factor given for the square panels supported on all edges in Ref. 17 was a significant improvement. However, the inappropriate interpolation used for all other transformation factors produces larger errors than the approximations in Ref. 16. Comparison with Mayor & Flanders [39] and Morison [6] shows that it would be more accurate to use the square panel transformation factor for any panel with all edges supported and an aspect ratio between 0.5 and 2 than to use the interpolation in Ref. 17.

There are other sources of approximation or error in the tabulated data in Ref. 16. K_L and K_M are rounded to two decimal places before calculating K_{LM} from the ratio. In a

number of cases, the rounding is inconsistent, and a few calculated rather than interpolated values appear to have been altered to give a more even step between aspect ratios at the expense of accuracy. In one elasto-plastic table, supposedly identical to the simply supported elastic table, an incorrectly typed value for K_M (equal to the value in the line above) has been used to calculate an incorrect value of K_{LM} that completely breaks the trend due to interpolation.

Overall, although the concept and principles of the Equivalent SDOF method were a significant advance, the implementation of the method in Ref. 16 for two-way panels left something to be desired, and the problems produced by this have extended forwards to the present. The interpolation of elastic K_{LM} in Ref. 17 spoils what would otherwise be a significant improvement in implementation of the Equivalent SDOF method.

4 Review of literature - The response of glazing to blast loading

4.1 Glass and glazing

4.1.1 Glass

Glass is formed from fused oxides [44]. The most common forms of glass are based on fused silica (SiO_2). The addition of soda (Na_2O) from wood-ash was found to reduce the melting point to under 700ºC, but resulted in a glass that can dissolve in water to form water glass, a viscous liquid. The further addition of lime (CaO), obtained by burning limestone, formed a more inert glass [45]. Almost all glass used in glazing is soda lime silicate glass, although borosilicate glass or aluminosilicate glass ceramics are also used where high resistance to thermal shock is critical [1].

Strictly speaking, soda lime silicate glass is a super-cooled liquid with viscous mechanical properties, as it is amorphous rather than crystaline. However, at room temperature glass possesses mechanical properties corresponding to those of crystalline solids. Glass has elastic properties and strength, but does not exhibit plastic flow, so fracture will occur before there is any permanent deformation [46]. Short term viscous flow becomes perceptible at elevated temperatures above a value known as the "strain point", but the timescale for viscous flow at room temperature is of the order decades to centuries. For most practical purposes at room temperatures, and certainly for consideration of response to blast loading, glass can be treated as a linear elastic-brittle solid.

Glass has been used by man since pre-historic times, in the form of obsidian, a volcanic glass, used to make tools [47]. Glass is reported to have been discovered accidentally by the Phoenicians and used for decorative beads by the ancient Egyptians. Glass making was distributed around Europe and first brought to Britain by the Romans.

4.1.2 Window glazing

Window glass was hand-made until the end of the 19th century [48]. The three main methods of manufacture were:

- Crown glass, produced by blowing a balloon and then spinning it very fast to produce a disk. The outer portion beyond the central knob was cut into panes. This predominated for quality glazing until the mid 19th century.

- Sheet glass, produced by blowing a cylindrical balloon, and then cutting and straightening the cylindrical portion. Improved techniques involving swinging the cylinder in a pit to lengthen it were introduced in Britain in 1834. These allowed larger panes to be produced with an improved surface finish.

- Polished plate glass, produced by casting on a table and then grinding and polishing to produce a smooth surface. This allowed larger panes of greater thickness to be produced, but was expensive, even when steam power was introduced for the grinding and polishing from 1800.

The early 20th century saw the mechanisation of sheet and plate glass production [48], and the elimination of significant crown glass production.

Machine drawn cylinder sheet glass was first drawn in the US in 1903, and produced in Britain from 1910 to 1933. Forty foot high hollow cylinders of glass were drawn vertically from a tank and annealed. The glass was then cut into shorter cylinders, which were cut lengthwise, re-heated and flattened.

Flat drawn sheet was invented in Belgium in 1913 and introduced to Britain in 1919. Production is still covered in modern standards [49], although it is no longer used extensively. The glass is drawn vertically in a flat sheet until it cooled sufficiently to be cut. It was noted for having a "wave" of optical distortion in one direction only, rather than in both directions in earlier production processes.

Drawn sheet window glass was made in large quantities, but only in a few thicknesses. Currently four thicknesses up to 6mm are available, of which the thinnest, 3mm, corresponds to a weight of 24 oz/ft^2 [1], but thinner sheet glass used to be available. In practice, thickness variations of at least 10% appear to have been normal for sheet glass.

Continuous polished plate glass was cast and then subsequently ground and polished on a conveyor belt. The process was introduced to Britain in 1923. The method was capable of producing a greater range of thicknesses than drawn sheet glass, to a fine quality without distortion. It was commonly used for large panes such as shop windows, in thicknesses greater than could be produced by drawing.

Rolled plate glass has been used since the mid 19th century for obscured glass where patterns are rolled into the surface. As well as domestic applications, this was used extensively for railway station roofs and similar roof lights, and it is still covered by modern standards [50].

Float glass was developed in Britain and launched in 1959. It is the standard modern method of producing window glass world-wide [51]. Molten glass flows over a weir on to a bath of molten tin, and is drawn off horizontally in a continuous process [48]. The molten glass floats on the denser molten tin and cools on the tin to a temperature below the melting point of glass, while remaining above the melting point of tin. The process produces a fine quality of glass to closer tolerances than drawing, with a mirror like reflection and without any wave or distortion. A wide range of thicknesses can be manufactured, typically up to 25mm [1], by adjusting the flow and draw rate of the glass.

As part of normal production, all types of sheet glass are annealed. Glass is passed through annealing ovens where stabilisation followed by a slow, controlled cooling occurs from a temperature above the "strain point" of about 250ºC, either on original

cooling or after re-heating. This will minimise locked-in stresses in the glass [46]. Normal float glass, used for the great majority of glazing, is often referred to as annealed glass.

4.1.3 Safety Glass

Safety glazing is specified for situations where there is a risk of people impacting glazing [51]. Safety glazing is identified by its resistance to impact and its breakage characteristics. In impact testing, safety glass should either not break or should break in one of two ways:

- Disintegration occurs leading to a large number of particles that are relatively harmless
- Numerous cracks appear, but the fragments hold together and do not separate. No significant openings should appear, and the mass of detached fragments should be limited

In addition to some plastics, two types of glass are most commonly used for safety glazing: toughened glass or laminated glass.

Annealed glass can be strengthened to form toughened glass by tempering heat treatment [46]. Sheets of glass cut to their final size are heated close to softening point, and then cooled rapidly, causing the surface to shrink and harden rapidly. Subsequent cooling of the core of the glass results in a compressive pre-stress in the surface of the glass, and a balancing tensile stress in the core. As breakage of glass is normally caused by tensile cracks that initiate at the surface, the surface pre-stress inhibits glass breakage.

Toughened glass (fully tempered in American parlance) has a surface compressive prestress in excess of 70 MPa, and typically about 100 MPa. The energy of the locked-in stresses is sufficient, once released, to cause propagation of cracking through the whole pane. The glass tends to break into small cubical pieces, with the size of the pieces reducing as the prestress, and hence locked-in energy, increases. The number of fragments per unit area is therefore often used as a quality control measure for the tempering process. This break-up process, called ‘dicing’ results in small fragments with fairly blunt edges [46].

Prior to the introduction of float glass, plate glass was subjected to toughening. Glass down to 3mm in thickness can be toughened, but because thinner glass will tend to warp, glass panes thinner than 6mm are rarely toughened [46], so only the thickest of sheet glass would have been suitable. Modern toughened glass is invariably float glass.

The greatly enhanced breaking strength, combined with the smaller, safer fragments when the glass breaks justifies the status of toughened glass as a safety glass.

“Heat strengthened” glass (partially tempered in American terms) has a surface compressive stress in the range of 20-50 MPa, most typically around 40 MPa. This will increase the breaking strength, although to a lesser degree. Heat strengthening

involves lower temperatures than toughening, and tends to avoid the surface ripple that often occurs in toughening [46]. However, the locked-in energy is insufficient to cause crack propagation throughout the pane, so the glass will tend to crack directionally into larger jagged sections, as for annealed glass.

Although in common use elsewhere in Europe, heat strengthened glass was not in regular use in the UK until the 1990s, and is not regarded as a safety glass. The lower strength enhancement and the jagged fragments when broken are substantial grounds for this exclusion.

Laminated glass is a sandwich of two or more plies of glass bonded to polymer layers. The most common polymer material used is plasticized polyvinyl butyral (PVB). Mechanically, PVB is a soft non-linear viscoelastic solid that, in addition to bonding the glass together, will stretch as a membrane after the glass has broken.

Lamination was originally developed to produce safer car windscreens, but today is used also in aviation and architectural applications. Sheets of PVB are placed between glass sheets and pressure and heat are used in an autoclave to exclude air and to bond the PVB to the glass surfaces. When broken, the glass fragments mostly adhere to the PVB, and the PVB membrane, anchored at the perimeter, retains the glazing in place.

This post-cracking retention of fragments and the residual strength of the PVB membrane are the reasons why laminated glass is treated as a safety glass in architectural glazing. Because most of the fragments are retained, the sharp edges and points of the broken glass are not exposed, and so can cause, at most, superficial cuts. There are also security benefits in resistance to intruders and in resistance to ballistic penetration, particularly from multi-layer laminated glass.

Lamination can be applied to heat strengthened and toughened glass as well as to annealed glass, although a minimum thickness of PVB of about 1.5mm is required to laminate toughened glass, to accommodate the surface ripple produced by the heat treatment.

4.2 Early research into blast resistance of glazing

4.2.1 British Research in World War II

In REN 585 [31], Philip summarised all of the UK blast research between 1939 and 1945. The research on blast effects on glazing is summarised by Philip in Part II, Section ii of the document.

A significant proportion of the research on glass was aimed at reducing the hazard from existing glazing, with free-field blast tests, blast tunnel tests and studies on various forms of strengthening, protection and substitute materials. The only one of these subjects likely to have relevance to today's problems was cellophane treatment [2], which can be considered as a predecessor of today's anti-shatter films. The rest tended to be suitable only for the emergency conditions that held in wartime.

Other research more relevant to the analysis and performance of glass under blast loading involved measurement of natural frequencies, the analysis of glass panes using the Equivalent Static Load SDOF method, prediction of glass breakage for different threats, spans, and aspect ratios and assessment of glass breakage from selected bomb attacks. Most of the testing papers were written by the Road Research Laboratory and most of the analytical papers by Philip.

The documented work mostly took place between 1939 and 1942. Some later UK papers apply this experience together with subsequent knowledge of blast effects to provide more general formulae for glass breakage.

4.2.2 Assessment of fundamental frequency of glass panes

A number of reports contain the results of measurements of the fundamental frequency of vibration of window panes of various sizes and types [53, 54, 55, 56]. Some of these window panes were existing windows at the Road Research Laboratory, and others were specially made for vibration measurement or blast testing.

The results were related to theoretical formulae, for simply supported plates from Timeshenko's "Vibration Problems in Engineering", and for clamped plates derived by the Rayleigh method in RC 58 [53].

In Ref. 53, measurements of existing windows puttied into timber frames gave frequencies with significant scatter compared to the formulae. One pane, unputtied and supported by a light wooden frame, gave a fundamental frequency of half the simply-supported value. Excluding this, the mean of the 11 other measurements, for windows puttied into frames of clamped in by wooden fillets, closely matched the simply supported formula.

In Ref. 55, glass panes, 0.12″ (3.0mm) thick with a 9″ (229mm) clear span, gave consistent results for aspect ratios between 1 and 4 when cast into concrete frames. For edges cast-in only 1/8″ (i.e. one thickness) the fundamental frequencies were about 125% of the simply supported formula, while edges cast-in 1½″ (12

thicknesses) gave frequencies about 85% of the clamped formulae. Forty panes 0.127″ (3.2mm) thick, 11.75″ by 16.5″ (298mm by 419mm) clear in a large frame with a 5 x 8 layout gave an average frequency 82% of the clamped frequency with a range +16.3% to -14.2%, and no significant correlation with position in the frame.

In ref. 54, sixty panes of 24 oz. (nominal 0.114″ or 2.9mm thick) sheet glass 12″ by 18″ (305mm by 457mm) were fitted into four frames in a 3 x 5 configuration for blast trials, some by putty alone, and others by sprigs and putty. Excluding 4 unsuitable records, the average frequency measured was 128% of the simply supported frequency.

The frequency of a number of plate glass roof panes ¼″ thick and 2′ by 7′ (610mm by 2134mm) were also measured, three rolled plate glass, two toughened and two wired. The mean frequency of the panes was 123% of the simply supported frequency.

In Ref. 56, two series of tests were conducted on 24oz (nominal 0.114″ or 2.9mm thick) sheet glass, the first with panes from 27″ (686mm) to 7.5″ (191mm), and the second with panes from 55″ (1397mm) to 7.5″, with 1, 4, 9 or 16 panes in a frame depending on size. Frequencies of tested panes were measured and averaged 110% of the simply supported frequency. Some frequency measurements of 55″ and 27″ panels were made in the first series, although these were not blast tested at the time. The 55″ mean frequencies were 4.4 times those of the second series, and the 27″ were 0.78 times those of the second series. It is not clear why they differ so much, but it is possible that the 55″ frequency measured was that of a higher mode of vibration.

Somewhat different conclusions have been drawn from these results at different times and by different people. Initially, Philip assumed sheet glass restraint (generally in domestic sash or casement windows) to be half way between pinned and clamped, but plate glass (typically in larger shop-fronts) to be pinned [32]. Later trials of sheet glass were subsequently analysed based on values at one tenth of the range between pinned and clamped [56]. Wise has assumed that newly puttied windows can be treated as restrained (i.e. partially clamped), old but still well fitting panes as pinned, and loose panes as ‘free’, i.e. as if pinned for a span 25% greater [33].

4.2.3 Blast testing of glass

Several blast trial series are reported, including, in some cases, interpretation of high speed filming of the glass damage [31].

In Ref. 57, twenty six panes of untreated glass and four of treated glass were tested and filmed at 1000 frames per second. Damage that occurred early in the pressure phase tended to form circumferential crack patterns, while damage that occurred later tended to form radial patterns similar to static damage. For panes with a static capacity of 0.72 psi, an equivalent static load of 0.6 psi failed to cause cracking, while an equivalent static load of 0.8psi caused 4 of 5 panes to crack, which was regarded as confirmation of the Equivalent Static Pressure method.

Further testing is reported in Ref. 56, with a range of charge sizes and pane sizes. This was primarily to provide a check on the Equivalent Static Load method. Panes up to

17" performed consistently with the analysis method, subject to some observations on possible conclusions drawn from tests using small charges, and a trend for larger panels to perform less well, which was tentatively attributed to the "Flaw Theory" of glass failure (see Section 4.3.5). The results for larger panes required abandonment of the "tentative assumption" in Ref. 30 of linearity with frequency for low natural periods described in Section 3.2.1.

One interesting test [58] included static tests to failure of fresh glass and glass that had been subjected to 20 blasts in a blast tunnel at a level below that required to fail the glass. No loss of strength due to repeated blast loading in the elastic range was noted.

4.2.4 Analysis of glass panes under blast

The key papers for analysis of glass were those of Philip, RC 163 [32] and its addendum REN127 [59]. REN 583 [60] provided later review, and data sheets [61,62] summarised the conclusions in 1945.

The maximum static pressure for a given modulus of rupture can be written in terms of the square of the shortest span and a coefficient α for different fixities and for the aspect ratio λ, the ratio of the short and long sides a/b. Similarly, for a given material stiffness, the natural period can be written in terms of the square of the short span and a coefficient β based on the fixity and aspect ratio.

These two coefficients, α and β, can be combined to give the maximum pressure as a function of the frequency, with a coefficient that peaks at an aspect ratio λ of 0.3 [32]. The values of the coefficients are different for clamped, pinned and mean fixity, but the shapes of the curves are very similar, as shown in Fig. 24.

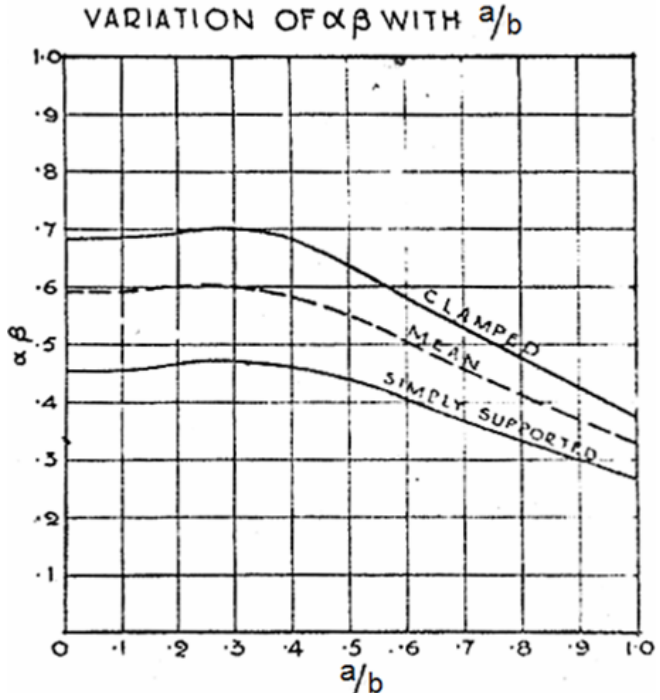

Figure 24. Variation of the coefficient product $\alpha\beta$ with aspect ratio [32]

From the blast measurements and analyses in Ref. 32, curves for the maximum values of the equivalent static load for side-on blast were plotted against frequency for a 500 lb bomb at 50 ft, 100 ft and less reliably at 200 ft. Values for reflected blast were assumed with a reflection factor of 2.0. By combining this with the two relationships above, a range of relationships were plotted, including the maximum allowable pane size against aspect ratio for a given glass thickness and strength, and a given charge and range. At longer ranges these curves can become asymptotic, and all sizes of panel above a certain aspect ratio may remain intact.
Plots were made of the panel size for marginal breakage against the range from the 500 lb bomb for several aspect ratios, using a theoretical blast decay with range. This was applied in analysis of the damage caused by similarly sized German 250 kg bomb as shown in Fig. 25. The ranges for the three measured trials fit reasonably onto these curves. For a given bomb and glass thickness there will be a range beyond which all sizes of panel should remain intact. Although this value will vary with the aspect ratio, the value for an aspect ratio of 0.3 will represent the worst case.

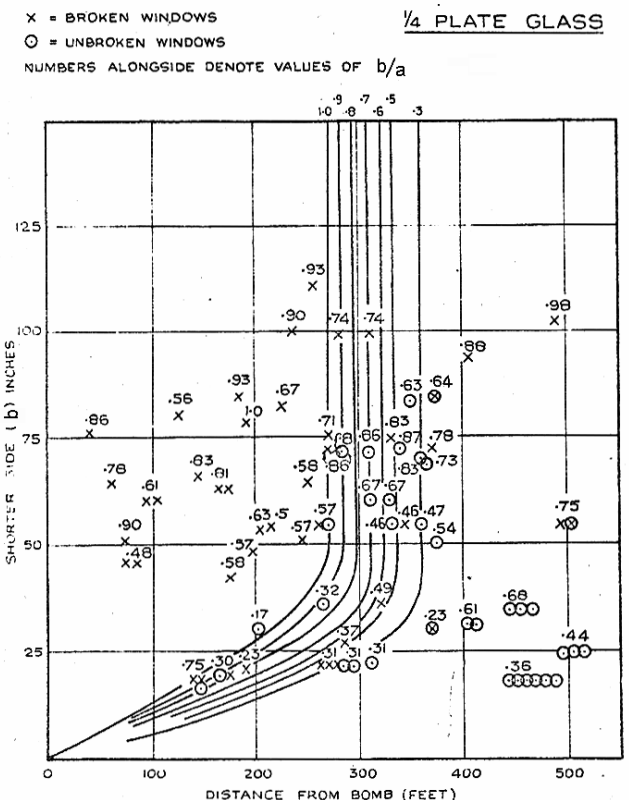

Figure 25. Panel size – range plot with data from Portsmouth [32] (¼″ plate glass, 250 kg bomb)

By assuming some relationships known to be approximately true, it was possible to produce a single curve for a particular bomb defining the theoretical breaking line, plotting 1/frequency against a strength parameter that takes account of aspect ratio. These two parameters could be plotted for any particular window. Windows above the line were expected to break, and those below the line were expected to remain intact. As with the panel size against range plots, the upper end of the curve for ‘large panes’ was a straight line, and the lower end for ‘small panes’ was a curve approximated to a parabola.

Data from a damage survey of plate glass due to damage from a 250 kg bomb in Portsmouth was plotted on both span-distance and 1/frequency plots, and a curve plotted through the zone of mixed breakage, as shown in figure 26. In practice there is significant scatter, so that a mean line and boundaries at about 5% and 95% breakage were drawn. Similar 1/frequency plots were also drawn for damage by similar bombs at New Malden and Tolworth. To get alignment of data from plate and sheet glass damage at New Malden, the breaking strength of sheet glass was assumed to be three times that of plate glass. Some of the scatter was thought to be the result of pane orientation and shielding due to factors like detonating on the same side of the street (giving side-on pressure) or the far side of the street (giving reflected pressure).

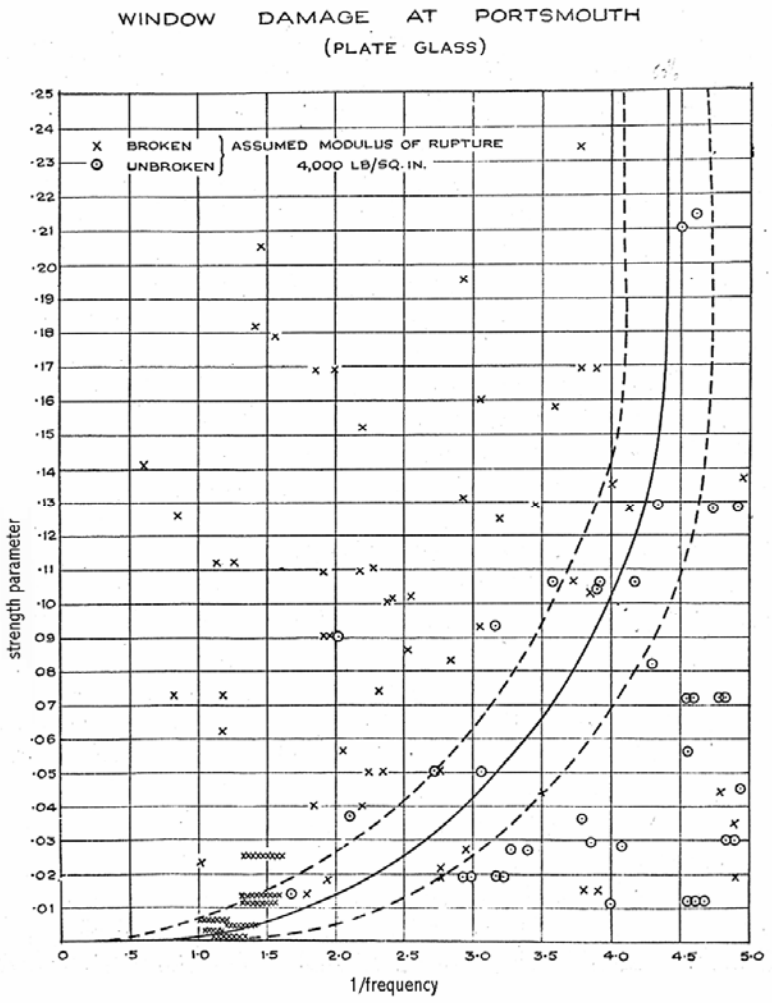

Figure 26. Strength –1/frequency plot with data from Portsmouth [32] (¼″ plate glass, 250 kg bomb)

The curves derived from damage were of similar shape to those derived from pressure histories of blast trials, but of lower amplitude. This was attributed to a surface detonation and full exposure of the gauges in the trials, as opposed to the bomb falling on and demolishing a building at the survey sites, with possible shielding by other buildings.

In REN 127, Philip [59] corrected a minor error arising from the Poisson's ratio for glass being taken as zero in Ref. 32, and indicated that further damage surveys suggested that sheet glass strength was double rather than triple that of plate glass, but that this justified a stronger plate glass rather than a weaker sheet glass.

In REN 119, Philip [60] used further blast trial data and further damage surveys to provide 1/frequency curves for a number of other types of bomb or mine. She was testing a "universal curve" that could be applied to all bombs based on the weight of the explosive charge, and derived from the results of a substantial number of damage surveys.

The "Universal Curve" was provided as formulae for 50% breakage of "small" panes and "large" panes of plate or sheet glass in RE 2/4 data sheet 8B6 [61], in terms of the charge weight in the bomb, together with tables of the parameters for aspect ratio. 95% breakage and 5% breakage were taken to be at half and double the range respectively, and the size of pane at the transition was a function of the charge weight in the bomb, so all normal panes might be "large" for a small charge and all normal panes might be "small" for a very large charge. The data sheet noted that the formulae would account for all but the occasional freak breakage, but, because breakage is dependant on the shape and size of the panes, general rules for the range of damage from a particular explosion could not be given with any certainty. However, a simplified table of approximate ranges for typical household glazing and a range of bombs and mines was also included. It would not be appropriate to other types of glazing.

In addition to containing a general formula for structural damage range, which was the source for the simplified table in data sheet 8B6, Data sheet 8B7 [62] contained guidance on increased ranges from built-up areas for carrying out trials. There is considered to be a very small risk of damage at three times the 50% damage range, and "certain safety" at four times this range.

The blast trial data in REN 583 [56] was also used to test the " universal curve" formulae in Data sheet 8B6 [61], referred to as the "air raid" formulae. The smaller panes showed reasonable agreement between the test results, the "air raid" formulae and Equivalent Static Pressure analyses based on blast profiles, allowing for some shielding and reduced reflection in air raid situations. The larger panes showed progressively lower strength in testing. This was believed to arise from a number of causes, including:

- The blast profiles used were based on larger experimental charges (100lb +) than were required for 50% damage to large panels (2.5-5lb). It was considered that the large difference in scaled ranges could be the source of some systematic error in calculating the Maximum Equivalent Pressure and Suction values.
- The semi-empirical "air raid" data was derived from bombs with charges 100lb-3000lb and might not be valid for smaller charges.
- The "tentative theory" of a linear relationship in RC23 [30] to account for the presence of higher modes of vibration in the response (see Section 3.2.1 of this thesis) might be producing a systematic error for the larger panels with low fundamental frequencies.

- The “Flaw Theory” of glass strength, which implied that larger panes will be weaker (presumably a reference to Griffith flaws, which are discussed in Section 4.7.1.4).

One factor not considered at the time was the slenderness. The larger panes would be more slender, and would be more influenced by large deflection membrane effects.

In REN 585, Philip [31] remarks that because so much more was known about blast pressure curves in 1945, the theory in RC 163 [32], on which all of this was based, might be revised. This revision does not appear to have been undertaken.

4.2.5 Early American analysis

The paper by Wise [33] was based on RC163 [32] and the earlier measurements of fundamental frequency, but was contemporaneous with REN 583 [56] and the Data Sheets [61, 62], and this appears to influence the fixity assumptions and material properties used.

The assumed deflected shape of the restrained case was intermediate between a fixed and pinned deflected shape, and the Rayleigh method was used to calculate the fundamental frequency, the amplitude and the maximum stress, which is taken to occur at the centre of the longer edge.

Wise [33] also considered a loosely supported pane, in the light of the exceptional pane in Ref. 52 (see Section 4.2.2). There is a substantial reduction in frequency, which over the frequency range considered would cause a reduction in response, but a corresponding increase in the static stress would cause a reduction in the resistance.

The Friedlander curve assumed for the blast loading allows a single curve of Equivalent Static Pressure against frequency to be used for a blast of a given peak pressure and positive phase length to be derived. However, only the first root of the equation was considered, with subsequent roots assumed to be smaller due to damping. This ignores the possibility of a larger negative phase response at the second root, as demonstrated in some of Wise’s references.

Wise [33] used his formulae to calculate one “exceptional” example from Ref. 32 for which a bomb and range were given, although he appears to have mis-understood the reason for it being considered an exception; Ref. 32 also concluded that the failure had been caused by the threat that Wise analysed. This example showed that loose panes were less likely to break at the margins, and that a restrained pane was marginally more likely to break than a simply-supported one.

For calculation of radius of breakage tables, Wise [33] used the simply supported formula with side-on pressures to calculate an ‘average’ range, and assumed a trade-off between face-on reflection to enhance breakage, and shielding from the blast to reduce breakage. He used a range of breaking stresses for glass to try and bound the uncertainty, but all the Modulus of Rupture values used are low even by early UK practice, even though three out of four references given for this were UK papers.

The methods used by Wise [33] give cleaner and easier calculation, but the approach is strongly theoretical, and has only been compared with two cases. In addition to that from Ref. 32 above, he analysed an accidental explosion of 2136 tons of explosive at Port Chicago, California, where he concludes that larger panes would be expected to be broken under favourable conditions at the 25 miles reported maximum range of damage. The radius of breakage tables lack adequate pragmatic or experimental verification.

4.3 Research on blast resistance of glazing into the 1980s

4.3.1 Introduction

The early analysis of glass was mostly related to the effect of aerial bombs in wartime, and gave average breakage ranges with a rough estimate of probability variation. However, glass breakage in wartime was generally not considered important in the subsequent decades when wartime scenarios were based on nuclear weapons. Instead, the main glazing interest switched to safety in the event of an accidental explosion during storage, processing and transportation of munitions or explosives, a vapour cloud explosion, and to the vulnerability of glazing to shock waves caused by sonic booms from aircraft.

Initially this was based upon statistical analysis of the extensive wartime damage surveys, and of surveys following accidental explosions [13], but experimentation and analysis continued through to the end of the 1970s, albeit at a lower pace and with a wider range of participants. A good summary of developments over this period is given by Prichard [63].

In the 1980s there was a resurgence of relevant glazing research in America, focused on two centres. The first, interested primarily in the response of glazing to blast, was at the US Naval Civil Engineering Laboratory, perhaps because the Navy controlled the largest munitions stores in the US. The work on glass, primarily by G Meyers, was part of an extensive program of research and development on Explosives Safety. The second was Texas Technical University, where a Glass Research and Testing Laboratory was set up, initially aimed at researching glass under conventional loading.

4.3.2 Non-linear analysis of glass

Prichard [63] considered non-linear large-deflection response of square glass panes, using a SDOF analysis with coefficients from Biggs [34]. The difficulty with analytical models arises from the in-plane restraint conditions in the support of most glazing. The load-deflection relationship given by Timoshenko [38] for full in-plane restraint:

$$p = E\left(\frac{h}{b}\right)^4\left[21.9\frac{z}{h} + 31.04\left(\frac{z}{h}\right)^3\right] \tag{16}$$

where p is the pressure, z the deflection, h the thickness, b the span and E the Young's modulus, was not considered appropriate for glazing. Instead he cited a load-deflection relationship:

$$p = E\left(\frac{h}{b}\right)^4\left[21.9\frac{z}{h} + 2.72\left(\frac{z}{h}\right)^3\right] \tag{17}$$

found by Bowles & Sugarman [64] from experimental measurements, and an empirical equation for tensile stress in the centre of the pane σ derived by Seaman [65] from the results of Bowles & Sugarman [64] and Freynik [66]:

$$\sigma = E\left(\frac{h}{b}\right)^2\left[4.40\frac{z}{h} + 0.82\left(\frac{z}{h}\right)^2\right] \tag{18}$$

These were used to analyse the results of glass damage from some large igloo explosions, and also of some gas cloud explosions. For these long-duration blast loads, the amplitude of the pressure rather than the duration of the shock wave was found to be critical, as the maximum deflection occurred early in the loading.

This work on square panels gave an insight into the non-linear nature of large deflections of thin glass panes. However the limitation of the formulae to square panels restricted its practical application.

Moore [67] performed a series of non-linear finite element analyses to assess the behaviour of glass in satellite solar cells under the acceleration of launch into space. The geometric non-linear analysis of two-way spanning panes calculated the effect of large deflections on the stiffness and stress of glass plates. This demonstrated the weakness in all of the earlier analysis that had used small-deflection plate bending theory for all elastic analysis, including that for slender glass panes.

Once the deflection of an elastic plate exceeds 50% of the thickness, membrane forces start to have a significant effect on the response, with tensile forces across the span anchored by a compressive ring around the perimeter. As the deflection increases, the tension membrane forces enhance the resistance above that of bending, resulting in a non-linear resistance curve. The maximum tensile stresses are initially a combination of the bending and membrane stresses at midspan, but as the deflections increase beyond about twice the thickness for square panes, or more for other aspect ratios, the torsion and membrane stresses near the corners increase more rapidly and become dominant.

Moore's [67] analysis reduced this to two graphs, Figures 27 and 28, which plotted the deflection as a ratio of thickness against non-dimensional load, and non-dimensional stress against non-dimensional load, with the non-dimensional factors adjusted to apply to any slenderness. Five curves on each graph covered five aspect ratios between 1 and 4.

For any particular pane, the load-deflection curve could define a non-linear resistance curve, and for a given tensile strength, the load-stress curve could define the maximum resistance at cracking, and hence the cracking deflection.

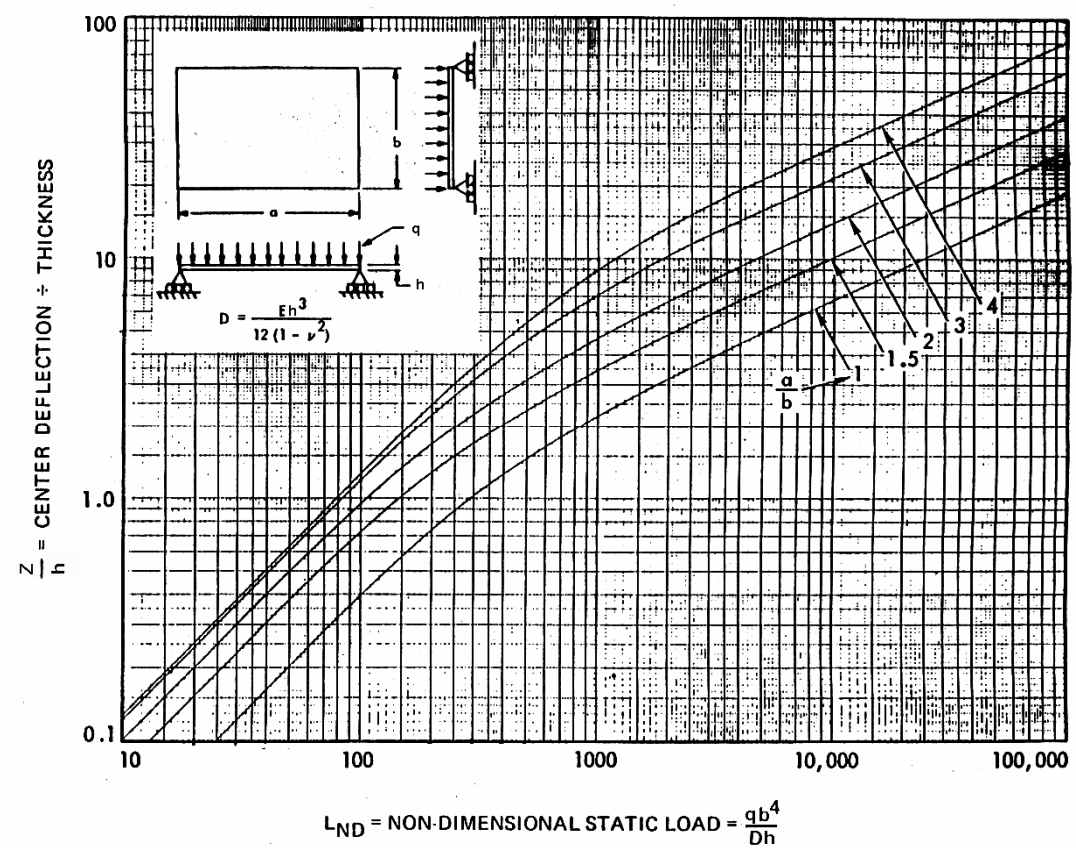

Figure 27. Moore's curves for deflection [67]

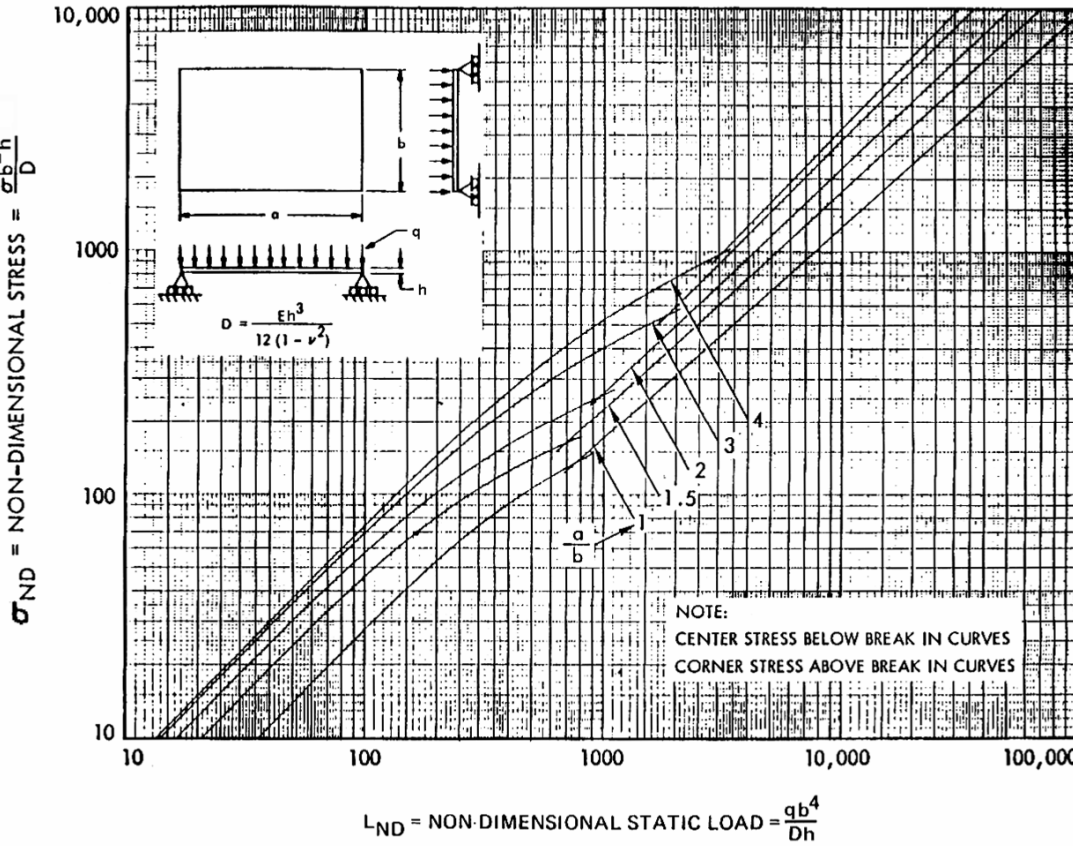

Figure 28. Moore's curves for stress [67]

Working around the same time as Moore, Vallabhan [68] at Texas Tech University also developed a non-linear analysis of glass plates, in his case using a finite difference method. His results compared closely with Moore's [67] for a worked example. He also compared it to a coarser finite element analysis in a PhD dissertation at Texas Tech University [69], which was similar, but not as close.

The finite difference analysis was faster to run on a computer than a finite element analysis, and greater detail was provided of the analysis of two numerical examples, as in Fig. 29, but the paper [68] did not provide the information required for use in a SDOF method.

The convergence parameters used by Vallabhan [68] were optimised for a quasi-static analysis with incremental loading. For suddenly applied loads the values were expected to require some modification, but further research would be required to identify the optimum parameter values. Each increment is solved independently of the previous one, which minimises cumulative error in an incremental solution.

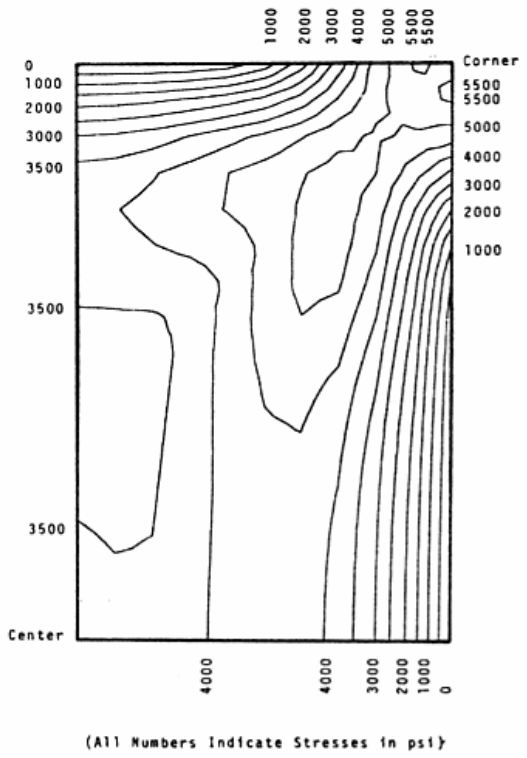

Figure 29. Typical contour map of principal tensile stress [68]

4.3.3 Blast resistant window design – Meyers and TM5-1300: 1990

Meyers [70] applied Moore's [67] resistance curve to an equivalent SDOF analysis under blast, and then used the curve of maximum stress to assess whether the glass would crack or not. However, the analysis used a triangular positive phase loading without a negative phase, and so did not model possible cracking on rebound.

As the objective of this work was to establish safe glazing designs at known ranges from explosives stores or process buildings, where the maximum licensed quantity of explosives was already known, Meyer was concerned with an acceptable low probability of cracking rather than a 50% probability. He used this analysis in conjunction with blast trials to estimate suitable design strength of different types of glass. He addressing annealed float glass, fully tempered (toughened) glass, and also polycarbonate.

At the US Department of Energy, Meyers wrote a computer program, BLASTOP [71], that employed large deflection SDOF analysis based on a resistance function of 10 linear stages derived from Moore's [67] data, to identify the maximum stress in a glass pane from a given triangular blast threat.

Although the Biggs-type numerical SDOF calculation extended beyond the first peak to pick up rebound response, the loading was limited to a triangular positive phase loading only.

The peak deflections were used to assess the 'bite' (as illustrated in Fig. 30) required to retain the glass during the blast response, assuming that cracking had not occurred.

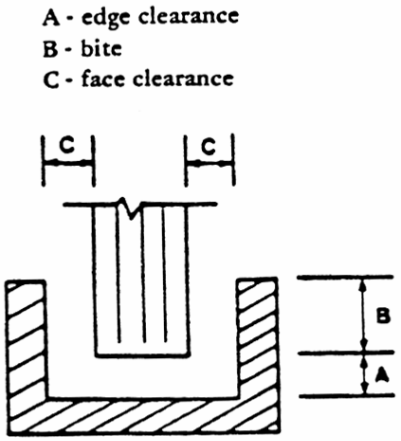

Figure 30. Identification of 'bite' [24]

Mean and standard deviation properties of various types of glass were used to calculate a probability of failure of the glass pane. Although different types of laminated glass were available options, all the calculations were based on failure at first crack.

Some of Meyers' work was incorporated into the 1990 revision of TM5-1300 [24], in a new section on blast resistant windows. Only monolithic toughened (fully tempered) glass was considered. The data was presented in two forms.

Firstly, graphs were presented that gave the blast loading as a peak pressure and time that would cause a less than 1% risk of glass breakage for a range of pane sizes, with different aspect ratios and thicknesses shown on different plots. These covered panes between 1 and 25 square feet and thicknesses between ¼″ and ¾″ (6.4mm and 19mm). Typical examples are shown in Fig. 31.

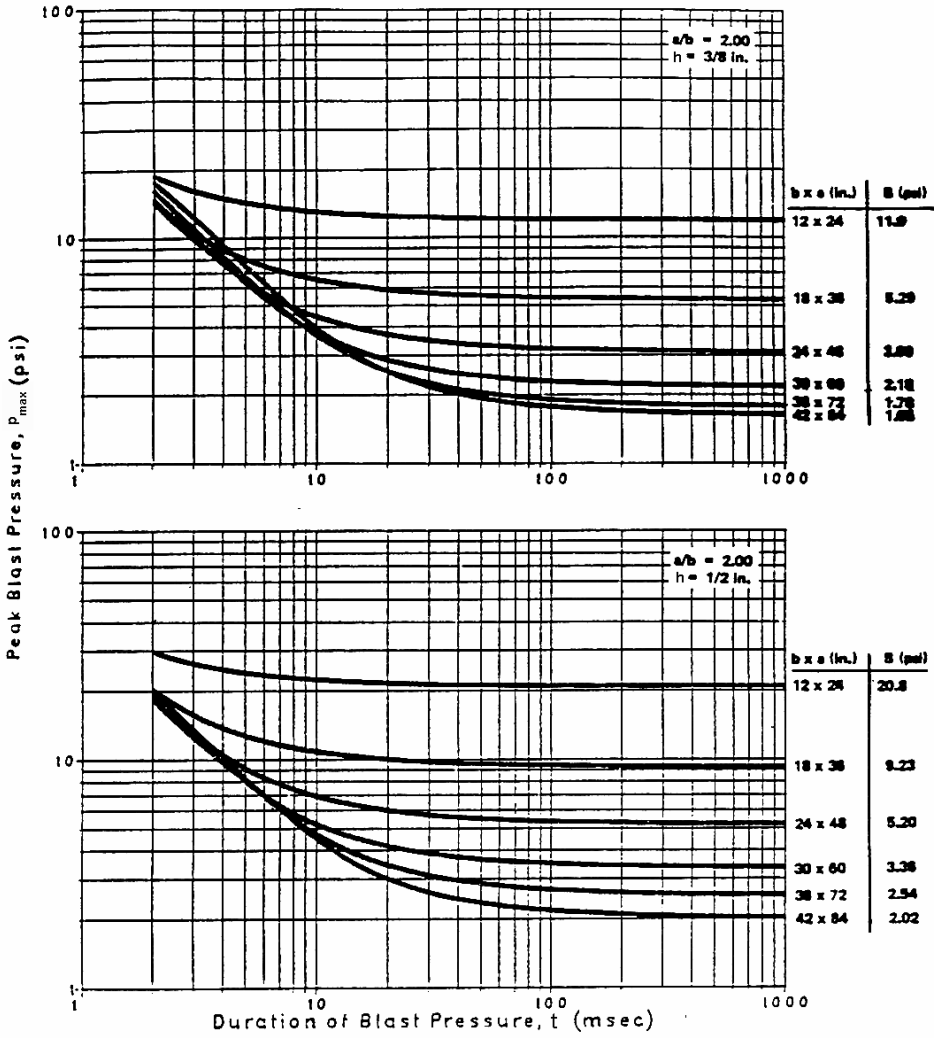

Figure 31. Typical plots of toughened glass blast capacity [24] (toughened glass panels 3/8″ and 1/2″ thick with aspect ratio of 2.0)

Secondly, where application of, or interpolation between, these curves was not considered appropriate, TM5-1300 gave a 10 step calculation process, and data tables to either identify panes for which small deflection theory was suitable, or to calculate a linearised approximation of the non-linear resistance curve. The TM5-1300 values of K_{LM} were used to estimate an equivalent mass and the mass and stiffness used to calculate a fundamental period. The SDOF chart for elastic response was then used to calculate the dynamic load factor and hence the load for a limiting deflection. As presented in Ref. 24, the method was based on a deflection that would cause either a maximum tensile stress of 16000 psi (110 MPa), or a deflection of 10 times the thickness.

The deflection limit of 10 times the thickness was included to ensure that the glass would not disengage from the bite of the supports specified. Ref. 24 cites work at Texas Technical University on edge displacement, and also on a glass failure prediction model and on non-linear analysis by finite difference.

Loading on the supports was specified from the maximum resistance, distributed in accordance with small deflection elastic theory, as half sine curves along the sides and

reverse concentrated reactions at the corner. It should be noted that this is substantially different from the reaction distribution prescribed even for elastic reinforced concrete elsewhere in Ref. 24, as shown in Fig. 32.

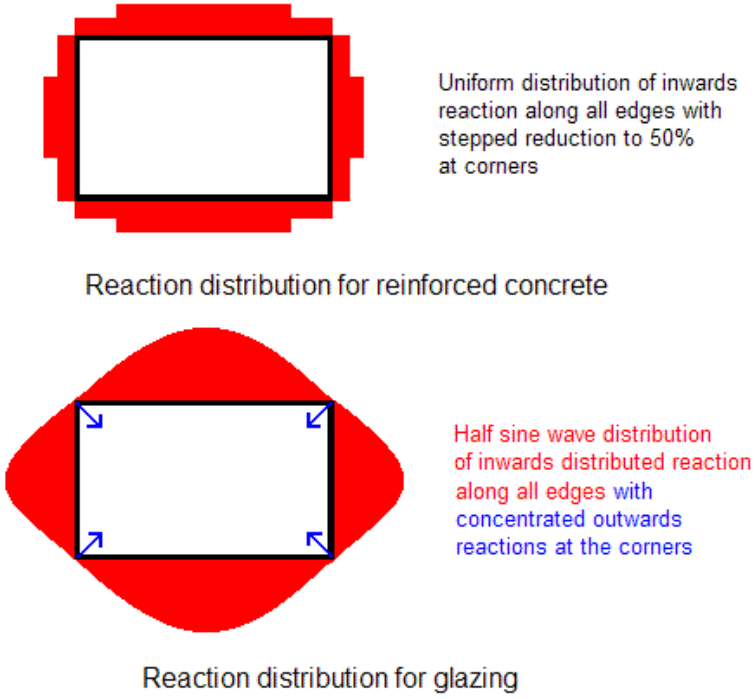

Figure 32. Different reaction distributions for reinforced concrete and glazing in Ref. 24

4.3.4 Mayor & Flanders – BLAST program

Meyers also supervised and advised Mayor and Flanders as they adapted a US Dept of Transportation computer program on behalf of the US State Department to provide blast resistance calculations for embassy walls and windows that might be subjected to attack by terrorists [40].

Mayor and Flanders incorporated a numerical SDOF calculation into the BLAST program, and so were able to use a non-linear resistance curve. A large deflection resistance function of glass has been used based on the curves produced by Moore [67], and linearised by Meyers [71].

As indicated in Section 3.5.5.3, Mayor and Flanders derived their own elastic SDOF transformation factors for walls. They acknowledged that for large deflection of glass, the deformed shape would deviate from that used to calculate the factors for small deflection, but a more accurate calculation would require knowledge of the deformation field of the FEA, which was not available to them. However, the small deflection factor as calculated for the elasto-plastic stage of solid RC walls of the same aspect ratio would be initially correct, so this value was used for the BLAST program.

4.3.5 The effect of weathering on strength

McLellan & Shand [45] state that it is generally accepted that fracture of glass originates in small imperfections or flaws, the large majority of which are found at the surface. Since glass does not yield, the applied stress, when high enough, causes these flaws to propagate. The stress concentration factor in the flaws, measured as the local stress over the nominal breaking stress, is of the order 100. If the distribution, size and orientation of flaws in the surface of a glass plate are random, then the cracking of the glass is a matter of probability, and this is the reason for the large variation of breaking stress among similar specimens. This is discussed further in Section 4.7.1.4.

Different methods of fabrication and treatment of glass will produce flaws of different characteristics and size. Hot casting as in float glass or flat drawn sheet is likely to produce the least number; hot working as for drawn cylinder sheet glass will produce more, while cold working as for polished plate glass will create more still. All window glass is likely to accumulate additional flaws in service, from contact and physical abrasion, from thermal cycling and from chemical attack of the atmosphere. Abrasion is often used in testing to increase the number of flaws to simulate aging. McLellan & Shand [46] indicate that abrasion reduces the average tensile strength, but also reduces the variability, as is shown in Fig. 33, where the modulus of rupture is the tensile failure stress for a particular flexural test configuration.

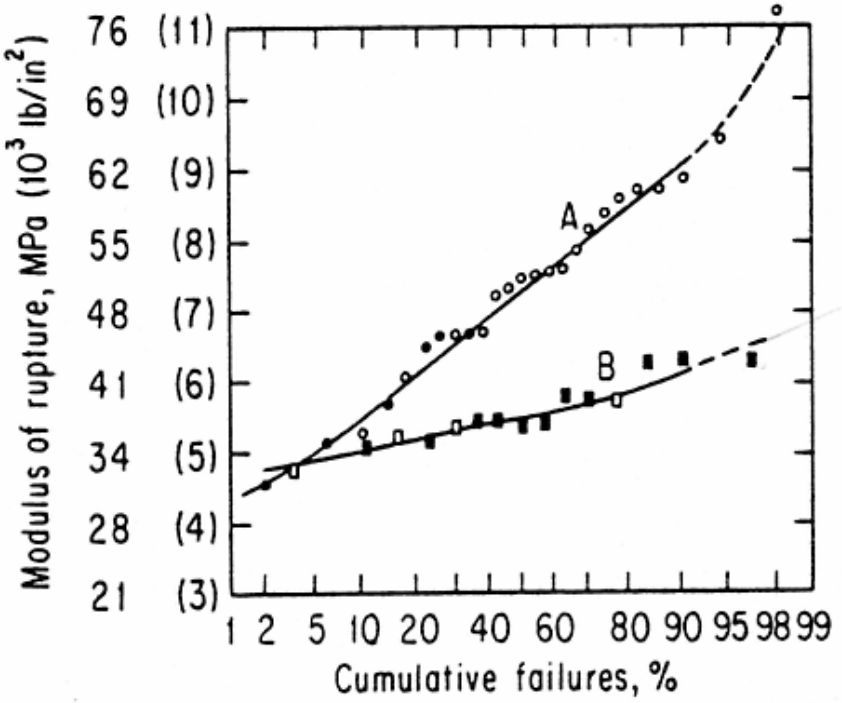

Figure 33. Effects of abrasion on the tension face of plate glass bars in flexure [45] (A – surface not abraded. B – tension face sand blasted)

McLellan & Shand [46] report that the fatigue characteristics exhibited by glass under static loads are somewhat similar to those of metal under cyclic loading. In both cases delayed failure results from slow propagation of flaws. Fatigue in glass is associated with the presence of water vapour in the surrounding atmosphere when the glass is under stress. Tests of annealed glass in a vacuum show very little loss of strength with

loading time. For loads of short duration, as in impact or blast, the atmospheric moisture has no appreciable effect, but fracture strength for sustained loading of 5 seconds in normal atmospheric conditions is of the order 40-55% of the short term strength.

Norville and Minor [72] addressed methods for characterising the strength of monolithic window glass plates arising from surface flaws, using data from 4 test series of new glass and 8 test series of glass weathered for between 8 and 25 years in buildings in Texas and Oklahoma, tested at Texas Technical University. Only the 78% of samples where fracture was initiated in the face of the glass were considered, with those where fracture was initiated at the edge discarded. In total, 383 tests of weathered samples and 77 tests of new samples were reported.

Tests were conducted by evacuating air from a chamber on one side of the glass sample to increase the loading in the glass linearly with time until the glass fractured. Loading rates which produced specimen failure in 3 seconds to 30 minutes were used for different series.

The Weibull cumulative probability of failure is given by:

$$P_f = 1 - \exp(-B) \tag{19}$$

where B is a risk function:

$$B = k \int_0^a \int_0^b [c(x,y)\overline{\sigma}_{\max}(x,y)]^m \, dxdy \tag{20}$$

In which $c(x,y)$ is a biaxial stress correction factor, $\overline{\sigma}_{\max}(x,y)$ is the maximum positive principal stress at any location x,y in a panel a by b, and m and k are surface strength parameters.

Norville and Minor [71] stated that it is impossible to measure m and k physically, although for a plate of unit surface area subject to uniform biaxial tension, the median failure strength (P_f=0.5) reduces to:

$$\sigma_0 = \left(\frac{0.693}{k}\right)^{1/m} \cdot Pa \cdot m^{-2} \tag{21}$$

Instead, the value of these parameters were calculated from a combination of a carefully controlled test of the sample to failure, a finite-difference nonlinear stress analysis, and a numerical integration of Eq. 20. Statistical analysis was then used to determine the best values of m and k for a given set of test specimens. The values from the new and weathered glass series are given in table 4 below.

Glass type in series	Range of parameters for series	
	m	k
New	8.0-9.9	$3.57\text{x}10^{-16}$-$1.75\text{x}10^{-23}$
Weathered	4.0-6.0	$1.19\text{x}10^{-12}$-$6.08\text{x}10^{-16}$

Table 4. Weibull distribution parameters for new and weathered glass

The cumulative probability functions for new glazing and glazing in-service for 20-25 years indicates a substantial difference in strength, although this may be due to the difference between sheet and float glass as well as due to weathering.

For float glass taken from cavity glazing in-service for 8 years, the outside face (OKC-1) had least strength, while the cavity faces (OKC-2 and OKC-3) had the greatest strength. Significantly, the reduction in mean strength was accompanied by a reduction in deviation so that the variation in strength for a low probability of failure was much less than for a median or high probability of failure, as shown in figure 34.

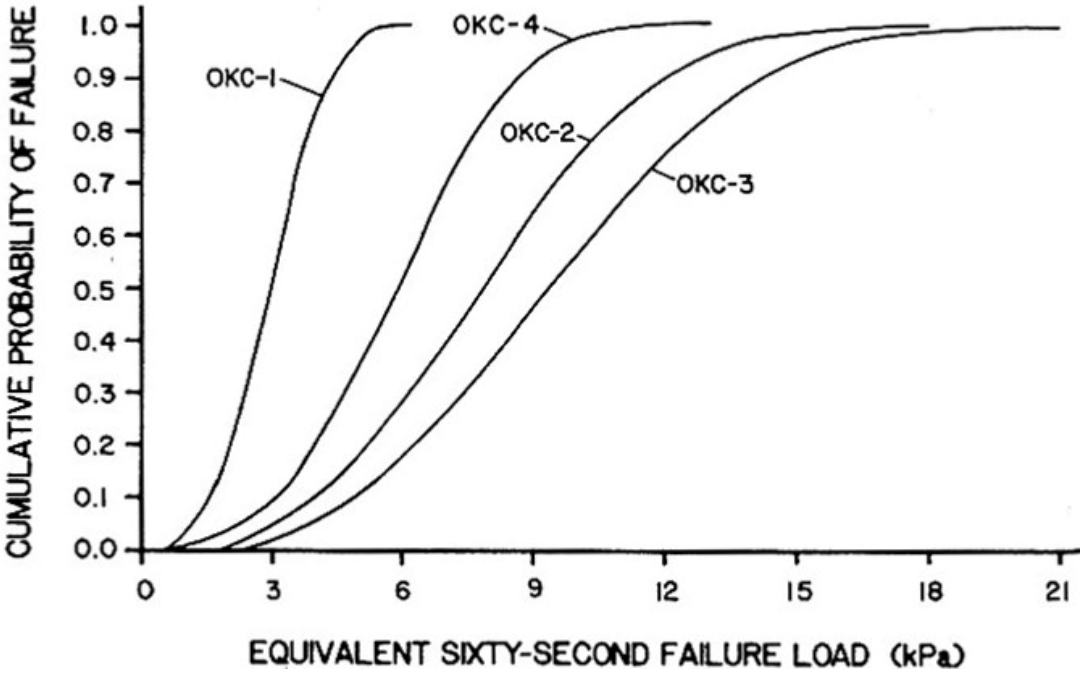

Figure 34. Effect of different degrees of weathering on the probability of failure [72]

4.4 Research on laminated glass

4.4.1 Low rate-of-strain behaviour of laminated glass

Minor and others at Texas Technical University [73, 74, 75, 76, 77] tested glass laminated with a PVB interlayer under low rate-of-strain loading. Ref. 73 summarized the work covered in the earlier reports.

Linden et al. [74] showed that, at room temperature, the deflections and corner stresses were close to values given by a monolithic non-linear model (implying near full composite action), although the mid-span stresses with a 0.76mm interlayer were midway between a monolithic and a layered model, and with a 1.52mm interlayer were closer to the composite model.

Behr et al. [75] conducted experimental and theoretical analyses of uncracked monolithic and laminated glass at a range of temperatures from 0 to 77ºC., looking at central deflections and central and corner principal stresses.

In Ref. 75, the monolithic glass, loaded to 5.17 kPa over 15 seconds at 22ºC, was used to validate the theoretical analysis based on the finite difference work of Vallabhan [68]. Deflections and centre stresses are within 5%. Theoretical corner stresses are about 15% low, but smaller grids near the corners in the finite difference model increase the corner stress and reduce the error.

It was also shown that laminated glass at 22ºC and 38ºC has similar deflections to monolithic glass equal to the total glass thickness, while the deflections at 49ºC and 77ºC are between monolithic and layered. Trends are similar for centre and corner principal stresses.

Behr, Minor & Linden [76] looked at the effects of interlayer thickness and at the effect of 1 hour sustained loading at different temperatures. At 22ºC doubling the thickness of the interlayer affected the stress by less than 10% and the deflection by no more than 5%.

For sustained loads at 38ºC, 49ºC, and 77ºC, Ref. 76 showed an increase of around 20% in the corner stress, close to the layered model, together with a slight reduction in centre stress and a 10% increase in the deflection, all relative to the initial values on loading to 1.4 kPa. This suggests that creep in the PVB interlayer makes the response to long term loading closer to the layered model compared to short term response.

Resnik & Minor [77] reported on eleven series of tests to failure on 20-25 units per series, all of laminated glass with a 0.76mm interlayer. These tests covered a range of annealed glass panel sizes and thicknesses at room temperature, a range of glass strengths for one size at room temperature, a range of temperatures for annealed glass of one size, and glass with initial damage. Conclusions included:

- At room temperature, the mean failure pressures were about the same as for monolithic glass.

- Mean failure pressures reduced by 12% at 49ºC and 25% at 77ºC.

- Prior minor damage to the compression face has little effect, but damage to the tension face caused a 41% reduction in mean failure pressure.

- Most failures initiated either in a broad central zone or a small corner zone. Most corner failures initiated at the edges within 2″ (3-5% of short span) of the corner. Most series had either predominantly corner or predominantly central failure, with a few series more evenly divided. *This is consistent with the stress distribution in Moore's data.*

- In any series with both corner and central failures, corner failures generally occurred at higher pressures than central failures. *This is consistent with failure based on pre-existing micro-cracks.*

- Thicker panes experienced more breaks in the centre, *which is consistent with a lower membrane effect at failure.*

- At higher temperatures, there were fewer breaks in the centre, *consistent with less composite action, and the glass behaving more like two thinner separate layers with greater membrane effect at failure.*

- With heat strengthened and tempered glass, all failures occurred in the corner zone, but almost all clear of the edges. *The former is consistent with greater membrane effect at failure, but the latter is not.*

The conclusions in Ref. 77 apply to low rate-of-strain performance, and are not necessarily relevant to blast resistance where PVB and glass properties may vary differently at high rates-of-strain. However, the relative performance is of interest, as is the observation of the point of initiation of cracking. The final conclusion could indicate that heat strengthening results in greater surface compressive stresses at the edges compares to the faces, so the maximum membrane stresses on the faces are generally more critical than the higher membrane and torsion combinations at the edges.

4.4.2 Blast testing of laminated glass

Barnard [78, 79] reported on a range of tests by the Home Office Advisory Branch in conjunction with the Property Services Agency (PSA), the Metropolitan Police and the Ministry of Defence in 1974 and 1975.

The tests were mostly aimed at evaluating possible protective methods that could be applied to existing windows to reduce injury from flying glass caused by terrorist bomb attacks. However, several different types of glazing were evaluated, including laminated glass in a range of thicknesses.

Preliminary trials at Waltham Abbey [77] used small charges between 1 and 2 lb (0.45 and 0.9 kg) at ranges between 18″ and 4′ (0.45 m and 1.22 m) loading glazed

targets inset into a timber target wall. The top and rear of the targets were not enclosed. Five of the 48 tests were on laminated glass, including 0.38, 0.76 and 1.5 mm thick interlayers in 6mm, 6.5mm and 7.5mm nominal thickness laminated glass.

Preliminary trials at Kirkcudbright [77] used line and cylinder charges between 100 lb and 230 lb (45 and 105 kg) at ranges of 14 ′, 25′, 35′ and 55′ (4.3, 7.6, 10.7 and 16.8 m). The glazing and frame was supported in heavy braced frames without enclosure at the top, side or rear. Five of 66 tests were on laminated glass, including 11.3mm 5-ply and double glazed 8mm 3-ply with 21.0mm 5-ply.

The tests described in Ref. 78 were described as an inexpensive method of determining the relative strengths of the materials under test in free-field or semi free-field conditions, prior to their evaluation under more realistic and fully instrumented test conditions. The variety of charge size, configuration and stand-off gave a substantial range of peak pressure and duration of the blast wave, but the fact that clearing occurred and back-face pressure was produced meant that the loading could not be related to loading on a building façade.

On laminated glass, Barnard [77] reported that no standard yet could be given for the thickness of glass that was required to withstand any given loading for a given window size. Laminated glass was reported as being considerably stronger than ordinary window glass, although even when the glass remained in the frame some high speed fragments could be produced when the inner face cracked.

It was noted that the thickness of the PVB interlayer was an important factor, as this provided the residual strength of the panel once the glass had cracked. The 0.38mm interlayer tore when, for the same loading, the 0.76mm interlayer remained in the frame. To utilise the strength of the laminated glass the frame also needed to be strong and securely mounted to the building structure. The glass needed to be bonded to the frame in an “amply deep” rebate with a strong but flexible adhesive. Epoxy polysulphide was suggested as a suitable adhesive, but surface preparation was critical – the thick laminated glass tended to fail at the polysulphide/ frame connection.

Trials at Shoeburyness [78] used 50 lb charges at ranges of 20′ and 35′. Ten shots were conducted with two, three or four targets for each shot, fixed in a frame at the front of a cubicle built of “Pendine” blocks (nominally reinforced concrete blocks 1800mm x 600mm x 600mm). The targets were either 1.17m by 1.07m or 1.17m by 2.29m in size. Eleven targets contained laminated glass as a single layer or as one or both layers of a double glazing unit. The laminated glass was reported as either 8mm nominal thickness with a 1.9mm interlayer, or 11.5mm “anti-bandit” glass that could have a 1.5mm interlayer.

In these trials [78], some laminated glass was retained in the frames by a mastic tape. These samples tended to fail with the cracked laminated glass being pulled from the frames, although some marginal failures still had one edge of the laminated glass anchored. Other samples were anchored to metal frames by epoxy resin. Under similar blast loading these were retained in the frame, with frame distortion, and some failure of the frame / epoxy bond. None of the laminated glass windows failed by tearing of the interlayer.

Following this, the PSA conducted two families of trials in the 1970s and 80s, under the aegis of the Forcible Attack Working Group (FAWG) and the Security Service special counter-terrorist research programme known as EDICTS. These have not been publicly reported, but included tests of laminated glass in a range of mounting techniques, adhesive materials and rebate depths.

EDICTS trials in the late 1980s, following terrorist attacks on army barracks, were aimed at assessing protection for accommodation buildings, and used standardised steel test cubicles with openings for test panels 1.55m by 1.25m (large) and 1.25m by 0.55m (small). A substantial database of test data was accumulated, which was used to create "isodamage" fragility curves that indicate the level of damage and fragment hazard that can be expected on a pressure /impulse chart, which is also marked with curves of charge size and range. A typical fragility curve is shown in Fig. 35.

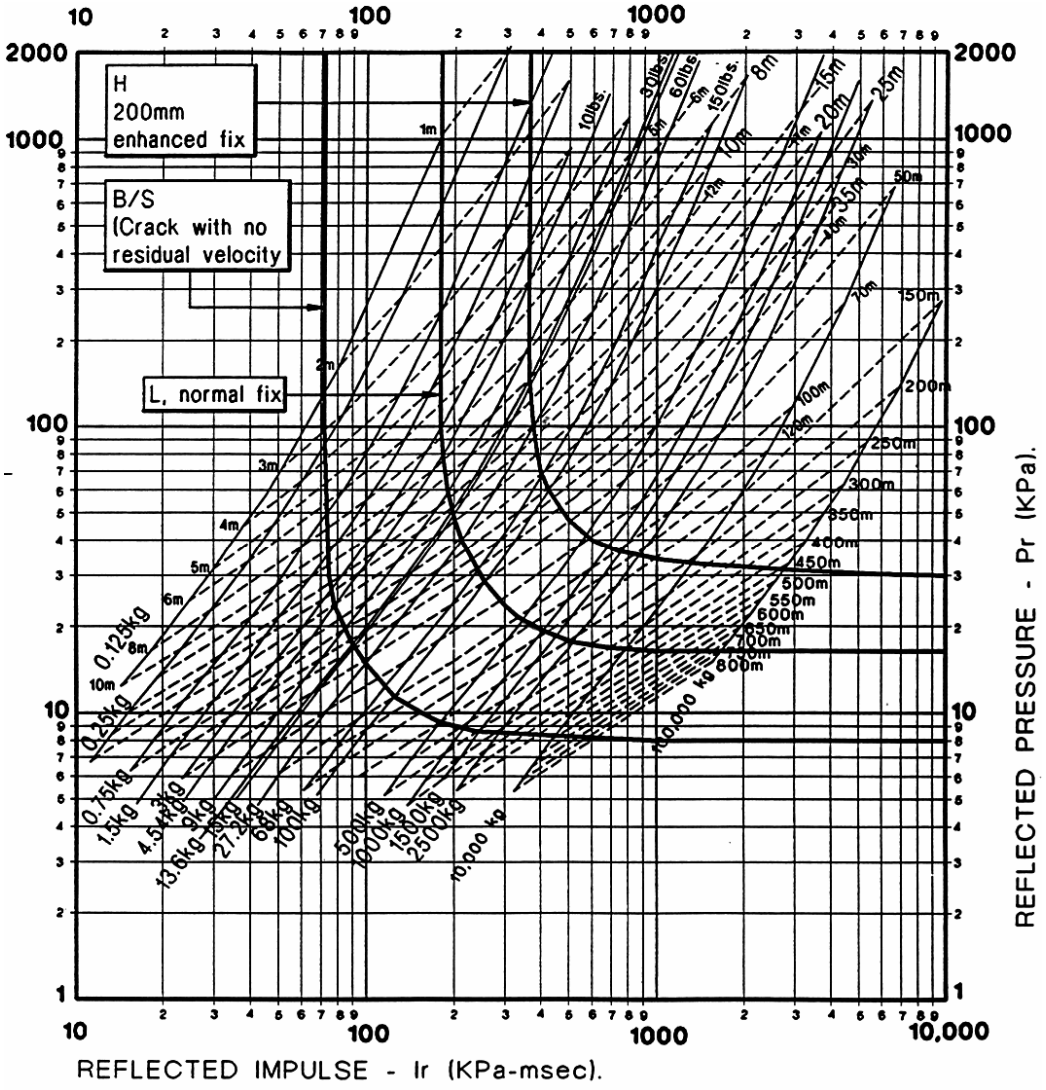

Figure 35. Fragility curves for "large" pane of 7.5mm thick laminated glass [81]

Early fragility curves for the two sizes of window tested [80] did not adequately allow for the clearing of the blast around the trial cubicles, and so over-estimated the blast impulse resisted by the glazing. Later fragility curves produced in a 1997 Glazing Hazard Guide [81] by the PSA's successor organisation, then part of the Security

Facilities Executive (SFE) and currently part of the Home Office Scientific Development Branch (HOSDB), compensated for the clearing, and presented the fragility in the face of the threat to the façade of a building.

As complete protection cannot always be assured from a threat of indeterminate size and location, attention was paid to the response after cracking. For conventional glass, a distinction could be drawn between glass just cracking ('break safe'), glass breaking and falling into the building at moderate velocity ('low hazard'), and glass breaking and flying into the building with sufficient velocity to cover a substantial volume and cause potentially fatal injuries ('high hazard'). There proved to be a substantial increase in the blast required to cause fatalities if damage to glazing and minor injuries could be accepted in the event of a terrorist attack. There was also a significant benefit if the probability of the response being exceeded was pitched at the 10% level implicit in most blast design for military attack, rather than the less than 0.1% criteria used for explosives safety in TM5-1300 [24].

For glass laminated with PVB, the benefits of considering the post-cracking response were considerably greater. Interlayers of 0.38mm thickness tended to be cut soon after cracking by the broken glass, but provided some enhanced resistance, and retained most of the broken glass bonded to the interlayer and often partially attached to the frame, reducing the hazard from flying glass. Greatest benefit was found with 1.52mm or more of interlayer anchored in a 25-30mm deep 'bite', where the PVB interlayer would stretch as a membrane and experience a substantial deformation before being cut or torn. This provided a substantial additional resistance after cracking of the glass, and the substantial stretching of a soft membrane spread the reactions over time, reducing the maximum forces exerted on the frame, and the risk of frame failure resulting in 'high hazard' fragments. It was also found that laminated glass used as the inner leaf of double-glazing would catch the debris from a monolithic outer leaf after it had cracked.

The fragility curves are based on the positive phase blast pressure and impulse, but the SFE Glazing Hazard Guide [81] acknowledges that the negative phase is influential, causing outwards cracking of most glass as the range is reduced from survival values, and reducing peak deflections and stresses in laminated glass membranes for large panes, particularly for small charges at short range.

This research resulted in recommended minimum glazing protection levels for UK government buildings [82, 83] that continue to be updated. Two other factors have resulted in these minimum standards of protection spreading into significant private sector use. One was the extension of the Provisional IRA terrorist campaign to economic targets in the UK mainland in the 1990s, and the other was the so-called 'COMBLAST' co-operative blast testing scheme first organised by the PSA, and continued by successor organisations. A series of testing weeks were organised in which glazing manufacturers were able to share facilities and costs for blast trials to develop and prove blast resisting glazing systems that have then been commercially available for incorporation into buildings. This has also increased the HOSDB database of test data.

The 1997 fragility curve charts [81] also incorporated tentative resistance tables, although only a few points on the curves are tabulated. The data up to cracking are

based on Moore's [67] data, but the laminated glass resistance beyond cracking was given by a peak value representing a near linear resistance curve. In practice, only the area under this curve is known, representing the capacity to absorb energy shown by the testing. For the standard sized panels, a limiting deflection was selected arbitrarily, and a tentative resistance curve scaled up to give this maximum deflection at zero velocity. The resistance of the scaled-up curve at the maximum deflection was taken as the maximum deflection.

The limiting deflections selected were not consistent, equal to 9.4% of the short span b for the small panel, but 16% of the short span b for the large panel. The reason for this discrepancy is not known, but it is understood that the limiting deflections may have been estimated by eye from oblique views in high speed video films of marginal tests.

4.4.3 Recent evaluation of uncracked laminated glass

Earlier analysis of laminated glass at Texas Technical University had used an upper-bound stiffness model equivalent to a monolithic pane of thickness equal to the total thickness of glass in the laminate, and a lower-bound model of two glass plies with no shear transfer. Norville, King & Swafford [84] instead considered a true upper bound model for laminated glass beams in which the plane sections remain plane and the PVB interlayer makes a significant contribution to the bending behaviour of the laminated glass beam, because various researchers had reported stiffnesses higher than the previous upper bound model.

A composite model was developed in which a shear transfer factor q of 1.00 represented the shear transfer across the centreline of a monolithic panel twice the thickness of the two glass plies. For q=1.00 in the laminated model, the stress in the glass at the boundary with the interlayer would be zero. This would still give a greater strength and stiffness than the previous upper bound model. The lower bound model would give a q value of 0, while the upper bound model would give a q value greater than 1.00, as the interlayer provides a separation of the glass plies. The stress distribution in one of the glass plies is illustrated in Fig. 36 for the different cases.

Beam tests using 6mm thick laminated glass with 2.69mm thick glass plies and 0.76mm interlayers were analysed with this model. For long duration loading (>60 s) the test stresses indicated the following:

- At 0ºC, q=1.07
- At 23ºC, q=0.84
- At 49ºC, q=0.31

Deflections of the laminated glass beams calculated from the model using these q values showed good agreement with measured deflections, strongly supporting the validity of the model.

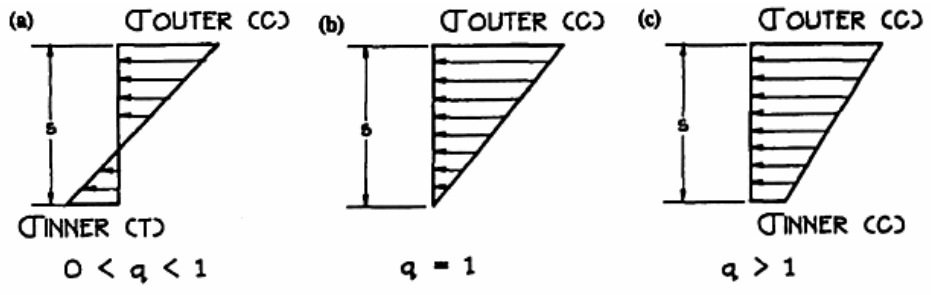

Figure 36. Stress distribution in a glass ply for different values of parameter *q* [84]

In tests on laminated glass panes at ambient temperature, the fracture strength of 6mm thick laminated glass panes incorporating a 0.76mm interlayer was in close agreement with the fracture strength of monolithic 6mm thick panes of the same size. Laminated glass panes composed of 3mm glass plies with a 2.28mm PVB interlayer showed a substantial increase in strength over the 6mm monolithic glass.

Wei, Shetty & Dharani [85] used finite element analysis to investigate an uncracked laminated glass plate 662.4mm square and 11.04mm thick with a 1.52mm thick PVB interlayer and 4.76mm thick plies, using a viscoelastic material model for the PVB interlayer. The stress relaxation modulus at time *t* is given by:

$$G(t) = G_{\infty} + (G_0 - G_{\infty}) \cdot e^{-\beta t} \tag{22}$$

and the deviatoric stress component is given by:

$$\sigma_{ij}(t) = 2 \cdot \int_0^t G(t-\tau) \cdot \dot{\varepsilon}_{ij} d\tau \tag{23}$$

where G_{∞} is the long term stiffness, G_0 is the short term (glassy) stiffness, β is a decay factor and $\dot{\varepsilon}_{ij}$ is the deviatoric strain rate.

A static solution was compared in Ref. 85 with test data for deflections up to about twice the thickness. Deflection and maximum principal stress showed large deflection non-linear curves in good agreement with the test data. The through thickness maximum principal stress in the glass at maximum deflection was co-linear between the glass plies, as can be expected where there is no shear, but the stress was offset in the tensile direction by the membrane tension. This is similar to one of the cases shown in Fig. 37.

In Ref. 85, a range of dynamic responses were analysed up to a maximum deflection of about 0.5 times the thickness. Deflection histories and maximum principal stress showed only minor differences than those for monolithic glass of identical total thickness under the same blast loading. The through thickness maximum principal stress was co-linear between the plies with negligible membrane stress. The slightly greater deflection and stress for the laminated glass is attributed to the lower shear stiffness of the PVB interlayer, but could also be caused by the lower mass due to the lower density of PVB. These are similar to two of the cases shown in Fig. 38.

The stress and displacement amplitudes, timing and distributions for the glass and true PVB short term modulii are almost identical, although the glass modulus is 87 times that of PVB.

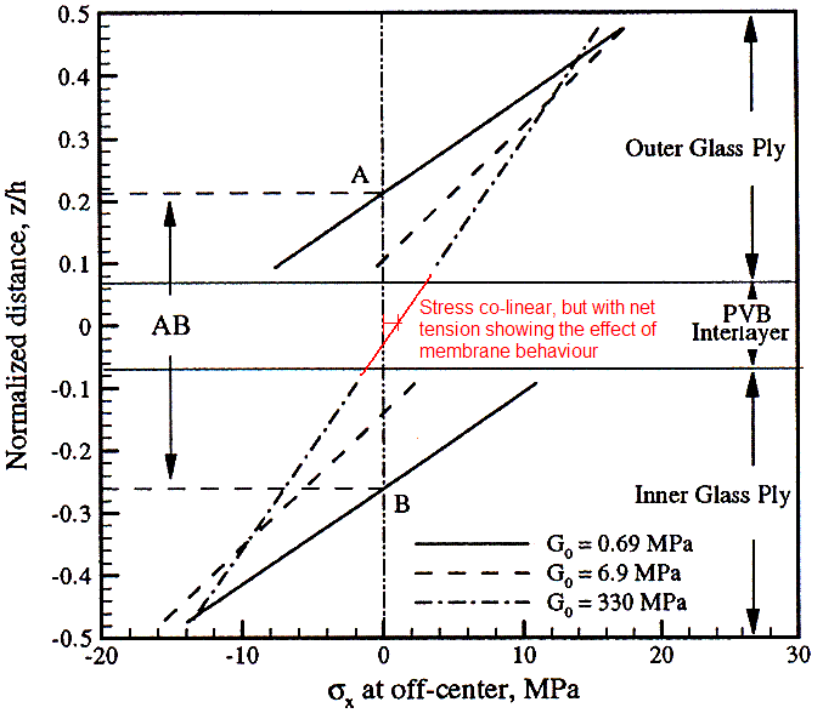

Figure 37. Effect of short term modulus of PVB on stress distribution at edge of laminated glass panel [85]

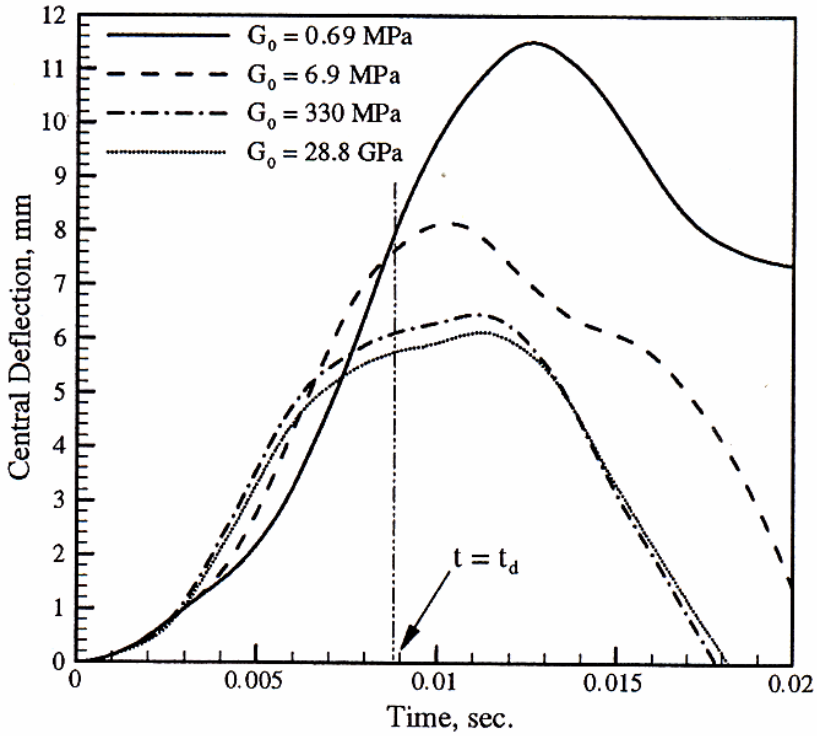

Figure 38. Effect of short term modulus of PVB on deflection of uncracked laminated glass [85]

A sensitivity study looked at the effect of varying the short term PVB shear modulus. Values of 330 MPa (true short term PVB modulus), 6.9 MPa (10 times long term modulus) and 0.69 MPa (long term modulus) were considered. Significant differences in both deflections (in Fig. 38) and stresses (in Fig. 37) were observed for the reduced short term stiffnesses, but the intermediate value gave results significantly closer to the true short term PVB modulus (48 times larger) than to the long term modulus (10 times smaller).

The deflections and stresses are not sensitive to the bulk modulus, whose normal value was taken to be 2.0 GPa. Increasing or decreasing the value by a factor of 10 had little effect on the results of the dynamic analyses.

Van Duser, Jagota and Bennison [86] addressed the question of load-bearing capacity for first glass fracture of laminate plates under uniform pressure loading by combining a three-dimensional finite element model for stress development using a viscoelastic model of PVB with a Weibull statistical model for glass fracture.

The viscoelastic material properties are based on the approach of Ferry [87], with the shear relaxation modulus represented by a generalised Maxwell series at a reference temperature:

$$G(t) = G_{\infty} + \sum_{1}^{n} G_i \cdot e^{-t/\tau_i} \qquad (24)$$

Where G_i is the modulus of individual terms and τ_i the associated relaxation times.

Derivation of viscoelastic material properties for DuPont "Butacite®" PVB are described by Bennison, Jagota & Smith [88]. The variation of shear relaxation modulus with time t is illustrated in Fig. 39. These values were used in Ref. 86.

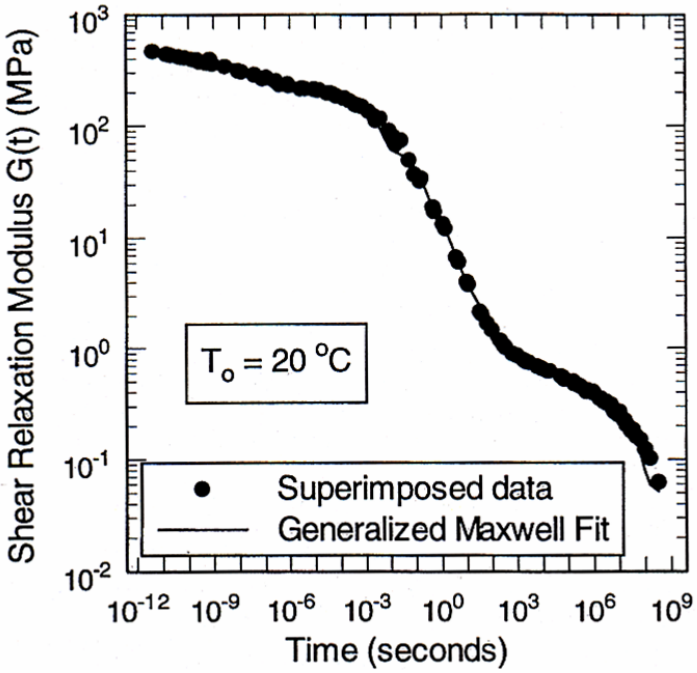

Figure 39. Variation of shear relaxation modulus with time [86]

A time shift function $a_T = t/\tau$ is used to adjust the modulus for temperature, where the reduced time τ at temperature T is related to the time t at reference temperature T_0 by:

$$\log_{10} a_T = \frac{J_1 \cdot (T - T_0)}{J_2 + T - T_0} \tag{25}$$

Where J_1 and J_2 are material constants.

For the Weibull distribution of glass strength in Ref. 86, the risk function B in Eq. 20 for cracking initiated on surface i is written as:

$$B = \left(\frac{\sigma_{wi}}{\sigma_{0i}} \right)^{mi} \tag{26}$$

Where σ_0 is as Eq. 13 and σ_w is the Weibull effective stress, which is less than the maximum principal stress. The probability of failure somewhere in the laminate is:

$$P_f = 1 - \exp\left[-\sum_{i=1}^{4} \left(\frac{\sigma_{wi}}{\sigma_{0i}} \right)^{mi} \right] \tag{27}$$

Ref. 86 indicates that for different temperatures and loading rates, the viscoelastic properties of the interlayer result in different stresses and stress distributions on each surface. As the membrane stresses increase with slenderness and loading, the tension stresses all increase and the possibility of failure initiating on an inside surface rather on the rear surface may become significant, and may marginally increase the overall probability of failure.

Even with this increase, the probability of failure of laminated glass is almost always less than for a monolithic glass pane with a thickness equal to the sum of the thickness of the glass leaves. For large deflections, where the membrane stress is substantial, the concept of upper and lower bound stiffnesses breaks down and the probability of failure converges on that of the solid glass pane irrespective of the stiffness of the PVB interlayer. The use of limits based on one-way laminated glass beams without membrane stresses can be highly misleading for two-way spanning panes of laminated glass, and will tend to underestimate the stiffness and strength.

4.5 Methods of analysis of blast loaded laminated glass

4.5.1 TPS Consult

TPS Consult inherited much of the PSA data and counter-terrorist experience after PSA was privatised in 1992, and continued to provide explosives safety and counter-terrorist advice and designs to the public and private sector.

From 1997, TPS Consult developed an analytical approach to SDOF analysis of laminated glass glazing using Mathcad [89] to calculate the response for a multi-stage resistance model. This was documented in the Author's 1999 MSc Dissertation [6].

An analytical method of assessing large deflections of plates using the Galerkin method described by Chia [90] was assessed. For a square panel it gave a resistance function of:

$$p = E\left(\frac{h}{b}\right)^4\left[21.05\frac{z}{h} + 3.90\left(\frac{z}{h}\right)^3\right] \qquad (28)$$

similar to equation 17 found experimentally by Bowles & Sugarman [64], but with a slightly lower linear term and slightly higher cubic term. Comparison with Moore's [67] curves indicated a higher resistance at large deflection, which would be consistent with the cubic term being too large.

The linear component was consistent with small deflection theory for other aspect ratios, but the trend for high aspect ratios was towards increasing rather than decreasing membrane action, which was both logically inconsistent and contrary to the trend shown by Moore [67]. The finite difference analysis of a simply supported plate by Aalami & Williams [91] was consistent with Moore [67], and so Moore's data was used in the first two stages, i.e. the non-linear resistance of the whole pane and of the front ply, up to the cracking of the rear and front plies respectively.

Two further stages were incorporated in the resistance function [6], representing first elastic and then plastic stretching of a PVB membrane. This approach was developed from observation of the apparent yielding of the PVB interlayer in tensile tests by Schmidlin on cracked laminated glass witnessed by the Author and recorded by Fullermann [92] and the "S" shaped resistance curve of laterally loaded panels tested by Ellis [93, 94] at the Building Research Establishment for PSA.

The plastic membrane deflected shape was taken as the "soap film" deflected shape from Timoshenko and Goodier [42] and described in Section 3.5.5.5. This has a uniform tension force throughout, and represents a pure plastic membrane. The resistance function and SDOF parameters were calculated for a range of aspect ratios up to 4.

Elastic membrane theory is an asymptotic large deflection theory for very thin plates. Mansfield [95] gives a general description and power laws for deflections and

membrane stresses, but does not give solutions for rectangular membranes. The power laws indicate that the resistance will be a cubic curve.

In Ref. 6, the cubic term from the Galerkin method was used as the elastic stiffness coefficient with a PVB elastic modulus factored up from the value from Schmidlin's low rate-of-strain tests [92]. The "pure-plastic" yield stress was also factored up from the low rate-of-strain tests, and these assumed high rate-of-strain material properties justified by back-analysis of the SFE [81] fragility curves for laminated glass.

It was found that, for realistic elastic-plastic resistance curves, the elastic stiffness factor varied significantly for high aspect ratios, which was felt to arise from the inconsistencies in the Galerkin analysis described above. In practice, stiffness enhancement was adjusted to give an approximately "S" shaped membrane resistance curve with a point of contraflection at the elastic-plastic transition between 10% and 20% of the span for all aspect ratios. Membrane theory does not provide a deflected shape of an elastic membrane, so SDOF parameters were taken as equal to those for the plastic membrane.

In Ref. 6, a limiting deflection of 27.8% of span was adopted; being the 90% confidence value calculated from the lateral loading tests for laminated glass with 1.52mm PVB interlayers [93,94]. The form of failure tended to be the cutting of the PVB interlayer at locations of high curvature by the attached glass fragments. This was considered not to be sensitive to strain rate.

A typical resistance function showing the four stages is illustrated in Fig. 40.

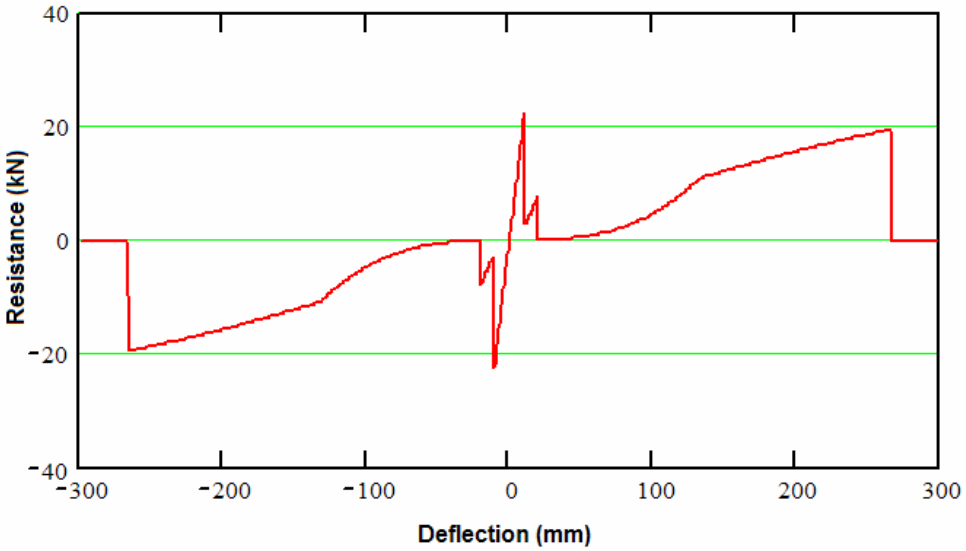

Figure 40. Typical TPS Consult resistance curve for laminated glass [6]

An unloading curve for the plastic PVB membrane in Ref. 6 was derived from the elastic membrane curve, using the relationship between the Von-Karman equations for initially flat plates and the Maguerre equations for initially curved shells reported by Chia [90]. This represents the elastic unloading / reloading curve for an initially flat membrane after plastic stretching, and is illustrated in Fig. 41. It was

acknowledged that this was an approximation, as the relationship was only proven for moderate initial deflections.

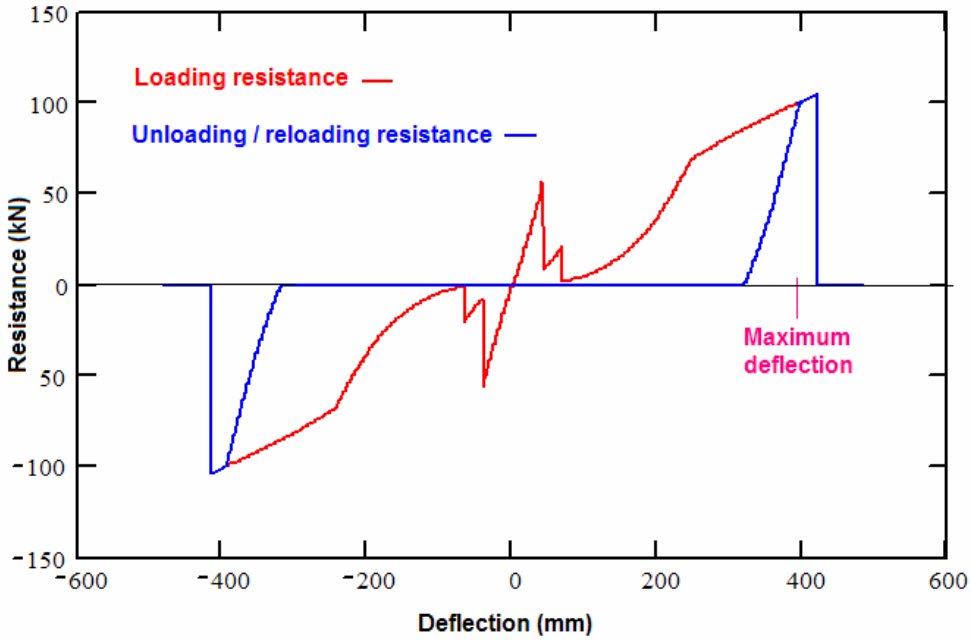

Figure 41. Typical loading and unloading resistance curves for laminated glass [6]

In Ref. 6, aeroelastic damping was incorporated into the analysis of blast response. This dominates the rebound response of a PVB membrane, particularly if it has already been stretched into the plastic zone, and provides much closer accordance with the response observed in high-speed video of blast trials.

The differential equation solver in Mathcad [89] can solve multiple differential equations simultaneously. In Ref. 6, double glazing was modelled using two SDOF differential equations with cavity air pressure loading both leaves, and calculated by treating the cavity as an adiabatic air spring. This provided a model for load sharing under blast loading on the outer leaf.

4.5.2 US Army Corps of Engineers

The US Army Corps of Engineers (USACE) digitised the UK fragility curves and compiled a database of around 1000 blast trials, including 600 from the UK, in WinDAS [96]. They are developing analysis software HAZL [97], although the post-cracking analysis of laminated glass is reported as being tentative at present.

In 2001, Norville and Conrath [98] proposed design procedures for blast-resistant glazing incorporating laminated glass, based on the understanding and experience of the material of both Texas Technical University and the USACE. Although proposed as a tool for the general construction professional rather than for the specialist practitioner, it does illustrate the limited penetration of dynamic design into normal US practice.

In Ref. 98, normal design of glazing for lateral loading such as wind was cited from ASTM standard E1300 [99]. This contained 12 charts, each of which plotted load capacity of panels of annealed glass of a different thickness for a range of lengths and widths, for loads of 1 minute duration with a probability of cracking of eight per thousand (0.008). Different types of glass, included laminated glass of different sizes and cavity construction incorporating such laminated glass, were covered by glass type factors, which, although they did not accurately map the glass response, should ensure a breakage rate less than eight per thousand.

Norville and Conrath [98] proposed an empirically developed chart that approximately relates charge size and stand-off range to an equivalent 60 second duration static design load, suitable for the design of a blast resistant façade incorporating suitably anchored laminated glass with the expectation that the glass will break under the blast loading but will:

- minimise flying and falling glass shards and their associated lacerative hazard
- maintain closure of most of the contained openings,

while performing the everyday glazing functions economically. In developing the chart, the authors claim to have considered the reflected pressure and positive phase impulse of the threats and the experimental results of laminated glass blast tests in WinDAS [96].

4.5.3 US General Services Administration

US consultants Applied Research Associates have developed a computer program WINGARD [100] for analysing the resistance of glazing to blast that incorporates the post-cracking resistance of laminated glass. This was commissioned by the US General Services Administration, and a variant is used for the US State Department.

Membrane theory has been applied to the interlayer resistance of laminated glass after cracking. Cubic curves are used in place of the HOSDB near triangular resistance curves to represent the energy absorption of the membrane. The validity of this model depends on the accuracy of the implicit assumption that the extension of PVB is essentially linear up to failure.

The 2005 release, WINGARD PE 5.5 includes an elastic-plastic membrane model as an option for thicker membranes, although the way in which this is treated for analysis is not made clear, and the default PVB yield stress is not consistent with data for room temperature PVB from other sources (see Chapter 8).

4.6 Analysis of polymers

Recent research into methods of analysing polymers for high rates of strain has generally been aimed at modelling their performance in vehicle crashes.

Du Bois, Kolling & Fassnacht [101] analysed PVB in laminated winscreens for both impact with the screen and roll-over accidents. They used hyperelastic rubber material models to reproduce test data up to 225% strain. For numerical analysis they tried various rubber material laws, but only the Ogden material model of order 6 came close to the test data for large deformation. This was based on principal stretch ratios (translational strains that exclude rotation effects), and used six material parameters to model the deviatoric behaviour, plus a high bulk modulus for the pressure response. For strains less than 100%, simpler models with two material parameters were adequate.

They suggested a laminated glass model consisting of two coincident finite elements: a shell element for the glass and a membrane element for the interlayer. In general, an Ogden material of order 6 is recommended for the PVB interlayer, but it was concluded that the assumption to neglect viscosity of the PVB was unsatisfactory.

Du Bois, Kolling, Kousters & Frank [102] considered analysis of elastomers, recoverable foams and thermoplastics.

For quasi-static problems, elastomers can be considered as incompressible, rubber-like materials (PVB is such an elastomer). In short-time dynamics, however, a strong strain rate dependency of elastomers can be observed. To consider this behaviour the Ogden material model in Ref. 101 must be generalised by viscous terms. This generally requires a large number of parameters that are complex and time consuming to identify.

Instead, they developed a new material model in LS-DYNA, based on the Ogden formulation. Stress-strain curves for uniaxial static and dynamic tensile tests were entered directly, and the Ogden function internally determined by defining a tabular function of the principal stretch ratio. LS-DYNA uses a Jaumann formulation to evaluate the viscous terms in a coupled hyperelastic-viscoelastic model.

Ref. 102 states that, where thermoplastic components undergo high velocity impact loading and large deformations to failure, they can be modelled as pseudo-metallic elastic-plastic bodies. Only when the forces during unloading may be important, as for pedestrian impact modelling when most of the bumper deflections will be elastic, then the viscoelastic behaviour on unloading may be of significance.

For thermoplastic polymers with significant viscoelastic behaviour, not only does the yield stress increase with strain-rate, often more markedly than for metals, but an increase in the elastic modulus is observed. Stress-strain curves for a typical polymer at different strain rates are shown in Fig. 42.

Ref. 102 states that this type of physical response can be modelled perfectly well using standard elastic-plastic material laws, with a simple damage model reducing the elastic modulus with plastic strain to approximate the softer unloading curve. DuBois et al. [102] report the use of such a model using a Von Mises yield model, and also using a Drucker-Prager model. The Drucker-Prager was preferred for modelling bending, as higher yield criteria could be set for compression than for tension.

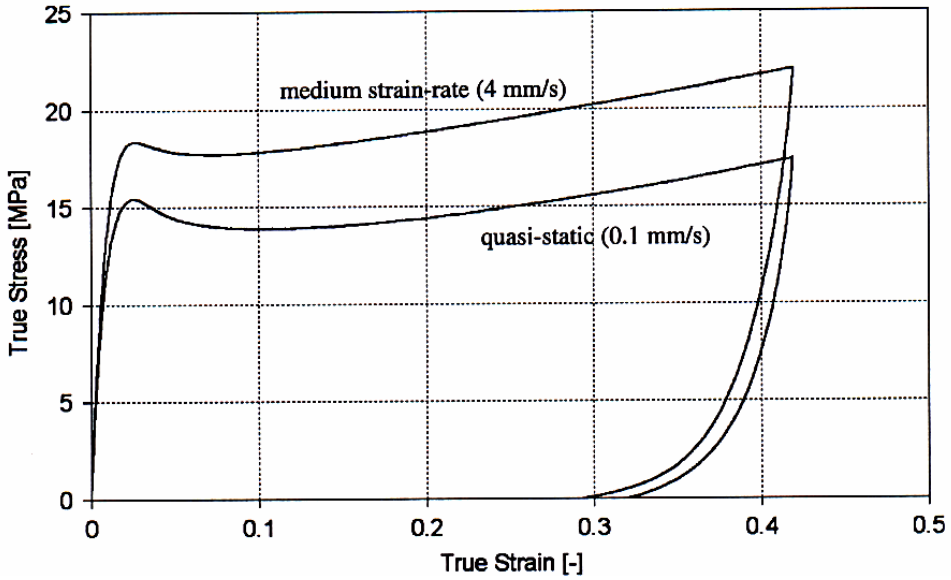

Figure 42. Stress-strain curves for a typical thermoplastic at different strain rates [102]

Specialised material models were developed in a 7 year research program to model the behaviour of a number of types of compressible polymer foams. As for the PVB models described above, these were based on quasi-static compression and tension tests, with the parameters determined internally. Typical stress-strain curves for different grades of polypropylene foams are illustrated in Fig. 43.

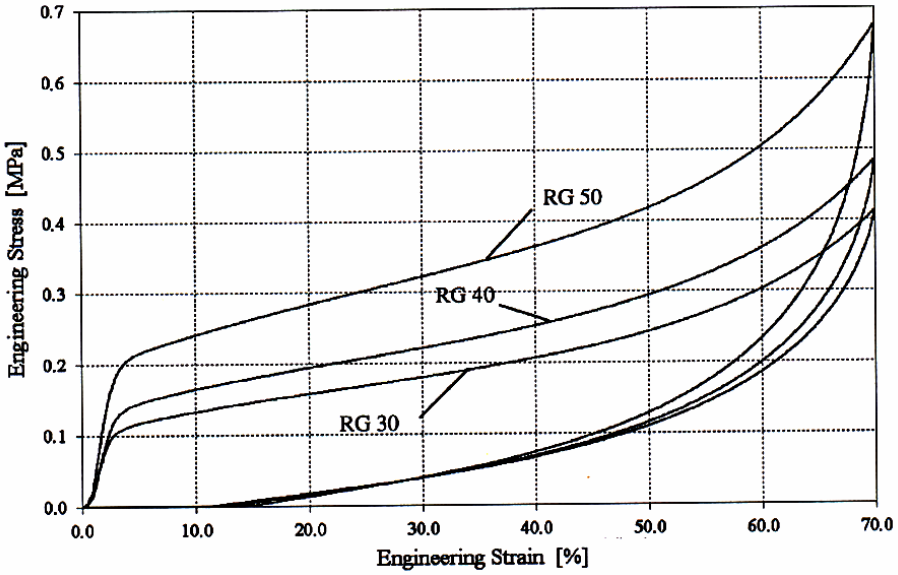

Figure. 43 Typical quasi-static stress-strain curves for polypropylene foams [102]

Mullerschon et al. [103] described a non-linear viscoelastic material model implemented in LS-DYNA as "*MAT_OGDEN_RUBBER", which comprised a three term Ogden model in parallel with up to six optional Maxwell viscoelastic components (although only two Maxwell components were used in this case). They concluded that the capability of this material law to adapt to experimental tension tests

of a high density polyethylene (HDPE) polymer at different constant strain rates was rather poor.

For better modelling of the HDPE tests, an alternative material model in an alternative finite element code PANDAS was developed that used two term non-linear springs in the Maxwell components. The comparison of the two models with test results from quasi-static and two speeds of dynamic tests are given in Fig. 44. The higher strain rate, $\dot{\varepsilon}_2$, represents about ten times the strain rate of $\dot{\varepsilon}_1$, and a deflection of 2.5mm corresponds to a maximum strain of about 10%.

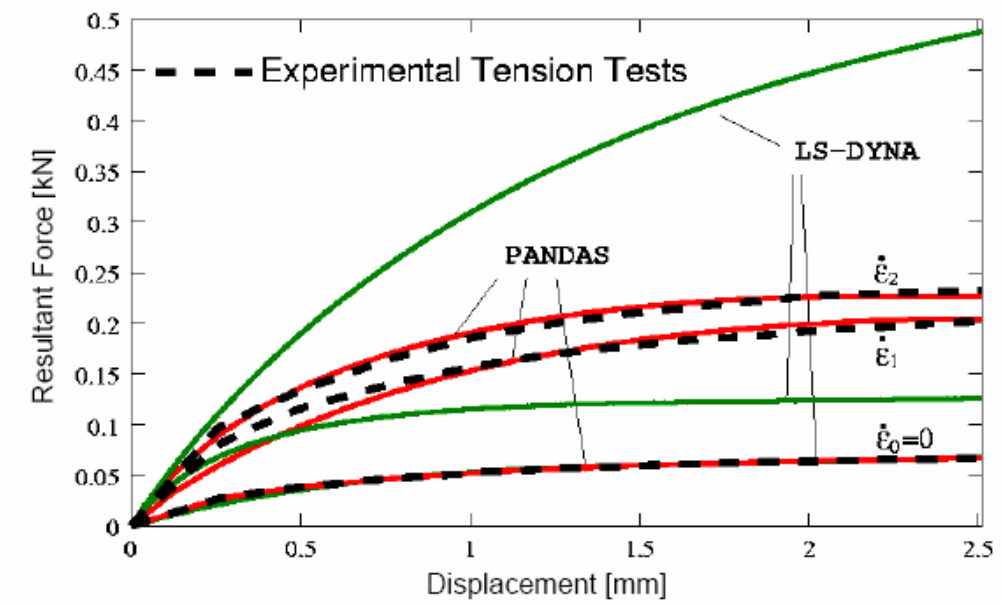

Figure 44. Modelling of HDPE tests in LS-DYNA and PANDAS [103]

Spingler [104] reviewed methods of developing material laws for polymers from test data. He stated that no typical process for material characterisation exists, and that for a polymer, parameters of an appropriate law of behaviour need to be determined individually, due to the different behaviour of each. The main method of material characterisation for finite element models consists of undertaking a range of tensile tests from quasi-static to dynamic velocities and using an inverse method that simulates the test to identify the parameters of a material behaviour law.

Springler proposes using a material model using G'Sell's law, or the modification by Tillier that expresses the stress as:

$$\sigma = K \cdot e^{\frac{\beta}{T}} \left(1 - e^{-w\varepsilon}\right)\left(1 + h_1\varepsilon + h_2\varepsilon^2\right)\dot{\varepsilon}^m \tag{29}$$

Where K is the "material consistency" (a standardised stiffness value), β the thermal dependency coefficient, w the viscoelastic parameter, h_1 and h_2 are strain hardening parameters and m is the strain rate hardening coefficient. Tensile tests at different temperatures, as illustrated in Fig. 45, can be used to calculate stress-strain laws at different temperatures, as shown in Fig.46.

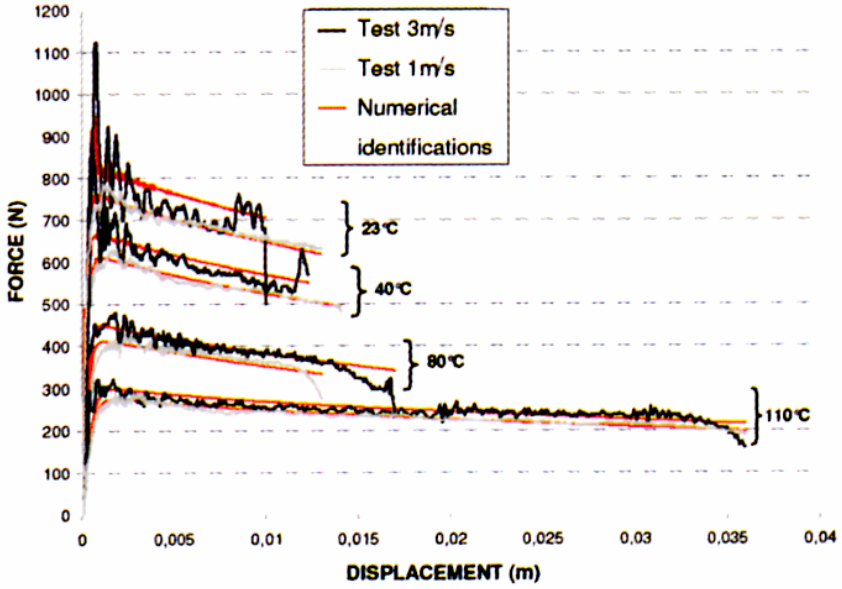

Figure 45. Tensile test traces and idealisations for polypropylene [104]

For impact, Ref. 104 indicates that there is a significant temperature increase, and allowance in the strength model must be made for this, but temperature changes in tensile straining are much smaller, so tensile response of polymers can be treated as isothermal.

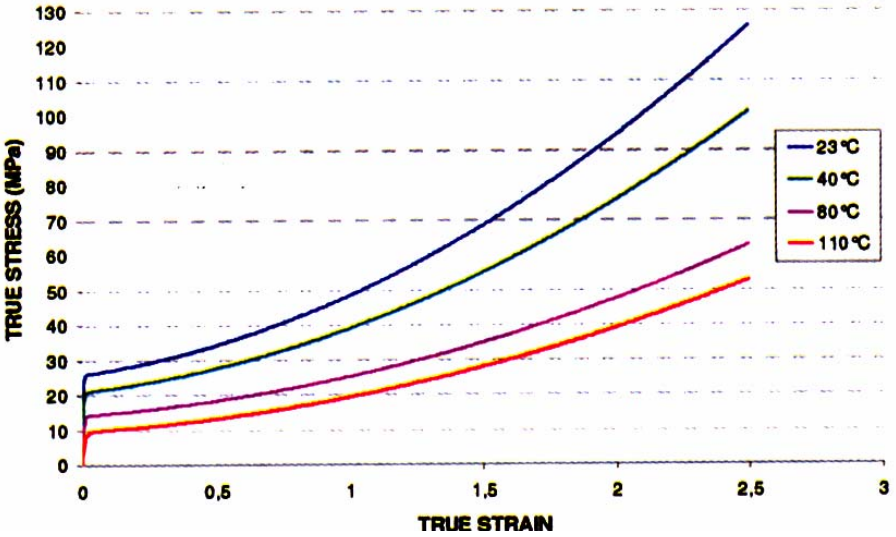

Figure 46. Stress-strain laws for polypropylene at different temperatures [104]

4.7 Properties of glazing materials under blast loading

4.7.1 Monolithic glass

4.7.1.1 Data measured or assumed in World War 2 research

The data used in UK research in World War 2 came from two sources; static or low rate-of-strain testing of small samples, and reverse engineering of the observations of blast damage surveys.

Tests on glass samples cut from a sheet glass window pane at the Road Research Laboratory were covered in RC58 [53]. Poisson's ratio ν was assumed to be 0.235, and the mean of the stiffness $E/(1-\nu^2)$ was measured as 10.25×10^6psi, giving a mean Young's Modulus E of 9.68×10^6psi (66.8GPa). This fell within a cited range for Crown glass of $9.42\text{-}11.31 \times 10^6$psi (65.0-78.0 GPa). The mean density ρ was measured as 0.091lb/in^3 (2519 kg/m^3).

These values were assumed to hold for other frequency measurements in RC 81 and RC 87 [54,55].

In RC163 [32], a standard modulus of rupture σ_f, of plate glass was taken as 4950psi (34.1 MPa). However, reverse analysis of damage to existing windows has been based on σ_f=4000psi (27.6 MPa) for plate glass and σ_f =12000psi (82.7 MPa) for sheet glass for 50% breakage under blast loading. REN 127 [58], an addendum to RC163 proposes an increased value of σ_f =6000psi (41.4 MPa) for plate glass.

REN 119 [59] reported several measurements of glass properties. Young's Modulus E, was reported as 8.67×10^6psi (59.8GPa) from a static test and $8.29\text{-}8.55 \times 10^6$psi (57.2-59.0 GPa) from dynamic tests of 24 oz sheet glass, and $8.25\text{-}8.55 \times 10^6$psi (56.9-59.0 GPa) from dynamic tests of 18 oz sheet glass. The modulus of rupture σ_f, of 24 oz sheet glass was reported as 6000psi (41.4 MPa).

REN 583 [56] reported mean measurements of glass properties for 24 oz sheet glass as Young's Modulus E, of 10.3×10^6psi (71.0 GPa) and modulus of rupture σ_f, of 11400psi (78.6 MPa).

REN 583 [56] noted a systematic variation of strength with size of blast test panels, with larger test panels appearing to be weaker than small panels in comparison to either formulae based on air raid data or to SDOF analyses based on a constant cracking strength. One possible reason advanced for this was the "Flaw Theory". This proposes that failure of a glass pane always begins at a flaw. The larger the pane, the greater the number of flaws, and hence the greater probability of failure.

Wise [33] cited three UK papers and a mechanical engineer's handbook for glass properties. Although Young's modulus E, at 10×10^6psi (68.9 GPa) and Poisson's ratio ν, at 0.235 are consistent, the modulus of rupture is not. Wise gives the modulus of rupture σ_f as 3000-4000psi (20.7-27.6 MPa) for sheet glass and as 4000-5000psi (27.6-34.5 MPa) for plate glass.

These are summarised in Table 5 below:

Source	Glass Type	Elastic Modulus E	Poisson's ratio σ	Modulus of rupture	Density
		GPa		MPa	kg/m^3
RC58 [53]	Sheet	66.8	0.235		2519
	Crown	65.0-78.0			
RC163 [32]	Plate			34.1 27.6	
	Sheet			82.7	
REN127 [59]	Plate			41.4	
REN119 [60]	24 oz sheet	59.8 (stat) 57.2-59.0		41.4	
	18 oz sheet	56.9-59.0			
REN583 [56]	24 oz sheet	71.0		78.6	
Wise [33]	Sheet	68.9	0.235	20.7-27.6	
	Plate	68.9	0.235	27.6-34.5	

Table 5. Properties of glass from World War 2 research

4.7.1.2 Data from the 1960s to 1980s

Bowles and Sugarman [64] did not calculate the breaking stress of glass, but, by comparing the mean failure strength of 41″ square panels of varying thickness, demonstrated that sheet glass is stronger than plate glass, as shown in Fig. 47.

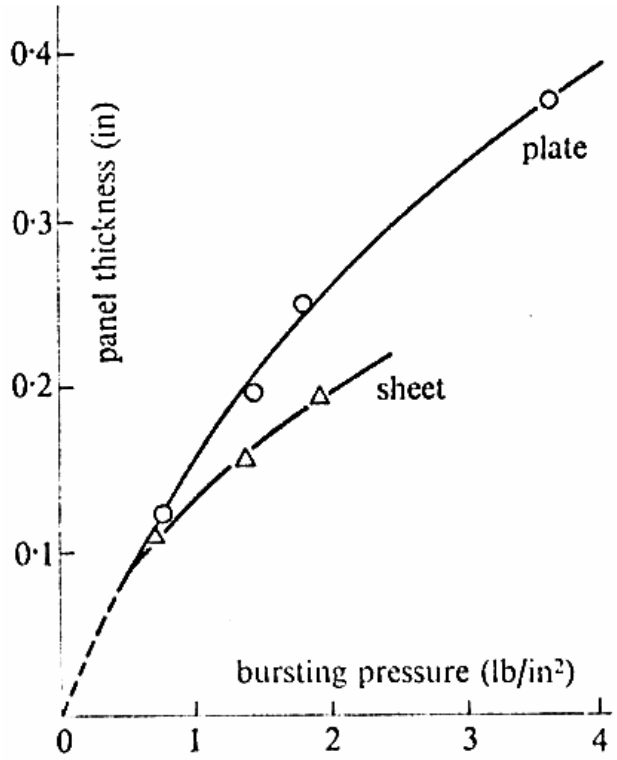

Figure 47. Comparative strength of sheet and plate glass [64]

Prichard [63] uses a value of Young's modulus "usually quoted in the literature" of 69 GPa. He termed the reduction of breaking strength of glass with increasing loading duration as "static fatigue". He states that the best data that could be found in the literature for short duration loadings was that obtained by the Pittsburgh Plate Glass Company and cited by Seaman [65]. This is listed in table 6.

Load duration (sec)	Modulus of Rupture (MPa)	
	Plate glass	Sheet glass
0.01	46.9	51.7
0.1	42.1	46.2
1.0	37.9	41.4

Table 6. Modulus of rupture values cited in Refs. 63 and 65.

McLellan & Shand [46] quote elastic constants for a range of glass types at 20ºC, measured by two different methods, namely resonant frequency and ultrasonic measurement. For soda-lime plate glass the values are:

- Elastic Modulus E = 72.4 GPa
- Shear modulus G = 29.6 GPa or 30.3 GPa
- Poisson's ratio ν = 0.21

A figure in Ref. 46 shows that the moduli reduce with increasing temperature to at least 550ºC, approaching the softening temperature.

Ref. 46 includes a wide range of data on breaking strengths, which is not always consistent, even if only those applicable to window glass are considered. A selection of breaking stresses are:

- Effective 3 sec. duration of breaking load in air: annealed widow glass 55-138 MPa; surfaces ground or sand blasted 10-28 MPa
- Fig. 33 in Section 4.3.5 shows a probability distribution of modulus of rupture on 6mm plate glass samples that indicates that a 5% failure rate will occur for both non-abraded and sand blasted glass at around 34 MPa, with a lower mean strength and smaller variation for sand blasted glass.
- Mean modulus of rupture for tests at 24ºC and loading rate of 69MPa/min: annealed plate glass 102 MPa; tempered (toughened) plate glass 221 MPa.

Bansal & Doremus [105] report elastic properties for a range of soda lime silicate glass compositions. Typical values are shown in Table 7.

For comparison purposes, BS952-1:1995 [1] specifies the composition of soda lime silicate glass for glazing by mass as 69-74% SiO_2, 12-16% Na_2O and 5-12% CaO, with optional minor quantities of magnesium or aluminium oxides, which will raise the modulus more than an equivalent quantity of calcium oxide.

Glass composition (mole %)			Young's modulus E (GPa)	Poisson's ratio ν
Na_2O	CaO	SiO_2		
7.5	22.0	**70.5**	78.8	0.224
9.5	15.8	**74.7**	73.3	0.209
10.0	**8.0**	82.0	70.5	0.193
10.0	**11.5**	78.5	71.7	0.202
10.0	13.5	76.5	73.9	0.201
10.0	15.0	75.0	74.3	0.207
10.0	17.5	**72.5**	75.1	0.212
10.0	19.5	**70.5**	76.2	0.221
11.0	18.5	**70.5**	75.2	0.216
13.5	**8.0**	78.5	69.1	0.198
16.0	**8.0**	76.0	68.0	0.203
17.5	**12.0**	**70.5**	70.3	0.225

Table 7. Modulus and Poisson's ratio for different glass composition [105]

The compliant proportions, shown in bold in Table 7, indicate that none of the compositions reported in Ref. 105 would comply with Ref. 1. However, they do indicate a Poisson's ratio of 0.22 +0.055 -0.011 for compliant silicon dioxide levels, with higher silicon dioxide levels giving lower Poisson's ratio. They also indicate a Young's modulus around 70 GPa, increasing with higher levels of calcium oxide (or magnesium or aluminium oxide in lieu) and decreasing with higher levels of sodium oxide.

TM5-1300: 1990 [24] gives the following as design values for tempered glass, on which the design charts and tables were based:

- Elastic modulus $E = 1 \times 10^6$ psi (6.90 GPa)(although this may be a typographical error)
- Poisson's ratio $\nu = 0.22$
- Design tensile stress of 16000 psi (110.3 MPa) for a probability of failure equal to or less than 0.001.

Mayor & Flanders [40] included tabulated data in the theory manual for BLAST, collated from several sources, including Meyers:

- Elastic modulus $E = 10 \times 10^6$ psi (69.0 GPa)
- Poisson's ratio $\nu = 0.22$
- Mean failure stress and coefficient of variation depending on the glass type and treatment as shown in Table 8.

Glass has a pronounced decrease in fracture stress due to long load duration. This suggests that there may also be an increase in fracture stress at blast duration loading compared to the strengths derived from mechanical testing. Moore is cited in Ref. 40

as recommending an enhancement of 1.5 for annealed glass, with lower enhancements for other glass types.

Glass Type	Treatment	Mean Failure Stress		Coefficient of variance
		psi	MPa	
Annealed	New	15,400	106	0.279
	Abraded	10,100	69.6	0.050
Fully tempered	New	33,300	230	0.171
	Abraded	24,400	168	0.033
Semi-Tempered	New	24,871	171	0.198
Plate Glass	New	14,000	96.5	0.297

Table 8. Glass failure strength data collated by Mayor & Flanders [40]

For annealed and tempered glass, values for an abraded surface show a reduced mean value but a greatly reduced deviation.

Failure mechanisms based on micro-cracks were discussed in Ref 40. Micro-cracks that trigger glass failure are normally found on the surface, and the Weibull statistical distribution that would arise from the weak-link failure mechanism was reviewed. The Weibull model predicts that larger specimens should fail at lower stresses, a phenomenon that glass is reported to exhibit. However, lacking suitable statistical data to justify a Weibull distribution, a normal distribution was used in BLAST to predict failure probabilities.

4.7.1.3 Data from the 1990s to the present

In the output of the 1994 version of BLASTOP, Meyer [71] presented design values and estimated 50% and 99.9% probability of failure values of different types of glass, whether monolithic or laminated. The steps between the columns are equal, so the rounded value for the design stress appears to be taken as the 0.1% probability of failure value, and a coefficient of variance (C of V) applied to estimate the other strength values, as shown in Table 9.

Glass Type	Design stress		50% break stress		99.9% break stress		C of V
	psi	MPa	psi	MPa	psi	MPa	
Annealed	4000	27.6	12300	84.8	20600	142	0.2184
Heat strengthened	9000	62.0	16775	116	24550	169	0.15
Fully tempered	16000	110	23154	160	30310	209	0.10

Table 9. Glass failure data used by Meyers in BLASTOP [71]

The SFE Glazing Hazard Guide [81] reports that glass breakage tensile stress values of 80 MPa for annealed glass and 180 MPa for toughened (fully tempered) glass under blast loading were derived from the tests and literature studies, and were used to extrapolate the break-safe lines from the test results.

It was noted in Ref. 81 that the breakage stress under short duration loading was higher than under long duration loading.

In Ref. 6, the Author used values of 2490 kg/m^3 for density, 70 GPa for Young's modulus and 0.22 for Poisson's ratio, and adopted the design tensile stresses from Ref. 81. It was noted that these strengths were marginally greater than the 90% confidence breaking strengths of glass based on the data collated by Mayor & Flanders [40] for both new and abraded glass which are very similar values for each glass type, implying a small increase in strength between testing and blast loading rates. This suggested that the design values should give at least 90% confidence of remaining uncracked throughout the life of the glazing, and were indicated as "whole life" characteristic design strengths in Ref. 6.

Ref. 100 incorporates design failure stress based on a normal distribution with the properties shown in Table 10.

Glazing type	Probability of failure (*Pf*)	Failure stress corresponding to *Pf*		C of V
		psi	MPa	
Annealed	8/1000	4000	27.6	0.28
Heat strengthened	1/1000	7600	52.4	0.15
Fully tempered	1/1000	16000	110.3	0.10

Table 10. Glass failure data in WINGARD [100]

The coefficients of variation were used to calculate the failure stress corresponding to a probability of failure of 750 breaks per 1000. This was then used to calculate design glass failure stresses for calculating fragment velocities, reactions and the transfer to membrane resistance.

Other properties used in parameter studies described in Ref. 100 include:

- Density ρ = 2489 kg/m^3
- Young's Modulus $E = 10^6$ psi = 6.9 GPa (possible typographical error)
- Poisson's ratio v = 0.22

Van Duser et al. [86] and Bennison et al. [88] used values of 72 GPa for Young's modulus and 0.22 for Poisson's ratio as properties of glass in the laminated glass model, citing trade literature.

Wei et al. [85] used values of 2500 kg/m^3 for density, 72 GPa for Young's modulus and 0.25 for Poisson's ratio, but did not cite a source.

Current European standards [106, 107, 108, 109] contain a number of mechanical properties for soda-lime glass used for glazing in buildings:

- Generally accepted figures for soda lime silicate glass [106] for use in calculations where a high degree of accuracy is not required are given as:
    - Density ρ =2500 kg/m^3

- Young's modulus E = 70 GPa
- Poisson's ratio v = 0.2

- A mechanical strength based on testing is not given for annealed glass, but a characteristic bending strength of 45 MPa is given for use in design [106]

- The 5% breakage probability of Heat Strengthened float glass shall be at a mechanical strength not less than 70 MPa [107].

- The 5% breakage probability of thermally toughened glass (including safety glass 4mm and thicker) shall be at a mechanical strength not less than 120 MPa [108, 109].

The mechanical strength values apply to a quasi-static loading over a short time, e.g. wind loading, and are defined by the statistically evaluated lower limit of the 95% confidence interval from tests on at least 10 specimens [107, 108, 109].

4.7.1.4 The fracture mechanics approach to glass strength

In 1921, Griffith [110] applied thermodynamics to describe crack growth in brittle materials, in terms of the energy required to create the two new surfaces of the crack. A crack in a brittle material grows if the elastic energy released upon crack extension is greater than that required to create the new surface of the crack. The Griffith criteria for crack growth assumes that a thin, sharp crack is already in place, that the material is stressed across the crack, and that the material is brittle [111].

Griffith's equations were demonstrated on glass, which is brittle at normal temperatures, and whose structure results in particularly sharp crack tips, which makes glass particularly vulnerable to small crack sizes. Crack sizes as small as a few tens of nanometres can control the tensile strength in normal use and reduce the critical stress at which the crack will propagate a hundred-fold, even for high strength glasses, and more for soda-lime-silica glasses. These small cracks appear to occur naturally only on the surface of the glass, and are referred to as Griffith flaws.

From thermal data, Griffith calculated that the theoretical cohesive strength of glass is of the order 23 GPa. Tensile strengths approaching this magnitude have been demonstrated remote from the glass surface by Joffé [112], by immersing a glass sphere suddenly in molten metal to generate an internal tensile stress due to thermal shock. Strength values around 14 GPa have been demonstrated at surfaces in exceptional cases, e.g. with fine silica glass fibres or flame-polished bulk silica glass, both protected from all mechanical contact and measured at -196ºC, and strength values around 3GPa have been demonstrated in fracture tests of flame-polished test specimens whose ordinary strength was less than 100 MPa [113].

The stress at which a crack will grow is a function of the fracture toughness of the material and the size of the pre-existing crack. The fracture toughness takes into account the strength of the bond in the material and the radius at the crack tip. The tensile strength of the flawed glass will reduce as the crack grows, so when the growth results from an externally applied load or restraint the crack growth will be

catastrophic, causing the whole glass section to crack. Only when the tensile stress is confined to a limited zone of the glass and can be relieved by the limited growth of the crack can controlled crack growth occur.

Although Griffith flaws in glass are too small to be observed directly under a microscope, Ref. 111 reports that visual evidence of their existence can be demonstrated using controlled crack growth. If chemical treatment at the surface and thermal treatment are combined to produce a shallow tensile layer in the surface of the glass, a pattern of cracks will occur in this surface layer without cracking the whole sample. Cracks in the pattern will normally intersect at right angles as the first crack will eliminate all stresses except those parallel to the crack, and the subsequent crack will therefore be perpendicular. This is the case everywhere except at the initiating flaw. Even then, a non-uniform stress has to be introduced to deflect the cracks from the orientation of the Griffith flaws so that they can be identified.

This was first demonstrated by Andrade & Tsien [114] using sodium vapours deposited on the glass at 400ºC in vacuum, but modern practice [111] is to use a blend of lithium nitrate and potassium nitrate salts in air, in contact with the glass surface at lower temperatures, following the practice of Ernsberger [115]. Exchanging the sodium ion in soda-lime-silica glass with a smaller lithium ion will induce tension in the glass surface, while exchanging with a larger potassium ion will induce compression. The surface stress can be changed by altering the mixture of the blend of nitrate salts and the time of the treatment. As only the pre-existing Griffith flaws with a critical stress below the stress induced in the surface will trigger the surface crack patterns, this can be used to analyse the distribution of Griffith flaws of different strengths in glass samples.

The random distribution of Griffith flaws in the surface of glass in position, orientation and size (and hence critical stress) all contribute to the variability of the breaking strength of glass test samples and of glass in service. Many of the variations in glass strength under various circumstances can be attributed to variations in these properties:

- Andrade & Tsien [114] found that there were more flaws in aged glass than in freshly drawn glass, which explains the combined reduction in strength and variability discussed in Section 4.3.5. This may arise from the growth of nascent flaws during service, e.g. due to repeated thermal shocks, or the creation of new flaws due to engrained dirt, cleaning etc.
- Many Griffith flaws are associated with working of the glass surface such as grinding and polishing as well as by abrading. This explains the lower strength of plate glass compared to sheet glass in Fig. 47 and elsewhere in Section 4.7.1, as well as the effects of abrading by sand blasting or rubbing with wire wool or other abrasives.
- Larger, blunter flaws in glass can also cause a local reduction in strength. This is a common cause of failure in service of glazing when the edges have not been cleaned up after cutting.
- Etching of glass with hydrofluoric acid increases the strength, presumably by removing the surface layers that contain the flaws or by blunting the crack tips. Ernsberger [115] showed that increased etching times resulted in a decrease in

the density of the crack patterns. When sufficient glass was removed by etching it was impossible to obtain any crack pattern at all, regardless of how long the ion exchange treatment with lithium nitrate salt was continued [111]. It is reported that this can increase the strength of glass between 10 and 20 times [116].

- Heat treatment at sufficiently high temperatures can cause Griffith flaws to heal. The size of Griffith flaws that can be detected by the sodium vapour method in Ref. 114 are limited by the healing of the smaller flaws at the 400ºC temperature required for the deposition of the sodium vapour [111]. During annealing of glass, many Griffith flaws produced during drawing or floating of glass are healed in whole or in part. This, as much as the elimination of adverse pre-stress, reduces the extreme brittleness of freshly made glass.
- It has been established that the "static fatigue" reduction in strength under sustained loading described in Ref. 46 and illustrated in Table 6 is linked with chemical attack by atmospheric agencies, primarily water vapour. Stress corrosion of the glass bonds at the crack tip where the glass bonds are most highly stressed and the glass is most chemically active reduces the strength of the glass bond [116]. If the glass is stressed above the static fatigue limit, the crack in the corroded glass grows into the uncorroded glass. As this glass corrodes in turn, the crack will grow slowly, gradually reducing the uncorroded critical stress until it reaches the applied stress, and the crack can grow catastrophically. The higher the applied stress, between the static fatigue limit and the dry cracking strength, then the shorter the loading duration before the glass cracks through.

4.7.2 Polyvinyl butyral (PVB)

Ward [117] subjected PVB to low and high loading-rate tests. Low strain-rate tests were undertaken by pulling a tensile test sample, with a width of 6.2mm and an effective length of about 50mm. The tests showed an increasing strength and stiffness up to failure at extensions of the order 4-6 times the initial sample length. The samples showed strain rate dependency, with higher failure loads and lower deflections for higher rates-of-strain.

The mean measured stiffnesses can be expressed as secant Young's Moduli to failure, as shown in Table 11. It should be noted that the resistance was not linear, so the secant moduli are not necessarily indicative of the stiffness at small deflections.

Strain-rate /min	Young's Modulus N/mm^2
0.1	3.4
1	4.5
2	4.7
10	5.8

Table 11. Secant Young's modulus of PVB for quasi-static loading [117]

In Ref. 117, high strain-rate tests were undertaken by impacting a weighted dropper with a 10mm diameter hemispherical contact on the centre of a 50mm diameter circular target of PVB sheet at a known velocity, and measuring the force exerted on the target against time. The velocity of the dropper was effectively constant over the short period of the test, so the displacement of the dropper and the deflection of the centre of the PVB at any time could be calculated and related to the reaction force measured by a sensor in the support for the PVB. The tests show a trend of increasing maximum load and decreasing failure deflection with increasing velocity from 3 m/s up to 12.3 m/s. Because of the geometry of the test, the strain and strain-rate was not uniform in the test samples, but these tests did indicate that the strain-rate dependency does continue into the high strain-rate range.

DuBois et al. [101] include a curve for the shear modulus of PVB between the temperatures of -5ºC and +58ºC, shown in Fig.47, citing experimental data from Solutia, the manufacturer of Saflex PVB. They also give a Poisson's ratio $\nu \approx 0.5$ for the nearly incompressible PVB interlayer, and states that a polymer behaves qualitatively the same if the strain rate is increased or if the temperature is decreased.

Ref. 101 draws the conclusion that the sensitivity to temperature shown in Fig. 48 implies a similar sensitivity to strain rate. It also states that the response of the PVB interlayer varies from rubbery elastic at low strain rates to glass-like linear elastic for high strain rates.

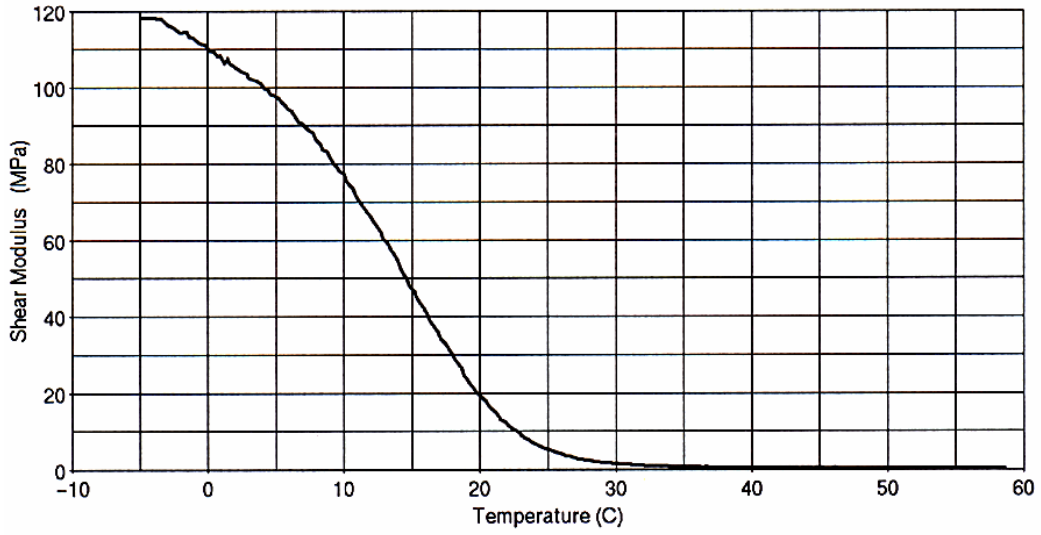

Figure 48. Shear modulus of Saflex PVB for different temperatures [101]

Reference to the Saflex web-site [118] gives other physical properties of the PVB used in architectural laminated glass as:

- Tensile strength 3220 psi (22.2 MPa)
- Tensile elongation 205%
- Specific Gravity 1.066

Warren and Millea [119] reported room temperature shear moduli for Monsanto architectural grade "Saflex" PVB, at one quasi-static pull rate and two dynamic strain rates, as listed in Table 12. The stiffness appeared to vary with the thickness.

PVB sheet thickness	0.06" (1.52 mm)		0.03" (0.76 mm)	
Shear Modulus *G*	psi	MPa	psi	MPa
Pull rate 0.5"/min	130	0.896	120	0.827
Strain rate 10%/sec	200	1.38	140	0.965
Strain rate 100%/sec	450	3.10	280	1.93

Table 12. Room temperature shear modulii of PVB at different rates

Ref. 119 also reported that at 140ºF (60ºC) the strength and stiffness was sufficiently reduced so that short, thick laminated glass will behave as a set of stacked plates

Bennison [120] provided a low rate-of-strain stress-strain curve for Butacite®, the plasticized PVB manufactured for architectural laminated glass by DuPont, which is shown in Fig. 49. The extension rate was given as 1mm/s, but the sample length and temperature were not given. The data provided included a Poisson's ratio of 0.499.

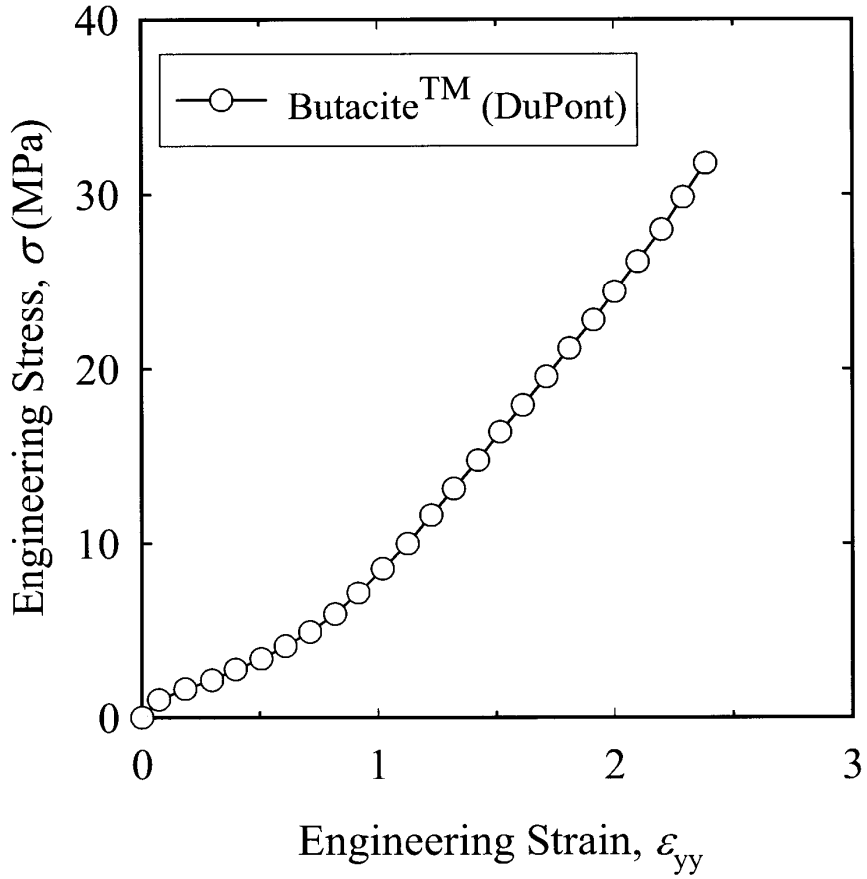

Figure 49. Low rate-of-strain stress-strain curve for Butacite® [120]

Bennison et al. [88] provided not only the chart in Fig. 35, but also a full listing of the parameters for an eleven term generalised Maxwell series for the viscoelastic properties of Butacite® PBV at a reference temperature T_0 of 20ºC. The parameters are listed in Table 13.

Term No i	Stiffness ratio G_i/G_0	Time constant τ_i (sec)
1	0.1606000	3.2557×10^{-11}
2	0.0787770	4.9491×10^{-9}
3	0.2912000	7.2427×10^{-8}
4	0.0711550	9.8635×10^{-6}
5	0.2688000	2.8059×10^{-3}
6	0.0895860	1.6441×10^{-1}
7	0.0301830	2.2646×10^{0}
8	0.0076056	3.5364×10^{1}
9	0.0009634	9.3675×10^{3}
10	0.0004059	6.4141×10^{5}
11	0.0006143	4.1347×10^{7}
G_∞	0.0001098	

Table 13. Terms in the Generalised Maxwell series description (Eqn. 24)

Additional parameters in Ref. 88 include:

- Instantaneous shear modulus $G_0 = G_\infty + \sum_{i=1}^{n} G_i = 0.471$ GPa
- Time shift constants for Eqn. 25, $J_1 = 20.5$ and $J_2 = 91.1$
- Bulk modulus $K = 2.0$ GPa

This approach assumes a linear viscoelastic response from PVB that Ferry [87] states is only exact for infinitesimal strains and strain rates, and that real viscoelasticity will vary from the idealised linear model as these values become finite.

Van Duser et al. [86] used the same data, and noted that plasticized PVB, tested under constant strain rate, exhibited increases in stiffness at large strains, but that linear viscoelasticity remained an accurate representation of the constitutive behaviour up to strains of approximately 0.1. This was appropriate for the analysis of laminated glass prior to breakage.

Ref. 86 noted that the time shift constants were derived from data from tests between 10ºC and 70ºC, and that deformation was mostly reversible within this range. It emphasised that it was not uncommon for viscoelastic properties of plasticized PVB to vary between manufacturers.

Wei et al. [85] used a simpler viscoelastic model, given in Eqn. 22. This is equivalent to a Maxwell series with only one term beyond the long term modulus. Two sets of data were used. For comparison with static test data, PVB properties were adopted from the Bennison et al. [88] Maxwell series data at a temperature of 46.5ºC to give the best fit to the experimental data:

- $G_0 = 0.471$ GPa
- $G_\infty = 0.376$ MPa
- $\beta = 1/\tau = 66.0$ s^{-1}

An alternative set of data was used in Ref. 85 for the dynamic analyses, but with no source stated:

- G_0 = 0.33 GPa
- G_∞ = 0.69 MPa
- $\beta = 1/\tau = 12.6\ s^{-1}$

Other properties of PVB given in Ref. 85 are a density of 1100 kg/m^3, and a bulk modulus K of 2.0 GPa, although sensitivity studies showed little effect on the dynamic response and stresses from variations between 0.2 GPa and 20 GPa.

WINGARD 5.5 PE [100] contained an elasto-plastic material model for membranes, with default material properties for PVB of:

- Young's modulus E = 50,000 psi = 345 MPa
- Poisson's ratio ν = 0.47
- Yield stress = 3000 psi = 20.7 MPa
- Allowable strain = 2.0

No strain rate or temperature was associated with these values.

4.7.3 Laminated glass

Tests on laminated glass up to cracking have already been reported [73-77,], but the results are described in terms of lateral loading at cracking, which do not provide insights into the material behaviour of laminated glass. The material properties of the glass and the PVB used for analysis of these tests have been reported above. However, there are two reports of tests that give some insight into the composite properties of laminated glass.

4.7.3.1 BRE tests

As part of the PSA testing program described in Section 4.4.2, low rate-of-strain, large deflection lateral loading tests of glazing panels of various makeup were undertaken by Ellis and Beak [93, 94] at the Building Research Establishment.

The majority of the tests were on PVB laminated glass. The test samples were clamped onto a test rig over a butyl sheet, and water was pumped into the space under the butyl sheet to cause the glass to deflect. Pressure and deflection histories were recorded from sensors, allowing pressure vs deflection graphs to be plotted. The duration of each test varied between about 8 minutes and about 28 minutes.

Three distinct stages were reported in the deformation of laminated glass:

- The glass deformed elastically under increasing pressure until the unloaded (i.e. top) glass lamina cracked. The pressure dropped abruptly, with no significant change in mid-span deflection.
- With the loaded (i.e. bottom) glass lamina intact, the pressure increased again while the deflection continued to increase, until the loaded glass lamina

cracked. The pressure dropped abruptly to a low level. An abrupt change in mid-span deflection sometimes indicated a significant change in deformed shape.

- The pressure increased gradually as the interlayer stretched like a balloon. The pressure vs deflection curve tended to follow an "S" shape. The pressure peaked as the interlayer was cut by edges of the glass fragments and the small cuts enlarged and the PVB interlayer tore. This occurred usually at the centre of a long edge, but occasionally at the mid-span parallel to the long edge. Ellis reported that further cracking could be heard during the early part of this stage.

A typical pressure vs deflection curve is shown in Fig. 50, that clearly shows the three stages described. The deflected shape of the glazing near the maximum deflection in the third stage is shown in Fig.51.

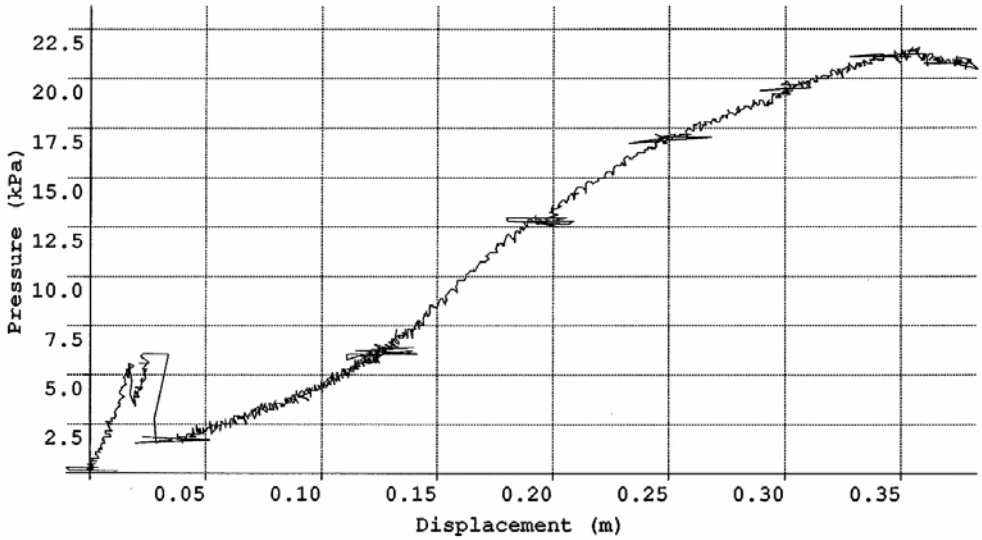

Figure 50. Pressure - deflection history of 1.59m by 0.96m panel of 11.5mm laminated annealed glass and butyl sheet [93]

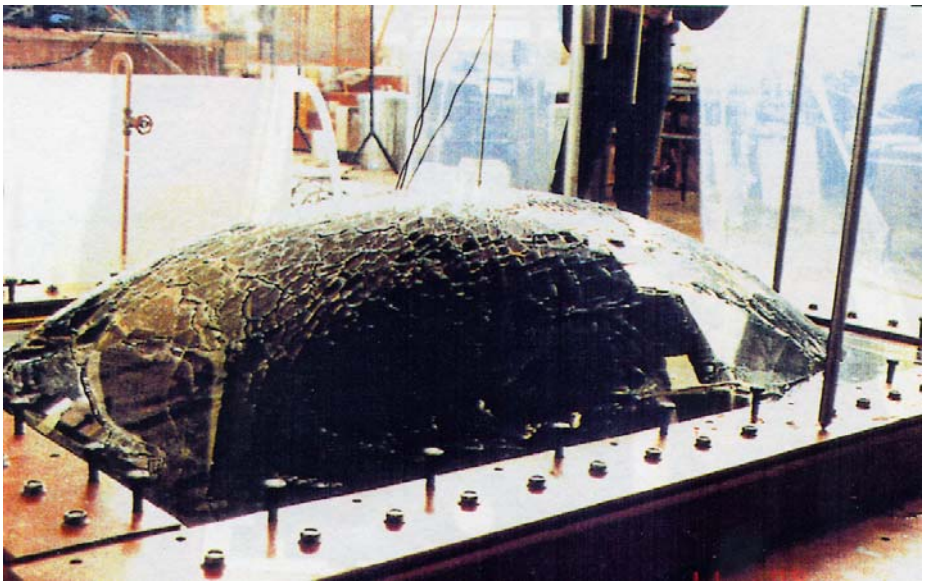

Figure 51. Glass panel from Fig. 50 near maximum deflection [93]

A pressure vs deflection curve of the butyl sheets of each size was measured without a test sample. By subtracting this from the corresponding test curves the resistance curves of the glazing alone could be calculated.

The deflection at maximum pressure in the different tests varied substantially. In most cases this represented the maximum resistance of the PVB interlayer, but in some cases where the butyl sheet was also cut by the glass fragments, they were limited by the capacity of the pumps to deliver additional water to overcome the leaks, and may under-estimate the failure resistance of the interlayer.

Two of the samples sealed with neoprene gasket failed by the glass pulling out of the support, and do under-estimate the failure resistance of the interlayer.

The mid-span deflection at maximum resistance of seven panels of two sizes with 1.52mm thick PVB interlayers ranged from 27% to 57% of the short span. The Author [6] applied the Student t distribution to these results to calculate the 90% confidence of the maximum deflection of a panel at maximum resistance to be 27.8% of the short span. There were insufficient test records for panels of other construction for statistical analysis.

4.7.3.2 Schmidlin tests

Some low rate-of-strain tensile tests were undertaken by Schmidlin for a specific project [92]. These tests were witnessed and analysed by the Author [6]. Although the objective of the test was to assess different silicone ‘bites’ against pull-out, many of the tests involved pulling of pre-cracked laminated glass samples 250 mm long by 150 mm wide with a 1.52 mm thick PVB interlayer, and recording a load vs extension curve. Twenty five suitable tests were undertaken at a temperature of 25°C.

There was a wide scatter of extensions at maximum load, between 68mm and 308mm. Failure generally occurred by tearing of the membrane, although a few shallow anchorages failed by the interlayer pulling out from between the anchored glass. The onset of tearing appears to be influenced by the pattern of cracking, which contained a large random element.

The load / extension curves showed an initial high stiffness, reducing gradually to a constant lower stiffness, as shown for the mean and bounding cases in Fig. 52. The shape is similar to an elastic-plastic yield curve for a material without an abrupt yield stress, but with significant strain hardening. There is significant variation in the initial stiffness and the transition stress (analogous to yield or 0.2% proof stress in metals), but less in the hardening stiffness. The mean elastic modulus at low strain was 52 N/mm^2, the transition occurred at around 20% extension, with a mean transition stress of 3.7 N/mm^2.

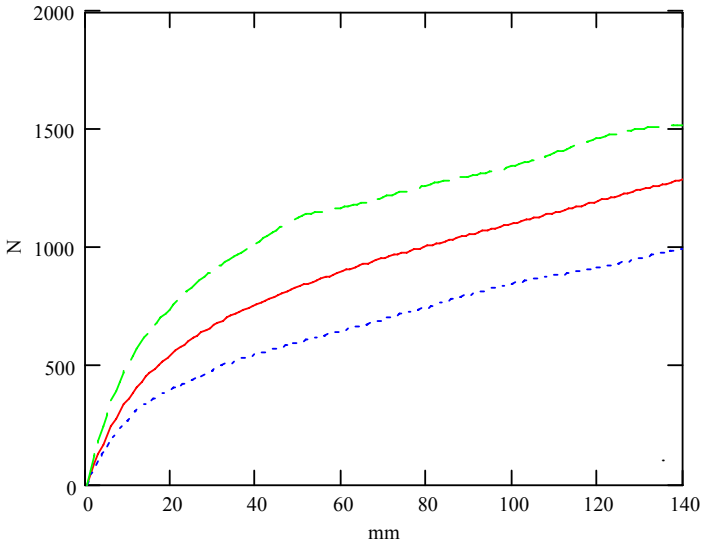

Figure 52. Mean and bounding force – deflection curves for cracked laminated glass under tension [6, after 92]

4.7.3.3 TPS Consult model

The Author [6] used an elastic-pure plastic model of cracked laminated glass. However it was generally not based on material properties of the PVB interlayer, which were not available.

The design maximum plastic deflection was based on the 90% confidence failure deflection of laminated glass in 4.7.3.1, and a yield stress of 8 N/mm^2 was assumed by back-analysis of cases used to define fragility curves of laminated glass [81], with consideration of strain rate enhancement over the transition stress in 4.7.3.2, and allowance for strain hardening in the equivalent elastic-pure plastic model.

The high rate-of-strain modulus was expected to be substantially higher than the low strain-rate value in 4.7.3.2, but a design value was not calculated by back-analysis. Instead a stiffness coefficient was adjusted for Young's modulus and aspect ratio to give a transition to the plastic resistance at around 45-50% of the design maximum deflection and an "S" shaped resistance curve.

4.8 Overview of research on glass response and properties

4.8.1 Analysis of glass response

The various early analyses of glass breakage that were based on small deflection theory are of limited value, as neglect of membrane effects will have distorted the analysis results substantially. Even in the 1960s and 1970s non-linear resistance data was only available for square panels. Realistic analysis of blast response of glazing became possible only at the start of the 1980s, when computing had developed to the point that non-linear numerical analyses [67, 68, 69] had become practicable.

Unfortunately, the significance of the negative phase loading and the elastic response on rebound, identified in the early research had been forgotten. The use of positive phase blast loading only had become the accepted norm for all blast analysis, and the original qualifications by Newmark [34] were not remembered.

Some of the qualitative lessons from the early analysis, informed by extensive observation of blast effects on glazing in the field, need to be married to the more modern methodology, based on decades of research and increasing computational power, to synthesize a reliable modern analysis of glass under blast loading.

The American analyses in the 1980s [24, 70] appear to have been oriented towards prevention of damage from accidental explosions at explosives storage and processing facilities, with very low probabilities of failure and no consideration of post-cracking response. Because the zone at risk was small, expensive designs for the limited glazing at risk to prevent cracking were acceptable. Even when the threat broadened to include a terrorist device [40, 71], the methodology and available data meant that the post-cracking benefits of laminated glass were ignored.

Most current methods of analysis of laminated glass are based on the research by PSA and successors in the 1980s and 1990s, either directly [81], or via the USACE WinDAS database [96]. This was directly aimed at assessing the threat from terrorist bombs, where the threat could be almost anywhere, but where damage and minor injuries could be accepted provided the risk of serious injuries and fatalities could be substantially reduced. This required a very different cost-benefit analysis, where the merits of laminated glass for new construction or major refurbishments became very clear.

Proscribed solutions based directly on this research for basic levels of threat [82, 83] have their place, to give simple solutions to set a base standard of protection for buildings whose threat profile is sufficiently low that expert review and tailored solutions are considered unnecessary. Even these can become quite involved; two different tables of equivalent static loads for different types of supports and fixings, further divided by panel size, and with further adjustments for different glazing make-up, all for just one level of threat. It is important that the need for more detailed analysis for more severe threats is recognised.

The method proposed by Norville & Conrath [98] is felt to take the attempt to simplify the selection of glazing make-up for blast resistance too far, particularly with the inclusion of laminated and monolithic glass in a single method. In practice, the curves are likely to match only commonly tested sizes of commonly tested make-ups, if that. They will not reflect the fact that the ultimate resistance of laminated glass to blast is more a function of the thickness of PVB than the thickness and type of the glass, as this will not be covered by the type factors for cracking of laminated glass. Similarly, the method cannot account for the different dynamic response factors over the range of panel sizes and cannot account for the different changes in non-linear response of panels of different slenderness as the cracking stress increases with higher loading rates, even though it may account for the higher strength.

The method cannot help with the design of the frame. Ref. 98 mentions that the loading transferred to the frame can be determined using dynamic analysis techniques, but does not elaborate. The recommendations for attachment to the frame, that the 'bite' depth should not exceed standard depths any more than necessary to facilitate the width of the structural silicone or adhesive tape sealant, is contrary to UK test experience for laminated glass, as the width of silicone recommended in Ref. 97 is limited to the thickness of the blast resisting material in contact.

The remaining methods, Wingard [100] and the TPS Consult analysis [6], are very similar in approach, using a numerical SDOF analysis with a non-linear resistance for glass cracking and a distributed reaction based on the SDOF reaction coefficients. The substantially different results arise from some of the different assumptions about the behaviour of the PVB interlayer, the source of the SDOF coefficients, and the additional factors taken into account.

WINGARD [100] originally included:

- SDOF coefficients from Biggs [35].
- Damping defined as a proportion of "critical damping" (default 2%) and varying with the non-linear stiffness.
- Reaction distribution using a Navier stress distribution [38,41].
- Glass resistance after Moore [67].
- A closed form non-linear elastic membrane interlayer resistance, calculated by equating strain energy and work done, giving a cubic curve compared to the solution of Timoshenko [38] for a square panel.
- An adiabatic gas spring model for calculating pressure in the cavity of double glazing, providing load sharing between the leaves.
- An impact model between leaves, calculating a common velocity from the combined momentum.

The 2005 version, WINGARD 5.5 PE [100] also incorporated an optional elastic-pure plastic membrane interlayer resistance. The yield point is calculated from the elastic model and the yield stress, but the yield is taken to be local, over 2.5% of the shortest span. Total failure is predicted to occur once the strains in this region exceed the

failure strain. The effect of this plastic straining on the membrane resistance is not described.

The TPS Consult [6] analysis started with a model similar to that in WINGARD [100], but various factors were modified in the light of observations to improve the accuracy of the modelled response:

- Glass resistance after Moore [67].
- SDOF transformation factors for glass calculated from the simply-supported elastic deflected shape for small deflections using the Navier equations [38, 41].
- Static reaction distribution from the associated stress equations [41] for the same analyses.
- SDOF dynamic reaction coefficients from equilibrium calculation based on the Navier deflections and stresses [38, 41].
- Elastic-plastic membrane model based on cubic elastic membrane theory [95] and plastic large deflection "soap film" membrane [42]
- A modified elastic rebound resistance for stretched membranes based on the relationship between the equations for plates and shells with initial curvature [90].
- SDOF transformation factors, static and dynamic reaction distributions from a large deflection plastic membrane based on the "soap film" membrane [42]. These were also used for the less critical elastic membrane.
- An adiabatic gas spring model of the sealed cavity volume to calculate the load sharing between the panes of double glazing, based on the small deflection uncracked and the plastic membrane cracked deflected shapes.
- An impact model between leaves, using conservation of momentum and energy to calculate bounce of uncracked panes, and momentum only to calculate a common velocity for the impact of debris.
- Aeroelastic damping equal to the impedance of air on the faces of the glazing. At the back of the window the impedance was taken as that of air at atmospheric pressure. At the front, the impedance was calculated from the loading pressure history using the Rankine-Hugoniot [7] equations, and in the cavity, the damping relative to the mean velocity was calculated from the cavity pressure history.

In 2003, a modified version was developed, using the large deflection glass parameters described in Chapter 6 of this thesis for resistance, transformation factors, cavity pressure calculations and static and dynamic reaction distributions.

Overall, it is felt that the current TPS Consult model [6] has a number of unique features that are worth developing further to improve the modelling of response of laminated glass under blast loading. However there are some features of the WINGARD [100] model such as the closed form equation for the elastic membrane resistance that deserve consideration for inclusion in future models.

At the same time there are assumptions built into the WINGARD [100] model that reflect specifically American window construction practice, such as the use of a narrow silicone bead on one side of the glazing only for "wet glazed" systems, rather than the enhanced supports developed by testing in the UK [81] to fully mobilise the resistance available in the interlayer.

4.8.2 Elastic properties of glass

The elastic properties of soda lime silicate window glass, with a few exceptions such as Ref. 60 and some possible typographical errors introducing a factor of ten difference, are clustered into fairly narrow ranges:

- Young's modulus E within the range in Ref. 52 of 65 MPa to 78 MPa, and most recent values between 69 MPa and 72 MPa. Ref. 104 shows that this variation could reflect chemical differences between test samples within the normal range of composition.
- Poisson's ratio between 0.20 and 0.25, with most recent values given as 0.22. Again, Ref. 104 indicates that variations between at least 0.209 and 0.225 could reflect chemical differences between test samples within the normal range of composition.
- Density between 2489 kg/m^3 and 2519 kg/m^3.

Ref. 108 indicated that the mechanical properties will be unchanged for continuous service up to 250ºC and are unaffected by sub-zero temperatures, although Ref. 46 indicated that a modest reduction in Young's modulus could be expected at elevated temperatures.

Design values used by the Author [6] were:

- Young's Modulus E = 70 MPa
- Poisson's ratio μ = 0.22
- Density ρ = 2490 kg/m^3.

These fall within the range of test and normally used values, and are appropriate for continued use. For all practical purposes, these design values can be considered to be constants.

4.8.3 Design breaking strength of glass

The identification of design fracture strengths for glass subjected to blast loading is far more complex. For deterministic analysis of laminated glass systems, in which cracking is not the end of the analysis, a deterministic design cracking strength is required. In practice, there is a substantial element of randomness in glass cracking. As a result, any deterministic design value will be associated with a probability of cracking rather than a certainty.

This uncertainty is common to most structural design. Normal practice is to choose a characteristic design strength with a high, but not extreme, confidence of survival,

typically 95% confidence. This can be established statistically from a moderate number of material tests without being overly dependent on the shape of the tail of the statistical distribution of results assumed for the test data.

In most cases, a normal distribution of strength is assumed. This distribution can be used directly to calculate the characteristic strength of the material from about 40 test results, where the distribution of the sample can be taken as representative of the material population. The "Student t" distribution can be used to calculate a confidence level strength value from fewer results. As the number of results reduces below about 40, the margin between the mean of the test results and the confidence level value increases.

In static design of structures for normal loadings, where only extremely low probabilities of failure would be acceptable under continuous or frequently occurring loads, characteristic strengths are reduced and characteristic loads are increased by partial safety factors to increase the confidence levels of the design values. This approach will not work in a deterministic dynamic analysis where the value of some loads are controlled by other strengths, and, for example, the reduction in flexural yield strength by a partial safety factor would reduce the maximum shear force, and where inertia will make the effects of scaling loads and strength non-linear.

In blast dynamics, it is normal to perform the analysis of the rare event, expected no more than once in the lifetime of a small proportion of buildings, using characteristic or notional forces or strengths to give a high, but not extreme, confidence level that the response will not be exceeded. A 90% confidence level is explicit [22,23] or implicit in most US military manuals. Where an increase in the failure strength used in the analysis would increase loadings in a secondary component or mechanism, and particularly where the secondary failure would not be ductile, it is normal to provide a factor of safety in the assessment of the secondary component. An overall factor of safety of 1.5 against ultimate capacity is common.

This approach was used by the Author in the TPS Consult analysis model [6], and is still considered to be appropriate. When applied to bomb blast on a large building façade, this could imply that one in every 10 panes could be expected to exceed the calculated response and possibly exceed the calculated hazard rating. However, the blast load distribution from any one event is not uniform, and the worst-case loading will only act on a small part of the façade. The design hazard rating could be exceeded at a few windows, but far less than 1 in 10. In assessing the overall risk from what will in any case be an uncertain threat, this is considered to be an acceptable risk.

In the light of this design philosophy, the design breaking strength of glass to be incorporated into an analysis should be such as to give about a 90% confidence of survival (or a 10% probability of breaking) under blast loading through the building's expected life.

Various references [46, 111, 113,116] indicate that fracture of glass is initiated at pre-existing sub-microscopic flaws in the surface of the glass, and that the probability of the glass cracking at any particular stress level is affected by the size, nature, number and distribution of the flaws. This is based on the fracture mechanics analysis of Griffith [110]. These references also indicates that the strength of the glass varies with

the loading duration as a result of corrosion of the stressed Griffith flaws by atmospheric moisture.

Initial flaws are formed in the surface of the glass during manufacture, and these are augmented and modified through the life of the glass, by mechanical treatment like abrasion [40], by weathering [72], and by thermal shock.

Cracking of a glass pane or ply under load is initiated when the stress at the first Griffith flaw reaches the failure stress of that flaw. This failure mechanism is often represented as the weakest link in a chain. A statistical distribution developed to model this failure mechanism is the Weibull distribution. This assumes a random distribution of flaws with a normal distribution of flaw strengths. Among other features, this model gives a lower mean strength for a larger glass pane or a longer chain with the same distribution of flaws per unit area or per link.

Analyses of glazing have been undertaken using the Weibull distribution [72, 86]. However, these required the probability of cracking to be integrated over the whole surface of the panel as a function of the distribution of principal stresses distributed over the surface. For large deflections of two-way spanning glass panels, where the maximum principal stress is not proportional to the loading [67] and the distribution changes with loading [68] this would require separate assessments over the whole range of loading levels for all permutations of Weibull statistical coefficients.

Although the Weibull distribution is a useful research tool, the statistical parameters are difficult to derive from testing, and the database is currently too limited for reliable generic design parameters to be identified. At the current state of knowledge, it is therefore not an appropriate tool for deriving glass design strengths for deterministic SDOF analyses, although research based on it can certainly inform the decision making process.

A statistical analysis of test data using the normal distribution can give an acceptable probability distribution for the test samples, but there remains the difficulty of relating the test results to glass panes under blast loading, bearing in mind the different loading durations of the tests and blast loading, the sensitivity of the glass strength to the treatment of the glass through its life, and even the difference in size of the test samples and window panes.

The selection of suitable probability criteria can greatly reduce the sensitivity of the analysis to the age, exposure and treatment of glass through the building life. The existing data shows that selection of a 90% or 95% confidence level for the design strength is particularly suitable, because the effect of abrasion or weathering of the glass surface on this design strength is minimal. This is illustrated for plate glass in Fig. 33, from McLellan & Shand [46]. This is also shown by an analysis of the normal distribution data collected by Mayor & Flanders [40], presented in Table 14.

Glass Type	Treatment	Mean Failure Stress	Coefficient of variation	90% confidence stress	95% confidence stress
		MPa		MPa	MPa
Annealed float glass	New	106	0.279	68.1	57.4
	Abraded	69.6	0.050	65.1	63.9
Plate glass	New	96.5	0.297	59.8	49.4
Fully tempered	New	230	0.171	179.6	165.3
	Abraded	168	0.033	160.9	158.9

Table 14. Calculation of confidence level values from data in Ref. 40

One explanation of this might be that, at low probabilities of cracking, a critical flaw might be at or close to the position and orientation of the maximum stress, and cause cracking as soon as the stress reaches the critical stress for the flaw. Increasing the number of such flaws by weathering or abrasion will not increase the stress required to cause cracking significantly. In abraded glass with a high density of flaws, on average there will still be a critical flaw close to the position and orientation of the maximum stress, so the coefficient of variation is very small. In new glass there are far fewer flaws, so as the probability of failure increases it is more likely that the flaws will be at less critical locations and orientations, so the maximum stress in the glass will have to increase above the critical level to generate critical stress at the flaw, and hence the larger coefficient of variation.

As the effect of the pane size on the mean strength arises from the different number of flaws in the pane, this should be affected by the same mechanism. The mean and the variation in results should be smaller for larger panes. The effect of pane size should be far less significant in the 90% confidence strength than in the mean strength.

Figure 34, taken from Ref. 72, shows a reduction in the effect of differential weathering of similar glass at low probabilities using the Weibull distribution also, although it does not show the overlap seen in the normal distribution. Other data in Ref. 72 suggests that there may still be a difference between different types of annealed glass, such as sheet, plate and float glass, even when weathered. This would be consistent with the data on plate glass from Ref.40 analysed in Table 12, which does not converge with the data on float glass.

This could occur in spite of the above explanation for abrasion if weathering tends to increase the size of the flaws as well as the number. The larger flaws are more critical and will trigger cracking with a lower stress at the flaw. Different manufacturing processes could also result in different sized initial flaws.

The mechanism that causes the sensitivity of the cracking strength to loading duration is complex and not well understood. It appears to involve interaction with water vapour in the atmosphere when the glass is stressed, but is not simply a cumulative crack growth mechanism, as repeated sub-critical blast loading does not cause a reduction in the failure strength [58]. Even when data on 90% or 95% confidence strength is analysed from various sources, as shown in Table 15, it is necessary to consider the loading duration of the tests.

Source	Float glass		Heat strengthened		Toughened	
	90%	95%	90%	95%	90%	95%
	MPa	MPa	MPa	MPa	MPa	MPa
Ref. 40 new	68.1	57.4	127.6	115.3	179.6	165.3
Ref. 40 abraded	65.1	63.9	-	-	160.9	158.9
Ref. 71	61.1	54.3	93.5	87.1	139.1	133.3
Ref. 100	54.3	45.7	78.9	73.6	139.1	133.3
Ref. 105-108	-	45	-	70	-	120

Table 15. Confidence level values for glass strength calculated from various sources

Ref. 105 gives a design characteristic value for float glass for a short quasi-static loading like wind loading, which implies a load duration of about 3-5 seconds, and Refs. 106-108 specify minimum test characteristic values for similar load durations. The other references do not state the duration of the tests upon which the data is based. The similarities with the values from Ref. 100 strongly suggest that the values are based on tests of a similar duration, while the similar structure of the data suggests that this is a revision of the data in Ref. 71.

Even for Ref. 40, it is not clear that the data was based on high strain rate testing, as there is discussion of Dynamic Increase Factors (DIF) that might be required to calculate dynamic design strengths. A value for a DIF of 1.5 for annealed float glass and lower values for strengthened glass types is discussed.

Ref. 100 does not use a lower bound characteristic strength for glass cracking, but used the 75% failure stress level for the short quasi-static test data. However, this could be regarded as applying a DIF related to the coefficient of variation for the different types of glass. For comparison, this has also been applied to the strength data from Ref.71, and results are included in Table 16. As a means of calculating the DIF this is very suspect as it would give inappropriate results for weathered or abraded glass.

Source	Glass type	90% confidence strength	Dynamic design Strength	Dynamic increase factor
		MPa	MPa	
BLASTOP, Ref. 71	Float	61.1	97.3	1.593
	Heat strengthened	93.5	127.4	1.363
	Toughened	139.1	170.4	1.224
WINGARD, Ref. 100	Float	54.3	100.7	1.854
	Heat strengthened	78.9	107.6	1.363
	Toughened	139.1	170.4	1.224

Table 16. Dynamic design strengths and implicit dynamic increase factors

An alternative source for dynamic design strengths for glass comes from back-analysis of blast trials of monolithic glass panes. This would overcome any questions

of strain rate and the differences between typical panel size and test sample size. However, the number of test samples are likely to be substantially smaller, the variability of the loading and other circumstances of the tests may add to the scatter, and systematic bias could be introduced by any error or approximation in the back-analysis.

The dynamic design strengths in Ref. 81 were derived in this way. The analysis used the non-linear resistance function from Ref. 67, but SDOF transformation factors from Refs. 35 or 24, which may have introduced some systematic error. The loading histories may have been based on measurements during the tests, or on idealised positive phase loadings, corrected for the clearing around the test cubicles. The characteristic design strengths of 80 MPa for annealed float glass and 180 MPa for toughened float glass in Ref. 81 appear to be lower bound values, but perhaps not calculated statistically for a particular confidence level.

The design strength for annealed float glass is lower than that used in WINGARD [100], or that calculated from BLASTOP [71] but less than the characteristic value from BLAST [40]. The small difference in WINGARD between the strengths for annealed and heat strengthened glass suggests that the annealed strength in WINGARD is upper bound due to the use of a very high coefficient of variation to define the dynamic increase factor, and that the value in Ref. 81 is more representative. This would be consistent with a coefficient of variation of 0.248 in the data in Ref. 100, which is midway between the values in Refs. 71 and 40.

The effect of heat strengthening or toughening is to induce a compressive pre-stress in the surface of the glass. If the pre-stress is uniform, which appears to be the case except possibly near the edges, then the breaking strength should equal the annealed glass breaking strength plus the surface pre-stress. The minimum breaking strengths specified in the European standards [106-108] therefore represent minimum pre-stress levels of 25 MPa for heat strengthened glass, and 75 MPa for toughening.

There is no specified maximum for toughening, and surface stresses up to at least 125 MPa can be achieved. In the UK and Europe surface stresses of at least 100 MPa are normal, but manufacturing practices in the USA are not identical, and lower prestresses of the order 80-90 MPa are reported to be more common. There may be a genuine difference between the dynamic design strength of 170 MPa from US data and 180 MPa from UK data.

Heat strengthened glass is often specified when some of the undesirable features arising from full tempering are unacceptable, most commonly the risk of spontaneous breakage due to nickel sulphide inclusions and the ripples in the surface. To avoid these, the maximum temperature is reduced, which will reduce the pre-stress that can be generated, and a significant margin below the minimum toughened stress will be used to avoid risking the break pattern for toughened glass occurring. In practice heat strengthening will not be undertaken to give surface pre-stress above about 50 MPa.

Heat strengthened glass is often specified to resist thermal shock or temperature gradients that might crack annealed glass. Depending on the resistance required, different degrees of surface pre-stress may be specified. The 108 MPa dynamic design strength in WINGARD [100] is consistent with a pre-stress close to the minimum of

25 MPa and an annealed glass dynamic design stress of about 80 MPa. With higher heat strengthening specified to give a surface pre-stress of 40 MPa, a design strength of 120 MPa would appear to be suitable.

The method of analysis will be independent of the exact dynamic strength used for design. However in any back-analysis of laminated glass trials, an appropriate cracking strength rather than a lower bound design strength will need to be considered for the glass so that the influence of the PVB membrane may be studied. This has to be considered in a case-by-case basis from the records of the trial, as each pane will have behaved differently due to random variability of Griffith flaw strengths and distribution.

4.8.4 Properties and behaviour of uncracked laminated glass

There are two main stages to be considered for laminated glass, i.e. before and after cracking. There have been extensive studies of uncracked laminated glass, but few studies of the post-cracking behaviour.

The earlier concepts of uncracked laminated glass were based mainly on tests of one-way spanning samples with no membrane forces, and looked at the stiffness relative to two layered glass plies or a single monolithic glass plate equal to the combined thickness of the glass plies, rather than the overall composite section thickness. The weaknesses in this model were finally pointed out by Norville, King and Swafford [84] in 1998, and were also noted by Van Duser et al. [86] in 1999.

With a stiff interlayer, the bending properties can approach that of a monolithic glass pane of equal thickness to the laminated glass, which may be substantially stiffer than a pane equal to the glass alone.

In a pane supported on four edges, membrane stresses will start to become significant for deflections greater than about half the thickness, and will dominate the stresses once the deflections reach 5-10 times the thickness. The membrane stiffness and stresses in the different laminated glass models all converge towards that of the glass section alone as the deflection increases, and the stiffness of the interlayer ceases to be significant. In blast analyses, the design strength of the glass is higher than for low rates of straining, so the glass can deflect further before it cracks, and the cracking stresses will tend to be dominated by the membrane behaviour except for small, thick panes.

Van Duser et al. [86] analysed laminated glass panels, with a viscoelastic PVB interlayer based on the data for Butacite [88], but with a temperature adjustment to allow for the softer PVB used in the test panels. The central deflections at room temperature for a loading duration of about 60 seconds corresponded to the monolithic glass model equal to the two plies, but at lower temperatures approached those of the full monolithic section. The probability of failure was found to be lower for laminates than for the monolithic glass plate of equal total thickness, so the treatment of laminated glass as fully composite would tend to underestimate the strength, demonstrating the previous concept that laminated glass was weaker to be erroneous.

Wei et al. [85] extended the analysis of viscoelastic PVB interlayers into the range of high strain rate response to blast loading, although remaining in the amplitude range where small deflection theory could be applied. Again the PVB was modelled as softer than Butacite, this time by using viscoelastic properties with a value of the short term shear modulus reduced by 30% rather than by a temperature adjustment. The results indicated that the deviation of the deflection history and stress distribution from that of a monolithic pane equal to the full thickness was negligible.

These analyses indicate that, at room temperature, a laminated glass pane under blast loading can be treated as a fully composite section, with flexural properties based on the full section, and tensile properties based on the glass section. However, there may be a reduction in the flexural stiffness of the composite section at higher temperatures.

4.8.5 Properties and behaviour of laminated glass after cracking

Ellis and Beak [93, 94] showed that cracking can occur in stages. In Ref. 6, the Author modelled the remaining uncracked ply as a thinner monolithic plate. This, on the whole, appears to underestimate the performance to second crack seen in Refs. 93 and 94. This may be because, with the exception of toughened laminated glass, the cracking of the first ply does not lead to a complete loss of strength and stiffness across the whole area of the ply. In some cases the initial crack would occur in the centre, while treating the more slender remaining leaf as monolithic would lead to the expectation of a corner failure. If the first ply is uncracked in the corner, the strengthening and stiffening could result in the second ply carrying additional load until it would crack in the centre.

This underestimate of the second cracking strength cannot always be relied upon to occur, and hence cannot be taken into account in assessing the design strength. In practice, this has less effect on the resistance to blast loading than for low strain rate loading. The higher failure stresses combined with the large deflection resistance curves stiffens the second ply more than the overall leaf, and the failure deflection to first crack increases more than that to second crack. In many cases second crack will occur instantaneously with first crack. Even when it does not, the displacement between first and second crack is shortened, and the resistance between them makes a smaller contribution to the overall resistance capacity.

After second crack, the “S” shape of the resistance curves measured in Refs. 93 and 94 indicate that the stress-strain properties of the PVB membrane are not simply linear elastic. Ref. 92 and the analysis by the Author [6] show that a bi-linear stress-strain curve with strain hardening could be a reasonable model.

The fairly crude elastic and pure plastic membrane models used by the Author [6] to approximate this could be improved with better and more appropriate materials data at high strain rates. The elastic membrane model with local plasticity used in WINGARD [100], although an improvement on an elastic-brittle model, does not seem realistic.

The linear viscoelastic properties used to model PVB in uncracked laminated glass [88] provides an alternative explanation of the bi-linearity to plastic yielding, but the modelling of laminated glass and other polymers for impact loading and high-rate-of-strain tensile testing [101-104] suggests that bespoke models combining multiple terms of non-linear viscoelasticity and rubber stretching might be required to model large deflection behaviour in this way. Unfortunately, this is unlikely to be suitable for generating simplified resistance functions for SDOF analysis.

However, a bilinear elastic-plastic model that provides a good approximate fit to test data and varies with strain rate might provide a suitable model for the resistance of a tensile membrane to a monotonically increasing load, even if the actual softening mechanism is other than true plasticity.

The failure strains from PVB tests in Ref. 117 are many times those observed in laminated glass under lateral loading, so the details of behaviour at the lower end of the force-deflection curve may be of more relevance than the behaviour to tensile failure, and other failure mechanisms such as cutting of the membrane on cracked glass edges need to be considered.

A statistical analysis by the Author [6] of the 7 results for laminated glass with a 1.52mm interlayer in Refs. 92 & 93 using the "Student t" distribution gave a 90% confidence deflection at maximum resistance of 27.8% of the short span. Most of the failures were due to cutting of the membrane at the supports, support failure and leakage through cut membranes. This gives an indication of a possible deflection limit that is independent of strain rate, but that does not preclude the possibility of tensile failure of the membrane at lower deflections for high strain rates, as appears to be arbitrarily assumed in Refs. 81 and 100. Measurement of the deflection of glazing under blast loading is required to assess appropriate membrane deflection limits.

5 The single degree of freedom method for small deflections of panels supported on four sides

5.1 Review of existing calculations

The original calculation of elastic, elasto-plastic and plastic coefficients in Ref. 16 are described in Section 3.5.4 of this thesis, with modifications by Biggs [35] and alternative transformation factors in TM5-1300 [17, 24], described in Section 3.5.5. The transformation factors in TM5-1300 are significantly at variance with the earlier values.

Calculations for simply supported elastic plates by Mayor & Flanders [40], and by the Author [6] are also presented in Section 3.5.5. These are in agreement with each other, but differ significantly from both the previous sources.

Because of these discrepancies, the accuracy of the existing parameters on which the implementation of the equivalent SDOF method of analysis has been based are questionable. Some of the causes of the discrepancies have been noted in the overview of the existing methods of analysis of blast response, in Section 3.6.3.

Because of the fundamental nature of these coefficients to the whole of blast analysis, a critical review of all of the existing coefficients for two-way spanning panels and the calculations that were used to derive them has been undertaken. This work has been presented by the Author in several papers [121, 122, 123].

5.1.1 Plastic analysis in Ref. 16

The plastic deflected shapes were based on simple yield line patterns. The interpolation process used resulted in a fixed yield line angle of 45° in the spans. The reactions are based on dynamic equilibrium calculations assuming that there is zero shear across the span yield lines.

Review of the plastic calculations shows a number of sources of inaccuracy:

- A 45º yield line approximation is justified in static analysis because it only affects the resistance. This has a stationary value at the critical angle, so a moderate error in yield line position will only cause a small error in the resistance. The SDOF parameters are not stationary, so the errors due to the approximation will be larger in these, as is illustrated in Table 17.

- The equilibrium method of yield line solution requires the use of nodal forces to represent shears and twists across yield lines [38], so the assumption of no shear transfer is not universally correct. A constraint such as 45º yield line angles will require non-zero nodal forces for equilibrium. Neglecting these forces in the dynamic equilibrium calculations can lead to larger errors in the reaction coefficients, as shown in Table 17.

Parameters for simply-supported plastic panel of aspect ratio of 0.5	Stationary node point	45 degree node point	Difference from stationary
Resistance coefficient, Ru/m	28.21	28.80	
Load factor, K_L	0.391	0.417	6.45%
Mass factor, K_M	0.225	0.250	11.2%
Load-mass factor, K_{LM}	0.574	0.600	4.49%
Load reaction coefficient, short edge, V_{FS}	0.054	0.042	-23.2%
Resistance reaction coefficient, short edge, V_{RS}	0.109	0.083	-23.2%
Load reaction coefficient, long edge, V_{FL}	0.098	0.104	6.45%
Resistance reaction coefficient, long edge, V_{RL}	0.239	0.271	13.2%

Table 17. Plastic parameters for alternative yield line models of simply-supported panels of aspect ratio 0.5

- A 1951 American Concrete Institute document is cited by Ref. 16 for the resistance coefficients relative to a uniform moment capacity m used in the tables. These values are not consistent with yield line analysis using the 45º assumptions and give more upper bound, i.e. less accurate, results, as shown in Table 18.

Resistance coefficient	Stationary Node Point	45 degree node point		Ref. 16	
Aspect ratio λ	Ru/m	Ru/m	Difference from stationary	Ru/m	Difference from stationary
1.0	24.0	24.0	0%	24.0	0%
0.9	24.10	24.13	0.12%	24.22	0.50%
0.8	24.44	24.55	0.45%	24.88	1.80%
0.7	25.13	25.34	0.84%	26.0	3.46%
0.6	26.31	26.67	1.37%	27.5	4.52%
0.5	28.28	28.80	1.83%	30.0	6.08%

Table 18. Plastic resistance coefficients of simply-supported isotropic panels from alternative models

- The plastic resistance is defined in terms of different span and support resistances, implying that the analysis can be applied to an orthotropic slab. In yield line theory, yield line angles are modified by orthotropy. The Affinity Theorem is used to convert the orthotropic panel to an isotropic affine panel with a modified aspect ratio [38]. If the yield line angles in the affine panel are solved assuming a 45º angle, the yield line angles in the real orthotropic panel cannot be 45º.

- A particular case of orthotropic slabs is fixity on two opposite sides only. If the reinforcement were otherwise isotropic, the Affinity Theorem would change 45º yield line angles to approximately 35º or 55º, depending on which edges are fixed. The interpolation used for long or short edges fixed assumes an unchanged 45º angle, and is not consistent with yield line theory.

5.1.2 Elastic analysis in Ref.16

The elastic and elastic-plastic analyses are based on a very crude approximation of two-way spanning deflected shape, using triangular and trapezoidal panels as for the yield line calculations, but with one-way spanning deflected shapes, so as to allow extrapolation from the square case to the one-way spanning. This gives rise to a number of sources of inaccuracy:

- The assumed deflected shape is substantially different from the deflected shape of a slab under static uniformly distributed load, as can be seen in Fig. 53. This introduces significant errors even for the symmetrical square panel, as shown in Table 19.

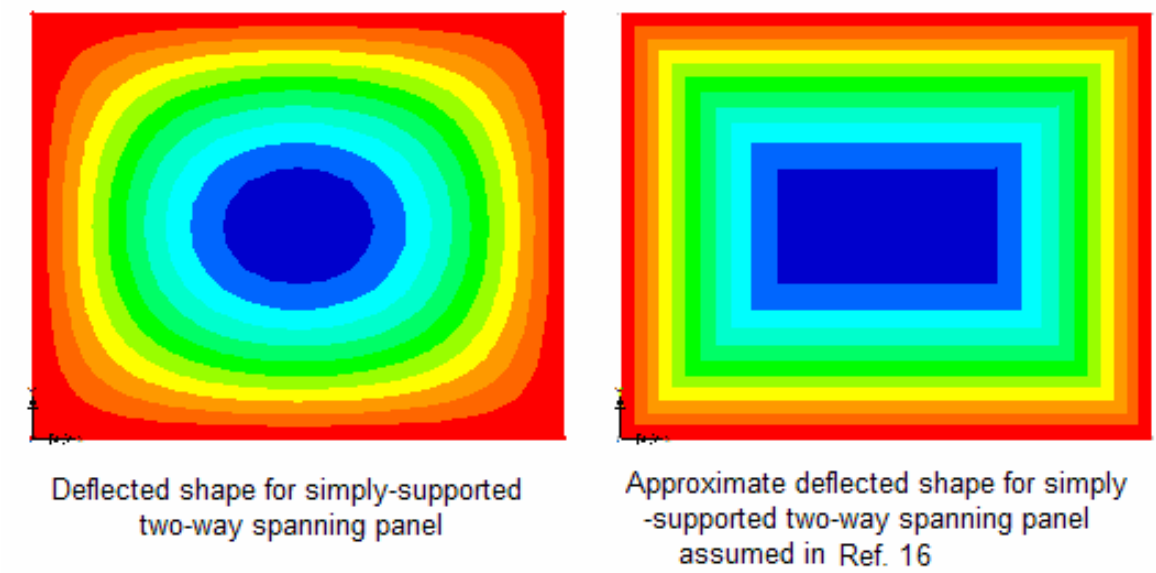

Figure 53. Comparison of typical true and approximate elastic deflected shapes

- The mixing of one-way deflected shapes for simple and pinned supports for the panels with fixity on two edges implies a deflected shape which does not even meet at the joins, and is therefore not kinematically compatible.

- There is no justification for the assumption that 45° lines in an elastic panel represent lines of zero shear except in symmetrical square panels. Ignoring any shear transfer will introduce substantial errors in the reactions.

- The spring constants are based on coefficients given by Timoshenko [38] for a Poisson's ratio of 0.3, suitable for steel plates, but twice the customary value for reinforced concrete. These have been used unaltered, which introduces

additional inaccuracy, as a simple adjustment in the formula can be made for Poisson's ratio.

Parameters for simply-supported elastic panel of aspect ratio 1.0, using Poisson's ratio of 0.3	Navier solution after Timoshenko [38]	Ref. 16	Difference
Spring constant coefficient $ke/(a^2/EI)$	270.5	271	0.18%
Load factor, K_L	0.418	0.45	7.66%
Mass factor, K_M	0.262	0.31	18.3%
Load-mass factor, K_{LM}	0.627	0.68	8.45%
Load reaction coefficient, short edge, V_{FS}	0.128	0.07	-45.3%
Resistance reaction coefficient, short edge, V_{RS}	0.122	0.18	+47.5%
Load reaction coefficient, long edge, V_{FL}	0.128	0.07	-45.3%
Resistance reaction coefficient, long edge, V_{RL}	0.122	0.18	+47.5%

Table 19. Elastic parameters for alternative deflected shapes

- The reference to Timeshenko [38] for spring constants is rather ironic, as he provides all the formulae required for a proper elastic deflected shape and stress calculation for different aspect ratios.

- In employing the simply-supported elastic model to represent the incremental elasto-plastic stage, no provision is made to allow for the elastic shear in the supports. Even though the panels are symmetrical in two axes, unequal fixity will give rise to an elastic shear transfer from the pinned edges to the fixed edges that will modify the reactions. This omission leads to inaccurate distribution of reactions for panels with unequal fixity.

Numerical accuracy is suspect in the original tables. Using rounded values of K_L and K_M to calculate K_{LM} results in rounding errors and inconsistent trends in K_{LM} from what is supposed to be a smooth interpolation. This helps to conceal a typographical error where a value of K_M repeats that of the line above, and is used to calculate an incorrect K_{LM}. There are also rounding mistakes where the same ratio has sometimes been rounded down where it has been correctly rounded up elsewhere, and cases where some of the few calculated values of K_L and K_M for square panels have been incorrectly rounded to try to equalize the interpolation steps.

5.1.3 Biggs 'Introduction to Structural Dynamics'

In 1964, Biggs [35] included tables extracted from Ref. 16 in his seminal textbook, although for two-way spans he considered only the simply-supported and fully-fixed cases. He stated that the factors given were based upon approximations to the classical plate theory for deflections in the elastic range and yield line theory in the plastic range, which in the light of foregoing comments may rather overstate their provenance.

Biggs did make two improvements to the two-way tables:

- the elastic spring constant corresponds to a Poisson's ratio of 0.15 rather than 0.3, as appropriate for reinforced concrete, although this is not stated in the text or tables.

- the elastic resistance of the fully-fixed panels was recalculated.

Biggs also tidied up the inconsistency between simply-supported elastic and various fixed elastic-plastic values of K_L for a square panel, giving a consistent, if not completely accurate, value of 0.46. However, other errors in the two-way tables that he included from Ref. 16 were not corrected.

5.1.4 Plastic Analysis in TM5-1300

There are extensive charts, tables and formulae in TM5-1300 [17] defining hinge or yield line location, resistance, and static shears for plastic analysis of uniformly loaded one-way spans and a variety of two-way spans. These include panels with one or two edges unsupported, so long as opposed supports have symmetric support fixity. The single chart for load-mass factor K_{LM} against yield line location covers all these cases.

This data is based upon the equilibrium method of yield line analysis for the classical yield line pattern, with the interior 'sagging' yield lines extending to the corners of the panels, and the nodes free to find the stationary position, as described by Jones and Wood [39]. The data incorporates the Affinity Theorem, and works equally for isotropic and orthotropic panels. As such, it represents a major step forward from the approximations of Ref. 16.

Even so, there are three areas of concern about the analysis used:

- An arbitrary modification of stress is used to reduce the resistance from the "classic" yield line values by between 11% and 17% to account for corner stiffness. This adjustment is at least 50% greater than can be justified by advanced yield line models, and fails to adjust the deflected shape and transformation factors.

- The equilibrium equations do not include nodal force terms, and will reach an incorrect equilibrium where these are non-zero, such as where diagonal yield lines reach free edges.

- TM5-1300 does not provide formulae for calculating the dynamic reactions. It uses a static plastic resistance as a generally conservative approximation for shear design, but does not allow calculation of a reaction history on a support. This makes it impractical for calculating successive degrees of freedom.

5.1.5 Elastic Analysis in TM5-1300

A table is provided in TM5-1300 [17] to give transformation factors for uniformly loaded elastic and elastic-plastic cases, both one-way and two-way spanning. This table gives values of K_{LM} only, for a range of support conditions and support fixity. For square panels supported uniformly on four sides, the values are more reliable than those produced by Ref. 16, being accurate within the 2 decimal places given for all sides simply-supported, and within 3% for all sides fixed. This implies more realistic two-way spanning shape functions.

However, outside these two values, the table is based on linear interpolation, mostly between one-way spanning values assumed at aspect ratios of 0.5 or 2.0, irrespective of the support conditions, which gives rise to anomalies:

- For the panels supported on all four edges this is interpolated to the square panel with an aspect ratio of unity. This is less accurate than the linear interpolation between aspect ratios of zero and unity in Ref. 16, as the true transformation factors are actually less sensitive to aspect ratio than a linear interpolation. It would actually be considerably more accurate to apply the K_{LM} value for the square panel as a constant value between aspect ratios of 2.0 and 0.5 than to use the table in TM5-1300.

- The situation is even worse for panels with one edge free. No two-way spanning case has been analyzed, and interpolation goes linearly from the one-way span at an aspect ratio of 0.5 to a cantilever at an aspect ratio of 2.0. There appears to have been no consideration that a two-way pattern might exist between these extremes with a K_{LM} value lower than either, or that the cut-off limit of 2.0 is wholly inappropriate for a panel with a free edge, when this is actually around the point of maximum two-way action.

- The interpolation between simply-supported and fully-fixed is again linear and is based solely on the number of fixed edges, taking no account of the distribution, or whether the long or the short edges are fixed. The true variation of K_{LM} with edge fixity is far more complex than assumed, with unequal fixity modifying the shape function.

Charts and tables are provided in TM5-1300 [17] to derive the elastic and elastic-plastic stiffness and resistance, to build up a multi-stage resistance curve. These plot peak elastic stresses, and so identify the onset of yield at each edge in turn. This allows quadri-linear resistance curves of fixed edge panels, which are, in principal, more accurate than the tri-linear curves of Ref. 16. However, using these as a basis to identify the change in stiffness without allowing for the gradual transition as more of the support yields systematically under-estimates the duration of the elastic stage and over estimates the duration of the elasto-plastic stage or stages.

When combined with the excessive downwards adjustment in the plastic resistance, TM5-1300 [17] systematically under-estimates the resistance from the point of first yield onwards.

TM5-1300 contains no data for calculating elastic reactions. The only recommendation is that, if the member does not go fully plastic, the elastic or elasto-plastic resistance at peak deflection is calculated, and then distributed between the supports in proportion to the static plastic reactions to approximate maximum elastic reactions.

5.1.6 Additions in the 1990 revision of TM5-1300

Some additional data was incorporated in the 1990 revision of TM5-1300 [24]. These additions occur primarily in static data that can be used to calculate dynamic properties, but their practical application in dynamic analysis is affected by the existing limitations of the dynamic parameters which have not been updated:

- Plastic resistance and shear data was added for asymmetric support fixity, but the K_{LM} chart is still limited to symmetric fixity by the text of the manual.

- Elastic resistance data for asymmetric support fixity is included, and the original K_{LM} table can be taken to apply, although this merely stretches further the already unreasonable interpolation.

- Cases with concentrated loads from Ref. 16 have been included in the one-way span tables. These are often used to analyze supporting members, but the usefulness is somewhat reduced by the inability to generate a reaction history for the supported members to use as a loading.

5.1.7 Application of SDOF in PSADS

PSADS [23] supersedes a 1986 edition of TM5-855-1 [21], whose SDOF approach was based on Ref. 16. It continues the use of this approach, except that the plastic resistances of panels with fixed supports are reduced by an arbitrary 10% to allow for the upper bound nature of simple yield line analysis. Some, but not all, of the improvements by Biggs [35] have been incorporated in the tables of SDOF coefficients. An additional two-way spanning table has been added, for a panel with one free edge and three fixed edges, based upon the 45° internal yield line assumption, covering aspect ratios from 0.5 to 2.0.

However, PSADS [23] does adopt a somewhat ambivalent approach by including the latest TM5-1300 [24] SDOF data as an Appendix. It leaves it to the user to find the conflicts between the data and to decide which to follow, although the supporting programs appear to be based on the values in the main text.

Although PSADS does allow calculation of dynamic reactions, it has adopted the use of the quasi-static reaction for shear calculations from TM5-1300 [17, 24] because of the artificially high initial reactions that can be produced by the simplified assumptions of a SDOF analysis.

This review of existing SDOF parameters and their derivation was included in a paper for the International Journal of Impact Engineering [122], which is appended to this thesis.

5.2 Assessment of alternative approaches for analysis

5.2.1 Alternative approaches to elastic analysis

Three types of small deflection analysis have been undertaken to calculate spring constants, SDOF transformation factors and reaction coefficients for simply supported plates. These have allowed comparison of the different methods for reliability and accuracy.

Two analyses are based on classical elastic plate formulae described by Timoshenko [38], the Navier and Levy formulae, dating from 1820 and 1899 respectively. The third is based on a linear elastic finite element analysis.

The Navier analysis uses a Mathcad [89] worksheet initially developed by the Author for Ref. 6. However, this has since been used to undertake sensitivity studies for comparison with the other methods.

5.2.1.1 Analysis using the Navier formulae

The Navier formulae for a uniformly loaded plate are based on the exact solution for the double Fourier deflected shape of a rectangular slab under a two dimensional sine wave shaped load distribution, together with the bending, torsion and reaction distributions derived from this. This exact solution can be extended to apply to any loading distribution of *n* by *m* half sine waves. A uniformly distributed load can be represented as a series of sine wave loads with *n* and *m* independently increasing from one to infinity, with amplitudes of each coefficient a function of *n* and *m*.

The deflection *w* of a uniformly loaded rectangular plate of size *a* by *b* at any point *(x,y)* can therefore be given by an infinite double Fourier series in *m*, *n*, *x* and *y*, for odd values of *m* and *n*:

$$w = \frac{16a^4 p}{\pi^6 D} \cdot \sum_m \sum_n \frac{\sin\frac{m\pi x}{a} \sin\frac{n\pi y}{b}}{m \cdot n \cdot (m^2 + \frac{a^2}{b^2} \cdot n^2)} \qquad (30)$$

where p is the pressure and $D = \frac{E \cdot I}{(1-\nu^2)}$

As the value of the successive terms decrease with increasing *n* and *m*, the series is convergent and a finite number of terms can be used to obtain results to a chosen accuracy. Using Mathcad [89] to undertake the calculations, including a numerical integration across the surface of the plate, the spring stiffness and transformation factors have been calculated. For *m* and *n* up to eleven, the first thirty six terms will give at least three significant figure accuracy for $\lambda=a/b$ between 0.25 and 4.0, and four significant figures between 0.5 and 2.0. These are consistent with the K_L values produced by Mayor and Flanders [40] from a similar calculation with thirty terms, and have a reasonable, if less close, relationship with their FE terms. They differ substantially from the values in Refs. 17 and 35, being lower and less sensitive to aspect ratio, as seen by comparison of the values in Tables 1 and 2.

Similar calculations have been undertaken to derive the moment across the centrelines, the reactions along the sides, and the location of the centroids of the deflection, moment and reactions for a quarter span. However, the reactions in particular are sensitive to the accuracy of the loading series close to the supports, and so require very large numbers of terms to converge. With *m* and *n* up to four hundred and one, giving forty thousand terms of the series, the sum of the reactions is still 0.2% less than the loading, indicating an accuracy less than three significant figures; Convergence is very slow as the last thirty thousand terms only halve the error of 0.4% for ten thousand terms.

The reaction coefficients are calculated from simultaneous equations using the above values, and this can amplify or reduce the error in some circumstances. The comparison of the sum of the dynamic reaction coefficients with the static reaction gives an error of 0.1% for each side of a square panel relative to the static reactions and up to 0.4% for the short side reactions with an aspect ratio λ of 2.0. Sensitivity studies show that this error derives mainly from the reaction and reaction centroid calculations. Even with the enormous number of terms used, the coefficients are only reliable to about two significant figures. However, the values calculated are substantially different from those in Ref. 16, with higher force terms and lower resistance terms.

The equations for stress derived from Equation 30 can be used to calculate a reaction distribution along each supporting edge. The Fourier series so calculated gives a distribution rather flatter than the single half sine wave assumed by TM5-1300 [24] for glazing reaction. A concentrated reverse reaction occurs at the corners, as in TM5-1300. For a right-angle corner, this is numerically equal to the sum of the distributed torsion (i.e. kN=kNm/m) at the ends of the two adjacent sides that meet at the corner. As a result, the concentrated reaction can also be calculated from the stress equations.

5.2.1.2 Analysis using the Levy formulae

The Levy formulae were developed to converge faster than the Navier formulae. They are based on calculating the deviations from the one-way deflected shape using an infinite single Fourier series containing a number of hyperbolic terms. The one-way-spanning deflected shape can be kept separate or can be expressed as a term in the single Fourier series:

$$w = \frac{4 \cdot p \cdot a^4}{\pi^5 \cdot D} \cdot \sum_{m=1}^{\infty} \frac{1}{m^5} \cdot \left[1 - \left[\frac{\frac{m \cdot \pi \cdot b}{2 \cdot a} \cdot \tanh\left(\frac{m \cdot \pi \cdot b}{2 \cdot a} \right) + 2}{2 \cdot \cosh\left(\frac{m \cdot \pi \cdot b}{2 \cdot a} \right)} \cdot \cosh\left(\frac{m \cdot \pi}{a} \cdot y \right) \right] \ldots + \frac{\frac{m \cdot \pi \cdot b}{2 \cdot a}}{2 \cdot \cosh\left(\frac{m \cdot \pi \cdot b}{2 \cdot a} \right)} \cdot \frac{2 \cdot y}{b} \cdot \sinh\left(\frac{m \cdot \pi}{a} \cdot y \right) \right] \cdot \sin\left(\frac{m \cdot \pi}{a} \cdot x \right) \tag{31}$$

for a panel from *+b/2 to –b/2* and from 0 to *a*, where the 1 inside the outermost square bracket covers the one-way span deflected shape.

The spring stiffness has been calculated in Mathcad [89] to three significant figures using four terms of this series. However, the higher terms are required mostly for the accuracy of the one-way span, as with this element extracted from the series and the exact deflection for the midspan substituted, a spring stiffness to three significant figures was calculated for aspect ratios $\lambda=a/b$ between 1.0 (square) and 2.0 with only one term of the series.

The series expression was found the more practical for calculation of the transformation functions, but even with this, four terms of the Levy formula were sufficient to give the same accuracy as thirty six terms of the Navier formula.

The full analysis of the reaction coefficients has not been undertaken using this approach because the total reactions for aspect ratios λ of 0.25 to 4.0 can only be calculated for the first seven terms in Mathcad . For higher terms, an intermediate value in the hyperbolic equation is greater than 10^{37}, causing an overflow error message. For seven terms the error in the static loading is 0.16%, which is similar to the accuracy given by 40,000 terms of the Navier series. For aspect ratios λ between 0.5 and 2.0, up to ten terms of the series can be used before overflow occurs in Mathcad, and the error reduces to 0.05%. This would give an improvement in accuracy over the Navier series as well as a massive reduction in calculation effort. However, without implementing the algorithm in higher precision calculations, the accuracy is limited to three significant figures by the large numbers generated by the hyperbolic functions in the formula.

5.2.1.3 Analysis using linear FEA

Linear FE analysis was undertaken using thin shell, eight-noded, semi-loof elements in the LUSAS general FE program [124]. Quarter panel models were analysed between two supported edges and two lines of symmetry. In linear analysis, panels were analysed with aspect ratios λ between 1.0 and 4.0. A uniform mesh of square elements was used with a minimum of ten elements in each direction, increasing to twenty by ten for a 0.5 aspect ratio and ten by forty for an aspect ratio of 4.0. A typical model is shown in Fig. 54. Further analyses with λ between 1.0 and 0.5, directly corresponding to the aspect ratios in the tables in Ref. 16, are described in Section 5.4.

Numerical output from the FE analyses was exported to Excel [125] for post processing. Deflections and back surface principal tensile stresses were analysed for all nodes, and reaction forces and moments at all supports, which include the nodes on the boundaries modelling the axes of symmetry.

Simply-supported panels were analysed for Poisson's ratios v of 0.15, 0.22 and 0.3, corresponding to reinforced concrete, glass and steel. Full moment fixity but no in-plane edge restraint was also analysed for reinforced concrete, corresponding to the results in Ref. 16.

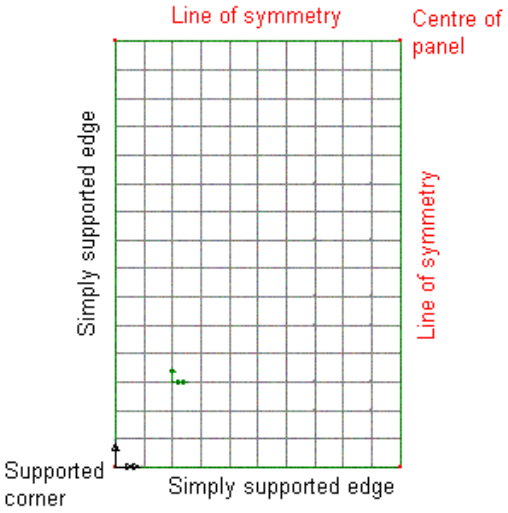

Figure 54. Typical regular mesh quarter panel model, for λ of 1.5

The spring constant was calculated from the maximum deflection at the centre point of the panel, and the transformation factors were calculated using all the node deflections and the trapezoidal rule for numerical integration. The maximum stress at mid-span was used to calculate a coefficient for the maximum pure elastic resistance. This is equivalent to the transition case used in Ref. 17, although this is not the same as the plastic or elasto-plastic transition resistances presented in Refs. 16 or 35. The reactions and moments around the perimeter of the model and the deflections of the whole model were used to calculate parameters for the reaction coefficients, with a Mathcad 'add-in' to Excel used to solve the simultaneous equations.

For six significant figure data exported from LUSAS, the static reactions are consistent with the applied loads within the rounding error, and the combined dynamic coefficients on each side are likewise consistent with the static reactions on each side, to better than five significant figures. However, this close equilibrium does not take account of the discretization error of the element mesh. Changing the mesh of a square panel from ten elements to twenty elements each way affected the fifth significant figure of some results, as did the secondary effects in a small amplitude non-linear analysis. The results are considered reliable to four significant figures, and are the basis of the new elastic analysis in Section 5.4.

5.2.1.4 Conclusions from small deflection analysis

The three forms of analysis used give results that are consistent with each other to at least 3 significant figures. The results calculated by FE analysis have a greater accuracy as well as covering a greater range of cases.

The Navier method gives good results for a simply-supported panel, albeit that it is slow to converge for the reactions. The slow convergence is not an insuperable problem for modern computer based analysis using tools like Mathcad. However, the method is limited to simple supports. There is not an equivalent double Fourier series for fixed supports, let alone for mixed supports.

The Levy method gives comparable accuracy to the Navier method both for deflections and reactions, but is limited in computer analysis by the very large intermediate values produced by the hyperbolic functions. This might be overcome by expansion of the hyperbolic formulae into their exponential forms and algebraic manipulation, or by coding the method in a double precision analysis. The Levy method, which calculates variation from a one-way span formulation, has been used for support conditions other than simply-supported [41], including the soap-film plastic membrane formula [42], but separate formulae would have to be identified for each case to be analysed.

This comparison has demonstrated that a moderately fine finite element mesh can give results that are consistent with accepted analytical methods to the levels of accuracy achievable in practice by the analytical methods, and that mesh refinement may give greater accuracy more practicably than any available analytical methods. Finite element analysis has several additional advantages for developing more complex analyses:

- Varying support conditions can be analysed as easily as simply-supported, and with only minor modifications to the models.
- Alternative loading conditions such as uniform edge moments can be analysed to build up a more consistent and realistic model of elastic-plastic transition.
- Membrane restraint and geometric non-linearity can be used to extend the analysis into the large deflection range.

This assessment of alternative means of elastic analysis for deriving SDOF parameters was included in a paper presented at the 11th International Symposium on the Interaction of the Effects of Munitions with Structures [121] which is appended to this thesis.

5.2.2 Alternative approaches to plastic analysis

Since Ref.16, the yield line method has been used for plastic analysis to identify the ultimate resistance and deflected shape of the yielding panels. However, the yield line models have always been the "classic" model with span yield lines extending into the corners, whether at a constrained 45º angle or at an optimal angle.

Yield line analysis gives an upper bound solution to the true flexural resistance. Many different yield line patterns are kinematically possible for the same loading, and each of them will have its own value of resistance. The flexural pattern that will actually occur in an elastic-plastic plate like a reinforced concrete slab is the pattern whose resistance value is reached first as the loading is increased. All the other mechanisms will have a higher resistance.

Other forms of solution, such as those involving stress analysis, can identify lower bound resistances, but only in a few, generally very simple, cases are upper bound and lower bound solutions found that coincide, so that the solution can be confidently taken as exact. Through the 1950s and 1960s, researchers like Jones and Wood [39] developed more advanced yield line mechanisms with more complex behaviour in the

corners, giving lower resistances that are less 'upper bound', and therefore more accurate, than the 'classic' mechanism.

Based on the differences between the classic and advanced resistances, current military manuals like TM5-1300 [17, 24] and PSADS [23] have proposed adjustments to the resistance, either by an arbitrary reduction in moment capacity near the corners or by an arbitrary reduction in resistance. However, none of these adjustments have refined the 'classic' deflected shape, and therefore they have not modified the transformation factors or reaction coefficients.

As part of this research, a range of five different symmetrical yield line patterns have been analysed over a range of aspect ratios and support fixities using the energy method of yield line analysis, which involves differentiating the energy equation by each independent variable required to define the geometry and equating it to zero, to find the optimal value of the independent variables when the resistance is a minimum.

The energy equations (Eqns. 32-34) have been derived from calculating the internal and external work due to a deflection at point E in Figs. 54-58, equating these, and eliminating the deflection from both sides of the equation to give the resistance R.

- 'Classic' yield lines extending to corners – one variable α, as shown in Fig. 55.

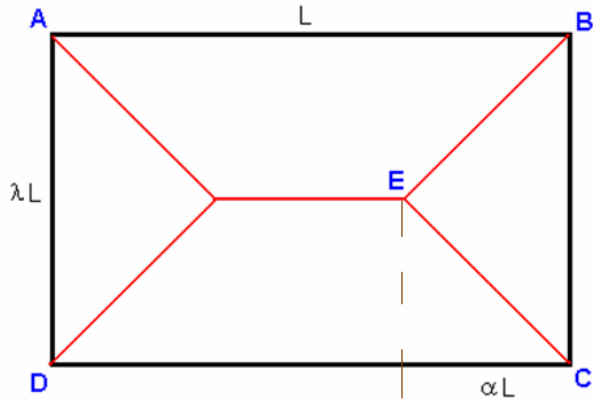

Figure 55. Geometry of classic yield line mechanism

$$R = m\left[\frac{(1+i_L)4/\lambda + (1+i_S)2\cdot\lambda/\alpha}{1/2-\alpha/3}\right] \tag{32}$$

For orthotropic moment capacity m and support fixity i_L on the long side and i_S on the short side

- Floating corner levers – four variables α, β, γ, and δ, as shown in Fig. 56.

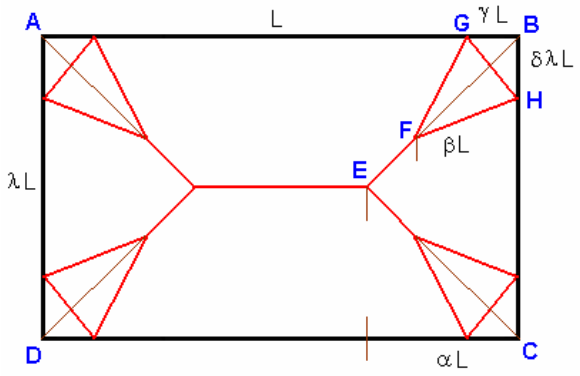

Figure 56. Geometry of floating corner lever mechanism

$$R = m\left[\frac{(1+i_L)\frac{4(1-2\gamma)}{\lambda} + (1+i_S)\frac{2\lambda(1-2\delta)}{\alpha} + (1+i_C)\frac{4\beta}{\lambda}\left(\frac{\gamma^2+\delta^2\lambda^2}{\beta\gamma/2+\alpha\beta\delta-\alpha\gamma\delta}\right)}{\frac{1}{2}-\frac{\alpha}{3}-\frac{2\beta\gamma\delta}{3\alpha}}\right] \quad (33)$$

For orthotropic moment capacity m and support fixity i_L on the long side, i_S on the short side and i_C on the corner fan respectively.

- Anchored corner levers – three independent variables α, γ and δ, as shown in Fig. 57.

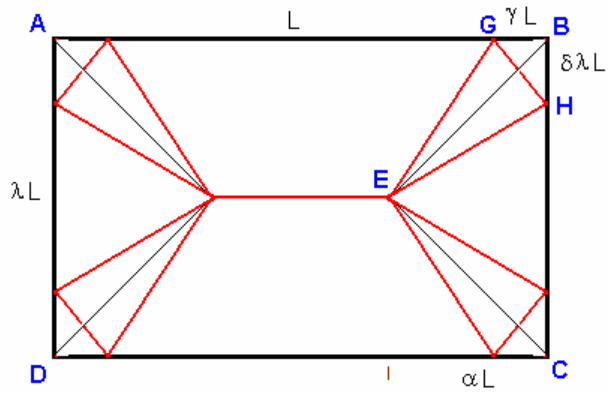

Figure 57. Geometry of anchored corner lever mechanism

This is as for the floating corner lever, but with F coincident with E, so that β is constrained to be equal to α. The same work equation (Eqn. 33) can be used as the basis of the analysis, but with a constraint of $\beta = \alpha$ applied instead of one of the differential equations equalling zero.

- Floating circular corner fans – three independent variables α, β and r, as shown in Fig. 58. Variables θ, θ_1, θ_2, γ and δ are dependent on these, and have been eliminated from Eqn. 34.

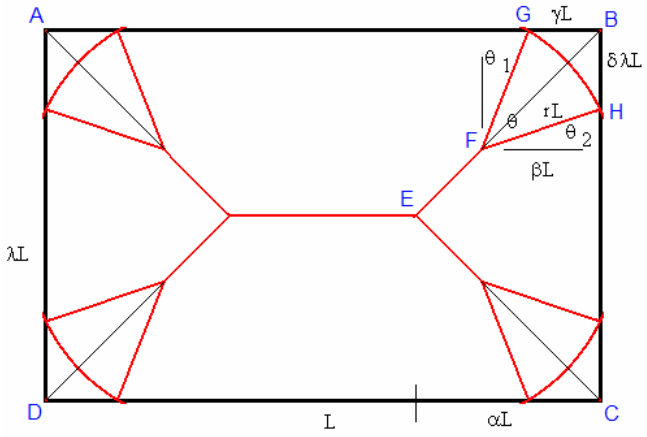

Figure 58. Geometry of floating corner fan mechanisms

$$R = m\left[\frac{\begin{array}{l}(1+i_L)\left(\frac{4}{\lambda}-\frac{8\beta}{\lambda}+8\sqrt{\left(\frac{r}{\lambda}\right)^2-\left(\frac{\beta}{2\alpha}\right)^2}\right)+(1+i_S)\left(\frac{2\lambda}{\alpha}-\frac{2\lambda\beta}{\alpha^2}+4\sqrt{\left(\frac{r}{\alpha}\right)^2-\left(\frac{\beta}{\alpha}\right)^2}\right)\cdots \\ +(1+i_C)\frac{4\beta}{\alpha}\left(\frac{\pi}{2}-a\cos\left(\frac{\lambda\beta}{2\alpha r}\right)-a\cos\left(\frac{\beta}{r}\right)\right)\end{array}}{\frac{1-2\alpha}{2}+\frac{2}{3}\left[\begin{array}{l}\alpha-\frac{\lambda\beta^2}{2\alpha^2}\left(\beta-\sqrt{r^2-\left(\frac{\lambda\beta}{2\alpha}\right)^2}\right)-\frac{\beta^2}{\lambda\alpha}\left(\frac{\lambda\beta}{2\alpha}-\sqrt{r^2-\beta^2}\right)\cdots \\ +\frac{\beta r^2}{\alpha}\left(\frac{\pi}{2}-a\cos\left(\frac{\lambda\beta}{2\alpha r}\right)-a\cos\left(\frac{\beta}{r}\right)\right)\end{array}\right]}\right] \tag{34}$$

For orthotropic moment capacity m and support fixity i_L on the long side, i_S on the short side and i_C on the corner fan respectively

- Anchored circular corner fans – two independent variables α and r, as shown in Fig. 59. Variables θ, θ_1, θ_2, γ and δ are dependent on these, and have been eliminated.

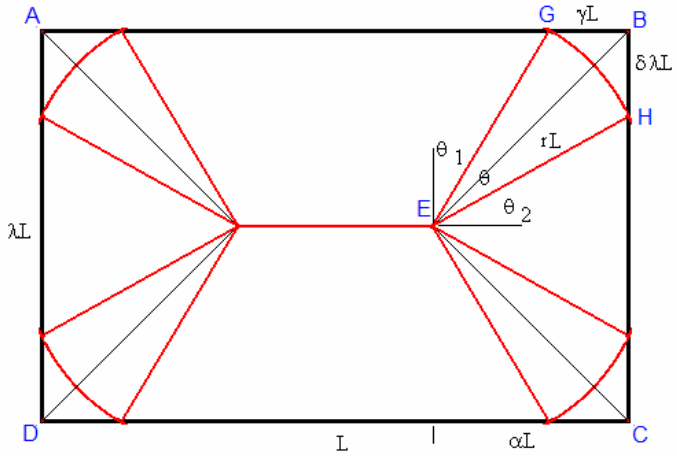

Figure 59. Geometry of anchored corner fan mechanisms

This is as for the floating circular fan, but with F coincident with E, so that β is constrained to be equal to α. The same work equation (Eqn. 34) can be used as the basis of the analysis, but with a constraint of $\beta = \alpha$ applied instead of one of the differential equations equalling zero.

Even these cases do not represent the least upper bound solutions known for rectangular panels, which Jones and Wood [39] identified as 'cosh' fans. However the four advanced mechanisms represent a practical advance on the conservatism of the classic mechanism with a manageable number of independent variables.

For each case, equations to calculate the stationary value of the variables were derived by differentiating the work equation with respect to each independent variable, using the symbolic mathematical capability in Mathcad. The non-linear equations in which the differential expressions were set to zero were solved simultaneously in Mathcad for selected values of aspect ratio and support fixity using a numerical solve block, except for the classic case where the single quadratic equation was solved analytically.

From the nature of optimising the geometry by differentiation, floating corners will be more lower case than anchored corners provided the geometry is physically possible. However, when the calculation would produce a value of β greater than the value of α, a value of α greater than 0.5 or a value of r greater than the diagonal length to the corner, a correctly optimised floating corner mechanism in isolation from the other corners is not possible. In these circumstances, the mechanism is constrained to anchored corners. When a valid floating corner mechanism could not be achieved, the equation arising from differentiation with respect to β was removed from the solve block, and replaced by the identity $\alpha = \beta$. This gave solutions for the corresponding anchored corner mechanism.

With the introduction of corner levers and fans, some of the hogging yield lines cross the interior of the panel corners. The yield line moment capacity on these yield lines will depend on the reverse reinforcement in the structural component, rather than on the edge fixity. As most panels designed to resist blast are reinforced equally on both sides to resist rebound and to provide adequate compressive resistance at large plastic hinge rotations, the panels have been calculated as isotropic panels with equal reverse moment in the corners, and the corners taken as held down, even when edges are simply supported.

With hogging moment capacity in the circular fans, no valid mechanisms are possible for either floating or anchored fans in a simply-supported panel. The square panel reverts to the classic pattern with zero fan angle, and the other aspect ratios give an invalid mechanism with negative fan angles for equilibrium.

With hogging moment capacity and simple supports, valid anchored corner lever mechanisms were found, but the corner levers were so narrow that there was no significant difference in resistance and SDOF parameters from the classic mechanism.

Except for nearly square, fully-fixed panels, the corner levers proved to be the mechanisms giving the least upper-bound resistance, as is shown in Table 20. This ran

contrary to expectations, fuelled by text books that list the solutions only for different square fully-fixed panels to illustrate advanced yield line mechanisms, in which circular and hyperbolic fans are less upper bound than corner levers. However, for any panel with more than minimal asymmetry at the corners, the independent intercepts on the two edges due to separate variables γ and δ are of more significance to minimising the resistance than the curvature of the fan yield lines.

Support		Simple	Fully fixed			Long side fixed			Short side fixed	
Analysis		All	Lever	Fan	Classic	Lever	Fan	Classic	Lever	Classic
Asp-ect ratio	1	**24.00**	44.00	**43.32**	48.00	**34.07**	34.08	35.44	**34.07**	35.44
	0.9	**24.10**	44.20	**43.88**	48.20	**35.09**	35.28	36.50	**33.32**	34.67
	0.8	**24.44**	**44.88**	44.91	48.88	**36.58**	36.91	38.01	**32.80**	34.13
	0.7	**25.13**	**46.22**	46.63	50.26	**38.72**	39.19	40.18	**32.64**	33.94
	0.6	**26.31**	**48.55**	49.35	52.62	**41.82**	42.71	43.32	**32.99**	34.28
	0.5	**28.28**	**52.44**	54.92	56.56	**46.47**	47.56	48.00	**34.16**	35.44

Table 20. Resistance constants *Ru/m* for alternative plastic mechanisms

With the short sides fixed, the "square" yield line pattern with an α value of 0.5 is reached with an aspect ratio of $1/\sqrt{2}$ (=0.7071). Panels with an aspect ratio greater than this have a transposed yield line pattern, and were analysed as panels with the "long" side fixed, but with an aspect ratio greater than 1. This is an aspect of the Affinity Theorem in yield line analysis [39].

For consistency, and to avoid steps appearing in the other properties due to the mixing of different deflected shapes in the tables, the calculations presented have been based on corner levers throughout, using floating corner levers where the optimal mechanism is valid and anchored corner levers where it is not. The avoidable exaggeration of the resistance due to the failure to use the circular fan mechanism when it is lower bound is no more than 1.6%. This is substantially less than the 11% discrepancy produced in some cases by use of the classic mechanism, or the 7% discrepancy that applying the PSADS [23] blanket 10% reduction for classic resistances with fixity would produce in other cases.

This assessment of alternative approaches to advanced yield line models was included in a paper in the International Journal of Impact Engineering [122], and a paper prepared for the 12th International Symposium on the Interaction of the Effects of Munitions with Structures [123], which are appended to this thesis.

5.3 New plastic analysis

The yield line optimisation of the corner lever models was used to calculate the minimum resistances and the positions of the corner points of the mechanism, defining the plastic incremental deflected shapes, for panels supported on four sides, with simple supports and with fixity on long sides, on short sides and on all sides, for a range of aspect ratios from 0.5 to 1.0. The range of cases considered matched those listed in Ref. 16 for two-way spanning slabs. The results of these calculations are shown in Table 21, and were used in two ways; for direct calculation of resistance and deflected shape, and as input for the creation of balanced finite element analyses.

Edge Fixity	Aspect ratio λ	Geometric variables			
		α	β	γ	δ
Simply Supported	1	0.5	=α	0	0
	0.9	0.4734	=α	0.0002	0.0002
	0.8	0.4433	=α	0.0006	0.0007
	0.7	0.4093	=α	0.0012	0.0018
	0.6	0.3707	=α	0.0021	0.0034
	0.5	0.3269	=α	0.0029	0.0058
Fully fixed	1	0.5	0.4487	0.1590	0.1590
	0.9	0.4761	0.4370	0.1523	0.1656
	0.8	0.4487	0.4213	0.1447	0.1732
	0.7	0.4192	0.4007	0.1359	0.1816
	0.6	0.3809	0.3741	0.1255	0.1911
	0.5	0.3389	=α	0.1132	0.2018
Long side fixed	1	0.4215	=α	0.1410	0.0751
	0.9	0.3956	=α	0.1329	0.0784
	0.8	0.3671	=α	0.1238	0.0820
	0.7	0.3357	=α	0.1136	0.0860
	0.6	0.3010	=α	0.1023	0.0904
	0.5	0.2627	=α	0.0897	0.0953
Short side fixed	1* (1.0)	0.4215*	=α	0.1410*	0.0751*
	0.9* (1.111)	0.4475*	0.4475*	0.1492*	0.0718*
	0.8* (1.25)	0.4758*	0.4606*	0.1579*	0.0680*
	0.7	0.4928	0.4627	0.0640	0.1677
	0.6	0.4559	0.4350	0.0595	0.1794
	0.5	0.4114	0.3989	0.0544	0.1933
	* transposed yield line pattern analysed as affine panel with "long" side fixed. Vertical & horizontal dimensions exchanged.				

Table 21. Optimised geometric variables for corner lever yield line analyses

The information on the deflected shapes of the optimised corner lever mechanism for a given aspect ratio and support fixity was used to calculate the transformation factors K_L and K_M, by applying the formulae in Equations 11 and 12 to individual elements of the corner lever mechanism as triangles and rectangles. The values of these transformation factors are less than for the corresponding values for the classic

mechanism because of the corners that do not deflect and the modified deflection of the corner levers. The composite transformation factor K_{LM} was calculated from the ratio of these factors.

The information on the geometry of the optimised corner lever mechanism for a given aspect ratio and support fixity was used to calculate the dynamic rotational equilibrium about the assumed centres of inertia of the individual components of the corner lever mechanism, as simple and compound triangles and simple or compound trapeziums depending upon whether the corner levers were anchored or floating. This enabled the force and resistance factors of the reaction for each component to be calculated, using the method from Ref. 16 illustrated in Fig. 22. However there are two qualifications about how these should be used to define the dynamic reactions on the supports of the panels.

The first and simplest is that the corner levers and the rigid corners distribute their reactions to both the long and the short edges, so that these dynamic reactions will require to be distributed between the edge reactions in an appropriate manner. The more complex qualification is the need to identify, quantify and account for forces acting across the yield line joints between the elements of the mechanism.

Although sagging yield lines are taken to form perpendicular to maximum principal bending moments, and are therefore assumed not to transfer shear forces, force transfer between components is required in some circumstances to enable the equilibrium yield line method to give identical results to the energy method. The exact mechanism by which twists and torsion transfer forces is debatable. Johansen [126] identified the requirement to model this effect, but avoided speculating on the mechanism by defining equivalent nodal forces to be used in the equilibrium method.

Jones and Wood [39] developed and clarified the rules that identify where non-zero nodal forces must be considered for equilibrium in a yield line model, and how they can be calculated. At three-line nodes in the span, the nodal forces will be zero only if the nodes are free to find the optimum position. If they are constrained to a sub-optimal position, then non-zero nodal forces will occur. Span nodes with more than three lines are equivalent to multiple three-line nodes constrained to a common location. As a result, non-zero nodal forces will occur at the apex of anchored corner levers.

These nodal forces could be calculated by the method of Jones & Wood [39], or could be calculated by comparison between the equilibrium and energy methods. However, a balanced finite element analysis of the corner lever yield line model offers the opportunity to confirm the results of the energy analysis, evaluate the corner levers, identify reaction distribution from the corners and assess peak support reactions.

In a balanced FE analysis, the separate components are modelled to the proportions calculated from the energy method calculations, with both transverse loading equal to the unit resistance acting on the face and unit sagging and hogging moments applied to the yield lines. The components are connected with the minimum number of joints to form an articulated mechanism, and converted to a structure by a single dummy support at the centre. The equilibrium of the yield line pattern and the correctness of

the resistance for that mechanism is demonstrated by the residual reaction on the dummy support being negligible.

To model the edge moments and to minimize the averaging length for peak reactions, a four-noded (linear) irregular shell element was used with dummy beams at the edges to which the moments are applied, because edge moment loading is not available for the quadratic shells in LUSAS [124]. For comparable accuracy this required a finer mesh than was used for the elastic models described in Section 5.2.1. Typically, the quarter panel was modelled with 50 to 80 elements to a side. A typical finite element model is shown in Fig. 60, and the supports and applied edge moments for this model are shown in Fig. 61, together with the deflected shape due to displacement of the dummy support, equivalent to incremental plastic deformation of the slab modelled

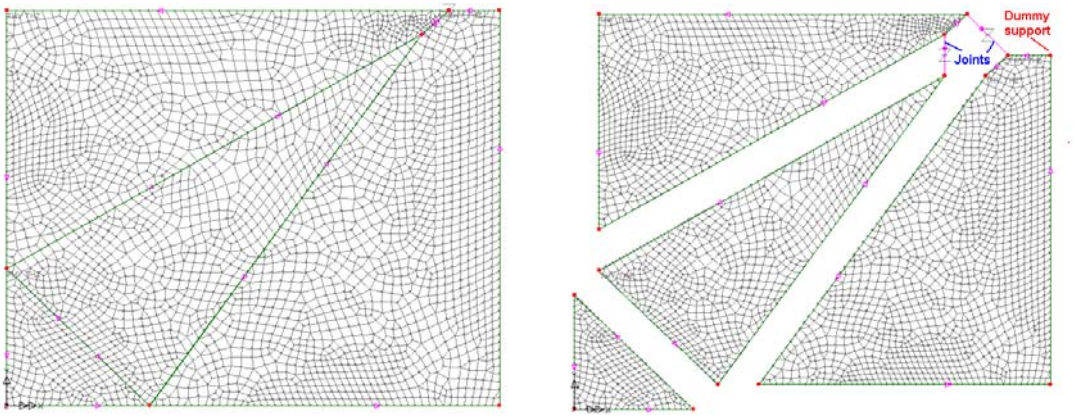

Figure 60. Typical quadrant balanced finite element model of corner lever yield line, exploded to show components, joints and dummy support

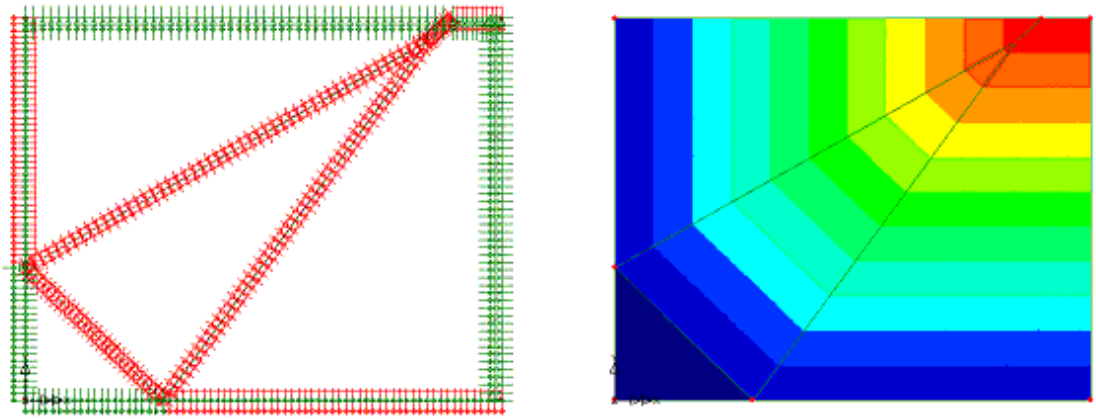

Figure 61. Typical supports and applied moments acting on the quadrant together with the transverse load, and the deflected shape

For such analyses, residual reactions of the order 10^{-6} of the transverse loading were found at the central support, caused by discretization error in representing a continuous system as discrete finite elements. This error reduced by a factor of three to four when the mesh size was halved, demonstrating that the loads, moments and

geometry based on the optimised energy analysis of the yield line model was in overall equilibrium.

For floating corner levers or fans, the zero shear transfer claimed for internal three-line nodes by Nodal Force theory for the equilibrium method of yield line analysis [39] was confirmed by the joint forces being of the same order as the residual reaction, and reducing by a similar factor when the mesh was refined. For anchored corner levers or fans, one of the variables is eliminated as the three-line nodes combine, being replaced by a five-line node with a geometrical constraint. The non-zero shear transfer for such nodes claimed by Nodal Force theory was also vindicated by joint forces of the order 100 times the residual reaction in the FE analysis, which only changed in the third significant figure when the mesh was refined.

For the floating corner levers and fans, the total static reactions from each component in the FE model are consistent, within the discretization error, with those calculated from the geometry. However, they are distributed onto the long and short sides in accordance with equilibrium and the elastic deformation within the components between yield lines. This distribution has been applied to the force and resistance components of the dynamic reaction, and coefficients have been summed along each edge to give the total dynamic reactions on each edge.

For the anchored corner levers and fans, the shear or twist transfer represented by the nodal forces in the joint modifies the static reactions in the panels. As these forces are part of the resistance, the difference between the two static reaction calculations has been used to modify the resistance coefficients of the dynamic reaction before summing along each edge to give dynamic reactions that allow for the nodal forces.

The FE analysis also gives the distribution of reaction along the edge of the components, which allows the peak reactions to be identified at mid-side. These have been calculated from the greatest average reaction along one element edge, but because of slight ripples in the reaction values from the FE model, these tend to be upper bound, and the maximum value may be found a few elements off the centreline.

The FE analysis demonstrated that the yield line solutions are upper bound, as expected. The bending moments in the components do exceed the unit yield line moments in some locations, by up to about 16% in parts of the span, and very locally by up to 70% at the tips of the fixed triangle for the example in Fig. 62. This demonstrates that there is not a matching lower bound solution for the corner lever mechanism.

The combined results of the optimised energy method yield line analyses, the analytical calculations of SDOF coefficients and the balanced FE analyses are summarised in Tables 22-25. These tables are presented in a layout similar to that in Ref. 16, based mostly on a 45º constrained classic yield line approach, and could supersede the values presented there and in the subsequent manuals and text books [19, 20, 21, 22, 23, 35]. They could also supersede the alternative values in Ref. 17, based on the equilibrium method calculations for a modified classic yield line approach, and subsequent manuals [23, 24].

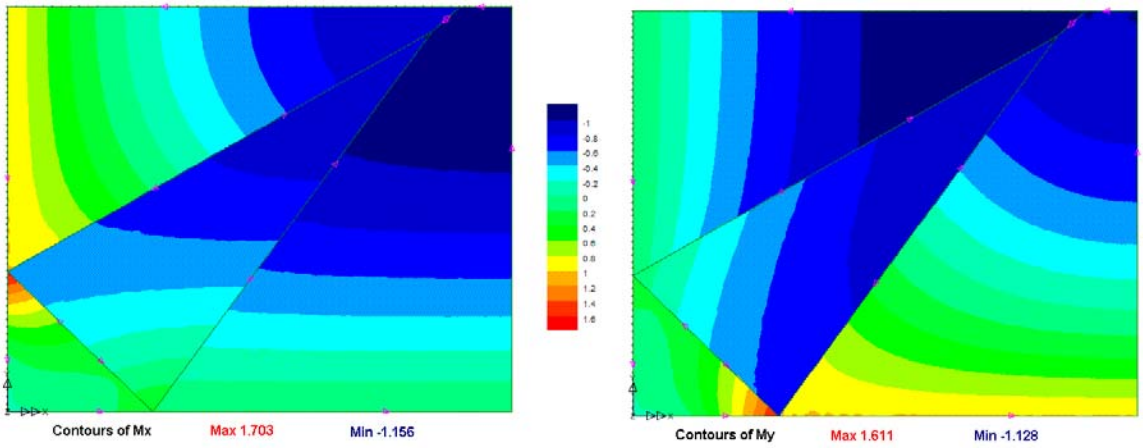

Figure 62. Bending moment distribution in typical panel with fully fixed supports

The approach could be extended to provide an updated analysis of panels with one free edge, currently covered by Refs. 23 and 24. However, optimisation of corner levers would need to be investigated for the alternative mechanism where diagonal yield lines intersect the free edge. This is one of the other cases where non-zero nodal forces have been identified in Ref. 39, even in an unconstrained mechanism.

The analyses undertaken have all been based on an isotropic plate model, but concrete is often reinforced orthotropically, or with different reinforcement in each face. Even with equal reinforcement in both directions, the different cover depth to the crossing reinforcement layers will result in orthotropic bending strength. Affinity theory relates panels with orthotropic strength to 'affine' isotropic panels with a modified aspect ratio [39]. The resistance factor of the orthotropic panel will be equal to that of this affine panel, and the proportions of the mechanism will be the same, giving the same SDOF coefficients.

The application of affinity theory to the panels in Tables 22 to 25 is shown in Fig. 63. Affinity theory can also be used to analyse single reinforced simply-supported panels, and partially fixed panels that have no secondary reinforcement in the corner zone of the supports, by affinity with the fully-fixed mechanism, but with the support resistance moments corresponding to the simple supports set to zero.

Aspect Ratio	Resis-tance	Transformation Factors			Dynamic Reactions			
		Load Factor	Mass Factor	Load-mass Factor	Short Side Total	Short Side Peak	Long Side Total	Long Side Peak
λ	Ru	K_L	K_M	K_{LM}	V_S	V_{PS}	V_L	V_{PL}
1	24.00*m*	0.333	0.167	0.500	0.083F+0.167R	1.718 V_S /a	0.083F+0.167R	1.718 V_L /b
0.9	24.10*m*	0.342	0.176	0.513	0.079F+0.158R	1.729 V_S /a	0.086F+0.178R	1.724 V_L /b
0.8	24.44*m*	0.352	0.186	0.527	0.074F+0.148R	1.731 V_S /a	0.088F+0.190R	1.704 V_L /b
0.7	25.13*m*	0.364	0.197	0.542	0.068F+0.136R	1.735 V_S /a	0.091F+0.205R	1.676 V_L /b
0.6	26.31*m*	0.376	0.210	0.558	0.062F+0.123R	1.743 V_S /a	0.094F+0.221R	1.629 V_L /b
0.5	28.28*m*	0.391	0.225	0.574	0.054F+0.109R	1.755 V_S /a	0.098F+0.239R	1.548 V_L /b

Table 22. Dynamic coefficients for uniformly loaded, simply supported, isotropic, plastic panel

Aspect Ratio	Resis-tance	Transformation Factors			Dynamic Reactions			
		Load Factor	Mass Factor	Load-mass Factor	Short Side Total	Short Side Peak	Long Side Total	Long Side Peak
λ	Ru	K_L	K_M	K_{LM}	V_S	V_{PS}	V_L	V_{PL}
1	44.00*m*	0.318	0.160	0.502	0.091F+0.159R	0.132F/b+0.269R/b	0.091F+0.159R	0.132F/b+0.269R/b
0.9	44.20*m*	0.327	0.168	0.514	0.086F+0.147R	0.140F/b+0.284R/b	0.096F+0.171R	0.138F/b+0.285R/b
0.8	44.88*m*	0.338	0.178	0.526	0.080F+0.135R	0.148F/b+0.299R/b	0.101F+0.184R	0.142F/b+0.300R/b
0.7	46.22*m*	0.350	0.189	0.540	0.073F+0.121R	0.158F/b+0.317R/b	0.106F+0.200R	0.147F/b+0.320R/b
0.6	48.55*m*	0.364	0.202	0.555	0.066F+0.106R	0.168F/b+0.337R/b	0.110F+0.218R	0.150F/b+0.340R/b
0.5	52.44*m*	0.379	0.217	0.571	0.057F+0.090R	0.183F/b+0.366R/b	0.115F+0.238R	0.150F/b+0.356R/b

Table 23. Dynamic coefficients for uniformly loaded, isotropic, plastic panel, fixed on all sides

Aspect Ratio	Resis-tance	Transformation Factors			Dynamic Reactions			
		Load Factor	Mass Factor	Load-mass Factor	Short Side Total	Short Side Peak	Long Side Total	Long Side Peak
λ	Ru	K_L	K_M	K_{LM}	V_S	V_{PS}	V_L	V_{PL}
1	34.07*m*	0.355	0.190	0.537	0.036F+0.138R	0.120F/b+0.240R/b	0.134F+0.192R	0.147F/b+0.312R/b
0.9	35.09*m*	0.364	0.199	0.548	0.031F+0.127R	0.126F/b+0.251R/b	0.137F+0.205R	0.149F/b+0.325R/b
0.8	36.58*m*	0.374	0.209	0.559	0.027F+0.115R	0.132F/b+0.261R/b	0.139F+0.219R	0.152F/b+0.340R/b
0.7	38.72*m*	0.385	0.220	0.571	0.023F+0.103R	0.137F/b+0.270R/b	0.140F+0.234R	0.152F/b+0.352R/b
0.6	41.82*m*	0.397	0.232	0.584	0.018F+0.090R	0.145F/b+0.282R/b	0.141F+0.241R	0.151F/b+0.363R/b
0.5	46.47*m*	0.410	0.245	0.596	0.014F+0.076R	0.153F/b+0.296R/b	0.141F+0.268R	0.151F/b+0.374R/b

Table 24. Dynamic coefficients for uniformly loaded, isotropic, plastic panels, fixed on long sides only

Aspect Ratio	Resis-tance	Transformation Factors			Dynamic Reactions			
		Load Factor	Mass Factor	Load-mass Factor	Short Side Total	Short Side Peak	Long Side Total	Long Side Peak
λ	Ru	K_L	K_M	K_{LM}	V_S	V_{PS}	V_L	V_{PL}
1	34.07*m*	0.355	0.190	0.537	0.134F+0.192R	0.147F/a+0.312R/a	0.036F+0.138R	0.120F/a+0.240R/a
0.9	33.32*m*	0.345	0.181	0.525	0.132F+0.179R	0.144F/a+0.301R/a	0.040F+0.149R	0.115F/a+0.231R/a
0.8	32.80*m*	0.335	0.172	0.512	0.127F+0.165R	0.141F/a+0.288R/a	0.046F+0.162R	0.109F/a+0.217R/a
0.7	32.64*m*	0.329	0.166	0.504	0.121F+0.150R	0.191F/b+0.384R/b	0.052F+0.177R	0.146F/b+0.293R/b
0.6	32.99*m*	0.342	0.179	0.522	0.113F+0.133R	0.212F/b+0.416R/b	0.059F+0.195R	0.154F/b+0.315R/b
0.5	34.16*m*	0.358	0.194	0.541	0.103F+0.114R	0.236F/b+0.473R/b	0.067F+0.216R	0.159F/b+0.339R/b

Table 25. Dynamic coefficients for uniformly loaded isotropic plastic panels, fixed on short sides only

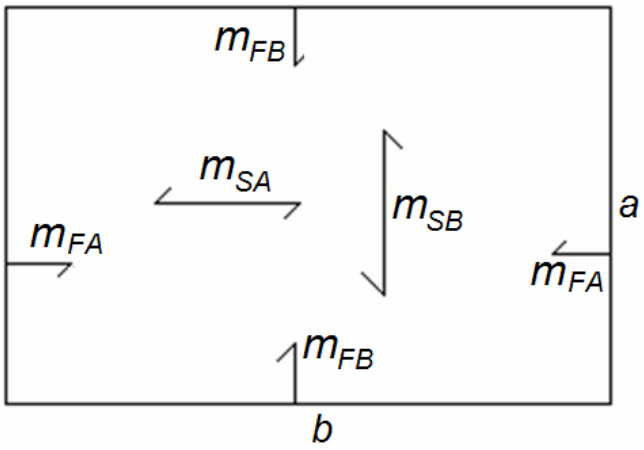

For analysis of Orthotropic Panels with λ = *a*/*b*

For simply supported panels with both faces reinforced and corners held:

Use Table 20 with $\lambda' = \lambda \cdot \sqrt{\frac{m_{SB}}{m_{SA}}}$ and take $m = \sqrt{m_{SB} \cdot m_{SA}}$

For fully fixed panels (or any panels with corner moments of resistance equal to the support moment of resistance in the same direction):

Use Table 21 with $\lambda' = \lambda \cdot \sqrt{\frac{m_{SB} + m_{FB}}{m_{SA} + m_{FA}}}$ and take $m = \frac{\sqrt{(m_{SB} + m_{FB}) \cdot (m_{SA} + m_{FA})}}{2}$

For panels with the long edges fixed and both faces reinforced (m_{FA}=m_{SA}) at corners

Use Table 22 with $\lambda' = \lambda \cdot \sqrt{\frac{m_{SB} + m_{FB}}{2 \cdot m_{SA}}}$ and take $m = \sqrt{\frac{(m_{SB} + m_{FB}) \cdot m_{SA}}{2}}$

For panels with the short edges fixed and both faces reinforced ($m_{FB} = m_{SB}$) at corners

Use Table 23 with $\lambda' = \lambda \cdot \sqrt{\frac{2 \cdot m_{SB}}{m_{SA} + m_{FA}}}$ and take $m = \sqrt{\frac{m_{SB} \cdot (m_{SA} + m_{FA})}{2}}$

Figure 63. Use of the Affinity Theorem for the analysis of orthotropic panels

This new plastic analysis was included in a paper in the International Journal of Impact Engineering [122], and a paper prepared for the 12th International Symposium on the Interaction of Explosives and Munitions with Structures [123], which are appended to this thesis.

5.4 New elastic analysis

The elastic phases of the SDOF response have been analyzed in LUSAS [124] using unit transverse loading on models of panel quadrants in linear elastic analyses, with the results post-processed in an Excel [125] spreadsheet.

The models used eight-noded (quadratic) square thin shell elements, varying between 20 x 20 and 20 x 10 regular element grids with the aspect ratio varying between 1.0 and 0.5. The quadratic elements give better deflection and stress accuracy than double the density of linear elements, but the peak reactions have to be averaged over three nodes, as the side and corner nodes have different weighting.

The analyses were similar to those described in Section 5.2.1.3 and Fig. 54, except that the aspect ratios were less than unity rather than greater than unity, so a higher resolution was used for the square panel; Also that fixed supports were modelled at the long sides, short sides and all sides, in addition to the simply supported cases. The Poisson's ratio used in the analysis was 0.15, suitable for modelling reinforced concrete. The different deflected shapes and maximum deflections with different edge fixities are shown in Fig. 64 for a typical panel (λ = 0.8) with other properties identical.

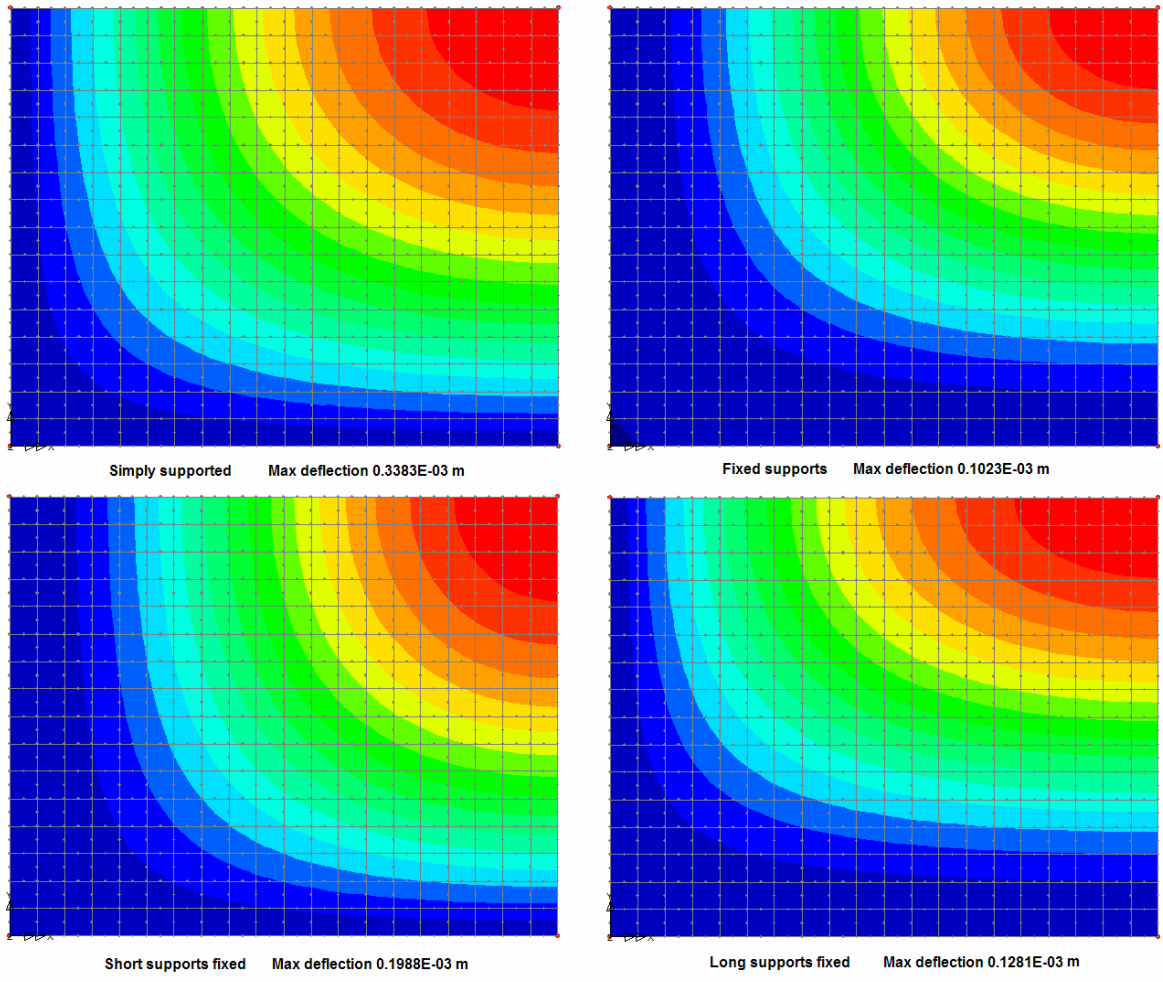

Figure 64. Deflected shapes of typical panel with varied support fixity

A spreadsheet was used to post-process the deflections, stresses and reactions from each case to establish the stiffness and SDOF parameters. The post-processing calculates the elastic spring stiffness from the maximum deflection and the transformation factors by numerical integration of the deflections at all nodes, using the trapezium rule.

The approach adopted to calculate the dynamic reactions for elastic panels was a numerical application of the analytical method developed by the Author in Ref. 6, as described in Section 3.5.5.5 and Fig. 23. This is different from the component-based analysis used in Ref. 16 or in the plastic analysis described in Section 5.3, although consistent with the principles in Ref. 15.

In the symmetrical panels with all edges supported, lines of symmetry have been taken as the lines of zero shear, isolating a quarter panel.

From the finite element nodal results output to the spreadsheet:

- Deflection output for all nodes was used to calculate the position of the centroid of the inertia forces in both axes
- The position of the centre of loading in both axes was calculated from the corner node coordinates
- The moments in both directions due to resistance were calculated from the reaction moments at the support nodes on the symmetry edges and supports (where fixed). The different moment distributions for different edge fixity are illustrated in Fig. 65 for the same analyses as Fig. 64.
- The position of the centre of the reaction along each edge of the quarter panel was calculated from the nodal reactions and coordinates of the support nodes.

These coordinates were used to define the rotational equilibrium of dynamic forces and resistance about the centroid of the inertia forces in two axes, giving four linear simultaneous equations. These were solved using a Mathcad [89] numerical solution for linear simultaneous equations via a Mathcad ‘add-in’ to the Excel spreadsheet, to give the total dynamic reaction coefficients presented in Tables 26 to 29.

The peak reaction at the middle of each side has been calculated from the mean of corner and mid-side node reactions on the side of the element adjacent to the panel centreline on each supported side. The different weighting on the nodes in the quadratic element composition means that individual nodal reactions are not indicative of the distributed peak value. The peaks are expressed as a factor applied to the mean reaction on each side.

The elastic properties in Tables 26 to 29 are only applicable to panels with isotropic stiffness. However, orthotropic strength is permitted, provided hogging of the supports is not so much stronger than sagging of the spans that yield will occur in the spans before the supports have yielded. The elastic resistances have been written in terms consistent with orthotropic strength.

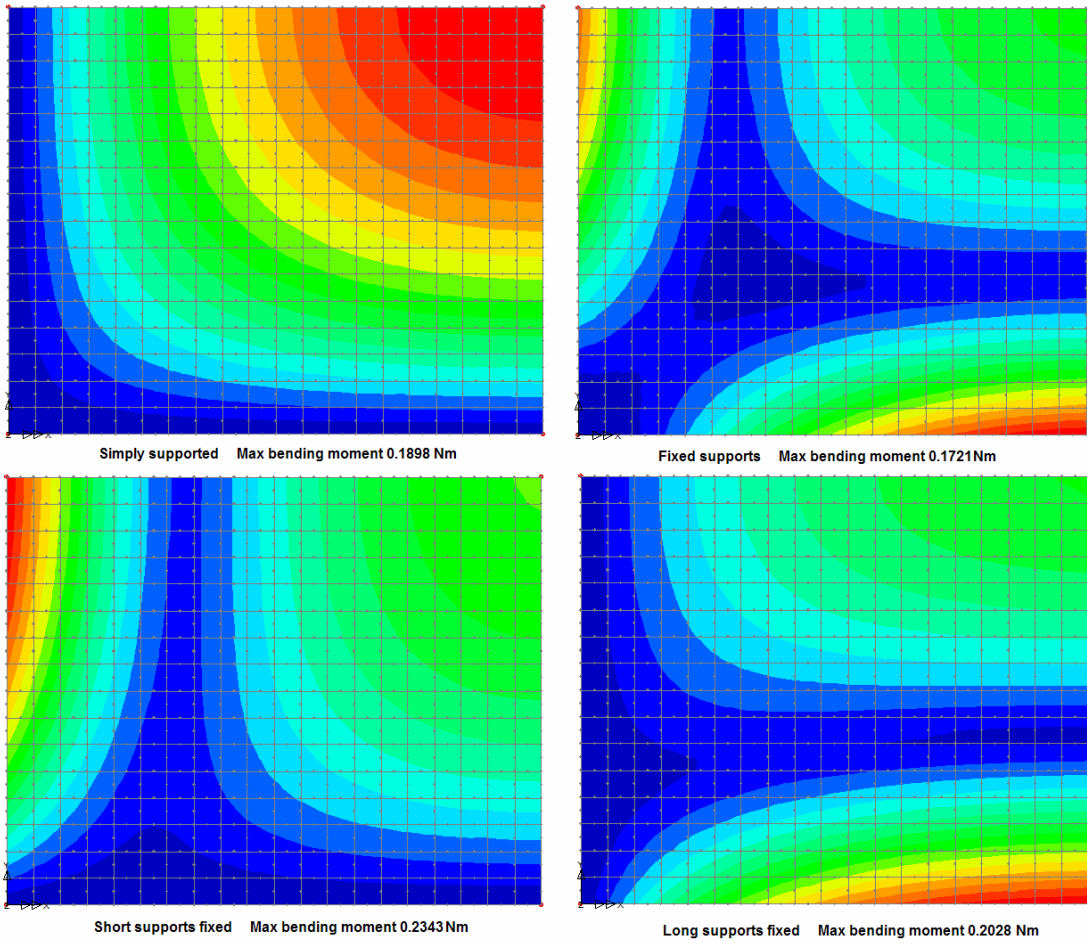

Figure 65. Absolute maximum bending moments of typical panel with varied support fixity

Aspect Ratio	Ultimate resistance	Elastic Stiffness Coefficient	Transformation Factors			Dynamic Reactions			
			Load Factor	Mass Factor	Load-mass Factor	Short Side Total	Short Side Peak	Long Side Total	Long Side Peak
λ	Re = Ru	$ke / (EI/a^2)$	K_L	K_M	K_{LM}	V_S	V_{PS}	V_L	V_{PL}
1	24.00*m*	251.8	0.419	0.262	0.626	0.136F+0.114R	1.752 V_S/a	0.136F+0.114R	1.752 V_L/b
0.9	24.10*m*	229.3	0.419	0.263	0.627	0.133F+0.098R	1.796 V_S/a	0.139F+0.130R	1.703 V_L/b
0.8	24.44*m*	212.2	0.420	0.264	0.628	0.128F+0.081R	1.839 V_S/a	0.142F+0.149R	1.644 V_L/b
0.7	25.13*m*	200.9	0.423	0.266	0.629	0.122F+0.064R	1.877 V_S/a	0.143F+0.171R	1.574 V_L/b
0.6	26.31*m*	196.7	0.427	0.270	0.632	0.115F+0.046R	1.908 V_S/a	0.143F+0.196R	1.493 V_L/b
0.5	28.28*m*	202.0	0.435	0.278	0.639	0.106F+0.029R	1.929 V_S/a	0.142F+0.223R	1.402 V_L/b

Table 26. Dynamic coefficients for uniformly loaded, simply supported, isotropic, elastic concrete panels

Aspect Ratio	Elastic resistance	Elastic Stiffness Coefficient	Transformation Factors			Dynamic Reactions			
			Load Factor	Mass Factor	Load-mass Factor	Short Side Total	Short Side Peak	Long Side Total	Long Side Peak
λ	Re	$ke /(EI/a^2)$	K_L	K_M	K_{LM}	V_S	V_{PS}	V_L	V_{PL}
1	12.93 m_{FA} +12.93 m_{FB}	808.5	0.308	0.182	0.593	0.134F+0.116R	1.763 V_S/a	0.134F+0.116R	1.763 V_L/b
0.9	11.40 m_{FA} +14.53 m_{FB}	741.2	0.308	0.183	0.594	0.132F+0.095R	1.797 V_S/a	0.136F+0.137R	1.718 V_L/b
0.8	9.76 m_{FA} +16.37 m_{FB}	701.8	0.311	0.185	0.596	0.128F+0.074R	1.822 V_S/a	0.137F+0.161R	1.657 V_L/b
0.7	8.05 m_{FA} +18.56 m_{FB}	693.4	0.317	0.190	0.600	0.123F+0.054R	1.836 V_S/a	0.138F+0.185R	1.579 V_L/b
0.6	6.29 m_{FA} +21.28 m_{FB}	723.3	0.328	0.199	0.608	0.117F+0.034R	1.840 V_S/a	0.138F+0.211R	1.485 V_L/b
0.5	4.50 m_{FA} +24.95 m_{FB}	807.3	0.347	0.216	0.624	0.107F+0.018R	1.837 V_S/a	0.139F+0.236R	1.378 V_L/b

Table 27. Dynamic coefficients for uniformly loaded, isotropic, elastic concrete panels fixed on all sides

Aspect Ratio	Elastic resistance	Elastic Stiffness Coefficient	Transformation Factors			Dynamic Reactions			
			Load Factor	Mass Factor	Load-mass Factor	Short Side Total	Short Side Peak	Long Side Total	Long Side Peak
λ	Re	$ke / (EI/a^2)$	K_L	K_M	K_{LM}	V_S	V_{PS}	V_L	V_{PL}
1	16.86 m_{FB}	533.6	0.359	0.220	0.611	0.090F+0.013R	3.111 V_S/a	0.187F+0.209R	1.304 V_L/b
0.9	17.44 m_{FB}	539.9	0.361	0.221	0.613	0.088F+0.003R	3.178 V_S/a	0.188F+0.220R	1.283 V_L/b
0.8	18.37 m_{FB}	560.6	0.365	0.225	0.617	0.086F-0.005R	3.212 V_S/a	0.187F+0.232R	1.256 V_L/b
0.7	19.80 m_{FB}	600.6	0.372	0.232	0.623	0.082F-0.012R	3.215 V_S/a	0.185F+0.244R	1.223 V_L/b
0.6	21.95 m_{FB}	669.3	0.383	0.243	0.633	0.077F-0.017R	3.190 V_S/a	0.182F+0.258R	1.184 V_L/b
0.5	25.20 m_{FB}	783.1	0.401	0.261	0.651	0.070F-0.020R	3.145 V_S/a	0.177F+0.272R	1.141 V_L/b

Table 28. Dynamic coefficients for uniformly loaded, isotropic, elastic concrete panels, fixed on long sides only

Aspect Ratio	Elastic resistance	Elastic Stiffness	Transformation Factors			Dynamic Reactions			
			Load Factor	Mass Factor	Load-mass Factor	Short Side Total	Short Side Peak	Long Side Total	Long Side Peak
λ	Re	$ke / (EI/a^2)$	K_L	K_M	K_{LM}	V_S	V_{PS}	V_L	V_{PL}
1	16.86 m_{FA}	533.6	0.359	0.220	0.611	0.187F+0.209R	1.304 V_S/a	0.090F+0.013R	3.111 V_B/b
0.9	16.55 m_{FA}	437.3	0.359	0.219	0.610	0.184F+0.197R	1.323 V_S/a	0.093F+0.026R	3.000 V_B/b
0.8	16.52 m_{FA}	361.0	0.359	0.219	0.610	0.179F+0.183R	1.341 V_S/a	0.094F+0.044R	2.839 V_B/b
0.7	16.94 m_{FA}	303.3	0.362	0.221	0.611	0.172F+0.164R	1.357 V_S/a	0.096F+0.068R	2.623 V_B/b
0.6	18.05 m_{FA}	263.5	0.366	0.225	0.613	0.162F+0.141R	1.370 V_S/a	0.098F+0.100R	2.358 V_B/b
0.5	20.31 m_{FA}	242.5	0.376	0.233	0.619	0.149F+0.111R	1.381 V_S/a	0.100F+0.139R	2.061 V_B/b

Table 29. Dynamic coefficients for uniformly loaded, isotropic, elastic concrete panels, fixed on short sides only

5.5 Assessment of elasto-plastic stage

The incremental deflection in the elasto-plastic range for panels with some edges fixed is the same as that for the plastic supports pinned. This approach was used in Ref. 15 and subsequently to evaluate the elasto-plastic stiffness and transformation factors by taking them as equal to the values for the simply-supported panels in the elastic range. Ref. 16 also used the reaction coefficients from the simply-supported panels.

This was incorrect, as the reaction coefficients should be based on the total resistance, so the effect of the support moments must still be considered after they have reached the moment capacity. Biggs [35] identified the problem in the one-way span propped cantilevers and introduced an elastic shear term. However, because he did not include the partially fixed two-way spanning cases, he did not identify the need for a corresponding elastic shear term in the reaction coefficients for these cases. This remains uncorrected in the current manual, PSADS [23].

Similarly, the resistance at which the transition from elastic to elasto-plastic is taken to occur must be considered. The values in Ref. 16 are stated to lie between the initial onset of plasticity at the supports and the case when full plasticity could be expected in the supports, but the value is not defined more closely. Biggs [35] revised the values for the fully fixed case, but did not present a basis for the revised values. Ref. 17 used the initial onset of plasticity to define the transition, and so systematically underestimated the stiffness.

A consistent basis for both has been provided by analyzing a quadrant of a simply-supported elastic panel with unit moment per unit length upon either edge. By equating midspan deflections of the elastic panel with edge fixity and the simply-supported panel combined with a unit bending moment on the fixed edge or edges multiplied by the support moment capacity, the value for the elastic resistance of the panels with support fixity has been calculated, as presented in Tables 27 to 29. By considering the deflections due to unit moments on the long and short edges of the fully-fixed panels separately, it has been possible to define the elastic resistance for this panel in a way that will account for orthotropic strength at the supports.

The edge moment reactions also indicate the elastic shear transfers due to a uniform edge moment, as assumed for the elasto-plastic stage.

The total elastic shear transfers are equal and opposite, increasing the reaction of the fixed sides, and reducing the reactions of the free side. The amplitude of the reaction transfer depends only upon the resistance moment at the supports, and the aspect ratio, as shown in Table 30.

For fixity on the long or the short sides only, the full elastic shear transfer must be applied. For fixity on all sides with isotropic support moment capacity, the transfers cancel out. However, for orthotropic support moment capacity there will be a net reaction transfer even for a fully-fixed panel, proportional to the difference in support moment capacity in the two directions.

The distribution of elastic shear is not the same as that from loading, being greatest at the corners and least in midspan. The changes to peak elasto-plastic reactions at the centre of the sides are given in Table 30 for fixity on long or short sides, and for isotropic fixity on all sides. For full support fixity with orthotropic support moment capacity, the net changes can be calculated by summing the effects of the long side and short side fixity.

It should be noted that the values given in Tables 30 and 31 are for initial deformation acting in the direction of the initial disturbing load. For rebound, the direction of the support bending moments will be reversed, so the sign of the transfer factors should be reversed when applied to the scalar value of the support moment capacity.

Even this loading model is somewhat artificial, as in real non-linear panels the full plastic support moment would only actually be generated at a larger deflection and a larger resistance, and this approach ignores the corner effects in the final yield line mechanism. The calculated elastic resistance lies between the true resistance with full support moments and the onset of plasticity calculated from the elastic analyses, as shown in Fig. 66.

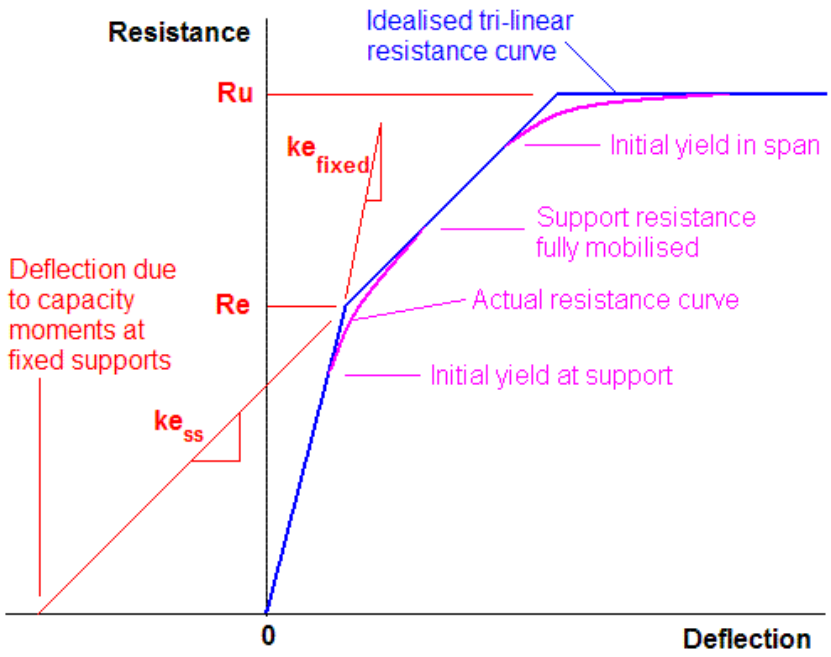

Figure 66. Construction of idealised tri-linear resistance curve

It was observed that this approach cannot produce a four line resistance curve similar to that from the approach in Refs. 17 and 24 with isotropic reinforcement, as the yielding of the long sides and short sides overlap. Such a separation would only be possible if the long side bending strength were much less than the short side strength. However, this is improbable as it represents a very inefficient reinforcement distribution.

Aspect Ratio λ	Magnitude of transfer
1	3.14 m_F
0.9	3.11 m_F
0.8	3.06 m_F
0.7	2.99 m_F
0.6	2.91 m_F
0.5	2.80 m_F

Sign of transfer to total reactions for elastic shear due to fixity on edges of panel		
Fixed Edges	To Short Side Total V_S	To Long Side Total V_L
Long	**Subtract**	**Add**
Short	**Add**	**Subtract**

Table 30. Total elastic shear transfers, to be applied to total dynamic reactions from simply supported panels when used for elasto-plastic range of panels with fixed edges

Aspect Ratio	Isotropic panel with all edges fixed		Panel with long edges fixed		Panel with short edges fixed	
	Short Side peak	Long Side peak	Short Side peak	Long Side peak	Short Side peak	Long Side peak
λ	Add to V_{PS}	Add to V_{PL}	Add to V_{PS}	Add to V_{PL}	Add to V_{PS}	Add to V_{PL}
1	-0.668 m_F/b	-0.668 m_F/b	-0.971 m_{FB}/b	+0.303 m_{FB}/b	+0.303 m_{FA}/b	-0.971 m_{FA}/b
0.9	-0.706 m_F/b	-0.622 m_F/b	-1.075 m_{FB}/b	+0.231 m_{FB}/b	+0.369 m_{FA}/b	-0.853 m_{FA}/b
0.8	-0.739 m_F/b	-0.562 m_F/b	-1.174 m_{FB}/b	+0.149 m_{FB}/b	+0.435 m_{FA}/b	-0.711 m_{FA}/b
0.7	-0.765 m_F/b	-0.485 m_F/b	-1.260 m_{FB}/b	+0.062 m_{FB}/b	+0.495 m_{FA}/b	-0.547 m_{FA}/b
0.6	-0.784 m_F/b	-0.389 m_F/b	-1.327 m_{FB}/b	-0.023 m_{FB}/b	+0.544 m_{FA}/b	-0.367 m_{FA}/b
0.5	-0.795 m_F/b	-0.277 m_F/b	-1.372 m_{FB}/b	-0.089 m_{FB}/b	+0.577 m_{FA}/b	-0.188 m_{FA}/b

Table 31. Adjustment for simply supported, peak elastic shears, when used for elasto-plastic range of panels with opposite edges fixed

5.6 Limitations of the analysis

The two-way spanning calculations are based upon a yield line criterion suitable for reinforced concrete, a Poisson's ratio of 0.15, elastic small deflection theory and thin shell finite element formulations. These limit the application of the tabulated data.

Metal plates, with a von Mises yield criterion, will be weaker near fixed supports, so the tables will overstate the plastic resistance of steel or other metal plates with fixed edges. Even for the simply supported tables, the higher Poisson's ratio for steel or glass will alter the elastic stiffness and dynamic reactions. Alternative simply-supported properties for small deflection elastic analysis of glass and steel are included in Tables 32 and 33. Other properties are as Table 26.

Aspect Ratio	Elastic Stiffness Coefficient	Elastic resistance coefficient	Dynamic Reactions			
			Short Side Total	Short Side Peak	Long Side Total	Long Side Peak
λ	$ke / (EI/a^2)$	$Re/\sigma Z$	V_S	V_{PS}	V_L	V_{PL}
1	258.7	11.12	0.133F+0.117R	1.719 V_S/a	0.133F+0.117R	1.719 V_L/b
0.9	235.5	10.93	0.130F+0.101R	1.760 V_S/a	0.136F+0.134R	1.673 V_L/b
0.8	218.0	10.93	0.125F+0.084R	1.799 V_S/a	0.137F+0.154R	1.618 V_L/b
0.7	206.4	11.21	0.119F+0.067R	1.834 V_S/a	0.139F+0.176R	1.553 V_L/b
0.6	202.1	11.89	0.113F+0.049R	1.863 V_S/a	0.139F+0.200R	1.477 V_L/b
0.5	207.5	13.25	0.105F+0.031R	1.882 V_S/a	0.138F+0.226R	1.392 V_L/b

Table 32. Alternative properties for small deflections of a simply supported glass pane (Poisson's ratio = 0.22).

The elastic resistance coefficient *Re* given for glass is for the principal tensile stress in the centre of the back face to reach the stress σ, which can be used to identify the resistance and deflection for a given cracking strength (for a squat pane).

Aspect Ratio	Elastic Stiffness Coefficient	Dynamic Reactions			
		Short Side Total	Short Side Peak	Long Side Total	Long Side Peak
λ	$ke / (EI/a^2)$	V_S	V_{PS}	V_L	V_{PL}
1	270.5	0.128F+0.122R	1.681 V_S/a	0.128F+0.122R	1.681 V_L/b
0.9	246.3	0.126F+0.105R	1.718 V_S/a	0.131F+0.139R	1.639 V_L/b
0.8	227.9	0.121F+0.088R	1.754 V_S/a	0.132F+0.158R	1.589 V_L/b
0.7	215.9	0.116F+0.070R	1.786 V_S/a	0.134F+0.180R	1.529 V_L/b
0.6	211.3	0.110F+0.051R	1.812 V_S/a	0.134F+0.204R	1.459 V_L/b
0.5	217.0	0.103F+0.032R	1.829 V_S/a	0.134F+0.231R	1.380 V_L/b

Table 33. Alternative properties for small deflections of a simply supported steel plate (Poisson's ratio = 0.3).

The small deflection elastic analyses are accurate only up to deflections of about half the member thickness. Beyond this point tensile membrane effects will modify not only the stiffness, but also all of the SDOF parameters. This is no handicap for reinforced concrete sections, which should be plastic well before this deflection, but makes these tables inappropriate for thinner steel plates approaching yield or normally proportioned glass window panes approaching cracking.

Thin shell finite elements do not incorporate shear deflection. The deflected shapes and stress distributions in the elastic and elastic-plastic ranges may not be accurate for very deep sections in which a significant part of the deflection is shear deflection. If flexural cracking occurs before shear cracking then the tables may still be accurate for deep sections after cracking, as the flexural stiffness will reduce by more than the shear stiffness as a result of flexural cracking.

These limitations of the analysis are important, and need to remain associated with the tables, if they are not to be applied inappropriately.

One of the remaining limitations for any flexural analysis of reinforced concrete is the appropriate flexural stiffness to use for a material whose strength is predicated on a cracked section, but where the location, strength and pre-existing condition of potential cracks prior to dynamic loading are all unknown quantities.

The practice in PSADS [23] and TM5-1300 [24] of using a value of *EI* averaged between the values of the uncracked section and the cracked and unstiffened section throughout the initial elastic analysis is a reasonable, but essentially arbitrary, assumption. For normal levels of reinforcement, this is around 55% of the uncracked stiffness. The variability and uncertainty in real cracked reinforced concrete makes the detailed calculation of the reinforcement stiffness spurious. Lacking more specific data, this arbitrary assumption is no worse than any other, so long as it is recognized for what it is.

Non-linear finite element analysis has been undertaken using a layered shell model of elastic-plastic reinforcement and cracking concrete to resist uniformly distributed loading. Although one analysis is indicative rather than definitive, the trend shown for a slab with fixed supports was that the adjustment of stiffness when cracks occur first at the supports tends to redistribute bending moment from the supports into the spans. Although yield does occur first at the supports, it occurs later and with higher resistance than the tri-linear resistance curve would suggest, and the elasto-plastic stage is of very limited duration, but of a somewhat lower relative stiffness. However, although the initial redistribution is due to cracking rather than yielding it does take place, so a change in the incremental deflected shape and SDOF coefficients will still occur, if not exactly in the way in the tri-linear model.

The unloading stiffness from a state where plasticity is just commencing was consistent with the averaged stiffness in the manuals [23, 24], although with significant plasticity, it dropped to about half the value, as shown in Fig. 67. This suggests that the current design elastic stiffness may be appropriate for a one-off response to an accidental or terrorist blast loading on an existing structure with pre-existing cracking due to normal loading, shrinkage etc. It may under-predict the stiffness in a new, uncracked structure subjected to an initial loading, and it will over-

predict the stiffness of a structure that has been previously taken into the plastic zone or is subjected to repeated dynamic loadings.

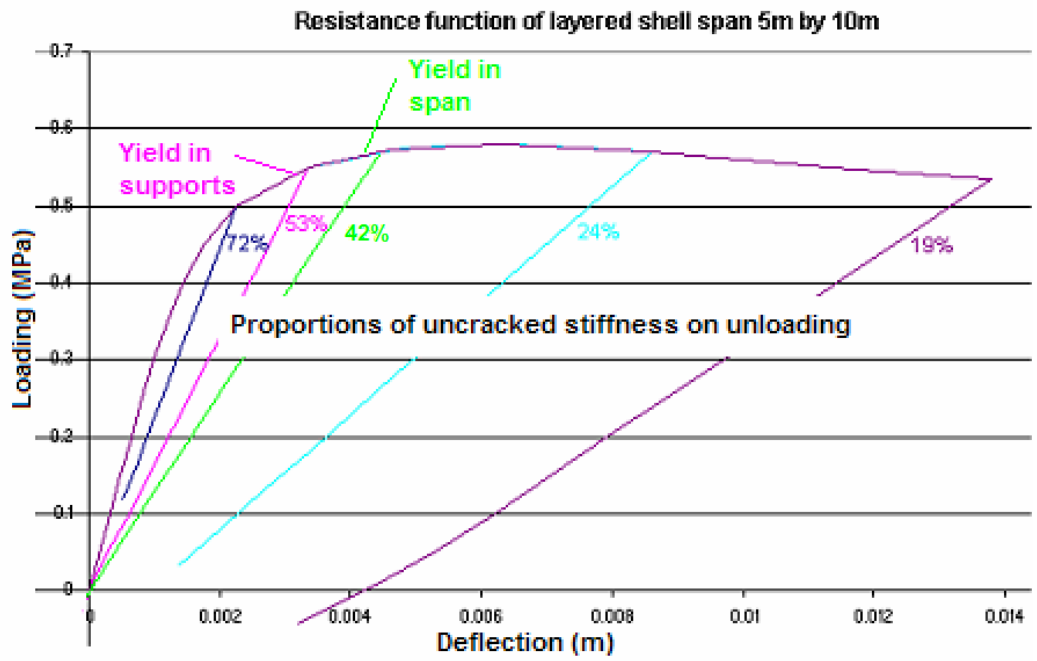

Figure 67. Resistance curves from non-linear finite element analysis of a reinforced concrete panel showing unloading stiffness

Without significant in-plane restraint, the plastic resistance of the nonlinear finite element model is within a few percent of the yield line calculation. With rigid in-plane restraint, tensile membrane action enhances the resistance, as shown in Fig. 68. Resistance based on pure bending analysis, even from an upper-bound yield line analysis, will still be lower-bound for a significantly restrained slab.

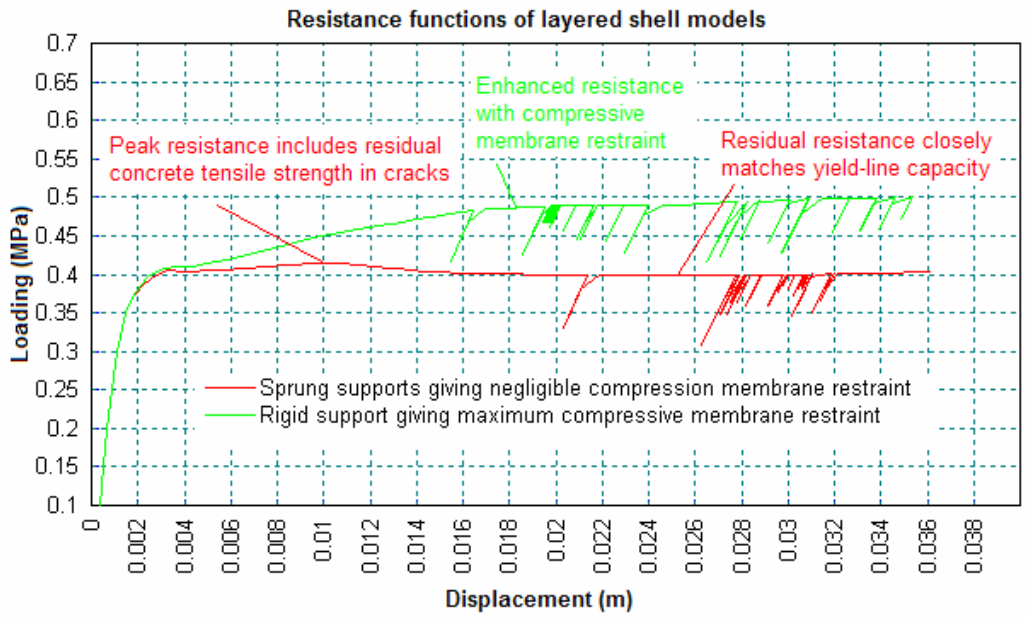

Figure 68. Resistance curves from non-linear FE analysis of RC panels

5.7 Comparative calculations

Comparative calculations of dynamic response have been undertaken of the reinforced concrete panel shown in Fig. 69, using PSADS [23] (after Ref.16), TM5-1300 [24] and the new data presented in this chapter.

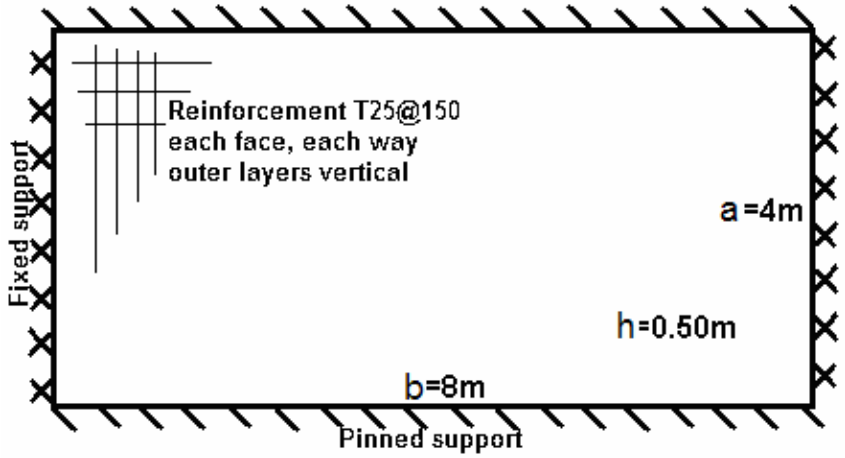

Figure 69. Panel analysed in comparative calculations

Assuming a depth to vertical reinforcement of 50mm and to horizontal reinforcement of 75mm, design properties common to all the analyses are:

- Second moment of inertia (after Refs. 23 & 24) $I = 6.533 \times 10^9$ mm^4/m
- Concrete Young's Modulus $E = 30$ kN/mm^2
- Mass $M = 38400$ kg
- Vertical bending moment in span $m_{SB} = 699$ kNm/m
- Horizontal bending moments $m_{SA} = m_{FA} = 657.5$ kNm/m

The PSADS [23] properties are all as Ref. 16, except that the stiffnesses have been adjusted for a Poisson's ratio of 0.15, and the plastic resistance *Ru* has been reduced by 10% to allow for corner fans in yield line mechanisms.

The elastic and elasto-plastic properties are all based on an aspect ratio *a*/*b* of 0.5.

The plastic properties from PSADS [23] are also based on an aspect ratio of 0.5, but the plastic TM5-1300 [24] properties are based on fig. 3-17 (reproduced here as Fig. 70) for a panel with four sided support and an affine aspect ratio of 1.458, giving a hinge position *x* of 3.188m from the side.

The plastic properties from the new analysis are based on a panel with the short sides fixed (Table 23) with an affine aspect ratio of 0.516 and an affine bending moment *m*` of 678 kNm/m, in accordance with Fig. 63.

Properties from the different design methods are summarised in Table 34. The resistance curves are illustrated in Fig. 71.

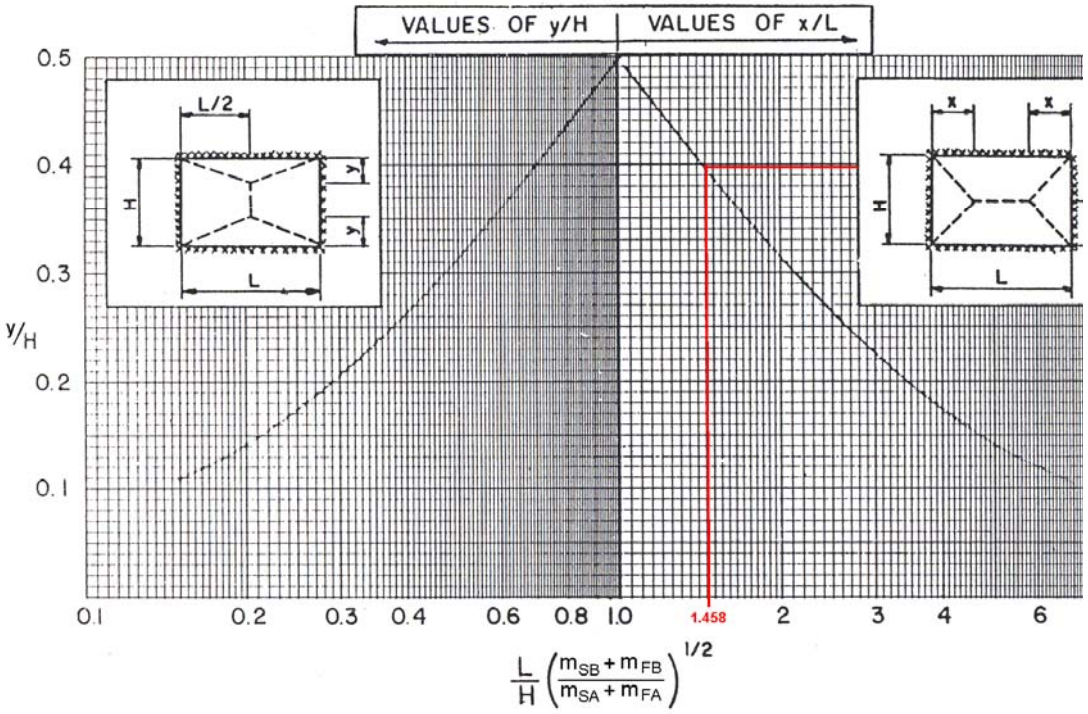

Figure 70. Figure 3-17 from TM5-1300 [24], used to derive the position *x* of the yield line node.

Property	PSADS [23]	TM5-1300 [24]	New Analysis
ke_{fixed}	240 EI/ba^3 91.87 MPa/m	$EI/0.0005277(1-\nu^2)b^4$ 92.76 MPa/m	242.5 EI/ba^3 92.81 MPa/m
Re	7.4(m_{FA}+2.43m_{SB}) 17435 kN	$m_{FA}a/0.02977b$ 11043 kN	20.31 m_{FA} 13354 kN
X_e	5.93 mm	3.72 mm	4.50 mm
ke_{ss}	201 EI/ba^3 76.94 MPa/m	$EI/0.000633(1-\nu^2)b^4$ 77.33 MPa/m	202.0 EI/ba^3 77.31 MPa/m
Ru	10.8(m_{FA}+m_{SA}+1.50m$_{SB}$) 25526 kN	5(m_{SA}+m_{FA})ab/x^2 20697 kN	33.97 m` 23029 kN
X_{ep}	9.22 mm	7.62 mm	7.23 mm
K_{LMe}	0.73	0.78	0.619
K_{LMep}	0.75	0.79	0.639
K_{LMp}	0.59	0.544	0.538
V_{Se}	0.05 F+0.08 R	-	0.149F+0.111R
V_{Sep}	0.04 F+0.09 R	-	0.142F+0.223R–2.80m_{FA}
V_{Sp}	0.04 F+0.08 R	1237 kN/m . 5/6 *a*	0.104F+0.117R
V_{Le}	0.09 F+0.28 R	-	0.100F+0.139R
V_{Lep}	0.09F+0.28 R	-	0.106F+0.029R+2.80m_{FA}
V_{Lp}	0.11F+ 0.27 R	897 kN/m . *b*-*x*/3	0.066F+0.213R

Table 34. Properties of panel for comparative calculations

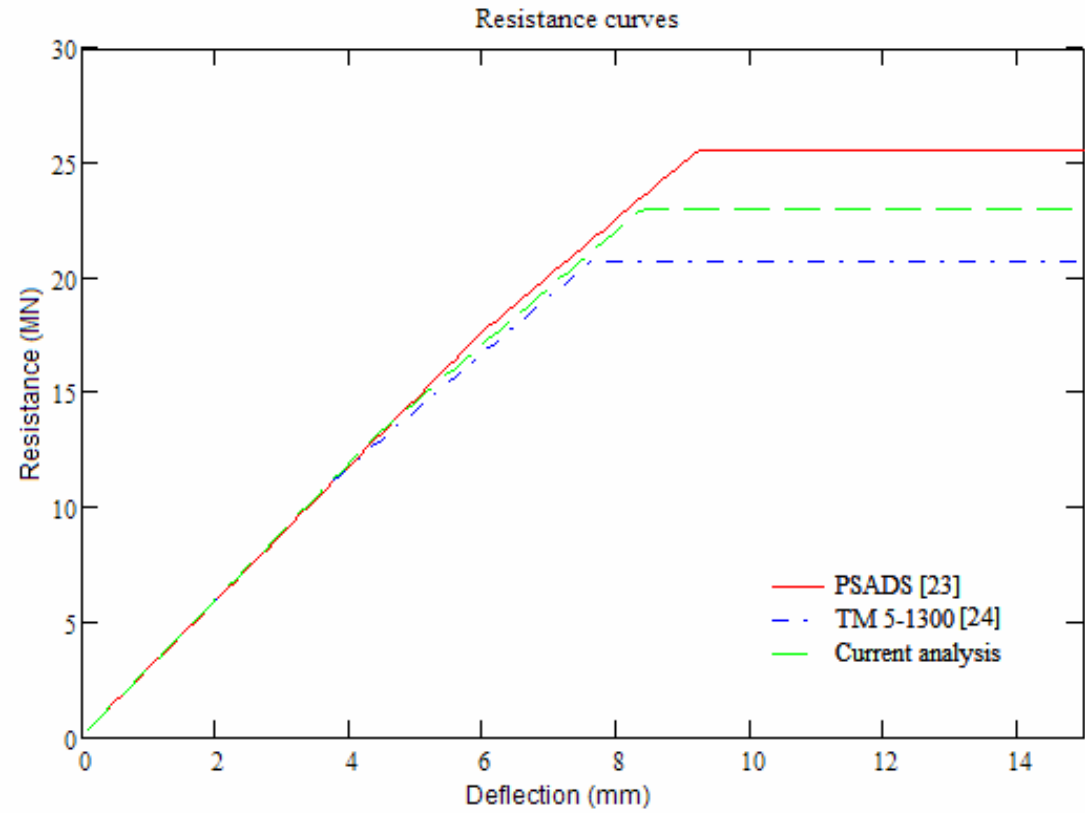

Figure 71. Resistance curves for comparative calculations

For a mainly plastic response, the panel has been analysed for the application of a triangular blast loading with a peak pressure of 1000 kPa and duration of 40 msec, giving an impulse of 2 x 10^4 kPa.msec. Numerical analyses with a structural damping of 3% of critical were undertaken. The results are summarised in Table 35, and illustrated in Figures 72 and 73.

Result		PSADS	TM5-1300	New Analysis
Maximum Deflection	z_{max}	52.8 mm	102.0 mm	83.7 mm
Time of Deflection	t_{max}	21.9 ms	30.1 ms	26.3 ms
Span Ductility	z_{max}/X_{ep}	5.73	13.4	9.96
Support Ductility	z_{max}/X_e	8.90	27.4	18.6
Support Rotation		0.756°	1.46°	1.20°
Short Reaction	V_S	3429 kN	4124 kN	5867 kN
Long Reaction	V_L	10005 kN	6224 kN	7154 kN
Distributed React	V_{SD}	857 kN/m	1237 kN/m	1467 kN/m
Distributed React	V_{LD}	1251 kN/m	897 kN/m	894 kN/m
Mid span React	V_{SP}	857 kN/m	1237 kN/m	2173 kN/m
Mid span React	V_{LP}	1251 kN/m	897 kN/m	1562 kN/m

Table 35. Results of comparative SDOF analysis into the plastic zone

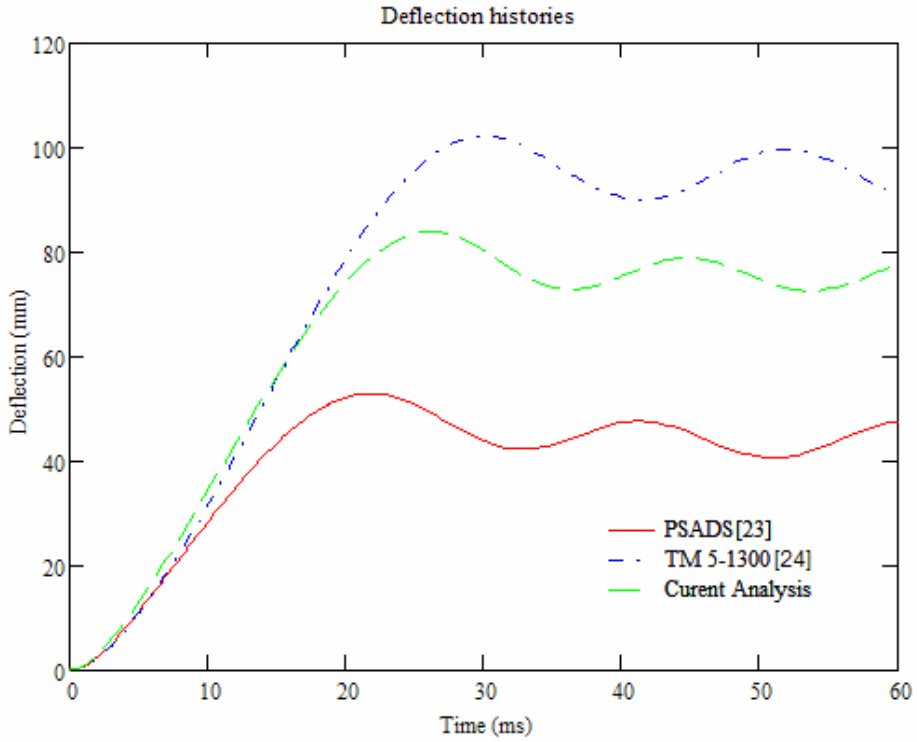

Figure 72. Deflection histories for comparative calculations for 2 x 10^4 kPa.msec impulse loading

The predominant factor in the different deflections is the plastic resistance *Ru*, but the SDOF reaction coefficients and the assumptions on how it is distributed have a major effect on the reactions.

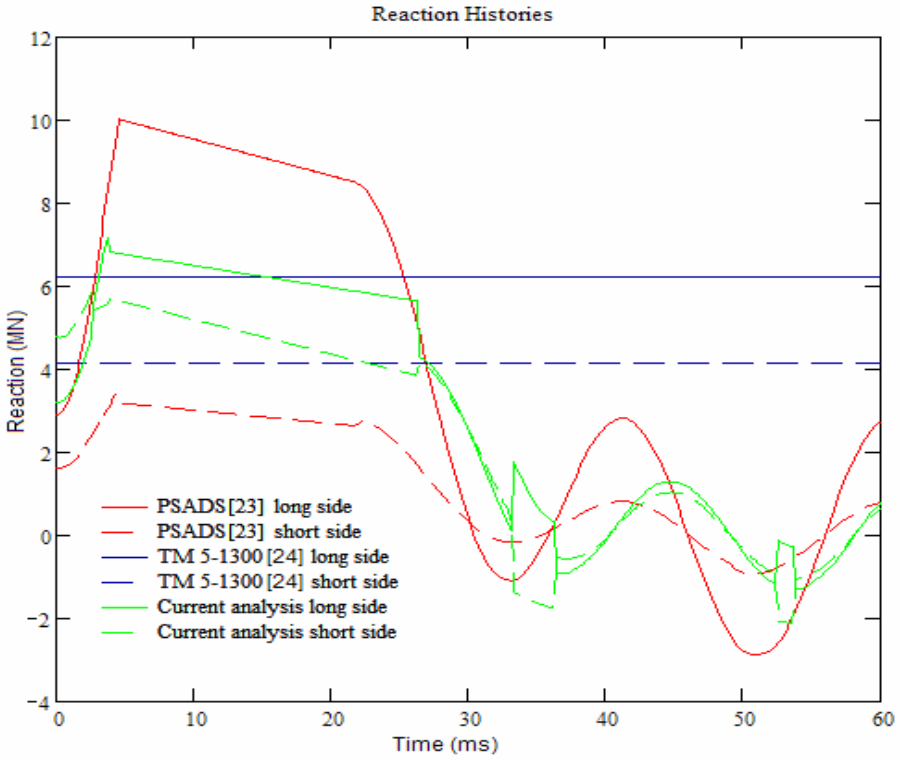

Figure 73. Reaction histories for comparative calculations for 2 x 10^4 kPa.msec impulse loading

For a mainly elastic response, the same panel has also been analysed for the application of a triangular blast loading with a peak pressure of 250 kPa and duration of 20 msec, giving an impulse of 2.5 x 10^3 kPa.msec. In addition to the numerical SDOF analyses, a linear elastic transient dynamic finite element model was analysed using a thickness and density selected to give the same *I* and *M*. The analyses were all undamped to make the SDOF analyses comparable to the FE analysis. The results are summarised in Table 36, and illustrated in Figs. 74-76.

Result	PSADS	TM5-1300	New Analysis	FEA
Deflection z_{max}	4.25 mm	4.193 mm	4.297 mm	4.808 mm
Time of Defln t_{max}	8.8 ms	9.05 ms	8.1 ms	8.4 ms
Support Ductility z_{max}/X_e	0.717	1.127	0.956	-
Short Reaction V_S	1228 kN	2433 kN	2101 kN	2273 kN
Long Reaction V_L	3907 kN	3672 kN	2203 kN	2768 kN
Distributed React V_{SD}	307 kN/m	730 kN/m	539 kN/m	568 kN/m
Distributed React V_{LD}	488 kN/m	529 kN/m	282 kN/m	346 kN/m
Mid span React V_{SP}	307kN/m	730 kN/m	739 kN/m	994 kN/m
Mid span React V_{LP}	488 kN/m	529 kN/m	580 kN/m	850 kN/m

Table 36. Results of comparative SDOF and FE analysis mostly in the elastic zone

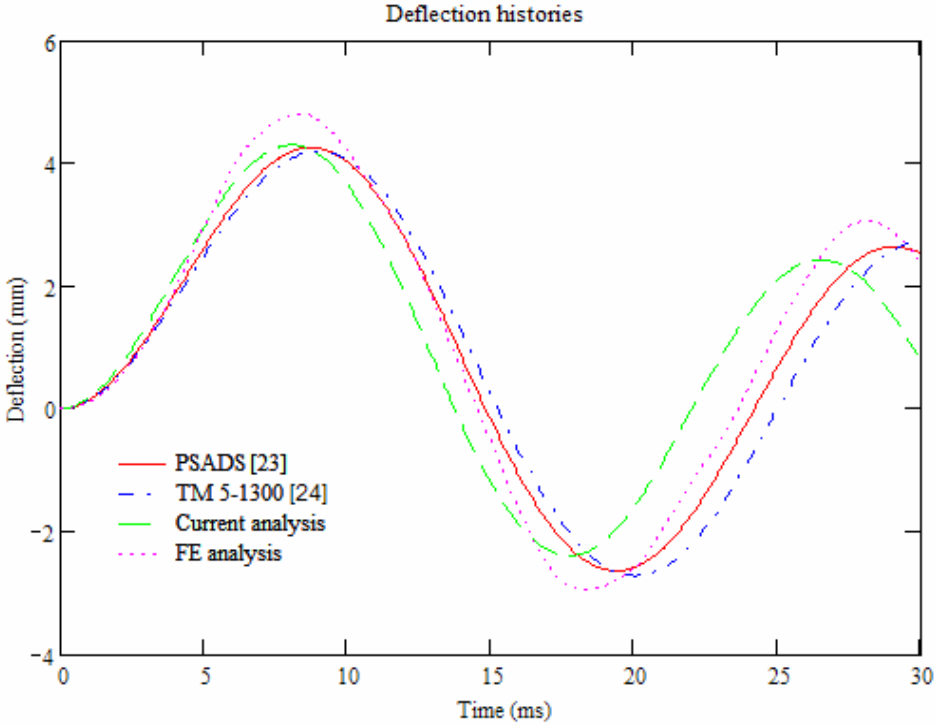

Figure 74. Deflection histories for comparative calculations for 2.5 x 10^3 kPa.msec impulse loading

The time of peak deflection in the new analysis is slightly early due to the inaccuracy of using the flexural shape from the start of the analysis. In the other SDOF analyses, the high K_{LM} values results in later peaks in spite of this effect.

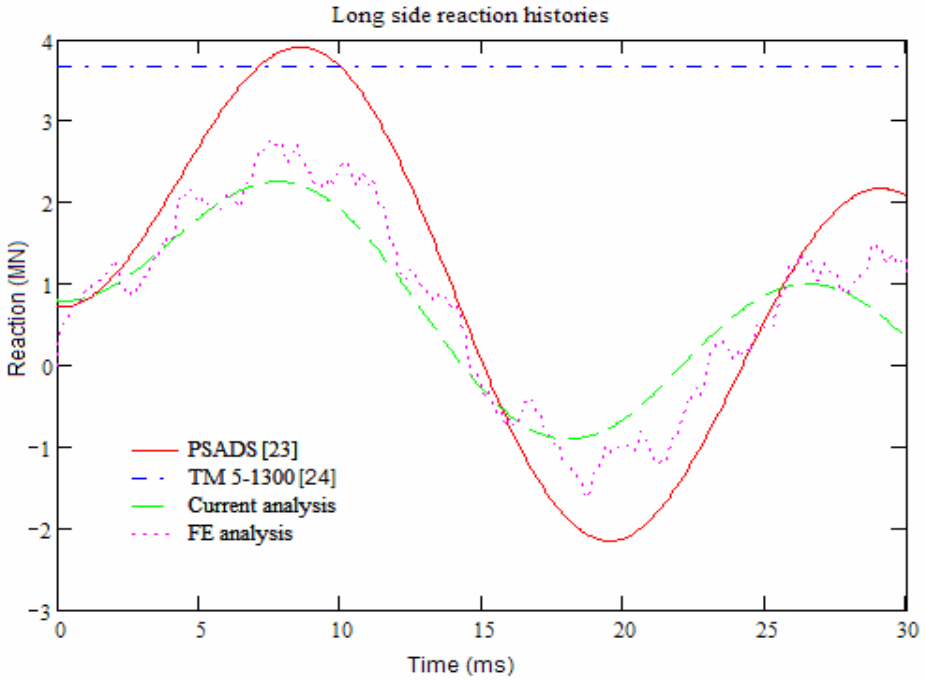

Figure 75. Long side reaction histories for comparative calculations for 2.5 x 10^3 kPa.msec impulse loading

In the FE analysis the higher modes of vibration contribute significantly to the peak reactions, and marginally to the peak displacement. In an analysis with damping, the contribution from the higher modes could be significantly reduced.

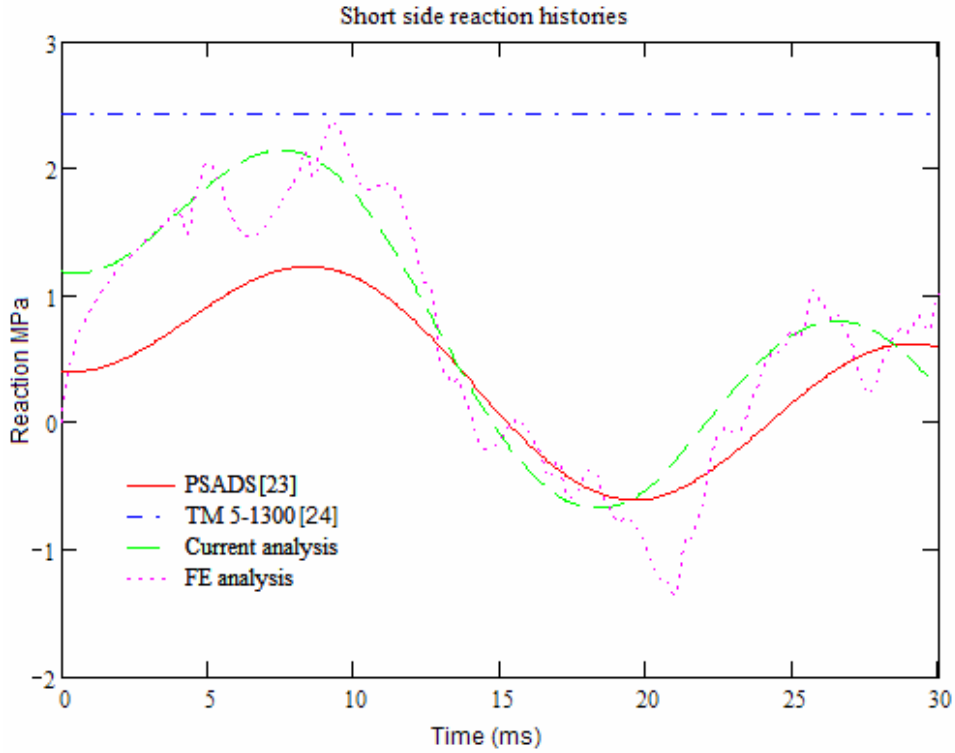

Figure 76. Short side reaction histories for comparative calculations for 2.5 x 10^3 kPa.msec impulse loading

5.8 Summary for the application of the SDOF method to panels

The earlier applications of the equivalent SDOF method to two-way spanning panels was based upon elastic small deflection theory and plastic yield line analysis [15, 16].

Although the approach was generally sound in theory, some of the assumptions and simplifications adopted to derive the SDOF parameters by hand calculations or to make the method straightforward to apply by hand calculations introduced significant errors into the calculations.

With the development of numerical methods of elastic analysis, improved understanding of plastic analysis and current availability of much greater computing power, the constraints on the development of more accurate SDOF solutions have been greatly reduced, and a fundamental review of the SDOF method as normally applied to reinforced concrete panels appeared to be timely.

Although it was demonstrated that classical analytical methods of analysis could be used to produce similar results for the elastic response, it was found that numerical analysis using finite element methods would readily produce accurate results for elastic response for a wide range of aspect ratios and support conditions, and that SDOF parameters could be calculated for a range of panels without the need for inaccurate interpolation between bounding cases [16, 17].

The consistent elastic deflected shape and stress field produced in such an analysis gave additional information on the distribution of the reactions on the supports. This allowed an alternative model to be used for calculation of the total dynamic reactions, based on the same principals of equilibrium [15], but without the use of inaccurate assumptions, and also made available information on peak reactions.

As understanding of the yield line method had increased since the initial development of the equivalent SDOF methods, attempts had been made to account for the inaccuracy in the 'classic' yield line model [23, 17, 24], but these ad-hoc adjustments were inconsistent, and were only applied to the calculation of the plastic resistance. The analytical calculation power now available has made it practicable to apply the energy yield line method to advanced yield line patterns, avoiding some of the complexities of the equilibrium method in the calculation of the resistance and the deflected shape, and to calculate SDOF parameters from the deflected shapes of the advanced yield line mechanisms.

Use of a balanced finite element approach has allowed verification of the yield line energy calculation, has confirmed the need to incorporate equivalent nodal forces in the equilibrium yield line method used in Refs. 17 and 24 to avoid breakdown cases, and has provided the additional information on reactions required to account for the nodal forces in the dynamic reactions. These analyses have also demonstrated that the common assumption of a uniform reaction along support yield lines is not correct, and that, as for the elastic case, the peak reaction will be greater than the mean value.

By considering a finite element model loaded with a unit edge moment, a consistent model has been created for the elasto-plastic transition, and the effects of elastic shear in two-way spanning panels on the dynamic reactions has been identified for the first time.

The comparative analyses indicate that the plastic response in general lies between the extremes of the two current alternative SDOF methods [23, 24]. The elastic analysis is more consistent with more advanced dynamic analysis by the finite element method than the current alternative SDOF methods, but none of the SDOF methods can be expected to account for the influence of higher modes of vibration.

Overall, this chapter has identified a more consistent and more accurate set of parameters for application of the equivalent SDOF method to rectangular reinforced concrete panels supported on four edges than had been available previously. The methods used can also be applied to produce similar parameters for panels supported on two or three sides.

Previously, SDOF analyses developed for reinforced concrete panels had been applied indiscriminately for other materials. In this chapter the limitations of applicability of the method and parameters have been identified. With some modifications, the analysis can be applied to simply supported steel or glass plates for elastic deflections that do not exceed half the thickness. The different yield criterion for steel will make the analysis unsafe for steel plates with fixed edges. The effects of non-linearity for larger deflections of glass plates are explored in Chapter 6.

6 Application of SDOF method to thin elastic plates with large deflections simply supported on four sides

6.1 Review of existing large deflection calculations

Large deflection analysis is required to evaluate the elastic response of slender rectangular panels supported on more than two sides, when tensile membrane behaviour starts to contribute to the resistance in addition to bending behaviour. This starts to become significant once the deflections exceed about 50% of the thickness. Most glass panes will deflect farther than this before cracking, so a large deflection analysis is required to model glazing up to cracking.

Existing large deflection analysis data is derived from three sources: analytical solutions, experimental data and numerical analysis. The ease with which analytical solutions can be done varies with the in-plane support conditions. The most straightforward solution is with full edge restraint, as produced by Timoshenko [38], which had applications in ship design. More complex was the solution for plates that were not restrained against shortening, but were restrained against warping, as given by Chia [90], which had applications in the aircraft industry. In theory, these methods could have been used to calculate the deflected shape and the stress field in the plate. In practice, only formulae for midspan deflections and a few critical stresses were ever derived.

Most complex were the large deflection solutions that allowed the edges to warp. The Author [6] attempted to use the Galerkin method presented by Chia [90] to analyse a simply-supported plate with no in-plane restraint other than symmetry. This was regarded as a representative model for window glazing. The Galerkin method involved using an initial coarse assumption of the deflected shape to derive an initial function for the stiffness, and then to use the principal of orthogonality of modes to refine the stiffness function. The approach does not derive a refined deflected shape or stress field, and so could not have been used to derive SDOF coefficients for large deflection cases. The results of the analysis were disappointing. The resistance formula was a reasonable fit for moderate deflections of a nearly square panel and for small deflections for all aspect ratios, but the trends for moderate or large deflections with non-square panels were counter-intuitive, and diverged dramatically from the data from other available sources.

Bowles & Sugarman [64] and Seaman[65] used experimental data to produce large deflection formulae for mid-span deflection and stress respectively in a square glass pane. This used the analytical basis of Timoshenko [38], but with the parameters modified pragmatically to account for the different in-plane restraint conditions. Deflections were not measured at additional points, so the deflected shape was not assessed. Prichard [63] used this approach to assess the non-linear resistance and cracking stress, but used SDOF transformation factors from Biggs [35], based on small deflection theory and the approximate elastic deflected shape in Ref. 16.

Aalami & Williams [91] used finite difference numerical methods to calculate large deflection response and stresses in steel plates with a variety of support conditions and loadings, including a uniformly loaded, unrestrained, simply-supported plate comparable to a glass pane. Only mid-span deflections and critical stress output was presented. This showed that stresses could become critical at the corners for large deflections, but the accuracy of applying the results to glass panes was limited by the difference in Poisson's ratio.

Moore [67], and Al-Tayyib [69] both used non-linear finite element analysis to model simply-supported glass panes numerically without in-plane restraint. This involved calculating the deflections at a grid of nodes over the model for each load step; Stresses can also be derived throughout the model. Moore identified that the corner stress may be more critical than the centre stress at large deflections, and produced resistance and maximum stress curves that were applied to SDOF analysis of blast loading by Meyers [70]. Neither Moore nor Meyers appear to have considered using the deflection or stress output from these analyses to assess other SDOF parameters for large deflections, and Moore's curves are combined with approximate small deflection transformation factors and an approximate small deflection static distribution of reaction in Ref. 24.

Vallabhan [67] used finite difference methods to analyse glass panes numerically. Contour maps of stress and deflection were produced, so all the data needed for calculation of large deflection SDOF coefficients was available. The initial convergence criteria used by Vallabhan were optimised for quasi-static loading, and most of the research to which the program was initially applied at Texas Tech University related to low strain-rate loading [71-76]. Although Vallabhan envisaged additional research to optimise the finite difference program for dynamic analysis, it was always intended as a multi-degree-of-freedom analysis tool, and was not used to derive SDOF parameters.

Currently there are no existing large deflection calculations that have been used to assess transformation factors or reaction coefficients for SDOF analysis.

6.2 Large deflection finite element analysis

A series of non-linear FE analyses of simply-supported glass panes was undertaken using thin shell, semi-loof elements in the LUSAS general FE program [124], which have eight nodes per element and quadratic interpolation, but with only eight bending degrees of freedom, two along each side. Quarter panel models were analysed between two supported edges and two lines of symmetry.

The analyses were used to cover the same range as that analysed by Moore [67] for aspect ratios λ from 1 to 4, and for non-dimensional loading L_{ND} (indicated by ND Load in subsequent figures) given by:

$$L_{ND} = p \cdot \frac{12 \cdot (1 - \nu^2)}{E} \cdot \left(\frac{b}{h}\right)^4 \quad [10<L_{ND}<100{,}000] \tag{35}$$

where p is the applied pressure, b the shorter span and h the thickness. A small deflection non-linear analysis with L_{ND} = 1 or 5 was included for comparison with linear analysis, and where convergence could be achieved, an analysis at L_{ND}=200,000 was also included. In the non-linear analyses, successive load increments were analysed at factors of 1, 2 and 5 times successive powers, to provide near equal spacing of data on a logarithmic scale.

Initially only five aspect ratios were modelled, 1, 1.5, 2, 3 and 4, to match the curves produced by Moore. Subsequently, additional intermediate values were added to provide a smoother numerical interpolation when applying the data in SDOF calculations.

For the models analysed, the span b was set at 1m, and t was generally chosen as 3.57383mm, so that for normal glass properties of E= 70 MPa and ν= 0.22 the non-dimensional load L_{ND} is equal to the pressure p. This gives a slenderness h/b of approximately 1:280, corresponding to a 6mm pane over a span of 1.67m, which is at the slender end of practical glazing.

The elements and loading type selected can produce follower forces in a non-linear analysis, as is appropriate for a true pressure loading on a surface with large deflection. However, a fully Eulerian solution for shells is not available in LUSAS where the follower forces are in equilibrium for the deformed shape of that increment. Instead, an 'Incremental Lagrangian' solution was used, where the follower forces are based on the deformed shape of the previously converged increment. To minimise the difference, intermediate loading steps were set in the calculation with a loading equal to 99% of that of the load steps that were post-processed.

For incremental calculations, an accurate deflection at the 99% increment was also required, so three increments were analysed for each step in the loading: one at 99% loading with follower forces based on the previous deformed shape at 40% or 50% of the loading, a second at 99% with follower forces based on the previous 99% loading, and one at 100% loading with follower forces based on the second 99% loading case. Output was taken from the second and third of these increments.

Both ‘Incremental Lagrangian’ analyses with follower forces and ‘Total Lagrangian’ analyses with conservative forces have been undertaken for comparison purposes. They represent alternative static models, either of which could be used as the basis of an approximate SDOF model. The true dynamic response is likely to lie between these two extremes. The question of which is the more appropriate approximate deflection model depends on the relative timing of the dynamic loading and the glazing response.

Conservative forces are most appropriate when the positive phase loading is of short duration compared to the duration of the elastic response, either to peak elastic deflection or to cracking. The bulk of the impulse is applied to the glass early in the response, when the deflections are small, and the momentum will continue to act conservatively as the deflection increases after the loading is past.

Follower forces are most appropriate when the positive loading is of long duration and will persist well beyond the peak elastic deflection and cracking. The pressure will be applied gradually throughout the deformation, and will still be high and acting perpendicular to the surface when the deflection is high. The difference between follower forces and conservative forces is illustrated in Fig. 77.

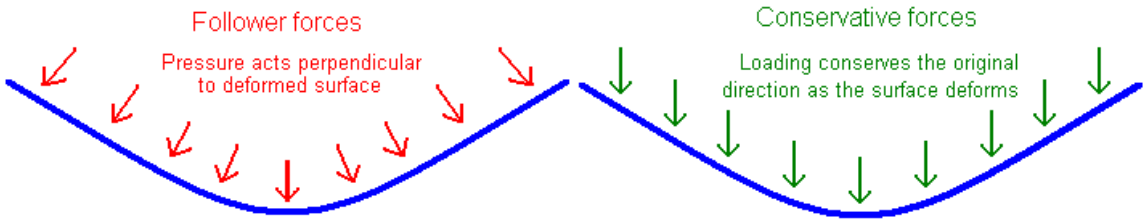

Figure 77. Large deflected shapes contrasting follower forces and conservative forces

The elastic stage up to cracking provides a relatively small proportion of the resistance capacity of laminated glass or systems containing laminated glass. For critical analysis of such systems, the glass resistance is likely to be overwhelmed quickly, and follower forces are likely to be a more appropriate model, although this will be more accurate for large charges at longer range such as vehicle bombs than for small package charges at close range.

Studies have been included to assess how sensitive the SDOF parameters are to the difference between the two models.

6.3 Non-linear deflection and maximum stress

Numerical output of the transverse deflection at each element from the 100% load increment for each loading step was exported to Excel for post processing, from analyses using a uniform mesh of 10 square elements along the shorter side and between 10 and 40 elements along the longer side. The maximum deflection was found always to occur at the node corresponding to the centre of the pane.

Charts of non-dimensional centre deflection d (indicated by ND Deflection in subsequent figures):

$$d = \frac{z}{h} = \frac{z}{b} \cdot \frac{b}{h} \tag{36}$$

where z is the deflection, h the thickness and b the shorter span, were plotted against the non-dimensional loading L_{ND} in Fig. 78 for the analyses using follower forces. This figure directly corresponds to the deflection chart produced by Moore [67] shown in figure 27, and is the non-linear equivalent of the spring stiffness values calculated for the linear analysis.

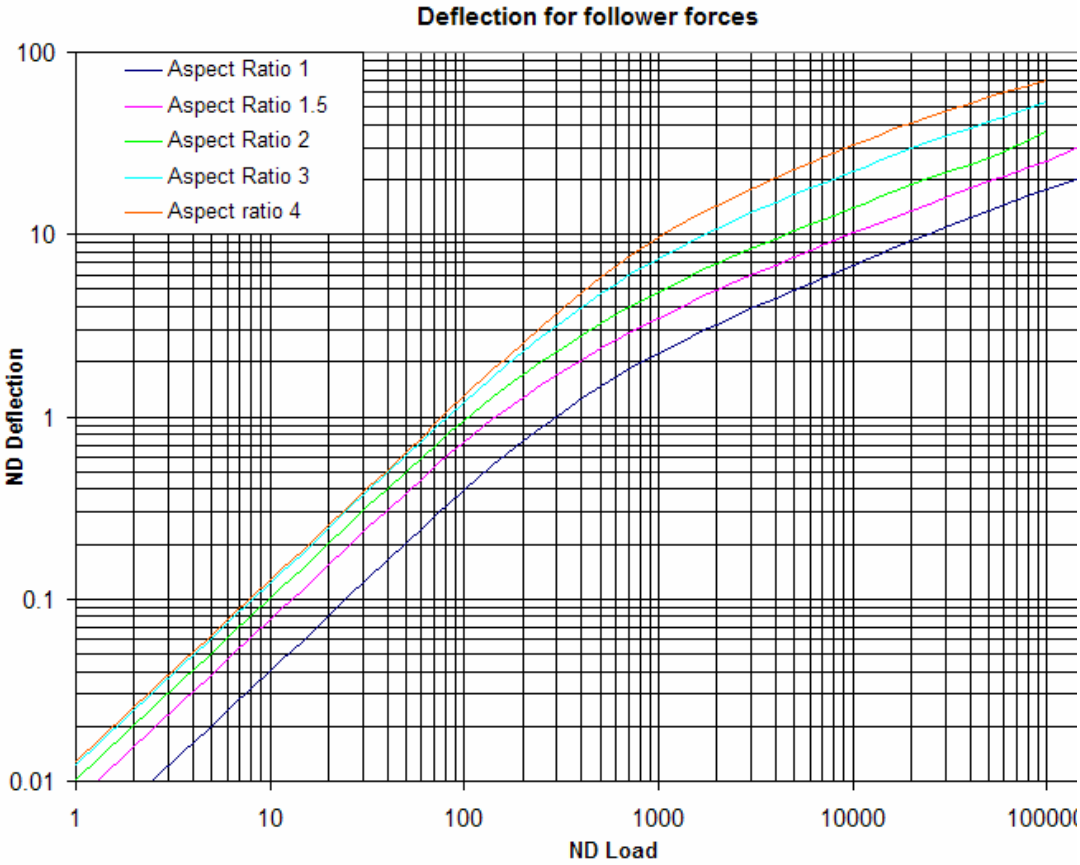

Figure 78. Non-linear deflections of simply-supported glass panes

The results of these analyses are similar, but not identical, to the data in Moore's charts. The deflections at the lower loaded end are identical, but the maximum deflections at the upper end of the scale are about 8% lower for the square panel, and

about 10% lower for an aspect ratio of 4. Although mesh refinement in this analysis would reduce the discrepancy, the effects of mesh refinement are small and diminishing.

A sensitivity analysis showed that, for λ=1 and L_{ND}=100,000, halving the size of the uniform grid increased the deflection by about 0.64%, and that the introduction of the refined mesh illustrated in Fig. 79 adds only a further 0.08%.

The source of the remaining 7-9% discrepancy is unclear at present, but might be explained by detailed differences in the FE models. For example, if Moore were more concerned with the effect of acceleration forces rather than pressure forces, he would not have included follower forces in his model. Inspection of Meyers' [70] application of Moore's curves does not provide any indication of which load application was used, but Moore's interest lay in the strength of solar panels on spacecraft launched into orbit, for which follower forces would not be appropriate.

An analysis for λ=1 and L_{ND}=100,000, using "Total Lagrangian" non-linear control which creates conservative forces, showed a 3% increase in deflection, still less than half the remaining difference. However, the maximum stress also increased by 12.5% for this analysis, so comparison of the stresses is also required to identify the likely differences between Moore and the current analysis.

The maximum principal stress in the unloaded surface at every node was exported to Excel for post-processing. At first inspection, using the element mesh from which the deflections were measured, the position of the maximum stress appeared to move sharply from the centre of the panel to the corner as the loading exceeded a narrow transitional band. This was consistent with the data provided by Moore who plotted variation of the centre and the corner stress. Inspection confirmed that even at the corner and at high loadings, the tensile stress was always higher on the unloaded surface.

However, sensitivity analysis showed that mesh refinement was required to produce a consistent value of stress in the corner of the panel, due to the high local stress gradient in the anticlastic surface close to the corner. To analyse the stresses a refined mesh was used, with three times as many elements along a side, and with a grading to make the largest elements 4 times the size of the smallest elements at the corner. This makes the largest elements in the centre of the panel about half the size of the uniform grid in each direction, and the smallest elements in the corner about 1/8 of the size

For the case with λ=1 and L_{ND}=100,000, a first level of mesh refinement with 50% more elements than the uniform grid, and the corner elements about ¼ of the uniform mesh size resulted in a substantial reduction in the maximum stress. However, doubling the number of elements to give corner elements $\frac{1}{8}$ of the uniform mesh, as illustrated in Fig. 79, results in a further 12% reduction. This demonstrated that there was still an unacceptable error in the coarser refined mesh. In contrast, increasing the gradation of the refined mesh further to reduce the mesh in the corner to about $\frac{1}{11}$ of the uniform mesh size decreases the maximum stress by only 0.6%, demonstrating that the error in the second level of refinement is acceptably small.

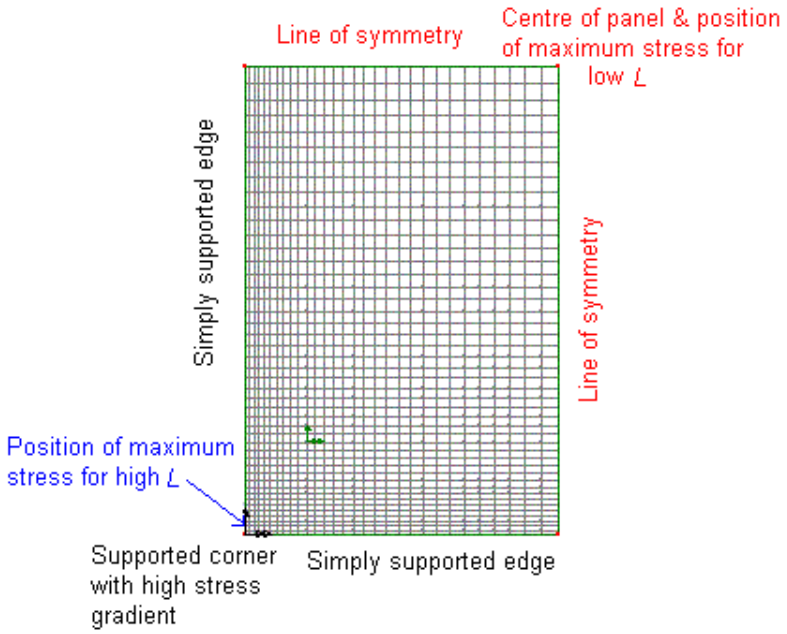

Figure 79. Typical refined mesh quarter panel model, for λ of 1.5

Maximum principal tensile stresses from analyses using this second level of refinement were expressed in non-dimensional form (indicated by ND Stress in subsequent figures):

$$\sigma_{ND} = \sigma \cdot \frac{12 \cdot (1 - \nu^2)}{E} \cdot \left(\frac{b}{h}\right)^2 \tag{37}$$

where σ is the actual stress, E is Young's modulus, ν is Poisson's ratio, h the thickness and b the shorter span. The stresses are shown in Fig. 80.

The maximum stresses in the centre of the pane are indistinguishable from Moore's, but maximum stresses found away from the centre are significantly higher than given by Moore for the corner. The introduction of the refined mesh reduces the maximum stress for λ=1 and L_{ND}=100,000 from almost double Moore's value to 1.31 times, or 1.46 times with conservative forces from 'Total Lagrangian' control.

However, for high values of L the maximum stress does not occur at the corner node, as assumed by Moore and as shown by coarser mesh FE analysis, but on the supported edge about 1.4% of the span from the corner, as shown in Fig. 81.

Unlike the eight-noded shell element, where the stresses are exaggerated in a coarse mesh, mesh refinement for four-noded shell elements converges towards the true maximum stress from lower bound values as the mesh is refined. For λ=1 and L_{ND}=100,000 a four-noded analysis with conservative forces will match Moore's corner stress with a 24 x 24 element uniform mesh for the quarter panel. However, the maximum stress two nodes up the side is 13.5% higher than this.

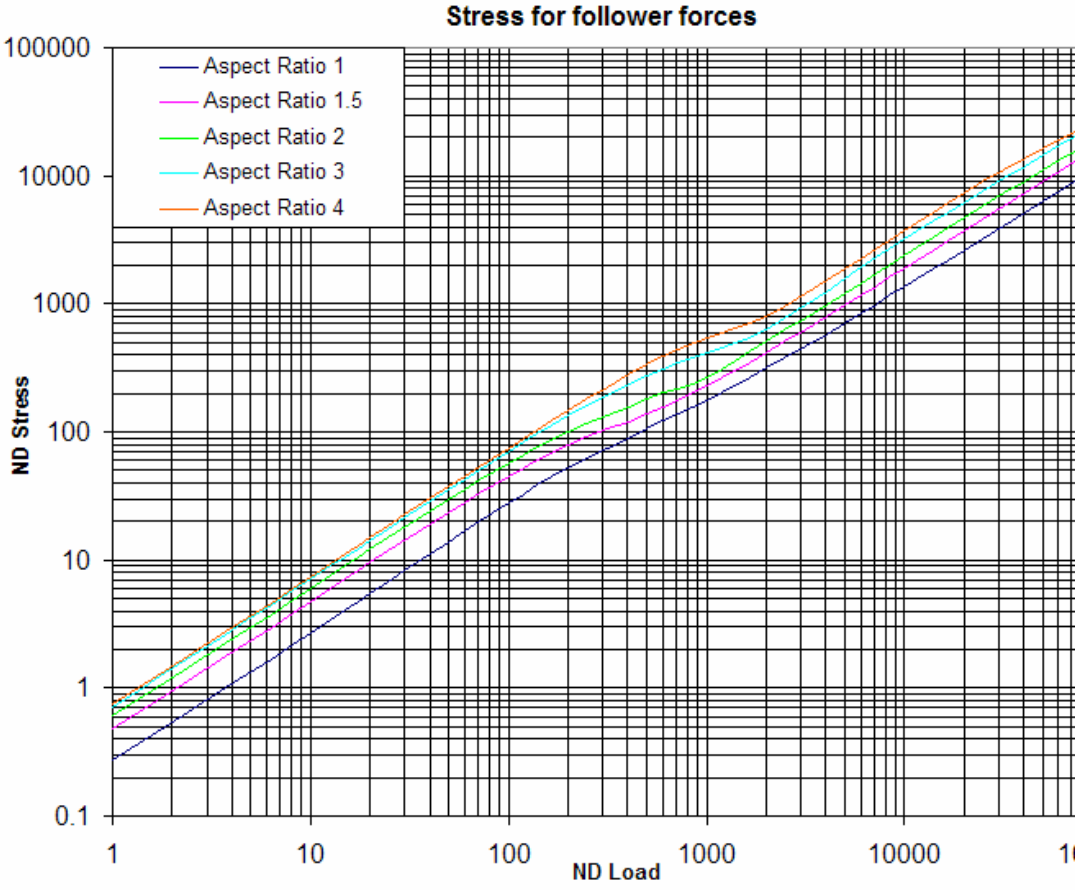

Figure 80. Non-linear maximum tensile stress in simply supported glass panes

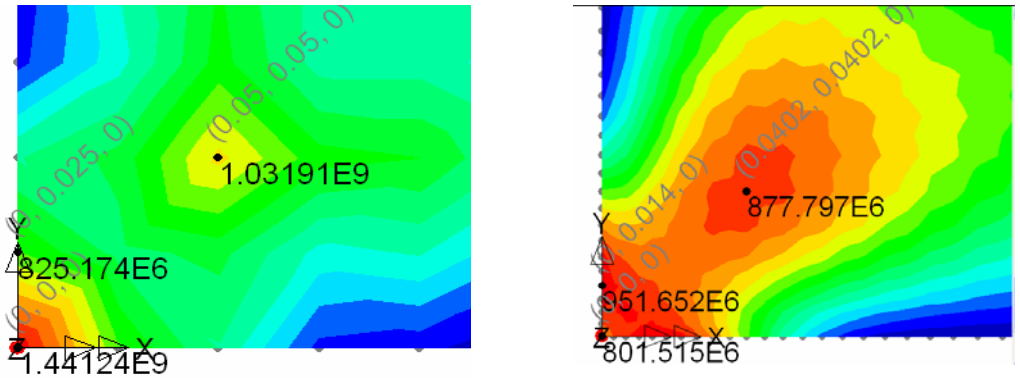

Regular Mesh Refined Mesh

Figure 81. Corner stresses in Regular and Refined meshes, λ=1, L_{ND}=100,000

If the mesh is refined, the corner stress first rises and then starts to drop, but the maximum stress continues to rise. Although the corner stress for a 30 x 30 graduated mesh with conservative forces is only 1% higher than for the 24 x 24 mesh, the maximum stress is 29% greater, being 88.4% of the maximum stress of the refined eight-noded analysis with conservative forces and 99.5% of the maximum stress of the refined eight-noded analysis with follower forces.

As four-noded elements are significantly less accurate than eight-noded elements with the same mesh density, it is probable that most of the remaining discrepancy lies in the four-noded element analysis.

It appears likely that Moore's analysis was based on a mesh of four-noded elements, and it is possible that the plateau of the corner stresses seen here may have convinced Moore that the mesh that he had used was sufficiently refined. However, consideration of nodes away from the corner could have increased the maximum stresses by more than 30%. Moore's analysis may have significantly exaggerated the deflection and loading of very slender glass panes before the failure stress was reached.

It is considered that the use of eight-noded elements, mesh refinement and testing for maximum stress throughout the model has resulted in a significant improvement in accuracy for this analysis over that reported to have been undertaken by Moore.

The use of follower forces is considered to have produced a more appropriate model for blast pressure loading from medium to large sized charges, ranging from terrorist vehicle bombs, up to accidental explosions from large explosives stores, where the positive phase blast loading will be significantly longer than the response time to cracking. Follower forces may be less appropriate for modelling the response to small package bombs at close range, but the approximation due to using curves based on follower forces is likely to be small compared to other approximations, such as modelling the blast loading as a uniform plane blast wave.

For SDOF analysis, the deflection curves can be used to define a non-linear resistance function for a glass pane, by plotting the non-dimensional resistance (equal to the non-dimensional loading) against the non-dimensional deflection, as shown in Fig. 82.

Plotting the deflection against the stress, as in Fig. 83, allowed the cracking deflection of the glass to be found for a defined cracking stress.

The figure shows a near linear relationship up to non-dimensional deflections between 2 and 12 depending on aspect ratio, controlled by the bending stress in the centre, with a narrow band of coefficients, corresponding to the elastic resistance in Table 30. There is then a transition towards a different power ratio, of the order 0.4, but with a much wider variation between coefficients with aspect ratio, dominated by the combination of torsion and membrane stress close to the corners.

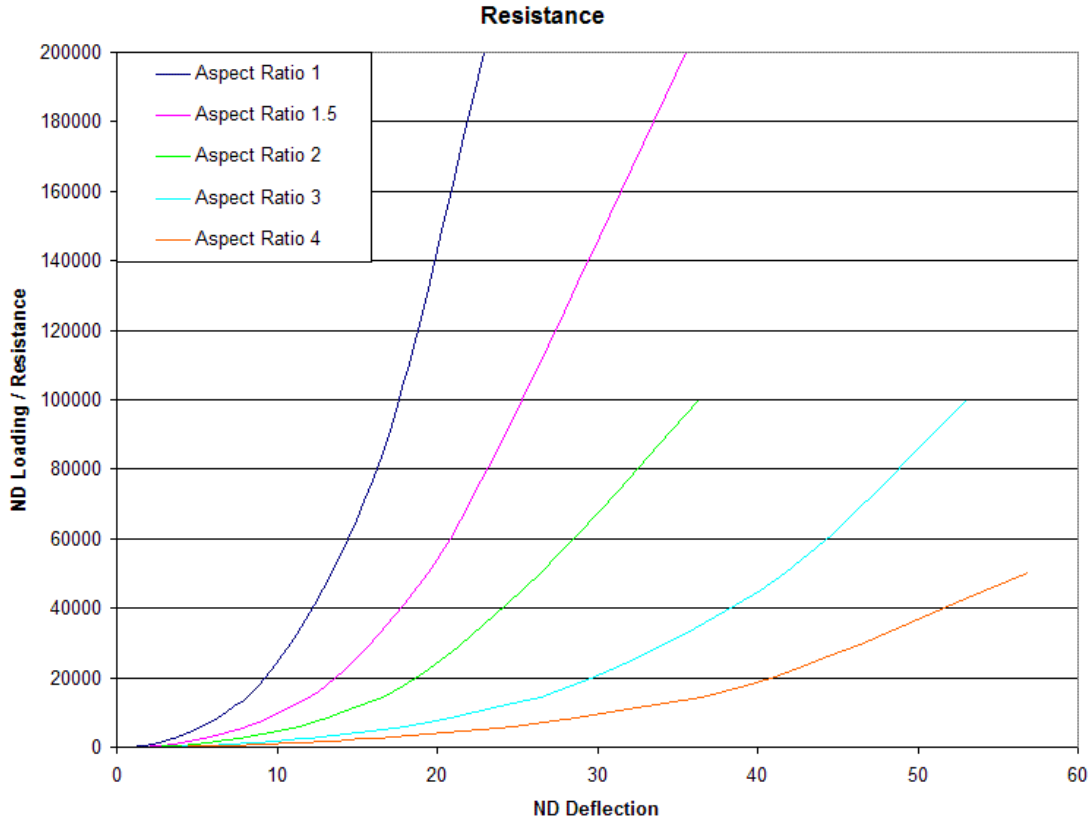

Figure 82. Resistance curves for simply-supported glass panes

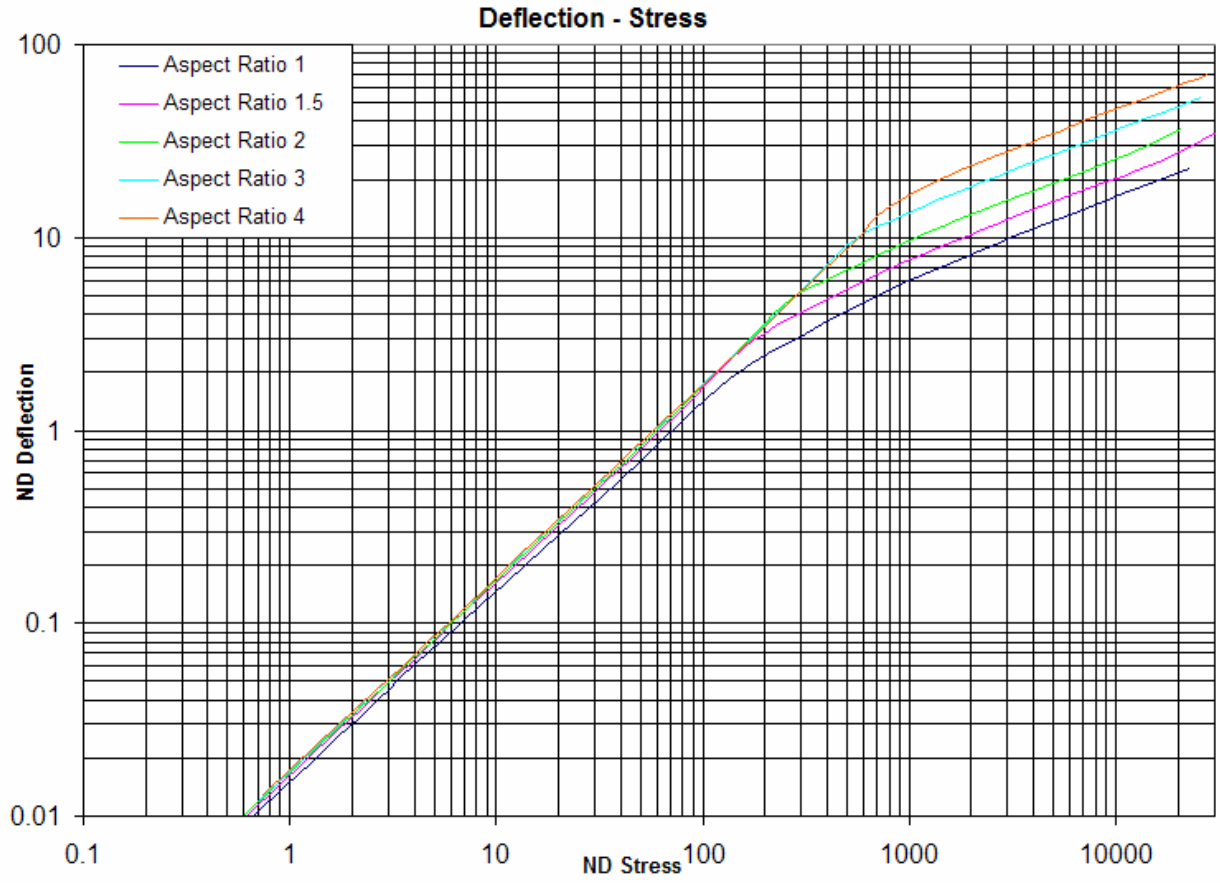

Figure 83. Deflection-Stress plot of simply-supported glass panes

6.4 Non-linear transformation factors

The SDOF transformation factors were calculated for each 100% loadstep of each analysis, using the deflections in three axes for the 100% loadstep, and the transverse deflection from the corresponding second loadstep with 99% of the load. These deflections were tabulated for the whole model in LUSAS [124] and then copied to an Excel [125] spreadsheet for post-processing.

The deflections of the nodes around the uniformly-sized square elements were weighted in accordance with the trapezoidal rule for numerical integration. All of the nodes in the interior of the model, both at the corners and mid-side of each element, were equally weighted, with the corner nodes common to four elements and the mid-side nodes common to two. Along the sides of the model, where the mid-side nodes are unique to each element and the corner nodes are common to two elements, the weighting was halved, and the weighting on the four nodes at the corners of the model was one quarter.

The automatic numbering of nodes in LUSAS for a single rectangular surface numbers the perimeter nodes first, and then the interior nodes, so the weighting pattern was systematic and was readily adjusted for each model. The weighted sum of nodes was three times the number of elements, i.e. from 300 for the square panel to 1200 for the panel with an aspect ratio of 4.0.

The load transformation factor K_L for uniform loading was based on the deflected shape of the loaded model at each timestep. This was calculated by weighting the transverse deflection of each node, summing the total deflections and then dividing by the weighted number of nodes and by the deflection of the node at the corner of the quadrant model corresponding to the centre of the panel, as given in Eqn. 38. For most calculations the reference point at the centre of the panel was also the location with the maximum deflection.

$$K_L = \frac{\sum_1^N z_n w_n p}{z_{centre} \cdot \sum_1^N w_n p} = \frac{\sum_1^N z_n w_n}{z_{centre} \cdot \sum_1^N w_n} \tag{38}$$

The mass transformation factor K_M for uniform distributed mass m was calculated similarly, except that the deflections were squared before being weighted, as given in Eqn. 39.

$$K_M = \frac{\sum_1^N z_n{}^2 w_n m}{z_{centre} \cdot \sum_1^N w_n m} = \frac{\sum_1^N z_n{}^2 w_n}{z_{centre} \cdot \sum_1^N w_n} \tag{39}$$

In initial analyses, the transverse deflections used for these calculations were the total deflections at each loading step, i.e. the values calculated for each of the 100% increments. This was the basis of the analyses by the Author presented in Ref. 121.

However, Biggs [35] identified that the transformation factors should be based on the incremental deflections rather than the total deflections. An analysis has therefore been undertaken using the difference between the 100% increments and the immediately preceding 99% increments for all the nodes as the incremental deflection. The difference between these approaches is illustrated for the load transformation factor K_L in Fig. 84.

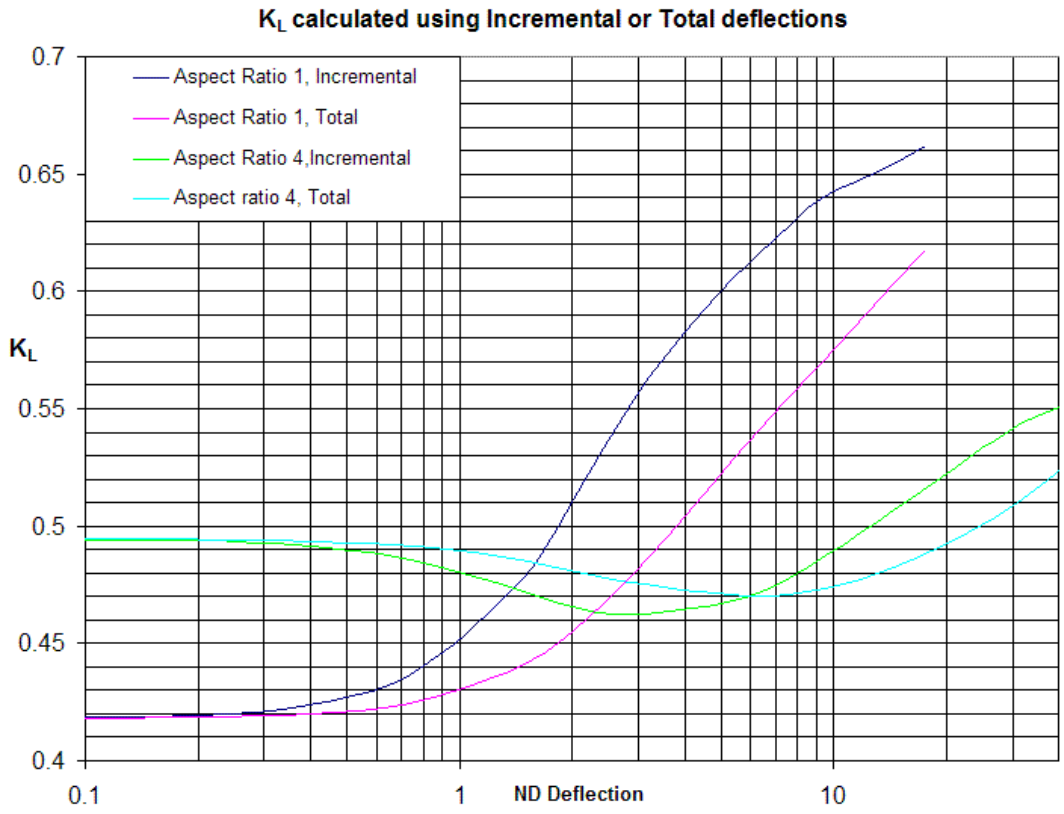

Figure 84. K_L coefficients calculated from Incremental and Total deflections

The incremental deflected shape amplifies the variation in the factor from the small deflection values shown by the total deflected shape, so the transformation factor varies sooner and more when the correct incremental shape is used for the calculation. The deviation from the small deflection values of transformation factors calculated from the non-linear incremental deflections is detectable from deflection values of about 0.3 times the pane thickness, rather than the commonly accepted limit of 0.5 times thickness based upon total properties.

Similar effects are seen in the mass transformation factor K_M, and in the ratio of these factors, K_{LM}. The transformation factors presented in Figs. 85, 86 and 88 are based on analysis of the incremental deflections.

Use of transformation factors based on the total deflected shape, as in Ref. 121, would tend to underestimate the variation from the small deflection transformation factors, although a SDOF analysis of glazing using them they would still be more accurate than one based on the small deflection transformation factors.

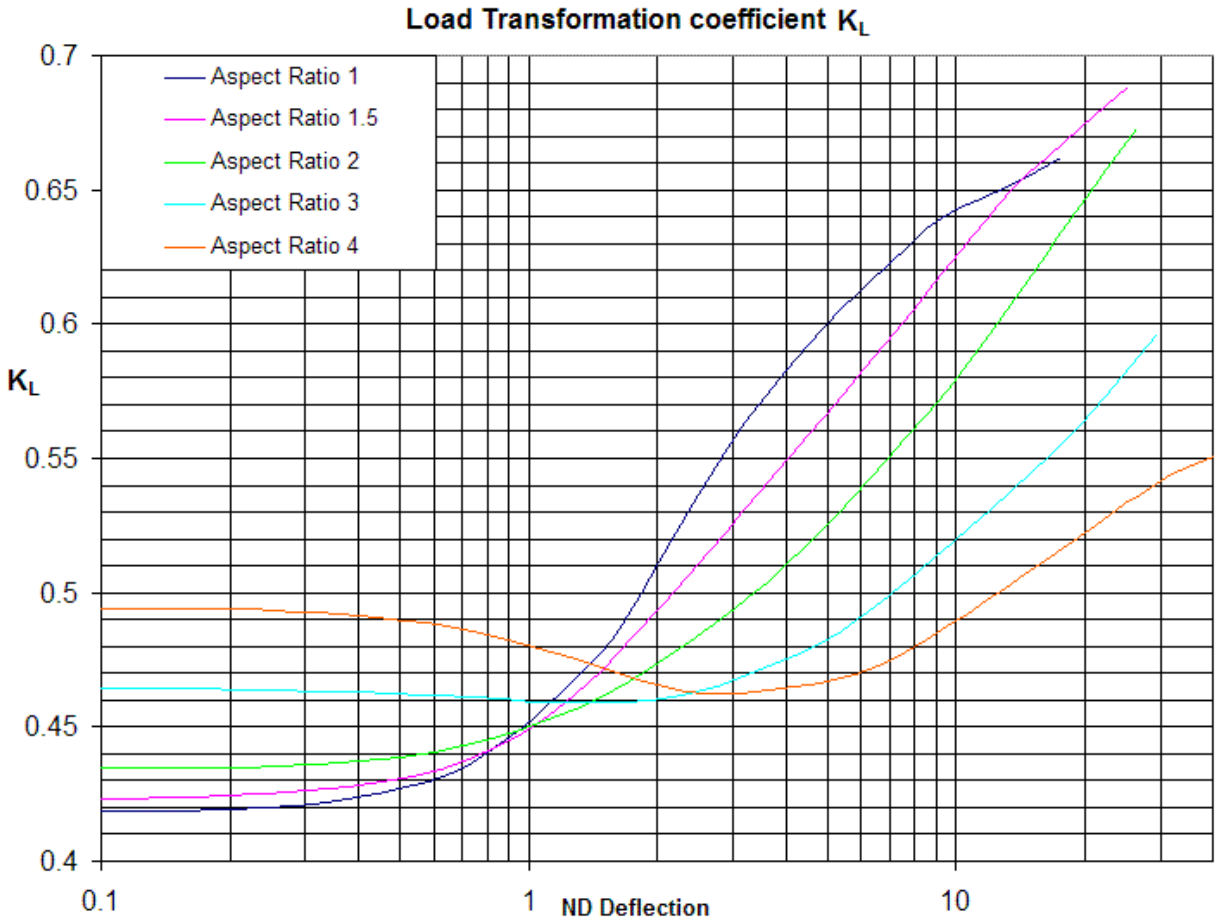

Figure 85. Load transformation factors for simply-supported glass panes

At very large loads, the geometric non-linear model of the pane can buckle locally near the centre of the supported edge due to the compression parallel to the support, as shown in Fig. 87. For higher aspect ratios, this tends to occur at lower pressures, but larger deflections, than for lower aspect ratios. In buckling, the deflections of a local part of the pane deviate from the general trend. When considering the total effects, this tended to be noticeable in the contour plot of tensile stresses only after the buckle was well-established.

In practice, the buckle has only a minor effect on central deflections and maximum stresses in the centre or near the corner, but has a significant effect on transformation factors that are based on integration of the deflected shape over the whole pane. The effects of the buckle are amplified when considering the incremental deflection, so the coefficients are significantly affected even at the early stages of buckling.

However, this sensitivity also makes it possible to identify the early stages of a buckle. One parameter that was found to be sensitive was the minimum incremental transverse deflection. For normal definition this is zero, at the supports. However, when buckling starts, the incremental deflections at some nodes become negative. This can be identified by checking the minimum value of the incremental deflection.

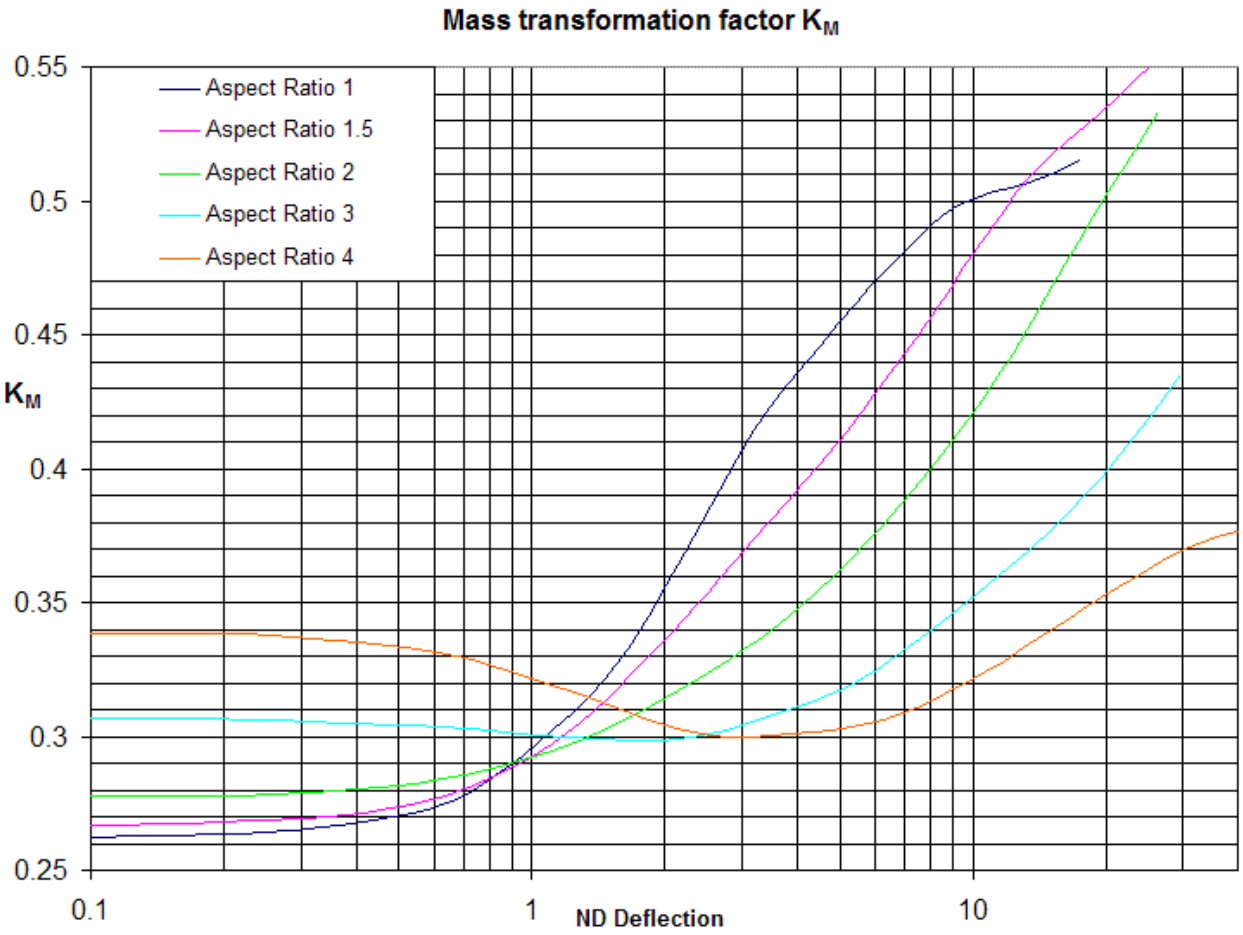

Figure 86. Mass transformation factors for simply-supported glass panes

Parameters calculated from load-steps where the incremental deflection was found to be negative have been discarded as unreliable. It is possible that there may be small distortions in the parameters calculated for the last retained load-step, if a buckling distortion small enough to avoid negative incremental deflection is occurring. However, the deflections at which these occur are still very large for a monolithic pane of practical slenderness, and cracking is likely to occur at smaller deflections, before this part of the curve is reached.

Single plies from laminated panes are more slender, and the non-dimensional deflections could possibly reach the less accurate levels for the SDOF coefficients before the cracking deflection is reached. However, when these cases are analysed the non-linear stiffness normally causes the final ply to crack immediately the laminated glass cracks. The SDOF coefficients for very slender plies are not normally required for the SDOF analysis of the glazing, so small distortions in the calculation of the coefficients for large deflections are not considered significant.

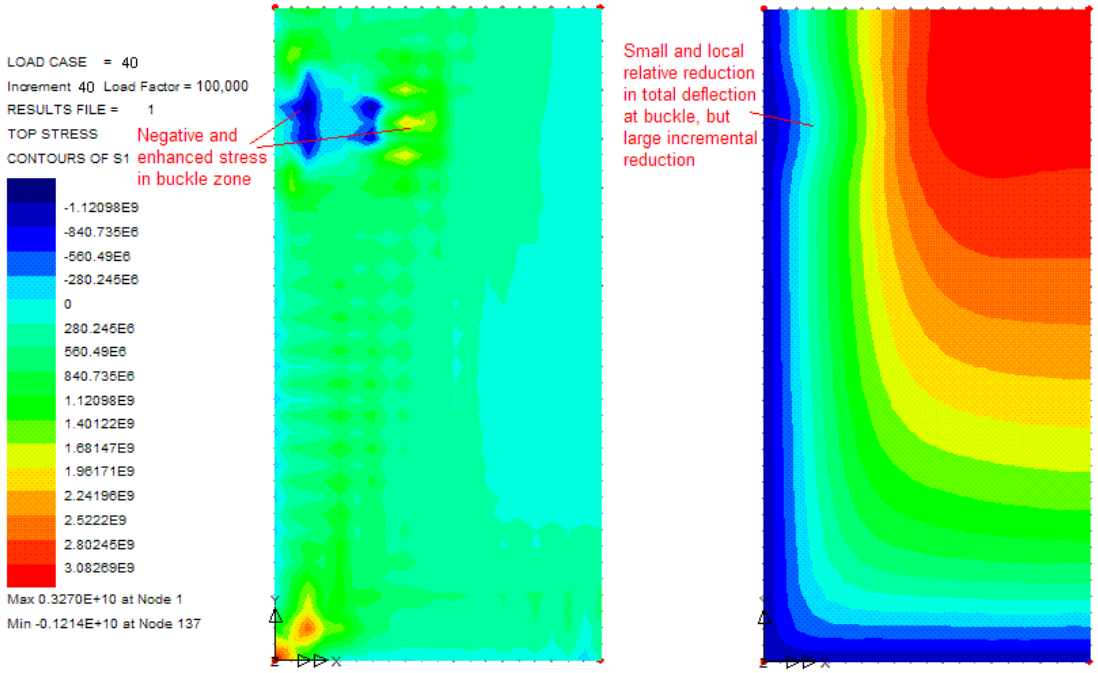

Figure 87. Typical stress and deflection plot at high load showing advanced buckling of the model

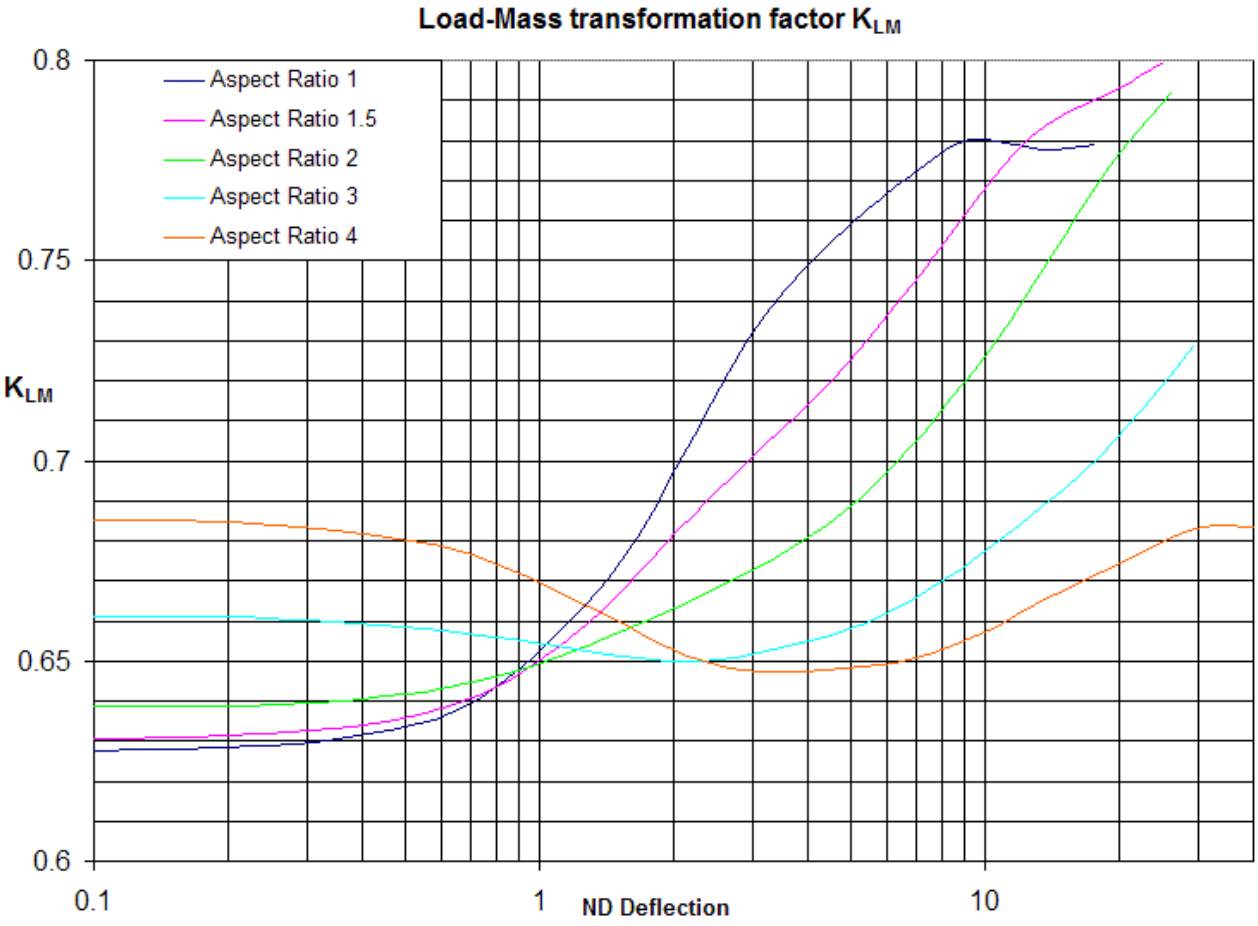

Figure 88. Load-Mass transformation factors for simply supported glass panes

Above a loading of L_{ND}=1000, a further weighting was included in the calculation. As the deflection increases the slope of the element becomes significant, and the projected surface perpendicular to the overall direction of loading reduces. For the calculation of K_L for higher loading, the nodes' weightings were adjusted by the projected areas of the associated elements. A linear approximation was used based upon the relative X and Y axis displacements of adjacent nodes nearer the lines of symmetry, and with symmetry nodes weighted as unity. Below L_{ND}=1000, where this modification affected the fourth or fifth significant figure, this weighting was ignored. At L_{ND}=100,000 it affects the second or third significant figure.

As the mass of the elements is not altered by their inclination, this weighting was not applied to the calculation of K_M. As a result, the incorporation of this additional weighting in K_L affects the second or third significant figure of K_{LM} for high loading levels.

Although it is not used for calculation of the SDOF transformation factors, the average total deflection can be a useful parameter in simultaneous SDOF analyses and multi degree-of-freedom analyses, e.g. in defining the volume swept by a leaf of a double glazed unit to calculate the volume change and hence pressure change in the sealed cavity. The average total deflection parameter is the same as the load transformation factor K_L for the total rather than incremental deflection, and can be calculated in the same way. This is included for completeness as Fig. 89.

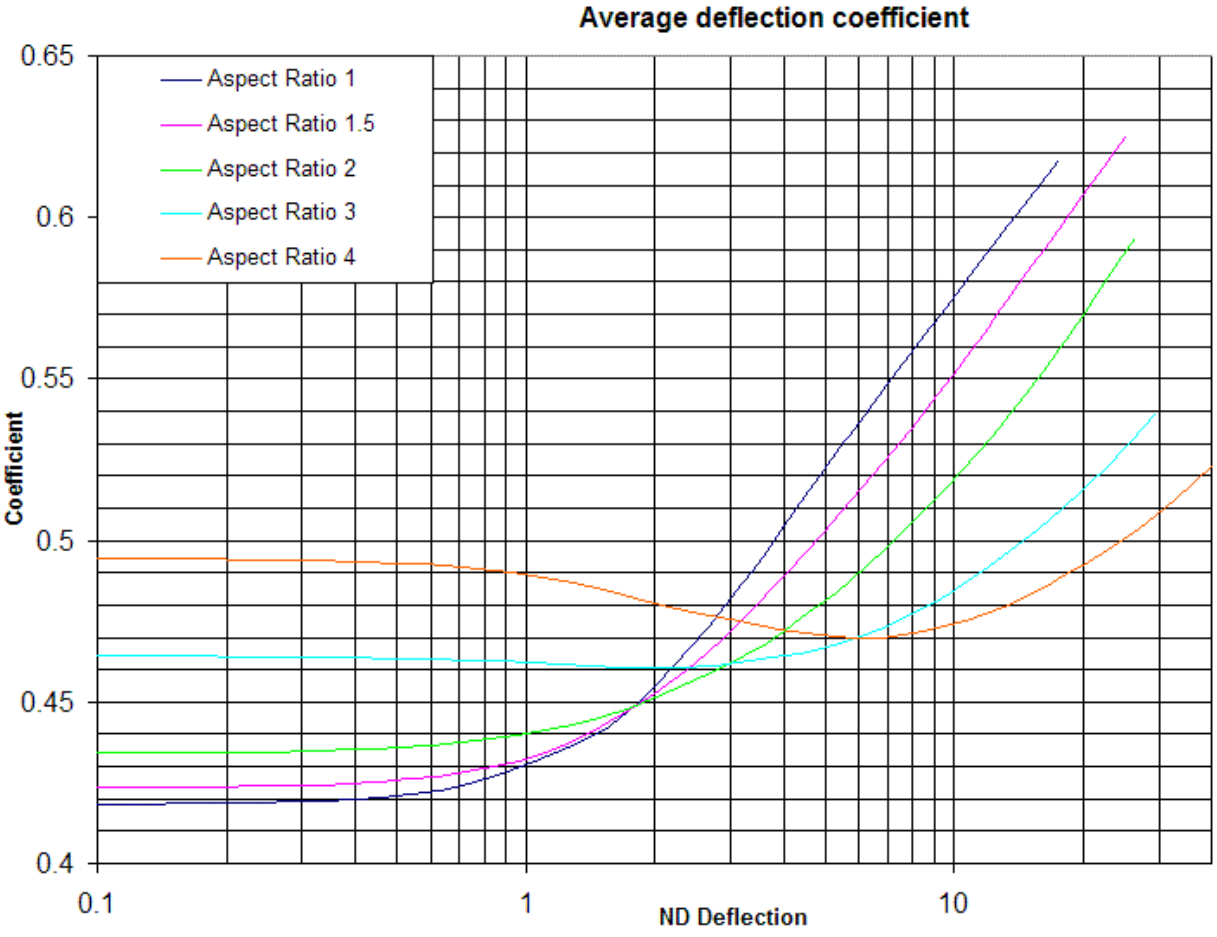

Figure 89. Average deflection factor for simply supported glass panes.

6.5 Non-linear reactions and reaction coefficients

The method of calculation of the reaction coefficients from the large deflection analysis is similar in principle to that used for the small deflection elastic analysis, developed originally by the Author in Ref. 6, described in Sections 3.5.5.5 and 5.4 of this Thesis and illustrated in Fig. 23.

One of the main assumptions of the method of calculating dynamic reactions in the Equivalent SDOF method is the use of the centroid of the deflected shape as the centre of the inertia forces. For elastic small deflections, the deflected shape is taken as invariable and independent of the time-based variation, so that the deflected shape, velocity shape and acceleration shape are taken as identical, with a common centre. The analysis of the propped cantilever in Section 3.5.4.1 and Fig. 18 showed the significance of using an appropriate definition of the centre of the inertial forces in a non-linear model; the abrupt changes in the position of the incremental deflection centre with plastic yield producing abrupt changes in the dynamic reaction coefficients.

For a continuously non-linear system, such as the large elastic deflection of glass panes, the deformed shape will be continuously changing, so the shape of the deflection, velocity and acceleration will not be identical, and the centres will be slightly different. From the static analyses undertaken, the incremental deflection is representative of the velocity distribution, but the acceleration distribution cannot be modelled.

The inertial forces primarily arise from acceleration, although the work of Zobec & De Bartoli [37] as described in Section 3.5.3 and Eqn. 13 show that there is a secondary velocity-related term to consider. In practice, the closest approximation available using a static analysis of non-linear deflection is to approximate the centre of inertia by the centroid of incremental deflection. Some idea of the order of approximation that this may introduce can be obtained by comparing reaction coefficients calculated in this way with those calculated using the centroid of total deflection.

The differences in reaction coefficients using the deflection and velocity centres are negligible for small deflections, and can reach about 3% for extreme values. The trend is that the difference is greatest where the rate of change is greatest, with the values based on the velocity (or incremental deflection) centre changing more. Where the change rate reduces again, the values converge.

A similar order of difference might be anticipated between values calculated from the velocity (or incremental deflection) centre and the acceleration centre. It should be noted that this difference will be a systematic error that will be over and above that from any numerical error or approximation in the numerical evaluation.

For large deflections, the size of the terms used in the differential equations to calculate the reaction coefficients change significantly from the small deflection case, and secondary effects that are zero in a linear analysis and negligible in a small

deflection non-linear calculation can substantially influence the results. These have been included simply and locally in each element by the non-linear FE analysis and produce an overall effect on the equilibrium state reached. However, in the post-processing it has been necessary to identify the overall effect from the local effects at each node to incorporate them into the two parallel simultaneous equilibrium calculations for force and resistance reaction coefficients.

Secondary effects that have been incorporated into the post-processing calculations for the non-linear analyses include:

- The horizontal movement of the centroid of acceleration and damping forces due to horizontal deflection of elements and edge pull-in. (for L_{ND}=1000 or more)

- The level of the deformed pane at the centroid, about which moments are taken.

- The horizontal components of applied pressure due to the follower forces, and the levels at which they act.

- The internal resistance due to the membrane forces acting at different levels in opposition, and the net force (balancing the horizontal pressures) and the level at which it acts.

- The modified lines of action of the reactions as the edge of the pane pulls in.

A number of these have been only approximated in the calculations with linear or first order solutions that do not fully account for the effects within the curved eight-noded elements. In addition, there will be other minor effects that have not been covered in the post-processing. All of these will contribute to error in the terms in the simultaneous equations. These incorporate the calculations based on small differences between relatively large numbers, so the reaction coefficients are prone to be inaccurate, particularly at large deflections when the secondary effects are at their greatest.

This has been monitored by calculating the ratio between the relevant dynamic reaction coefficients and the static reaction on the long and short sides and overall. The errors at small deflection are in the fourth significant figure or less, and increase with increasing deflection. All overall and long side coefficient combinations, and all but one short side coefficient combination for non-buckled load-steps are within 2% of the static load distribution, and those at realistic glass cracking deflections are all within 0.5% of the static load distribution. The exceptional short side coefficient combination has an error of 2.7%, but the aspect ratio is high so this is applied to a small absolute value.

The general pattern is for the short side coefficients to be upper bound and the long sides to be lower bound, with the balance resulting in a smaller, lower bound error overall. The nature of the secondary effects, the greater error amplification in the simultaneous equations and the sharp changes in trends on graphs when errors

increase, all indicate that force coefficients appear to contribute most of the error rather than resistance coefficients.

However, high deflection coincides with high resistance, and is associated with blast loading at a time after the blast peak has passed. Conversely, the peak loading occurs when deflection is small and the post-processing error is orders of magnitude smaller. Both of these indicate that in practice the errors in calculation of reactions arising from calculation error in the coefficients in Figures 90 & 91 will be significantly less than 2% at extreme deflections, and will be less than 0.5% in all practical cases.

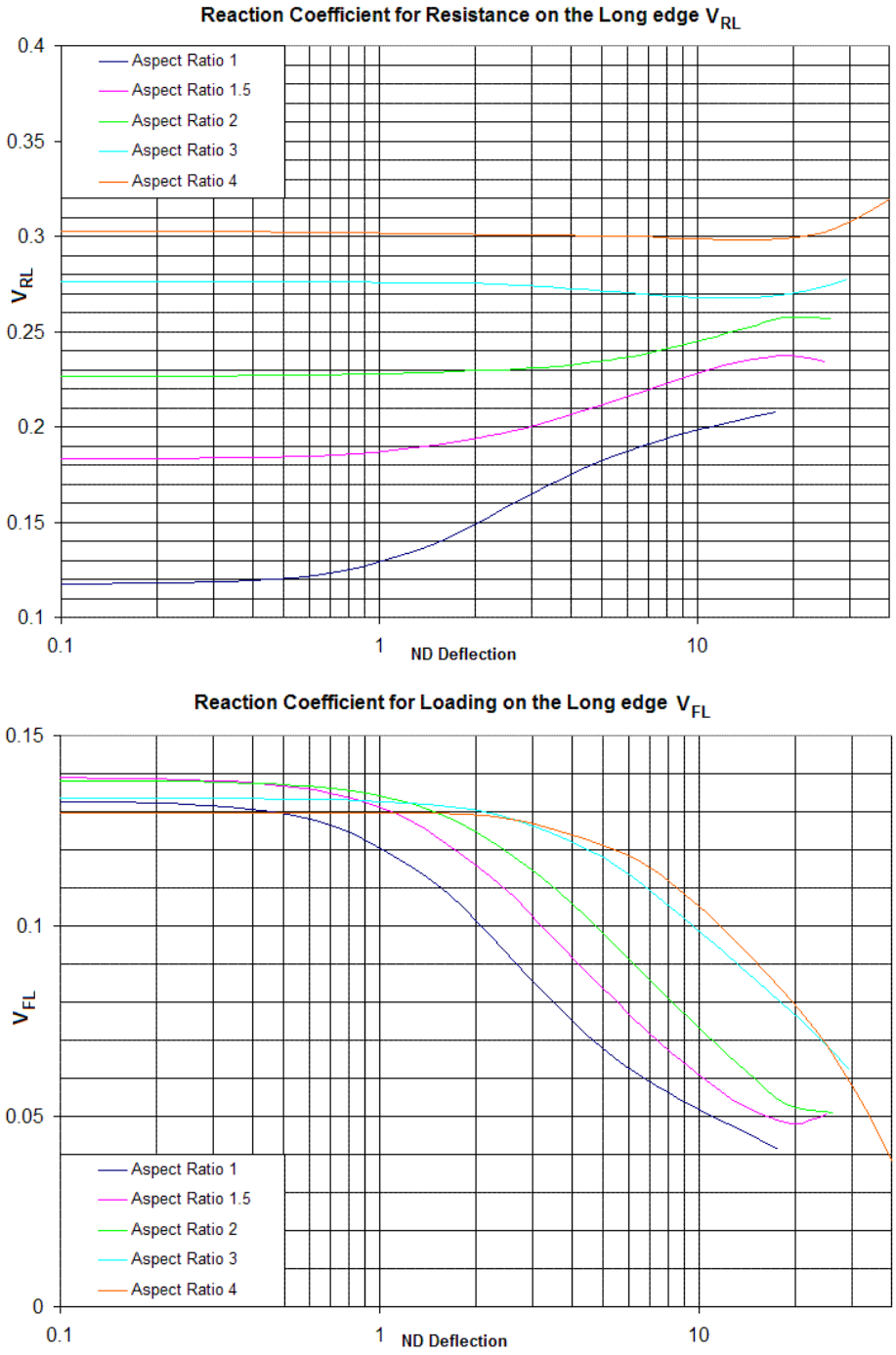

Figure 90. Reaction coefficients for the long edges of simply-supported glass panes

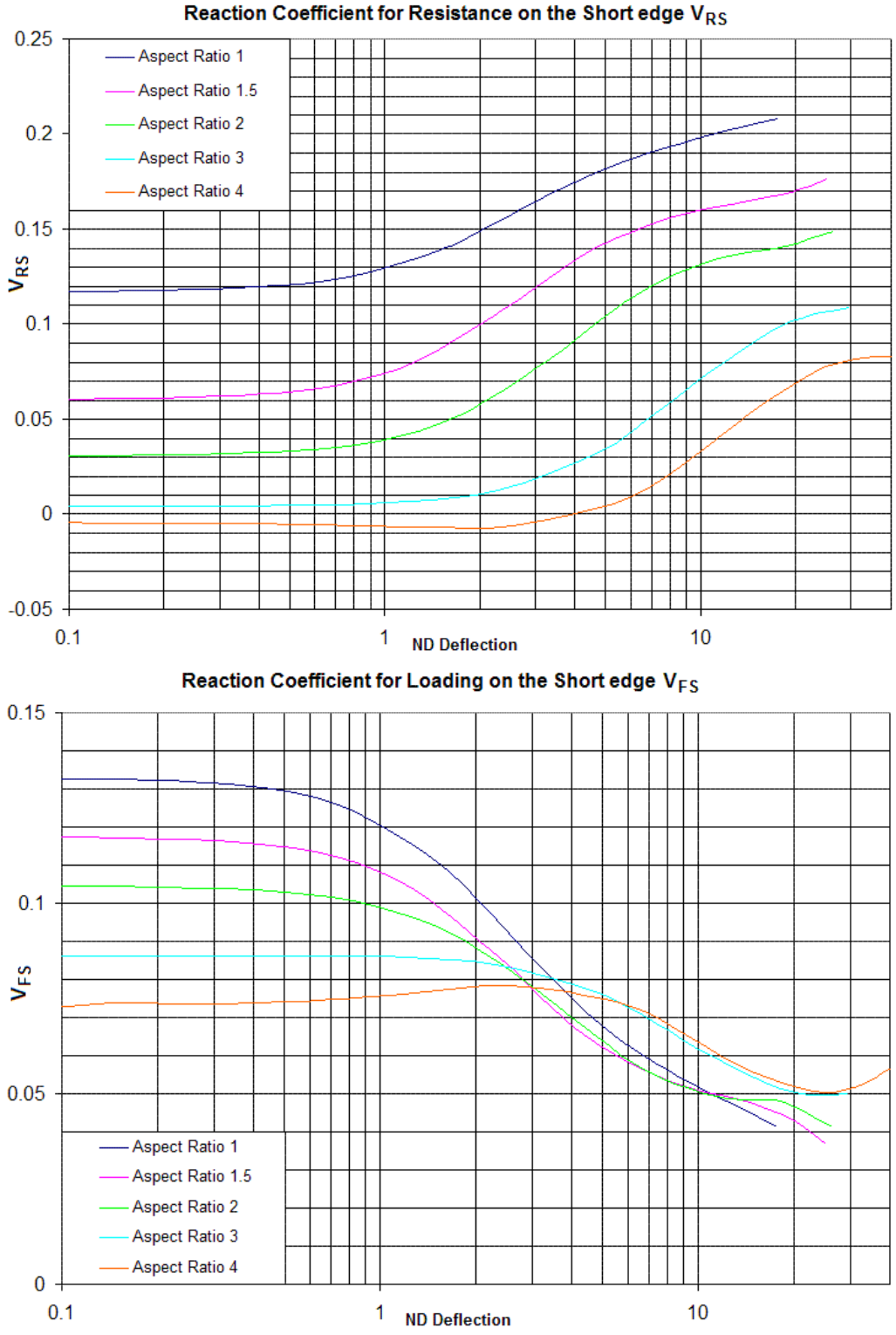

Figure 91. Reaction coefficients for the short edges of simply-supported glass panes

Where *z(t)* is the deflection history, the SDOF reaction histories can be defined as:

$$V_L(t) = V_{RL}(z) \cdot R(z) + V_{FL}(z) \cdot f(t) \text{ and } V_S(t) = V_{RS}(z) \cdot R(z) + V_{FS}(z) \cdot f(t) \quad (40)$$

6.6 Distribution of reactions with large deflection

The distribution of the reaction along the edges of the glass pane also varies significantly with deflection. The SDOF reaction calculation assumes that the force and resistance components of reaction both have the same distribution along the sides as the static loading, and that reverse reaction at the corners is distributed evenly between the two sides.

The local reverse reaction at the corners is evaluated as a point load by classical small deflection formulae and linear finite element analysis, although this is in fact an artefact of the modelling assumptions. If shear stiffness or less than perfect simple-supports were included, it would be seen that the reverse reaction is distributed over a small but finite width. This can be calculated even for a simply-supported thin plate if analyses are used that take more accurate account of the complete plate edge boundary conditions than is normal for the 'classical' plate analysis [41].

The distributed reaction between the corners has to balance the reverse corner reaction as well as the applied load. However, the shape of the distribution varies substantially with the deflection. For small deflections, the reaction distribution peaks at the centre, but is a little flatter than the half sine wave assumed in TM 5-1300 [24] for glazing reactions, with a peak of 1.72 times the mean reaction for a square panel.

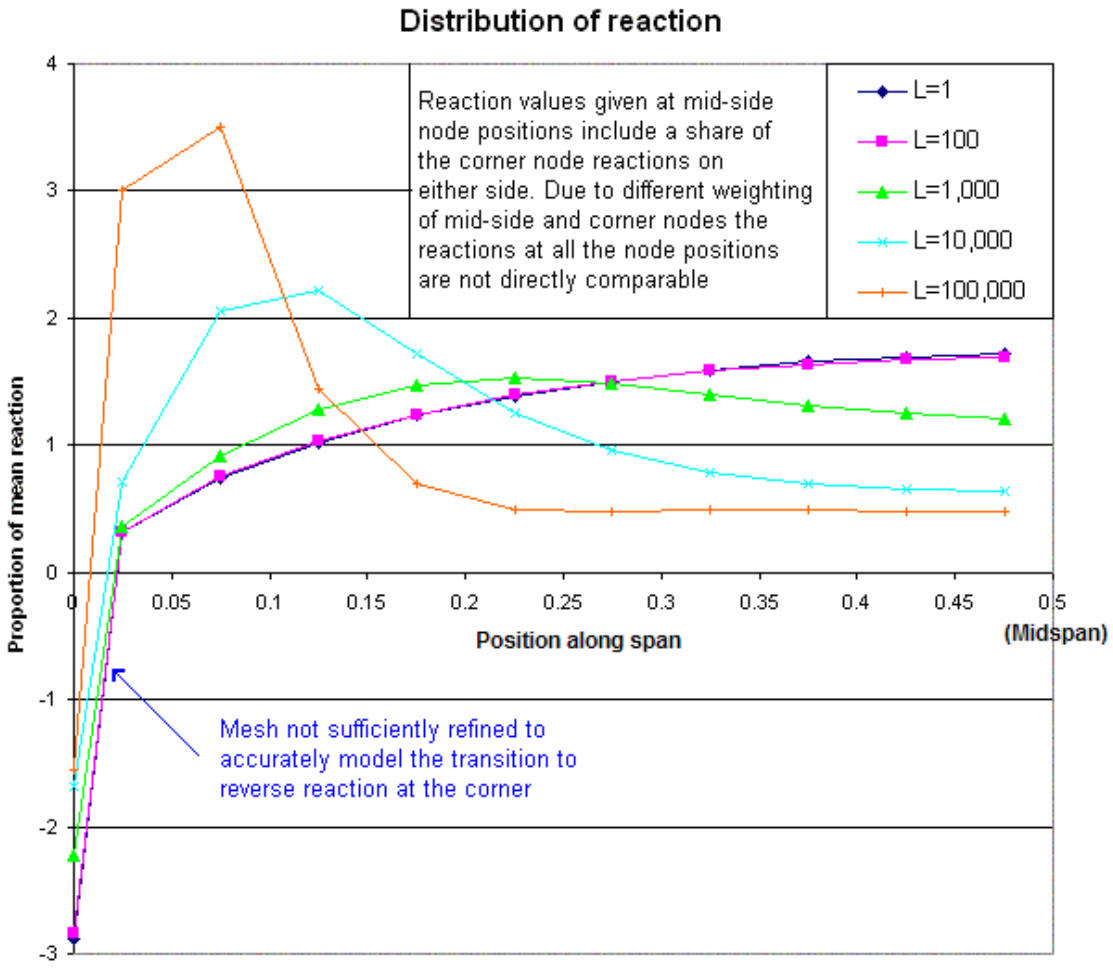

Figure 92. Relative reaction distributions for varying load on a square glass pane

As illustrated by Fig. 92, for λ=1.0 and a non-dimensional load L_{ND}=1000, corresponding to a deflection of just over twice the pane thickness, the maximum reaction has moved from the centre of the span to beyond the quarter point, with a minimum peak value of 1.53 times the mean reaction. For greater deflections the peak reaction becomes higher and closer to the support.

The values of the peak reaction factors in Figs. 93 and 94, i.e. the peak distributed reaction as a proportion of the average reaction, have been derived from the reactions of the refined mesh analyses used to assess the peak stresses, as shown in Fig. 78, because the refined mesh at the corner provides better resolution for the peak resistance at high loads than is shown in Fig. 92.

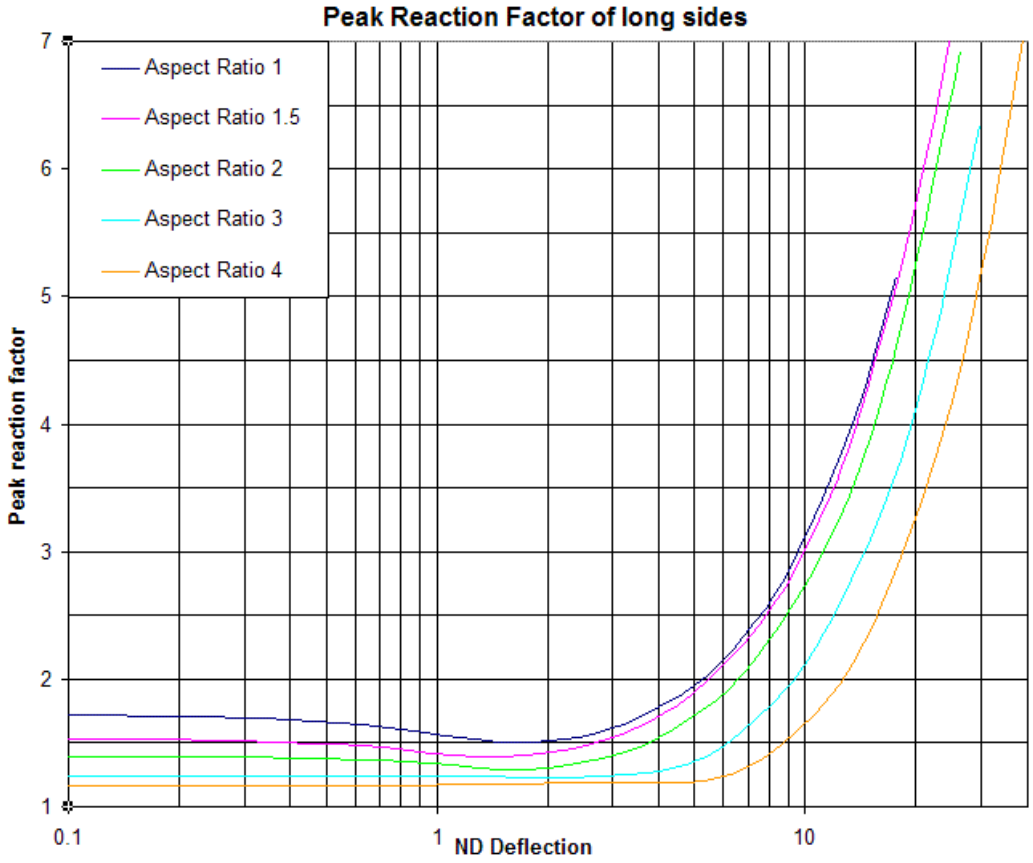

Figure 93. Reaction factors for peak reactions on long edges of glass panes

By plotting the peak factors against the deflections, these can be combined with the SDOF deflection history and the dynamic reaction history to calculate a history of the dynamic peak distributed reactions and identify the maximum inwards and outwards reactions on the glass restraint.

The magnitude of the reverse reaction at each corner as a proportion of the total reaction from the pane has been plotted in Fig. 95.

The distribution of the reactions on the glazing support members is far from uniform, and varies as the glass deflects. The analysis of these is beyond the objectives of this Thesis, but the reaction distributions can be used to provide a more accurate

approximation, e.g. a varying combination of uniform and half sine wave distribution to match the ratio of midspan moment and support shear from the glass reactions.

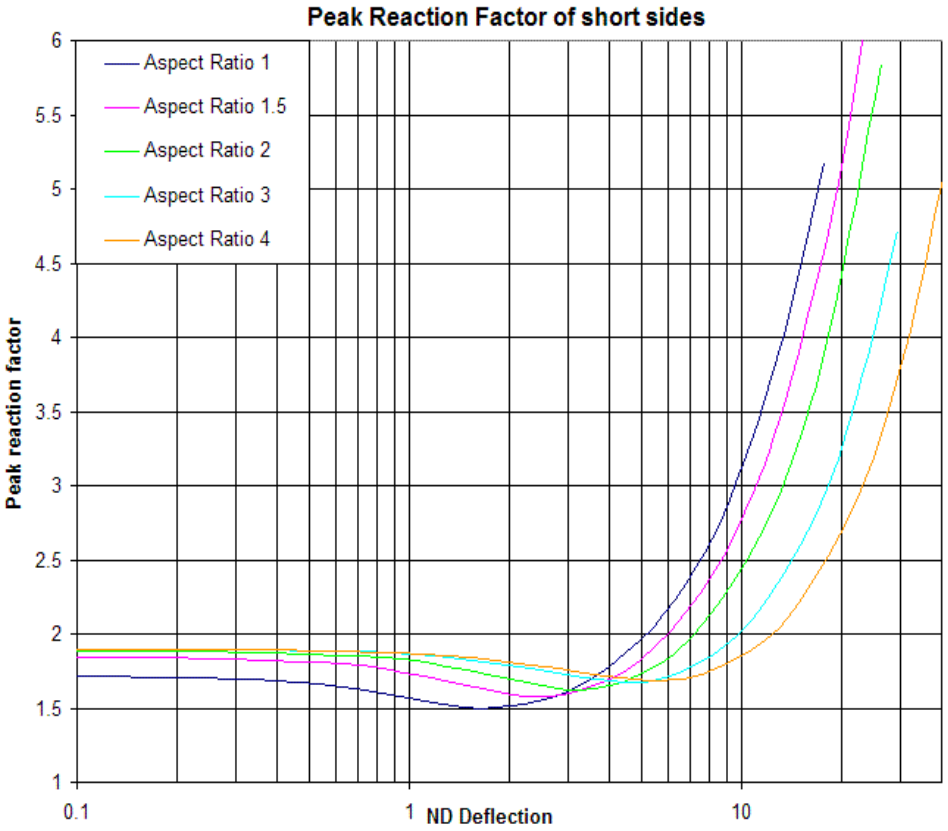

Figure 94. Reaction factors for peak reactions on short edges of glass panes

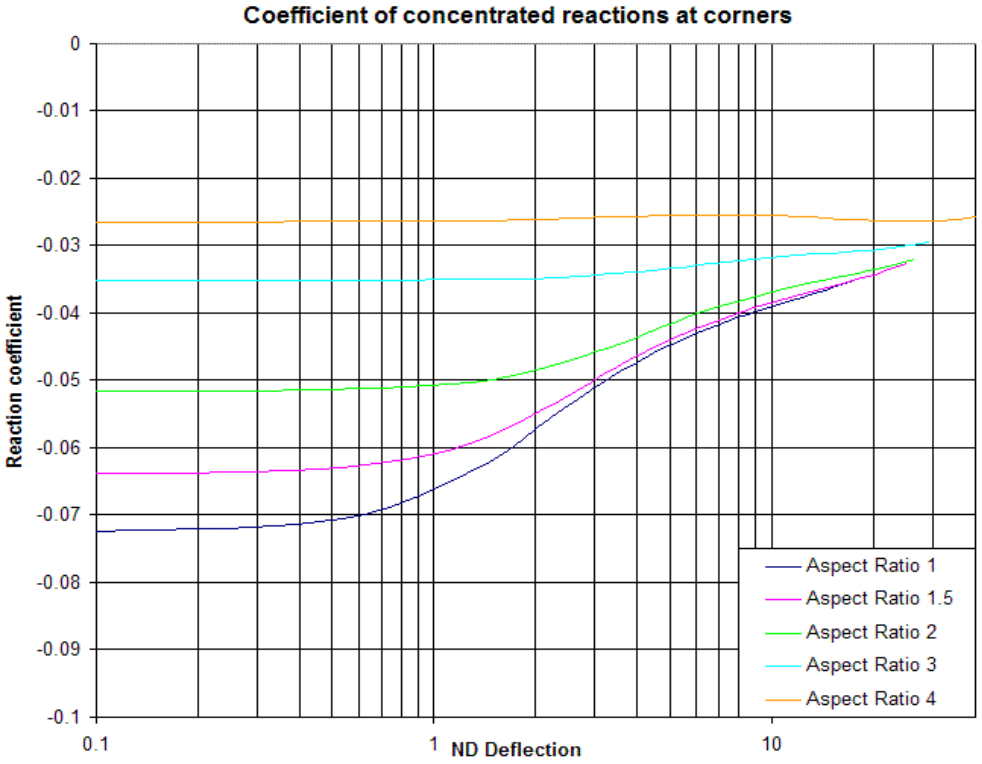

Figure 95. Factors for concentrated reverse reactions at corners of glass panes

6.7 Sensitivity studies

A number of studies have been carried out to assess the sensitivity of the analyses to some of the assumptions, to see how well the idealised model is likely to represent more realistic cases.

6.7.1 Sensitivity to slenderness of the pane

As described above, the main analysis was undertaken on models with a slenderness ratio of 1:280. Although this represents about the practical limit of slenderness for window construction, individual glass plies in laminated glass could be more slender, and most blast resistant glazing will be significantly less slender.

The non-dimensional loading formulae defined by Moore [67] and used here contains a fourth power slenderness term, while the stress contains a second power term and the deflection a single power term. This pattern should give relationships independent of slenderness for pure bending, but not for pure membrane behaviour, so the response of panes of different slenderness could be expected to diverge at high deflections when membrane behaviour is significant.

Analyses were undertaken for aspect ratios λ of 1, 2 and 4 for panes of relative thickness of 0.5, 2 and 5 and compared with the original analyses to study the sensitivity to different slenderness of the glass. The divergence of deflection shown in Fig. 96 and similar downwards divergences of maximum stresses and K_{LM} demonstrate that the non-linear deflection is not independent of slenderness.

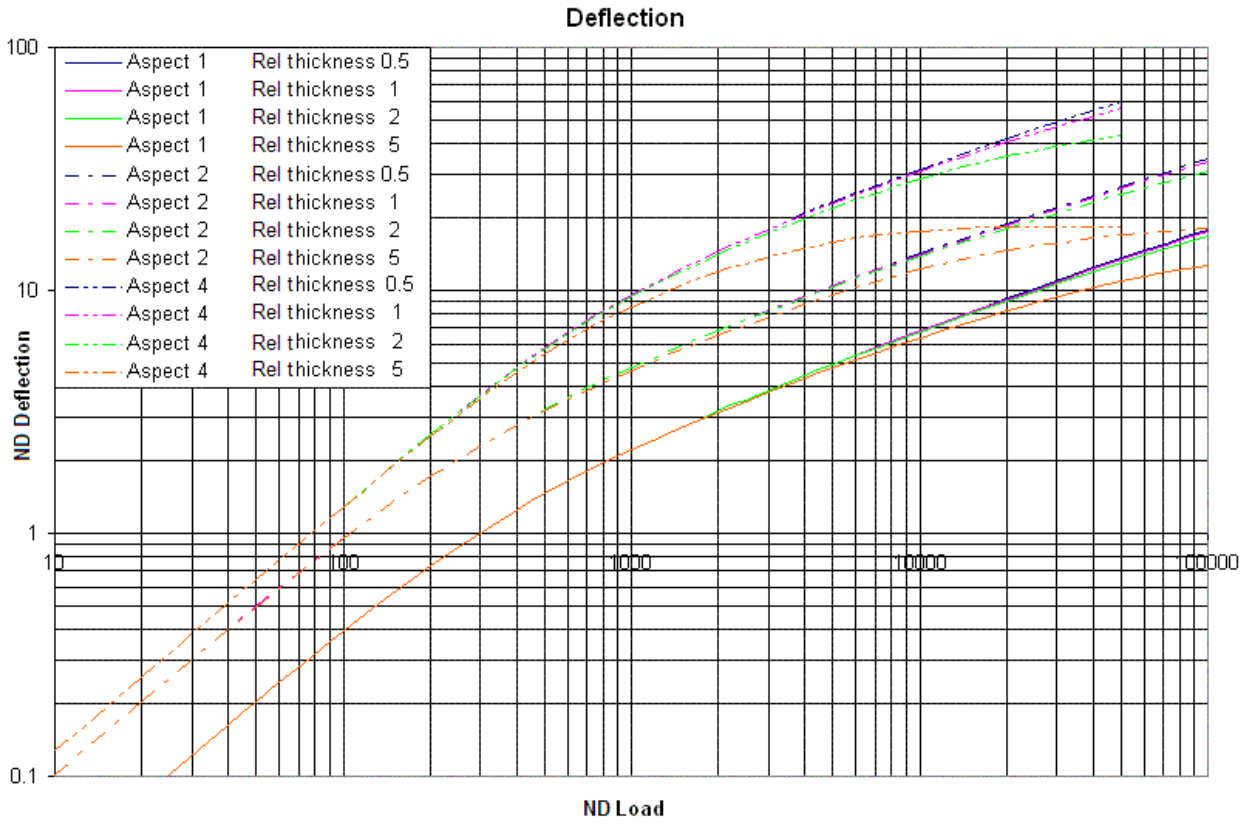

Figure 96. Variation in deflection of glass panes with slenderness

However, the effect of this sensitivity to slenderness will not be very significant for practical applications. The reduction in deflection is not noticeable until non-dimensional deflections of about 4 for five times thickness and about 10 for two times thickness, both corresponding to 20 times unit thickness. Even for toughened (fully tempered) glass strengths, slender windows will rarely reach this level before failing, and the non-dimensional failure stresses will reduce by the square of the reducing slenderness, so the actual failure deflection will decrease with increasing thickness.

Practical problems with glass should be confined to the parts of the original 1:280 slenderness curves where the divergence is not significant, and so the original curve can be used for all analyses of monolithic glass.

Greater error could actually occur in assessing very slender laminated glass plies. However, the breaking deflection of these under blast loading tends to be lower than the breaking deflection of the intact laminated glass, so the error introduced by using the original slenderness curve is unlikely to have any practical significance.

6.7.2 Sensitivity to lack of rigidity in the transverse support

The concept of a simple support is a tool to simplify analysis, but a perfect 'simple support' condition is never achievable in practice. Glazing is mounted in a frame using gaskets or a gap- filling adhesive such as silicone rubber, which is not perfectly rigid. In addition, there is likely to be some 'give' between the mounting for the glass and the connections to the supporting wall, even in a hole-in-the-wall window frame.

The stiffness of the support can vary between a stiff, blast-enhanced frame using substantial areas of structural silicone to support the glass, to a light aluminium frame with finned neoprene gaskets or to UPVC domestic window frames with narrow neoprene gaskets, as illustrated in Fig. 97. Analyses were undertaken for aspect ratios λ of 1, 2 and 4 with different linear spring stiffnesses at the supports to assess the effect that this has on the glazing response and SDOF parameters.

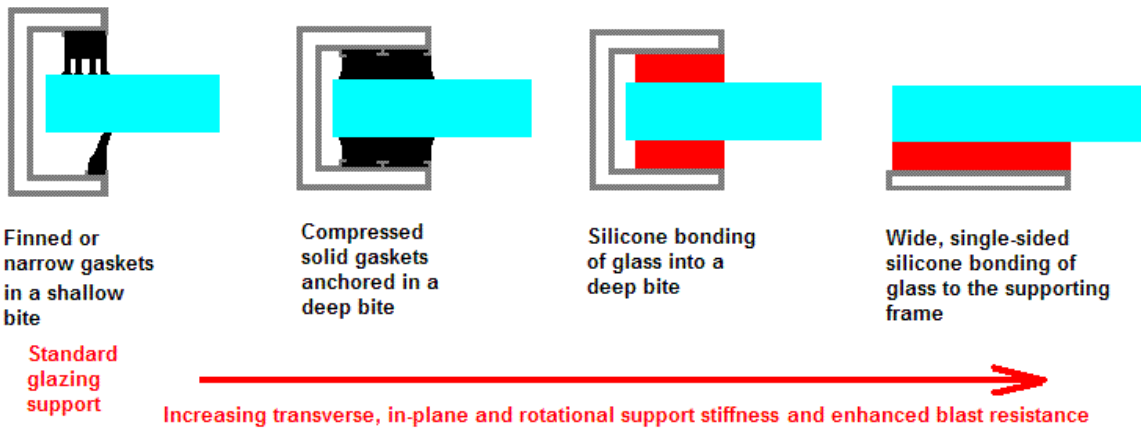

Figure 97. Typical variety of glazing supports

A non-dimensional flexibility parameter for the support was chosen that set unity as the stiffness of support that, for a rigid body, would be equal to the small deflection spring stiffness for the pane. The transverse stiffness of the supports was set to give a proportion of the unit flexibility, e.g. for 1% flexibility a stiffness 100 times that of the pane was modelled as distributed equally around the supported perimeter. Support flexibility values of 0.01% to 1% were considered to cover the likely range between stiff and soft supports.

With the exception of maximum stress, the differences are negligible for all parameters for flexibilities less than 1%. For 1% support flexibility, the deflections increase generally by 1-3% depending on aspect ratio until higher deflections are reached, when greater increases occur, as shown in Fig. 98. The curves for 0.01% support flexibility have been omitted from Fig. 98 for clarity, as they are indistinguishable from the rigid support.

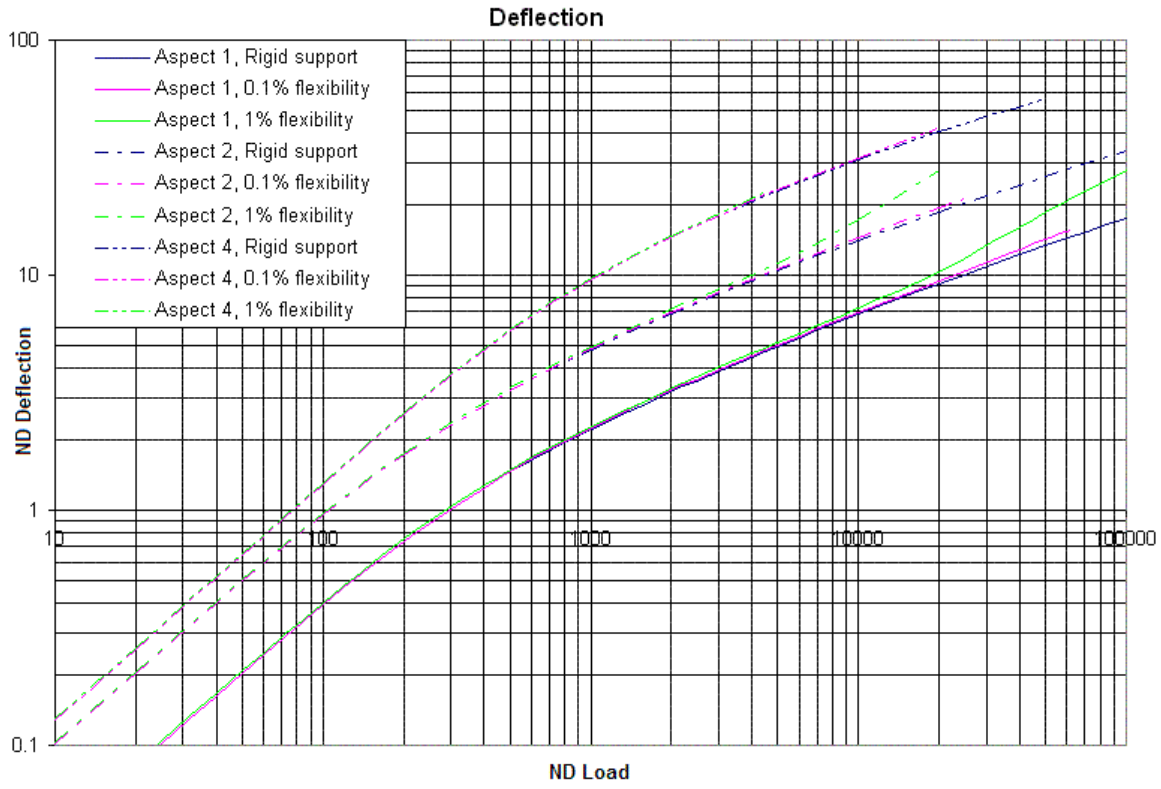

Figure 98. Variation in deflection of glass panes with transverse support flexibility

K_L and K_M are both increased for all deflections and a support flexibility of 1%, such that K_{LM} increases only about 0.2% at small deflection and no more than 0.5% generally when plotted against non-dimensional load. If plotted against non-dimensional deflection, allowance would have to be made for the increase in deflection in Fig. 97. Similarly, changes in the reaction coefficients occur only in the third decimal place if plotted against load.

The effect on the maximum stresses is complex. For all of the cases assessed, the flexibility of the support allows a lifting of the corner and a significant reduction of the torsion stress not only at the corner, but also in the area near the corner where the

maximum membrane stresses are enhanced by a lesser level of torsion. This will have little effect on the bending stress that controls the maximum stress at lower loads, and can reduce the maximum stress at higher loading; however, in the middle, either a lower bending and membrane combination may control, or, in some cases a membrane stress enhanced to compensate for the loss of torsion stiffness may control. Fig. 99 illustrates the effect on the maximum, corner and centre stresses for an aspect ratio λ of 1. Note that the figure is based on the regular mesh analysis that produces an exaggerated torsion stress at the corner, but this highlights the influence of the support flexibility more strongly.

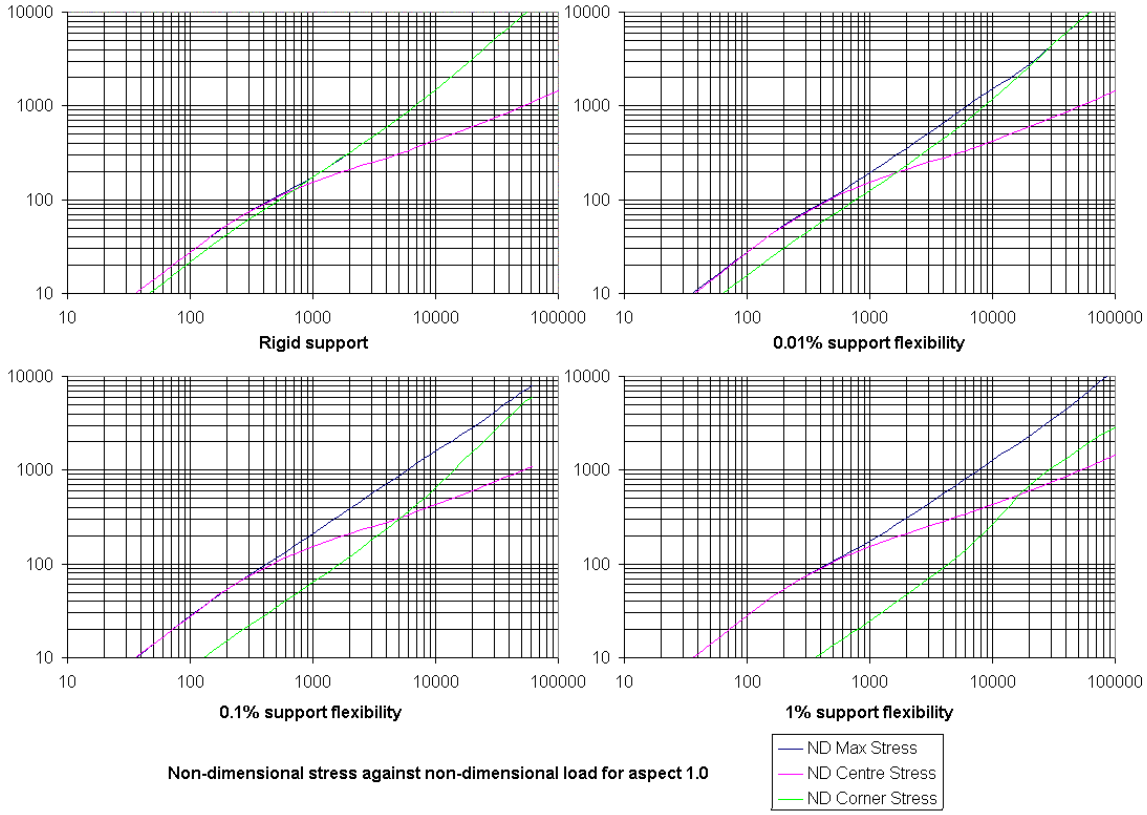

Figure 99. Variation of stresses with support flexibility for a square glass pane

The interaction of the different stresses at different locations leads to complex changes as the support flexibility changes. In the middle zone around L_{ND}=500 to 10,000 there are increases in maximum stress relative to the rigid support up to 20% for stiffer supports, but reductions of about 10% for softer supports. In the higher zone there are reductions up to about 25% for stiffer supports, but less reduction for softer supports except for low aspect ratios, where the reductions can increase to about 40%.

Most windows expected to resist blast will have stiffer supports from at least solid neoprene gaskets, and will be of a slenderness to break in the middle zone. The increased stress means that the deflection at breaking may be lower than expected from Figure 83. Conventional windows with narrow or finned gaskets will have softer support flexibility. Annealed glass is likely to fail in the middle zone, but toughened glass could survive into the higher zone. The reduced stress means that the deflection at breakage may be higher than expected, but the degree of enhancement will vary from case to case.

6.7.3 Sensitivity to in-plane and rotational stiffness in the support

Just as the rigid lateral support of a simple support is not achievable in practice, neither is the complete lack of in-plane and rotational restraint assumed in the idealised support.

The degree of support will depend on the stiffness of the frame and the glass support mechanism.

The non-dimensional unit stiffness per metre width for in-plane restraint has been taken as the plane-stress one way axial stiffness of the glass pane $= E \cdot \frac{h}{b}$ (41)

For an 'enhanced support' of 25mm double-sided silicone 'bite', the high-rate-of-strain stiffness against in-plane forces in the glazing is approximately 1% of the axial stiffness of a 1:280 slender pane, provided the stiffness of the frame is high. However, an enhanced support will normally be supporting laminated glass, and most usually will support a double-glazed unit or single glazing of substantially lower slenderness. For these the glazing stiffness will be significantly more, and the support restraint proportionally less.

For gasketed glazing systems there will be a non-linear in-plane resistance with a 'plastic' stage when the static friction of the gaskets has been overcome. The in-plane resistance of such systems will depend upon the pressure of the gaskets on the glass, but will be substantially lower than for silicone supports.

Analyses were undertaken for aspect ratios λ of 1, 2 and 4 with in-plane stiffnesses from 0.01% to 1% to cover the likely range of support stiffnesses.

The non-dimensional unit stiffness per metre width for rotational restraint has been taken as the rotational stiffness of the one-way span

$$= \frac{24 \cdot E \cdot I}{(1-\nu^2) \cdot b^2} \text{ which for a solid glass pane } = \frac{2 \cdot E \cdot b}{(1-\nu^2)} \cdot \left(\frac{h}{b}\right)^3 \quad (42)$$

Most real rotational restraints are likely to be significantly non-linear over the degree of support rotation compatible with large deflection. Stiffest are likely to be wide single-sided silicone bonding and silicone 'enhanced supports' for blast. Flexing of the frame, cover plates, thermal breaks etc. are likely to contribute significantly to the rotational stiffness value, not just the immediate glass support.

Analyses were undertaken for aspect ratios λ of 1, 2 and 4 with rotational stiffnesses from 0.1% to 10% to cover the likely range of support stiffnesses. A 10% stiffness will result in support moments of the order of 20% of midspan moments. A 0.1% rotational stiffness gives results that are not significantly different from the unrestrained cases, so these have been omitted from Fig. 98 for clarity.

The effect of greater in-plane restraint is to reduce deflections, but the amount is very sensitive to the aspect ratio, as shown in Fig. 100. The maximum stresses undergo

comparable reductions. Plotted against the deflections, the value of K_{LM} diverges downwards only at high deflections for aspect ratios λ of 1 and 2, but for $\lambda = 4$, it diverges upwards from non-dimensional deflections as low as 1.0. The force reaction coefficients experience minor changes at high deflections, but for high aspect ratios and high deflections there is a substantial transfer of resistance reaction from the short span to the long span, with changes of up to 0.04 to the coefficients.

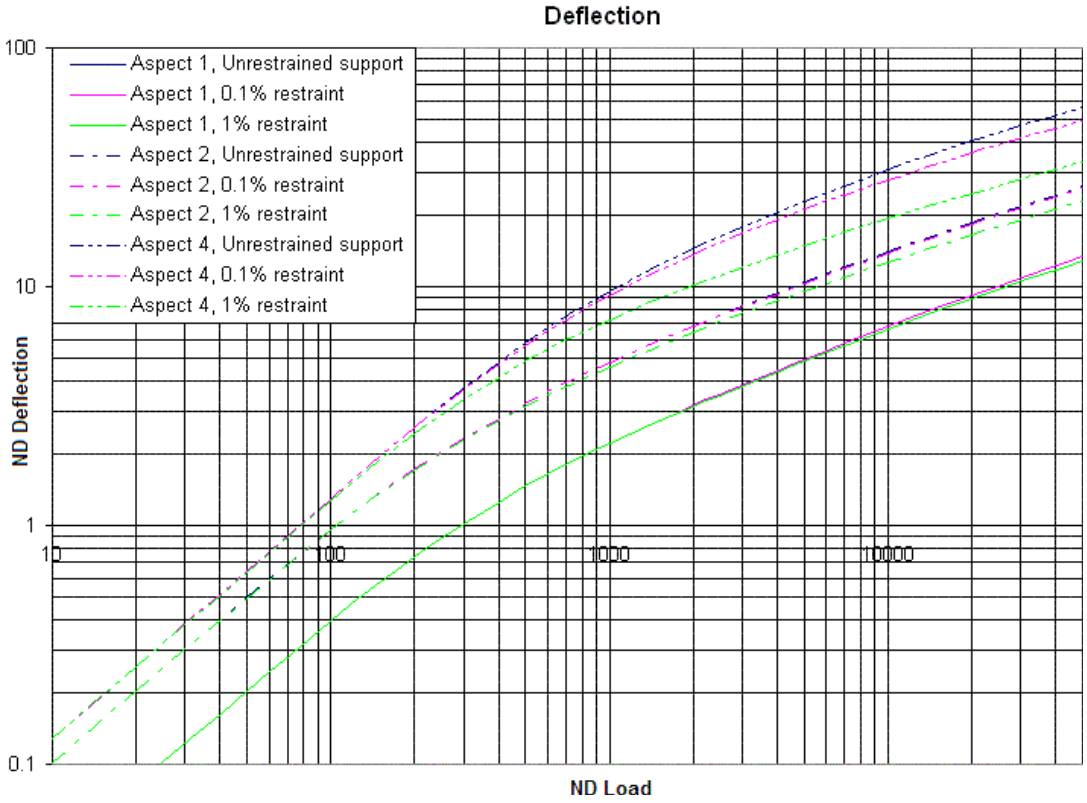

Figure 100. Variation in glass pane deflection with in-plane restraint

The effect of substantial rotational constraint is also to decrease deflection significantly, particularly at high aspect ratios, but the effect is very different as the decrease is greatest at low loading, and reduces as loading increases, as shown in Fig. 101.

Stresses show a similar pattern of reduction at low load levels. K_{LM} values show a near uniform reduction of the order 0.01, except for small deflections at $\lambda = 4$, which shows a comparable increase, with a change-over point at a non-dimensional deflection of 2.0. The reaction coefficients undergo somewhat smaller changes, with the greatest at low deflections and low aspect ratio, as the pane becomes partially fixed in bending.

In practice, high in-plane restraint and high rotational restraint are often combined in the same mounts, using silicone adhesive and either a deep rebate for an “enhanced support” for blast resistance, or a wide single-sided joint for architectural reasons. However, the unit stiffnesses are both sensitive to slenderness, and restraint levels will reduce as the glass thicknesses increase. The likelihood of a very slender glass pane very strongly mounted is low in practice, but if it occurred, there would be a significant shift of many of the design parameters. A typical change in deflections for

such cases is shown in Fig. 102, assuming 1% in-plane and 10 % rotational constraint.

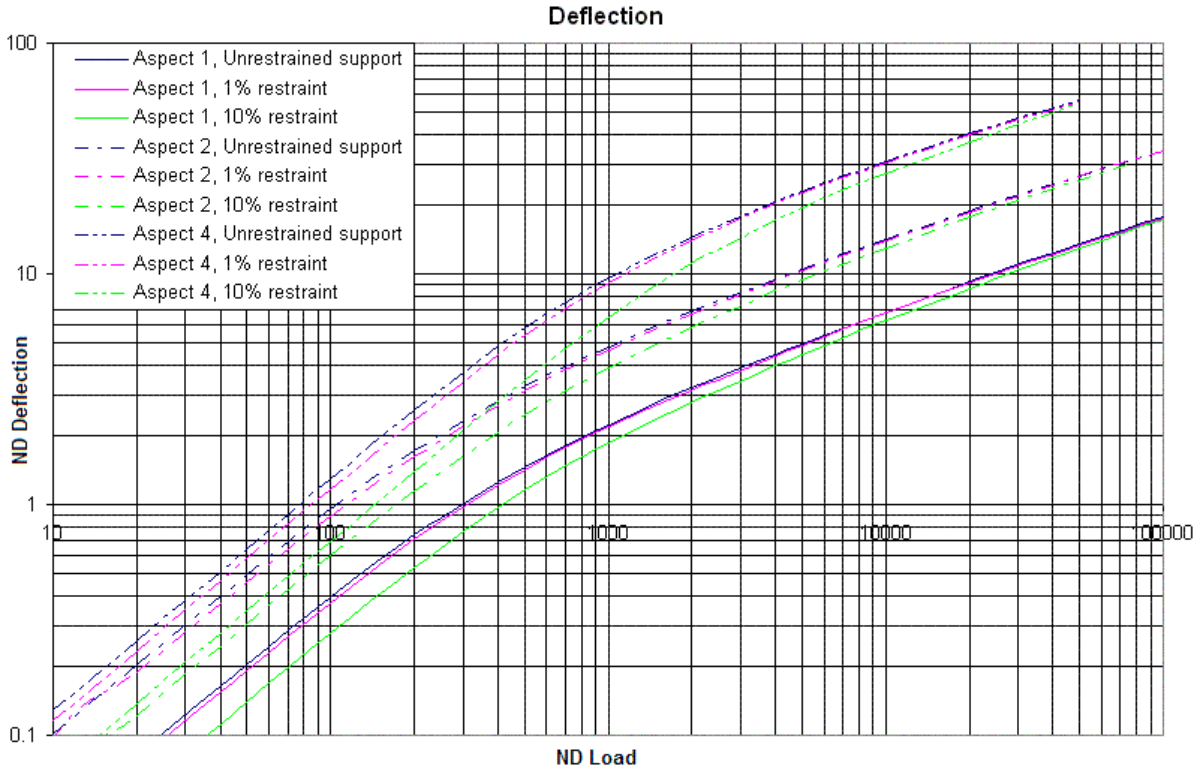

Figure 101. Variation in glass pane deflection with rotational restraint

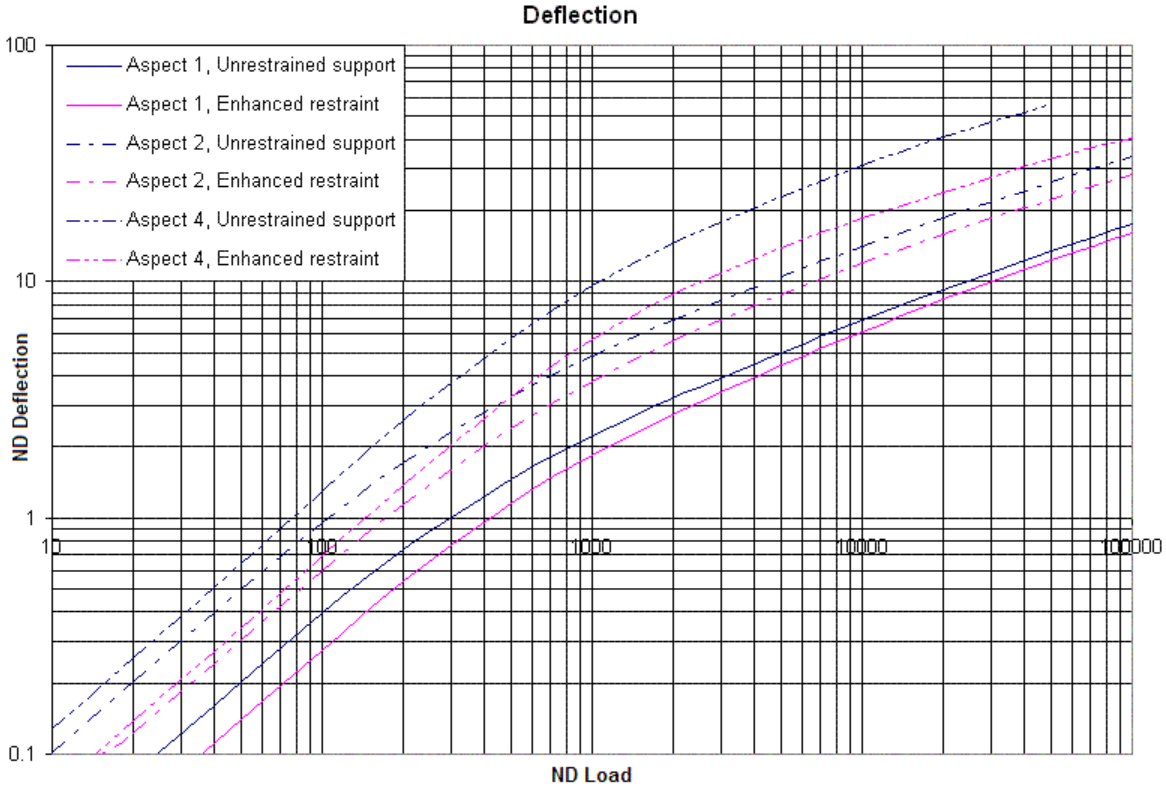

Figure 102. Variation in deflections for 1:280 slenderness glass panes in enhanced supports

The stresses also reduce, so that cracking deflections plotted against stresses are within 10% of Fig. 88, higher for the upper part of the curves for all aspect ratios, and lower for the lower part of the curve for an aspect ratio of 1, with no significant change for larger aspect ratios.

The change to K_{LM} is fairly uniform with deflection, but varies with aspect ratio, from a reduction of 0.013 for $\lambda = 1$ and of 0.008 for $\lambda = 2$ to an initial increase of 0.012 for an aspect ratio of 4, becoming 0.003 for deflections between 4 and 10 times thickness, and then 0.007 for large deflections.

Changes to reaction coefficients depend on deflection and aspect ratio. One general trend is a reduction in force coefficients at low deflections, reversing for high deflections, generally around 2 times the thickness. There is an increase in the long side reaction coefficients for aspect ratios of 2 and 4, but neutral to reduction for aspect ratios of 1. There are substantial reductions to the short side reaction coefficients for aspect ratios of 2 and 4 at large deflections, but smaller changes for aspect ratios of 1.

For a slender pane in a highly restraining frame, the dynamic response and reaction history are likely to be significantly changed, and an alternative analysis may be desirable. However for most double glazing and blast designed glazing in blast-enhanced frames the restraints will be substantially less significant, and a design based on a simply-supported analysis will still be a reasonable approximation.

6.8 Comparison of SDOF and dynamic transient analysis

A number of SDOF analyses of a simply-supported pane have been undertaken in Mathcad, and compared with a non-linear transient dynamic FE analysis undertaken on LUSAS.

The example used has been chosen as convenient for analysis rather than representative of any real case. For comparable analyses, the following parameters have been used throughout the exercise:

Glass properties

Young's modulus E	70 GPa
Poisson's Ratio ν	0.22
Cracking Stress	Ignored – assumed for the analysis not to crack.
Density ρ	2490 kg/m^3

Pane configuration

Pane thickness h	12 mm
Short span b	1.679 m
Long span a	3.358 m
Aspect ratio λ	2.0
Slenderness	~1:140
Support conditions	Simply-supported

Transient reflected load definition

Peak pressure p_r	30 kPa
Impulse I_r	300 kPa.ms
Triangular load duration t_r	20 ms

Damping has been taken as aeroelastic for atmospheric pressure on both sides. (The enhanced damping on the loaded face during loading has been ignored to simplify the transient FE analysis).

The cases analysed were:

- Non-linear transient FE analysis, using the regular mesh model, 'Incremental Lagrangian' non-linear control, an implicit Newmark time integration scheme and a transient pressure loading defined as a variation curve with time. Newmark integration gives unconditionally stable time integration without numerical dissipation of higher modes of vibration.

- SDOF using linear resistance and transformation factors and reaction parameters from the table for a simply-supported slab from Biggs [35]

- SDOF using non-linear resistance after Moore [67] and factors and parameters from Biggs

- SDOF using non-linear resistance from Fig. 78 and small deflection parameters from linear analysis with a Poisson's ratio of 0.22 (Tables 24 and 30)

- SDOF using non-linear resistance from Fig. 78 and non-linear parameters from Ref. 121 for unit thickness based on a slenderness of 1:280, calculated from the total deflections.

- SDOF using non-linear resistance from Fig. 78 and non-linear parameters based on incremental deflection from Figs. 85, 86, 90 and 91, for unit thickness based on a slenderness of 1:280.

- SDOF using non-linear resistance for a relative thickness of 2 from Fig. 96 and corresponding non-linear parameters based on incremental deflection for a slenderness of 1:140.

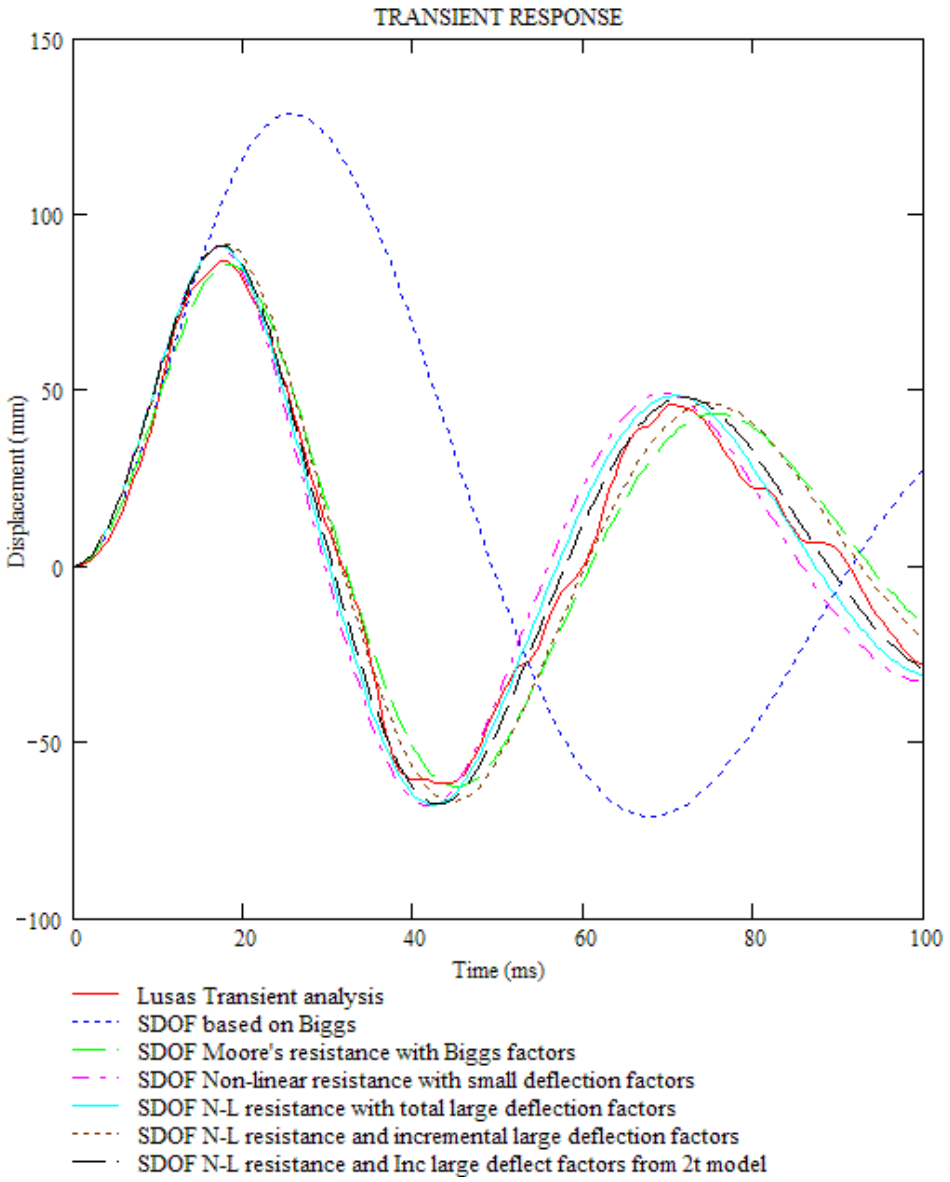

Figure 103. Midspan deflection history of the pane in cases analysed

In the response of this example using the linear analysis in Biggs, it can be seen in Fig. 103 that the linear stiffness calculated from small deflection theory gives predictions of amplitude of the response for large deflections that are significantly at variance with the assumptions, being of the order 10 times thickness, and which are substantially greater than the response based on all the alternative assumptions. Also, the timing of the peak response is approaching 40% greater (26 ms compared to 18 ms) than the other analyses.

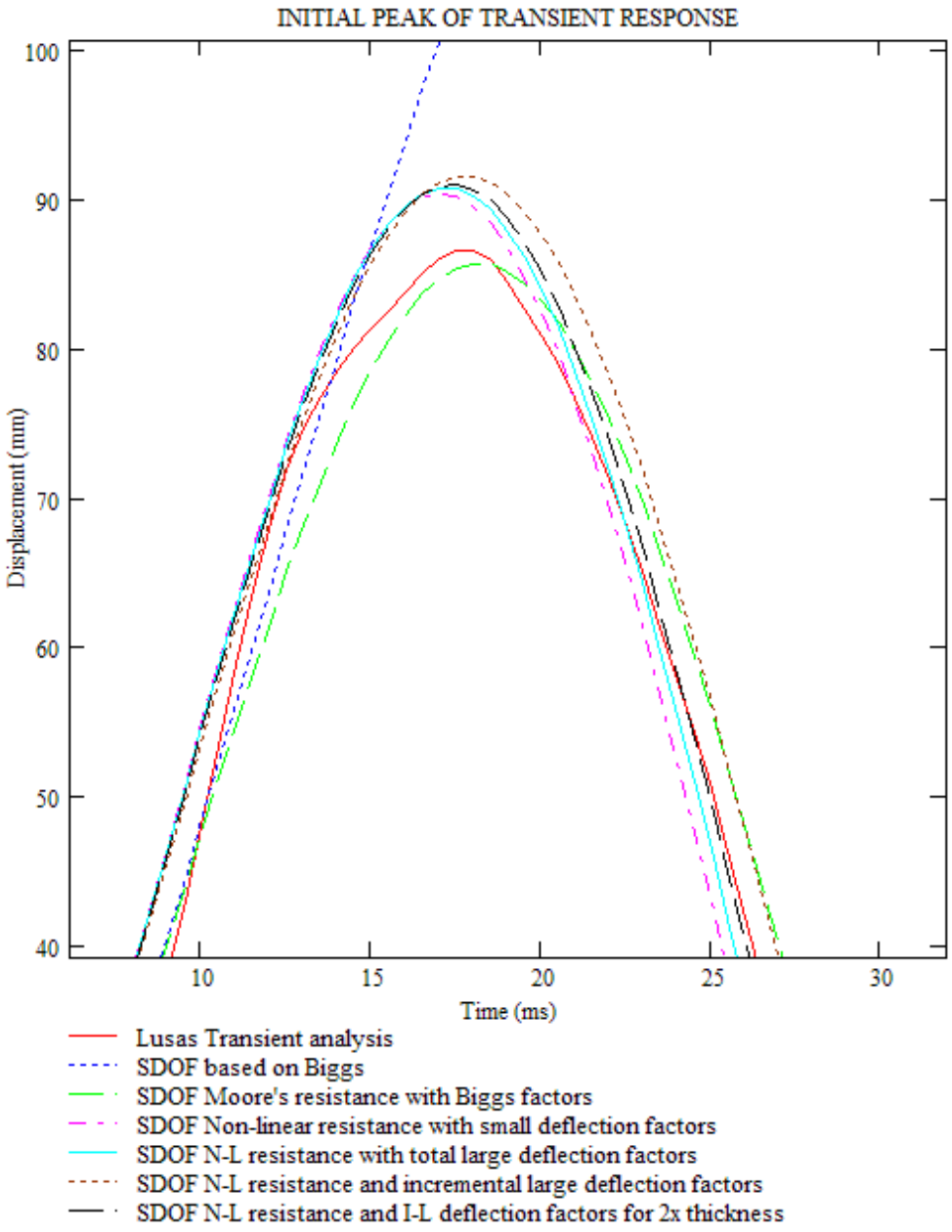

Figure 104. Detail of first peak of response from Fig. 103.

With Moore's non-linear resistance, the fit is much closer for the initial pulse, as can be seen in Fig. 104, but over several cycles it can be seen in Fig. 103 that the response

time is a bit longer than for the transient analysis, an indication that the effective mass is too high, and/or the non-linear stiffness is too low. For maximum deflections of the order 7 times thickness, most of the cumulative delay will come from a K_{LM} that is too high.

Using the slightly different non-linear resistance curve from Fig. 78 and the small deflection K_{LM} from Table 24, the timing of the initial pulse is improved, although the amplitude is a little high. Over several cycles the SDOF results tend to lead the transient FE results, indicating that the K_{LM} is a little low.

The three analyses with non-linear resistance and large deflection factors give very similar peak initial responses to the small deflection factors and transient responses between the Biggs and small deflection cases, as shown in more detail in Fig. 104.

The SDOF analysis with the best overall timing fit with the finite element analysis is the incremental large deflection case based on a thickness twice the standard analysis, as this most closely resembles the finite element model.

The standard thickness has a longer response, with a response closer to that from the analysis using Moore's resistance and Biggs transformation factors. The difference due to halving the thickness is less than half a percent difference in the stiffness and in K_{LM} at peak deflection, but these differences reinforce each other.

Using the total deflection to calculate K_{LM} gives a larger error in the average transformation factor, but the sign of the error is reversed, so that the error from the stiffness partially cancels that from K_{LM}, leaving a response only marginally faster than the finite element analysis.

Apart from the very early reactions, there is little difference between the amplitudes of the long side reactions from the various large deflection analyses, as shown in Fig. 105. The timing varies with the response, as described above, and the variations in the reactions due to the higher modes of vibration cannot be modelled by a SDOF analysis.

The difference between the different large deflection analyses becomes apparent when considering the reaction on the short side, as shown in Fig. 106. Small deflection coefficients fail to model the critical peak at all, while the total large deflection coefficients give an exaggerated reaction for the fundamental mode that is nearly equal to the finite element reaction peak from all the modes. The analyses with incremental coefficients give reaction histories that are identical except for the small difference in timing mentioned above, and which give a reasonable initial response.

The reaction histories highlight the 'ringing' of higher frequency responses in the transient FE analysis. One of the fundamental assumptions in the SDOF approach is that the higher frequency response of the real glass panes is sufficiently low as to be negligible, as by its very nature the SDOF analysis can only consider the fundamental mode of response. It is expected that in a real window the higher frequency effects would be substantially reduced by hysteresis (structural) damping, particularly in the glass supports, but no damping of this type has been included in this transient FE analysis.

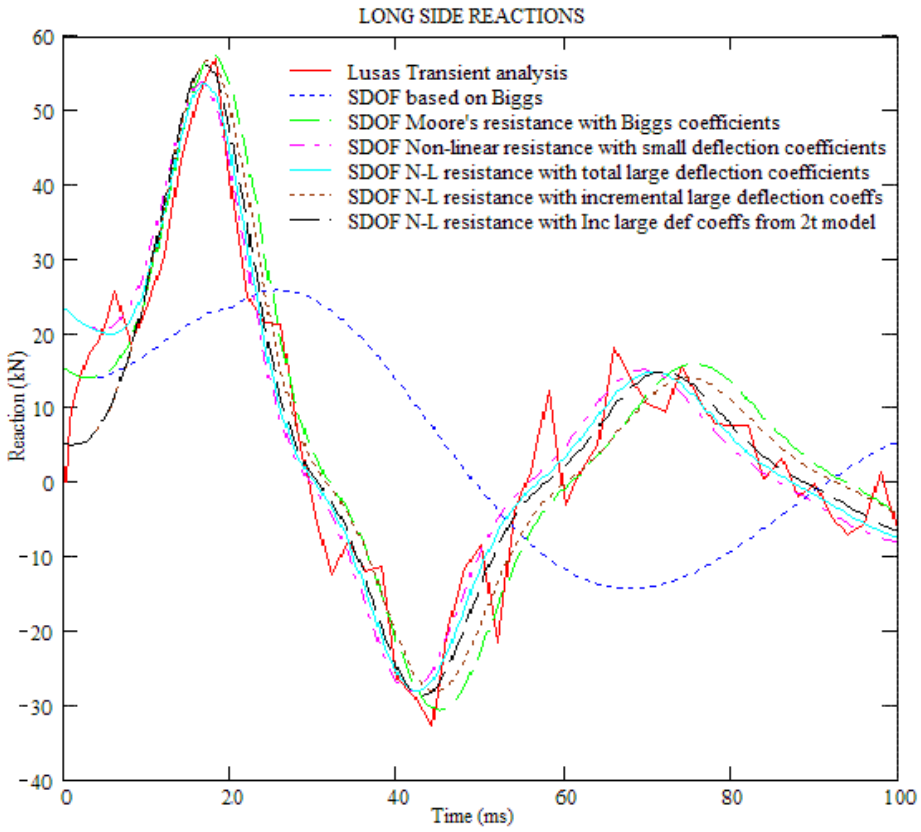

Figure 105. Reaction history on the long side of the pane in the cases analysed

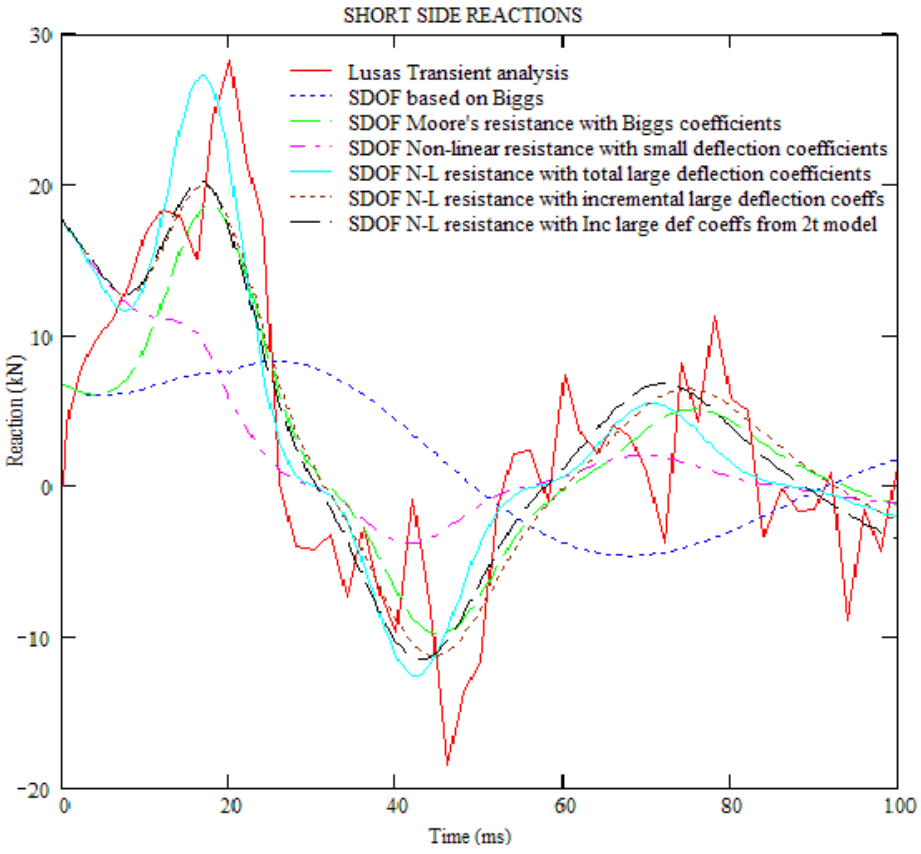

Figure 106. Reaction history on the short side of the pane in the cases analysed

6.9 Summary of SDOF analysis for thin glass plates

The small-deflection formulae for elastic deformation have only been considered an accurate model for two-way spanning plates for deflections up to about half the plate thickness. For deflections greater than this, the membrane stresses start to become significant and modify the deflection stiffness and the deflected shape, and a large-deflection analysis, such as undertaken in this chapter, will be required to model the behaviour of the plate.

The large-deflection analysis presented here has shown that, for a dynamic analysis, the variation in the deflected shape will begin to affect the response even at smaller deflections than previously thought. The SDOF transformation factors, based on the incremental deflected shape, show variation from the small deflection solution at deflections as low as one tenth of the plate thickness, and may have changed by up to 10% when the deflection reaches half the thickness.

The SDOF parameter that is most non-linear at large deflections is the resistance, which is based on the loading for a given deflection, and can be derived from the calculation of the central deflection for a given pressure. At deflections of the order ten times the thickness the resistance is many times the linear small-deflection resistance. Analytical methods indicated that the additional resistance was a cubic function of the deflection, but evaluation of the value of the cubic parameter was unreliable for unrestrained, simply-supported panes. A value for square panes were derived from testing [64], but it was only with the introduction of non-linear numerical analysis [67, 68] that reliable solutions became available over a range of aspect ratios. The comparative analyses in Section 6.8 show that any method of assessment of glazing response based on small-deflection resistance will be substantially in error.

The elastic small-deflection analysis in Chapter 5 showed that the K_{LM} transformation factor from Ref. 16 was too high for small deflections. The large-deflection analysis shows that for aspect ratios up to at least 2.0 the value increases by up to around 25% at large deflections. As the deflection history calculation integrates the transformation factor over the response time and the Ref. 16 value is not far from an average value over typical ranges, the use of the historic small-deflection transformation factor may result in smaller errors for large-deflection analysis of glass, as shown by the analysis in Section 6.8, than for small-deflection analysis of reinforced concrete. However, this is fortuitous rather than deliberate, and it would not apply for panes with higher aspect ratios, for which the K_{LM} transformation factor initially reduces with deflection.

It is in the calculation of reaction histories, and particularly of reaction on the short supports, where the use of the large-deflection deflected shapes and large-deflection reaction distributions to calculate the dynamic reaction coefficients shows substantial improvements in accuracy. Even this does not overcome two limitations of the equivalent SDOF method in calculating reaction histories, the false initial reactions that arise from the assumption of the static deflected shape from the start, and the inability to allow for the effect of higher modes of vibration on reactions.

An important feature identified in the large-deflection analysis is the variation in the location and value of the peak reaction as the deflection increases. This provides a basis for calculating the local forces in the glazing supports that was previously not available.

The charts produced in Sections 6.3 to 6.5 are based on the analysis of a slender pane, with a slenderness ratio of about 1:280. The sensitivity studies in Section 6.7.1 show that the non-dimensional response will vary with slenderness ratio at high non-dimensional loading, although it is indistinguishable at lower loading. In practice, this allows the charts based on the slender pane to be used to analyse all panes. When the panes are less slender, the cracking strength of the glass will be reached at lower non-dimensional stress, and hence at lower non-dimensional load where the response is indistinguishable. Significant error could, in theory, arise from using these charts to analyse the very slender glass plies in laminated glass up to final crack. However, the non-linear behaviour and high cracking strength under dynamic loading means that these plies normally would crack at smaller deflections than the deflection at first crack of the composite section of the laminated glass. As a result, these plies will crack immediately the first crack in the laminated glass occurs. The accuracy of the analysis of the final ply ceases to be relevant, because its immediate failure means that it does not contribute to the calculation of the response.

The sensitivity to the transverse support stiffness assessed in section 6.7.2 is more related to local support distortion, particularly near the corners, rather than the flexing of a supporting frame, which can be analysed as an additional degree-of-freedom. This support distortion can arise from the compressibility of gaskets or Silicone adhesive, and from the flexibility of the frame components forming the ‘bite’ around the glazing. The major effect with increasing support flexibility is to allow increasing lifting of the corner locally. This slightly increases the midspan deflections, but greatly reduces the torsion stresses at or close to the corners, and modifies the peak stresses once they move to a location close to the corner. With a very slender pane this might allow the glass to deflect further before it cracks compared to the standard analysis, making the standard analysis more conservative, and increasing the confidence level of the design cracking strength. However, the support flexibility has been expressed in terms of the flexibility of the glass. As a slender pane is more flexible, so the support must be softer to achieve the same degree of flexibility for a more slender pane. In practice, blast resistant supports are normally fairly firm, so the practical effects of variations in transverse support stiffness are not expected to be significant.

The sensitivity to in-plane and rotational support stiffness is less clear. The restraint of enhanced supports on thick glazing to resist substantial blast loading will not be very significant, but if for architectural reasons an enhanced support is provided for light glazing, the resistance will be greater than calculated from the charts. Using the standard charts for design of this case would be conservative.

Analysis using the SDOF charts derived from this analysis will be generally representative of the actual behaviour in most practical circumstances, and the resistance will generally be conservative in extreme circumstances where deviation may be significant. A conservative resistance can result in conservative deflections

but unconservative reactions, so design safety factors to allow for uncertainty and inaccuracy in analysis should generally be applied to reactions, not deflections.

7 Laminated glass up to cracking

7.1 Previous testing and analysis

7.1.1 Low strain-rate testing

Low strain-rate testing of a two-way laminated glass plate in which deflection and stress histories were recorded was reported by Vallabhan et al. [127]. With the exception of that by Behr et al. [76], which was also described in Ref. 127, most similar testing had previously been undertaken using one-way spanning beams rather than two-way spanning plates.

The testing in Ref. 76 was for a slender laminated panel 1.52 m by 2.44 m with an overall thickness of 7.1mm. This was found to behave non-linearly from a small loading level, but the maximum deflection was found to be consistent with that of a monolithic glass panel of thickness equal to the two glass plies, i.e. 6.35 mm.

In the new tests in Ref. 127, a laminated pane 1.52 m square and 11.05mm thick, comprising two glass plies 4.763mm thick bonded to a Monsanto (now Solutia) PVB interlayer 1.52mm thick, was mounted in a support frame with Teflon fasteners to give continuous simple support 12-13mm from the edge without in-plane edge restraint. Quasi-static pressure was applied to the sample rising from 0.69 kPa to 6.9 kPa (0.1psi to 1.0 psi) over a 60 second period. A series of tests were run in the temperature range 70ºF to 80ºF (21ºC to 27ºC), although the tests are not reported individually. In addition to the pressure sensor and the displacement sensor at the centre, the pane was fitted with strain gauge rosettes at various locations on both faces. The strain gauges were used to calculate principal stresses.

Previous tests referred to in Ref. 127 indicated that the shear modulus of this PVB varied between 100 psi (0.69 MPa) at low strains and 600 psi (4.14 MPa) at a shear strain of 3.0. These tests are incorrectly cited in Ref. 127, so further details have not been obtainable. Ref. 127 indicated that the deflection and stress curves for the two-way span are reasonably consistent with an analysis using a PVB shear modulus of 0.69 MPa. The maximum deflections were of the order 22mm, twice the overall thickness.

The testing in Ref. 127 has been used to help evaluate a number of analysis methods.

7.1.2 Linear viscoelastic analysis of PVB

Ferry [87] describes the way in which viscoelastic polymers deform. The material is formed of long, tangled polymer chains. There is a hierarchy of distortion mechanisms:

- Distortion of bonds in the polymer chain
- Straightening of loops and curves of the chain

- Sliding of polymer chains against each other, changing their configuration.
- Breaking and re-forming secondary polymer bonds

For any particular polymer, there is a glassy transition temperature below which there is almost no configurational or bond change for small strains. The remaining mechanisms give an effectively elastic behaviour, like glass at room temperature. Above the glassy transition temperature, the behaviour varies between glass-like and rubber-like with temperature and strain rate.

Linear viscoelasticity can be represented by a Generalised Maxwell model of parallel units with elastic springs and viscous dampers in series, as shown in Fig. 107. The long term stiffness of a viscoelastic solid is included as an undamped spring.

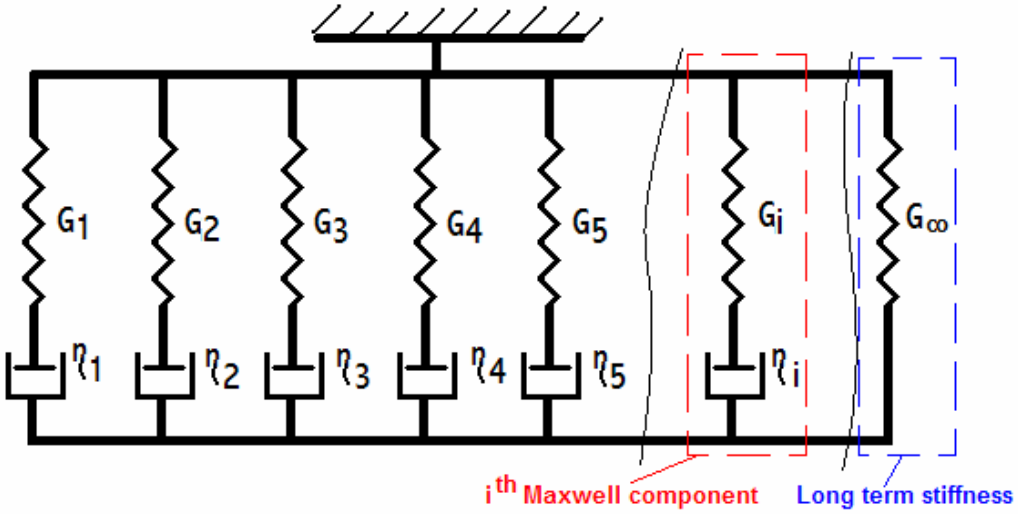

Figure 107. Schematic of the Generalised Maxwell viscoelastic model

For each elastic-viscous pair forming a Maxwell component, the relaxation modulus is given by:

$$G(t)_i = G_i \cdot e^{-t/\tau_i} \tag{43}$$

where the time constant $\tau_i = \eta_i / G_i$ as illustrated in Fig.107.

The relaxation modulus for the material is given by:

$$G(t) = \sigma(t)/\nu = \sum_i G_i \cdot e^{-t/\tau_i} + G_\infty \tag{44}$$

The shear moduli and associated time constants for the different Maxwell components can be derived by measuring the amplitude and phase difference in shear vibration tests over a wide range of frequencies. Different methods, such as broadband viscoelastic spectroscopy and resonant ultrasound spectroscopy, will be required to cover the full range of frequencies. Because the strain amplitudes measured become smaller at higher frequencies in these tests, these measurements give properties at small strains and small strain rates only.

Ferry [87] has proposed that the effect of temperature can be taken to modify the time constants uniformly throughout the Generalised Maxwell series by a time shift function $a_T = t/\tau$, where the reduced time τ at temperature T is related to the time t at reference temperature T_0 by:

$$\log_{10} a_T = \frac{J_1 \cdot (T - T_0)}{J_2 + T - T_0} \tag{45}$$

where J_1 and J_2 are material constants. By performing the shear vibration tests at a range of temperatures, the sensitivity of the Generalised Maxwell viscoelastic model to temperature can be established and the constants calculated.

Linear viscoelasticity strictly applies for infinitesimal strain and strain rate. Real viscoelasticity will vary as these values become finite, but can usually be approximated by linear viscoelasticity over a limited range. The range of accurate application of the test data will be dependent on the strains and strain rates generated in the vibration tests.

Viscoelastic deformation is based on the principle that the effect of sequential strains is additive, so that in pure shear the stress σ_{21} at time t can be written as:

$$\sigma_{21} = \int_{-\infty}^{t} G(t - t') \cdot \dot{\gamma}_{21}(t') dt' \tag{46}$$

where $\dot{\gamma}_{21}$ is the shear strain rate.

A simpler viscoelastic model, with one spring in parallel and one spring in series with the dashpot, is called the Standard Linear Solid Model, as shown in Fig. 108. It is equivalent to the Generalised Maxwell model with a single Maxwell component. With only a single time constant, this implies that the relaxation occurs over a fixed time period. This is more commonly implemented in commercial non-linear finite element programs because it requires less data, but it is less versatile. It is easier to fit to specific data from a test, but will be less accurate when circumstances diverge from the test.

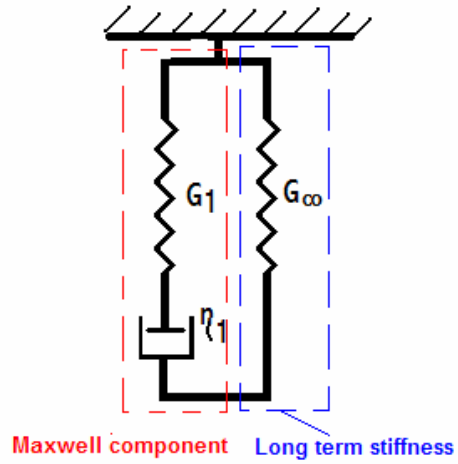

Figure 108. Schematic of the Standard Linear Solid Model

7.1.3 Low strain-rate analysis

The analysis in Ref 127 uses a finite difference solution of a layered plate to calculate deflections and surface stresses using various constant shear modulus values. These were compared to the data from the trials to show that the results were generally consistent with a shear modulus of 0.69 MPa.

The assessment of this analysis, and of similar analyses up to that time, was flawed by the theory that postulated that the composite section varied between two bounding cases: a stiff case equivalent to monolithic glass of a thickness equal to the two glass plies, and a soft case equivalent to two layered plies flexing independently. This was only refuted in 1998 by Norville, King & Swafford [84], who proposed a beam model that took account of the PVB interlayer as a layer of finite thickness. The bounding stiff case could have a stiffness equivalent to monolithic glass equal to the total thickness of the composite section, which can be significantly affected by the thickness of the PVB interlayer.

Ref. 84 and Fig. 36 showed that laminated glass beams transferred forces q through the interlayer equal to proportions of the force in the plies when the stress distribution is triangular and the inner surface would be unstressed. For long duration loading (>60 sec), laminated glass with the interlayer forming 12% of their thickness, where q = 112% would represent full composite action and 0% would represent fully layered action, were shown in tests to transfer the following forces, implying the degrees of composite action:

- 107% at 0ºC (32ºF) – 96% composite
- 84% at 23ºC (74ºF) – 75% composite
- 31% at 49ºC (120ºF) – 28% composite

Ref. 84 reported that in some cases for short duration loading at temperatures up to 49ºC (120ºF) test results corresponded to values above 100% transfer force, i.e. above 89% composite action.

Van Duser, Jagota and Bennisson [86] pointed out that the model in Ref. 84 was for beams in which there were only bending forces, and that slender two-way spanning panels were subjected to a combination of bending and axial membrane forces. Results for the bounding cases can be scaled.

Thus, for the small deflection, linear bending regime, the monolithic limit gives maximum stress σ_{max} and deflections at the centre δ as:

$$\sigma_{\max} \propto \frac{pL^2}{h_t^{\,2}} \qquad\qquad z_{\max} \propto \frac{pL^4}{Eh_t^{\,3}} \tag{47}$$

while for the layered limit the same equations apply, but the load on each ply is half that of the monolithic plate. However, the thickness is less than half, so the stress more than doubles, while the deflection more than quadruples.

For the large deflection non-linear limit of purely membrane behaviour, there is no shear stress in the interlayer and the monolithic and layered limits are identical, so that:

$$\sigma_{\max} \propto \left(\frac{Ep^2 L^2}{h_g{}^2} \right)^{\frac{1}{3}} \qquad z_{\max} \propto L \left(\frac{pL}{Eh_g} \right)^{\frac{1}{3}} \tag{48}$$

where h_t is the total thickness of the section, and h_g is the total thickness of glass, either excluding the interlayer, or adding it in by modular ratio.

Ref. 86 also applies the Generalised Maxwell series viscoelastic properties derived in Ref. 88 and given in Table 13 for Dupont Butacite PVB to analyse the low strain-rate response of the testing reported in Ref. 127. Two approaches were considered.

In the first approach, under constant loading rate, each material point experiences approximately proportionate loading, and over the period of loading the modulus of the interlayer decreases monotonically. Because the PVB displays a spectrum of relaxation times it was considered that it could be approximately considered as an equivalent elastic solid with a shear modulus corresponding to the shear relaxation modulus at mid-time of the experiment. Ref. 86 listed 30 second shear relaxation modulus values for various temperatures and indicated that the value of 0.69 MPa corresponded to a temperature near 40ºC.

In fact, the listed shear modulus values are not consistent with the data from Ref. 88 (listed in Section 4.7.2, Table 13 and Eqns. 24 and 25 of this thesis). Corrected values for 0.69 MPa are 31.81ºC for 30 seconds or 30.15ºC for 60 seconds. This can be compared to a 30 second modulus value of 0.917 MPa for 25ºC, the mean of the temperature range over which the testing was undertaken, so the difference between the measured material and that used in the test in Ref. 127 is less than stated in Ref. 86.

In the second approach, finite element analysis of the testing reported in Ref. 120 was undertaken with the interlayer explicitly modelled as elements with viscoelastic properties. The properties used were those reported in Ref. 88 using the Generalised Maxwell series, adjusted to various temperatures. Ref. 86 indicated that there was relatively little deviation from the monolithic case for temperatures of -3.5ºC and limited deviation at16.5ºC, but that there was significant deviation at 26.5ºC, and that the best fit to the measured data was given by a temperature of 46.5ºC.

For comparison purposes, the sensitivity of shear relaxation modulii to temperature and timing around the parameters of this testing is shown in Fig. 109, and the 30 second values for a range of temperatures, calculated from the data in Ref. 88, are given in Table 37.

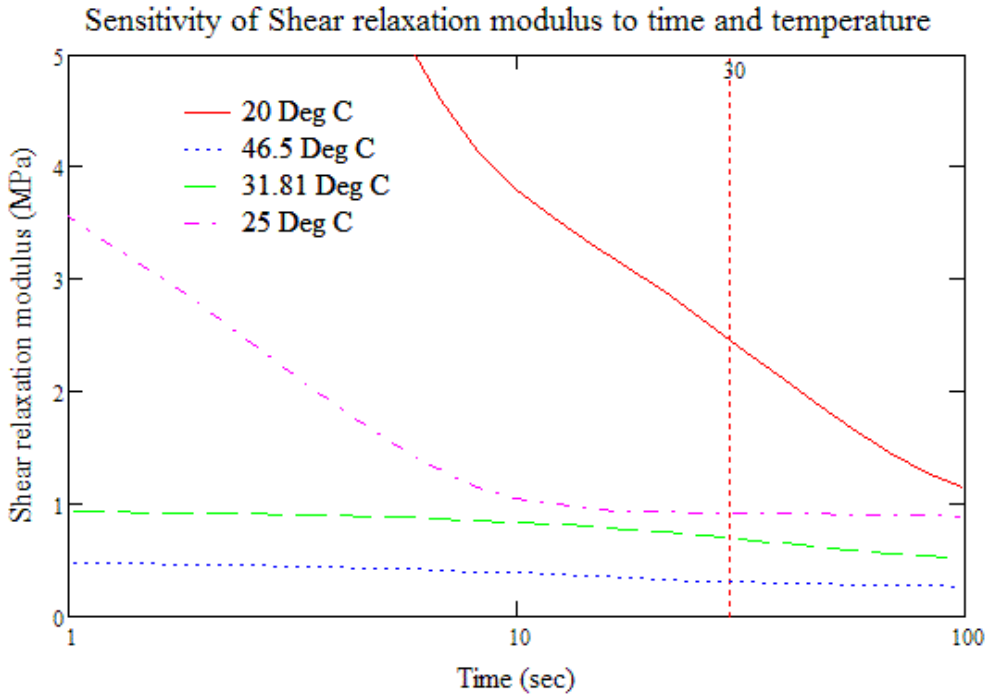

Figure 109. Sensitivity of shear relaxation modulus for quasi-static testing

Temperature	Shear relaxation modulus at 30 secs.
ºC	MPa
-3.5	215
16.5	6.07
20	2.47
25	0.917
26.5	0.901
31.81	0.690
46.5	0.302

Table 37. Variation of shear relaxation modulus for quasi-static testing with temperature.

The difference in the 30 second shear relaxation modulus between 31.81 seconds and 46.5 seconds is more than a factor of 2, which suggests that the use of the 30 second modulus as an equivalent linear modulus is very approximate. However, it should be noted that significant deviation from the monolithic stiffness required a modulus of the order units of MPa at half the loading duration, and that modulus values of the order tens and hundreds of MPa will result in response similar to that of monolithic glass.

Too much weight should not be placed on the temperature differences from the test analysis in Ref. 86. Ref. 88 makes clear that different plasticized PVB material from different manufacturers can vary significantly. Quite small variations in the Maxwell series coefficients could result in a factor of three variation in modulus at the low end

while having only a marginal effect at shorter time periods when the modulus values are two to three orders of magnitude higher.

The shear modulus values being considered in Ref. 86 are of the order 0.1% of the instantaneous modulus, and the PVB in the test is not the same as that from which the viscoelastic properties were established. It would be unreasonable, for example, to project the time factor differences between 25ºC and 46.5ºC, a time ratio of almost 4000, onto a high strain-rate response that is affected by a different part of the viscoelastic modulus-time curve.

The discrepancies may merely reflect the inaccuracy reported by Ferry [87] in using small strain and small strain rate linear viscoelastic properties to analyse moderate to large strains in polymers. Ref. 103 and Fig. 44 illustrate the need for nonlinear viscoelastic material properties in modelling polymer response at less than 10% strain.

7.1.4 High strain rate analysis

Wei et al. [85] analysed both the testing from Ref. 127 and blast loading up to 3 psi (20.7 kPa) with a duration of 7.72 milliseconds. A simplified linear viscoelastic model was used for the PVB (Eqn. 22 and Section 4.7.2 of this thesis). This was equivalent to a single Maxwell component in parallel with a spring representing the long term stiffness, sometimes called the Standard Linear Solid Model. This single viscoelastic term gives a relatively narrow time range for the transition from the instantaneous to the long term stiffness, centred on a time that is the reciprocal of the time constant β in Eqn. 22.

For the low strain-rate analysis, β was given as 66 sec^{-1}, which set the centre of the transition at 15 milliseconds, and resulted in a constant shear modulus equal to the long term modulus of 0.376 MPa for any time after 0.2 seconds. For a 60 second test analysed with an implicit finite element code (Abaqus) the time steps would probably be greater than 0.2 seconds, and the analysis would be indistinguishable from an analysis with a linear elastic PVB model. The long term modulus had been set equal to the 10 second shear relaxation modulus from the full viscoelastic model in Ref. 85 at a temperature of 46.5ºC, which is about 25% higher than the 30 second shear modulus for 46.5ºC in Table 37. It is therefore not surprising that there is good agreement with the results of the analysis in Ref 127, but this agreement arises from the value chosen for the long term modulus, and the selection of a time constant that eliminates any viscoelastic response, rather than any accuracy in modelling a viscoelastic response.

For the high strain rate analysis of blast response, the time constant β was given as 12.6 sec^{-1}, which set the centre of the transition at 79 milliseconds. For the blast analyses considered, with a peak deflection at 12 milliseconds, the 6 millisecond shear relaxation modulus is 306 MPa, close to the instantaneous value of 330 MPa. In Ref. 85, a viscoelastic dynamic analysis of an 11.04mm thick square laminated glass panel with a span of 1325mm was compared with that of a monolithic glass pane of the same size using an explicit finite element program (LS-DYNA). The analysis showed a negligible variation in the peak deflection and stresses. Sensitivity studies

were then conducted by scaling the instantaneous shear modulus, but retaining the time constant. Analyses with instantaneous shear stresses of 6.9 MPa and 0.69 MPa (ten times the long term modulus and equal to the long term modulus respectively) show substantial deviation in deflection and stress history from the original values.

As a general comparison intended to cover all likely blast cases, in Ref. 128, Wei & Dharani also compared the viscoelastic analysis above with elastic analyses using constant shear modulus values of 330 MPa, the instantaneous shear modulus, and 94 MPa, the shear relaxation modulus for 100 milliseconds. The maximum panel deflection for 330 MPa was identical to that of the viscoelastic analysis, while that for 94 MPa was only 0.01mm (0.16%) larger, indicating that the deflection and stresses are not significantly changed from those of a monolithic pane down to interlayer shear modulus of 94 MPa.

The simplified Wei shear relaxation modulus curves from Refs. 85 and 121 have been compared with the comprehensive measured shear relaxation modulus curves from Ref. 88 at various temperatures in Fig. 110. This indicates that, over the typical time range for blast response of uncracked glass to cracking or peak deflection, the simplified curves are substantially over-stiff. Even the 94 MPa modulus value corresponds to only a 4 millisecond shear relaxation modulus at 20ºC. This would confirm that a response to cracking or maximum deflection in 8 milliseconds can be treated as being similar to a monolithic pane.

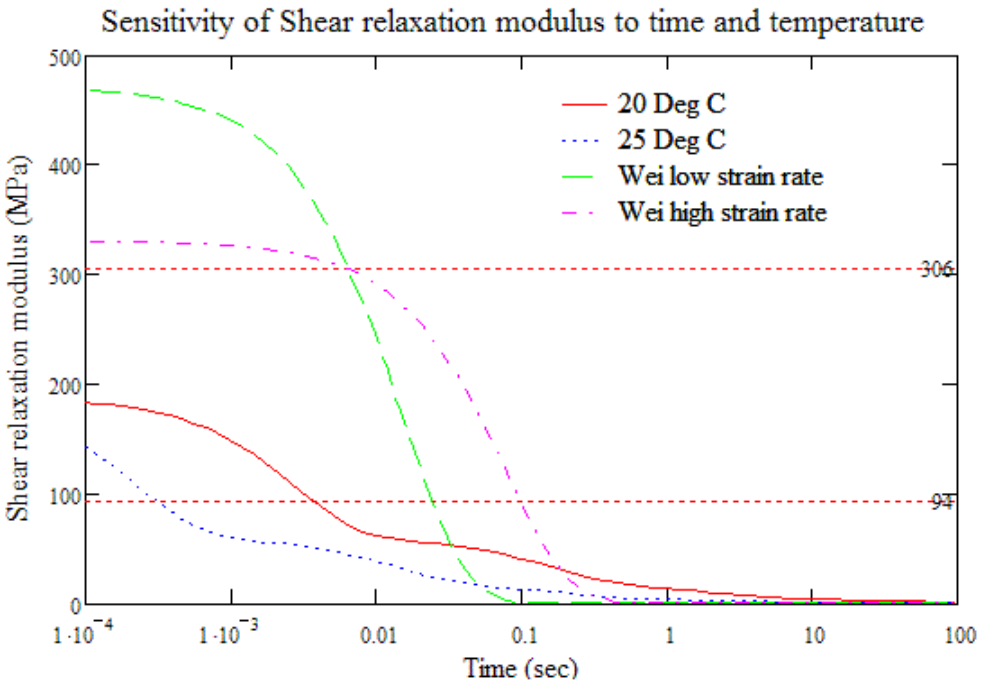

Figure 110. Comparison of shear relaxation modulus for blast testing

Six millisecond shear relaxation modulus values are listed in Table 38. In conjunction with the dynamic analyses described above, these indicate that laminated glass up to 15ºC certainly and 20ºC probably can be treated as if fully composite, but that by 35ºC the PVB modulus corresponds to analyses that indicate significant variation from the composite case. Unfortunately, the area of uncertainty between 20ºC and

35ºC contains the zone where inhabited room temperatures are most commonly found.

Temperature	Shear relaxation modulus at 6 milliseconds.
ºC	MPa
10	193
15	172
20	74.3
25	45.6
30	15.7
35	5.56

Table 38. Variation of shear relaxation modulus for blast testing with temperature.

It should be noted that the composite dynamic analyses reported here had a maximum deflection of 58% of the total pane thickness, and so can generally be taken as small deflection, with negligible membrane forces.

It should be further noted that, as indicated in Ref. 86, membrane stresses and deflections controlled by membrane effects are independent of the shear stiffness of the interlayer, so that the significance of the shear stiffness of the PVB on the failure deflections will decline with increased slenderness and cracking strength. However, the reduced stiffness at higher temperatures will reduce the initial bending stiffness and allow earlier transition to membrane resistance, so the shape of the resistance curve will vary appreciably even though the peak is at a similar deflection and resistance. As a result, the deflection curve should vary appreciably as the temperature rises from 20ºC to 35ºC.

7.2 Application of large deflection data for monolithic panes to laminated glass

To model the deflection of a laminated pane similar to that shown in Fig. 111 using curves derived from the analysis of monolithic plates, it is necessary to identify equivalent monolithic thickness T_e and modulus E_e that will result in the same flexural and axial unit stiffness.

The typical flexural stiffness per unit breadth of the laminate and of the equivalent monolithic material can be expressed alternatively as:

$$FS = F_1 \cdot EI = F_2 \cdot E_g \cdot \frac{h_t^3}{12} = E_e \cdot \frac{h_e^3}{12} \tag{49}$$

Where EI is the stiffness of a fully composite laminated section and F_1 is a reduction factor to allow for any reduction in composite action due to the shear deformation of the PVB. Section 7.1 suggests that F_1 can be taken as 1.0 for the blast response in temperatures below about 20ºC, but will be significantly below 1.0 for temperatures around 35ºC.

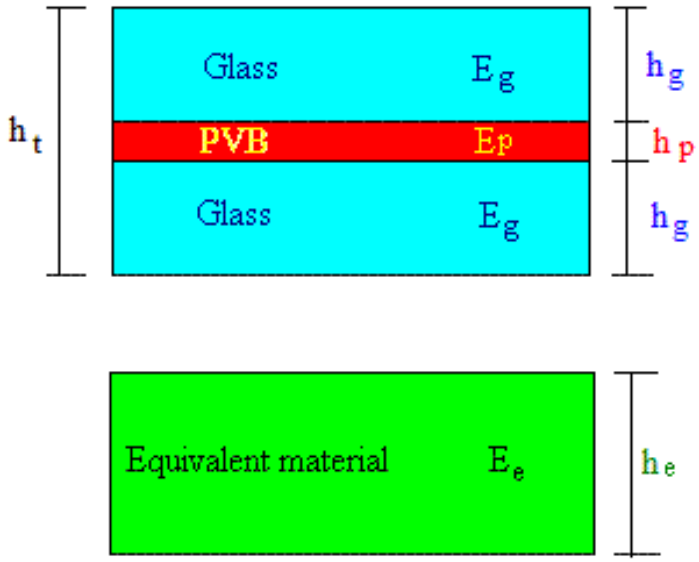

Figure 111. Typical makeup of two-ply laminated glass and an equivalent monolithic material

F_2 combines with F_1 a reduction factor to account for the lower stiffness of the fully composite section from a monolithic glass section of the same total thickness. The additional reduction is small for two ply glass, typically from 0.992 for laminated glass with 20% PVB to 0.999 with 10% PVB. With more plies, some of the PVB may be closer to the surface and the reduction could be greater.

The typical axial stiffness per unit breadth of the laminate and of the equivalent monolithic material can be expressed alternatively as:

$$AS = \sum A \cdot E = E_g \cdot \sum h_g + E_p \cdot h_p = F_3 \cdot E_g \cdot \sum h_g = E_e \cdot h_e \tag{50}$$

Where F_3 is an increase factor to allow for the contribution of the PVB to the tensile stiffness. The increase is small, typically from 1.001 for laminated glass with 20% PVB reducing to 1.0005 for laminated glass with 10% PVB, and for a PVB Young's modulus of around 350 MPa.

Dividing equation 49 by equation 50 to eliminate the Young's moduli gives:

$$h_e = F_4 \cdot h_t = \sqrt{\frac{F_2 \cdot h_t}{F_3 \cdot \sum h_g}} \cdot h_t \approx \sqrt{\frac{F_1 \cdot h_t}{\sum h_g}} \cdot h_t \tag{51}$$

For a fully composite two-ply section, the error introduced by using the approximate term in Eqn. 51 would be 0.5% in a laminated glass with 20% PVB, reducing to 0.075% with 10% PVB.

Substituting equation 50 into equation 51 allows calculation of the equivalent modulus:

$$E_e = F_5 \cdot E_g = \sqrt{\frac{F_3^{\,3}}{F_2} \cdot \frac{\sum h_g^{\,3}}{h_t^{\,3}}} \cdot E_g \approx \sqrt{\frac{\sum h_g^{\,3}}{F_1 \cdot h_t^{\,3}}} \cdot E_g \tag{52}$$

For a fully composite two-ply section, the error introduced by using the approximate term in Eqn. 52 would be 0.6% in a laminated glass with 20% PVB, reducing to 0.13% with 10% PVB.

For fully composite sections, the equivalent thickness T_e will tend to be slightly greater than the total thickness T_t, while the equivalent modulus E_e will tend to be significantly lower than the glass modulus E_g. As the flexural stiffness reduces due to shear deflection in the interlayer, the effective thickness will reduce, while the effective modulus will increase.

Using the equivalent section properties in the formulae for non-dimensional loading and non-dimensional load, the resistance curve for any laminated pane can be calculated from the monolithic curves in Figs. 77 and 81. In addition, other parameters based on the deflected shape for different levels of non-dimensional loading, such as the transformation factors K_L and K_M, their ratio K_{LM} and the average total deflection can be taken from the monolithic curves in Figs. 85-88. These provide all of the data required to calculate the deflection history of an uncracked laminated glass pane.

7.3 Blast testing of uncracked laminated glass

7.3.1 Permasteelisa tests at BakerRisk, August 2006

In August 2006, a series of 12 trials of Permasteelisa double glazing units were conducted in the BakerRisk shock tube at San Antonio, Texas. These tests were preliminary trials for façade units for a new high rise office block.

The first four tests were witnessed by the Author, and records, observations and photographs of the remaining tests were provided by Mike Lowak of BakerRisk [129]. From this information, the Author [130] back-analysed the trials and provided a report to Permasteelisa. Tests 1, 2 and 6 caused no damage to the glazing units, and so are suitable for consideration as tests on uncracked laminated glass.

The three test samples were all double glazing units with overall dimensions 2952 mm by 2157 mm, with a 25 mm 'bite' on the supporting frame, giving a clear glazed area 2902 mm by 2107 mm. The makeup of the samples and the test conditions are given in Table 39.

Dynamic pressure waves are produced in the BakerRisk shock tube by the release of compressed air from a large pressure vessel by the rupturing of two aluminium sheet diaphragms. The two diaphragms in combination can contain the pressure in the vessel when the thin void between is held at an intermediate pressure. Controlled venting of this void is used to overload the inner diaphragm and cause both diaphragms to rupture in quick succession. This leads to an explosive release of the compressed air, which forms a shock wave in an expansion cone leading to the target.

Sample Makeup	Units	Test samples		
		1	2	6
Inner leaf plies	mm	12	12	10
Inner leaf PVB interlayer	mm	1.52	1.52	1.52
Inner leaf thickness	mm	25.52	25.52	21.52
Cavity	mm	12.7	12.7	12.7
Outer leaf	mm	10	10	10
Overall unit	mm	48.2	48.2	44.2
Test Conditions				
Temperature at test	ºC	31	43	29
Specified peak pressure	kPa	59	59	48
Specified blast duration	ms	40	40	40

Table 39. Sample makeup and test conditions for uncracked tests at Baker Risk

Pressure histories produced by the shock tube are an approximately triangular pulse, followed by some smaller and shorter positive and negative pulses. The shock tube does not emulate the negative phase of an open air explosion, but for a long duration load on an uncracked sample, with a peak response during the initial positive phase, this is not significant. The peak reflected pressure at the target is controlled primarily by the pressure in the vessel, while the duration and impulse can be varied by altering the air volume in the pressure vessel with a movable water backed bulkhead.

Pressure histories for each test were measured using three pressure transducers mounted on the steel frame supporting the target sample in the shock tube, one at each side and one below, immediately adjacent to the sample. The transducers used were PCB sensors with a Baker Risk modification to reduce signal loss at low frequencies. The mean of the three sensor records was taken as a representative pressure history for tests 1 and 2. In test 6, one of the sensors failed, and the pressure history was taken as the mean of the records from the other two.

Displacement histories were measured at one location at the centre of the rear face of the inner leaf, using a Baumer Electric laser distance sensor. The sensor used has a working range of 800 mm, and will give a constant value ('peg') when the target is less than 200 mm or greater than 1000 mm from the sensor, resulting in the data being 'clipped'. The sensor was mounted on a timber frame attached to the sample mounting frame, generally at a range of approximately 800 mm, to give deflection measurements between approximately 600 mm inwards and 200 mm outwards. The measurements for uncracked glass used only about 20% of the full range, but the possibility that the glass could crack required most of the range to be provided for inwards deflections. Indeed, for test 6 it appears possible that the measurement 'pegged' at a rebound of only 25 mm.

At the time of the tests, the shade temperatures varied from the high 90s Fahrenheit in the afternoon to the high 70s or low 80s Fahrenheit around dawn. The shock tube is located out of doors and exposed to the sun for most of the day. Test temperatures around 30ºC (86ºF) on the inside face could only be achieved by testing by mid-morning, and by setting-up the sample the previous afternoon and running an air cooler overnight beneath a tarpaulin draped over the sample. Test 2 was the only test conducted in the afternoon, and the 43ºC temperature occurred in spite of the cooler and tarpaulin. The analysis in section 7.1.3 indicates that, even for high strain-rates, a significant reduction below the fully composite stiffness can definitely be expected for test 2, and some reduction probably also for tests 1 and 6.

Each sample unit has been analysed as two simultaneous single degree of freedom systems, representing the inner and outer leaves, and an adiabatic gas spring between them representing the gas in the sealed cavity, applying equal and opposite forces to the two leaves as changes in the cavity volume due to deflection of the two leaves causes changes in cavity pressure. Aeroelastic damping is taken to act on the inner and outer faces of the unit, and to damp the cavity vibration, although these damping levels are small for uncracked glass, and have only a minor effect on the response.

The peak measured deflections of all three tests were greater than was calculated assuming fully composite sections in the inner leaf, and the average pressure histories for loading. A sensitivity study was undertaken to identify the reduced stiffness of the inner leaf that would result in the same maximum deflection in each case.

The peak measured deflection for test 1 corresponds to a stiffness of 77% of fully composite, and the recovery curve, if not the rebound, appears to be consistent with this, as shown in Fig. 112.

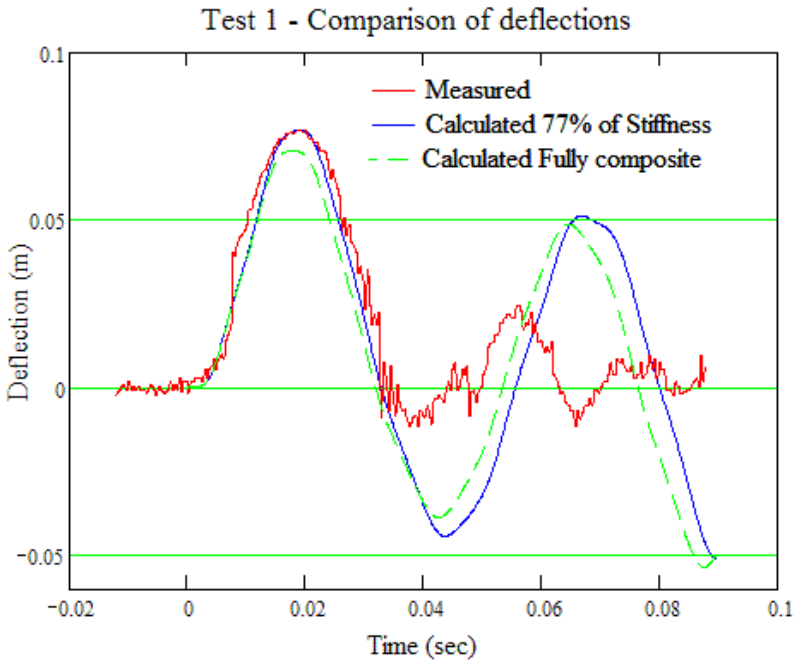

Figure 112. Measured and calculated deflections of the inner leaf for test 1

The peak measured deflection for test 6 corresponds to a stiffness of 45% of fully composite, but the subsequent measured response is faster than calculated, suggesting that this is too soft. A better fit for the timing of the response occurs with a stiffness of 66% of fully composite, although this gives a peak deflection 5% lower than measured, as shown in Fig. 113.

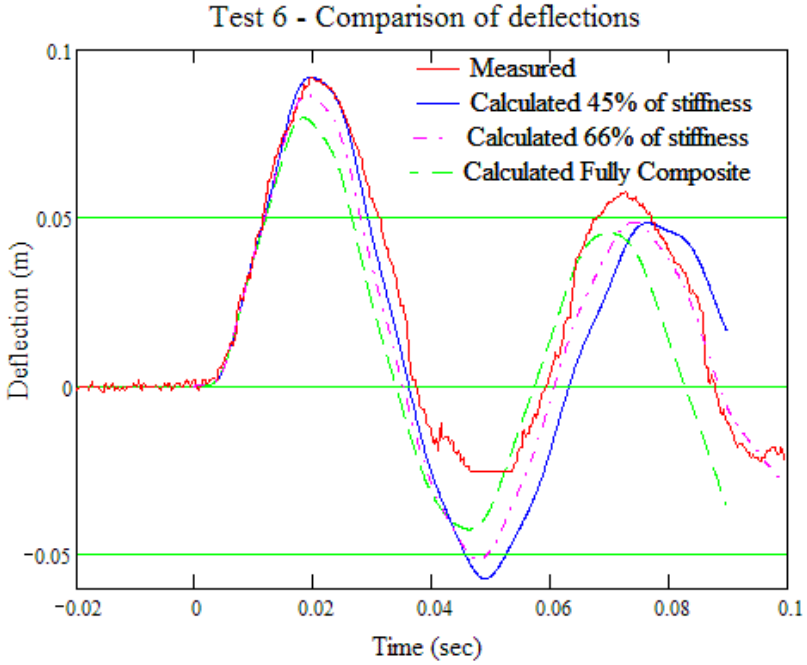

Figure 113. Measured and calculated deflections of the inner leaf for test 6

Considering stiffness alone, the peak measured deflection for test 2 corresponds to a stiffness of 56% of fully composite, but the measured recovery is much slower than

calculated for this stiffness. A sensitivity study suggested that there could be a significantly lower stiffness combined with an increase in the damping.

Additional damping will reduce the amplitude of the deflection, balancing the reduction in stiffness. A good fit is achieved with additional damping equal to three times the aeroelastic damping of the surrounding air, and a flexural stiffness of only 26% of the fully composite stiffness, as shown in Fig. 114.

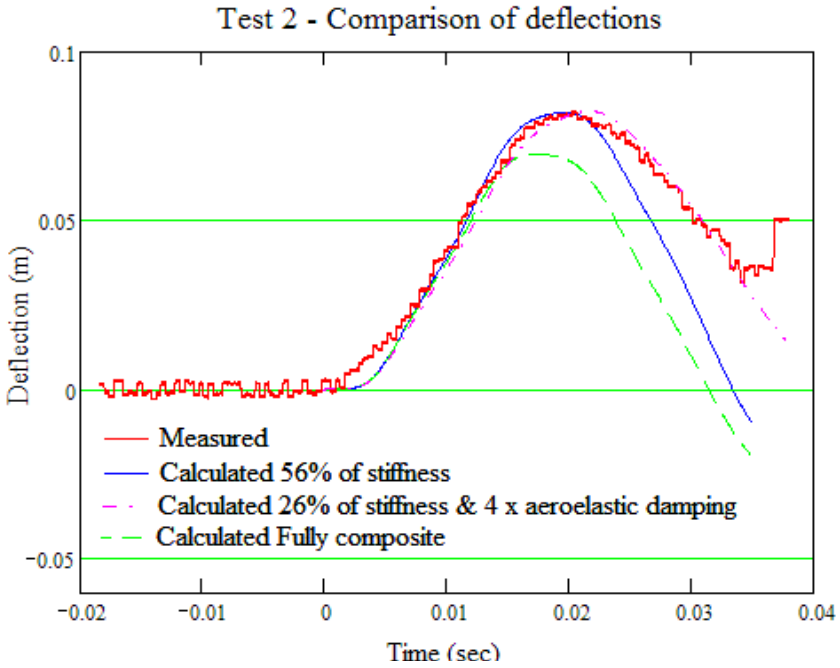

Figure 114. Measured and calculated deflections of the inner leaf for test 6

This reduced stiffness is approaching that of the independent plies, which for this glazing would be 21% of the fully composite stiffness. In turn, this suggests a source for the additional damping. There would have been significant shear strain induced in the viscoelastic PVB interlayer as the glass plies slide relative to each other, even though the material is soft at a temperature of over 40ºC, and the shear stress will be low. As reversal occurs the stress will reverse much more quickly than the strains reverse, resulting in a large hysteresis loop. The additional damping in the measured response may be hysteresis damping in the soft PVB interlayer.

7.3.2 Permasteelisa tests at Advantica, November 2005

In November 2005, a series of 9 arena blast trials were undertaken for Permasteelisa by Advantica at their test site at Spadeadam, Cumbria. These tests were used to load curtain-wall samples with double glazed units 4.2m high by 1.5m wide, mounted in pairs in specially commissioned test cubicles. The tests were witnessed and reported on by the Author [131]. The tests were undertaken in near freezing ambient temperatures, although the use of heaters meant that the inner glass temperatures were typically 15-20ºC at the time of testing.

Small curtain-wall panels below the main panels were used to provide normal curtain-wall support, with the panels supported by a bracket attached below the top of the

mullions and supported by RHS sections at the front of the cubicle, representing the support from floor structures in a building, and restrained at the base by the head of the panel below.

Five of the tests used charges of 100kg TNT equivalent at a range of 42m, to envelope the blast loading level "C" specified by the GSA [132], and the test loading EXV-45 in accordance with draft ISO standard DIS 16933 [133]. Two of the tests, numbers 2 and 4, were of units comprising a framed double glazed panel the full size of the unit, with relatively stiff frames, that remained elastic during these tests. For both these tests the glass comprised a 10mm annealed glass outer leaf and a 9.5mm (4mm / 1.52mm / 4mm) laminated annealed glass inner leaf, with a 12mm wide sealed cavity.

The glass in these tests was cracked in whole or in part, but laser displacement measurement of one of the panels for each test suggested that the glass cracked on first and/or second rebound. These laser measurements were the first direct measurements of deflection history under blast loading known to the Author.

These two tests are suitable for assessment of the stiffness of the glazing, but this assessment is complicated by the flexibility of the mullions. The central mullions of the paired units were interlocked to provide effectively a single shared mullion. The side mullions were interlocked with unglazed mullion sections which were restrained by RHS sections in the Test cubicle. The restraints were provided to prevent in-plane displacement, but also provided out-of-plane restraint, more stiffly for the 200mm deep mullions in test 4 than for the 160mm deep mullions in test 2.

The response of the glazing and mullion was modelled by solving SDOF analyses for the two glass leaves and for the flexing central mullion simultaneously in a three degree of freedom analysis. The two leaves were modelled with a gas spring representing the cavity and with aeroelastic damping, as for the tests described in Section 7.3.1, but also with support motion from the flexible mullion. The mullion was loaded with the edge reaction from the two supported panels. This is not uniformly distributed and varies with the glass deflection. This was approximated in the model by a varying proportion of uniformly and half sine wave loading to give the same midspan moments and endspan shears as the glazing reactions. SDOF parameters calculated for the range of load distributions were used to calculate the mullion motion and deformation history, treating the mullion as supported at the panel corners. The stiffer transoms and the restrained mullion were initially treated as being rigid.

The temperature of the Test 2 sample was not measured close to the time of testing, but the weather conditions, ambient temperature (3.5ºC) and time of day were similar to Test 4, which was measured by contact thermocouple on the inner face as 20.7ºC just before the final clearance of the test pad, and 17.2ºC immediately after the safety clearance following the detonation, suggesting a temperature at detonation around 19ºC.

The comparisons of the glass deflection for these two tests are shown in Figs. 115 and 116.

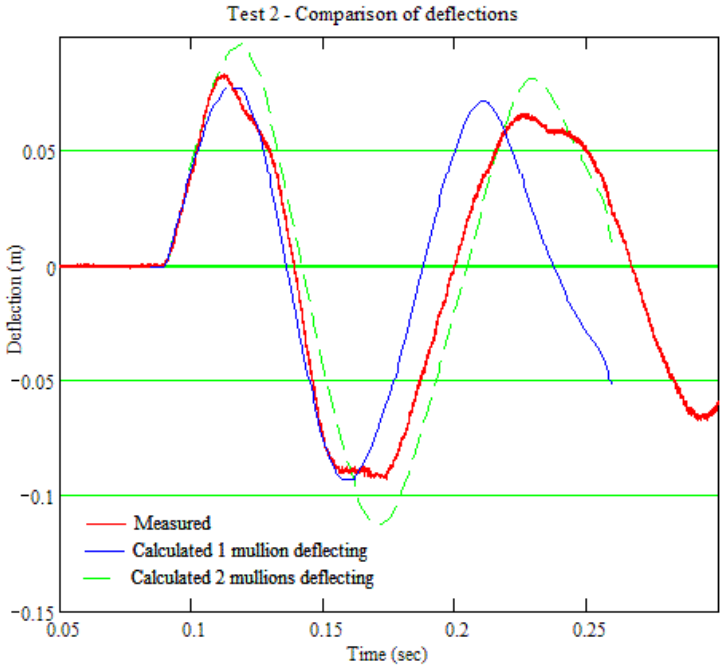

Figure 115. Measured and calculated deflections of the inner leaf for test 2

Fig. 115 shows that the peak calculated deflection for the glazing with one 160mm mullion modelled as flexing and the other as a rigid support was slightly lower than the measured deflection, while the initial rebound was slightly earlier than that measured. However, if the second mullion is also taken as deflecting, but with half the loading from the glazing, the glass deflection modelled in conjunction with the average mullion deflection is higher than the measured peak deflection, and the rebound is slightly earlier, as shown by the dashed line in Fig.115.

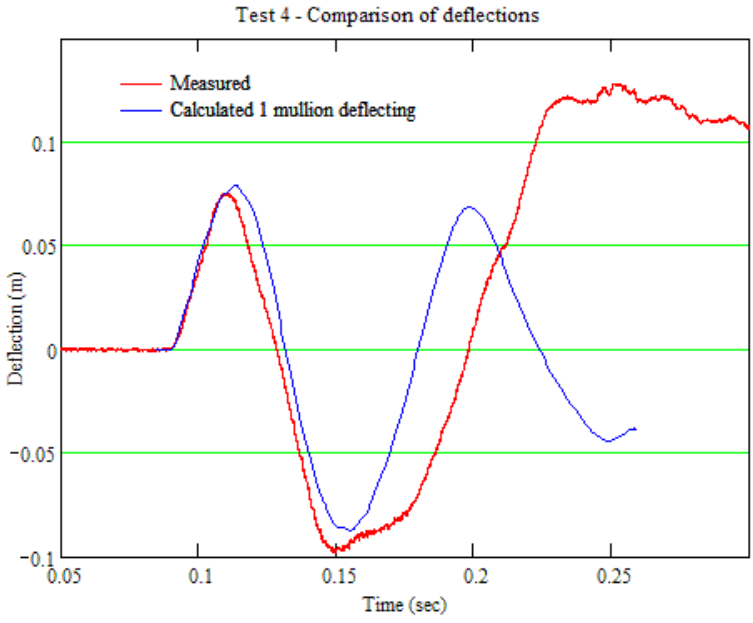

Figure 116. Measured and calculated deflections of the inner leaf for test 4

As the side mullions 160mm deep were incompletely restrained, the measured response should lie between these two models, as it does. As the laminated glass was modelled as fully composite for both analyses, this test is consistent with laminated glass behaving as fully composite under blast loading at a temperature of around 19ºC.

Fig. 116 shows that the peak calculated deflection for the glazing with one 200mm mullion modelled as flexing and the other as a rigid support was slightly higher than the measured deflection, while the initial rebound was slightly later than that measured. Although the modelling is not perfect, this suggests that the actual stiffness was slightly higher than that in the model, which is also is consistent with the laminated glass stiffness being fully composite at a temperature of around 19ºC.

7.4 The cracking process for laminated glass

Variability of glass strength means that the relationship between cracking of laminated glass and the stress in the equivalent monolithic model cannot be demonstrated by test, only by analysis. Currently, analysis has only been undertaken for a fully composite model.

Laminated glass with a single PVB interlayer forming 20% of the thickness, consistent with 7.5mm thick laminated glass, was modelled using a layered shell construction. This calculates the cross-section properties from the layered construction, but models the deformation with a single layer of nodes and elements, so shear flexibility of the interlayer was not modelled, and plane sections remain plane. In the layered analysis the PVB interlayer was taken to have a Young's modulus of 345 MPa and a Poisson's ratio of 0.49, but the modelling implies an infinite through-layer shear modulus.

These analyses were compared with monolithic shell analyses of the same aspect ratio using the equivalent thickness and Young's modulus calculated in accordance with the equations in Section 7.2. Non-dimensional stresses and deflections were calculated for both analyses using the equivalent properties, so that the relationship between the non-dimensional values and actual values are proportionate. The non-dimensional deflections and stresses are plotted in Fig. 117.

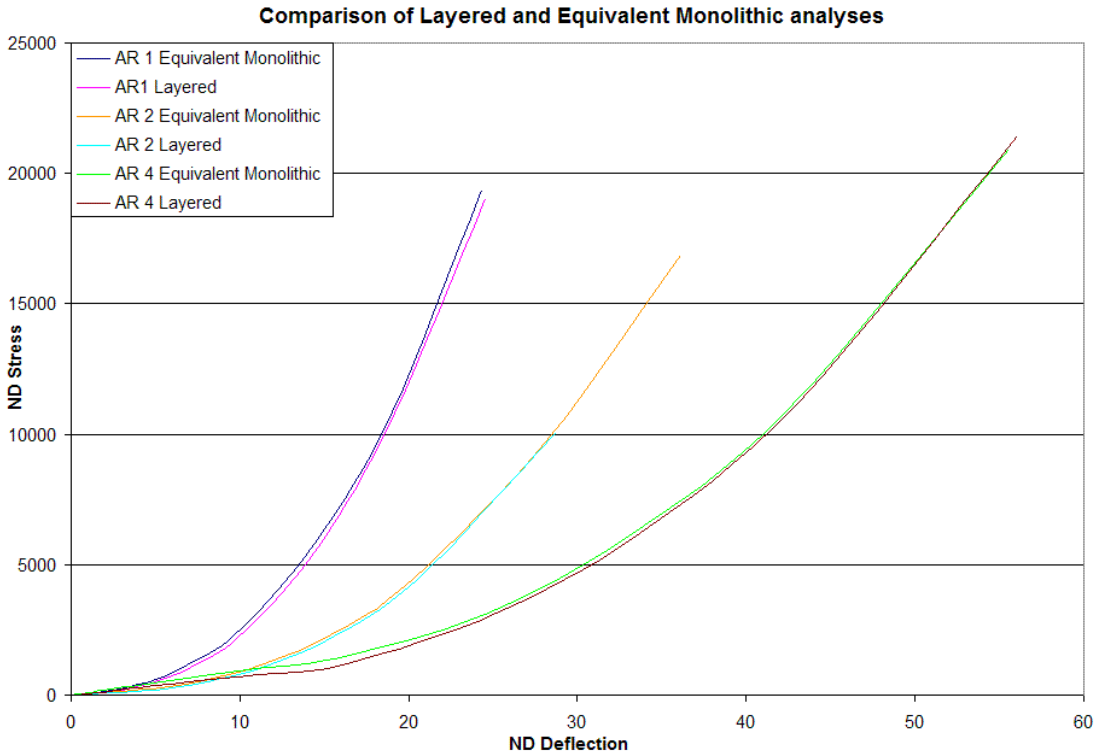

Figure 117. Stress-deflection comparison of layered and equivalent monolithic analyses for three aspect ratios

The results of these analyses show that for a given deflection, the maximum stress in the equivalent analysis is generally higher than in the layered analysis. The difference

is greatest at low non-dimensional stress levels when the maximum stress occurs at the centre and is primarily bending in nature. The differences are much smaller when the maximum stress occurs near the corner and is primarily membrane stress.

For a given cracking strength, this indicates that the equivalent monolithic analysis will generally give a slightly lower cracking deflection than the laminated analysis. Applying the actual cracking stress in an equivalent monolithic calculation without modification will marginally underestimate the cracking deflection and hence the cracking resistance. The underestimate in resistance at cracking will be conservative in calculating deflections of the cracked laminate glass. This conservatism will tend to be greatest for low non-dimensional cracking stress, i.e. for less slender sections and lower glass strengths, and for larger proportions of PVB, and will be smaller for slender panes, stronger glass and less PVB.

For design purposes, using the monolithic glass deflection-stress plot, Fig. 83, with the equivalent section properties to model laminated glass will underestimate the cracking deflection for fully composite sections, and is therefore expected to be conservative at and below room temperature. For back-analysis of individual cracked panels, as in Chapter 9, this conservatism cannot be separated from the difference between the random margin of strength of the laminated glass plies over the design cracking strength, and so may appear as a higher margin for laminated glass than for monolithic glass.

Cases with partial composite action, where some shear slippage occurs in the interlayer, have not been analysed. In theory, the bending stresses should increase less slowly than the deflection as composite action reduces, while the membrane stresses should remain proportional to the deflections. This suggests that the conservatism of the cracking deflection shown by fully composite models should increase as the composite action reduces with increasing temperature, but that the conservatism will increase least for slender panes, stronger glass and less PVB.

Although the lower bound resistance will be conservative for deflections and failure of the PVB, the maximum resistance at cracking will be underestimated by the equivalent monolithic analysis. For laminated glass with lower slenderness and lower PVB proportions where the cracking strength gives the greatest resistance and the greatest real reactions, this can underestimate the peak reactions. For slender panes with larger PVB thickness where the maximum resistance occurs in the PVB at maximum deflection this will not be significant.

7.5 Summary of laminated glass up to cracking

The viscoelastic analyses in Section 7.1 suggest that the linear Generalised Maxwell model of viscoelasticity is not sufficiently accurate to model the behaviour at finite shear strains and strain rates, even at the limited strains and strain rates found in uncracked shear in laminated glass. Artificial temperature adjustments to modify the stiffness were used in several papers to relate the material properties to the test results.

In any case, the shear stresses and strains in the PVB interlayer are unevenly distributed through the pane, with low values in the centre of the pane and high values at the perimeter. Shear stress and transfer forces can be used as indicators of the degree of composite action in a distributed analysis, but the deflections are the only practical indicator that can be used in a SDOF analysis.

This is the basis of the method of analysis of uncracked laminated glass proposed in Section 7.2, where the response of the laminated glass is related to that of an equivalent monolithic panel with modified properties which gives the same relationship between bending and membrane behaviour.

The few tests described in Section 7.3 are not inconsistent with the analyses in Section 7.2, and the high speed testing in Section 7.1. They suggest that the flexural stiffness under blast loading at temperatures around 19ºC is effectively fully composite, and that it reduces at elevated temperatures. At 30ºC the stiffness may be of the order 70% of fully composite, and that this may reduce to about 26% of fully composite at a temperature of 43ºC, probably with an increase in damping due to hysteresis losses in the PVB.

However, the deflection histories in these analyses are not particularly sensitive to the flexural stiffness, and as the test units were relatively complicated, requiring more complex analyses with two or three independent degrees of freedom. The results from the tests may therefore be affected by many other factors not considered here, or modelled inaccurately or incompletely, in addition to the stiffness of the laminated glass. Because of the uncertainty, many more results would have to be considered before this trend could be confirmed. The limited blast test data available supports the modelling described in Section 7.2, and also the sensitivity to temperature inferred from the previous work described in Section 7.1, but cannot be taken as adequate confirmation.

Given the variability of glass cracking strength, even a substantial number of tests would be unlikely to reliably assess the relationship between the laminated cracking deflections and the cracking deflections of the equivalent monolithic panels from Section 7.2. Numerical analysis shows that the use of an equivalent monolithic panel to analyse the cracking deflection will generally underestimate the cracking deflection and resistance, although the conservatism is greatest at small non-dimensional cracking stresses which will occur when the slenderness and the glass cracking strength are low, or when the PVB proportion of the overall thickness is high.

If the equivalent monolithic section is used with the design cracking strength to define a resistance function up to cracking of the laminated glass, the resistance will be lower bound, which will result in an upper bound maximum deflection of the cracked laminated glass, and a conservative estimate of the risk of PVB failure. This is a desirable bias in design, but when a test is back-analysed and the cracking strength of the glass is estimated from the deflection history, this bias will tend to result in estimated glass cracking strengths that are higher than the true cracking strengths.

In some circumstances, the underestimate in the cracking strength of laminated glass will result in an underestimate of the peak reactions on the supporting frame. It is desirable that glazing design incorporates a factor of safety in the design of glass retaining structures and their fixings which will be sensitive to the peak reactions, to allow for such uncertainties and inaccuracies in the analysis.

8 PVB in tension at high strain rates

8.1 Objective of tensile testing

The previous analyses considered in Chapter 7 indicated that the linear viscoelastic model of PVB in shear in uncracked laminated glass was not particularly reliable using the parameters derived from low amplitude vibration tests to model strains up to about 10%.

Once laminated glass cracks and the PVB interlayer becomes mobilised in tension, mean strains of about 50% or more can be projected from the observed transverse deflections, with strain rates substantially higher than in uncracked shear, and much higher than in the vibration material tests. It was expected that the low strain and low strain-rate material data from vibration tests might not be representative of the material behaviour in these circumstances. This was examined in this chapter by comparing tested and modelled behaviour.

High rate of strain tensile tests of PVB sheet were undertaken to attempt to typify the material properties of PVB in laminated glass, with a view to modelling the response of PVB membranes. Sufficient data was obtained from two sets of tests to evaluate alternative approaches to modelling PVB material and to evaluate coefficients for the selected material model.

8.2 Linear viscoelastic analysis of PVB in tension

The Generalised Maxwell viscoelasticity model was described in Section 7.2. The shear modulus *G(t)* was defined in Eqn. 45, with temperature adjustment of the time constants in accordance with Eqn. 46.

For uniaxial extension, Ferry [87] indicates that Young's modulus *E(t)* can be written as:

$$E(t) = \frac{\sigma_u(t)}{\varepsilon} = 2\left[G(t) + \int_{-\infty}^{t} G(t-t') \cdot \nu(t') dt' \right] \tag{53}$$

For soft viscoelastic solids, including PVB, the bulk modulus is much greater than the shear modulus, and the Poisson's ratio *v* is very close to 0.5 and does not vary significantly, so to a close approximation:

$$E(t) = 3 \cdot G(t) \tag{54}$$

For a sample pulled at a strain rate $\dot{\varepsilon}(t')$ at time *t`*, the uniaxial tensile stress $\sigma_u(t)$ at time *t* is:

$$\sigma_u(t) = 3 \cdot \int_{-\infty}^{t} G(t-t') \cdot \dot{\varepsilon}(t') dt' \tag{55}$$

For a test with a constant strain rate from time 0, this reduces to:

$$\sigma_u(t) = 3 \cdot \dot{\varepsilon} \cdot \int_{0}^{t} G(t-t') dt' \tag{56}$$

For linear viscosity, this indicates that the shape of the stress curve with time should be the same for all strain rates, with the amplitude proportional to the strain rate. The corresponding strain at time *t* is the product of the time and the strain rate.

From this, stress-strain curves for Butacite PVB can be calculated using the small strain and small strain-rate data from Ref. 88 listed in Table 13, which corresponded to a temperature of 20ºC, together with the time shift constants listed in Section 4.7.2.

Taking room temperature as 22ºC, room temperature tensile linear viscoelastic stress-strain relationships have been calculated. Large strain curves are presented in Figure 118.

It can be seen that, even with the viscoelastic softening, the linear viscoelastic material could be expected to reach a failure stress for even a strong polymer at a relatively small strain, and certainly well below a strain of about 2.0.

If only the initial part of the curves are considered, as in Fig. 119, an initial secant Young's modulus can be measured. For example, secant moduli to a stress level of 10 MPa are given in Table 40.

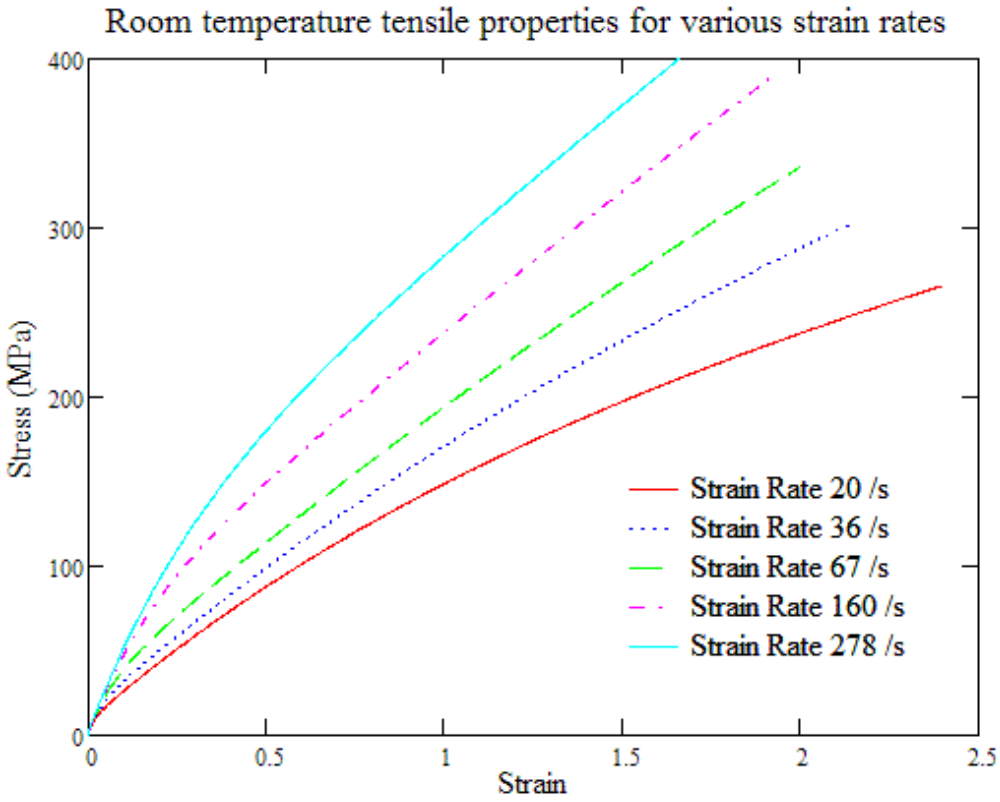

Figure 118. Linear viscoelastic tensile stress-strain relationships of PVB at 22ºC

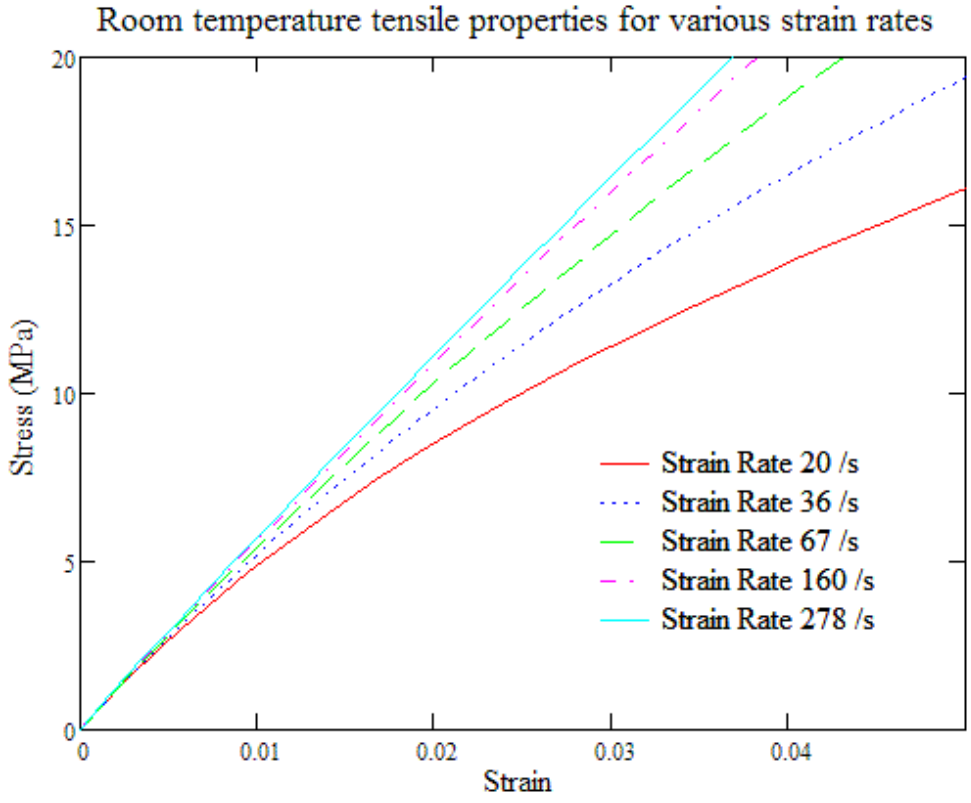

Figure 119. Initial stress-strain relationship from Fig. 118.

Strain rate	Secant Young's modulus to a stress level of 10 MPa	Corresponding secant shear modulus
/s	MPa	MPa
20	393	131
36	469	156
67	512	171
160	544	181
278	581	194

Table 40. Secant stiffness of linear viscoelastic PVB at room temperature

The secant shear moduli lie above the value of 94 MPa considered by Wei and Dharani [128] in the dynamic analysis of uncracked laminated glass, as described in Section 7.1.4, and the Young's moduli are also above the value of 345 MPa used by WINGARD [100]. However, the average strain rates for laminated glazing that is expected to crack, but to successfully resist blast loading as a PVB membrane without rupture, is expected to be towards the bottom of the range considered here, so they are of a similar order of magnitude.

A similar analysis has been undertaken for linear viscoelastic PVB at a temperature of 5ºC. The results are show in Figs. 120 and 121. Secant Young's moduli up to a stress level of 20 MPa are shown in Table 41.

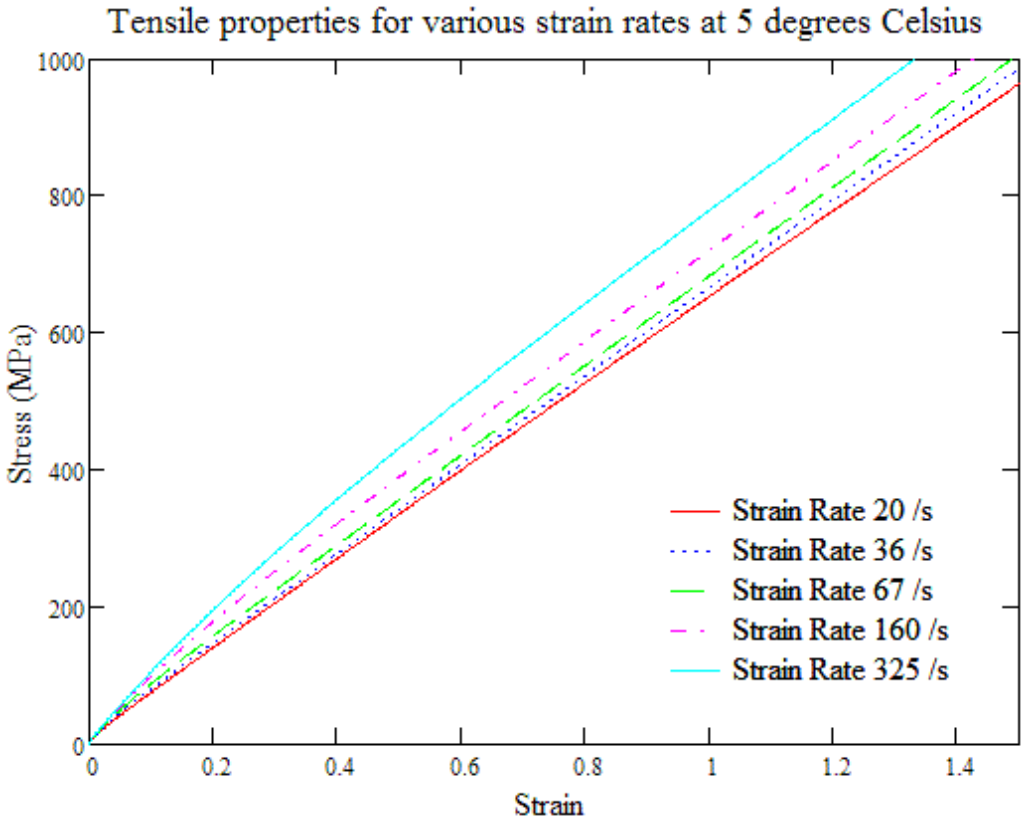

Figure 120. Linear viscoelastic tensile stress-strain relationships of PVB at 5ºC

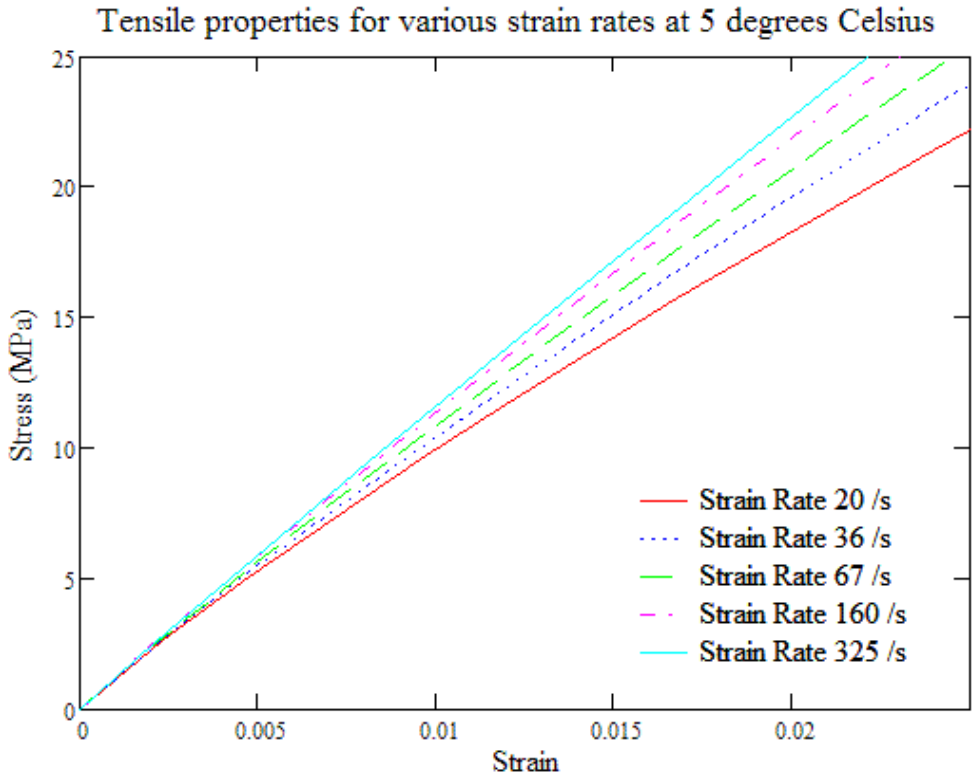

Figure 121. Initial stress-strain relationship from Fig. 120.

Again, it can be seen that a linear viscoelastic PVB could be expected to fail at a fairly small strain, and certainly well below a strain of about 1.4.

Strain rate	Secant Young's modulus to a stress level of 20 MPa	Corresponding secant shear modulus
/s	MPa	MPa
20	905	302
36	971	324
67	1033	344
160	1096	365
325	1138	379

Table 41. Secant stiffness of linear viscoelastic PVB at 5ºC

A similar analysis has been undertaken for linear viscoelastic PVB at a temperature of 35ºC. The results are show in Figs. 122 and 123. Secant Young's moduli up to a stress level of 2 MPa are shown in Table 42.

At a temperature of 35ºC, the linear viscoelastic PVB is sufficiently soft that strains of around 2.0 could be expected, at least at the lower strain rates, before rupture of the PVB. The stiffness is far more sensitive to strain rate than it is at lower temperatures, and the change from the initial stiffness to the residual stiffness is much greater.

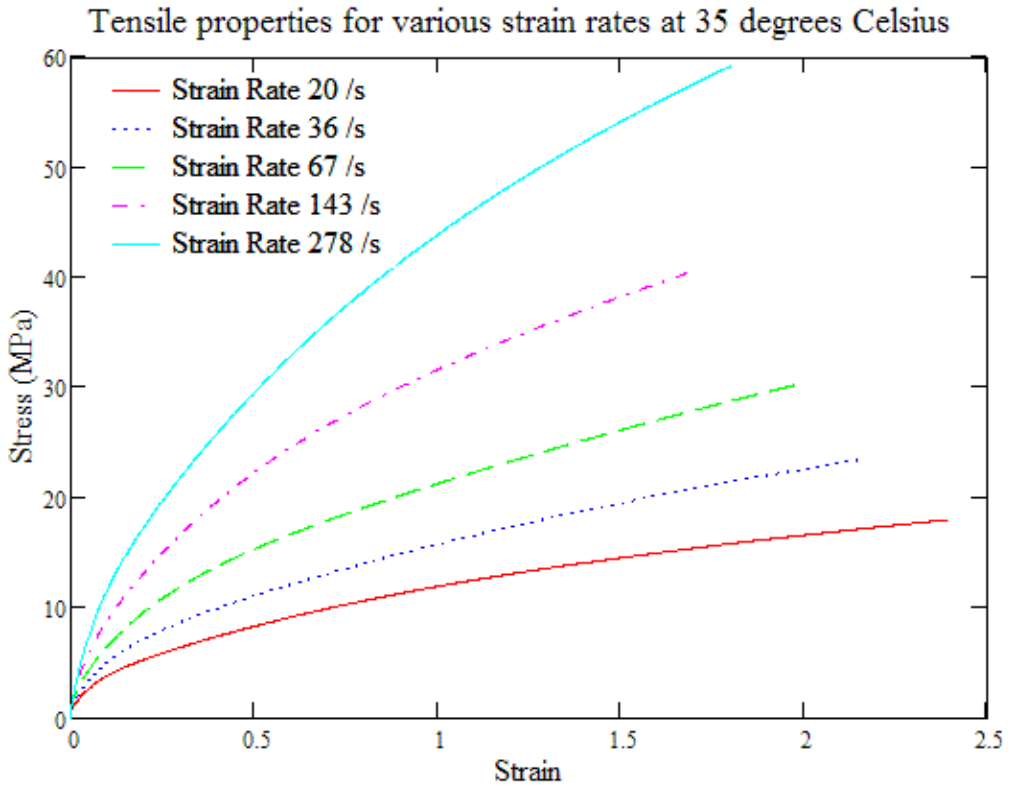

Figure 122. Linear viscoelastic tensile stress-strain relationships of PVB at 35ºC

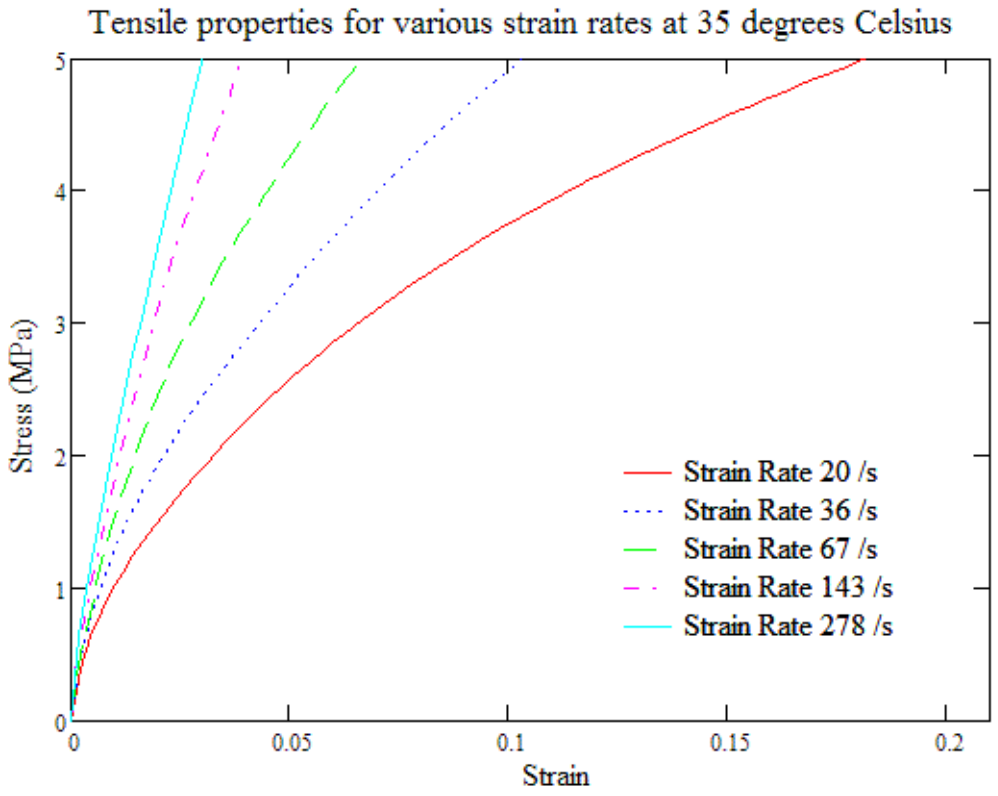

Figure 123. Initial stress-strain relationship from Fig. 122.

Strain rate	Secant Young's modulus to a stress level of 2 MPa	Corresponding secant shear modulus
/s	MPa	MPa
20	60.4	20.1
36	93.0	31.0
67	132	44.1
143	173	57.8
278	203	67.7

Table 42. Secant stiffness of linear viscoelastic PVB at 35ºC

To assess the relevance and significance for these analysis results requires comparison with high strain rate tensile tests of PVB.

8.3 Tensile tests at Cranfield University DCMT Shrivenham

8.3.1 Testing equipment and specimens

Initial tensile tests of PVB were undertaken at Cranfield University at the Defence College of Management and Technology (DCMT), Shrivenham (formerly the Royal Military College of Science) between July 2003 and October 2004, using an Imatek impact test machine, with elastic bungee cords to supplement gravity acceleration of the drop weight for high test velocities, shown in Fig. 124. A forked striker and anvil fittings on the impact test machine allowed the impact to produce a sudden extension at known velocity to a tensile test sample.

Figure 124. The Imatek impact testing machine at Cranfield University DCMT Shrivenham

The Imatek machine was configured for tests on metal specimens up to 25mm wide, 110mm long and 3mm thick, secured between a top anchor instrumented with a strain gauge to measure force, and an impact anvil at the base, using a single bolt through an 8mm diameter hole in each end of the sample.

The drop weight was fitted with a forked striker that dropped either side of the sample and impacted the anvil, bringing the anvil and the base of the sample up to the velocity of the drop weight. The moving components and the sample setup are shown in Fig. 125. A displacement transponder measures the position of the drop weight during the test. This enables the displacement to be measured over time, and the velocity of the test to be calculated.

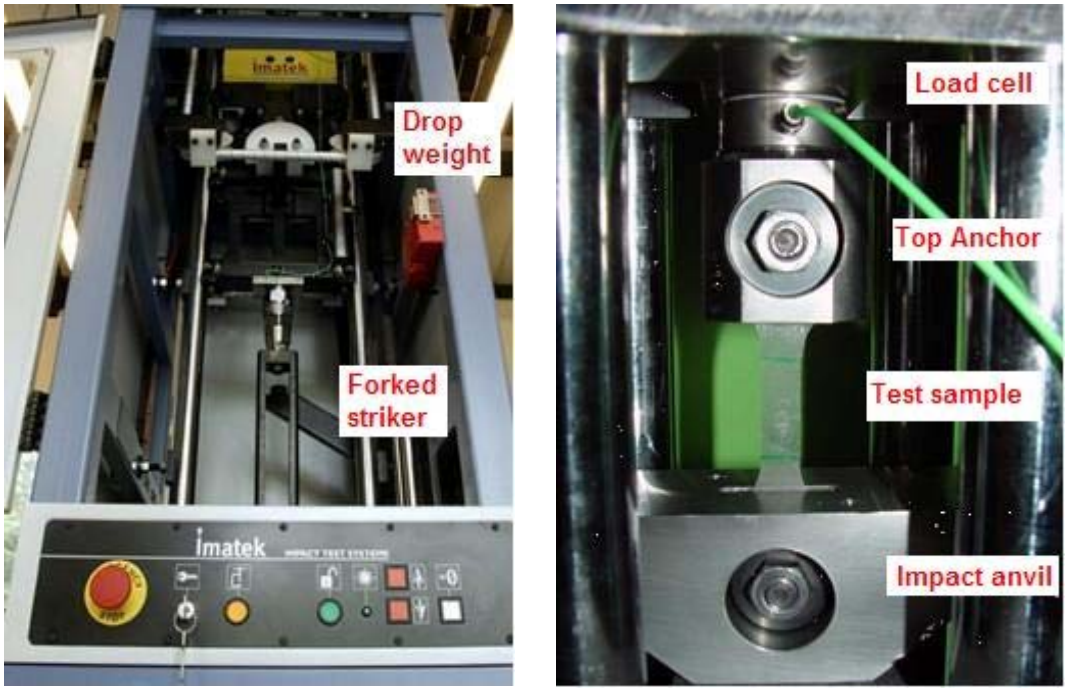

Figure 125. Components and sample set-up on the impact test machine

The PVB used for these tests was a nominally 30/1000 inch (0.76 mm) thick sheet donated by Romag Ltd. Micrometer measurement of the thickness indicated variation was less than 1/1000 inch. The test specimens were cut and fabricated by the Author. Rectangular steel tags 1mm thick with 8mm diameter holes were bonded to the PVB sheet using Loctite "Super Plastix", a Cyanoacrilate adhesive with an N-Heptane activator applied to the PVB face.

8.3.2 Preliminary tests

Five initial specimens were made with two layers of PVB bonded either side of a single steel tag at each end, leaving a 40mm length of PVB between the tags. These samples were tested in a tensile testing machine at a rate of 100mm per minute (approximately 0.028 strains per second). Both straight-sided specimens and specimens with a narrow waist showed a near linear increase of resistance with deflection until failure of the PVB at the face of the tag, at a load of around 600 N, giving a typical stress in the PVB about 15 MPa for the straight specimen, and a higher stress for the waisted sample. The fact that the shallow waisted specimen failed at the face of the tag and at a similar loading to the straight specimen indicated that the failure was occurring at a local stress concentration where the PVB was bonded to the tag. It was felt that a single layer of PVB with tags on both sides would reduce the stress concentration.

Five preliminary specimens were made in this format with straight sides, and were trimmed into a waisted shape before each test, to establish suitable test sample proportions. The samples were tested in the Imatek impact machine with a drop weight velocity of about 2 m/s, giving an average strain-rate of about 33 strain per second. The trimming was undertaken by hand using scissors, so the cross section and sample shape was not sufficiently consistent and accurate for further analysis.

These indicated that specimens waisted down to 40% of the width at the tags generally failed in the span, and showed non-linear elongation before failure.

8.3.3 Main tests

Twenty-six test specimens were hand-made by the Author in batches of up to ten, using a steel template and craft knife to cut the PVB waists to shape, before attaching the steel tags. After testing, the tags were reused for the subsequent batch of specimens.

The first batch of test specimens, numbers 6 to 15, were made in the shape of a standard steel test specimen, 100mm long, which left only a 40mm length of PVB between the tags, and only a 20mm straight gauge length, as shown in Fig. 126. These tended to fail in the radiused shoulder of the PVB.

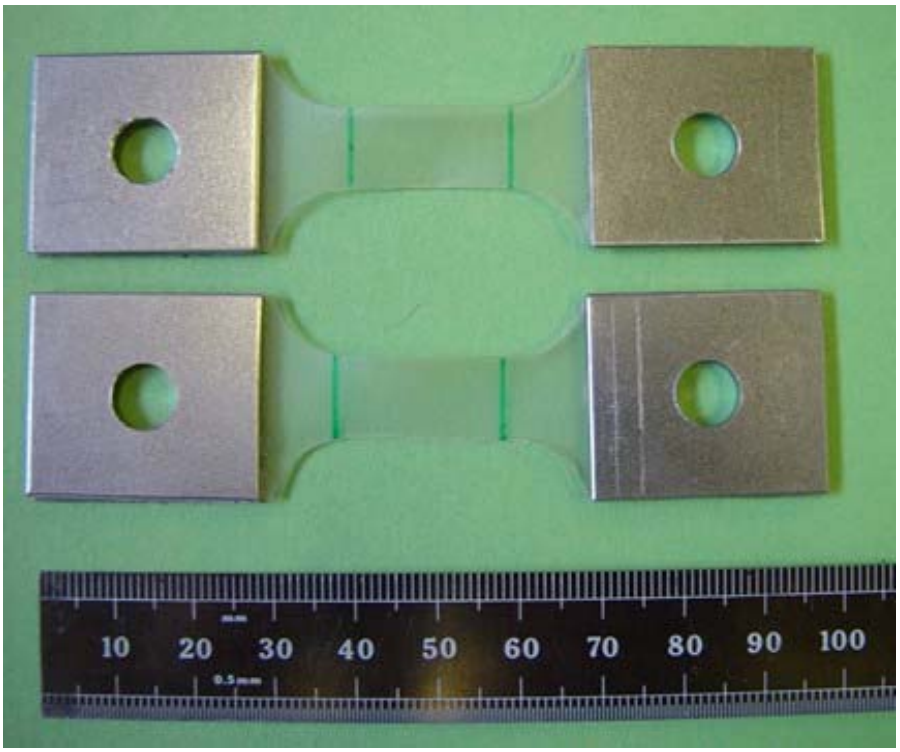

Figure 126. Typical test specimens from the first batch

A linear static plane stress finite element analysis of a quadrant of the test specimen, shown in Fig. 127, indicated that there was a stress concentration near the root of the curve, which suggested that yield should occur at that position initially, and that strains there would always be higher there than in the straight section, so that failure at that location was generally to be expected.

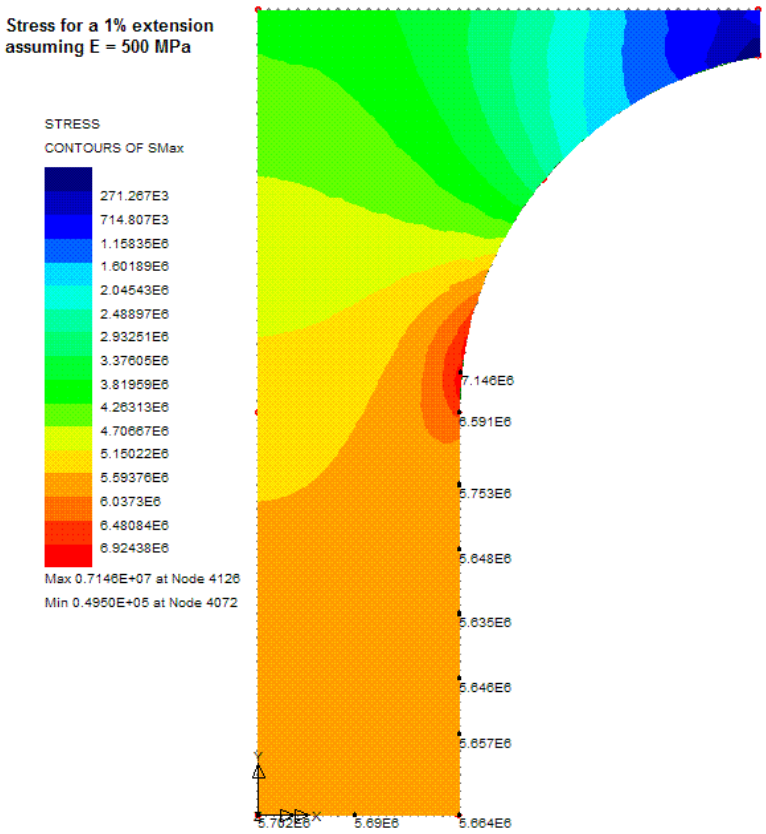

Figure 127. Elastic stress distribution in the first test specimen shape

The average stresses at the centre indicated that the sample was 1.137 as stiff as a rectangular specimen, and the peak stress was 1.257 times the average.

Following the first batch of testing, an alternative specimen shape was used for the remaining test samples, numbers 16 to 32. The revised specimen shape was an additional 10 mm longer to use the full capacity of the equipment, and had the tags shortened between the PVB and the hole, to leave a 60mm PVB length. The straight section remained 20mm long, but the radius of the shoulder was increased from 9 mm to 20 mm. A linear static plane stress finite element analysis of the revised shape is shown in Fig. 128.

The average stresses at the centre of this model indicated that the sample was 1.192 as stiff as a rectangular specimen, and the peak stress was 1.146 times the average. This reduced by almost 40% the stress concentration at the shoulder, but modifies the strain and the strain rate for a given velocity.

The data from these analyses allowed a first approximation of stress and strain to be drawn from the forces and extensions measured in the tests.

The tests were conducted over a range of impact velocities in three temperature ranges. Some tests were undertaken at room temperature, which was measured between 22ºC and 24ºC at the time of testing. Some tests were conducted with the specimen at a lower temperature, nominally 5ºC, while others were conducted with

the specimen at an elevated temperature, nominally 35ºC. In general, two specimens were tested at each velocity-temperature combination.

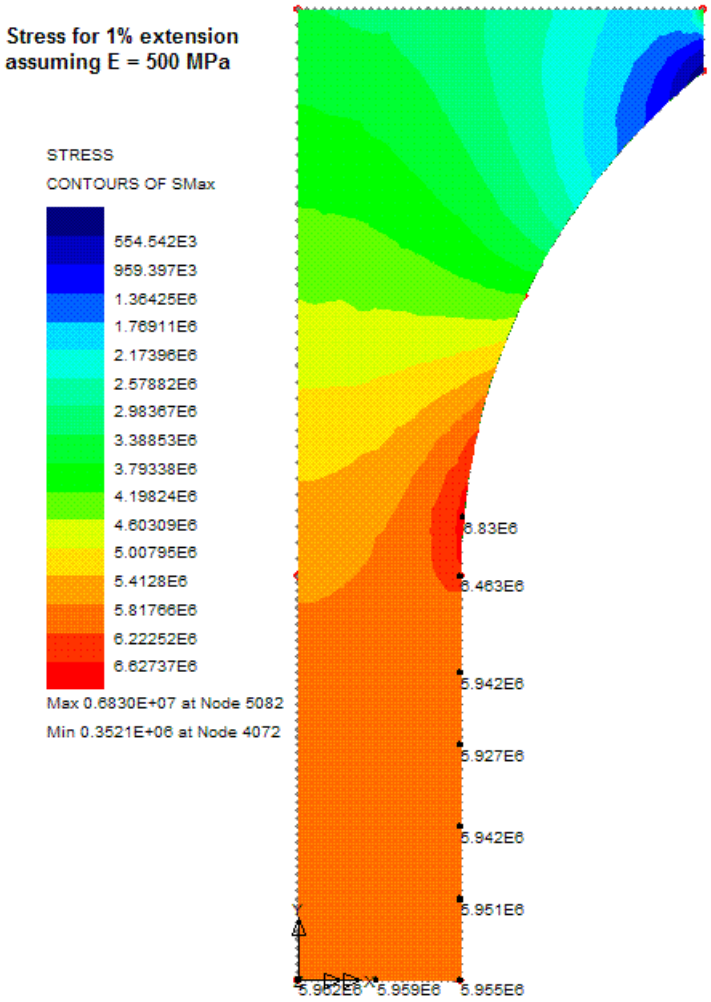

Figure 128. Elastic stress distribution in the second test specimen shape

The specimen temperatures were varied by binding a thermal pack around the specimen. The thermal packs had previously been conditioned in either a freezer or in hot water to a temperature beyond that required. The temperature of the specimen was measured with a contact thermocouple, bound inside the pack. Once the temperature was stabilised beyond the test temperature, and the equipment was ready for test, the thermal pack was removed, and the temperature of the sample was monitored with the thermocouple held in contact by hand. As the temperature approached the test temperature the thermocouple was withdrawn and the impact rig armed and triggered. The few seconds required after the thermocouple was removed meant that some anticipation and judgement was required to time the test, but following some preliminary timing trials it is felt that the tests were undertaken within +- 2ºC of the nominal temperature reading.

During the preparation for each test, the anvil block was supported from below to prevent the PVB from being stretched significantly by a quasi-static load, bearing in mind the viscoelastic nature of PVB and its potential to creep. However, the support

had to be removed before the test, so there was always a short period when the PVB was supporting the weight of the anvil block. This was not considered significant at room and lowered temperatures, but could have had a more significant effect on the results of the high temperature tests when the PVB was softer.

When the impact machine was triggered, the drop weight and forked striker were released, impacted the anvil and stretched the specimen to breaking. A reference load cell reading was taken at the start, and time, loadcell and drop weight position measured digitally. A digital record of these readings was stored covering a pre-selected duration from about 5 milliseconds before a significant rise in the loadcell reading. In some cases, the pre-selected period proved too short to capture the entire response to failure. In one case the start period was incorrectly set and the initial part of the record was lost, and in one case (Test 23) the equipment failed to record the data. The data records have been truncated to the point where the force becomes negative when the sample breaks and the load-cell rebounds.

8.3.4 Results of room temperature tests

The main tests undertaken at room temperature are listed in Table 43.

The measured velocity is the average velocity, calculated from the displacement divided by the time interval of the test record. The strain rate is calculated from the measured velocity by dividing by the PVB length of the sample between the faces of the tags, and multiplying by the appropriate stiffness factor calculated from the elastic analyses in Section 8.3.2. Although this is an accurate measure of the strain rate in the linear stages of the tests, it may be less representative of the actual strain rate as the material becomes non-linear and the strain distributions vary. In any case, this always represents engineering strain rates rather than true strain rates.

Test no	Sample type	Nominal velocity	Measured velocity	Strain Rate	Comments
		m/s	m/s	/s	
22	2	1.83	1.69	33.5	Failed in straight
16	2	1.85	1.778	35.3	Data ends early. Failed at shoulder
17	2	1.8	1.78	35.4	Failed in shoulder
6	1	1.5	1.44.	40.9	Data ends early.
19	2	3.72	3.49	69.4	Failed in straight
18	2	3.72	3.57	71.0	Failed in shoulder
8	1	6	4.69	133	
7	1	6	5.66	161	
23	2	7.5			No data record, but video
24	2	15	14.0	278	

Table 43. Room temperature PVB tests at Shrivenham

The average stress history for each test has been taken as the force history measured at the load cell, divided by the initial area of the straight length of the specimen, a

measure of engineering stress. This does not include the quasi-static stress from the weight of the anvil, of about 1.3 MPa. The average strain history has been taken as the elongation divided by the PVB length between metal tags, and multiplied by the stiffness factor, which gives a measure of the engineering strain in the specimens. The results of the tests are shown in Figs. 129 to 131.

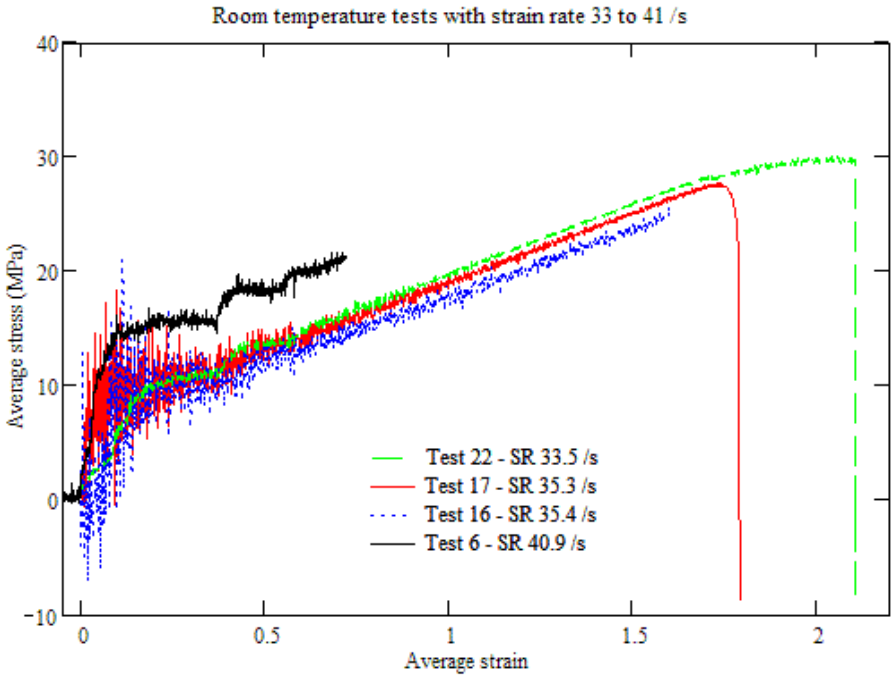

Figure 129. Engineering stress-strain relationship from room temperature tests at lower strain rates.

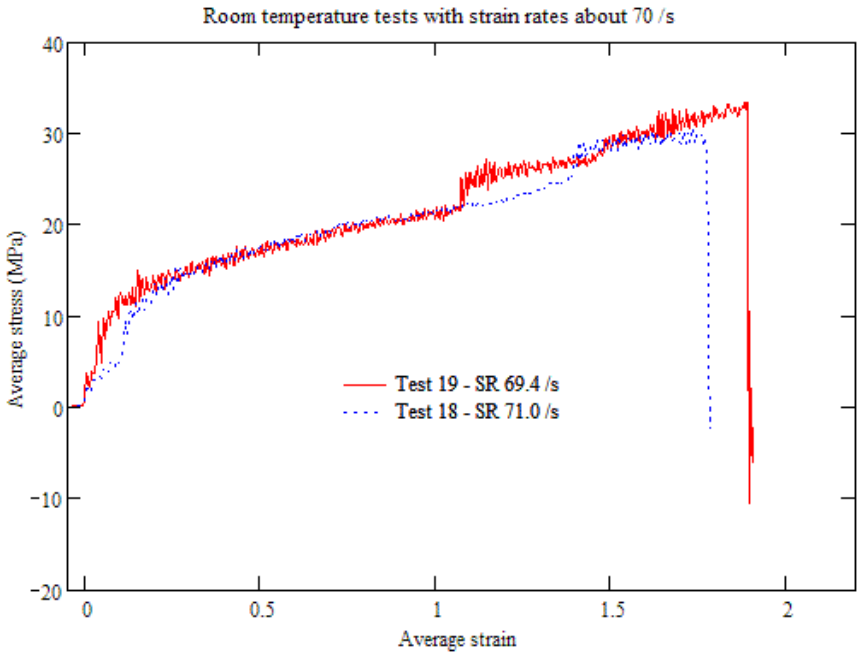

Figure 130. Stress-strain relationship from room temperature tests at strain rates about 70 /s

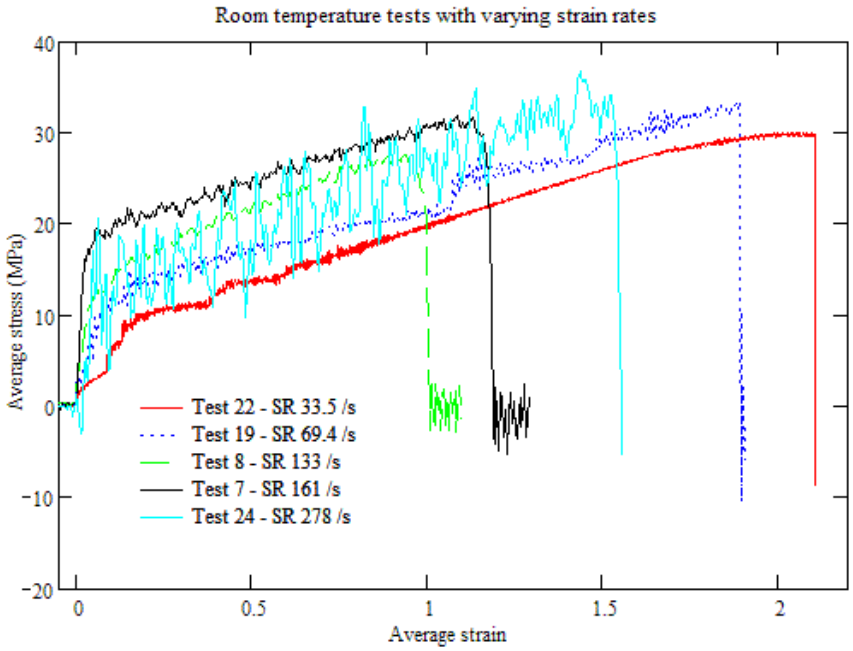

Figure 131. Stress-strain relationship from room temperature tests at varying strain rates

The room temperature tests showed engineering failure strains up to approximately 2.0 at the lower strain rates, and in excess of 1.0 for all tests, but failure stresses far lower than the linear viscoelastic analysis shown in Fig. 118. Even if the viscoelastic analysis is taken as an analysis of true stress and strain, the test results can be compared to it by converting them to true stress and strain terms using the relationships:

$$\sigma_T = (1 + \varepsilon_E) \cdot \sigma_E \tag{57}$$

$$\varepsilon_T = \ln(1 + \varepsilon_E) \tag{58}$$

where σ is stress, ε is strain and E and T subscripts indicate engineering and true respectively.

At the lowest stain rates, where the discrepancy is smallest, Fig. 132 shows that, even in true stress terms, the test specimens are substantially less stiff than the linear viscoelastic model.

This appears to arise from an abrupt and substantial transition in stiffness at a stress level varying between about 10 MPa and 20 MPa, and increasing with strain rate. The initial gradients appear to be of a similar order to the linear viscoelastic stiffness, but after the transition point the stiffness reduces by about an order of magnitude. In engineering stress and strain terms, this non-linear stress-strain relationship was approximately bilinear, similar to an elastic-plastic relationship with strain hardening observed in many metals. However, the deformation was viscoelastic rather than plastic; the broken specimens returned to their original shape after they were no longer loaded.

The results show that tests at similar strain rate on similar test specimens give very similar looking results, particularly for the transition stress analogous to yield stress, and for the hardening gradient. The initial "elastic" stiffness is more variable, as is the failure strain.

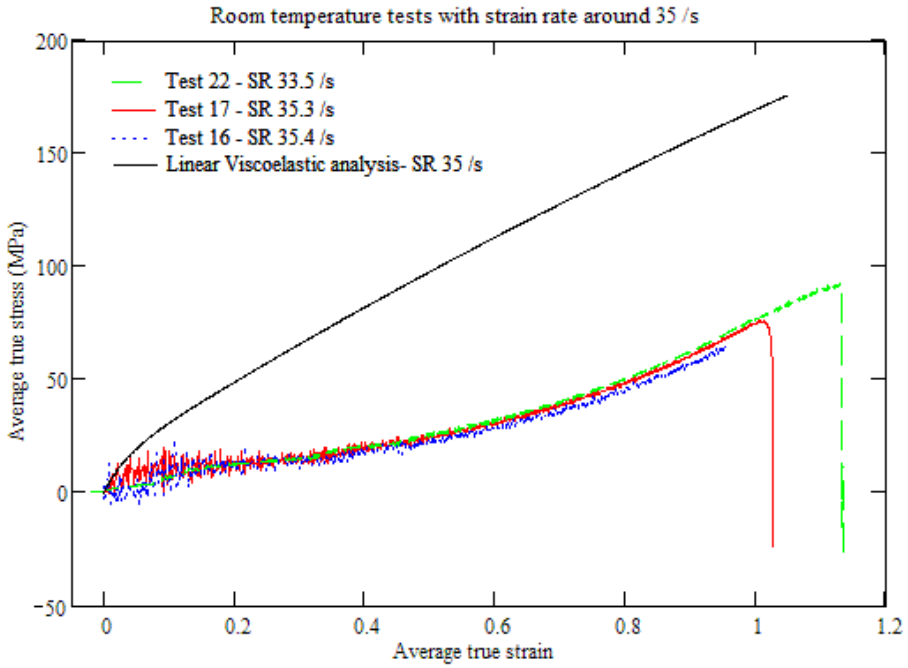

Figure 132. True stress-strain relationship from room temperature tests at lower strain rates, with a corresponding viscoelastic analysis.

High speed video of tests shows that failure tends to initiate at the side of the sample, usually in the zone of stress concentration shown in the elastic analysis. With non-linear deformation with strain hardening, this will still be the location of maximum stress, and will also be the area of highest strain. However, the test samples were hand cut, and the performance of PVB at the cut edge will be dependant on the smoothness of the curve at this location. Raggedness or notches in the edge of the sample at this location could cause premature failure. It is likely that the upper bound failure strains are more realistic representations of the performance in the interior of a sheet of PVB.

For a given sample type, there is a trend with increasing strain rate for a higher elastic stiffness and 'yield stress' and a lower failure strain, but a similar 'hardening stiffness'. The shorter sample shape 1, with the tighter radius, appears to be relatively stiffer and stronger than sample shape 2 for the same strain rate, and is less ductile, with a lower failure strain.

The difference in failure strain could be a result of the greater stress concentration at the shoulder in sample shape 1, but the greater elastic stiffness and strength are harder to explain. It is possible that the elastic stiffness calculation is sensitive to the response of the equipment, and that testing different length samples at different velocities will give a different degree of bounce in the equipment. There was a change to the striker to introduce a vibration damper, but this did not occur until after Test 22. It is difficult to draw firm conclusions on this with only one or two tests at any velocity.

8.3.5 Results of tests at reduced temperature

The main tests undertaken at a nominal temperature of 5ºC are listed in Table 44.

Test No	Sample type	Nominal Velocity	Measured velocity	Strain Rate	Comments
		m/s	m/s	/s	
11	1	1.5	1.25	36.0	Data ends early
9	1	1.5	1.27	36.2	Data starts late
10	1	1.5	1.32	37.4	
21	2	3.66	3.40	67.5	Failed in shoulder
20	2	3.72	3.51	69.8	Failed in shoulder
13	1	6	5.58	159	
12	1	6	5.60	159	
14	1	12	11.4	324	
15	1	12	11.4	325	

Table 44. PVB tests at Shrivenham at a nominal temperature of 5ºC

The results of the tests are shown in Figs. 133 and 134.

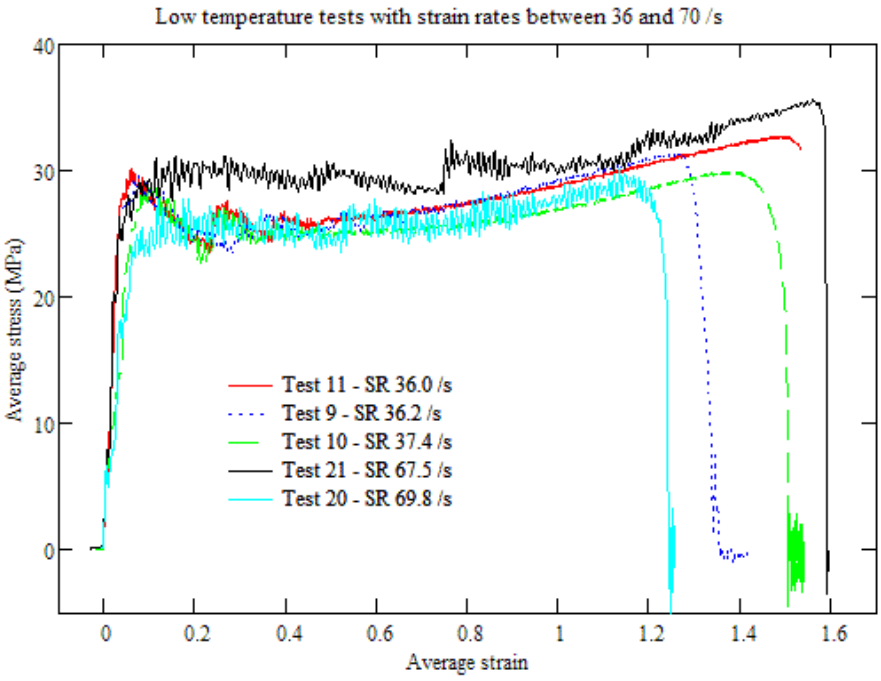

Figure 133. Stress-strain relationship from tests at 5ºC and strain rates up to 70 /s

The stress-strain relationships at strain rates of 36 /s to 70 /s shown in Fig. 133 are very similar, and with the stiffness, strength and failure stress at a strain rate of 36-38 /s enveloped by the properties at a strain rate of 67-70 /s, any variations appear to be random rather than systematic.

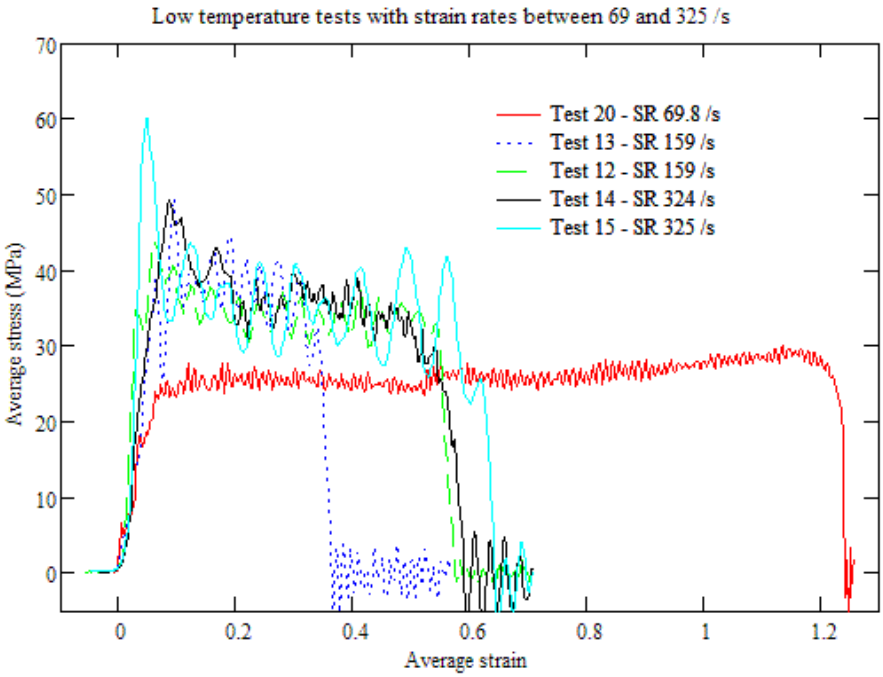

Figure 134. Stress-strain relationship from tests at 5ºC and strain rates from 70 /s

Again, it is not possible to distinguish the results at strain rates of 159 /s from those at 324-325 /s in Fig. 134. However they are significantly different from those at 70 /s and below, being stiffer, stronger and less ductile. There appears to be a step change in material properties between strain rates of 70 /s and 159 /s.

The small difference between the initial gradients is consistent with the linear viscoelastic analysis shown in Fig. 120, where the stiffness is not very sensitive to strain rate at low temperatures. The experimental variability and randomness from a few tests may conceal such a small systematic variation. However, the non-linear change that occurs between about 25 MPa and 40 MPa is similar in nature as that observed at room temperature, but is more severe.

There does appear to be a consistent trend in the hardening gradient. The apparent gradient in engineering stress – engineering strain terms is shallow but positive at 36-37 /s, shallower at 67-70 /s, shallow negative at 159 /s and more steeply negative at 324-325 /s. However, it should be noted that when the stresses and strains are transformed from engineering stress and strain format to true stress and strain format, even the apparent softenings turn out to represent marginal material hardening, as shown in Fig. 135.

Even this is likely to underestimate the true material hardening. The non-linear analyses in Section 8.4 show that for small hardening gradients, plastic strains tend to be more concentrated in the centre of the specimen than the elastic strain distribution. This will mean that the true local material hardening will be higher. This is illustrated

hypothetically in Fig. 136 if the local material engineering strains are assumed to be twice the average elastic values in Fig. 134.

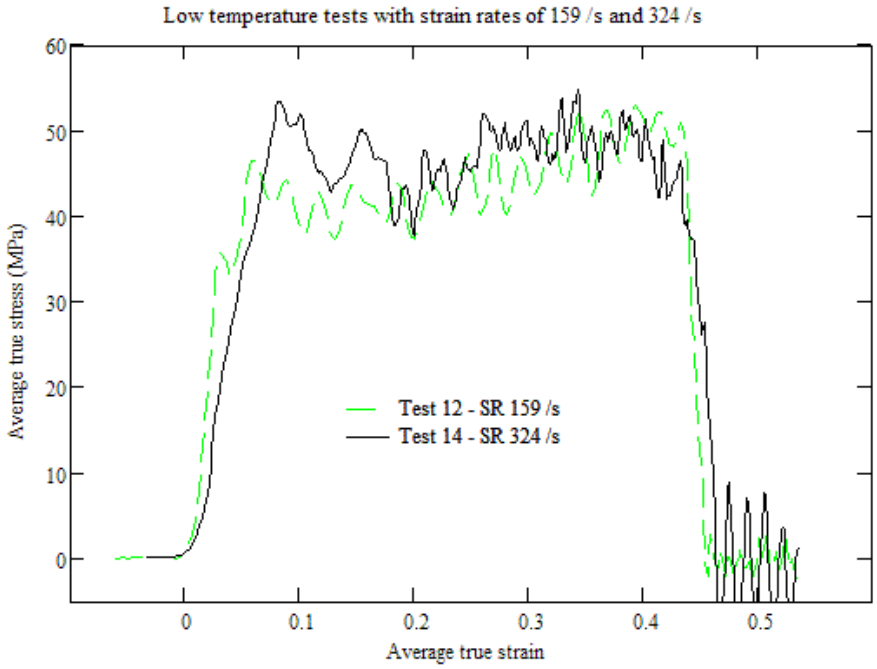

Figure 135. Average true stress – true strain relationship for tests 12 and 14

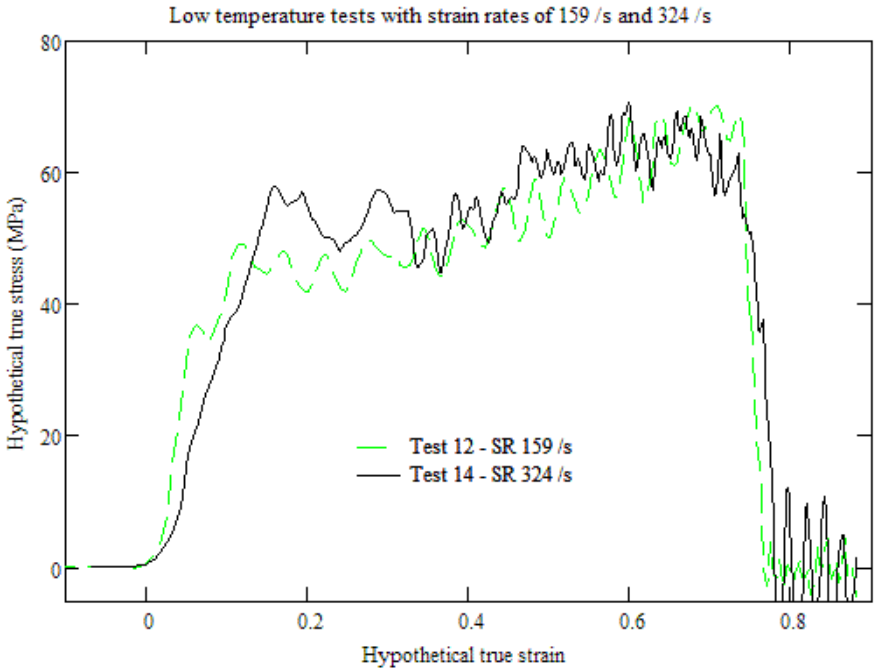

Figure 136. Hypothetical true stress – true strain relationship for tests 12 and 14 with local engineering strains twice the average

The failure strain in Test 13, at a strain rate of 159 /s, was substantially lower than those in the three other tests at similar or higher strain rates. This is more evidence that some premature failures could occur due to flaws in preparation of the test

samples, and that the true failure strain of PVB sheet can be expected to be similar to the upper bound values.

The anvil with the attached lower section of the sample dropped to the base of the testing machine after the sample failed, and could be observed closely. In several samples when the sample failed in the top shoulder, the viscoelastic recovery of the stretched middle sections was observed. The samples shortened visibly to their original proportions over a period of around three seconds.

8.3.6 Results of tests at elevated temperature

The main tests undertaken at a nominal temperature of 35ºC are listed in Table 45.

Test No	Sample type	Nominal Velocity	Measured velocity	Strain Rate	Comments
		m/s	m/s	/s	
32	2	1.875	1.81	36.0	Failed in shoulder
31	2	1.875	1.82	36.1	Data ends early. Failed in shoulder
29	2	3.75	3.37	66.9	
30	2	3.75	3.40	67.6	
27	2	7.5	7.14	142	Failed in shoulder
28	2	7.5	7.27	144	Failed in straight
26	2	15	14.0	278	Failed in straight
25	2	15	14.0	279	Failed in shoulder

Table 45. PVB tests at Shrivenham at a nominal temperature of 5ºC

The results of the tests are shown in Figs. 137 and 138.

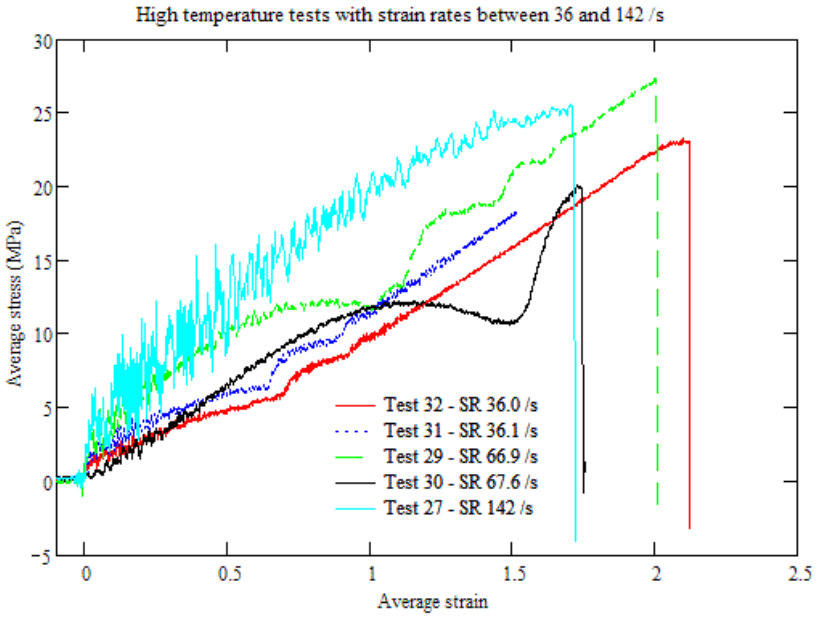

Figure 137. Stress-strain relationship from tests at 35ºC and strain rates up to 142 /s

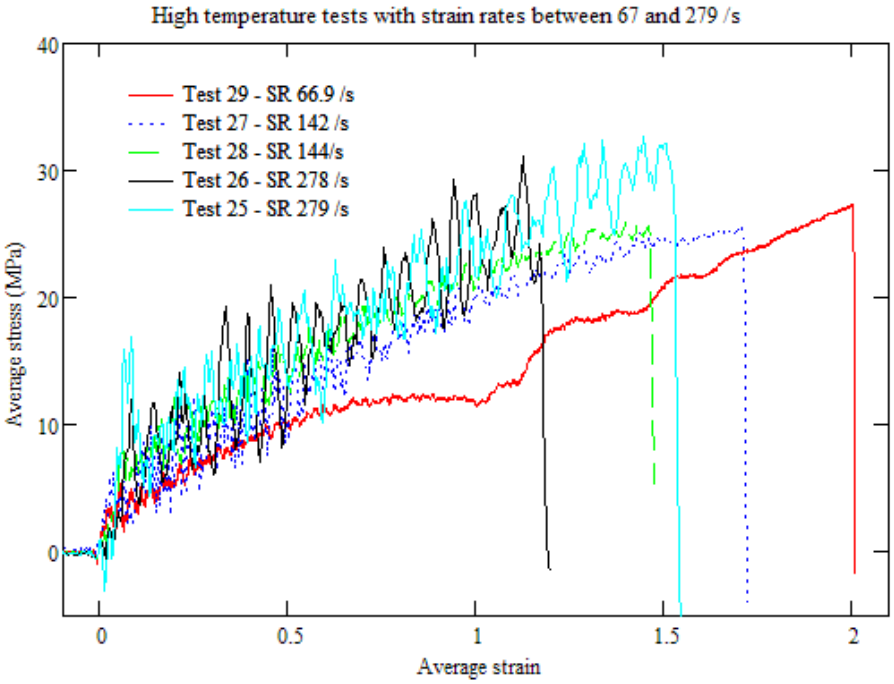

Figure 138. Stress-strain relationship from tests at 35ºC and strain rates from 67 /s

At high temperatures the stress-strain relationships are much closer to the relationships calculated from the linear viscoelastic analysis in Section 8.2 and shown in Fig. 122, in amplitude if not in shape. The test results are therefore shown against linear viscoelastic analysis results for similar strain rates and a temperature of 35ºC in Figs. 139-142.

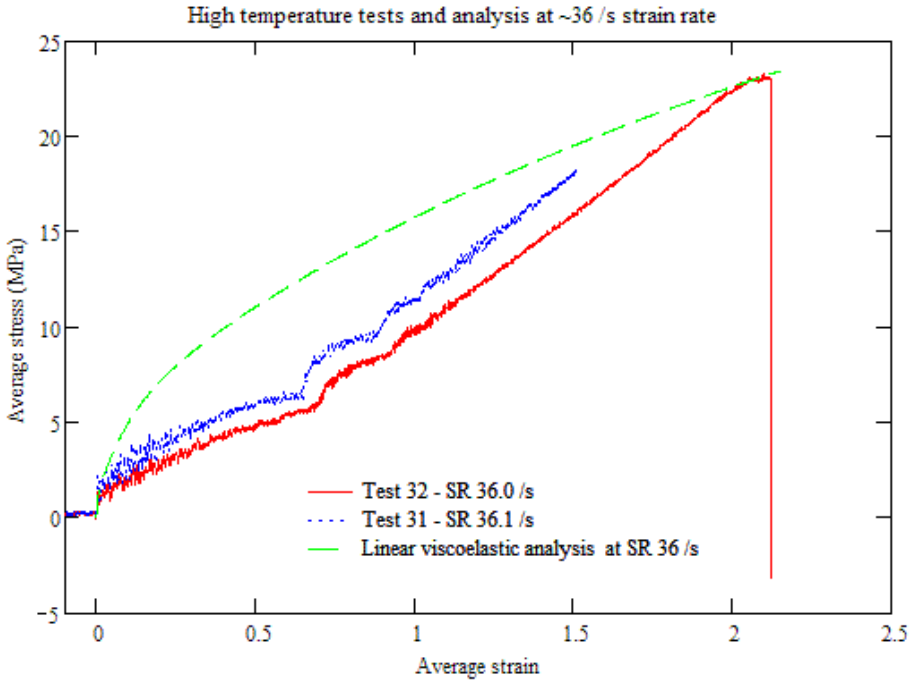

Figure 139. High temperature tests at a strain rate of 36 /s, with a viscoelastic analysis taken to be in engineering stress & strain terms

Because the linear viscoelastic properties were defined from small strain data, the question of whether they represented engineering stress and strain or true stress and strain was academic, as the measurable difference would have been negligible. However, it becomes critical to the interpretation of the analysis of large strain test results.

At a strain rate of 36 /s, the high temperature tests in Fig. 139 show a very short initially stiff stage that appears to be consistent with linear viscoelasticity, and then a transition to a reduced stiffness, as at lower temperatures. However, the hardening gradient is proportionally steeper than at low temperatures, and beyond a strain of about 0.7 a further rubber-type non-linear hardening occurs. In contrast, if the linear viscoelastic analysis is taken as engineering stresses and strains, this shows greater softening than at lower temperatures, so the two reach a similar stress at the failure strain.

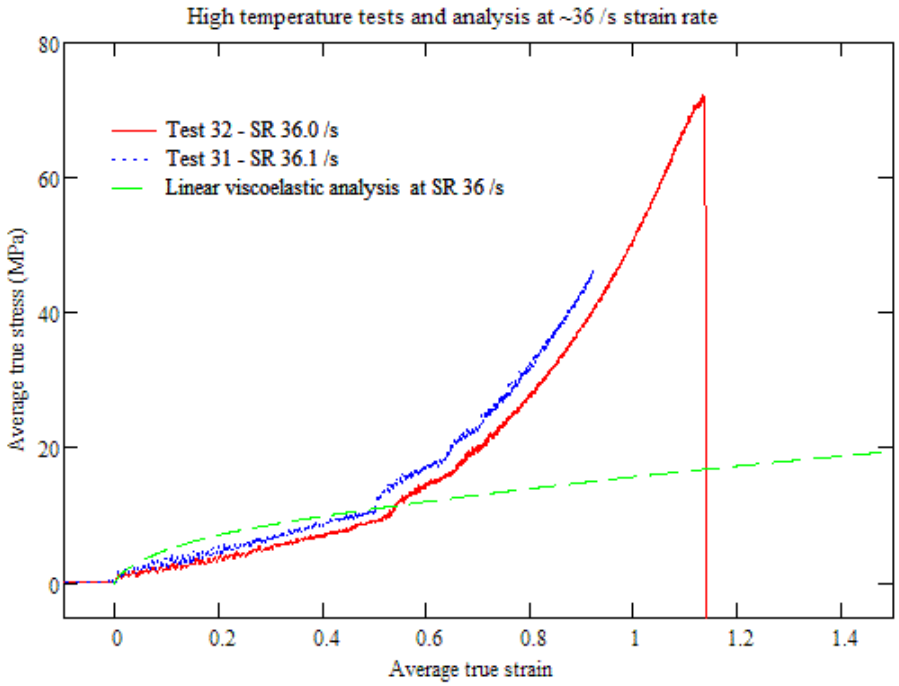

Figure 140. High temperature tests at a strain rate of 36 /s, with a viscoelastic analysis taken to be in true stress & strain terms

The interpretation is different if the viscoelastic stresses and strains from the analysis are taken to be equivalent to true stresses and strains, as in Fig. 140. The transition still causes the test curve to be softer than the linear viscoelastic curve, but greater hardening of the true strains means that they are of a similar magnitude at a true strain of around 0.5 to 0.6. The rubber like hardening of the PVB thereafter shows a large increase over the viscoelastic curve, to around a factor of four at failure.

With the exception of Test 30, which gives an anomalous trace, increasing strain rate shows the viscoelastic model increasing in stiffness faster than the test results, so that a comparison shows the tests becoming progressively softer than the viscoelastic model, with the engineering stress at failure of the order half the viscoelastic stress for a strain rate of 278 /s, as shown in Fig. 141. However, if the true stress and strains

are compared with the viscoelastic model the stress at failure is of the order twice the viscoelastic stress, as shown in Fig.142.

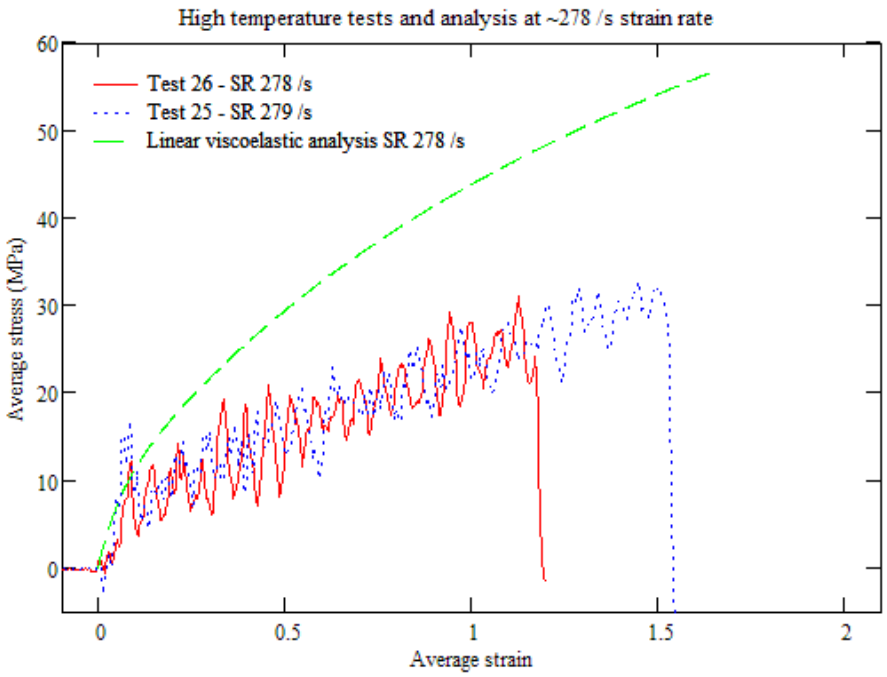

Figure 141. High temperature tests at a strain rate of 278 /s, with a viscoelastic analysis taken to be in engineering stress & strain terms

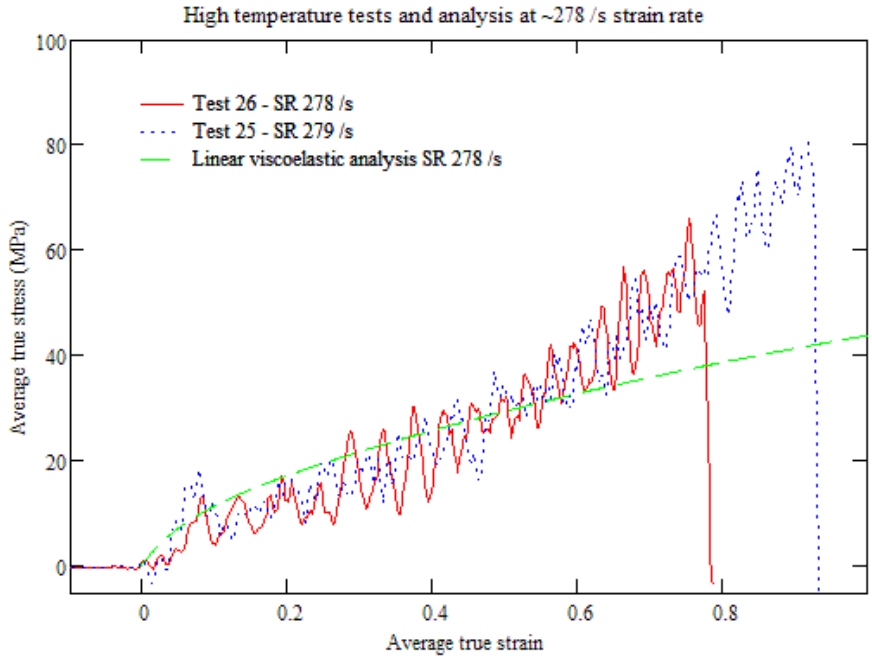

Figure 142. High temperature tests at a strain rate of 278 /s, with a viscoelastic analysis taken to be in true stress & strain terms

At elevated temperature, the failure strains appeared to be broadly similar to those at room temperature, although the absolute value will be different depending on whether it is expressed in terms of engineering or true strain.

8.3.7 Observations from PVB tensile tests

The results of the tests show a marked viscoelastic effect in the large strain and large strain-rate response of PVB. However the pattern is not consistent with the expectations for linear viscoelasticity, as shown in Section 8.2.

When PVB is stretched there is an initial stiff stage, where the behaviour of the PVB is generally compatible with the linear viscoelastic analysis, i.e. increasing in stiffness with reduction in temperature and increase in strain rate, and with greater sensitivity to strain rate at higher temperatures. As the curvature of this stage in the analysis is not great, this could be modelled by a linear resistance. As the bounce of the test equipment is likely to be greatest at this stage, the average gradients of this stage in test results is likely to be variable; a secant Young's modulus from the viscoelastic analysis may be a more reliable guide to this stiffness.

In all of the tests there is an abrupt non-linear transition with a reduction in stiffness. This is analogous to yield in metals, but the mechanism is different and the material remains viscoelastic, as the additional deformation is gradually recoverable on unloading. The stress at which this transition occurs can be estimated from the test results from the trends either side, but bounce in the test equipment at this transition makes it difficult to simply pick a point on the trace. The trends in the transition stress are similar to those in the initial stiffness, i.e. an increase with increased strain rate and reduced temperature, but the effect is too irregular to say from these test results whether a constant transition strain would be a reasonable approximation.

The stiffness of the test specimens after the transition is analogous to strain hardening in metals. The overall reduction in stiffness means that real PVB will be consistently softer at large strains and high strain rates than the linear viscoelastic model based on small strain and small strain-rate material properties treated as engineering stress and strain.

If the viscoelastic model is taken to represent true stress and strain, the test specimens at room temperature and below are still consistently softer, although by a smaller margin. At 35ºC, the stiffness reduces below the model at the transition, but the greater softening of the viscoelastic model at high temperatures and the high and increasing strain hardening in the test specimens mean that the curves cross, and at high strains the measured stress is greater than the calculated value.

The shapes of the tested and measured stress-strain curves are so different that, even when the amplitudes occasionally coincide, the linear viscoelastic model is not a realistic representation of the behaviour of PVB in tension up to high strains.

The hardening gradients behave very differently than linear viscoelasticity, with lower hardening stiffness relative to the initial stiffness at lower temperatures and higher strain rates, and higher relative stiffness at higher temperatures and lower strain rates. One effect of this reverse pattern is to reduce the differences in the work

done to failure per unit volume of PVB (proportional to the area under the stress-strain curve), over the variations of strain rate and temperature.

Even in engineering stress-strain terms, some of the hardening curves show a gradual upwards curve or an upwards kink that is typical of a soft rubber non-linearity. This is more marked in true stress-strain terms, when the changing geometry does not dilute the effect.

There appear to be at least three trends at work:

- an initial viscoelastic curve
- an abrupt change in viscoelastic properties to a lower stiffness, with the degree of change generally contrary to linear viscoelasticity
- a gradual hardening at large strains, showing hyperelastic rubber non-linearity.

Although polymer models with both viscoelasticity and hyperelastic non-linearity have been developed for use in some finite element packages [101-104], it should be noted that the abrupt changes in gradient are not easily represented by a gradual non-linear material model such as the Ogden material model, often used to model rubber hyperelasticity, and will need a high order Ogden model to even approximate the transition.

Ref. 103 and Fig. 44 showed the inaccuracy at different strain rates of the DYNA model (similar to that used in Refs. 101 and 102) without non-linearity in each stiffness term of the Generalised Maxwell viscoelastic mode. However, the local inaccuracy of the PANDAS curves in Fig.44 at lower strains illustrates the limitations of low order non-linearity when modelling a smooth transition, let alone an abrupt one.

A complete and accurate non-linear viscoelastic model of PVB is likely to require a sixth order or higher Ogden non-linear term in each Maxwell element of a Generalised Maxwell model. The amount of data required to create the model would be very large, and could vary between different makes of PVB. This model could only be used in a finite element analysis, and the large number of variables would make this impractical to simplify for SDOF analysis of PVB membranes.

An alternative to such a complex model would be to approximate the material stress-strain curve to a bilinear, or at most trilinear, curve with a von Mises yield criterion. This will give a simple idealised model with only a few parameters which will vary with the strain rate and temperature. These parameters could be derived from tensile tests at various strain rates and temperatures, and could be used to calculate membrane resistance curves suitable for interpolation. This approach is similar to that used in Ref. 104 for some polymers.

It is expected that an analysis using a bilinear material in engineering stress-strain terms will model the force deflection behaviour in the test better than a bilinear material in true stress-strain terms, which will tend to show softening in the force-deflection curve at high strains.

The PVB used for the Shrivenham tensile tests was uncured PVB sheet, as supplied by the manufacturer. When incorporated into laminated glass, this material is subjected to a combination of heat and pressure in the laminating autoclave, which has been observed to change its appearance from translucent to transparent. It is likely that some change in physical properties will also occur, so although the Shrivenham tests are indicative, properties measured from the test data will still not be representative of PVB interlayers in laminated glass.

8.4 Tensile tests at Imperial College

8.4.1 Test equipment

In October and November 2004, Permasteelisa organised high rate of strain testing of PVB samples at the Mechanical Engineering laboratories of Imperial College, London, to obtain material properties of PVB to be used in analysis and design. The Author [134] participated in the testing and analysed the results for Permasteelisa.

The samples were tested in a 20 kN Instron VHS high-rate servo-hydraulic testing machine, shown in Figs. 143 and 144, whose actuator moves upwards under the control of rapid-acting hydraulic rams mounted on an adjustable crosshead, with the hydraulic fluid pressurised by compressed air. The Instron actuator was fitted with a lost motion device to allow some initial motion in an acceleration stage so that the sample is tested when the actuator is moving at a constant velocity. The device was fitted with a single 1mm thick rubber washer for minimum damping and bounce, while still eliminating ringing due to impact.

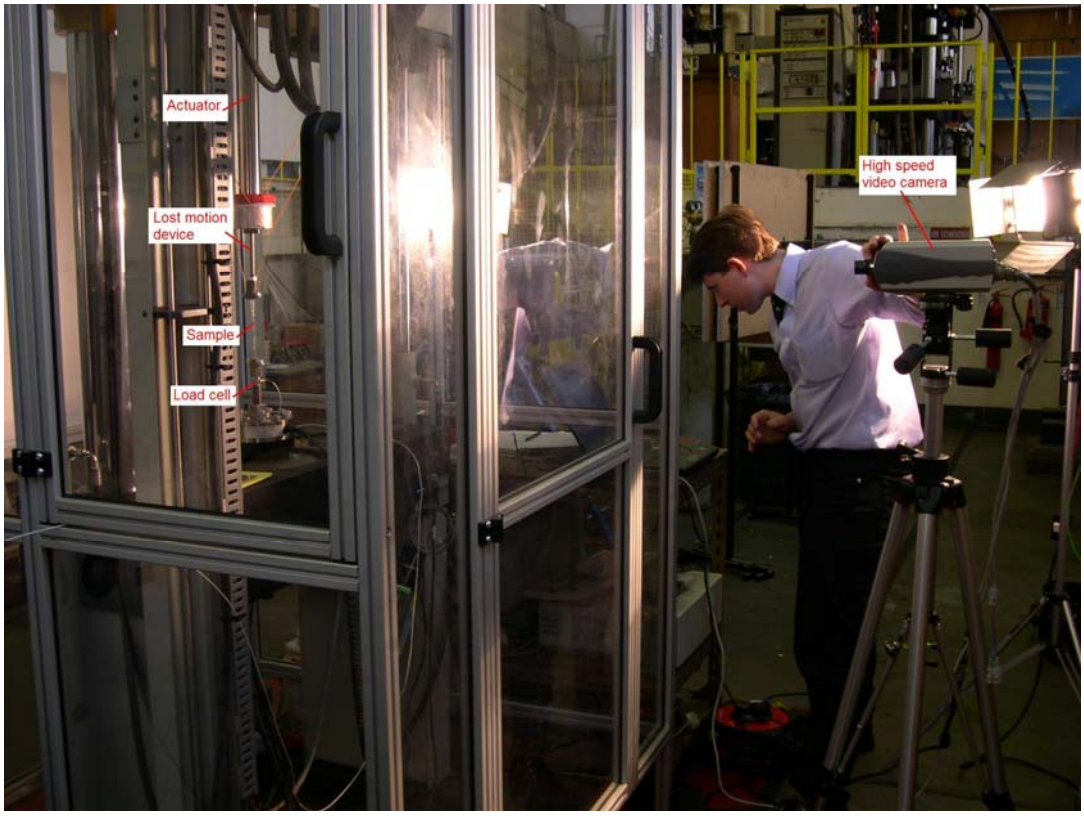

Figure 143. Inston test actuator and safety cubicle, with video equipment

Forces in the PVB samples were measured using a PCB Inc. piezoelectric loadcell of nominal 2.2 kN capacity, connected to a PCB amplifier and mounted at the static mount of the test machine. The manufacturer's calibrations for the load cell were used

to calculate the forces. These are checked at intervals and have been found to be accurate and consistent within about 1-2%.

Displacement was measured using the Instron machine's built-in 400 mm travel displacement transducer, which measures the position of the actuator. Ram velocity was evaluated at the time of test using the Instron's internal recorder, and valve settings were adjusted in dry runs and preliminary tests to obtain velocities appropriate for the tests. With the displacement of the actuator during acceleration until the lost motion device made contact, and the displacement during deceleration, the useful travel of the test machine at constant velocity was between 200mm and 250mm, substantially greater than the useful range of the Imatek machine at Shrivenham.

The forces and displacements were recorded on a Nicolet Sigma 60 Digital Oscilloscope Workstation. This is a 4-channel digital transient recorder set to record 10 bit resolution at up to 870 kHz. For most tests one channel recorded the displacement transducer and two channels recorded the loadcell voltage, with the channels displayed on the oscilloscope screen at different scales. This ensured at least one force trace at a good resolution, while avoiding the risk of an unexpectedly high signal being 'clipped' at the maximum scale voltage for the screen.

The digital data was saved as fixed length text files of voltage on each channel at fixed sampling intervals after the trigger signal. The recorder was set to trigger at a displacement reading shortly before the lost motion device bottomed out and the pull of the sample commenced.

For tests at room temperature, the test area was left exposed apart from the safety cubicle. Some room temperature tests were filmed with high speed video through the safety cubicle, using a Phantom IV high speed video camera with a Pentax C-mount lens at f2.0, shown in Fig. 143. Frames were composed of 512 pixels high by 128 pixels width, and were recorded at 1000 frames per second (fps) for 1 m/s and 2 m/s tests, at 2000 fps for 4 m/s tests and at 3000 fps for 8 m/s tests. The video data was converted to .AVI digital video files set to play back at 10 fps.

For tests at elevated and reduced temperatures, an Instron-SFL thermal chamber was fitted around the test area of the test machine, as shown in Fig. 144. Electrical heating was used to elevate temperatures above ambient, and liquid nitrogen from a vacuum flask was used to depress temperatures below ambient, under control of a thermostat built into the chamber structure.

The thermal chamber was designed to function over a range of -150ºC to +600ºC, a much wider range of temperature than that used for these PVB tests. Although the built-in thermostat read to 1ºC, there was generally a range of several degrees within which fine adjustment was difficult.

A separate thermocouple reading to 0.1ºC was used to measure the air temperature adjacent to the lower sample grip within the chamber. The thermocouples were generally in agreement at constant temperature, but the chamber thermostat responded slower to changes, presumably to avoid over-sensitivity in the oven controls.

The presence of the chamber prevented video of tests at elevated or reduced temperatures being recorded, because of the limited lighting in the thermal chamber and the poor visibility through the multi-layered thermal window in the chamber door.

Figure 144. Test equipment with thermal chamber in place around actuator

8.4.2 Test specimens

Advantage was taken of the larger travel available in the testing equipment to test larger specimens. A specimen with an overall length of 150 mm was chosen. This was a standard ISO specimen type (type 1B) for low strain-rate testing of plastics films or sheet [135].

Between 20mm by 22.5mm end tags, a 115mm long central section of PVB tapered down in a radiused curve from 20mm width at the tags to 10mm uniform width over a central gauge length of 60mm, giving a waist that was 50% of the width at the tags. After the specimens were cut to shape by hand against a steel template, the tags were glued in position and the tag ends were drilled with a 6mm diameter hole for attachment to the test equipment. The specimen shape is illustrated in Fig. 145.

This gives a substantially larger radius in the shoulder, and a correspondingly smaller stress concentration where the shoulder meets the straight than the previous specimens, but a higher stress concentration at the tags. However, the reduced waisting compared to the Shrivenham samples increased the risk of failure occurring at the stress concentration at the tags.

The test specimens were cut from 0.76 mm thick PVB sheet, as for the Shrivenham tests. However, as well as uncured PVB sheet, Permasteelisa had arranged for a PVB sheet to be laminated using glass sheets treated to prevent the normal glass-PVB bond forming, so that the laminations could be separated afterwards and an undamaged sheet of cured PVB was obtained and made into test specimens. In addition to being transparent rather than translucent, these specimens were noticeably more flexible than the uncured specimens, indicating a modification of the physical properties.

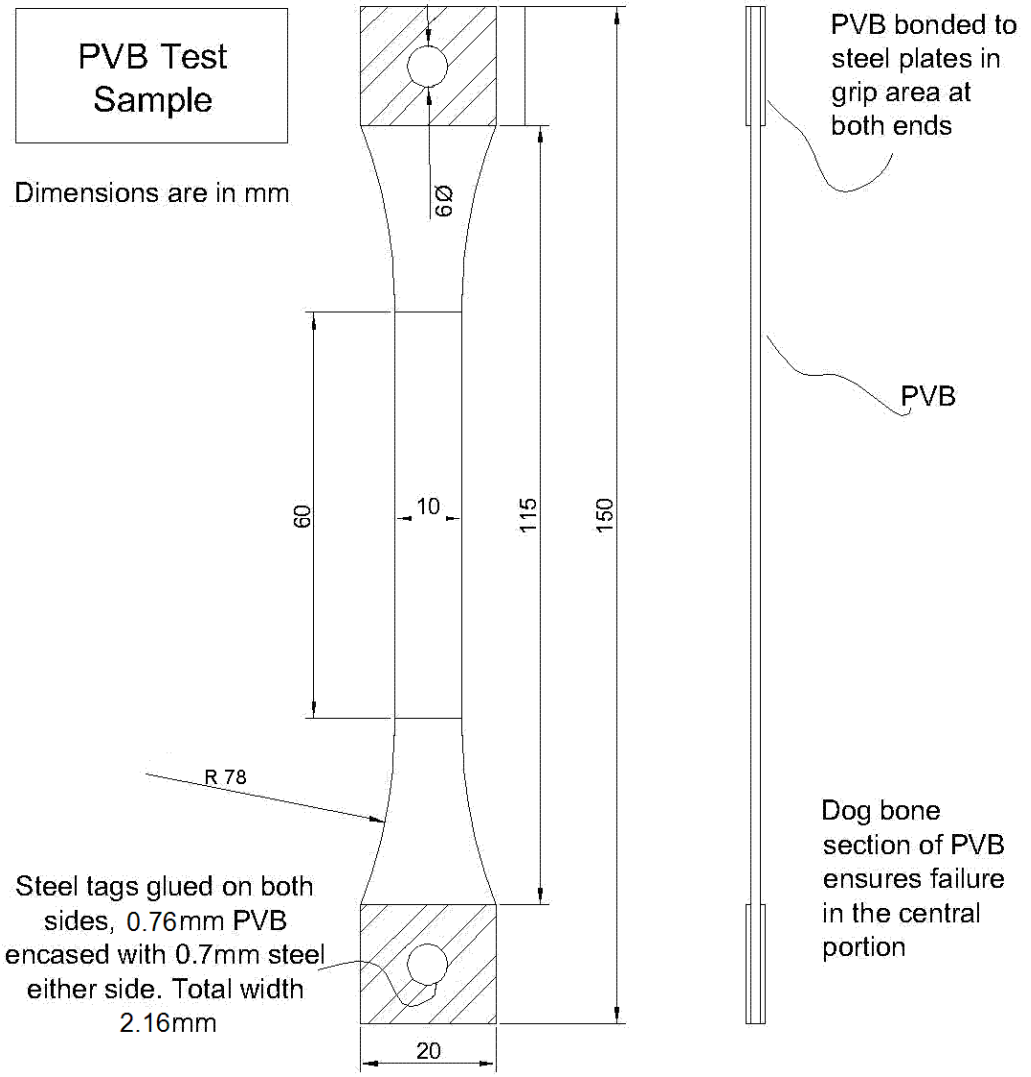

Figure 145. Details of PVB specimens tested at Imperial College

8.4.3 Test procedures

So far as they were applicable for high strain rate testing, the ISO general principals for low strain rate testing of plastics [136] were applied to these tests. The most critical of these principles was that a minimum of five specimens should be tested for each case considered.

From back-analysis of blast trials and SDOF analyses of glazing, the higher strain rates tested at Shrivenham are likely only to occur in laminated glass that is being overwhelmed by a blast loading, and which is certain to fail. Typical average strain

rates for laminated glass membranes that are predicted to just survive are expected to be of the order 10 /s – 20 /s. As a result, tests at velocities of 1 m/s, 2 m/s, 4 m/s and 8 m/s were chosen to give strain rates between about 10 /s and 80 /s.

Five specimens of the cured PVB were tested at each loading velocity at room temperature (22ºC) and at 5ºC and 35ºC, in addition to some preliminary tests. There were only sufficient test specimens of uncured PVB prepared for three or four to be tested at each velocity at room temperature only.

The machine cross-head was initially adjusted to give about 50 mm of pre-travel of the actuator before loading the sample, about 250 mm of extension at a fixed velocity, and about 100mm of end travel at a reduced velocity. For tests at 8 m/s velocity the pre-travel was increased to 100 mm, with extension reduced to about 200 mm. Most test samples failed before the reduction in the actuator velocity. One of the two that did not was videoed, and showed a jerky motion of the lost motion device that explained the data trace on this and the other similar test. This might introduce some error into the failure load and associated displacement of a few specimens, but would not affect the main properties of interest.

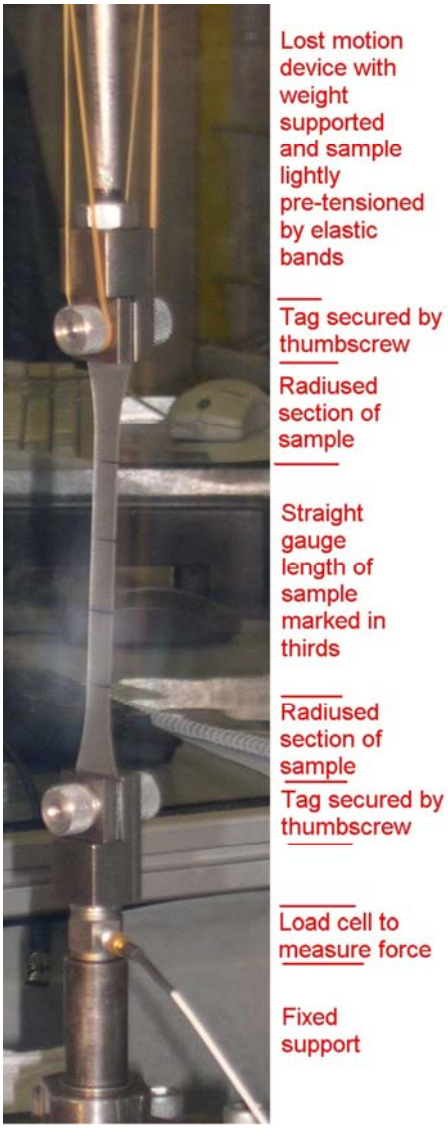

Figure 146. PVB test sample in testing rig

The PVB specimens were secured between the 2.2 kN load cell at the fixed support and the lost motion device connected to the actuator, using titanium grips with thumbwheel screw clamps through the holes in the sample tabs, as shown in Fig. 146. The use of lightweight grips & fixings was important to minimise inertial effects in the equipment given the light sample weight, and the fittings used were fabricated specifically for these tests.

As the PVB specimens had no compressive strength and were unable to support the weight of the lost motion device and the upper grip, two rubber bands were used to support this mass and to lightly tension the specimens to avoid any snatch of the specimens on load take-up. The rubber bands were suspended from sagging wires supported from fixed points of the testing rig or the thermal chamber. The sag in the wires allowed initial adjustment to achieve a suitable tension in the rubber bands, and allowed full deflection of the moving test head without risk of being restrained by projections catching on the wires. Preliminary tests without this pre-tensioning demonstrated that the effect of snatch in a slack specimen could obscure important features in the response.

The low mass and strength of the specimens resulted in negligible variation in the test velocity due to the presence of the PVB specimen from that found in dry runs. Variations in velocity that did occur were generally attributed to warming up of the machine with repeated use. Where a systematic variation appeared to be occurring, a small adjustment of the controls was made. Fresh dry runs were made for each new velocity setting, rather than relying on preliminary tests from previous sessions.

For each test, the gauge length of the specimen was marked and the specimen was secured in the grips and the screws tightened by hand, the elastic bands were fitted to the upper grip, and the safety door was closed.

The actuator was then taken to the start position, the rams switched to the high pressure hydraulic setting, the Instron taken through its start-up routine, the recorder armed and the Instron fired. A typical test is illustrated in Fig. 147 with selected frames from high speed video of the test, showing:

- Initial movement of the actuator
- Initial stretching of the specimen
- Final stretching of the specimen
- Recoil of the specimen after failure near the top.

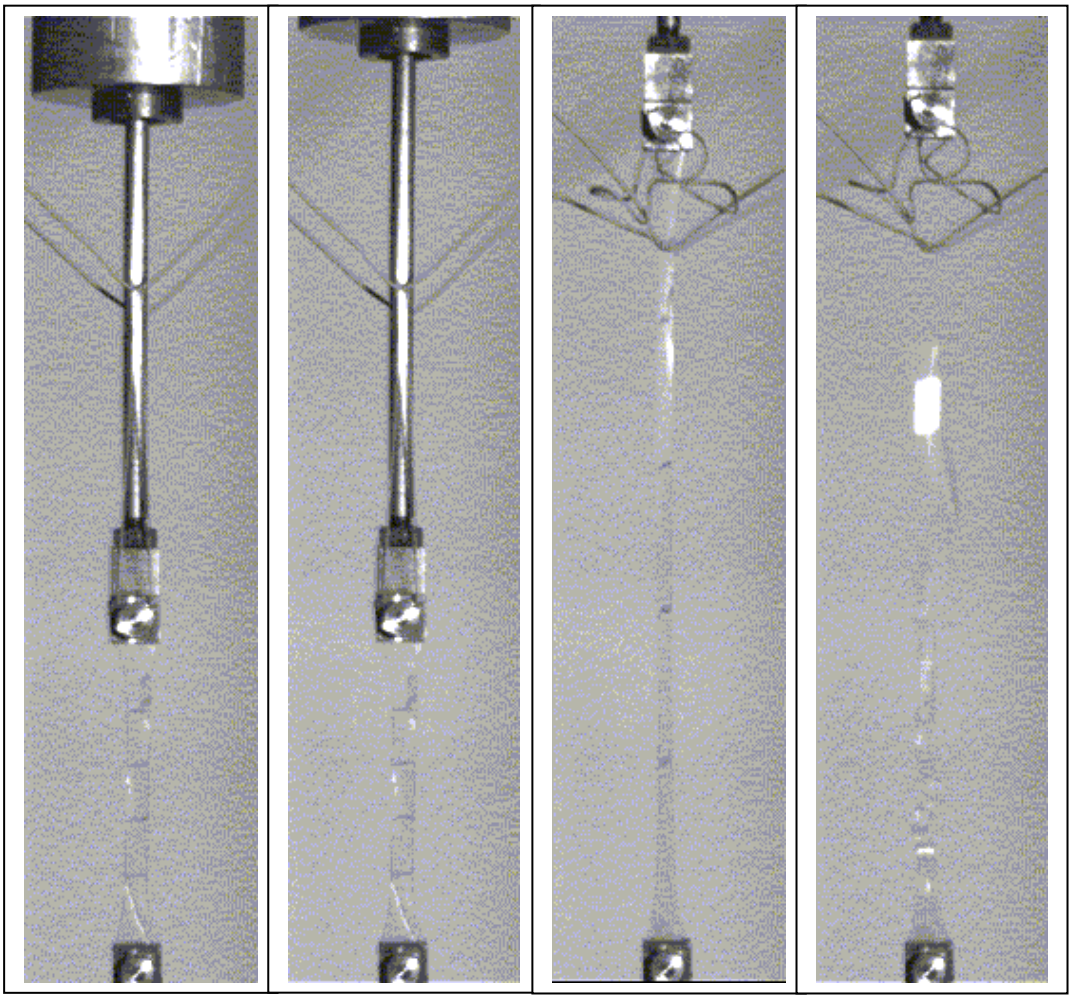

Figure 147. Selected frames from high speed video of a typical test

After each test, the velocity and the position of the failure were noted, and the sample number, matching the data file name was marked on the pieces. The tested samples were later photographed in batches. A typical batch is shown in Fig. 148.

The position of failure in the PVB showed some systematic differences due to sample construction and temperature, with de-bonding of the tags only for the uncured samples, end failure at the tab face more common at high temperature and failure in the gauge length more common at low temperature. There was a scatter of failures at both ends, but a bias towards failure at the top rather than the bottom that suggests that the weight and inertia of the sample had a minor but detectable effect on the stresses. The distribution of failure locations is shown in Fig. 149.

The de-bonding failures of the uncured PVB samples was caused in great part by poor bonding of the tags, although this will have been compounded by the high stress concentrations at the interface. However, the significant number of samples that failed at the stress concentration in the PVB at the interface indicates that the waisting of the sample was not sufficient to reliably take the body of the sample to failure, and that the 40% width of the Shrivenham samples was more suitable. However, the 50% waisting was sufficient to generate large elongations in the body of the test samples, sufficient for the main purpose of the tests.

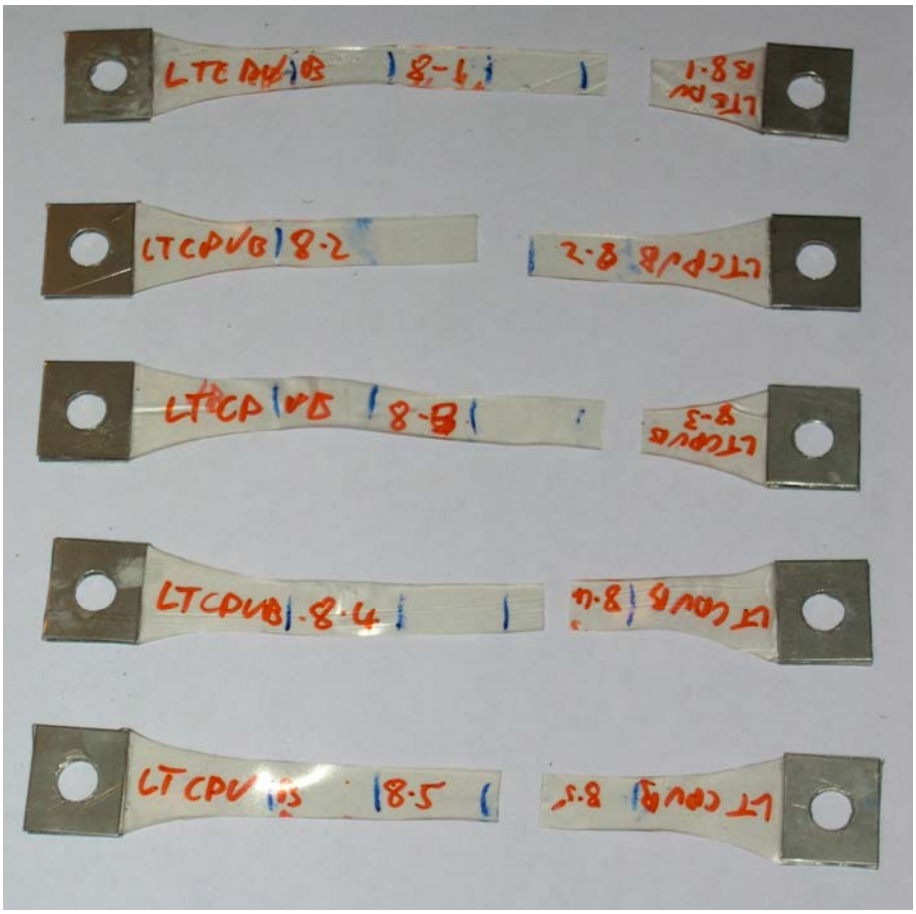

Figure 148. Typical specimens after test (cured PVB tested at 8 m/s)

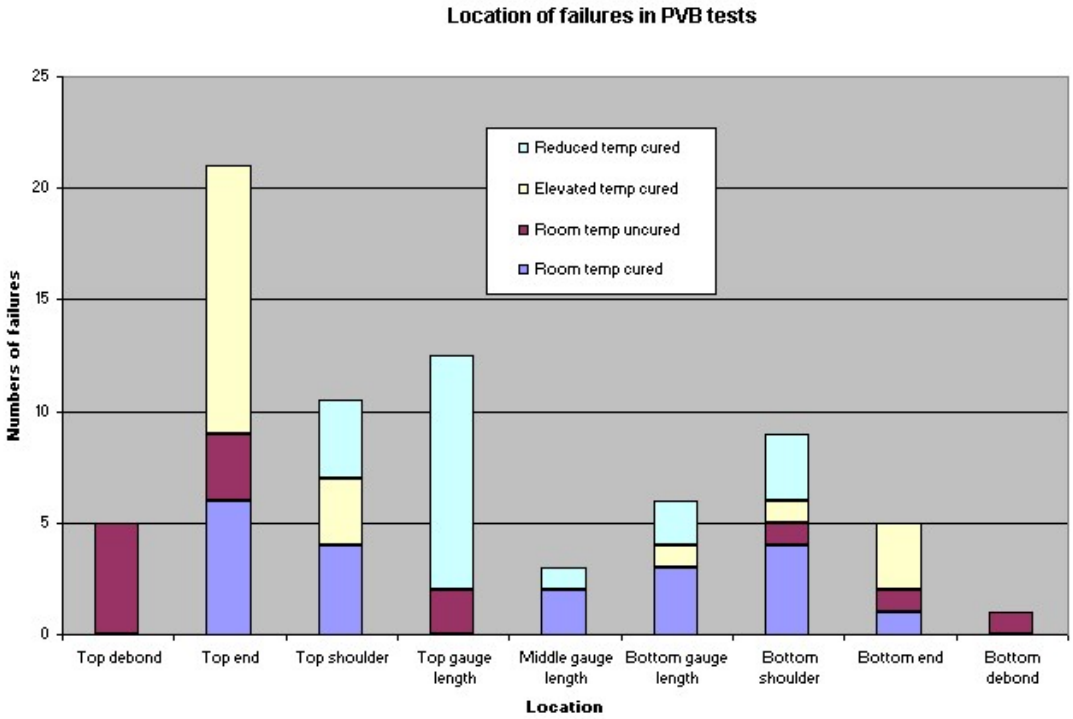

Figure 149. Distribution of failure locations for all PVB tests

When the thermal chamber was being used to produce elevated or reduced temperatures, two sets of 5 samples were initially loaded into the chamber and were left to condition at the set temperature. Once the temperatures were stable at the desired value, the chamber door was opened and a sample fitted into the grips. The door was then closed and the temperature allowed to stabilise on both thermostats before the sample was tested.

Typically the initial chamber adjustment and conditioning took at least 30 minutes, but stabilisation after the door opening generally took only 2-3 minutes. Care was taken to minimise the period of door opening. The chamber was rigged either for heating or cooling, not for both simultaneously, so if the temperature overshot it might take significantly longer to adjust by conduction or radiation. In these circumstances, the door was sometimes cracked open or a side port opened to allow limited air change to assist the chamber reach the desired temperature. Tests were only taken once the mean of the two thermostats was within 1ºC of the nominal temperature.

The first ten samples were stored in the chamber while it was initially brought to temperature and allowed to condition. Once five samples had been tested, a further five were added to the chamber and started to condition while dry runs were undertaken to set the correct velocity for the next series of tests. These would then be conditioned through the next 5 tests and further dry runs before being tested. The temperature control of the chamber and the conditioning and stabilisation times in the chamber are expected to have resulted in samples being close to the nominal temperature at the time of test, but the temperature of the specimens was not measured directly.

8.4.4 Analysis of tests

The digital data traces of the load cell and the displacement transducer voltages were recorded in a directory for each test, and were provided to the Author for analysis. The timestep of the recordings is listed in the data headings, and other observations were noted at the time of test.

The traces were loaded into an Excel workbook for each test. A worksheet was created in which a time line was defined from the sampling rate given in the header for the traces and displacement and force lines were calculated from the recorded voltages using the calibration coefficients for the load cell and the displacement transducer.

A start point was identified both graphically and from the numerical data where the force started to rise, and time and displacement traces were zeroed from that point. A sample of these time and displacement traces, with the corresponding force value trace, was identified to a point after the failure of the sample (usually when the force first went negative). This sample of data was then saved as a text file.

This sample trace was read into a Mathcad worksheet for analysis, where the time, force and displacement data can be plotted against each other, and sections of the

trace can be analysed to derive a simplified bilinear response model. Velocity, peak force and corresponding displacement were all calculated from the data traces.

The results of each test up to an elongation of about 60% of the specimen length was considered as a bilinear curve, and analysed to identify the elastic and 'plastic hardening' linear stiffnesses, and the force at which the transition occurs. This was done by identifying data ranges representing the two linear stages and using linear regression to calculate a gradient and intercept. The data in the immediate zone of the transition was generally not included in either line, as it often contained significant oscillations arising from the abrupt change in behaviour of the material.

A significant number of test results contained transient data spikes, which appear as large, short term variations in the record from the load cell, often both above and below the general trend, followed by resumption of the previous trend. The source is unknown, and could possibly be electrical, but one possible physical explanation is a local slip at the leading edge of the glue bond resulting in a 'release and impact' transient event. Detailed examination of the traces shows that the initial movement is normally a reduction in force, which would be consistent with this hypothesis. The higher stresses in the glue bond due to the lesser waisting in the test specimens may have increased the risk of such transient spikes.

In some cases, the sections of the trace considered for further analysis were selected to ignore the slowing up of the ram towards the end of its travel if this occurred before the failure of the sample, or to ignore data spikes that were not considered to represent actual forces in the sample. In other cases a section containing a data spike may have been analysed when considering the data on one side of the spike only would not give a representative result. In general a trend line based on data containing the whole spike event is not badly affected by the presence of the spike. However significant distortion can arise if part of the spike event is included at the end of a trend line.

At strains above 0.7, many of the force-deflection traces deviate upwards from the 'plastic hardening' line, as they did in some of the high temperature tests at Shrivenham. This is typical of soft rubber non-linearity. A second intercept and a third line would be possible to model the material into this higher strain range. This was not pursued because some LUSAS finite element models failed to converge at about this strain level, and because the average failure strains of laminated glass membranes were substantially lower, leaving the additional information both unusable and unnecessary.

8.4.5 Results of tests

8.4.5.1 Cured PVB at room temperature

The mean results of measurements and bilinear models from five tests of cured PVB at each pull velocity are shown in Table 46.

Typical force-elongation curves at 1 m/s and at 8 m/s are shown in Figs. 150 and 151, including the bilinear models and the sections of data used to define them.

Nominal pull velocity	Mean pull velocity	Initial stiffness	Transition force	Hardening stiffness	Ultimate resistance (U R)	Elongation at U R
m/s	m/s	N/m	N	N/m	N	mm
1	1.00	10333	35.8	639	186	172
2	2.06	11340	46.1	688	206	180
4	4.03	15229	60.6	709	198	157
8	8.02	31982	78.8	572	220	170

Table 46. Mean results from room temperature tests on cured PVB

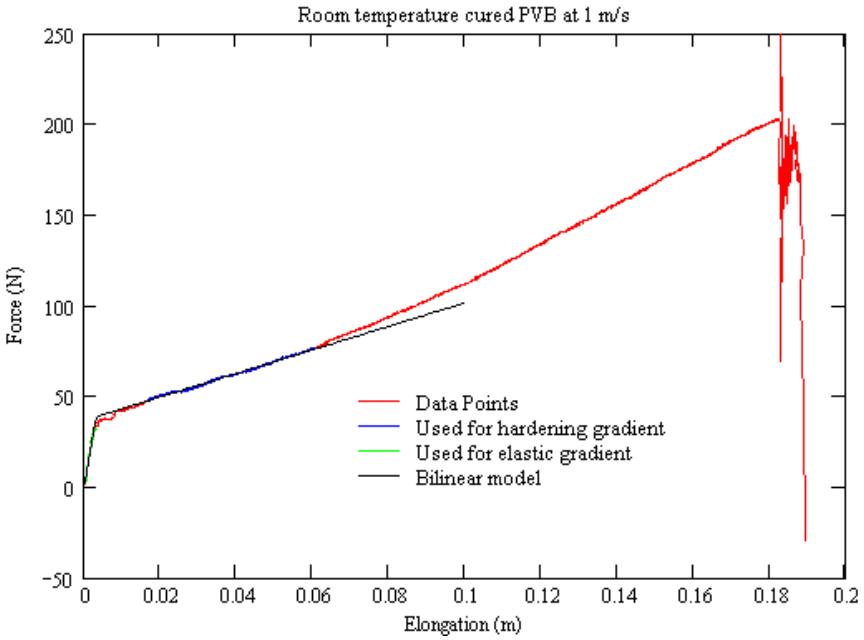

Figure 150. Typical force – elongation curve of cured PVB at 1m/s pull rate

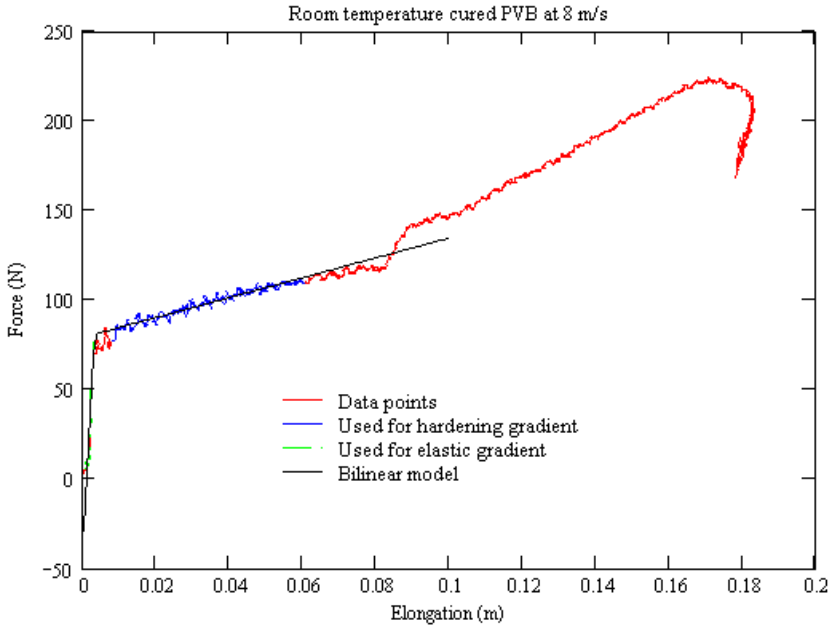

Figure 151. Typical force- elongation curve of cured PVB at 8 m/s pull rate

It can be seen from the two typical curves that extrapolation of the hardening line beyond the data used to define it will be reasonably accurate at first, and will only underestimate the force significantly at larger elongations.

Fig. 150 shows a typical transient data spike shortly before failure, while Fig.151 shows sign of the actuator decelerating before failure of the PVB.

8.4.5.2 Uncured PVB at room temperature

The mean results of measurements and bilinear models from five tests of uncured PVB at each pull velocity are shown in Table 47.

Nominal pull velocity	Mean pull velocity	Initial stiffness	Transition force	Hardening stiffness	Ultimate resistance (U R)	Elongation at U R
m/s	m/s	N/m	N	N/m	N	mm
1	1.03	8136	26.7	649	152	166
2	2.05	8726	34.6	679	173	177
4	4.01	11364	45.6	668	177	165
8	8.03	20102	69.3	645	193	172

Table 47. Mean results from room temperature tests on uncured PVB

The trends of the uncured PVB at room temperature are very similar to those of cured PVB. However, comparing Tables 45 and 46, it can be seen that the initial stiffness and transition forces in the uncured PVB is less than for the cured PVB. This was contrary to the expectations raised by the greater flexibility of the cured specimens. As the hardening stiffness was very similar for both materials, the ultimate resistance of the uncured PVB was lower than that of cured PVB pulled at the same velocity.

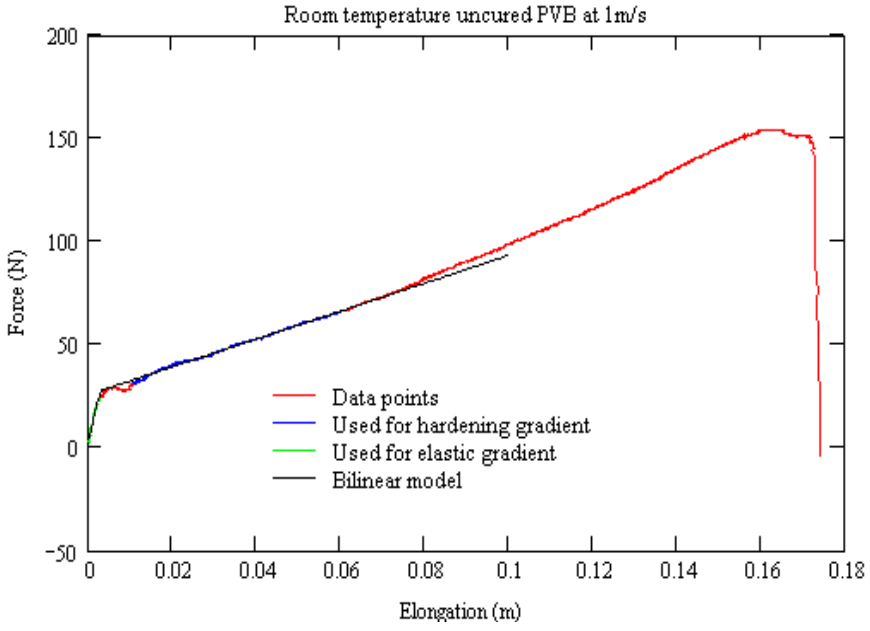

Figure 152. Typical force – elongation curve of uncured PVB at 1m/s pull rate

Typical force-elongation curves at 1 m/s and at 8 m/s are shown in Figs. 152 and 153, including the bilinear models and the sections of data used to define them.

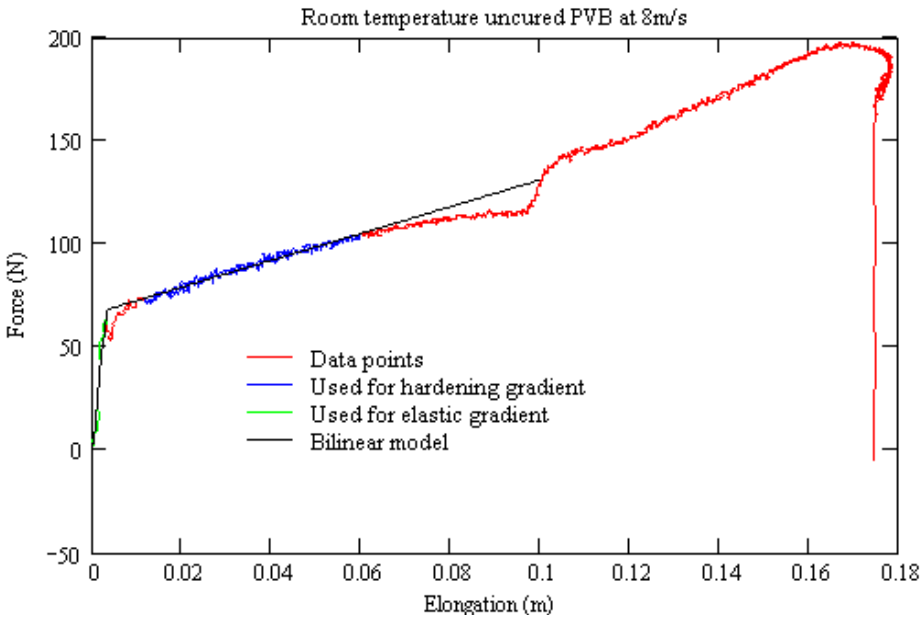

Figure 153. Typical force – elongation curve of uncured PVB at 8m/s pull rate

The 'notch' in Figs. 151 & 153 is a common feature of the faster pull rates. It is unclear whether this is the result of wave effects in the sample or bounce of the test equipment, or a true feature of the material, as a similar notch is visible on some of the Shrivenham tests in Figs. 137 and 139.

8.4.5.3 Cured PVB at reduced temperature

The mean results of measurements at 5ºC and bilinear models from five tests of cured PVB at each pull velocity are shown in Table 48.

Nominal pull velocity	Mean pull velocity	Initial stiffness	Transition force	Hardening stiffness	Ultimate resistance (U R)	Elongation at U R
m/s	m/s	N/m	N	N/m	N	mm
1	1.00	26076	161	0	236	157
2	2.08	27507	179	0	240	141
4	4.07	40795	199	0	257	139
8	8.01	54428	206	0	260	155

Table 48. Mean results from reduced temperature tests on cured PVB

Typical force-elongation curves at 1 m/s and at 8 m/s are shown in Figs. 154 and 155, including the bilinear models and the sections of data used to define them.

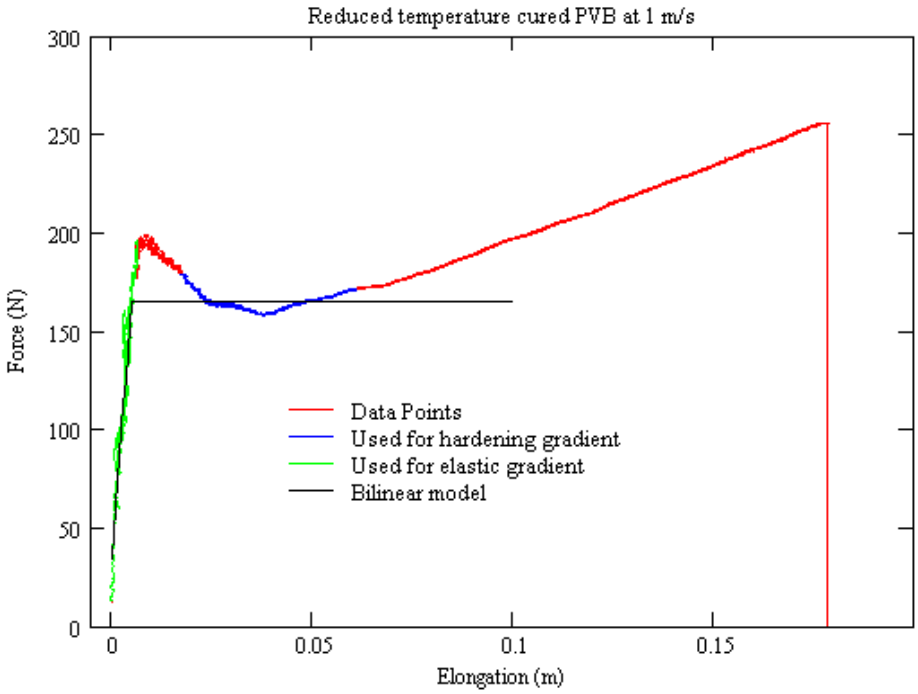

Figure 154. Typical force – elongation curve of low temperature cured PVB at 1m/s pull rate

The dip in the force after the transition and the subsequent increase is a feature in all the tests at 5ºC. It is uncertain whether this is a true reflection of the material behaviour or an artefact of the testing, but it is reminiscent of the material properties of other polymers shown in Fig. 42. In the bilinear modelling, the data used for the hardening gradient has been deliberately selected to give a constant force at the average force level. This ignores the transient peak.

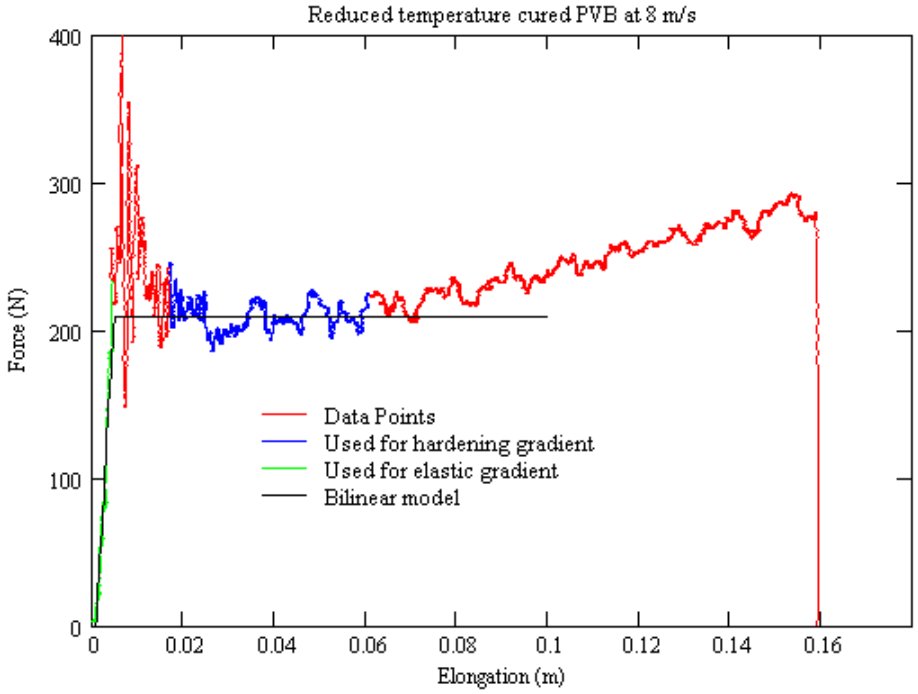

Figure 155. Typical force – elongation curve of low temperature cured PVB at 8 m/s pull rate

At these pull rates, with strain rates up to about 80 /s, the drop in force from the transition is temporary, and there is always a subsequent increase in force before the PVB fails. This is consistent with the Shrivenham tests at similar strain rates shown in Fig. 133.

An alternative bilinear analysis is possible, with the hardening gradient calculated from the data after the low point only, to maximise the hardening gradient to be more accurate when extrapolated beyond the 60% elongation range, at the expense of a lower transition stress that cuts out more of the transient peak. The mean results of this analysis from five tests of cured PVB at each pull velocity are shown in Table 49, and typical curves are shown in Figs. 155 and 156.

Nominal pull velocity	Mean pull velocity	Initial stiffness	Transition Force	Hardening stiffness	Ultimate resistance (U R)	Elongation at U R
m/s	m/s	N/m	N	N/m	N	mm
1	1.00	26232	135	574	236	157
2	2.08	27507	160	405	240	141
4	4.07	40795	189	233	257	139
8	8.01	54428	195	241	260	155

Table 49. Alternative mean results from reduced temperature tests on cured PVB

It should be noted that as the pull velocity increases the amount of noise in the signal increases. This makes the calculation of the hardening stiffness in particular more sensitive to the choice of the data points used to define the trend. This can be seen by comparison between Figs. 156 and 157.

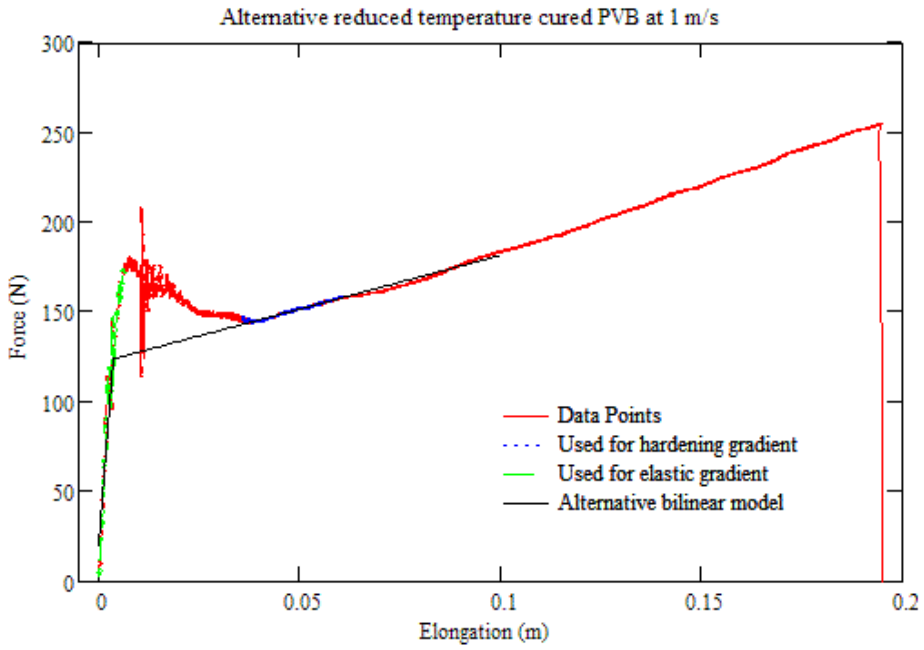

Figure 156. Typical alternative force – elongation curve of low temperature cured PVB at 1m/s pull rate

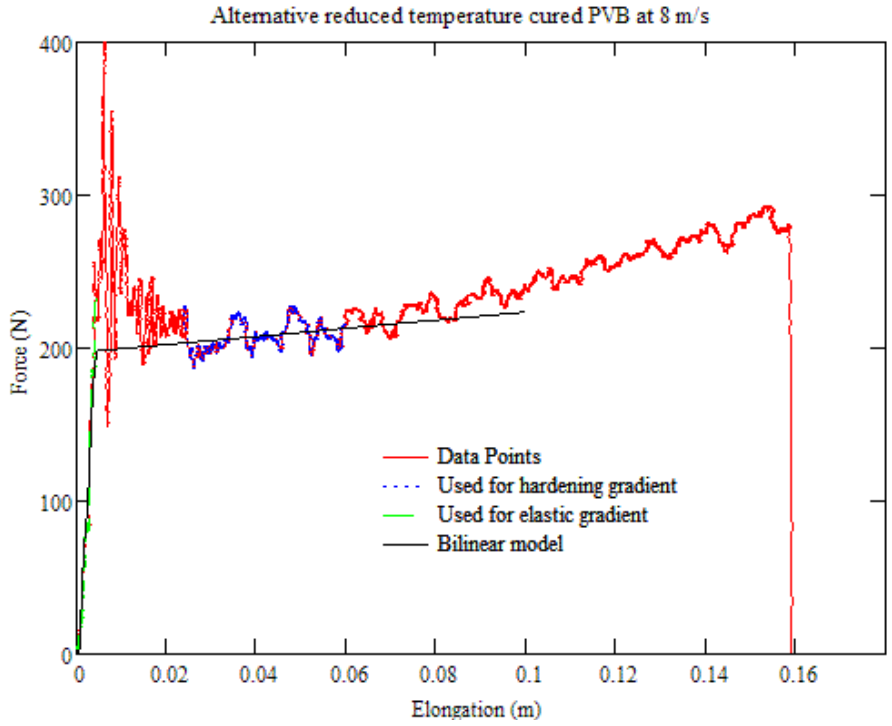

Figure 157. Typical alternative force – elongation curve of low temperature cured PVB at 8m/s pull rate

8.4.5.4 Cured PVB at elevated temperature

The mean results of measurements at 35ºC and bilinear models from five tests of cured PVB at each pull velocity are shown in Table 49.

Nominal pull velocity	Mean pull velocity	Initial stiffness	Transition force	Hardening stiffness	Ultimate resistance (U R)	Elongation at U R
m/s	m/s	N/m	N	N/m	N	mm
1	0.99	1587	6.5	148	131	228
2	2.05	2946	9.5	222	157	216
4	4.06	6675	17.1	359	176	205
8	8.03	11149	24.3	643	198	200

Table 50. Mean results from elevated temperature tests on cured PVB

Typical force-elongation curves at 1 m/s and at 8 m/s are shown in Figs. 158 and 159, including the bilinear models and the sections of data used to define them.

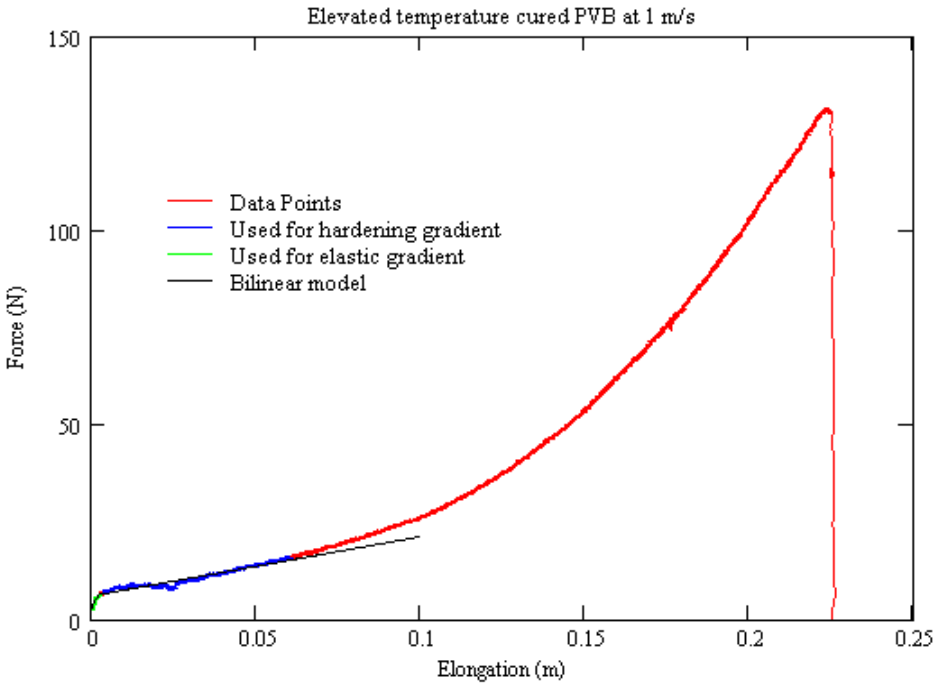

Figure 158. Typical force – elongation curve of elevated temperature cured PVB at 1m/s pull rate

After the transition to the lower hardening stiffness at a very low force, Fig. 158 shows a marked gradual non-linear hardening typical of soft rubber materials. The use of a bilinear model here would significantly underestimate the resistance if the engineering strain exceeds about 1.0.

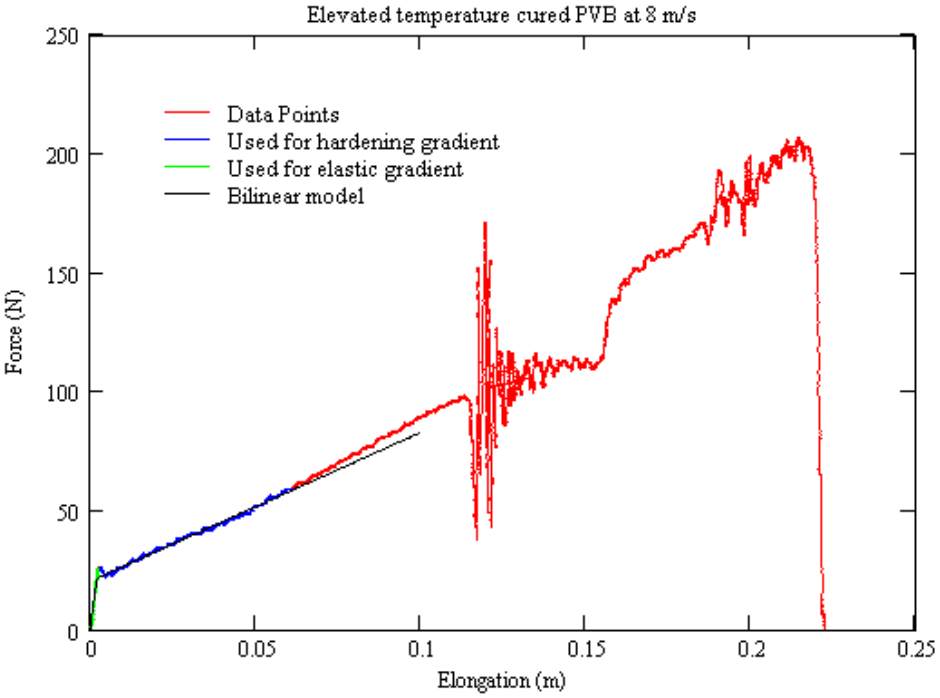

Figure 159. Typical force – elongation curve of elevated temperature cured PVB at 8 m/s pull rate

At the higher pull rate shown in Fig. 159, the transition force is higher, but the hardening curve is flatter, although there is still an upwards trend. Other 8 m/s pull rate tests also show the characteristic notch, so this is not a feature of the data spike that occurred shortly before in this test. At the higher pull rates, the bilinear approximation is still a reasonable model for PVB at 35ºC.

8.5 Bi-linear analysis of tensile tests

8.5.1 Approaches to analysis

Because of the shape of the PVB samples, the accurate conversion of these test sample response properties to material properties is not direct. Instead, non-linear finite element analyses of the test specimens were used to derive a relationship.

Several approaches to analysing the large strain nonlinear deformation of the test samples have been undertaken. These were chosen with consideration for applying the same material properties to the analysis of tensile membranes.

Because the test specimens were of uniform thickness and were thin compared to the length, and fairly thin even compared to the width, a two dimensional plane stress model is a reasonable approximation. This uses a single layer of nodes in the analysis, with an initially declared thickness, but with a through-thickness strain assumed to occur so as to give no through-thickness stress. This is functionally equivalent to a flat shell element loaded in-plane, and shell elements will normally give identical results.

An alternative approach that was also used was to model the specimen using three dimensional solid elements, either one layer thick or a few layers thick. With a thin flexible specimen the in-plane stresses should be nearly uniform, and the results should be insensitive to the number of layers. This had a significant bearing on the analysis times, as additional layers of elements increased the number of nodes and the size of the analysis.

Edge supports in the solid element model were applied to the edge surfaces, so that all the nodes were restrained. This should have made no difference to the tensile test models, although it was expected to provide local flexural constraint at the edge of a laterally loaded membrane. In practice, the highly constrained nodes show localised higher stresses and strains that are a function of the numerical treatment, rather than any reflection of the physical stress concentrations at these locations.

The method of handling the geometric non-linearity can significantly affect the stability of the analysis, and can affect the result. Analyses of uncracked panes in Chapter 6 used Lagrangian formulations, either ‘Total Lagrangian’ for conservative forces or ‘Updated Lagrangian’ for follower forces, although conservative forces can also be used in the ‘Updated Lagrangian’ formulation.

Both of these assess element stresses and strains relative to a rigid reference system, using Green’s strain tensor and the Second Piola-Kirchhoff stress tensor. The ‘Updated Lagrangian’ formulation updates the reference geometry at the start of each increment to the resulting geometry from the previous converged increment. However, the updating of the reference comes with a penalty, as each increment is not converged absolutely, but only within a tolerance, and the cumulative effect of the tolerances over many increments may produce a significant error.

As will be discussed in Chapter 9, it was decided that for most analyses of PVB membrane deformation, follower forces would not be required, and so it was not necessary to use the 'Updated Lagrangian' formulation for that reason, while the analyses it produced were found to be very sensitive to small variations in material properties.

The PVB test specimen was therefore analysed with a bilinear material model using a 'Total Lagrangian' non-linear formulation in a plane stress model, with a view to using the same material models in shell analyses of PVB membranes.

The Lagrangian formulations are described in the LUSAS handbooks [124] as being suitable for large deflections and rotations, but only for small strains, as the strain definition used, Green's strain, is only applicable to small strains. Significant errors could arise in the analyses for large extensions of the specimens, which implied large plastic strains. Alternative Eulerian and Co-rotational formulations were therefore also explored, which are described as being suitable for large strains.

The Eulerian formulation updates the geometry of the problem every iteration, and not simply every converged iteration. The logarithmic or natural strain tensor and Cauchy stresses naturally describe the material response, and infinitesimal elastic and inelastic material models can be used directly in the presence of large strains. In application in LUSAS, in three dimensional solid elements the deformation tensor is decomposed into a solid body rotation and the right stretch tensor, and a rotated logarithmic strain algorithm used, while in two dimensional plane stress and plane strain models the decomposition is into the left stress tensor and the solid body rotation. In either case, this gives a three dimensional true stress-strain behaviour.

This may be an advantage in analysing a structure where the material is well-typified in true stress-strain terms, but can be a positive disadvantage in trying to map simplified test specimen behaviour at large strains back to a material property, as it will tend to model the microscopic accurately, but to give a complex macroscopic response.

The Co-rotational formulation uses a reference system for each element that rotates with the element, so that the material model for the element experiences primarily distortions due to the stretches in the strain tensor, rather than solid body rotation. In LUSAS, a reference system rotation for the centroid of the element rather than for each Gauss point is applied to the stiffness matrix for each element in defining the overall stiffness matrix. After the rotations have been removed the stress measure used within the analysis are non-conventional Biot type stresses, but these are converted to Kirchoff stresses, the three dimensional equivalent of engineering stress.

This method is the required method in LUSAS for the use of rubber material models such as the Ogden model. However, it is currently only implemented for two and three dimensional linear continuum elements, not shell elements or quadratic continuum elements.

In addition to the Lagrangian plane stress analysis, the PVB test specimen was therefore analysed with a bilinear material model using a Co-rotational non-linear

formulation in a model using solid volume elements, with a view to using the same material models and elements in analyses of PVB membranes.

8.5.2 Lagrangian plane stress analysis of the PVB specimen

Plane stress, non-linear finite element analyses of a quarter model of the test specimen were under taken using the LUSAS [124] finite element program, with a bilinear material and a von Mises yield criterion used to calculate elastic stiffness, transition force and plastic hardening stiffness for a range of material properties. A 'Total Lagrangian' non-linear formulation was used, after an initial linear elastic analysis shown in Fig. 160.

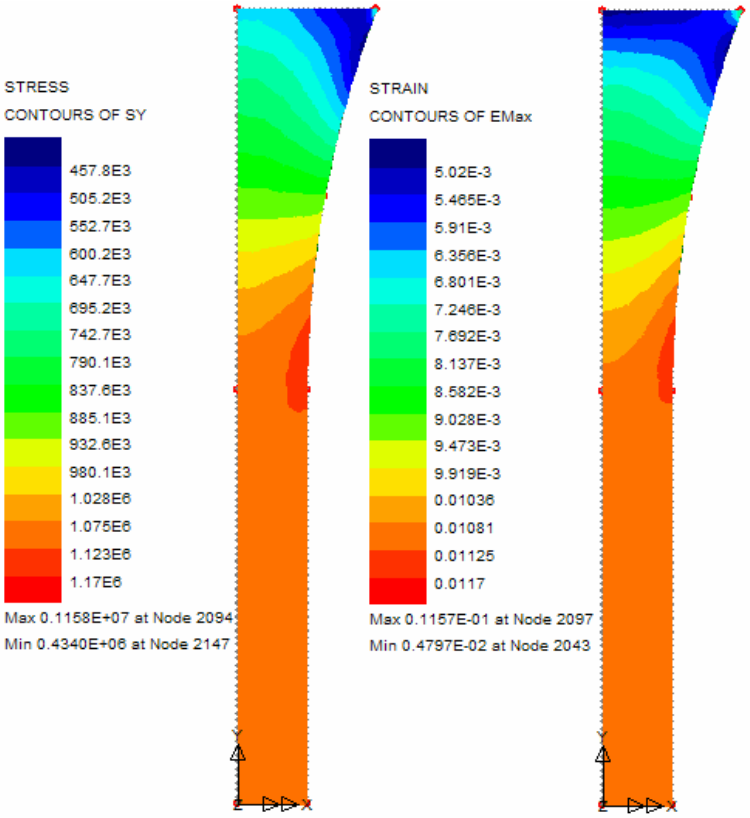

Figure 160. Typical elastic stress and strain distribution in FEA model

The loading was applied as increments of prescribed displacement in the longitudinal direction. This deflection-controlled analysis was expected to cope better with the abrupt change in stiffness due to the yielding of the material than a force-controlled analysis. Two incremental step sizes were used. Initially, elongation per step was set to 0.5% elongation of the specimen, with step reduction enabled when the iteration failed to converge. This was run to an elongation beyond that expected to cause general plasticity in the specimen. Thereafter, an analysis with 2% elongation per step was used until the increment failed to converge to a force and deflection norm of 0.001% in 30 iterations.

In the linear elastic analysis, the distributions of stress and strain were similar to the distributions in the different specimens in Figs. 127 and 128, except that the average stresses at the centre indicate that the sample was 1.117 as stiff as a rectangular specimen, and the peak stress was 1.035 times the average over the straight section.

Analyses were undertaken using several different values of Young's modulus, primarily values of 100 MPa and 250 MPa. It was demonstrated that with a constant ratio of the yield stress and hardening modulus to the Young's modulus, the force could be scaled with the Young's modulus. Thereafter, all analyses used a Young's modulus of 100 MPa, so that the various values of yield stress (σ_y) and hardening modulus (H) could be conveniently expressed as percentages of the Young's modulus.

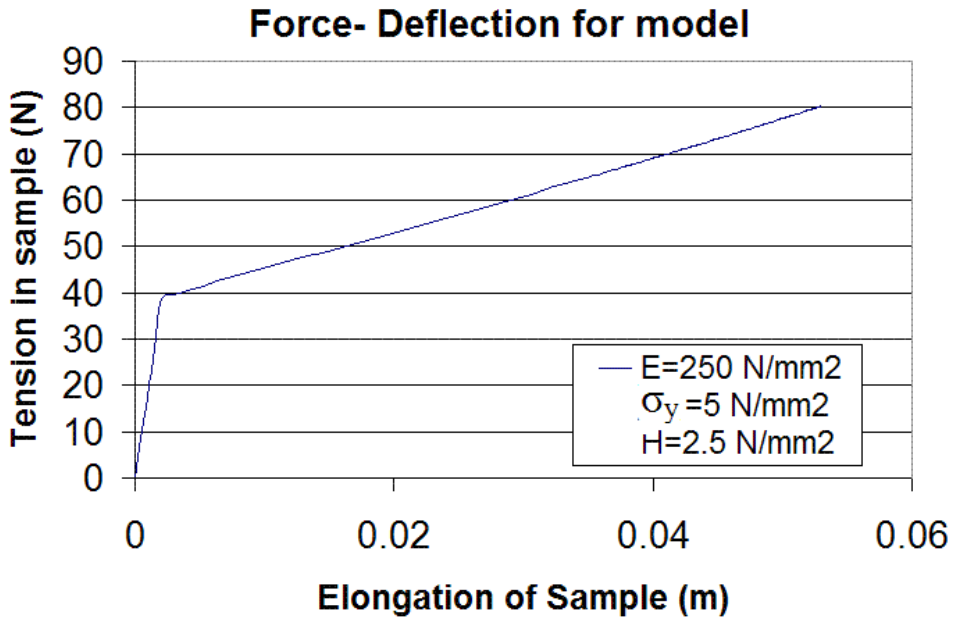

Figure 161. Typical force-deflection curve for von Mises plastic model of test

In the non-linear analyses, the force-deflection relationship in the specimen model was established from the sum of the longitudinal reactions at the mid-length edge, and from the prescribed displacements at the same positions. A typical force-deflection curve is shown in Fig. 161. Checks showed that the sum of the reactions at the tag end of the model were the same.

The non-linear analyses showed the force-deflection line in the elastic stage to stiffen slightly, rather than to be an exact straight line. The tangent stiffness typically increases by a few percent before the onset of yield. The relationship between Young's modulus and the elastic stiffness depends principally on the shape of the sample, but there is a minor variation with the yield stress as a proportion of Young's modulus as a result of the use of Green's strain.

For different yield stress values relative to Young's modulus, the strain at yield will vary, and the effect of Green's strain on the average elastic stiffness will vary slightly. As a result, the average elastic stiffness varies slightly with the yield stress. A linear approximation of this relationship was established by linear regression. The same relationship gives the elastic strain rate from the velocity of the test.

With a fine enough increment step, it is possible to observe a small reduction in stiffness one increment before the major drop in stiffness. Examination of the strain data shows that this represents a local onset of plasticity at the stress concentration

spot at the edge of the specimen, prior to general plasticity of the section. For convenience, this increment has been included in the calculation of the average elastic stiffness.

As the non-linear FE analysis is undertaken in a range of incremental steps, it is not possible to identify exactly the transition force, but only the force at the step immediately above the transition. This makes no significant difference in the calculation of the average elastic stiffness, but does give a slight variation of the calculated hardening stiffness with the hardening modulus, as this affects how steeply the curve rises between the transition point and the next FE result. The step containing the transition point is easily identified as the gradient at that step is intermediate between the elastic and plastic stiffness, and the force at the end of that step will always be upper bound for the transition force.

This upper bound effect was minimised by selecting the transition force as the lowest value of force at the step above the transition over a range of analyses with different hardening moduli. This was generally for an analysis with a low ratio of hardening modulus to elastic modulus, as this reduces the force difference per step, but the critical analysis was not always that with the lowest hardening modulus value. This process allowed the transition stress to be estimated from the transition force and the ratio of transition force to elastic stiffness without consideration of the hardening stiffness.

The factors, derived as described above, that allow a Young's modulus and yield stress to be selected for a Lagrangian finite element analysis to match a linearised test response from a sample of the shape tested are given in Table 51. The material properties to match any particular test result can be derived by interpolation.

Transition stress/ Young's modulus	2%	3%	4%	5%
Transition force/ (Elastic stiffness x specimen length)	1.78%	2.66%	3.53%	4.43%
Young's modulus/ (Elastic stiffness x sample length/ gauge area)	87.2%	86.1%	85.0%	84.3%
Transition stress x gauge area/ transition force	98.1%	97.1%	96.2%	95.2%

Table 51. Relationship of material and specimen properties up to transition, from a Lagrangian finite element analysis

The hardening stiffness in the FE analyses is a function of both the ratio of the hardening modulus to the Young's modulus and the ratio of the yield stress to the Young's modulus, with significant variation for both. The force deflection curve is not a straight line, because the as the elongation increases the distribution of

However with Young's modulus and yield stress evaluated above, interpolation over a range of analyses can eliminate the yield stress from consideration and produce a

relationship between the hardening stiffness to elastic stiffness ratio and the hardening modulus to Young's modulus ratio.

The hardening stiffness in the FE analyses is a function of both the ratio of the hardening modulus to the Young's modulus and the ratio of the yield stress to the Young's modulus, with significant variation for both. However with Young's modulus and yield stress evaluated above, interpolation over a range of analyses can eliminate the yield stress from consideration and produce a relationship between the hardening stiffness to elastic stiffness ratio and the hardening modulus to Young's modulus ratio.

The hardening stiffness is not a true uniform gradient in the analyses, but forms a shallow "S" shape as a result of two opposing influences.

The first influence is the specimen shape. The entire specimen does not yield simultaneously, but first yields across the straight gauge length where the specimen is narrowest. With reduced stresses in the broader curved section, as shown in Fig. 159, the yield there will be delayed until strain hardening causes a general increase in the stress level. This is illustrated in Fig. 162, where the higher strains extend further into the curved section when the elongation of the sample is greater. The effect of this is that the initial plastic elongation occurs only over part of the sample with a greater hardening stiffness, and the stiffness gradually reduces with increasing elongation.

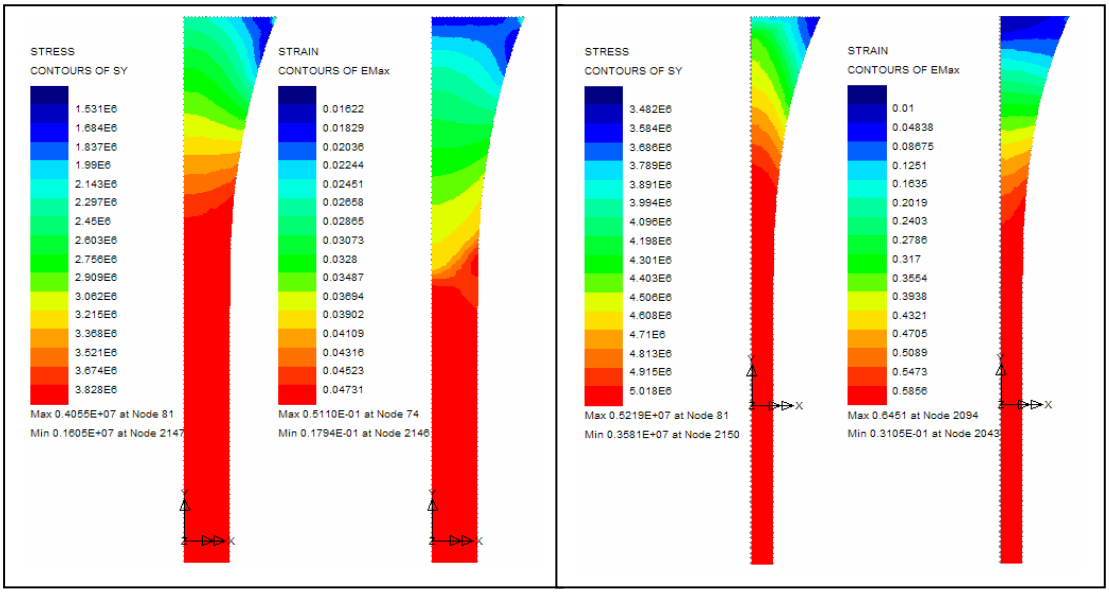

Figure 162. Typical stress & strain distribution for 4% and 44% elongation

The second influence was the gradual stiffening of the model introduced by the use of Green's strain in the Lagrangian non-linear formulation. This was observed in the elastic stage, but continues during the plastic stage.

In the early part of the plastic response the softening due to the sample shape gives a net softening. However, as the shape softening reduces with increased strain while the Green's strain hardening increases, in the later part of the plastic curve there is a net hardening. The point of contraflecture in the curve varied from an 11% elongation for a low yield stress and a high hardening modulus, to 41% elongation for a high yield and a hardening modulus ratio of 0.4%.

Even the most stable Lagrangian analyses, with the highest hardening moduli, required step reduction to negotiate the transition from the elastic to plastic state, and were generally only able to model the test specimen to an extension of about 71 mm. The failure of the analyses occurred because of excessive volumetric strains in some elements, and no significant improvement was obtained by remodelling the element shapes or refining the mesh. With less hardening, the analyses generally failed at smaller deflections, but deflections close to 60 mm could still be obtained for a hardening modulus of 0.6% of the Young's modulus, while the stability of the analysis dropped rapidly below this hardening level. This, as much as the typical shape of the test force-deflection curves, suggested that the bilinear approximations in Section 8.4 be based on data up to deflections of 60 mm.

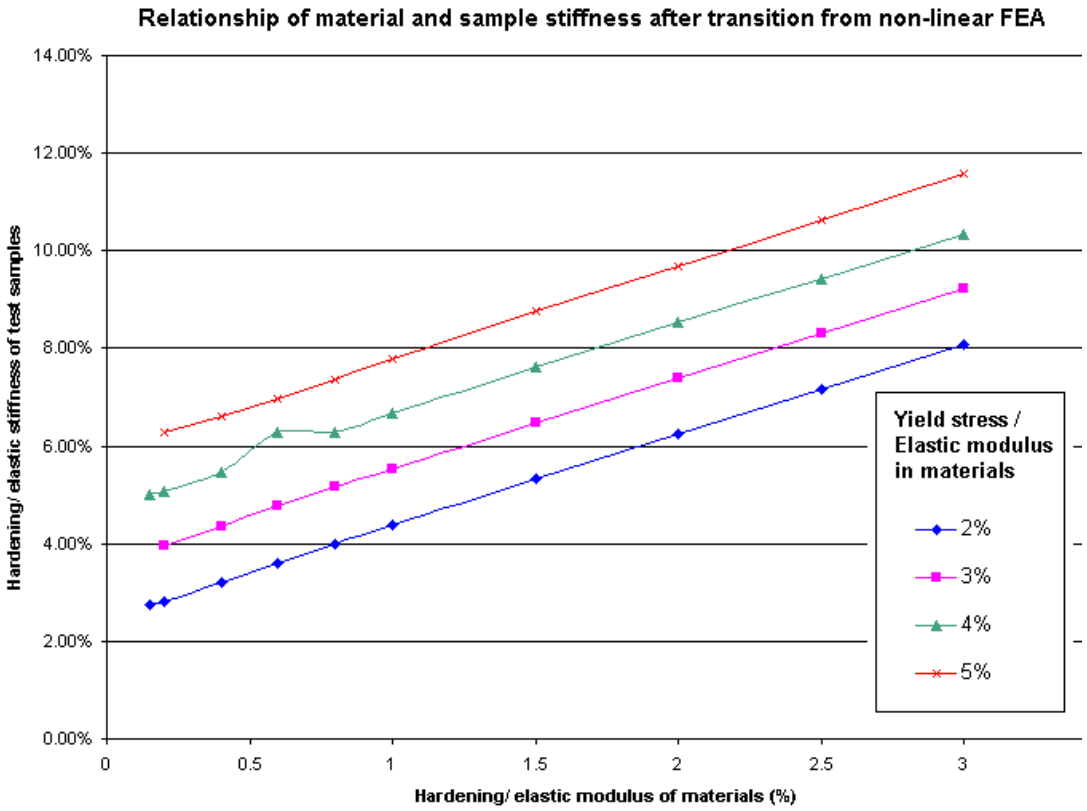

Figure 163. Relationship of material and sample stiffness after transition, from Lagrangian finite element analysis

Fig. 163 shows a plot of the mean hardening gradient of a test specimen from the transition point up to an extension of 60 mm, as a proportion of its mean initial stiffness below the transition point, in terms of the yield stress ratio and the hardening modulus ratio with the Young's modulus. Given the bilinear approximation of the test data and the other properties already derived using the data in Table 51, this can be used to calculate a suitable hardening modulus for a material to use in a Lagrangian model of a particular test, and by extension a Lagrangian model of a PVB membrane at the same temperature and extension rate.

There is one anomalous data point on Fig. 162, for 4% yield stress and 0.6% hardening modulus ratios. This has been confirmed by repeated analyses. It could still

be incorporated into back-analysis of the test results by linear interpolation, but alternatively a trend line can be used to smooth the data in this area.

The data lines in Fig. 162 have been extended to incorporate results for analyses with hardening ratios less than 0.4%, even though these analyses did not extend to 60 mm extension, and so are less accurate, and the material models may be less able to model PVB membrane deformation.

Even with this additional data, it is clear that the hardening of the modelled specimen is substantially greater than the material hardening gradient would suggest. There appears to be an additional hardening rate built into the Lagrangian formulation over and above the material hardening, with an apparent magnitude marginally greater than the value of the yield stress per unit strain.

In practice, this means that the Lagrangian model may be suitable for back-analysis of the room temperature and raised temperature tests, where the hardening gradient is high, but will be unsuitable for analysing the low temperature tests where the hardening is low to negligible, and by implication, for analysing low temperature PVB membranes.

8.5.3 Application of the Lagrangian analysis to the test results

8.5.3.1 Cured PVB at room temperature

The material properties for Lagrangian analysis of cured PVB at room temperature are given in Table 52, based on the average test data in Table 46.

Nominal pull velocity	Elastic strain rate	Young's modulus	Yield stress	Hardening modulus	Ultimate stress	Elongation / gauge length
m/s	Strain/s	N/mm^2	N/mm^2	N/mm^2	N/mm^2	Strain
1	10.2	134	4.55	1.46	24.5	2.87
2	21.1	146	5.84	1.05	27.1	3.00
4	41.2	196	7.67	0.50	26.1	2.61
8	80.4	420	10.13	0.46	28.9	2.83

Table 52. Lagrangian material properties derived from room temperature tests on cured PVB

A quadratic regression analysis of the design properties with respect to elastic strain rate gives material properties that can be used for interpolation, or limited extrapolation in Lagrangian finite element analyses. The results of such a regression analysis on the data averaged in Table 52 are given in Table 53. The test values and quadratic trend lines are shown in Figs. 164-166.

Property	Equation relative to Strain Rate (SR) (/s)
Elastic modulus (N/mm^2)	$135.91 – 0.6966 \times SR + 0.0526 \times SR^2$
Transition stress (N/mm^2)	$3.3084 + 0.1293 \times SR – 0.0006 \times SR^2$
Hardening modulus (N/mm^2)	$1.960 – 0.0529 \times SR + 0.0004 \times SR^2$

Table 53. Room temperature PVB Lagrangian material properties relative to strain rate.

The ultimate stress and corresponding average strain are not expected to be of practical interest in analysing PVB membranes in laminated glass, as the average deflection at failure of laminated glass loaded by water bags measured by Ellis and Beak [93, 94] are expected to require a substantially lower average strain, and in any case, the Lagrangian analysis is not capable of analysing to such strain levels.

8.5.3.2 Uncured PVB at room temperature

The mean material properties for Lagrangian analysis of the uncured PVB at room temperature are given in Table 54, based on the test data averaged in Table 47. Although this might be used for back-analysis of the tests, it will not be required for analysis of PVB membranes in laminated glass, because, by definition, all PVB in laminated glass will have been cured in the lamination process

Nominal pull velocity	Elastic strain rate	Young's modulus	Transition stress	Hardening modulus	Ultimate stress	Elongation / gauge length
m/s	Strain/s	N/mm^2	N/mm^2	N/mm^2	N/mm^2	Strain
1	10.5	105	3.41	2.30	19.9	2.77
2	21.0	115	4.38	1.84	22.8	2.95
4	41.1	146	5.79	0.93	23.3	2.75
8	81.4	261	8.82	0.38	25.4	2.70

Table 54. Lagrangian material properties derived from room temperature tests on uncured PVB

The Young's modulus, transition stress and ultimate stress of the uncured PVB are shown to be consistently lower than the corresponding properties of the cured PVB. There are variations in the hardening modulus and on average it is higher for the uncured PVC, but it is not sufficient to affect the relative ultimate strengths.

On average the elongations at failure are very similar, so although a number of the uncured samples failed by de-bonding of the steel tags and then tearing of the PVB at the mounting hole, this does not appear to have been significantly premature, and would in any case only have affected the ultimate stress and strain.

8.5.3.3 Cured PVB at a reduced temperature of 5ºC

For comparison purposes, the mean material properties for Lagrangian analysis of cured PVB at a reduced temperature of 5ºC are given in Table 55, based on the test

data averaged in Table 48, except that the zero hardening modulus is assumed from the zero hardening stiffness.

Nominal pull velocity	Elastic strain rate	Young's modulus	Transition stress	Hardening modulus	Ultimate stress	Elongation / gauge length
m/s	Strain/s	N/mm^2	N/mm^2	N/mm^2	N/mm^2	Strain
1	10.2	335	20.0	0	31.1	2.62
2	21.3	354	22.2	0	32.4	2.35
4	41.9	522	24.9	0	33.9	2.32
8	81.7	702	26.1	0	34.2	1.92

Table 55. Mean Lagrangian material properties derived from reduced temperature tests on cured PVB

These are provided for comparison purposes only because a Lagrange analysis would not be capable of running with these properties through yield.

In the low temperature tests there were a substantial number of spikes in the initial elastic gradient. The data samples used had to incorporate the spike data to be representative of the whole gradient, as the use of a short run of data before the spike could result in a significant variation in the calculated value of Young's modulus.

To reduce the sensitivity of the calculations to spikes, an alternative calculation method was employed for comparison. The force and displacement curves for the five tests were averaged up to the first failure time and the composite force-deflection curves were analysed. This reduced the amplitude of any spike relative to the mean trend to 20%, as spikes in different tests do not correspond. The results of this analysis are given in Table 56.

Nominal pull velocity	Elastic strain rate	Young's modulus	Transi-tion stress	Hardening modulus
m/s	Strain/s	N/mm^2	N/mm^2	N/mm^2
1	10.3	321	19.9	0
2	21.6	360	22.2	0
4	42.3	498	24.9	0
8	83.2	671	26.1	0

Table 56. Material properties derived from averaged data for reduced temperature tests on cured PVB

This analysis generally gives a Young's Modulus lower than the mean from the individual analyses. However the values fall within the range of the individual tests.

The results of a regression analysis on the data averaged in Table 55 with respect to elastic strain rate are given in Table 57. The test values and quadratic trend lines are shown in Figs. 164-166.

Property	Equation relative to Strain Rate (SR) (/s)
Elastic modulus (N/mm^2)	$248.56 + 6.7884 \times SR - 0.0150 \times SR^2$
Transition stress (N/mm^2)	$17.645 + 0.2483 \times SR - 0.0018 \times SR^2$
Hardening modulus (N/mm^2)	0

Table 57. Reduced temperature PVB Lagrangian material properties relative to strain rate.

A similar exercise could have been undertaken using the alternative bilinear interpretation of the test results in table 49. However, the hardening stiffnesses are too low to allow a hardening modulus to be estimated from Fig. 162.

8.5.3.4 Cured PVB at an elevated temperature of 35ºC

The mean material properties for Lagrangian analysis of cured PVB at an elevated temperature of 35ºC are given in Table 58, based on the test data averaged in Table 50.

Nominal pull velocity	Elastic strain rate	Young's modulus	Transition stress	Hardening modulus	Ultimate stress	Elongation / gauge length
m/s	Strain/s	N/mm^2	N/mm^2	N/mm^2	N/mm^2	Strain
1	10.1	20.5	0.82	0.49	17.3	3.80
2	20.8	38.4	1.21	0.76	20.6	3.60
4	40.8	87.5	2.19	1.07	23.1	3.42
8	80.2	147	3.12	2.44	26.1	3.34

Table 58. Mean Lagrangian material properties derived from elevated temperature tests on cured PVB

The results of a regression analysis on the data averaged in Table 58 with respect to elastic strain rate are given in Table 59. The test values and quadratic trend lines are shown in Figs. 164-166.

Property	Equation relative to Strain Rate (SR) (/s)
Elastic modulus (N/mm^2)	$-7.8694 + 2.6358 \times SR - 0.0088 \times SR^2$
Transition stress (N/mm^2)	$0.2058 + 0.0587 \times SR - 0.0003 \times SR^2$
Hardening modulus (N/mm^2)	$0.4378 + 0.0073 \times SR + 0.0002 \times SR^2$

Table 59. Elevated temperature PVB Lagrangian material properties relative to strain rate.

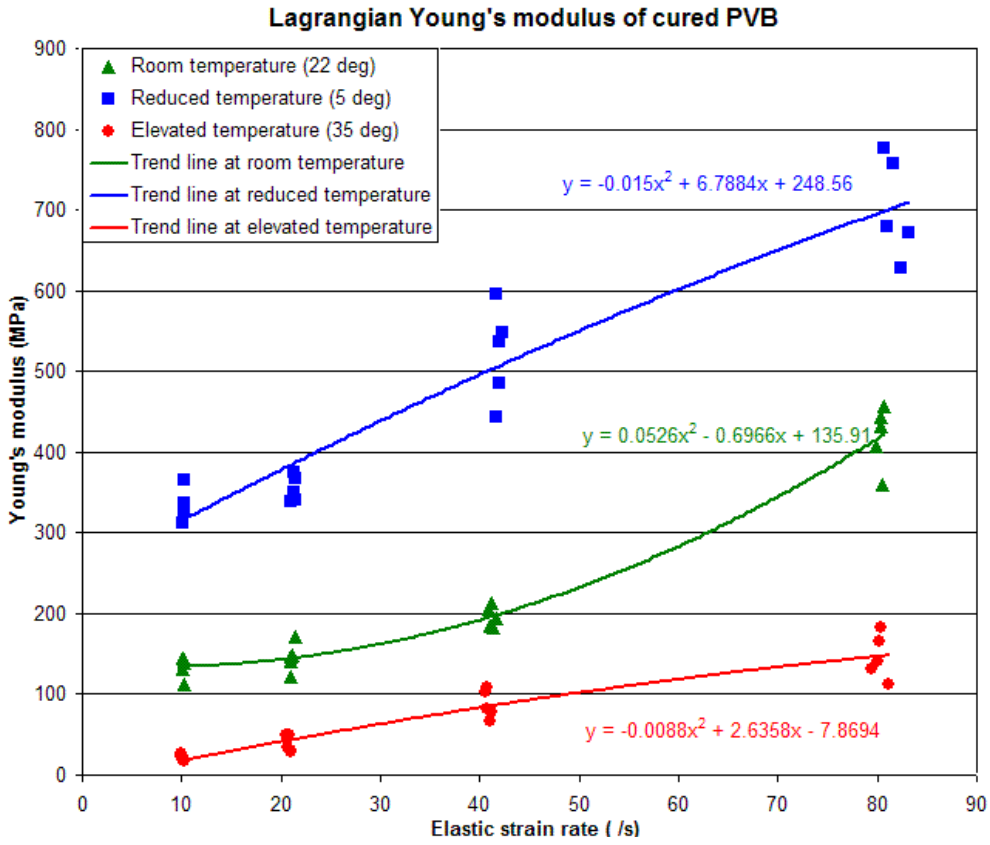

Figure 164. Lagrangian Young's modulus test values and trend lines

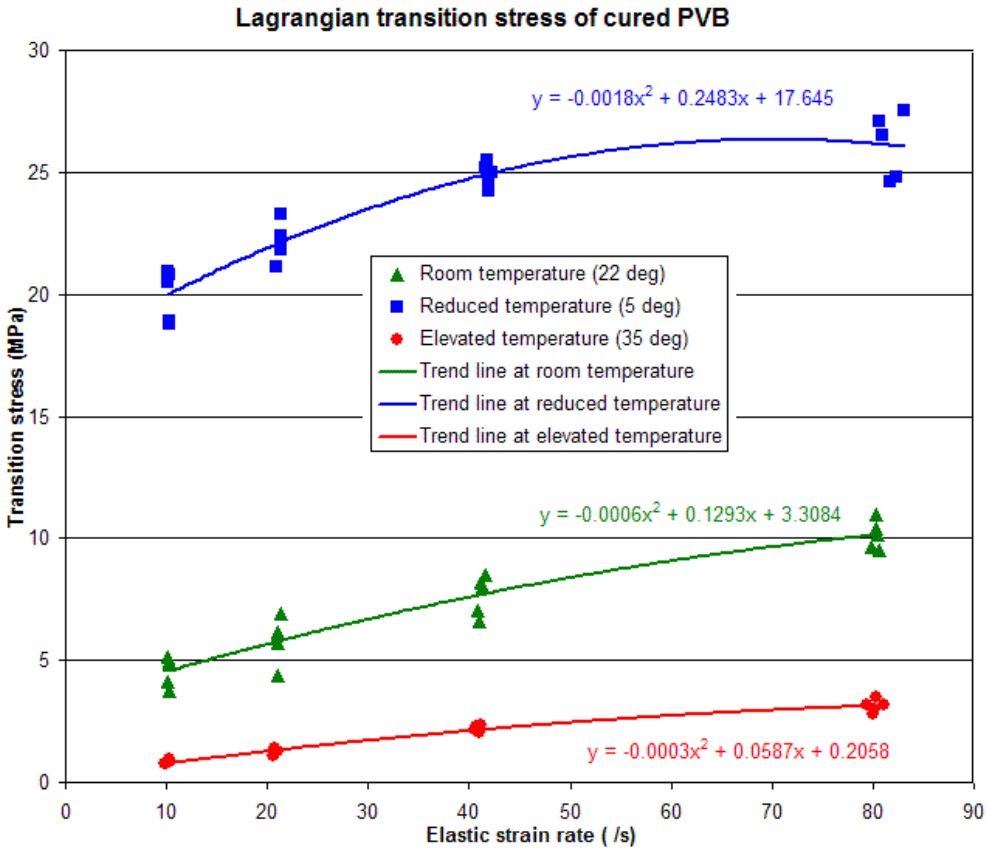

Figure 165. Lagrangian transition stress test values and trend lines

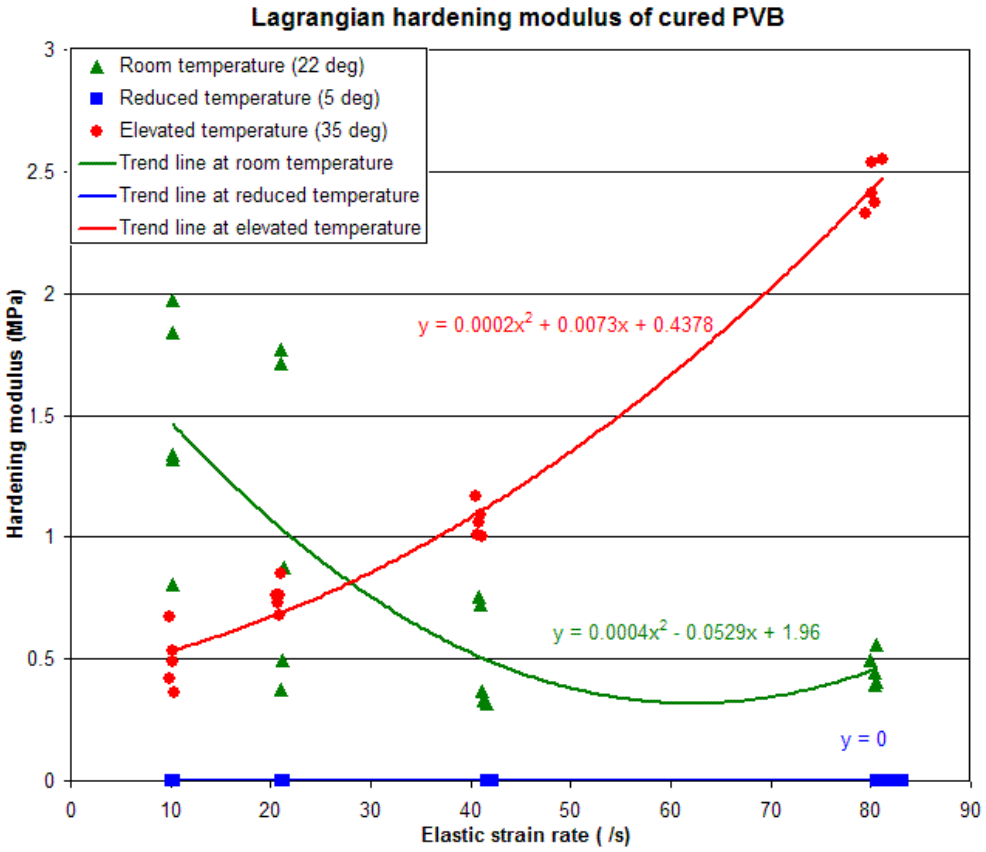

Figure 166. Lagrangian hardening modulus test values and trend lines

8.5.4 Three dimensional solid Co-rotational analysis of the PVB specimen

The plane stress model could also be analysed using a Co-rotational non-linear formulation. This gave a similar elastic stage to the Lagrangian analysis, but had no difficulty in transitioning into the plastic stage, even for a zero hardening material. It could model elongation to a length greater than three times the initial length, and modelled the specimen response with far less increased hardening over the material hardening. However, because of the limited range of element types supporting the Co-rotational formulation in LUSAS, the material properties calculated from such an analysis could not be used to analyse a shell element model of a PVB membrane.

By extruding the surfaces used to model the plane stress geometry into volumes 0.76mm thick, and assigning a volume mesh, the same test specimen could be modelled as a three dimensional solid, which could also be used to model the PVB membrane in laminated glass using a Co-rotational non-linear formulation.

The analysis process was very similar to that used for the Lagrangian plain stress analyses, but the results were significantly different in some respects.

The elastic stage is still not quite a straight line, although typically the variation from the straight is somewhat lower. However, the stiffness is noticeably smaller for the same Young's modulus. There appear to be two causes for this. One is the use of a strain measure other than Green's strain, which has little or no hardening built into

the formulation, and the other is the softening of the sample model introduced by the local stress concentrations in the model close to the tabs as a result of the high level of restraint modelled in the boundary elements of the model.

These two effects can be distinguished separately because the Co-rotational plane stress model has no such stress concentrations, and has an intermediate stiffness. For a typical example the strain formulation made about 6% difference to the average stiffness between Lagrangian and Co-rotational plane stress analyses, while the stress concentrations made about 4% difference between Co-rotational plane stress and solid analyses.

The Co-rotational formulation can analyse the transition from predominantly elastic to predominantly plastic without requiring any step reductions, even for an elastic – pure plastic material with zero strain hardening. This allows a lower value for the upper bound transition force to be identified, improving the accuracy of that calculation.

The Co-rotational analyses of the three dimensional solid model fail at different extensions, from 87-88mm for zero hardening to 198-201mm for a 10% hardening modulus ratio. All of them fail when the maximum principal strain first exceeds 2.0. The reason for this failure can be found in the minimum principle strain, which is listed as fractionally under -1.0, implying a negative cross section. The same limit was also observed in an Euler analysis

This appears to have arisen from a small deflection approximation used in LUSAS for modelling plastic yield in the von Mises yield criterion, even in the Co-rotational and Euler formulations. The transverse strain appears to have been taken as equal to the elastic approximation:

$$\varepsilon_y = -\nu \cdot \varepsilon_x \tag{57}$$

with the Poisson's ratio ν taken as 0.5 for plastic deformation, rather than the more accurate formula for plastic deformation without volume change:

$$\varepsilon_y = -\varepsilon_x^{-0.5} \tag{58}$$

As the material strength properties and the output stresses and strains are in engineering stress and strain terms, the analysis keeps good accuracy up to this failure, although the true stresses approaching failure would be completely unreal. This suggests that the modelling of a PVB membrane may still be realistic in engineering stress and strain terms and in overall forces and deflections, but that the analysis is likely to be limited to a biaxial strain of 1.0 or a uniaxial strain of 2.0.

It is interesting to note that the Co-rotational plain stress analysis of a test specimen does not fail at this point, but models even greater extensions. This appears to be because both transverse dimensions change sign at the same increment, so that the area never becomes negative.

The difference in the failure extensions for the different hardening gradients, shown in Fig. 167, highlighted a difference in the strain distribution in the models of the test specimens with variation of the hardening modulus.

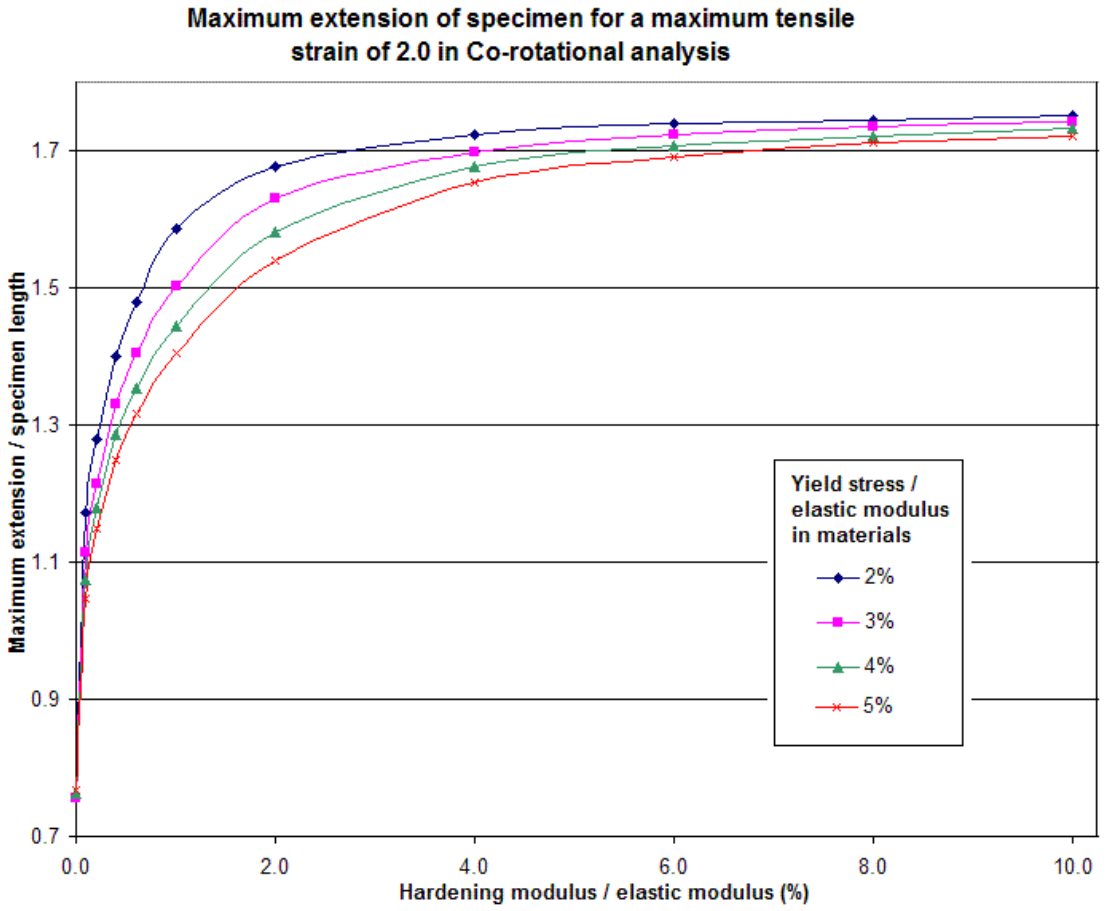

Figure 167. Modelled extensions of specimens for a limiting extension strain of 2.0

At zero hardening, the extension was less than that half of that for a hardening modulus ratio of 4% or more, and increased sharply for even a 0.1% hardening modulus ratio. The cause of this was a near triangular distribution of strain along the straight section of the test specimen at zero hardening, relative to a near uniform distribution of strain for significant hardening, as shown in Fig. 168.

The triangular distribution of strain at zero hardening is not considered to be representative of the real elongation pattern of the PVB samples tested, even those at low temperatures and high strain rates. Although high speed video could not be taken of the low temperature tests, the breaking pattern for these tests in Fig. 149 show that the centre of the specimen was the least likely position for the PVB to reach its failure strain, even when the hardening of the sample was at its lowest.

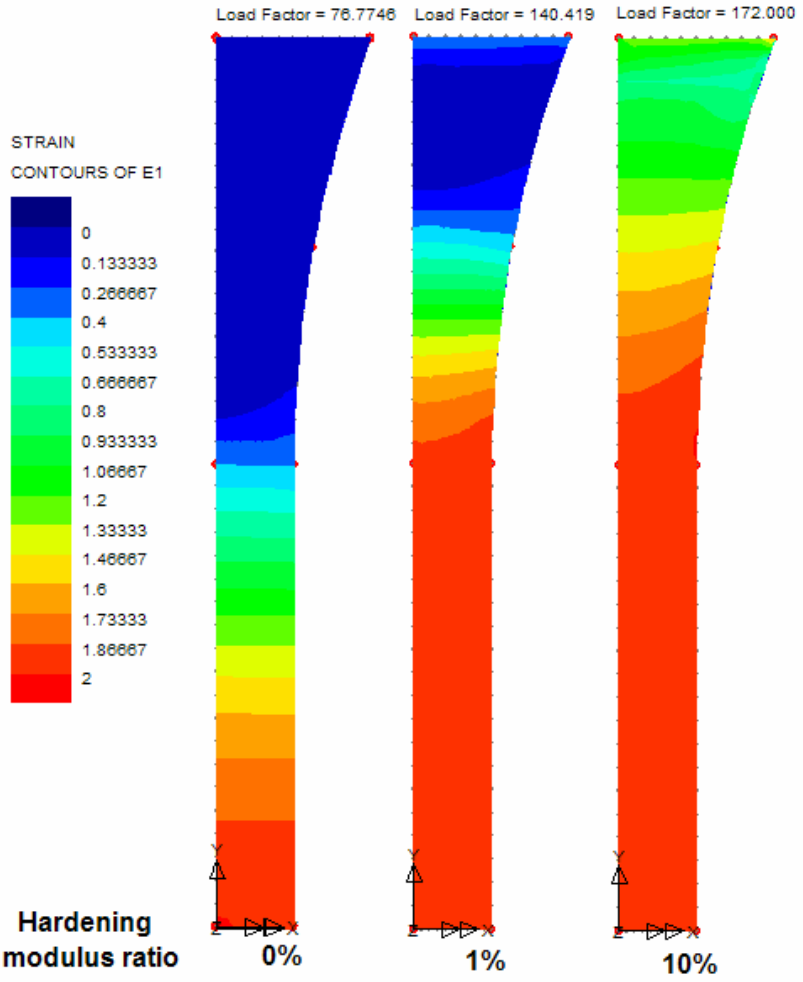

Figure 168. Strain distributions at analysis failure for different hardening modulus ratios and a yield stress ratio of 5%

The factors that allow a Young's modulus and yield stress to be selected for a Co-rotational finite element analysis to match a linearised test response from a sample of the shape tested are given in Table 60. The material properties to match any particular test result can be derived by interpolation.

Transition stress/ Young's modulus	2%	3%	4%	5%
Transition force/ (Elastic stiffness x specimen length)	1.88%	2.80%	3.70%	4.61%
Young's modulus/ (Elastic stiffness x sample length/ gauge area)	94.5%	93.2%	92.6%	92.2%
Transition stress x gauge area/ transition force	98.3%	98.8%	98.95%	99.0%

Table 60. Relationship of material and specimen properties up to transition, from a Lagrangian finite element analysis

Fig. 169 shows a plot of the mean hardening gradient of a test specimen from the transition point up to an extension of about 60 mm, as a proportion of its mean initial stiffness below the transition point, in terms of the yield stress ratio and the hardening modulus ratio with the Young's modulus. Given the bilinear approximation of the test data and the other properties already derived using the data in Table 60, this can be used to calculate a suitable hardening modulus for a material to use in a Co-rotational model of a particular test, and, by extension, a Co-rotational model of a PVB membrane at the same temperature and extension rate.

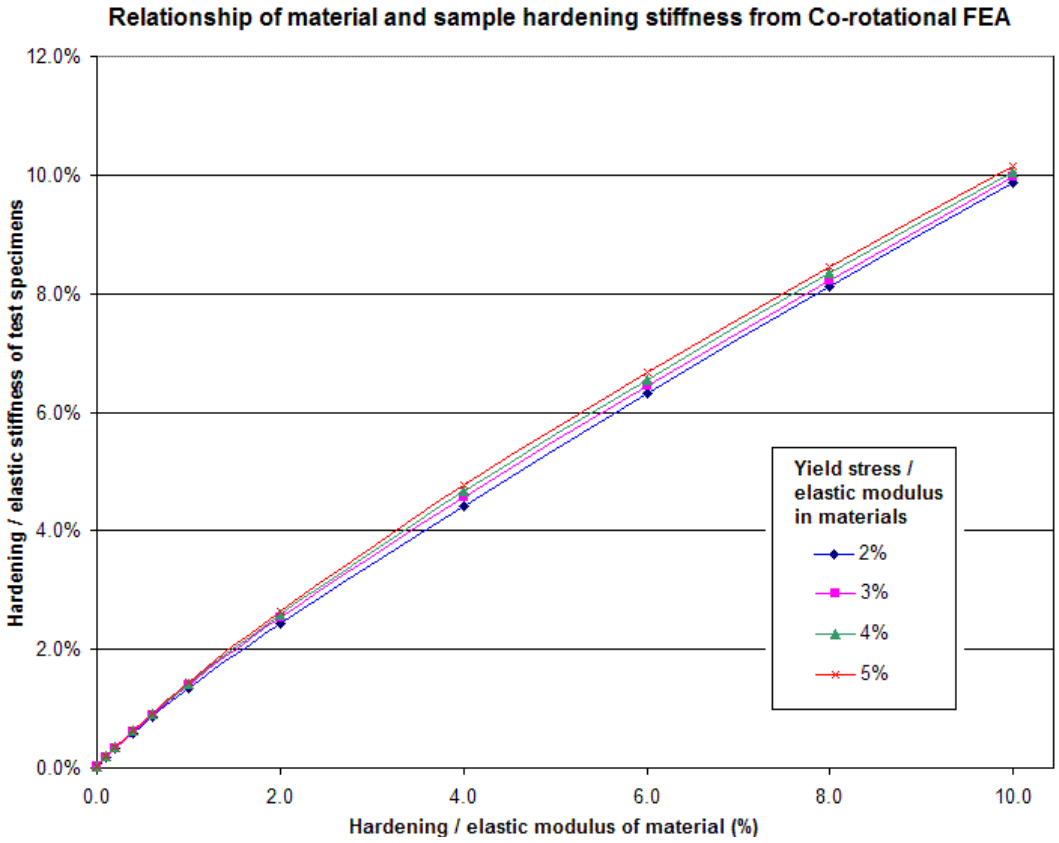

Figure 169. Relationship of material and sample stiffness after transition, from Co-rotational finite element analysis

Even for a zero hardening modulus there is a small positive hardening stiffness in the model, with the tangent stiffness never dropping to zero, and the secant stiffness increasing from 0.011% for a 2% yield stress ratio to 0.025% for a 5% yield stress ratio.

8.5.5 Application of the Co-rotational analysis to the test results

8.5.5.1 Cured PVB at room temperature

The average material properties for Co-rotational analysis of cured PVB at room temperature are given in Table 61, based on the test data averaged in Table 46.

Nominal pull velocity	Elastic strain rate	Young's modulus	Yield stress	Hardening modulus	Ultimate stress	Elongation / gauge length
m/s	Strain/s	N/mm^2	N/mm^2	N/mm^2	N/mm^2	Strain
1	9.39	145	4.65	8.31	24.5	2.87
2	19.36	159	6.01	8.76	27.1	3.00
4	37.80	214	7.91	8.60	26.1	2.61
8	74.16	455	10.21	6.30	28.9	2.83

Table 61. Co-rotational material properties derived from room temperature tests on cured PVB

A quadratic regression analysis of the design properties with respect to elastic strain rate gives properties that can be used for interpolation, or limited extrapolation. The results of such a regression analysis on the data averaged in Table 61 are given in Table 62. The data and trend lines are shown in Figs. 170-172.

Property	Equation relative to Strain Rate (SR) (/s)
Elastic modulus (N/mm^2)	$146.52 - 0.6711 \times SR + 0.0652 \times SR^2$
Transition stress (N/mm^2)	$3.3076 + 0.1527 \times SR - 0.000803 \times SR^2$
Hardening modulus (N/mm^2)	$7.8522 + 0.0647 \times SR - 0.00116 \times SR^2$

Table 62. Co-rotational material properties derived from room temperature tests on cured PVB relative to strain rate.

8.5.5.2 Cured PVB at a reduced temperature of 5ºC

The average material properties for Co-rotational analysis of cured PVB at a temperature of 5ºC are given in Table 63, based on the test data averaged in Table 48. A small softening modulus has been derived by extrapolation to give a zero hardening stiffness in the test specimens. Average material properties are given in Table 64, based on the alternative evaluation of these tests, as presented in Table 49.

Nominal pull velocity	Elastic strain rate	Young's modulus	Yield stress	Hardening modulus	Ultimate stress	Elongation / gauge length
m/s	Strain/s	N/mm^2	N/mm^2	N/mm^2	N/mm^2	Strain
1	9.46	362	20.9	-0.053	24.5	2.87
2	19.75	382	23.2	-0.058	27.1	3.00
4	38.32	570	25.9	-0.070	26.1	2.61
8	75.1	765	26.8	-0.075	28.9	2.83

Table 63. Co-rotational material properties derived from reduced temperature tests at 5ºC on cured PVB

Nominal pull velocity	Elastic strain rate	Young's modulus	Yield stress	Hardening modulus	Ultimate stress	Elongation / gauge length
m/s	Strain/s	N/mm^2	N/mm^2	N/mm^2	N/mm^2	Strain
1	9.41	366	17.6	5.94	24.5	2.87
2	19.67	383	20.8	3.91	27.1	3.00
4	38.29	571	24.6	2.04	26.1	2.61
8	75.06	726	25.4	2.10	28.9	2.83

Table 64. Alternative Co-rotational material properties derived from reduced temperature tests at 5ºC on cured PVB

A quadratic regression analysis of the alternative design properties with respect to elastic strain rate gives properties that can be used for interpolation, or limited extrapolation. The results of such a regression analysis on the data averaged in Table 64 are given in Table 65. The data and trend lines are shown in Figs. 170-172.

Property	Equation relative to Strain Rate (SR) (/s)
Elastic modulus (N/mm^2)	$258.32 + 9.2638 \times SR - 0.0404 \times SR^2$
Transition stress (N/mm^2)	$14.127 + 0.401 \times SR - 0.00334 \times SR^2$
Hardening modulus (N/mm^2)	$7.8731 - 0.235 \times SR + 0.00211 \times SR^2$

Table 65. Co-rotational material properties derived from reduced temperature tests at 5ºC on cured PVB relative to strain rate.

8.5.5.3 Cured PVB at an elevated temperature of 35ºC

The average material properties for Co-rotational analysis of cured PVB at an elevated temperature of 35ºC are given in Table 66, based on the test data averaged in Table 50.

Nominal pull velocity	Elastic strain rate	Young's modulus	Yield stress	Hardening modulus	Ultimate stress	Elongation / gauge length
m/s	Strain/s	N/mm^2	N/mm^2	N/mm^2	N/mm^2	Strain
1	9.28	22.3	0.846	2.05	17.3	3.80
2	19.1	41.7	1.24	3.02	20.6	3.60
4	37.7	94.9	2.20	4.71	23.1	3.42
8	73.9	159.4	3.14	8.73	26.1	3.34

Table 66. Co-rotational material properties derived from elevated temperature tests at 35ºC on cured PVB

A quadratic regression analysis of the design properties with respect to elastic strain rate gives properties that can be used for interpolation, or limited extrapolation. The results of such a regression analysis on the data averaged in Table 66 are given in Table 67. The data and trend lines are shown in Figs. 170-172.

Property	Equation relative to Strain Rate (SR) (/s)
Elastic modulus (N/mm^2)	-8.3798 + 3.1009 x SR – 0.0112 x SR^2
Transition stress (N/mm^2)	0.2445 + 0.0625 x SR – 0.00032 x SR^2
Hardening modulus (N/mm^2)	1.292 + 0.0830 x SR + 0.000223 x SR^2

Table 67. Co-rotational material properties derived from elevated temperature tests at 35ºC on cured PVB relative to strain rate.

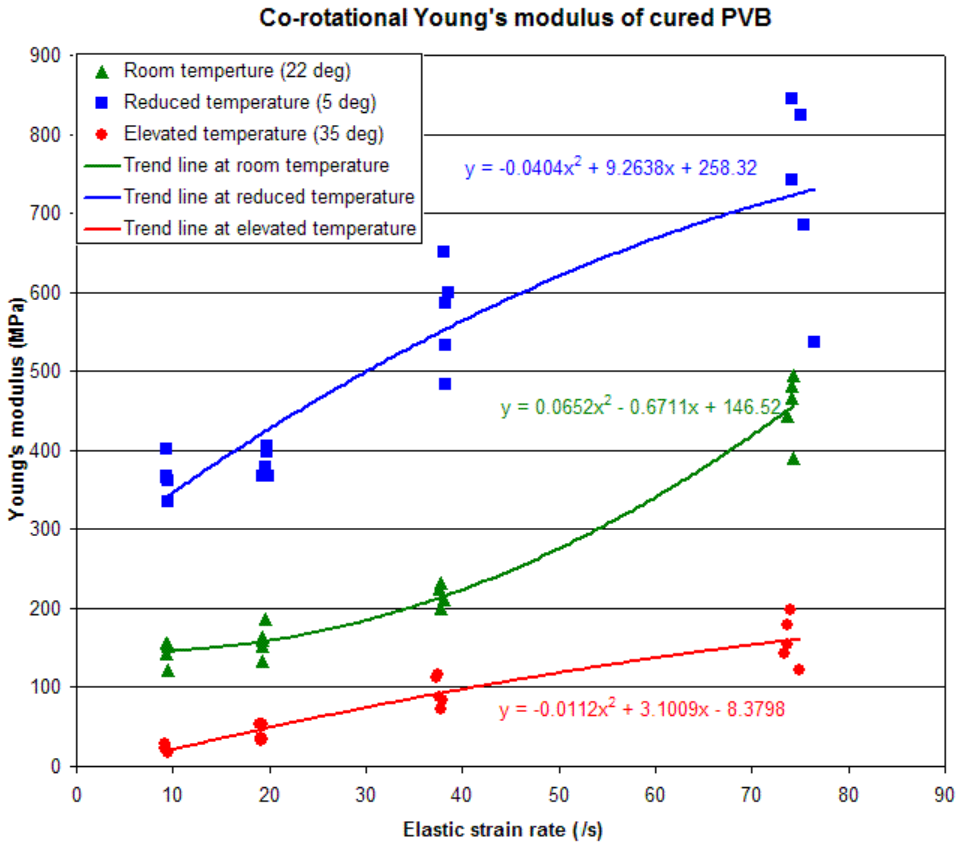

Figure 170. Co-rotational Young's modulus test values and trend lines

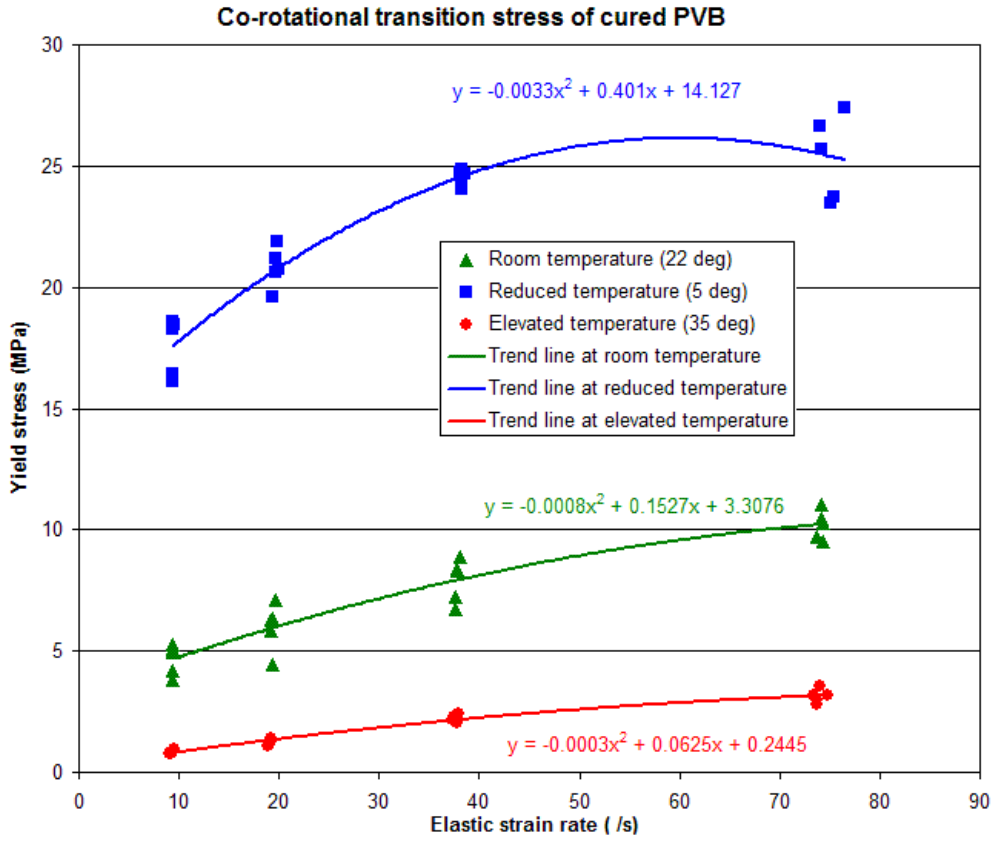

Figure 171. Co-rotational transition stress test values and trend lines

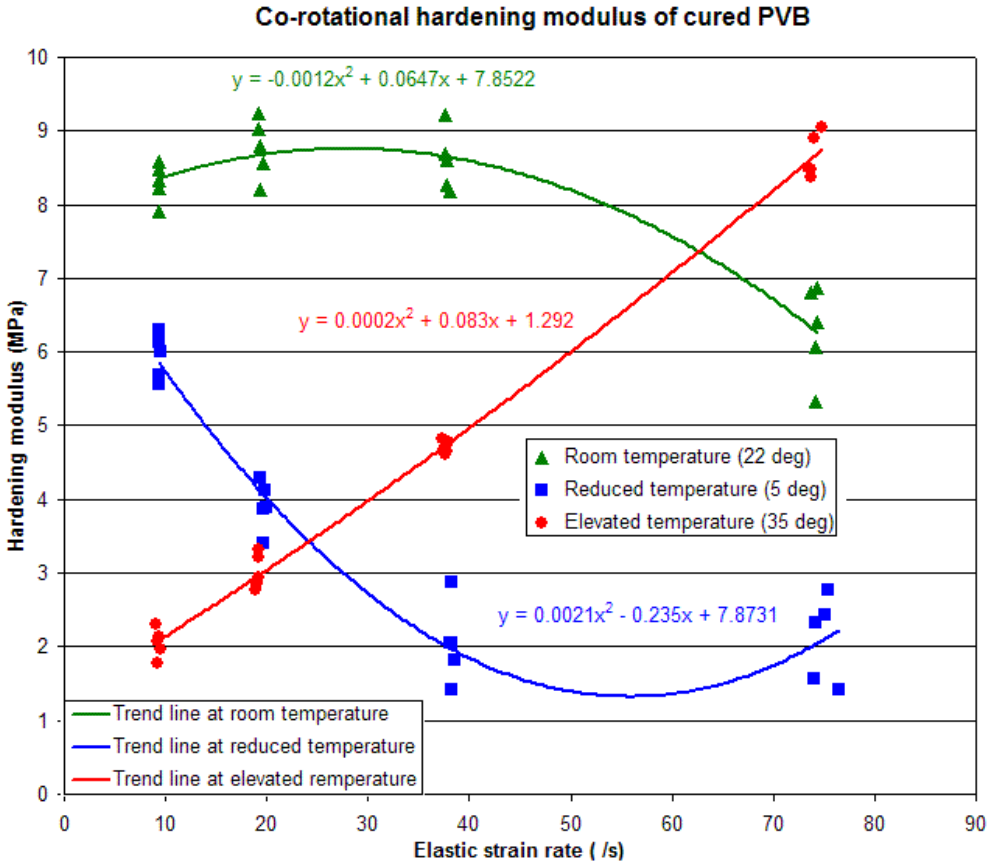

Figure 172. Co-rotational hardening modulus test values and trend lines

8.6 Summary from testing and analysis of PVB in uniaxial tension at high strain rates

8.6.1 PVB tensile tests

The high rate of strain tensile testing of PVB specimens has demonstrated that the behaviour of the material is far from linear. This suggests that existing methods of analysis that assume that PVB material behaviour is linear, and that only geometric linearity need be considered in analysis of a PVB membrane, will not be accurate.

The non-linear reduction in stiffness observed in low strain-rate testing [92, 120] also occurs at high strain-rates. Methods of analysis that allow for a change in stiffness [6, 37, 100] should be more accurate, but the accuracy can be improved by modelling the pattern of the resistance more accurately, and the analysis methods will only be as accurate as the material properties used.

The tests performed at Shrivenham were undertaken on uncured PVB, and covered a wide range of test velocities. These were useful in gaining an insight into the qualitative behaviour of PVB, but were not directly useful in the modelling of laminated glass, because the lamination process cures the PVB and changes the properties. The Imperial College tests were primarily of cured laminated glass, although sufficient tests were undertaken of uncured PVB to allow comparison, and to demonstrate the relevance of the Shrivenham tests. Unexpectedly, the cured PVB proved to be slightly stronger and stiffer than the uncured PVB.

The preliminary tests of straight samples, in which failure at the stress concentration at the specimen anchors occurred before the transition stress was reached in the sample generally indicates one of the pitfalls that may have lead to the previous assumption of linear behaviour, if simple test samples were used. The use of waisted samples overcame this problem. The 40% waist width used in the Shrivenham test specimens was sufficient to prevent failure from occurring at the supports. It is noticeable that some of the Imperial College specimens with a 50% waist width failed at the supports, although only after extensive elongation in the central section of the specimens.

The test specimens were narrow strips of PVB cut from a PVB sheet. However the peak elastic stress (other than the stress concentration at the support) occurs at the edge of the specimen, and high speed video showed that failures initiated at the edge of the sample. Failure is sensitive to the sample preparation, and the failure of some specimens at significantly lower extensions than similar specimens is likely to be due to this. The failure strains observed in the tests are expected to be lower bound for failures in a PVB sheet without stressed free edges. However, failure of cracked laminated glass is not expected to be due to direct stretching of the PVB, so this is not expected to be critical.

Analyses of tests with zero or very small hardening stiffness indicate a concentration of strain in the centre of the uniform section of the specimens, even though the force is constant along the length. The low temperature tests that are most closely

represented by these analyses could not be videoed because of the presence of the thermal cabinet, so there is no direct evidence for or against this pattern of behaviour. However, the preponderance of failures away from the centre of the specimens suggest that the analyses are not typical of the tests.

Models with localised high strains are not considered truly representative of PVB behaviour, but may explain the statements in the WINGARD manual [100], based on elastic-pure plastic FE analyses, that the plastic strain only occurs close to the support, and only allows limited additional deflection.

8.6.2 Analysis models for PVB

The uniaxial tensile properties of PVB have been demonstrated to show complex, non-linear viscoelastic behaviour at high strain rates. To analyse the response of more complex geometric arrangements, such as PVB membranes with large deflection, requires the use of a material model that can be demonstrated to reproduce the important features of the test behaviour, and which can then be applied in analysing the more complex geometries of real interest. The three major features of the response appear to be:

- Viscoelasticity causing gradual softening over time in a dynamic response, together with sensitivity to strain rate and temperature
- Hyperelasticity typical of soft rubber-like materials, causing gradual increase in stiffness at large strains
- An abrupt transition, with a large reduction in stiffness from a small strain regime to a large strain regime. However, this is not true plasticity, which it resembles, because the deformation is recoverable.

Two main approaches appear to be possible to modelling PVB behaviour. The first approach is the complex, comprehensive material model, which incorporates a number of different forms of behaviour into a single model to try to fully model the material behaviour. These tend to need large numbers of parameters to describe the material, and need results from a variety of different tests to find values for these parameter by a combination of back-analysis of the tests and curve fitting. Once this is achieved, the material model can be used to analyse the material in many different situations.

The alternative, empirical, approach is to use a relatively simple model with few parameters to approximate the response to individual tests, and to undertake the tests at various values of conditions to which the material is known to be sensitive. This is then used to define the sensitivity of the parameters to those conditions.

In recent years, considerable research effort has been directed towards comprehensive material models of polymers in general, and PVB in particular, led and funded in great part by the German motor industry. Most of the effort has been aimed at exploring the combination of rubber-like hyperelastic behaviour with viscoelastic behaviour. There is still a healthy debate on the degree of non-linearity needed in combination with a Generalised Maxwell approach to model behaviour of polymers.

Most of this is incorporated in research finite element codes or user-defined models in commercial finite element codes. The only current commercial implementation of a non-linear viscoelastic model in DYNA has one low-order non-linear term combined with a Generalised Maxwell viscoelastic model, and has been shown to be incapable of modelling polymer behaviour over a range of strain rates [103]. Even the more advanced models are not effective at modelling the abrupt transition in stiffness shown in the tests.

Other attempts at comprehensive models available are similarly incomplete. LUSAS, for example, can implement a single Maxwell viscoelastic term with plastic non-linearity, or a 'Generic Polymer' model with a viscoplastic term in series with a Generalised Maxwell viscoelastic model, but cannot combine these with its hyperelastic model in the same material.

The conclusion reached is that the comprehensive models are not yet sufficiently mature for general use, and that, at present, it would be unwise to rely on such a PVB model to analyse PVB membranes in laminated glass when it cannot model the abrupt transition in stiffness.

The approach adopted in this thesis is therefore to use a simple bi-linear elastic-plastic material model with a von Mises yield criterion, and three variable material properties:

- Initial elastic modulus (Young's modulus)
- Transition stress (yield stress in plasticity)
- Strain hardening modulus

which are sensitive to strain rate and temperature.

A constant Poisson's ratio of 0.49 has been used throughout, to reflect the fact that PVB is nearly incompressible with a high bulk modulus which is insensitive to strain rate or temperature.

Even with this material model, there were choices of the geometric non-linear formulation to be used in conjunction with the non-linear material model. The difference in hardening stiffness found between the well established Lagrangian formulation, commonly used for modelling plasticity, and the more recent Co-rotational formulation in similar models was unexpected. Significant differences did not simply occur at high strains, but from the onset of plasticity in what should still be a small strain regime.

The systematic higher hardening stiffness in the Lagrangian formulation for identical material models and mesh sizes might suggest shear-locking of the elements as they distort plastically, but the elements used had a modified matrix that should eliminate shear-locking, and refinement of the mesh in the model did not significantly affect the model.

Without having to account for the distortion that this has introduced to the Lagrangian hardening modulus, the material properties back-analysed from the test results using

the Co-rotational analysis are likely to be closer to the true material properties, and should be more reliable in analysing PVB membranes. However, the Co-rotational formulation is not available in LUSAS for shell elements, so there will be a penalty in model size and running time using this formulation.

In practice, only the Co-rotational formulation will be practicable for analysing PVB at reduced temperatures, but for other analyses both will be used.

Even the analysis using the Co-rotational formulation is not without its flaws. The von Mises plastic yield model is still not truly suited for large strain modelling, and the error in the transverse strain as a result of this limits the maximum strain that can be analysed, although the force-deflection relationship still appears to be correct up to the limiting strain.

The only material models in LUSAS that are not expected to suffer from this limitation are the various rubber models, of which the most versatile is the Ogden model. These are defined in terms of a bulk modulus and a non-linear shear modulus defined by equations of different forms and with different numbers of parameters required. Although they can be used to model smooth non-linearity of several forms, none of them can reliably model abrupt changes in stiffness, and cannot be used in combination with other material models such as viscoelasticity.

9 Cracked laminated glass membranes

9.1 Elastic tensile membrane behaviour

9.1.1 Previous analyses

In his description of membrane theory, Mansfield [95] indicates that under lateral loading any very thin elastic plate, taken to the extreme case of a membrane, will deflect in proportion to the cube root of the force. However, he offered no coefficients for any rectangular membranes.

Timoshenko [38] analysed rectangular elastic plates with large deflections, but only gave coefficients for a square steel panel with simply-supported but fully-restrained edges. The relationship between pressure p and central deflection z can be written as:

$$p = E\left(\frac{h}{b}\right)^4\left[21.9\frac{z}{h} + 31.04\left(\frac{z}{h}\right)^3\right] \tag{59}$$

where b is the length of the plate, h the thickness and E is Young's modulus. The first linear term in the square bracket represents the bending resistance, while the second term represents the membrane resistance. As the deflection increases relative to thickness, the second term dominates. For a deflection equal to the thickness, 59% of the loading corresponds to membrane behaviour, while for a deflection ten times the thickness 99.93% of the loading corresponds to membrane behaviour.

For thin PVB membranes with the span of the order 1000 times the thickness, the linear bending term can be ignored, and Eqn. 59 reduces to a cubic equation, with a coefficient of 31.04. Even though this was calculated for steel, with a Poisson's ratio close to 0.3, it has been applied to many other materials.

The WINGARD technical manual [100] gives a closed form equation for the cubic coefficient in terms of length, breadth and Poisson's ratio. The manual states that this reduces to Timoshenko's solution for a square membrane, and the coefficient does equal 31.04 (to four significant figures) for a Poisson's ratio of 0.304.

Considering a material such as PVB with a Poisson's ratio of 0.49, a plot of the coefficient W_C produced by this closed form solution in the equation:

$$p = W_C \cdot E\left(\frac{h}{b}\right)^4\left(\frac{z}{h}\right)^3 \tag{60}$$

is given in Fig. 173 for a range of aspect ratios a/b, where b is the short span and a is the long span. For the square membrane the coefficient value is 40.16.

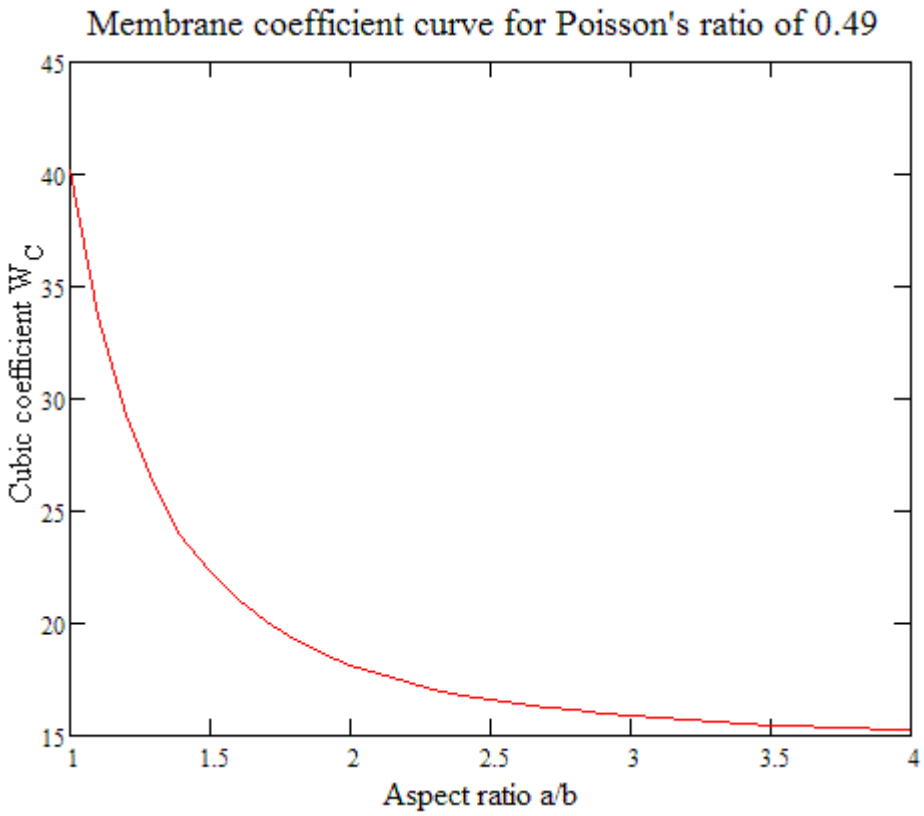

Figure 173. Membrane coefficients from the WINGARD closed form solution for Poisson's ratio of 0.49

The WINGARD manual reported reasonable correlation of this formula with finite element analyses up to deflections of 15% of the span. However, the HAZL [97] help screens state that this solution was not adopted in HAZL for resistance calculations because other finite element analyses indicated that it understated the stiffness.

9.1.2 Finite element analyses

A series of geometric non-linear analyses was undertaken using thin shell elements with a linear elastic material and a 'Total Lagrangian' non-linear formulation. The aspect ratio of the analyses varied from 1.0 to 4.0.

A corresponding series of non-linear analyses were undertaken using solid elements and a Co-rotational non-linear formulation, using the same geometry and material, for the same range of aspect ratios.

Both these series of analyses take the load as acting as a conservative force perpendicular to the original plane of the membrane, rather than as a follower force acting perpendicular to the membrane as it deformed. The difference between these forms of loading is illustrated in Fig. 77. The difference in response between these can be expected to be substantial, given the large deflections and rotations experienced by a thin membrane of relatively soft PVB under lateral loading.

Conservative forces were selected for the analysis of the membranes, even though follower forces had been used for the non-linear analysis of glass plates in Chapter 6, because of the relative slow response expected from PVB membranes under blast loading.

A blast loading transfers impulse to the membrane as momentum normal to the surface when it is loaded by the blast pressure wave. This imparts an initial velocity which is a vector and conserves its original direction. If most of the blast loading occurs early in the response of the membrane, the velocity vector will be close to perpendicular to the original membrane direction, and the dynamic loading will be close to a conservative load. On the other hand, a long, persistent transient pressure loading (which is still substantial by the time of the peak membrane deflection) will have loaded the membrane throughout the deformation period. The net impulse vector will have been intermediate between the conservative and follower force direction, and the deflected shape at maximum deflection will be intermediate between the two cases. No transient loading from a shock wave will give a deflected shape matching that from a static follower force.

The error in the dynamic response curve due to the use of a resistance based upon conservative loading will be least for large panes, for over-designed façades in which the PVB membrane deflections are well short of failure, and for small charges at close range. The errors will be greatest in the analysis of small panes loaded to their capacity, particularly when subject to long duration transient loads such as arise from accidental explosions of petrochemicals or bulk explosives stores, or from nuclear weapons. The assessment of deflection of curtain-walling subjected to blasts from vehicle borne improvised explosive devices is likely to be subject to moderate error from this approximation.

The sensitivity study on conservative and follower forces on non-linear glass plates in Section 6.3 showed that conservative forces gave a stiffer response than follower forces. Some preliminary analyses were undertaken using the ‘Incremental Lagrangian’ formulation and follower forces on shell element models of membranes. These confirmed that a lower stiffness can be expected with follower forces, which suggests that the membrane stiffness calculated from analyses with conservative forces will tend to be upper bound. The preliminary membrane analyses also showed a degree of chaotic variability in the results, with variations in the third or fourth significant figure of the Poisson’s ratio resulting in significant random variations in the stiffness of the membrane, presumably from the accumulation of rounding errors in the use of many successive increments to calculate the force-deflection curve.

An elastic material was selected with a Poisson’s ratio of 0.49, consistent with other models of PVB, and the high measured bulk modulus reported by Benneson et al. [88]. A Young’s modulus of 80 MPa was assumed for analysis, but the conclusions from the analysis were expected to be independent of this assumption.

A short span dimension of 1.5 m was used for the panel, although only a quadrant of the panel was modelled in the analyses. A membrane thickness of 2.28 mm was assumed in the model. This is the overall thickness of PVB in laminated glass 11.3mm thick, and the model slenderness ratio of 658 falls in the middle of the likely range of practical PVB membranes intended to provide blast resistance.

A uniform mesh of square elements (either shell elements or solid elements) was used. A finer mesh than that used for glass plates in Fig. 54 was required to allow the analysis of the first step to converge. This step was the most difficult to analyse because of the low initial stiffness that led to a high initial non-linearity. It proved necessary to use a minimum of 30 elements across a half span, in combination with lower convergence criteria, to obtain convergence of the first step with a very low initial loading.

The analysis does not result in a high stress concentration in the corner, unlike the glass plate analysis, so a graduated mesh, as in Fig. 79, was not required. A typical finite element model is shown in Fig. 174.

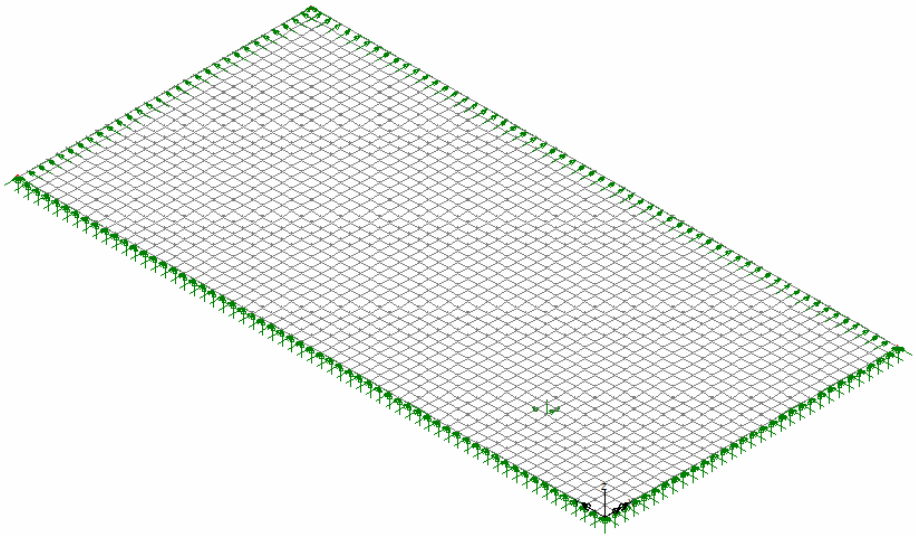

Figure 174. Typical mesh for membrane analysis with an aspect ratio of 2.0

The results of the analyses are presented in terms of a non-dimensional pressure P and non-dimensional deflection d :

$$P = \frac{p}{E} \cdot \left(\frac{b}{h}\right)^4 \qquad \text{and} \qquad d = \frac{z}{h} = \frac{z}{b} \cdot \frac{b}{h} \tag{61}$$

where the terms are as for Eqn. 60. It should be noted that d is the same non-dimensional deflection as that used by Moore [67] and in Chapter 6 for non-linear analysis of glass plates, and that P is proportional to, but not identical to, the non-dimensional load L for glass plates.

Although these definitions of P and d were chosen so that the results of the finite element analyses could be directly compared with Eqns. 59 and 60, a sensitivity study, reported later in this section, showed that the results of the analyses presented in this way were sensitive to slenderness. The variations from the cubic curve appeared to be a function of the deflection as a proportion of the span rather than as a multiple of the thickness.

Equation 60 can be re-written as:

$$p = W_C \cdot E\left(\frac{h}{b}\right) \cdot \left(\frac{z}{b}\right)^3 \tag{62}$$

The results of the analyses can therefore also be presented in terms of revised non-dimensional pressure P_{ND}' and revised non-dimensional deflection d' (indicated by 'ND membrane pressure' and 'ND membrane deflection' in subsequent figures) using the same cubic coefficient W_C from WINGARD:

$$P_{ND}' = \frac{p}{E} \cdot \frac{b}{h} \qquad \text{and} \qquad d' = \frac{z}{b} \tag{63}$$

with the terms as defined for Eqn. 60. The results presented in this form are still comparable with the WINGARD cubic formula, but are shown later in this section to be less sensitive to the membrane slenderness.

The results of the Lagrangian shell and Co-rotational solid analyses are compared with the cubic curves defined by the closed form solution in WINGARD for aspect ratios between 1.0 and 4.0 in Figs. 175 to 179.

These figures show that there are substantial differences between the two finite element analyses, although the geometry modelled and the material models are identical, and that the differences vary with the aspect ratio of the membrane. In square and nearly square membranes, where much of the membrane is in near equal bi-axial tension, the Lagrangian shell analysis shows higher stiffness than the Co-rotational solid analysis, as seen in Figs. 175 and 176. In long membranes where the central part of the membrane is one-way spanning in near uniaxial strain the reverse is true, as shown in Figs. 178 and 179.

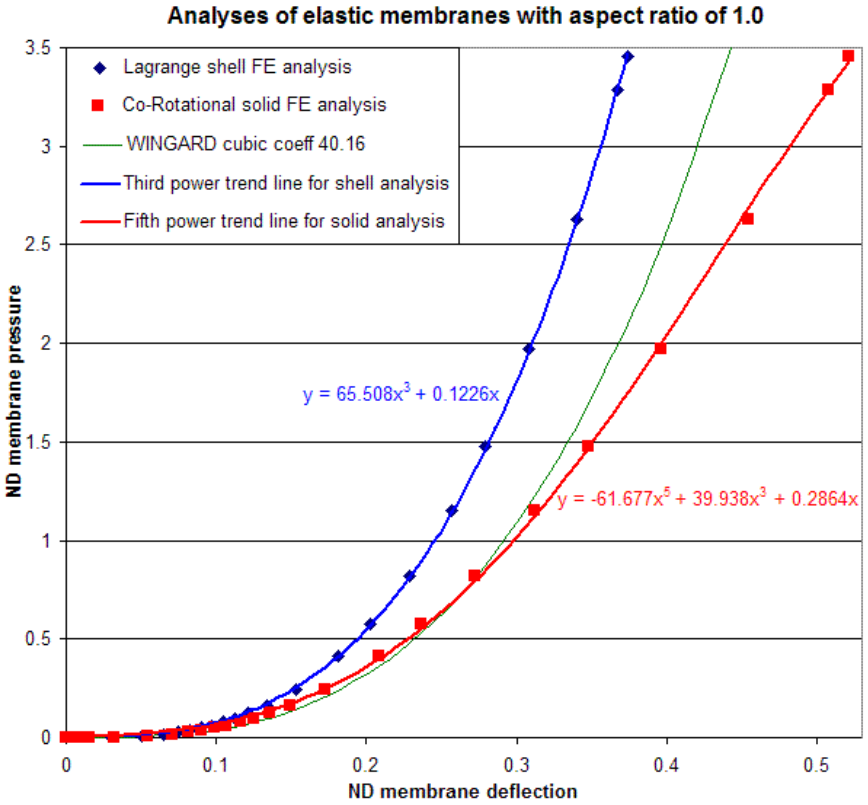

Figure 175. Analyses of elastic membranes with an aspect ratio of 1.0

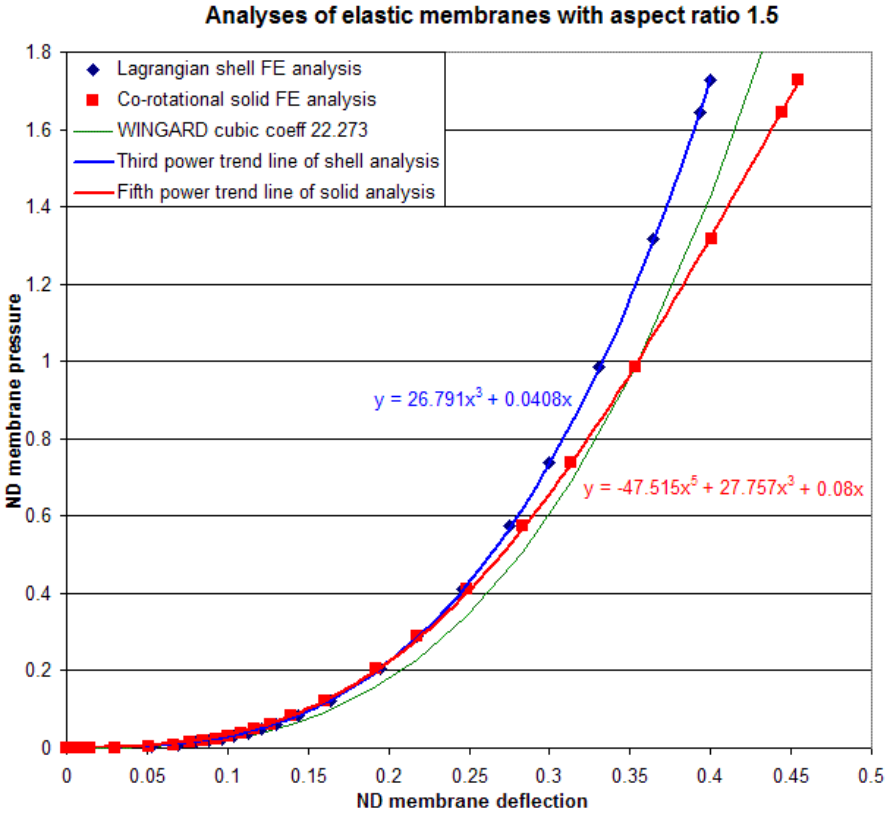

Figure 176. Analyses of elastic membranes with an aspect ratio of 1.5

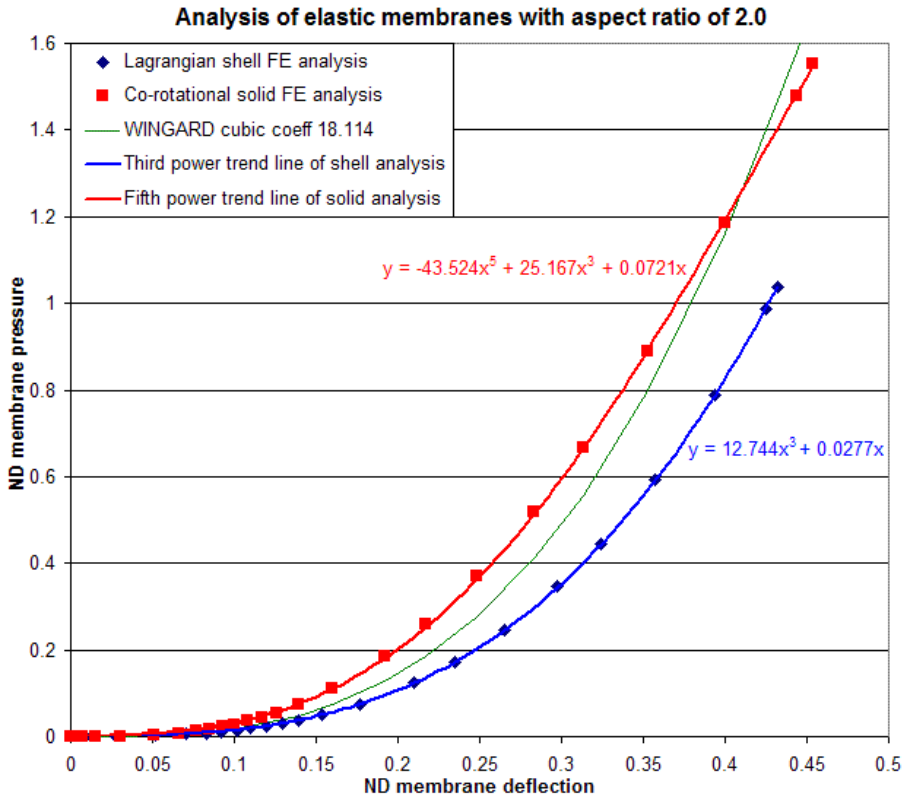

Figure 177. Analyses of elastic membranes with an aspect ratio of 2.0

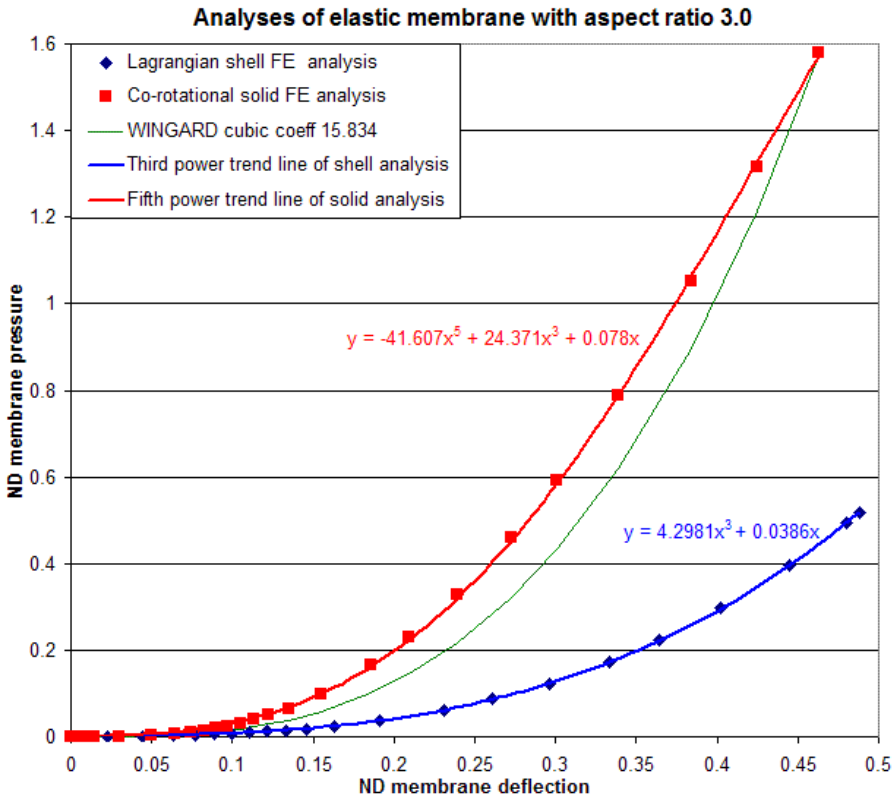

Figure 178. Analyses of elastic membranes with an aspect ratio of 3.0

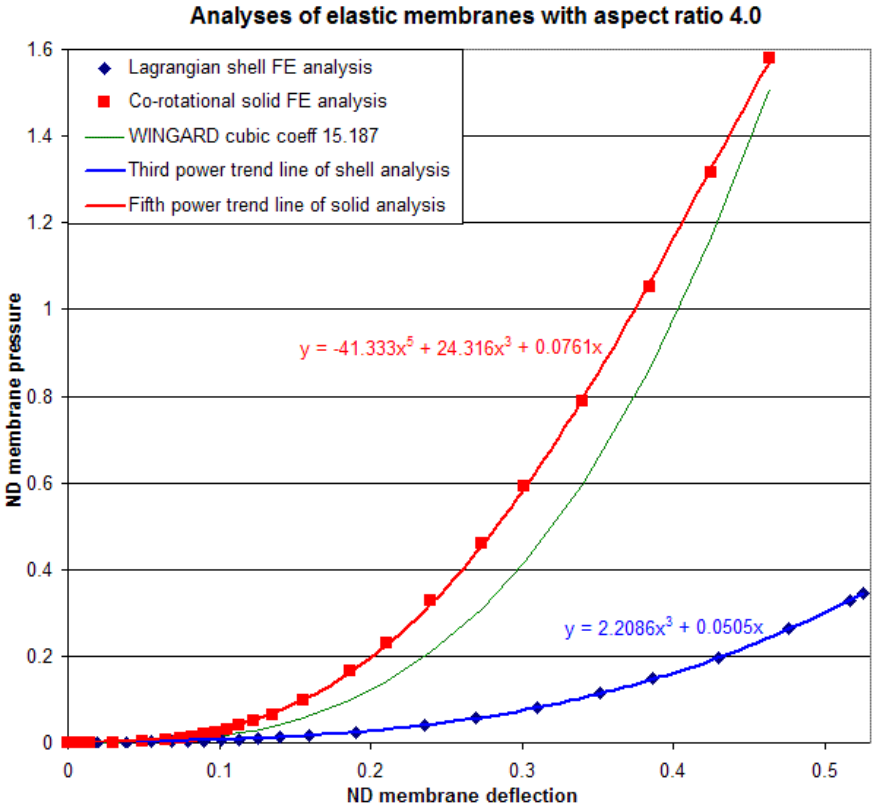

Figure 179. Analyses of elastic membranes with an aspect ratio of 4.0

Neither of the finite element analysis formulations result in pure cubic curves as calculated by the closed form solution in WINGARD, although the stiffness of the solid element analyses remains of a similar magnitude, while for larger aspect ratios the shell element analyses result in substantially lower stiffnesses. The results of the shell analyses could explain the observation in the HAZL help pages mentioned in Section 9.1.1, while the results of the solid element analysis in Fig. 175 is consistent with the FE results presented in the WINGARD manual [100] for a square panel.

Both the finite element analyses show results that follow the WINGARD cubic curve initially, up to a deflection of about 3% of the span. Typical results are shown in Figs. 180 and 181, which are close-in views of the lower parts of Figs. 176 and 178 respectively.

For deflections greater than about 3% of the span, the Co-rotational solid analyses show stiffness increasing faster than the WINGARD cubic curve up to about a deflection of 25% of the span, and a lower stiffness increase at higher deflections, so that the curves cross at deflections between about 27% and over 45% of the span, depending on the aspect ratio.

To reproduce this, a polynomial least-squares trend line requires a polynomial of at least the fifth power, with a higher cubic coefficient than the WINGARD coefficient, or a similar cubic coefficient combined with a large positive linear coefficient, to model the middle part of the curve, and a small negative fifth power coefficient to reduce the stiffness at the higher deflections. However, the least-squares trend curves result in a much closer proportionate match to the large values than the small values. The linear coefficients are much larger than the bending coefficient in Eqn. 59, and make the trend lines much too high at small deflections, as seen in Figs 180 and 181.

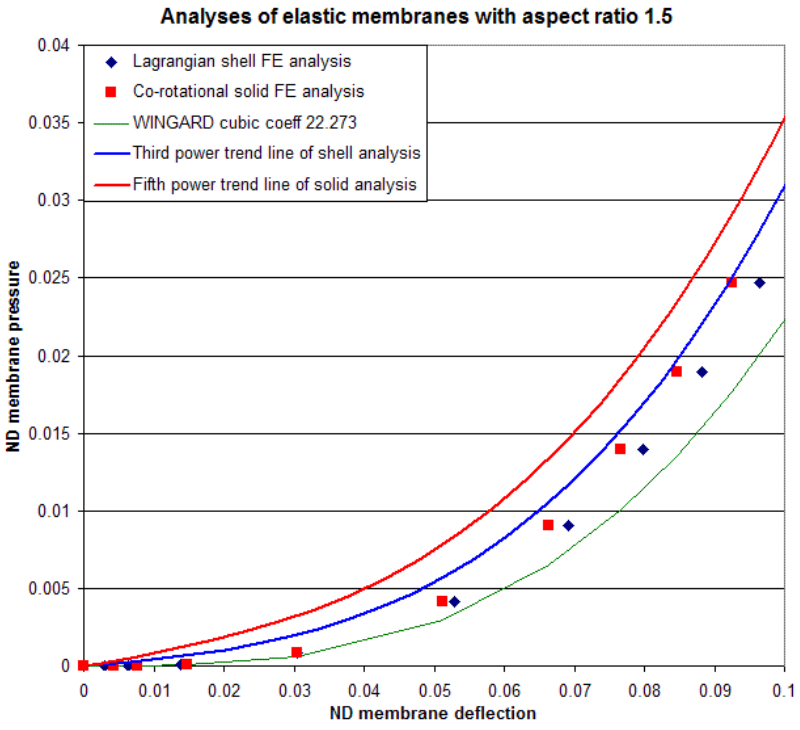

Figure 180. Initial part of analyses of elastic membranes with an aspect ratio of 1.5

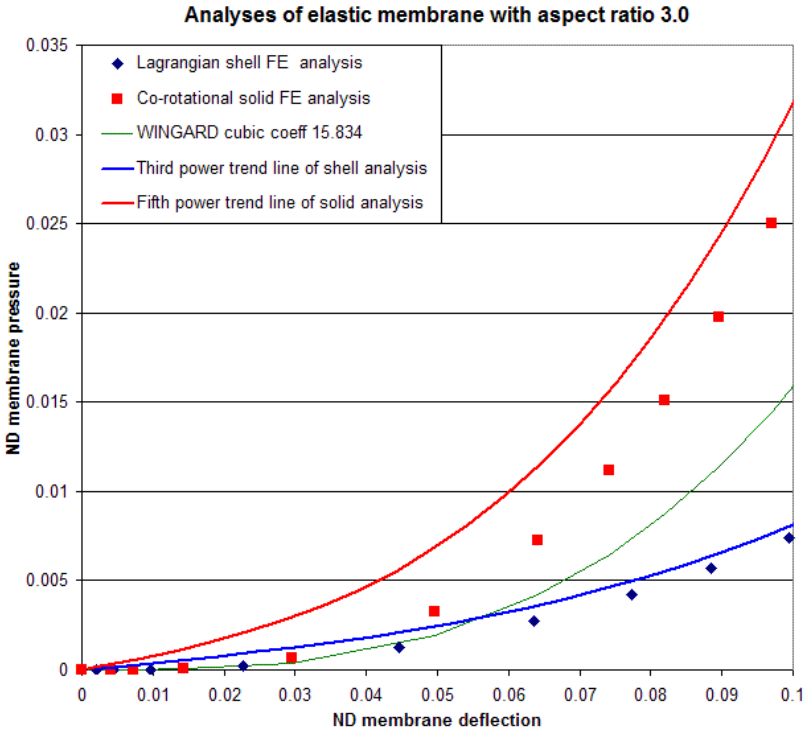

Figure 181. Initial part of analyses of elastic membranes with an aspect ratio of 3.0

The Lagrangian shell analyses start to diverge visibly from the Co-rotational solid analysis and the WINGARD curve for deflections above about 3% of the span, as shown by Figs. 180 and 181. However, alternative Lagrangian and Eulerian analyses using solid elements, shown in Fig. 182, suggest that the cause of the large change in stiffness with aspect ratio lies in the behaviour of the thin shell elements rather than the small strain basis of the Lagrangian non-linear formulation.

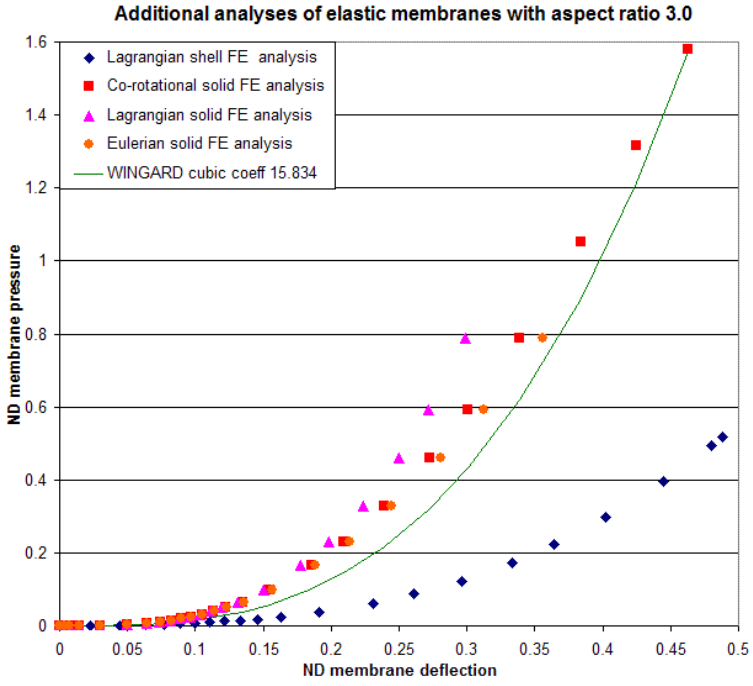

Figure 182. Additional analyses of elastic membranes with an aspect ratio of 3.0

The Lagrangian and Eulerian analyses of solid elements do not reach the maximum deflections of the Co-rotational or shell analyses: the former fails to converge, while the latter crashes with a "negative Jacobean" error message, which suggests instability in the analysis, such as wrinkling of the PVB in the corners. However, the trend of the results increases confidence in the reliability of the analysis using solid elements and the Co-rotational formulation, which is specifically recommended for large deformation, large rotation and large strain modelling.

The inaccuracy of the least-squares trend lines at smaller deflections shown in Figs. 180 and 181 indicates that an analytical approximation of the finite element results will not generate a reliable resistance function for an elastic membrane at small deflection. A numerical interpolation between the results of a Co-rotational analysis will be more reliably accurate across the full range of deflections in generating a resistance function for the membrane. The cubic coefficient from the WINGARD equations will give a rough approximation of the resistance of a membrane of a linear elastic material.

9.1.3 Sensitivity studies

9.1.3.1 Mesh density

Sensitivity studies were conducted on the mesh density of the Co-rotational solid analyses. Initially, the same mesh density was used as for the Lagrangian shell model, with a minimum of 30 square elements per half-span.

For the solid element models, this fine uniform mesh gave an aspect ratio of 10.96 for each element, which is high, but not unreasonably so. A coarser mesh or a thinner membrane would give a higher aspect ratio still. This could result in reduced accuracy in the analysis, as the ratio of coefficients in the element matrix would become large, which could reduce the accuracy of the matrix solution. Although the solid elements converged more easily in the initial load step, the slenderness of the elements encouraged a similar mesh.

However, only linear elements can be used with the Co-rotational formulation, while the shell elements were quadratic elements with mid-side nodes. The Co-rotational mesh can be expected to be less accurate, although the enhanced-strain linear solid elements used should model curvature well without experiencing shear-locking, and so are closer in performance to a quadratic element than could be expected from a simple solid element.

One analysis was run with the mesh doubled in both plan directions, to 60 elements per half-span. The mesh refinement increased the maximum deflection by only 0.04%.

One analysis was run with the standard plan mesh, but modelled two elements thick rather than one element thick. The mesh refinement increased the maximum deflection by only 0.1%.

The changes in performance from doubling the mesh density are sufficiently small that analyses using the original mesh are considered to be a reasonable representation.

9.1.3.2 Membrane slenderness

A sensitivity study of the effects of varying the slenderness of the membrane showed that similar deflections can be produced by varying the load in proportion to the membrane thickness for the same span. However, plotting this in terms of the non-dimensional pressure and deflection defined in Eqn. 61 resulted in curves with a similar relationship to the WINGARD cubic curve, but at different scales, as shown in Fig. 183 for an aspect ratio of 3.0, indicating that using those non-dimensional properties did not eliminate sensitivity to slenderness.

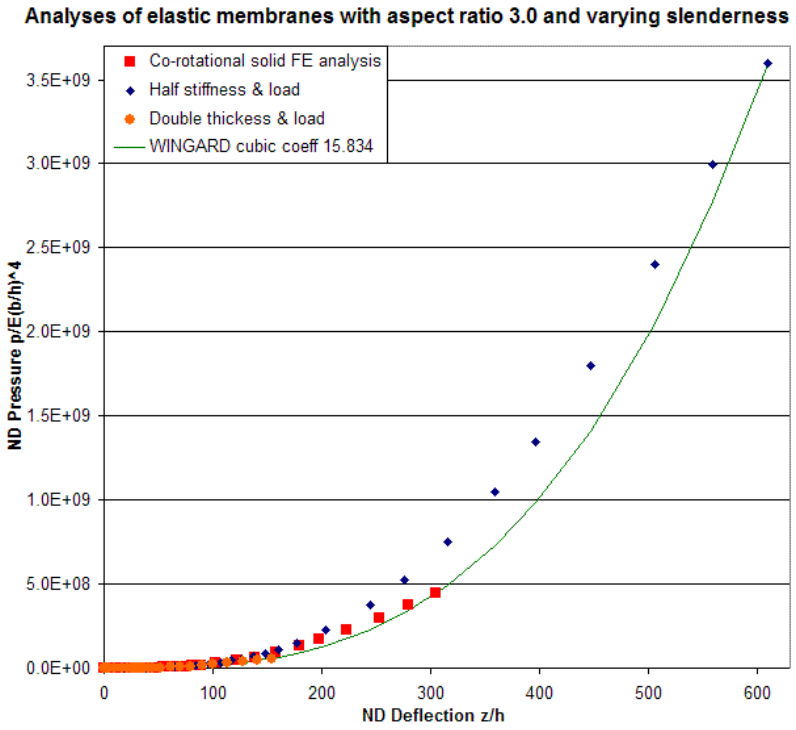

Figure 183. Analyses of elastic membranes of varying slenderness with respect to non-dimensional parameters in Eqn. 61.

Presenting the same results of the sensitivity study of membrane slenderness in terms of the non-dimensional properties in Eqn. 63 in Fig. 184, shows a close correlation when the thickness is half or double that of the original analysis, and hence the slenderness is double or half the original slenderness.

The higher slenderness corresponds to the membrane in a 6.8 mm thick laminated glass pane with a span of 1.0 m or an 11.5 mm thick laminated glass with a span of 2.0 m. This is approaching the practical limitation for slender PVB membranes in laminated glass to resist significant blast loading. The lower slenderness corresponds to the combined membranes in a 19.5 mm thick multi-ply laminated glass with a span of 1.0 m. Only extreme cases are likely to require a lower slenderness than this for blast resistance. With rare exceptions, most laminated glass with large thicknesses of

PVB uses multiple PVB layers no thicker than 1.52mm, for which the more slender analyses will, in any case, be more representative.

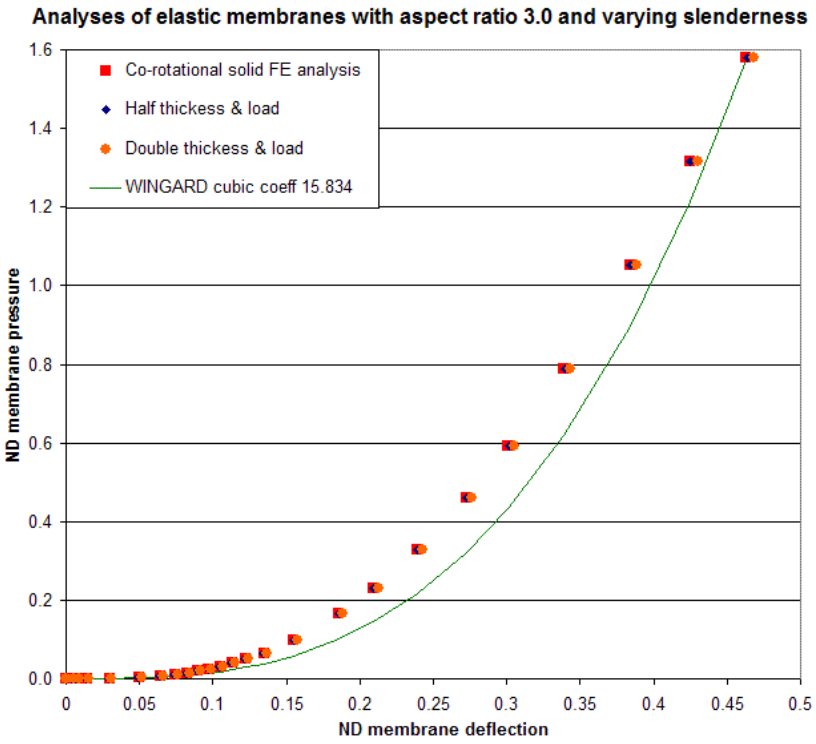

Figure 184. Analyses of elastic membranes of different slenderness with respect to non-dimensional parameters in Eqn. 63.

The close-in view of this data in Fig. 185 shows that there is a systematic increase in small deflections as the slenderness reduces, but the effect reduces in proportion as the deflections increase.

Considering the numerical data, at a deflection of 3% of span the deflection increased by 5% when the slenderness was halved, and decreases by 2% when the slenderness was doubled. These percentage variations were approximately halved for double the deflections, and reduced to about 1% or less at larger deflections.

As the PVB membrane will not be active at small deflections when the glass is still uncracked, these variations in stiffness with slenderness will not be significant in analysing the response of laminated glass. The original analyses can reasonably be used to represent membranes of any normal laminated glass with minimal error, and are still likely to be within about 1% even for unusual PVB configurations.

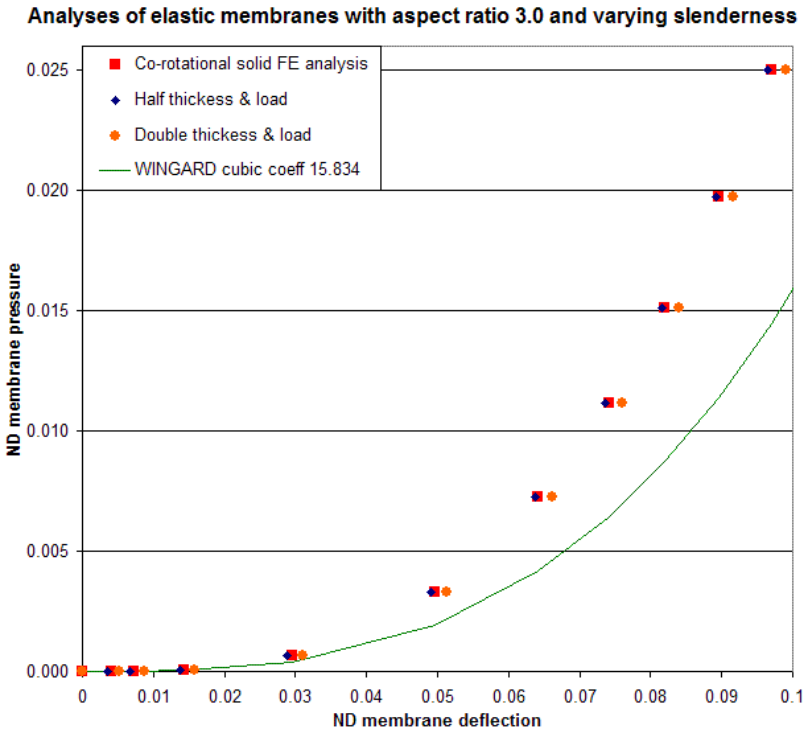

Figure 185. Initial part of analyses of elastic membranes of different slenderness with respect to non-dimensional parameters in Eqn. 63.

It was noted that Fig. 185 demonstrates that the accurate fit of the WINGARD cubic curve up to 3% of the span (identified in Section 9.1.2 and shown in Figs. 180 and 181) is indeed related to the deflection as a proportion of the span, rather than in proportion to the membrane thickness.

9.1.4 Design resistance of elastic PVB membranes

The results of the original Co-rotational solid finite element analyses can be used to represent the resistance of all likely PVB membranes in laminated glass. Elastic analyses are presented for a range of aspect ratios in Figs. 186 and 187. Fig. 187 plots the 'ND membrane pressure' against the cube of the 'ND membrane deflection', so the variation from the WINGARD cubic relationship, which appears as straight lines, can be observed.

Figs. 186 and 187 show that the sensitivity to aspect ratio is greatest for aspect ratios between 1.0 and 1.5, with little variation for aspect ratios above 2.0, with the results for aspect ratios 3.0 and 4.0 being indistinguishable.

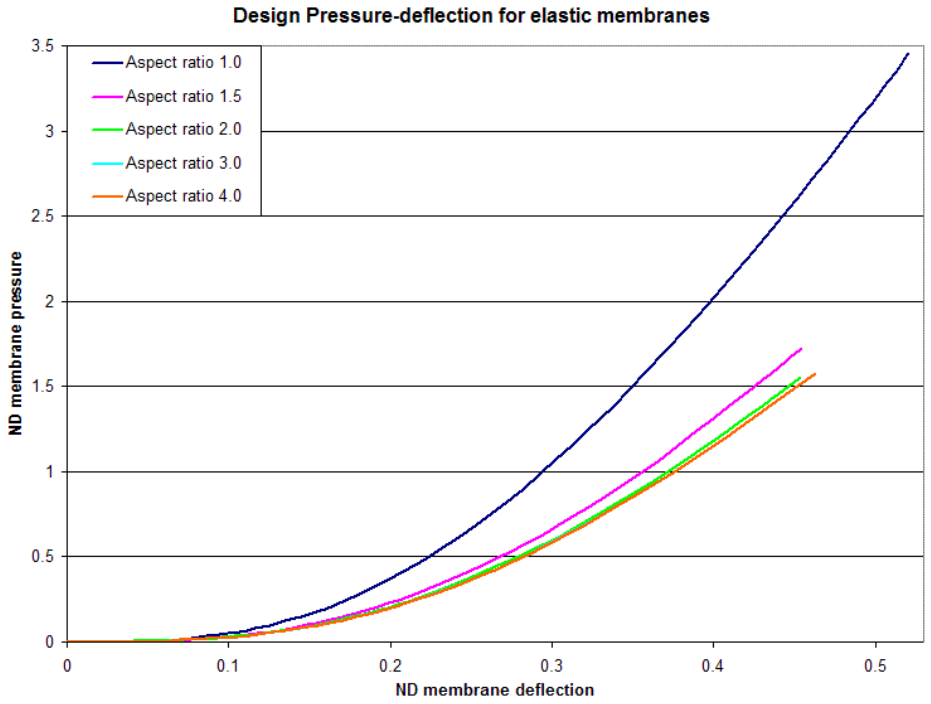

Figure 186. Design pressure-deflection relationship of elastic membranes

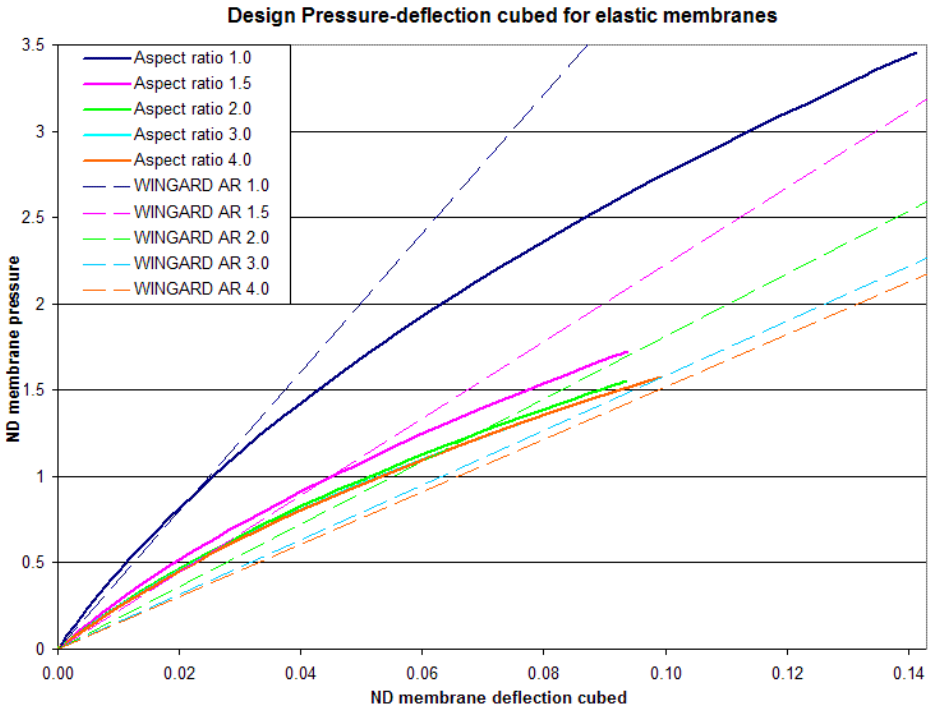

Figure 187. Design pressure-deflection relationship of elastic membranes

Chapter 8 showed that PVB behaviour in tension is non-linear, and can be approximated by a bilinear material model that varies with strain rate and temperature. The resistance curve of a PVB membrane will therefore only follow the curve for a linear elastic material up to the deflection when the transition stress is reached, and will diverge thereafter. Although the analysis of elastic membranes has

been useful in identifying solid elements and the Co-rotational non-linear formulation as most suitable for analysing the membrane deformation, the results will have limited application in the development of the PVB loading resistance function.

However, there is another part of the resistance function that will benefit from an understanding of the properties of elastic membranes, namely the resistance on rebound.

In a viscoelastic material, once the stretching force has been removed, the material will return to its original length gradually, with immediate elastic shortening at a rate that will depend on the unloading speed, followed by a gradual shortening of the slack material at a slower rate. When a viscoelastic membrane rebounds after stretching, the initial shortening rate will be considerably faster than the initial stretching rate, because the membrane will start from the geometry of maximum deflection, rather than from an initially flat shape. The initial unloading modulus will therefore not necessarily be identical to the initial elastic loading modulus.

The Author [6] has previously used a relationship between the von Karman differential equations for the transverse deformation of plates and the Maguerre differential equations for initially curved plates or shells, given by Chia [90], to derive an unloading resistance curve from an elastic loading resistance, as shown in Fig. 41, based on a cubic elastic membrane resistance. However, although the differential equations hold for large deflections, the relationship has only been demonstrated for approximate solutions of these equations that are accurate up to moderate deflections and moderate initial curvature only. Although the application of the relationship to the large deflections appears qualitatively reasonable, there is considerable uncertainty as to the accuracy of the calculation at large deflections.

Given the uncertainty in the appropriate unloading rate and material properties, and the uncertainty in relating that to the unloading resistance of a membrane, there seems to be little benefit in requiring the unloading resistance to be based on an interpolation of numerical data to model the geometric non-linearity of the membrane. The use of the WINGARD cubic curve for elastic resistance is an approximation, but it allows a straightforward calculation of an unloading resistance function. The uncertainty of the unloading resistance will be increased by this approximation, but this uncertainty is already high, so little will be lost by adopting the simpler approximation.

9.1.5 Stress distribution in elastic membranes

The distribution of principal tensile stress was examined for both shell and solid element analyses at different levels of loading. Typical distributions at four different loading levels are shown for a shell analysis in Fig. 188, and for a solid element analysis in Fig. 189.

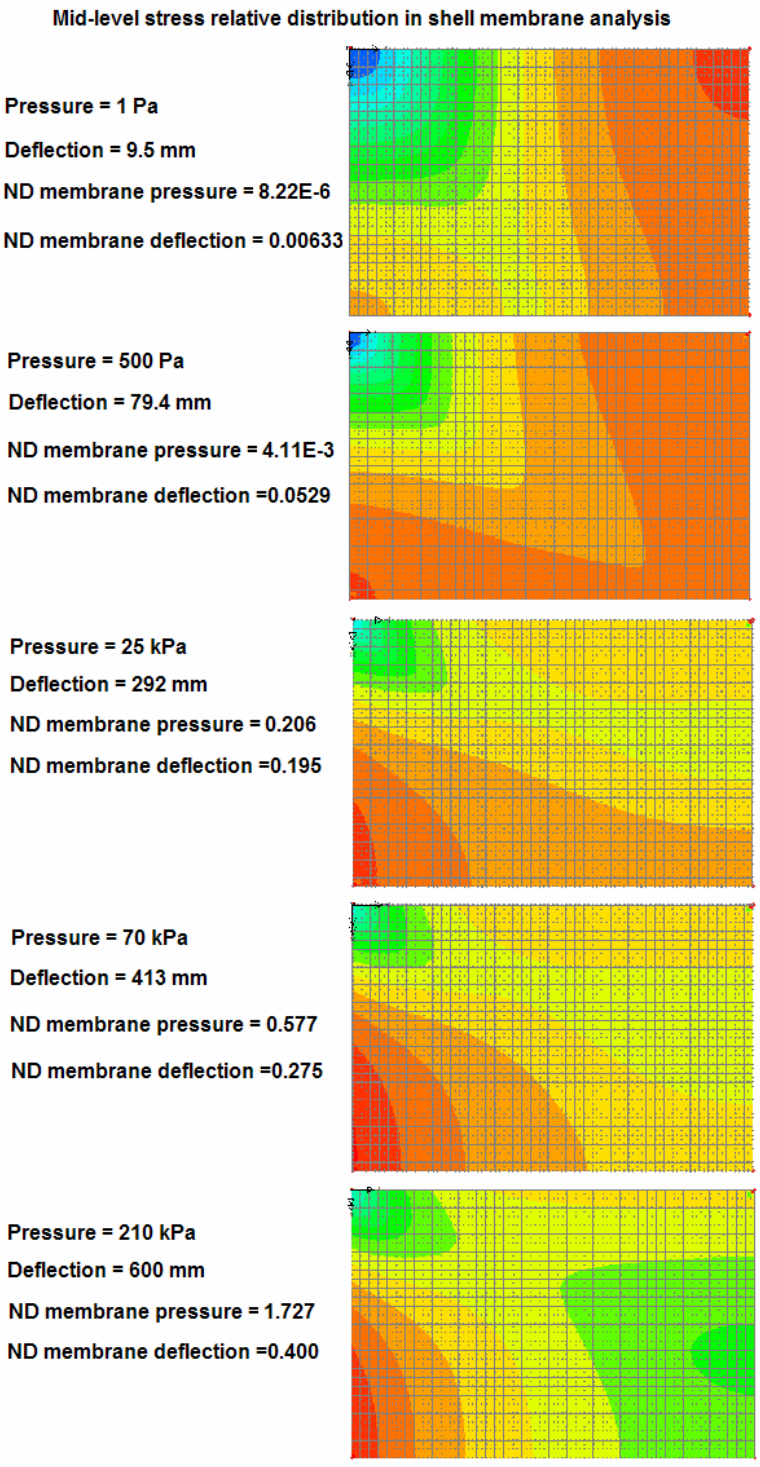

Figure 188. Tensile stress distribution for typical shell analysis at increasing loads

Fig. 188 shows that the maximum tensile stress occurs in the middle of the sides, with a minimum stress at the corners, with intermediate stresses in the centre. In the shell analysis the maximum stress occurs initially at the middle of the long side, but as the load and deformation increases it appears to move to the middle of the short side. Over a substantial range the maximum stress in the centre of the membrane is higher than that at the long edges, indicating that the longitudinal stresses and strains are

higher than the transverse stresses in the centre. This was confirmed by inspection of the directional stresses and strains.

This result is contrary to strain compatibility, as for a given deflection at the centre, the short span must be elongated more than the long span, and so should give higher strains in the transverse direction. This may explain the abnormal deflection behaviour in the shell deflections, and their sensitivity to the aspect ratio.

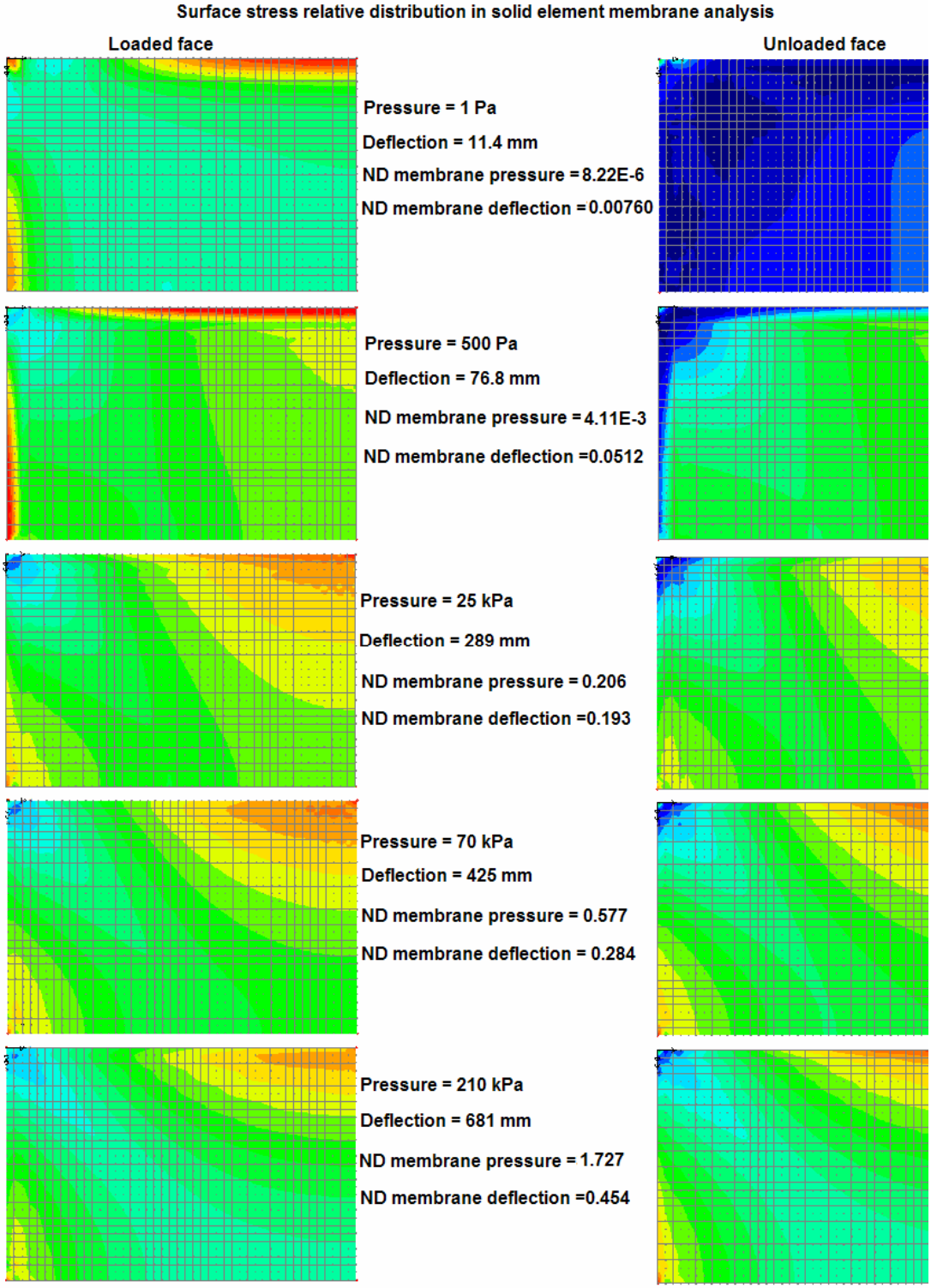

Figure 189. Tensile stress distribution for typical solid analysis at increasing loads

There is no calculation of mid-level stress in the solid model one element thick, so the membrane stress must be interpreted from the stress at the two surfaces, as shown in Fig. 189. To prevent the restraint against in-plane movement from providing a restraint against rotation at the supports, this restraint is only provided at the edge of the unloaded surface, while the out-of plane support is provided at the edge of the loaded face instead. This can be expected to affect the surface stresses locally. The support distribution in the solid model is illustrated in Fig. 190.

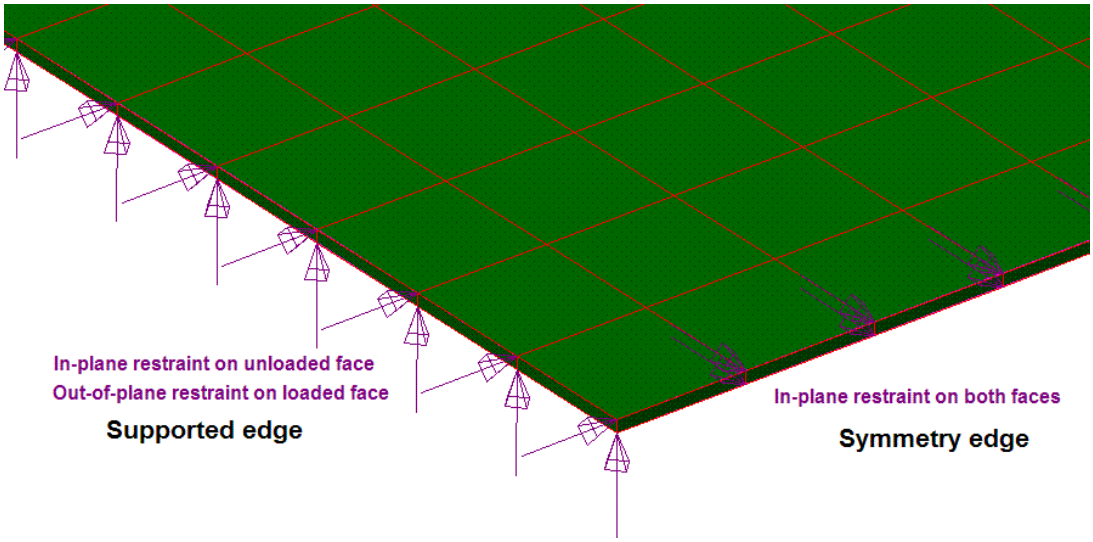

Figure 190. Distribution of supports in solid element model

At lower loading levels, the peak stresses occur at the loaded surface at the edges. Throughout the span, the tension in the unloaded face is less than the corresponding tension in the loaded face.

As the loading level increases, the influence of the element bending becomes proportionately less, and the stress distribution in the two surfaces becomes more similar. The main exceptions are close to the supports, where the stress reduces in the unloaded surface while still increasing in the loaded surface, and in the corner, where the low stress is lower still in the unloaded surface.

At very high loading levels, with large deflections and large rotations at the supports, the tension at the support becomes higher in the unloaded face, and the maximum on the loaded face no longer occurs at the support, but one element line into the membrane. This may be caused by the way in which the support is modelled. The principal stress distribution at the support may be influenced by the local shear distortion in the supported elements.

In the solid element models, the maximum membrane stress is associated with the centre of the long side at all levels of loading, which is both consistent with strain compatibility and explains the convergence of the curves for large aspect ratio in Figs. 186 and 187, as the central part of the membrane is essentially spanning one-way across the short span, with minimal curvature in the long direction.

9.2 Bi-linear tensile membrane resistance of PVB

Bi-linear material properties for PVB at various strain rates and temperatures were developed in Chapter 8 by back-analysis of tensile tests, using both Lagrangian plane stress and Co-rotational solid finite element models.

To calculate the resistance of PVB membranes at these strain rates and temperatures, these material properties will need to be incorporated into non-linear membrane analyses at various aspect ratios. The analysis of non-linear elastic membranes in Section 9.1 demonstrated that the Lagrangian thin shell model gave results that could be substantially different from other solutions, and that only the Co-rotational non-linear formulation could reliably continue the solid element analyses up to the deflection levels at failure which have been observed in static tests [93, 94].

To fully develop a design method based on this it will be necessary to undertake analyses with sufficient permutations of aspect ratio, strain rate and temperature to allow resistances and other properties for intermediate cases to be calculated by interpolation. This will require a very large number of analyses. For the purpose of the research described in this thesis, analyses have been undertaken only for aspect ratios and temperatures that correspond to blast trials for which deflection records are available, and which are reported in Sections 9.4 and 9.5.

9.2.1 Bi-linear analyses for HOSDB tests at Spadeadam

The Home Office Scientific Development Branch (HOSDB) [137] tests at Spadeadam in June 2006 were undertaken on standard "large size" HOSDB panels of 7.5mm thick laminated glass, 1.25 m by 1.55 m, at temperatures close to 20ºC [138]. This gives a 1.52 mm thick interlayer with a span of 1.25 m and an aspect ratio of 1.24.

By linear interpolation between the values in Tables 62 and 65, design material properties at 20ºC for use in Co-rotational solid element finite element analyses have been derived and are given in Table 68 for a range of elastic strain rates.

Elastic strain rate	Young's modulus	Transition stress	Hardening modulus
Strain / s	MPa	MPa	MPa
10	169.9	6.342	8.072
20	190.7	7.884	8.134
30	222.1	9.205	8.041
40	264.0	10.306	7.793
60	379.4	11.847	6.832
80	537.1	12.507	5.251

Table 68. Material properties of PVB at 20ºC for Co-rotational solid FE analysis

These non-linear material properties have been applied to Co-rotational solid membrane analyses in LUSAS, using the dimensions given above.

9.2.1.1 Deflection

The force-deflection relationships from these analyses are given in Fig. 191, and the non-dimensional versions in Fig. 192.

The analyses were taken to deflections between 37% and 50% of the span, which are the mean and the upper bound of the deflections at maximum pressure from the quasi-static water pressure tests of laminated glass reported by Ellis and Beak [93, 94], and substantially beyond the 90% confidence characteristic value of these deflections calculated by the Author [6].

Fig. 191 shows an increase in the resistance force with increasing strain rate, although at high strain rates and large deflections the increase is less, because of the reducing hardening modulus with strain rate.

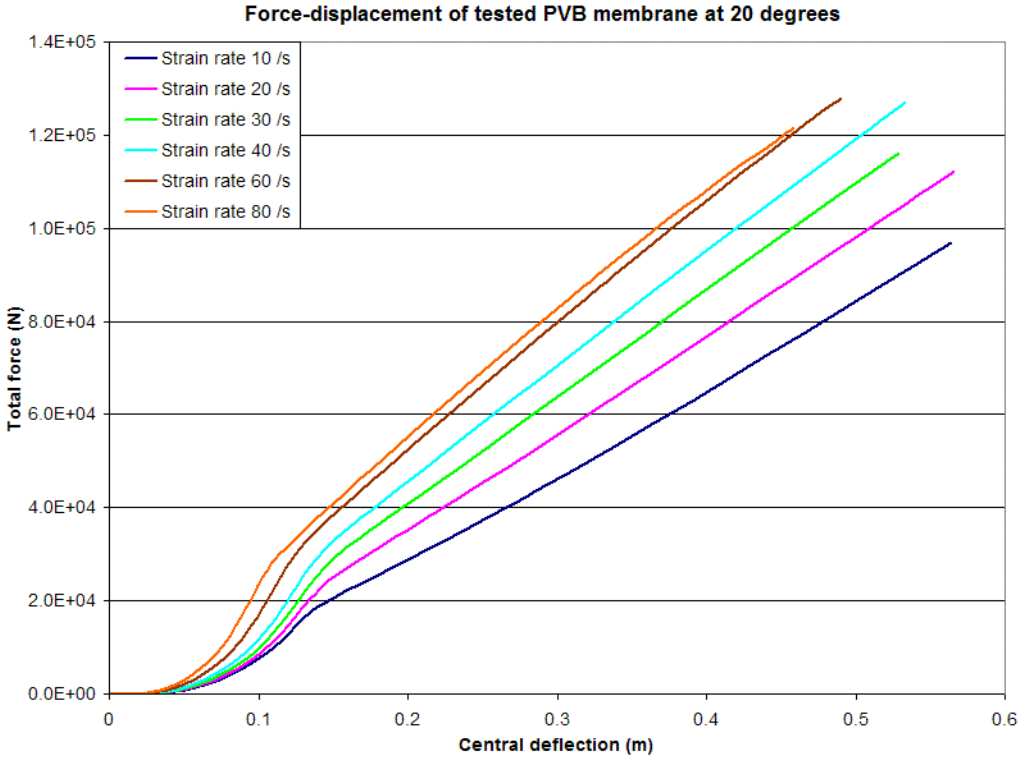

Figure 191. Force-displacement relationship calculated for HOSDB test panels

Fig. 192 shows that, for strain rates up to 40 /s at 20ºC, the increase in resistance with strain rate is approximately proportional to the increase in Young's modulus, as the non-dimensional curves are closely clustered. The deviation from the elastic curve occurs at deflections between 8% and 12% of the span depending on the strain rate, with the deviations occurring earlier for higher strain rates.

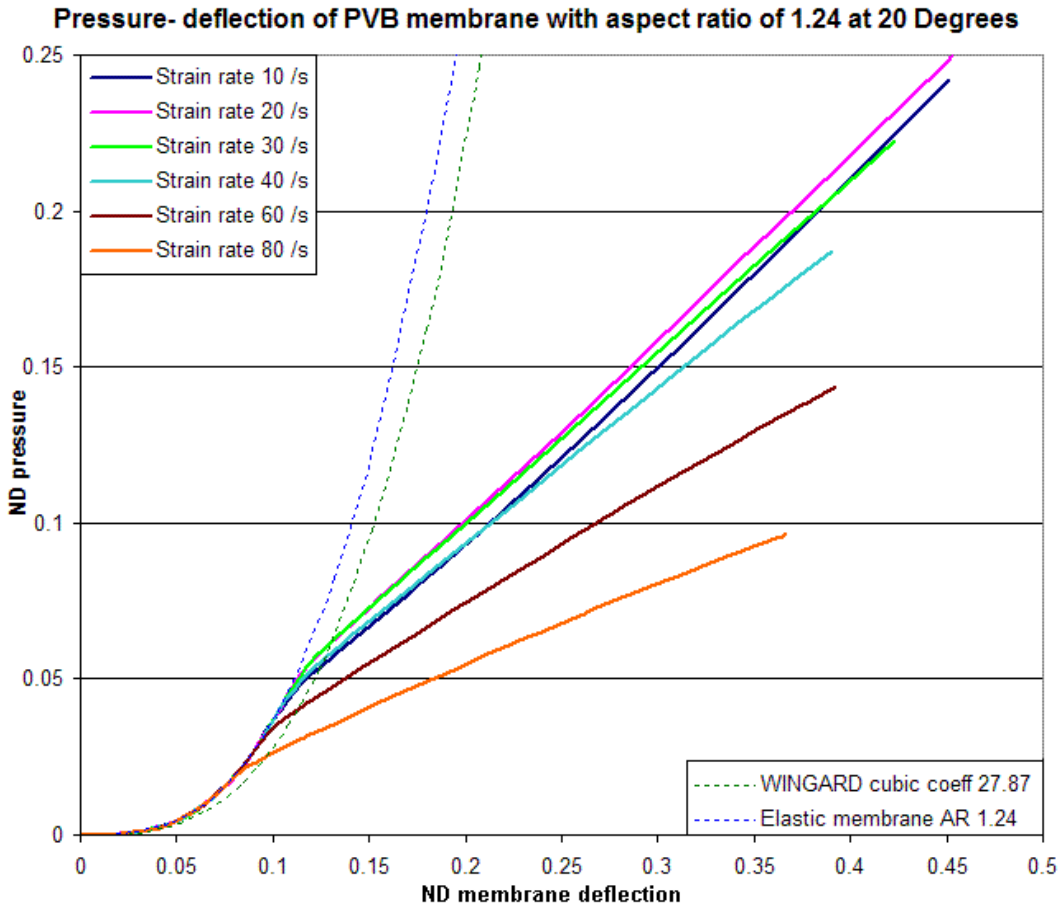

Figure 192. Non-dimensional pressure-deflection for PVB membrane in panels with aspect ratio 1.24 at 20ºC

9.2.1.2 Plastic strain distribution

The distributions of principal tensile plastic strain in the membrane analyses were reviewed. The build-up of the plastic strain in the 80 /s analysis with the most extreme strains is shown in Fig. 193.

The maximum plastic strain at the maximum deflection in each analysis occurred close to the middle of the long edge, with values that varied from 1.077 at a strain rate of 80 /s to 0.959 at a strain rate of 10 /s. The maximum plastic strain at midspan varied in reverse, from 0.144 at a strain rate of 10 /s to 0.115 at a strain rate of 80 /s. For these analyses with an aspect ratio of 1.24, the maximum plastic strains at the short sides were between 86% and 94% of the peak plastic strains on the long side, if the local high values at the corner of the model were dismissed as artefacts of the local constraints on the corner element.

In all the analyses, the plastic strain started locally near the centres of the supports and expanded out into the span. The elastic zone, shown as the darkest blue in Fig. 193, retreated into the corner, so that at maximum deflection only the corner node had no plastic strain. There was a gradient in plastic strain that became proportionally lower as the loading increased. The sharpest final ratio in plastic strain of 9.37 between the support and the span at a strain rate of 80 /s corresponded to the

resistance with the lowest degree of hardening relative to the elastic stiffness, and the softest gradient of 6.66 at a strain rate of 10 /s corresponded to the resistance with the highest degree of hardening.

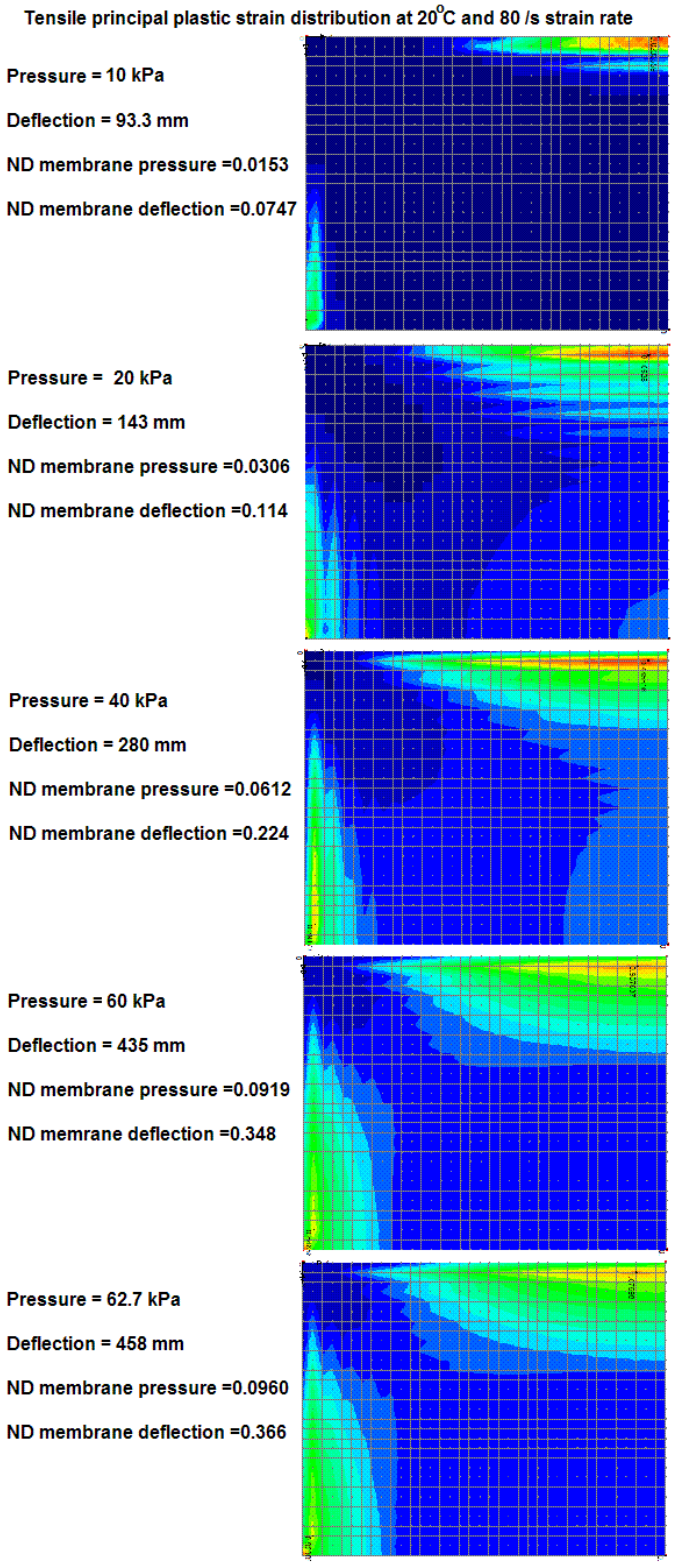

Figure 193. Plastic strain distribution from an analysis using material properties corresponding to a strain rate of 80 /s at 20ºC.

The effect of the strain peak near the support is illustrated in Fig. 194, where the ratio between the peak total strain and mean total strain across the short span has been plotted.

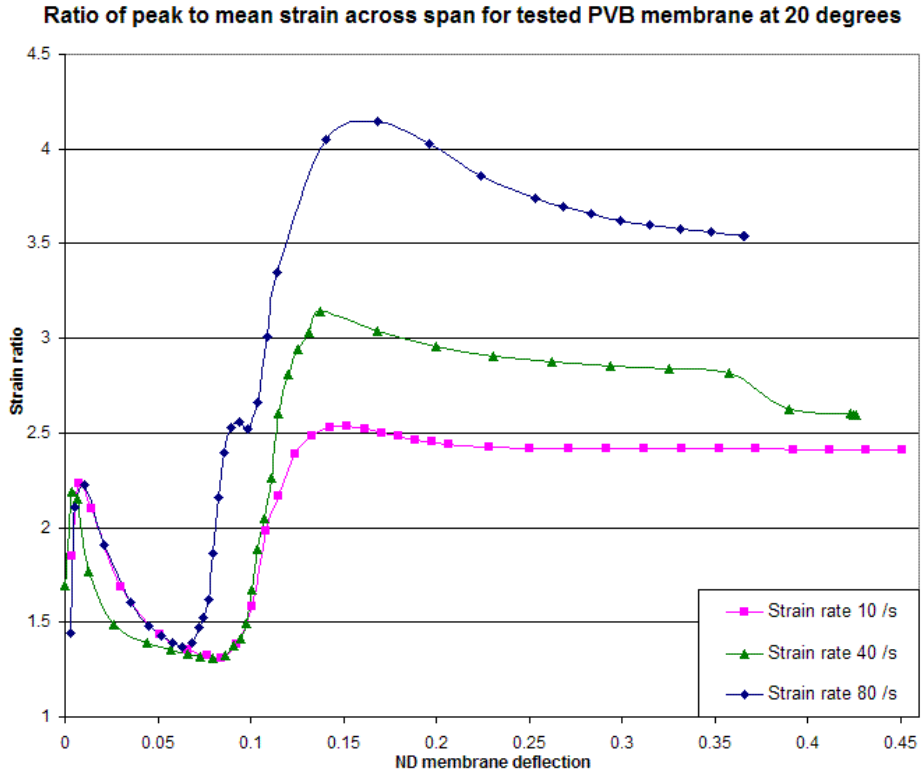

Figure 194. Ratio of peak to mean strain across the short span

The strains compared are total strains across the short span on the loaded face where the strains are higher, with the peak value taken as the mean of five to seven nodes to smooth out the variations due to hourglassing, and the average value is based on one line of thirty-one nodes. Fig. 194 shows some of the local variability in the analyses, but also shows a general sequence, where the local elastic strain ratio first peaks as bending becomes negligible and then reduces as strain spreads into the span. A large local peak occurs as the plasticity occurs first at the support, gradually reducing as the plasticity develops. The amplitude of the peak is inversely related to the ratio of hardening modulus and Young's modulus.

The mean strain across the short span varies consistently with the mid-span deflection, as shown in Fig. 195, indicating that the deflected shape across the centre of the span is consistent, so that the elongation-deflection relationship is independent of the strain distribution. This relationship might vary with aspect ratio, but should be effectively independent of the PVB temperature.

The quasi-static analyses described here with uniform material properties is likely to overestimate the peak plastic strain and the peak strain ratio that would be experienced in a dynamic response of a viscoelastic PVB membrane. The higher plastic strain rate near the supports would increase the resistance locally compared to the span and reduce the concentration of the plastic strain. The maximum strains from these analyses are likely to be upper bound.

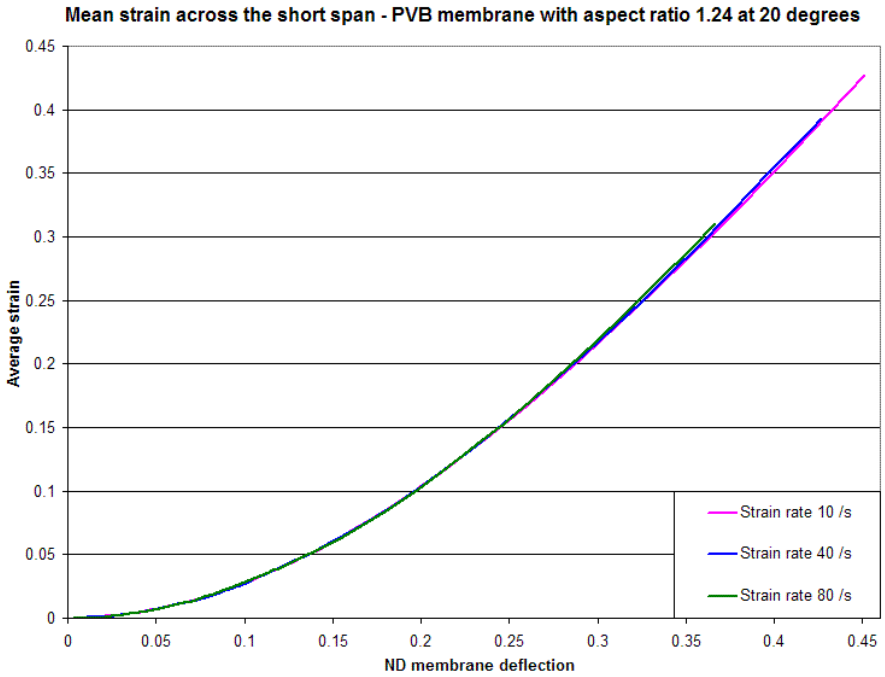

Figure 195. Mean strain vs deflection for a membrane with an aspect ratio of 1.24

The maximum plastic strain of 1.077 is around half of the elongations at failure found in the high strain rate tensile tests of PVB described in Chapter 8, for a deflection of around 45% of span, close to the upper bound of the deflections for maximum load observed in quasi-static tests [93, 94].

For an elastic-pure plastic material model and a plastic strain limited to 2.0, as described in the WINGARD manual [100], it can be seen that a finite element analysis might show the plasticity to occur only locally at the edge of the membrane. However, these analyses based on measured material properties of PVB, in which deflections in excess of design limits ate achieved with peak strains barely half this limit, indicate that this is not a realistic model of PVB membranes.

9.2.2 Bi-linear analyses for Permasteelisa tests at BakerRisk

The Permasteelisa tests [129, 130] at BakerRisk, San Antonio in August 2006 were undertaken on large double glazing units, with a clear glazed area of 2.107 m by 2.902 m, at temperatures between 26ºC and 29ºC. Two glass make-ups contained a 1.52 mm thick PVB interlayer, and one make-up contained a 2.28mm thick PVB interlayer, all with a clear span of 2.107 m and an aspect ratio of 1.3773.

By linear interpolation between the values in Tables 62 and 66, design material properties at 26ºC and 29ºC for use in Co-rotational solid element finite element analyses have been derived and are given in Tables 69 and 70 for a range of elastic strain rates.

These non-linear material properties have been applied to Co-rotational solid membrane analyses in LUSAS, using the dimensions given above.

Elastic strain rate	Young's modulus	Transition stress	Hardening modulus
Strain / s	MPa	MPa	MPa
10	107.9	3.591	6.464
20	125.3	4.686	6.497
30	151.0	5.651	7.284
40	185.1	6.485	7.473
60	278.2	7.761	7.412
80	404.7	8.515	6.763

Table 69. Material properties of PVB at 26ºC for Co-rotational solid FE analysis

Elastic strain rate	Young's modulus	Transition stress	Hardening modulus
Strain / s	MPa	MPa	MPa
10	79.1	2.673	5.024
20	99.9	3.581	5.646
30	125.5	4.379	6.184
40	156.0	5.070	6.639
60	231.2	6.127	7.300
80	325.7	6.753	7.629

Table 70. Material properties of PVB at 29ºC for Co-rotational solid FE analysis

9.2.2.1 Deflection

The force-deflection relationships from the analyses at 26ºC are given in Fig. 196, and the non-dimensional versions in Fig. 197. The force-deflection relationships from the analyses at 29ºC are given in Fig. 198, and the non-dimensional versions in Fig. 199.

As before, the analyses were taken to deflections between 37% and 50% of the span, which are the mean and the upper bound of the deflections at maximum pressure from the quasi-static water pressure tests of laminated glass reported by Ellis and Beak [93, 94], and substantially beyond the 90% confidence characteristic value of these deflections calculated by the Author [6].

The patterns shown in these analyses are very similar to those at lower temperature, with the stiffness increasing with the strain rate, but with lower overall stiffness, and less convergence of higher strain rate curves at higher temperature. When considered in non-dimensional form, again the pattern is very similar, with the curves up to a strain rate of 40 /s closely grouped, with similar proportions relative to Young's modulus, but with the gradient reducing with increased temperature, and the non-dimensional stiffness reducing with strain rate above 40 /s.

As the temperature increased, the deflection at which the non-linear curves departed from the elastic curve reduced to between 7% and 10% of the span, and the elastic stage of the analysis tends to be slightly softer than the non-dimensional curve for the elastic membrane analysis.

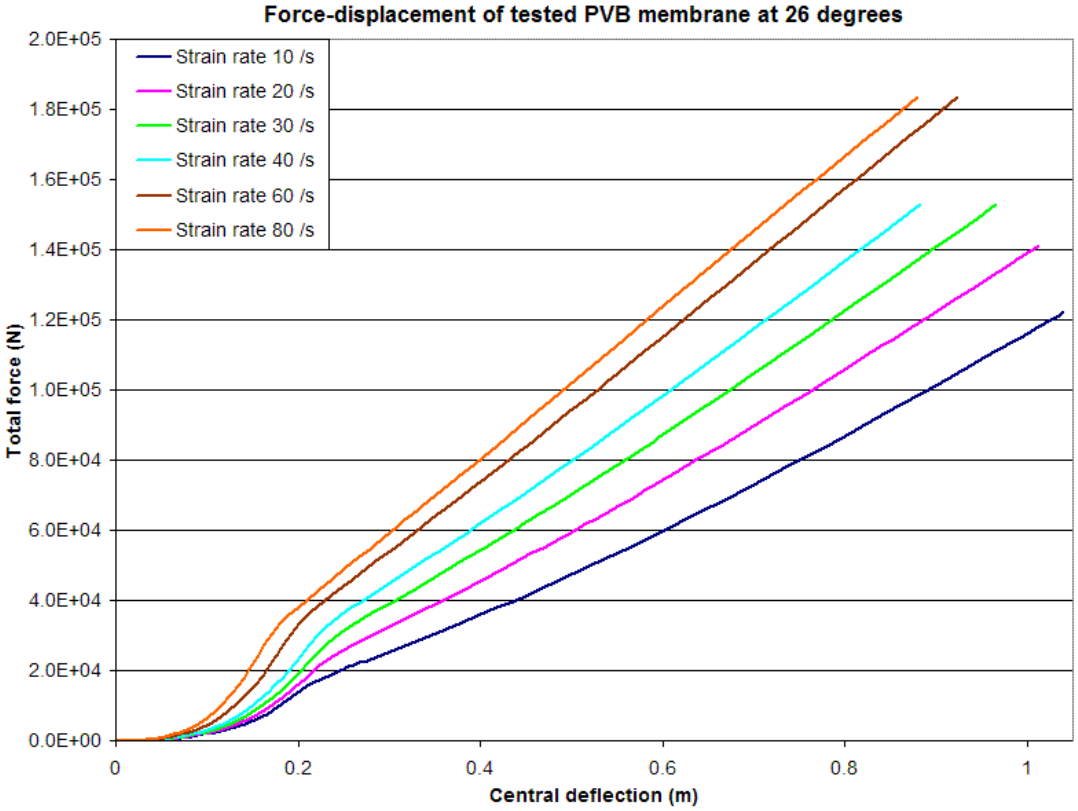

Figure 196. Force-displacement relationship calculated for Permasteelisa test panels at 26ºC

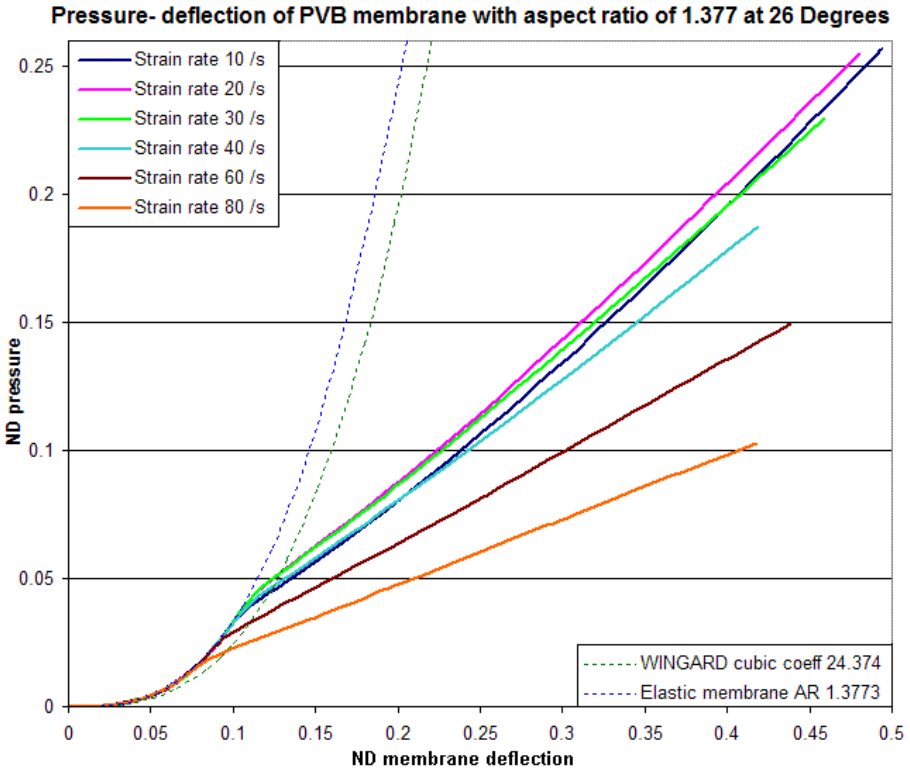

Figure 197. Non-dimensional pressure-deflection for PVB membrane in panels with aspect ratio 1.377 at 26ºC

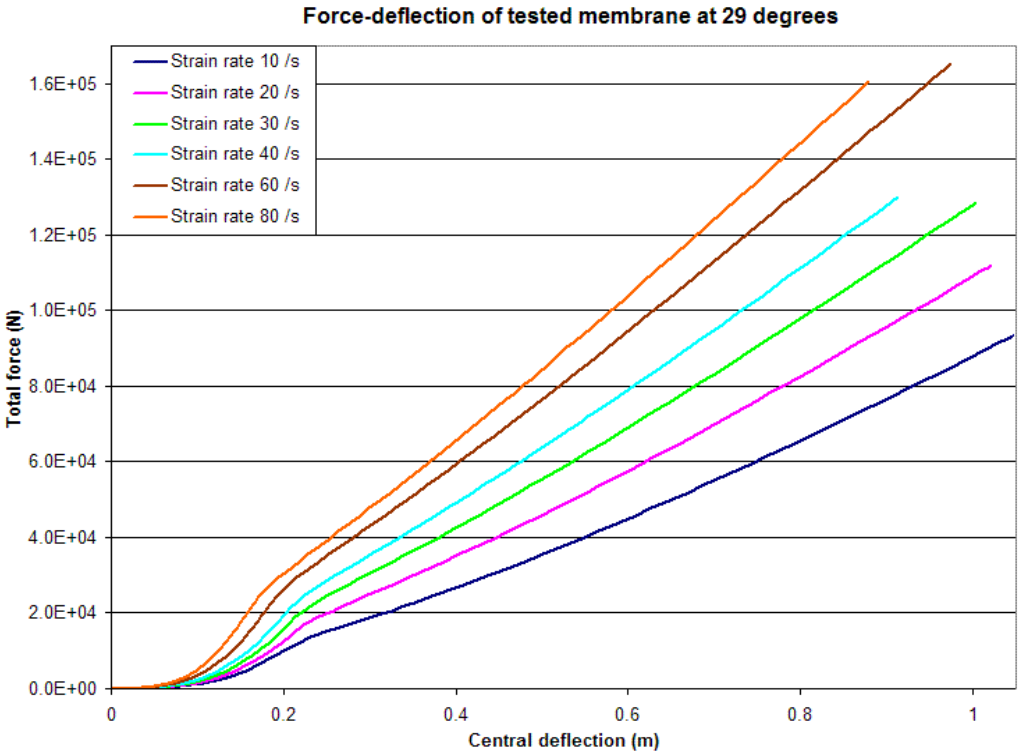

Figure 198. Force-displacement relationship calculated for Permasteelisa test panels at 29ºC

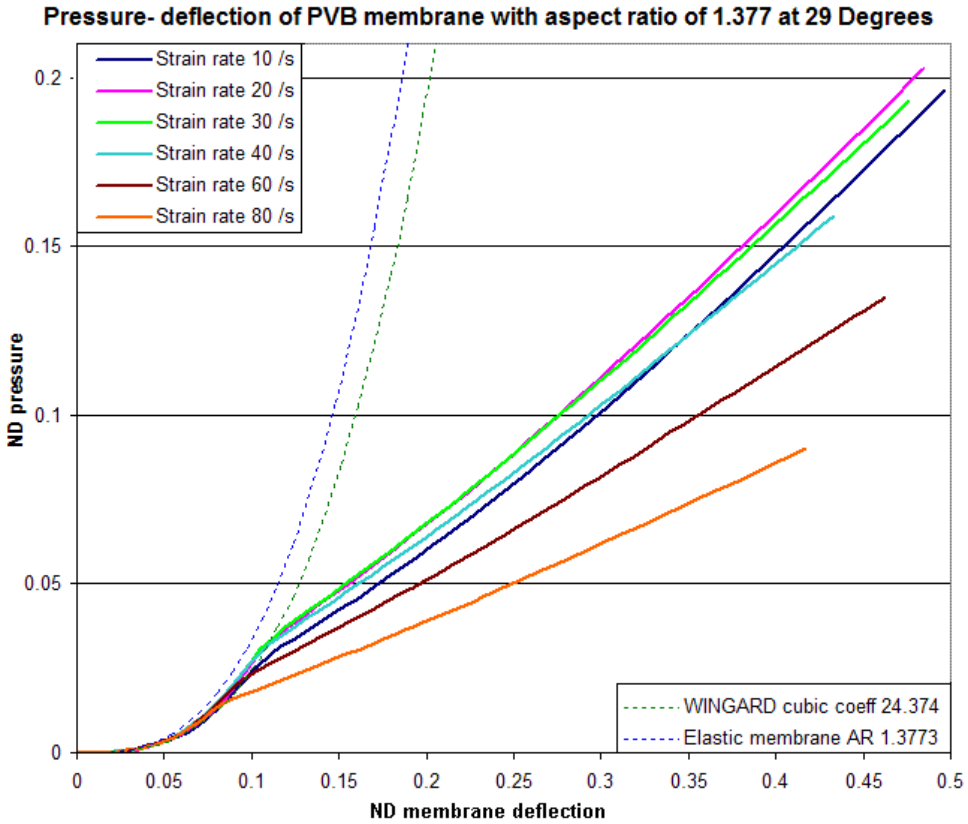

Figure 199. Non-dimensional pressure-deflection for PVB membrane in panels with aspect ratio 1.377 at 29ºC

9.2.2.2 Plastic strain distribution

The patterns of plastic strain distribution at 26ºC and 29ºC are similar to those at 20ºC, as shown in Fig. 200, except that the lower Young's modulus means that peak strains and strain ratios are lower, as shown in Fig. 201.

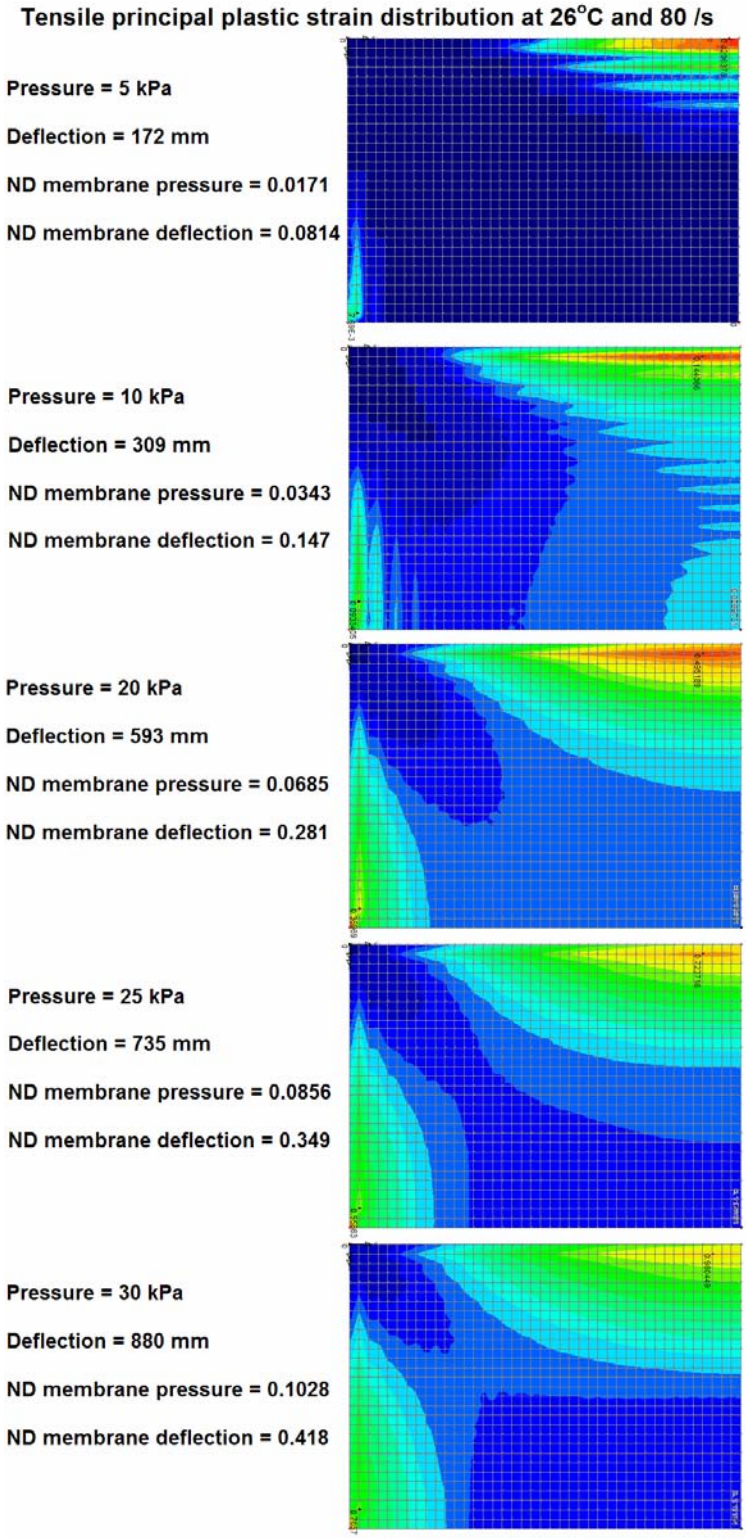

Figure 200. Plastic strain distribution from an analysis using material properties corresponding to a strain rate of 80 /s at 26ºC.

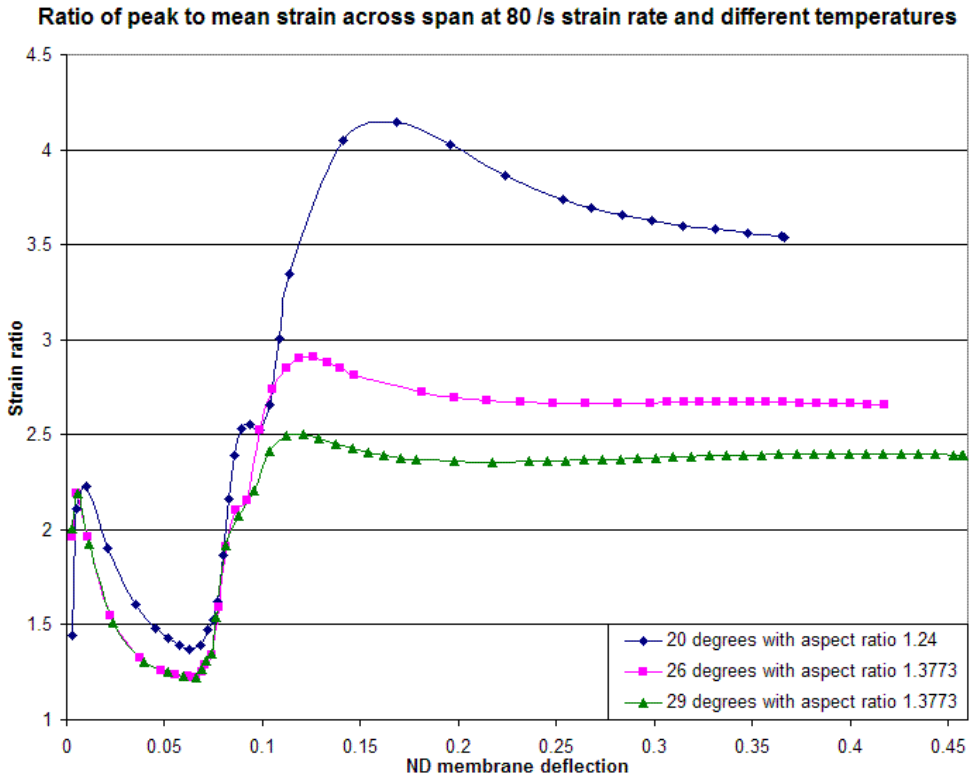

Figure 201. Ratio of peak to mean strain across the short span for different temperatures

Fig. 202 shows that the mean strains across the short spans of the different panels, as expected, are similar for the different temperatures and also that the mean strain – deflection relationship is not sensitive to small differences in the aspect ratio.

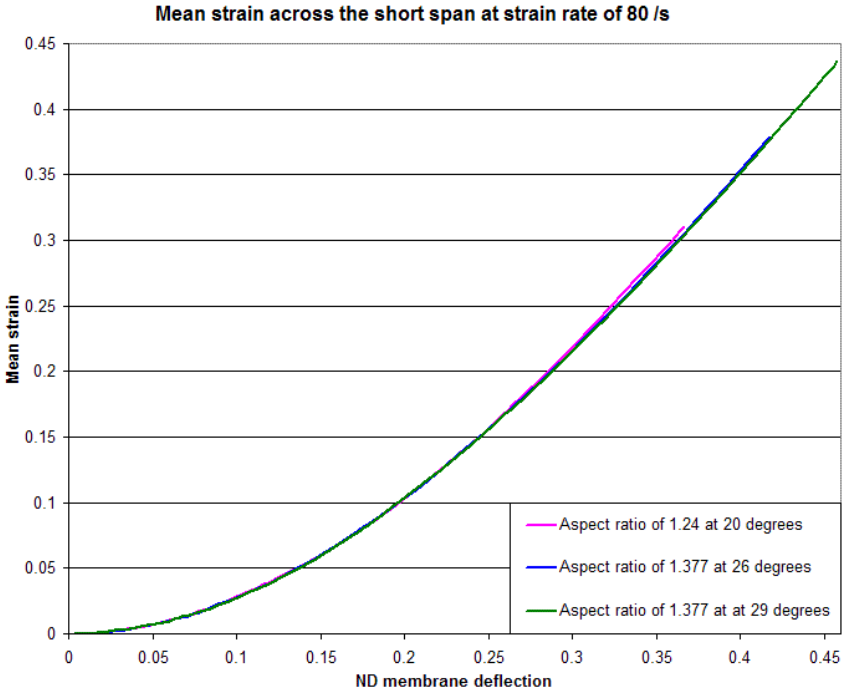

Figure 202. Mean strain vs deflection for membranes at different aspect ratios and at different temperatures

9.3 SDOF transformation coefficients of PVB tensile membranes

The SDOF transformation factors for the tensile membranes were calculated by a similar method to that described in Section 6.4 for non-linear analysis of glass plates. Because the analyses used conservative loading, there was no requirement to add additional increments to give accurate results. The requirement to produce a small step to analyse incremental deflections was met by re-running the analysis with the unit load reduced by 1%. This gave corresponding output for each load-step with 99% and 100% of loading. The incremental deflected shapes, and the transformation factors based on these, were calculated on the difference in the deflections between the corresponding cases from the two analyses.

Because of the differences in the finite element models and support conditions between the shell models of the plates and the solid models of the membranes, some of the details of the post-processing are different. For ease of processing, only the deflections of the nodes on one surface were analysed. This will have introduced a small error in the deflected shape, as the thinning of the membrane due to straining will should have introduced a small systematic deviation between the face deflections and the mid-surface deflection. In practice, with the thickness of the membrane being much smaller than the deflection, and the change in the thickness being smaller still, this systematic error will be acceptably small.

9.3.1 SDOF parameters for HOSDB tests at Spadeadam

The transformation factors K_L and K_M from the analyses of membranes with an aspect ratio of 1.24, using material properties for PVB at 20ºC are shown in Figs. 203 and 204. The ratio of these, K_{LM}, is shown in Fig. 205.

These show that the transformation factors initially follow a common curve in the elastic range. At the onset of plasticity there is initially a gradual deviation from the elastic membrane trend, as yielding zones develop first adjacent to the long side, and then adjacent to the short side.

Following a small ‘up-tick’, there is a sharp drop in the value of all the transformation factors between the onset of plastic strain in the centre of the membrane, which forms an isolated zone of yielding under biaxial stress, and this zone joining with the yielding zones extending from the long sides. This occurs over a narrow range of membrane deflection, and is reminiscent of the step changes in transformation factors between elastic, elasto-plastic and plastic phases in Chapter 5.

The small ‘up-tick’ before the drop is closely associated with the onset of yielding in the centre of the membrane. Sometimes, but not always, the ‘up-tick’ in the curves on Figs. 203 to 205 occurred at a load-step when there was yielding at 100% of the load, but not at 99%. For other curves this point occurred between load-steps, and the ‘up-tick’ appeared at the first load-step after this.

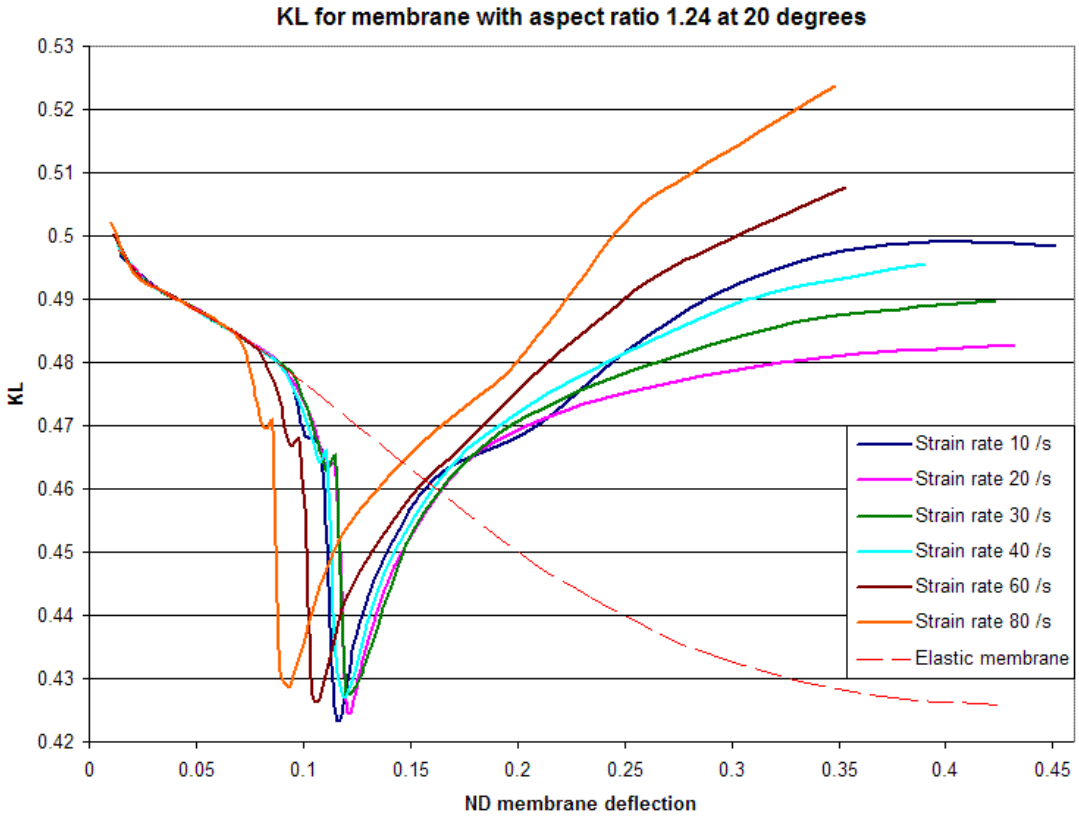

Figure 203. Factor K_L for PVB membrane with aspect ratio of 1.24 at 20ºC

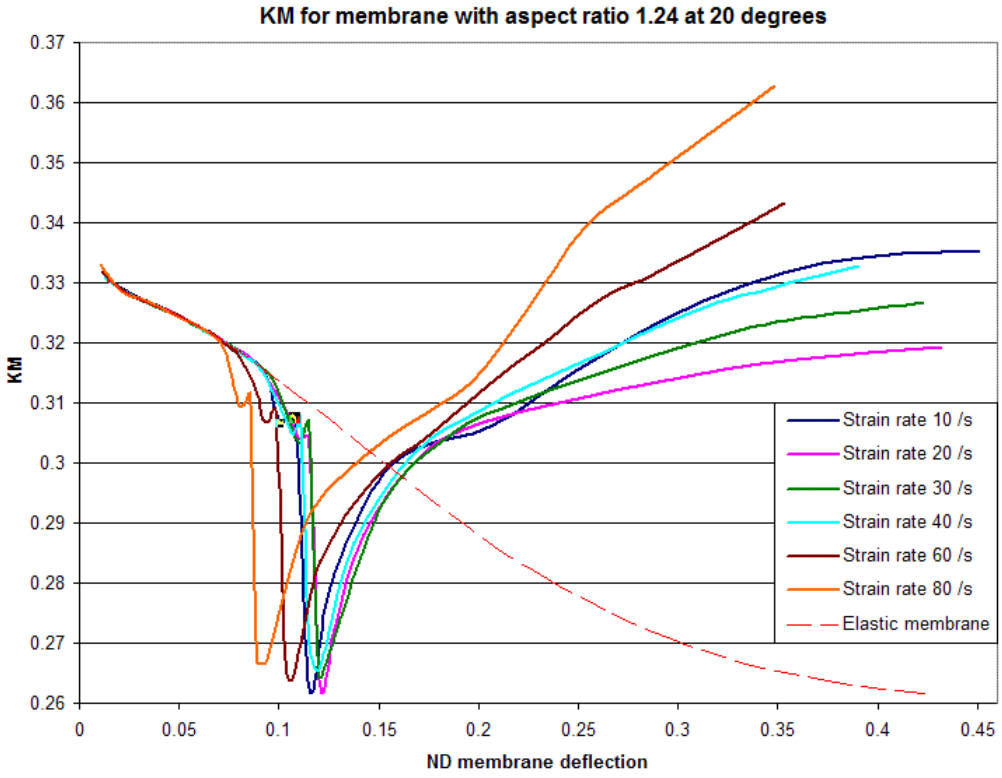

Figure 204. Factor K_M for PVB membrane with aspect ratio of 1.24 at 20ºC

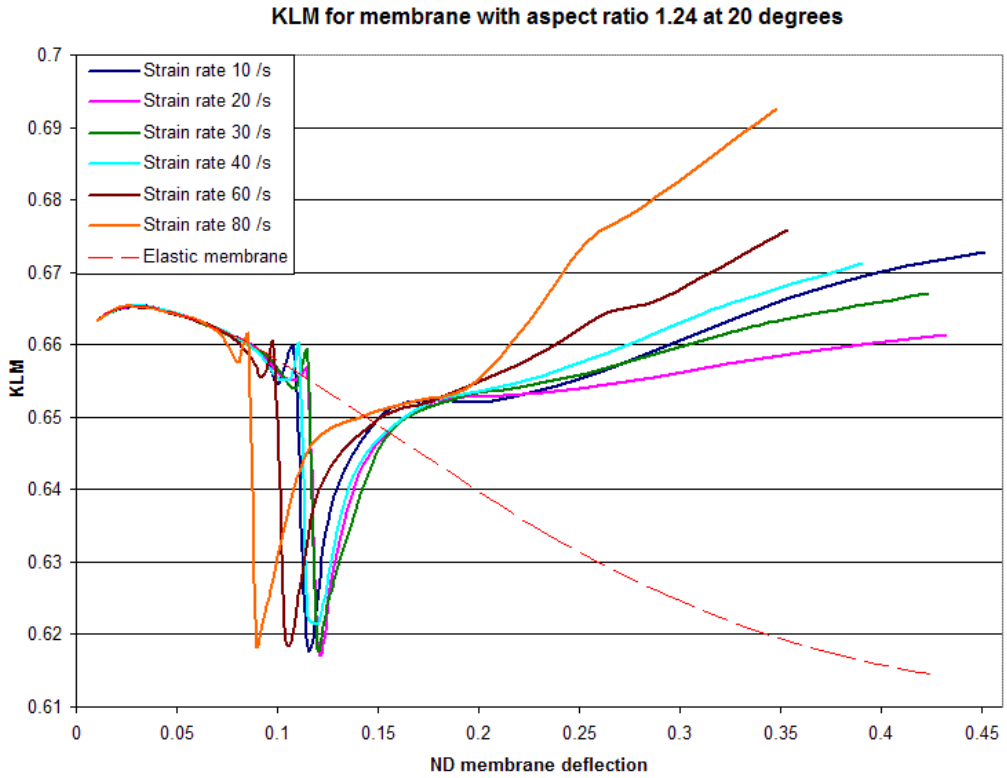

Figure 205. Factor K_{LM} for PVB membrane with aspect ratio of 1.24 at 20ºC

All the load steps on the down-slope after the 'up-tick' and before the trough in the curves in Figs. 203 to 205 showed isolated yielded zones in the centre of the membranes, while all the load steps after the trough have a yielding zone across the whole width of the membrane, although not necessarily along the whole length. The exact position of the trough in the figures is sensitive to the load-steps used in calculating the membrane response.

For all of these factors, Figs. 203 to 205 show that plastic yielding causes moderate but significant deviations in SDOF transformation factors from the trend for elastic membranes. These figures show that the trends for plastic membranes are more complex than the monotonic elastic membrane curve, but even these curves show that there must be a change in the deformed shape of elastic membranes as the amplitude changes. However, the figures have been scaled to emphasise the variation, and these variations can be seen in perspective in Fig. 216 where the variation is shown to be less than the variation in the parameters for uncracked glass derived in Chapter 6.

9.3.2 SDOF parameters for Permasteelisa tests at BakerRisk

The transformation factors for the panels at temperatures of 26ºC and 29ºC show a small systematic difference in the elastic trend line compared to that for the panels at 20ºC because of the small difference in aspect ratio, but a greater variation of the elastic-plastic trend lines due to the different material properties at different temperatures. The trends of the load-mass transformation factor K_{LM} is shown for 26ºC in Fig. 206 and for 29ºC in Fig 207. These can be compared with the trends for 20ºC in Fig. 205.

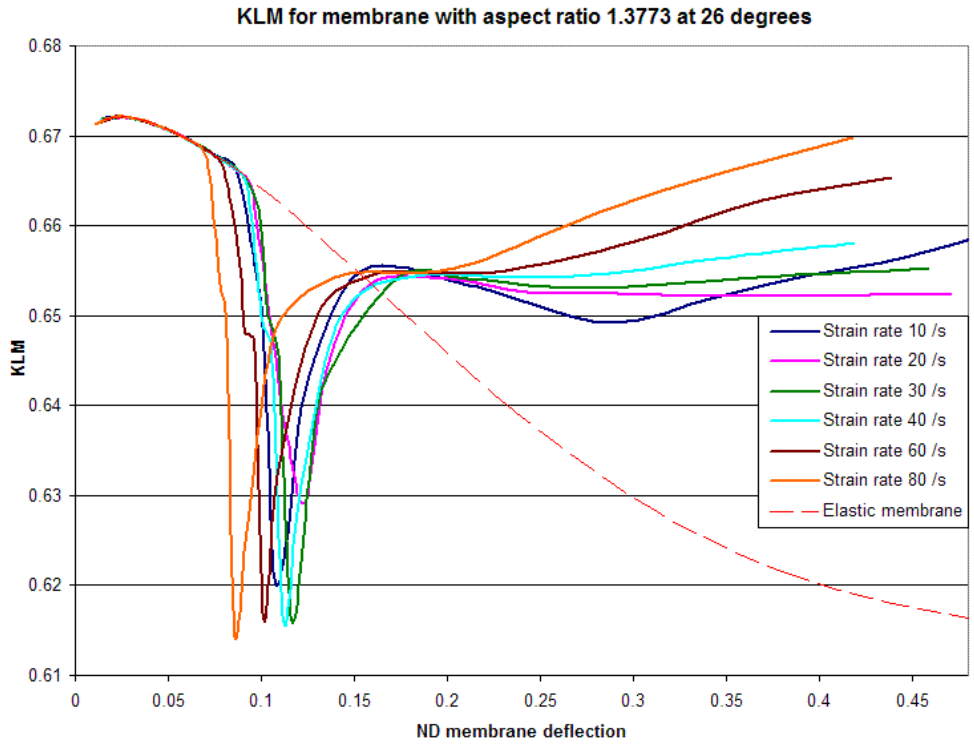

Figure 206. Factor K_{LM} for PVB membrane with aspect ratio of 1.3773 at 26ºC

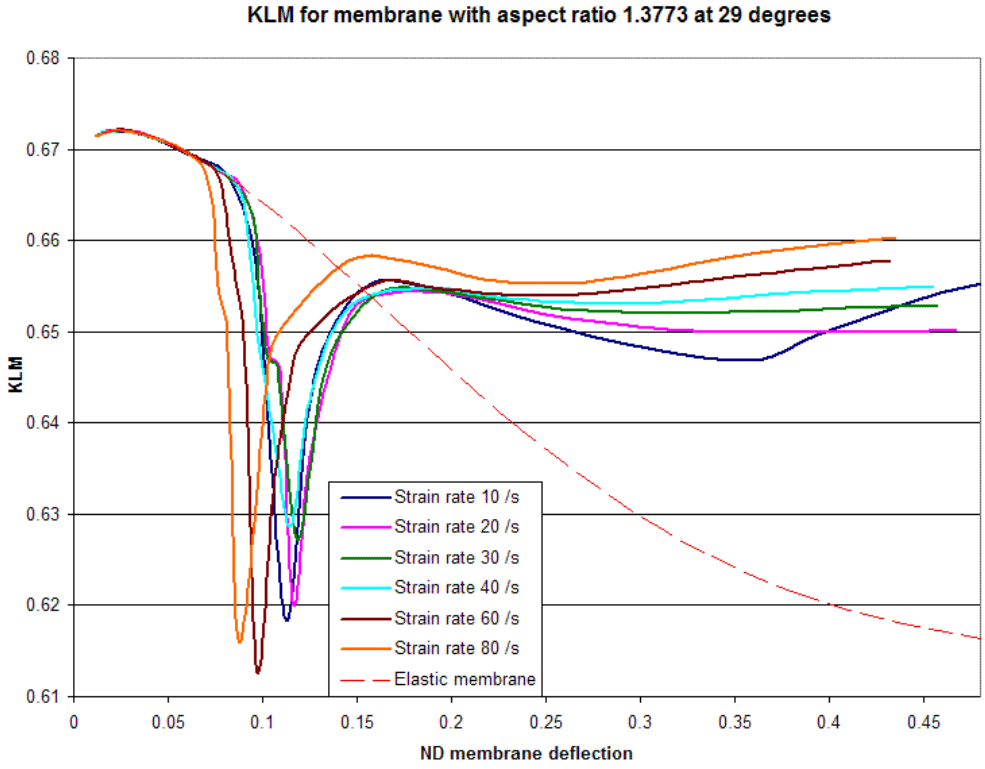

Figure 207. Factor K_{LM} for PVB membrane with aspect ratio of 1.3773 at 29ºC

At 26ºC, the transformation factors drop more in the early plastic stages with only the edge zones yielded, and the 'up-tick' at 20ºC when the centre of the membrane yields has become only a small kink in some of the curves, while not being isolated in some of the other curves, as shown in Fig. 206. This is because the whole of the kink lies between two data points in these curves, and is smoothed out in the presentation of the data.

There is still a spread of deflections at which the transformation factors reach their minima. However, the values rise more sharply, back to a constant value, independent of strain rate, at a deflection of about 18% of the span. Thereafter, the values of the transformation factors vary relatively little, suggesting a fairly stable deflected shape above this deflection.

This trend continues for transformation factors at higher temperatures as shown by Fig. 207 for PVB at 29ºC. The curves are more closely bunched, and after the dip and recovery the trends are flatter, with barely half the variation in value between ND membrane deflections of 0.15 and 0.45 shown by Fig. 206 at 26ºC.

The tests at BakerRisk were undertaken on double glazed units. To analyse the effect of the double glazing cavity on the response of the glazing, as described in Chapter 10 of this thesis, the average deflection of the glass panes on either side of the cavity needs to be known, so that volume and pressure changes in the cavity can be tracked. When the cavity remains closed after a laminated glass leaf has cracked, this requires the average deflection of the PVB membrane to be calculated from the deflection output of the finite element analysis of the 100% loading case, in the same way that K_L is calculated from the incremental deflection.

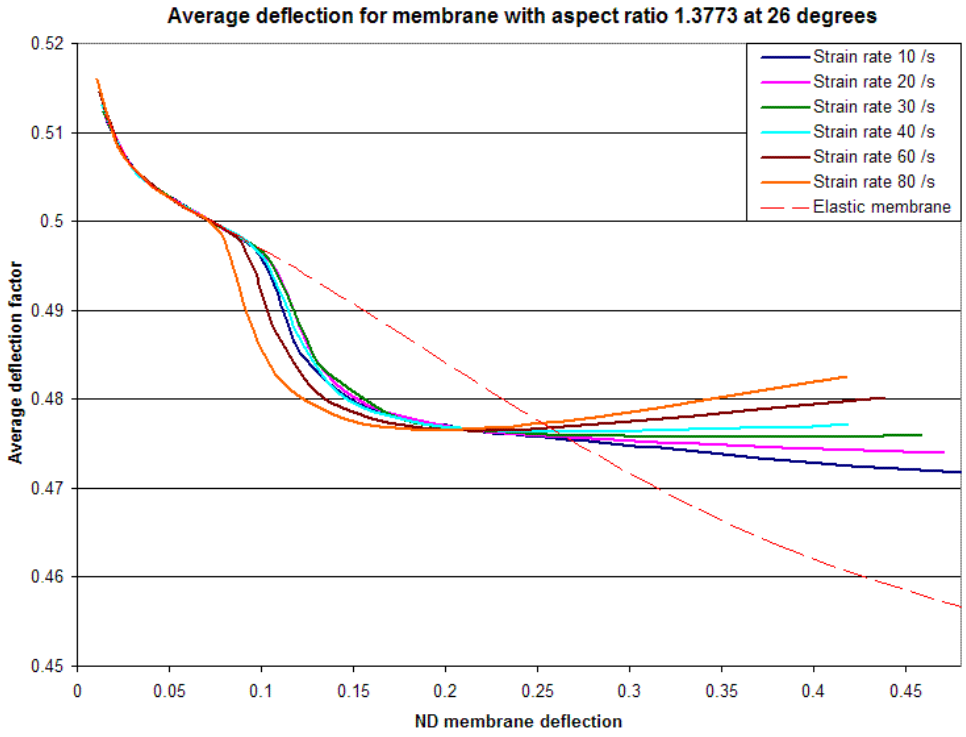

Figure 208. Average deflections for PVB membrane with aspect ratio of 1.3773 at 26ºC

The average deflection of the membrane as a proportion of the peak deflection at 26ºC is shown in Fig. 208, and at 29ºC is shown in Fig. 209. Being based on total rather than incremental deflections, these show sharp gradient changes as opposed to the sharp value changes in Figs. 205 to 207.

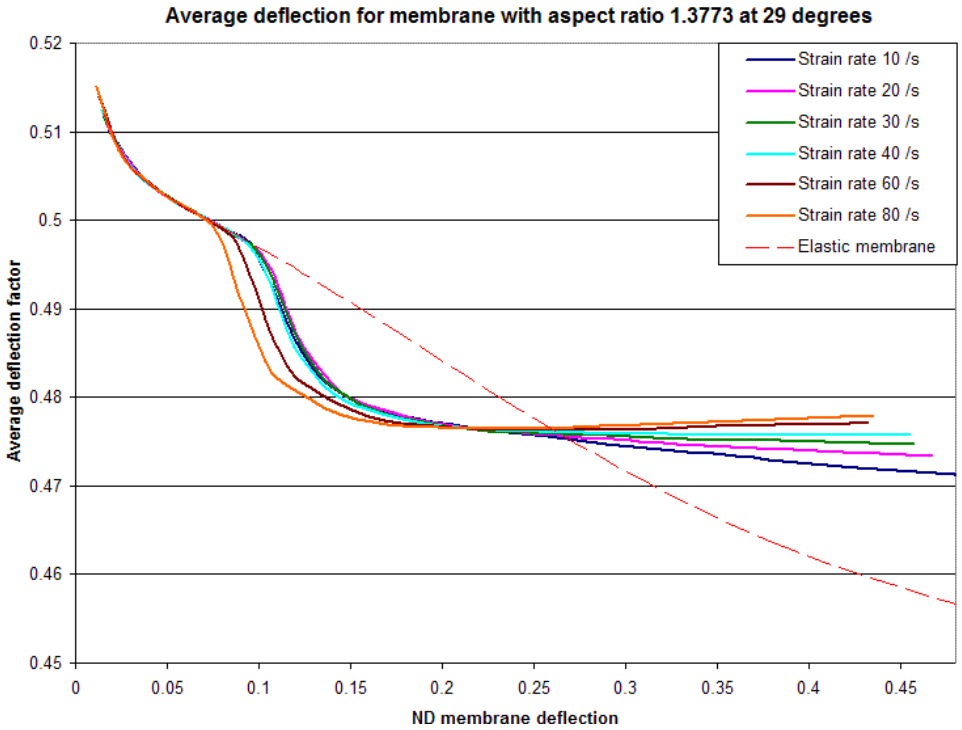

Figure 209. Average deflections for PVB membrane with aspect ratio of 1.3773 at 29ºC

9.4 Reaction coefficients and other data

Additional information can be derived from the deflections and reactions calculated in the finite element analyses of PVB membranes. SDOF dynamic reaction coefficients were calculated by considering the rotational equilibrium of the membrane quadrants in the finite element models, using the algorithm described in Section 3.5.5.5 and illustrated in Fig. 23, and which has already been applied in Section 5.4 to small deflection analysis of two-way spanning slabs, and in Section 6.5 to calculate the reaction coefficients for glass plates in Figs. 90 and 91. The different coefficients V_{RL}, V_{FL}, V_{RS} and V_{FS} are as defined in Section 6.5 and Eqn. 40.

As the loading was applied conservatively in the transverse direction, unlike in Section 6.5, the net in-plane forces were limited to the reactions at the supports and symmetry lines. However, the straining of the membranes was uneven, so calculation of both the centroid of the loading and the centroid of the inertial forces had to take account of the in-plane deflections of the nodes.

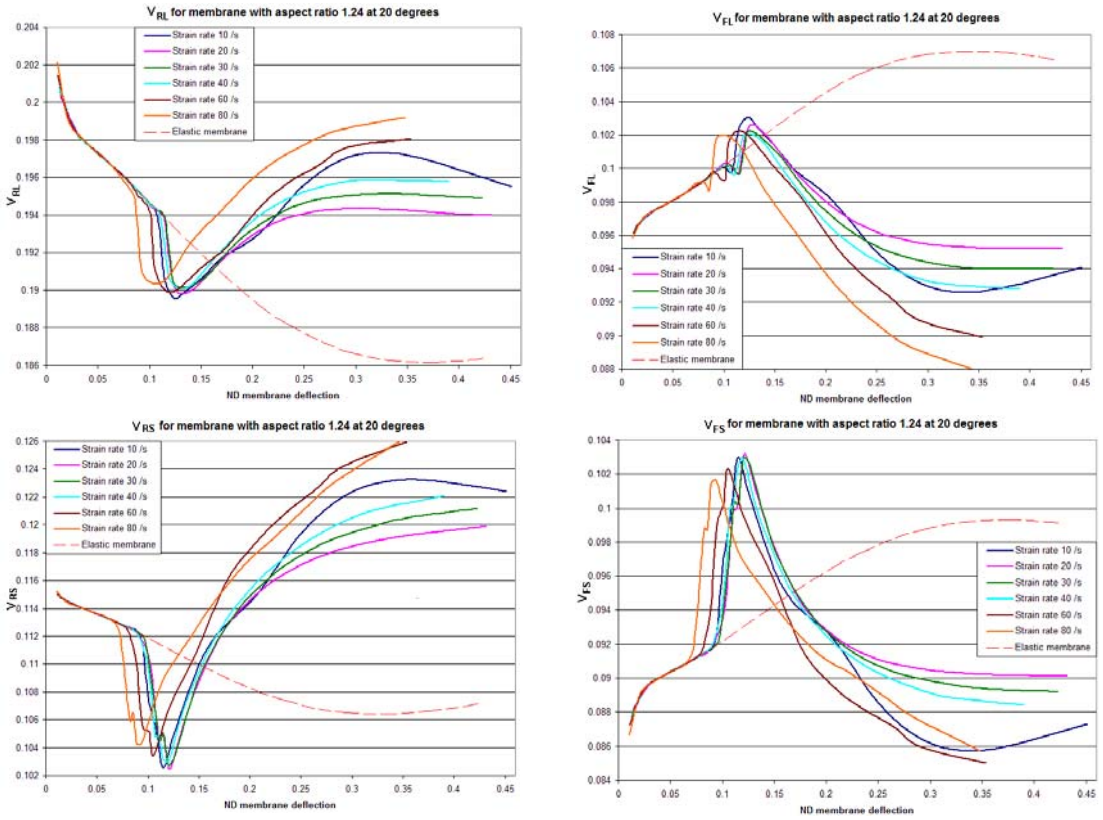

Figure 210. Membrane reaction coefficients for an aspect ratio of 1.24 for 20ºC

The sum of the reaction coefficients calculated separately from the loading distribution and the moments resulting from the internal reactions and the deflections of a single surface, but allowing for the initial membrane thickness, were accurate to within 0.4% for the 20ºC analysis and about 0.2% for the 26ºC and 29ºC. The maximum error occurred at a non-dimensional membrane deflection of about 0.25, and thereafter reduced for increasing deflection. This is expected to be greater than the error in the transformation coefficients due to the use of the deflections from a single surface.

The reaction coefficients from the analyses of membranes with an aspect ratio of 1.24, using material properties for PVB at 20ºC are shown in Fig. 210. These are not required for analysis of the blast trials in this chapter, but would be required to calculate the dynamic loading on the 'bite' and frame if used for design.

The reaction coefficients from analyses of membranes with an aspect ratio of 1.3773, using material properties for PVB at 26ºC are shown in Fig. 211, and at 29ºC are shown in Fig.212.

The reaction coefficients for the elastic membrane show a trend of reducing reaction sensitivity to resistance and increasing sensitivity to loading as the deflections increase.

The different reaction coefficients show different sensitivities to the initial plastic yield at the edges and to the plastic yield at the centre, but overall these increase the trend shown by the elastic membrane. However, after a yielded zone is established across the whole width of the membrane, the trend reverses, reducing or reversing the earlier effects.

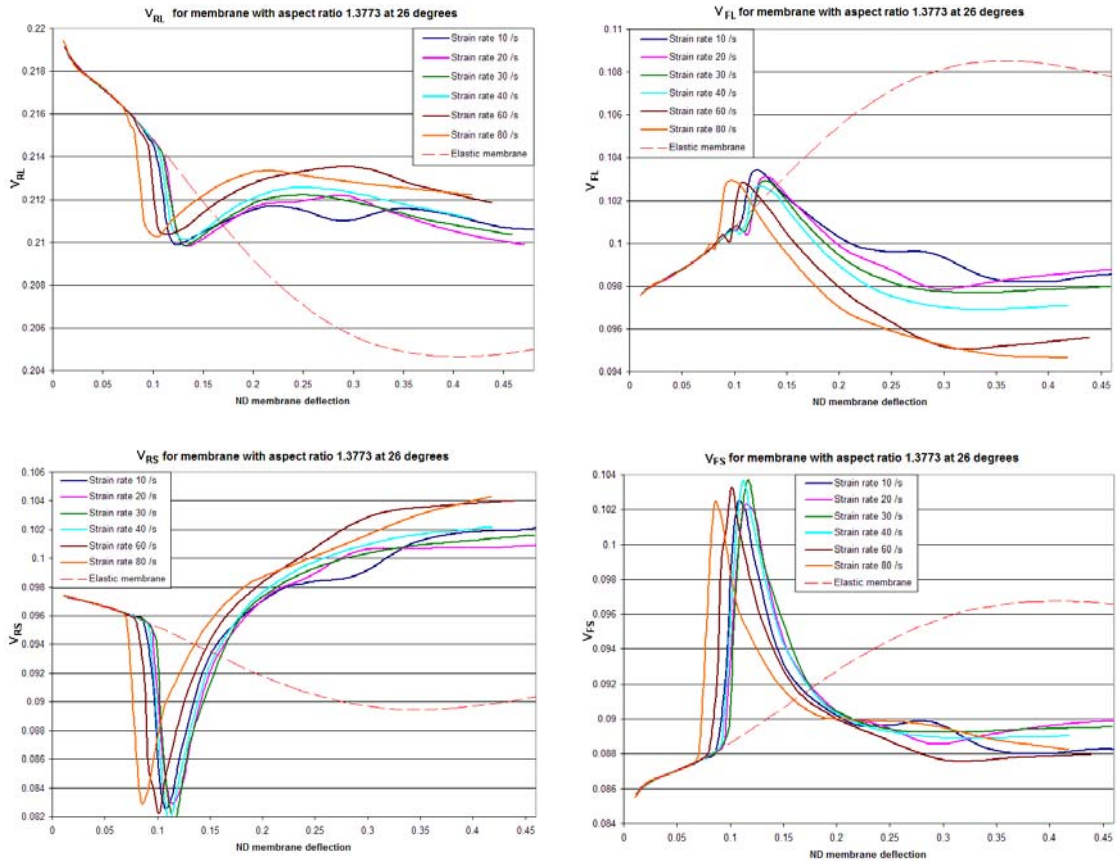

Figure 211. Membrane reaction coefficients with an aspect ratio of 1.3773 for 26ºC

Overall, the variability of the reaction coefficients is not very great in the elastic – plastic membrane model, with individual coefficients varying over a range of between 5% and 20% of the initial values.

As the temperature increases the pattern of the reaction coefficients appears to become smoother and more consistent, with only the 10 /s curves showing variation from a consistent pattern at 29ºC in Fig. 212.

Other design data that can be derived from the finite element reactions include:

- the ratio of the peak to average transverse reactions on the long and short sides, which can be used to identify the peak load in the bite of the frame anchoring a cracked laminated glass pane.

- the location of the peak transverse reactions, which are consistently close to the centre of the spans (unlike for uncracked glass panes) as shown in Fig. 92.

- the amplitude of the total in-plane reactions in each direction.

- the ratio of the peak to average in-plane reactions on the long and short sides.

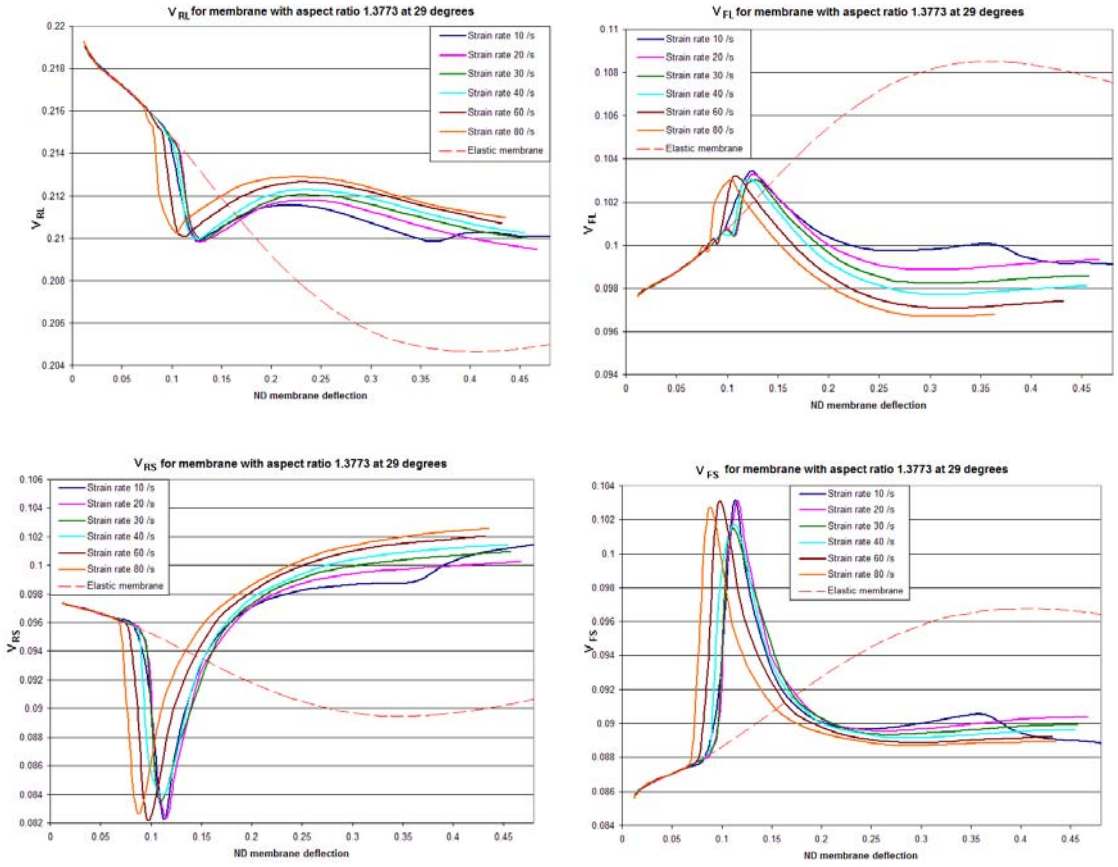

Figure 212. Membrane reaction coefficients with an aspect ratio of 1.3773 for 29ºC

9.5 Analysis of membrane response of blast trials at Spadeadam

9.5.1 Blast trials

In June 2006, five glazing panels were tested by HOSDB at the Advantica test site at Spadeadam, Cumbria. The results of these tests have been made available courtesy of HOSDB [137], in the form of pressure and deflection readings of the five tests, together with some photographs of the configuration. The tests were reported to have been undertaken at ambient temperatures of about 20ºC [138], but temperature measurements at the time of each test were not available.

The test panels were all single glazed 7.5mm thick laminated annealed glass panels of size 1250mm by 1550mm. These are HOSDB standard "Large panes", similar to those documented in Refs. 80 and 81, which fit into openings of existing test cubicles used for arena blast trials.

A cubicle capable of accommodating two panels was used. One opening was used for the glazing test panel, while the other opening was occupied by a steel plate fitted with three pressure transducers, as shown in Fig. 213. The three transducers were grouped around the centre of the plate, and will have been subjected to the same blast loading from a charge placed in front of the centre of the cubicle as the corresponding locations on the mirror image glazing test sample.

Figure 213. HOSDB test cubicle at Spadeadam

Although the reflected peak blast pressures on the face of the cubicle will be effectively uniform, the impulse from the blast wave will not be uniformly distributed, because rarefaction waves will extend from the free edges of the cubicle, reducing the pressure sooner near the edges than at the centre, and hence reducing the reflected impulse more at the edges than in the centre, a process known as 'clearing'. The pressure histories at the transducers will be a reasonable approximation of the mean pressure histories over the whole of the test panel. However, the actual distribution over the panel will not have been uniform, with greater impulse at the bottom left corner, and less impulse at the top right corner.

9.5.2 Pressure measurement

The pressure histories from all five of the trial shots were measured on each transducer. These were provided nominally for pressure in millibars at intervals of 10 microseconds, although the records of Shot 5 appear to have been provided in kPa units and have been corrected for analysis.

However, examination of the three pressure records for each of the trials shows a systematic difference between the sensors, with the first consistently giving the largest reading, the second consistently giving pressures and impulses as low as 60% of the first, and the third consistently gives intermediate pressures and impulses. The pressures and impulses from each transducer are given in Table 71, and the typical pressure histories for shot 1 are shown in Fig. 214.

Test	Transducer No	Peak pressure kPa	Impulse kPa.ms
Shot 1	25	**109.7**	**441**
	26	80.4	309
	27	86.4	378
Shot 2	24	**117.3**	**451**
	25	75.2	296
	26	99.5	430
Shot 3	24	**116.2**	**455**
	25	71.0	294
	26	93.8	417
Shot 4	24	**180.4**	**638**
	25	115.2	450
	26	151.1	595
Shot 5	24	**172.0**	**611**
	25	111.6	395
	26	153.6	566

Table 71. Pressure and impulse from transducers for HOSBD tests

These systematic differences were not caused by clearing effects because they affect the peak pressures as well as the impulses. From discussions with Advantica and HOSDB, it is most likely that the differences are caused by signal loss in joints in the cables between the transducers and the digital recorders, and that the higher values

are the most accurate. The tests have therefore generally been analysed using the first pressure history for each shot, with the blast properties shown in bold in Table 71.

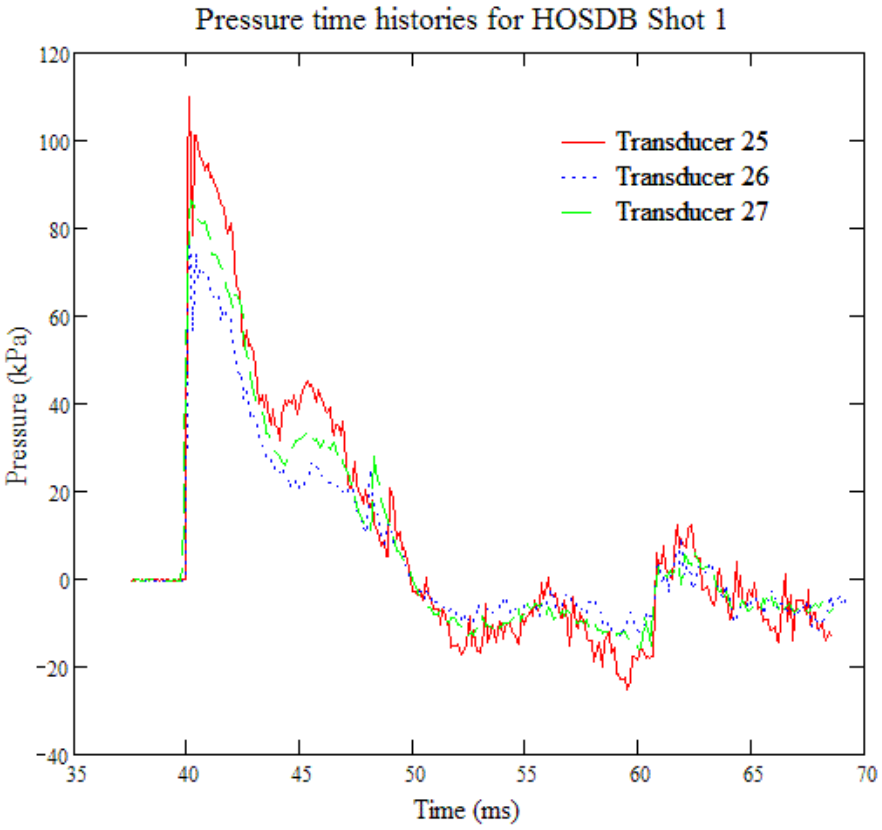

Figure 214. Transponder pressure histories for Shot 1

All of the pressure history records provided by HOSBD ran to a time after the maximum deflection, but did not always run until after the glass had rebounded back to its initial position. To allow for this, some analyses have been run using a different time history that runs longer, scaled up in proportion to the measured positive impulses.

9.5.3 Deflection measurement

The deflections of the laminated glazing panels were measured by two different methods.

A Baumer Electric laser displacement sensor was positioned inside the cubicle behind the window, and was used to measure the distance to a point on the inside of the window, where a matt reflecting target was located, at ten microsecond intervals as the glass deflects under the blast loading. The rest of the glass was blacked out with aluminium foil to prevent the sensor being blinded by the flash of the detonation and the glow of the fireball.

In addition, a high speed video camera above the window was aimed through an inclined mirror at a scale on the floor of the cubicle, so as to minimise parallax error.

As the laminated glass deflected, it intruded into the camera view, and the inwards deflections were measured later from video frames at one millisecond intervals.

The laser displacement sensor can measure small deflections and outwards deflections with the same accuracy as inwards deflections, within the 500mm range of the instrument. However, the distance that the sensor is mounted behind the glazing must be set in advance of the test, and once the glass reaches the 200 mm minimum range from the sensor the reading will 'peg' and the displacement curve data will be 'clipped' until the glass passes that point on rebound. In addition, if the glass sheds fragments they can tear holes in the foil, and either the glass or foil fragments can reflect the laser beam and cause false readings of large deflection, or the light can blind the sensor and give false readings. However, true readings will still occur early in the event, and some true readings can still sometimes be observed between the periods of false data. In practice, the laser data provided by HOSDB was truncated at the point where the glass rebounded to its original line. Little additional true data was reported [138].

The high speed video data is not as prone to false data, although similar measurements at BakerRisk [129] were sometimes obscured by a cloud of fragments, and fragments of the foil could also obscure the glass. However, the glass must be deflected more than the depth of the frame behind before it will register on the scale beyond, and an outwards deflection would take the glass out of the frame of view, and cannot be registered by this method. The early deflections at the start of the response may not be registered, so the identification of the time at which the response starts will not be accurate, and the coarser timesteps at which measurements are taken may also affect the accuracy.

The maximum measured deflections of the glazing in the five shots are shown in Table 72. A mean strain rate has been calculated by deriving an average strain from the maximum deflection using Fig. 195, and a rise time between the initial movement and the maximum deflection.

Test	Laser sensor			High speed video		
	Deflection	ND deflection	Strain rate	Deflection	ND deflection	Strain rate
	mm	%	/s	mm	%	/s
Shot 1	N/A	N/A	N/A	308.8	24.7	9.6
Shot 2	260.2	20.8	7.4	266.7	21.3	7.6
Shot 3	271.9	21.8	7.8	256.1	20.5	7.7
Shot 4	>307.7*	N/A	N/A	409.5	32.8	15.8
Shot 5	407.7	32.6	17.4	402.4	32.2	17.5

* Deflection limited by minimum range

Table 72. Measured maximum deflections from shots, and associated strain rates

The timing of the digital record of deflection from the laser sensor is different from the timing of the pressure record, so it is not possible to say whether it is based on a consistent zero time trigger. In initial response discrepancies suggest that they are based on separate trigger times. The video camera timing is based on the frame rate and frame counting, but the time zero setting is not based on a time zero signal, with

the cameras being started several seconds before detonation, and record the video data separately from the instrument data. There is therefore sometimes a systematic timing discrepancy between the two deflection measurement records. The small deflection timing of the video record is less accurate than the large deflection timing, so for comparison with the analysis, the start time of the video record has been adjusted where necessary to give a best fit with the laser record over the upper part of the rising curve.

9.5.4 Analysis of tests

The tests were analysed using a single degree of freedom analysis with a resistance function that combines the resistance of a laminated glass plate in accordance with the method described in Chapter 7, with the resistance of a PVB membrane at various strain rates. A typical resistance function is shown in Fig. 215.

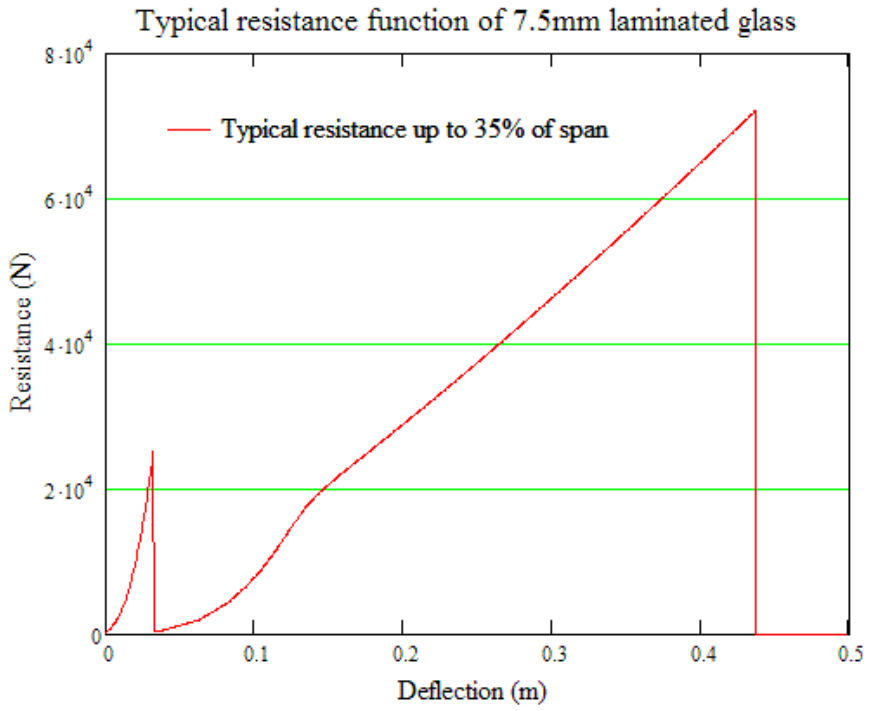

Figure 215. Typical resistance function for 7.5 mm laminated glass

The cracking deflection of the laminated glass is greater than the cracking deflection of a single 3mm thick glass ply. Both plies of glass are taken to crack simultaneously. The design strength of the annealed glass was taken as 80 MPa. However, the glass contributes relatively little to the resistance, as shown in Fig. 215, and sensitivity studies showed that increasing the strength to 100 MPa made only 0.35% difference to a deflection of about 300mm.

The transformation factors used in the analysis varied with deflection, in accordance with the curves calculated in Section 6.4 up to cracking of the equivalent monolithic plate, and in Section 9.3 after cracking. The transformation factors corresponding to the resistance in Fig. 215 are shown in Fig. 216.

The analyses incorporated aeroelastic damping on both faces, in accordance with analyses using the TPS Consult model [6]. The calculation of this is described in Chapter 10.

The resistance on rebound was modelled using a cubic resistance curve based on the WINGARD [100] coefficient, with the adjustment for the plastic deflection used in the TPS Consult model. However, the Young's Modulus used was taken to be independent of the initial elastic modulus, which allowed the rebound stiffness to be adjusted independently.

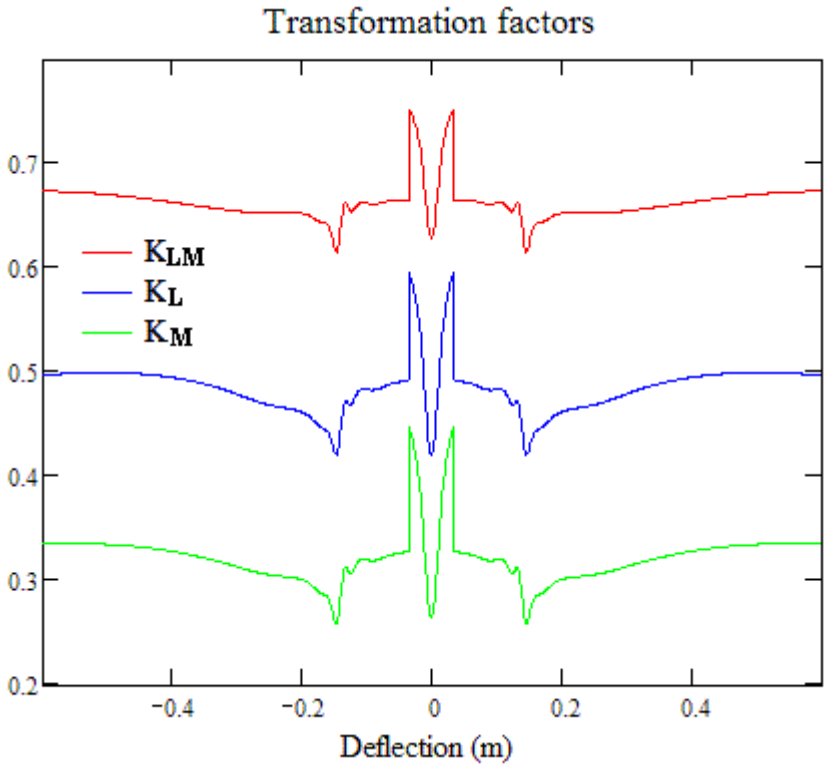

Figure 216. Transformation factors corresponding to resistance in Fig. 215

9.5.5 Results of the analyses

The deflection history of an analysis of Shot 1 with a resistance based on the material properties from the tensile material properties at 20ºC and 10 /s strain rate in PVB is shown in Fig. 217. The mean strain rate over the inwards deflection is shown in Table 73.

The laser displacement sensor appears to have been blinded before the peak deflection was reached, but it was in good agreement with the high speed video measurements in the early part of the analysis once a 1millisecond adjustment had been made to the timing, and there appear to be some points of agreement on the rebound.

Loading case	Material strain rate	Maximum deflection	ND membrane deflection	Mean strain rate	Strain rate ratio
	/s	mm		/s	
1	**10**	**306**	**24.5%**	**8.7**	**1.1**
2	30	269	21.5%	7.7	3.9
	40	**261**	**20.9%**	**7.2**	**5.6**
3	**30**	**270**	**21.6%**	**7.7**	**3.9**
	40	261	20.9%	7.1	5.6
4	**10**	**405**	**32.4%**	**14.3**	**0.7**
5	**10**	372	29.8%	14.1	N/A
5 + 10%		**406**	**32.5%**	**16.4**	**0.6**

Table 73. Strain rate comparison of analyses of HOSDB tests

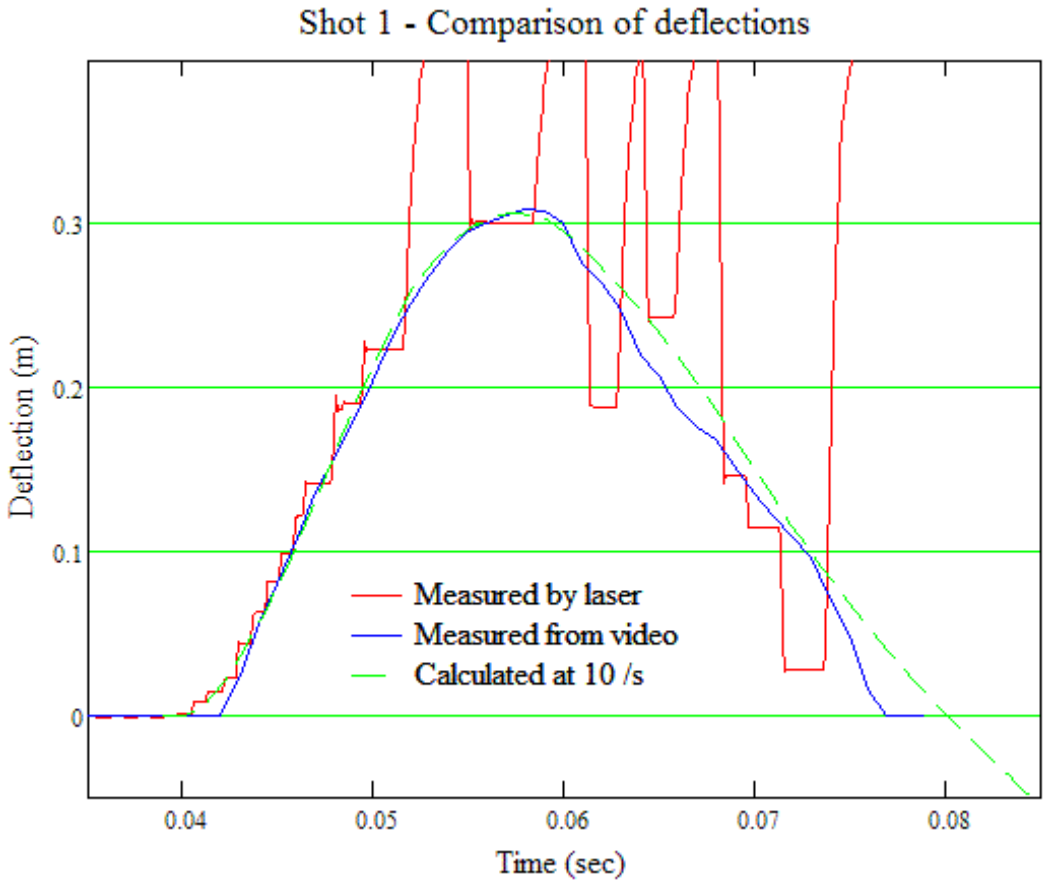

Figure 217. Deflections of Shot 1 for material at 20ºC and 10 /s

The calculated deflection history shows good agreement with the measurements over the inwards deflection once a 2 millisecond adjustment had been made to give agreement of the initial response. The agreement on rebound is fairly close for a cubic elastic rebound stiffness reduced to 29% of the initial elastic stiffness, so that the membrane only goes slack when the deflection reduces to 23 millimetres. The loading history only extended to 68 milliseconds, truncating the negative phase loading. A longer loading history would have increased the steepness of the curve after 68

milliseconds, which would have improved the correlation between the calculated curve and the video measurements.

The deflection history of an analysis of Shot 2 with a resistance based on the material properties from the tensile material properties at 20ºC and 40 /s strain rate is shown in Fig. 218. An analysis using 30 /s material properties showed a peak deflection 8mm greater, which is close to that measured from the video record, but showed less accurate correlation on the rebound. The mean strain rates over the inwards deflections are shown in Table 73.

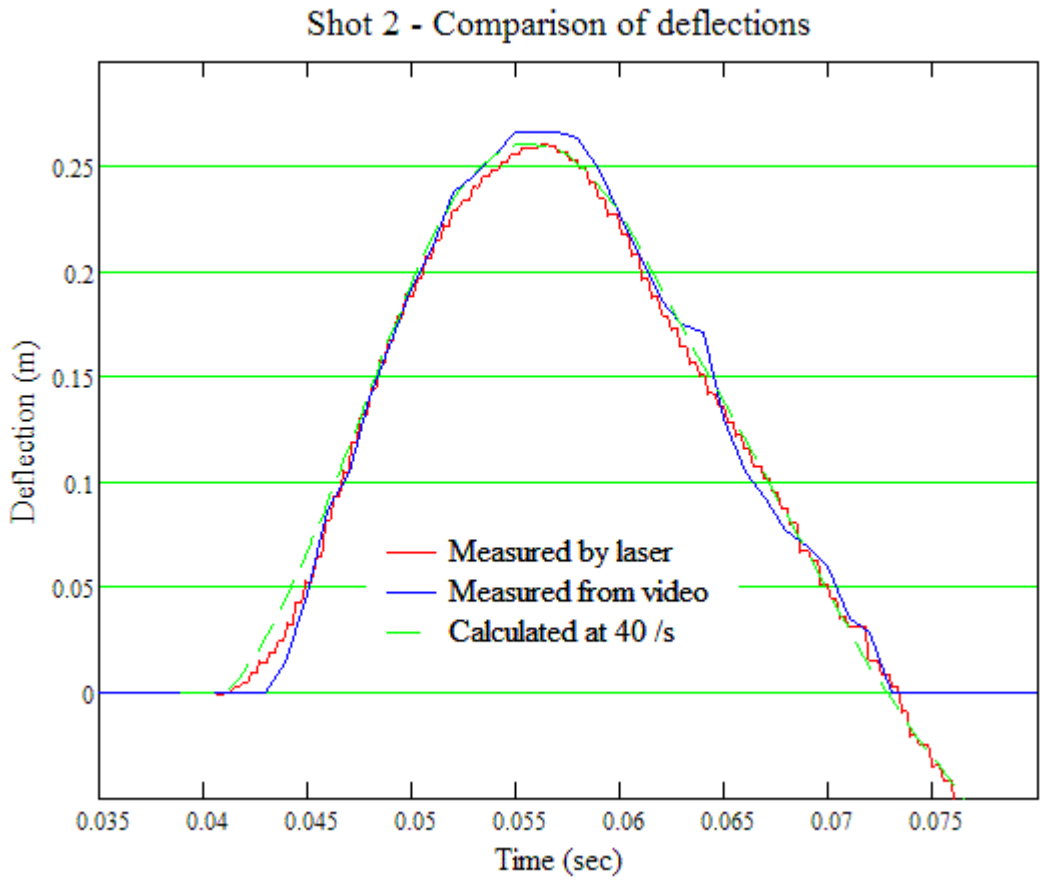

Figure 218. Deflections of Shot 2 for material at 20ºC and 40 /s

The measured deflection histories show good correlation on both the rising and falling curves with a 0.5 millisecond adjustment. There is some divergence in the initial small deflections when the camera cannot be expected to be accurate, and near the peak deflection.

The calculated deflection history shows good correlation with the laser measurements throughout the rising and falling curves using material properties for 20ºC and 40 /s strain rate in PVB, with a 1.5 millisecond adjustment for agreement on the initial response time and a rebound material stiffness 40% of the initial PVB stiffness, giving a slack deflection of 47 millimetres. Material properties for 30 /s in PVB make 3% difference to the peak deflection, which corresponds to the difference on the two measured results, but results in a later rebound, which reduces the correlation of the

falling curve. The loading history extended to 72 milliseconds, and so effectively covers the whole analysis.

The deflection history of an analysis of Shot 3 with a resistance based on the material properties from the tensile material properties at 20ºC and 30 /s strain rate is shown in Fig. 219. An analysis using 40 /s material properties showed a peak deflection 9mm greater, which is closer to that measured from the video record, but showed less accurate correlation on the rebound. The mean strain rates over the inwards deflections are shown in Table 73.

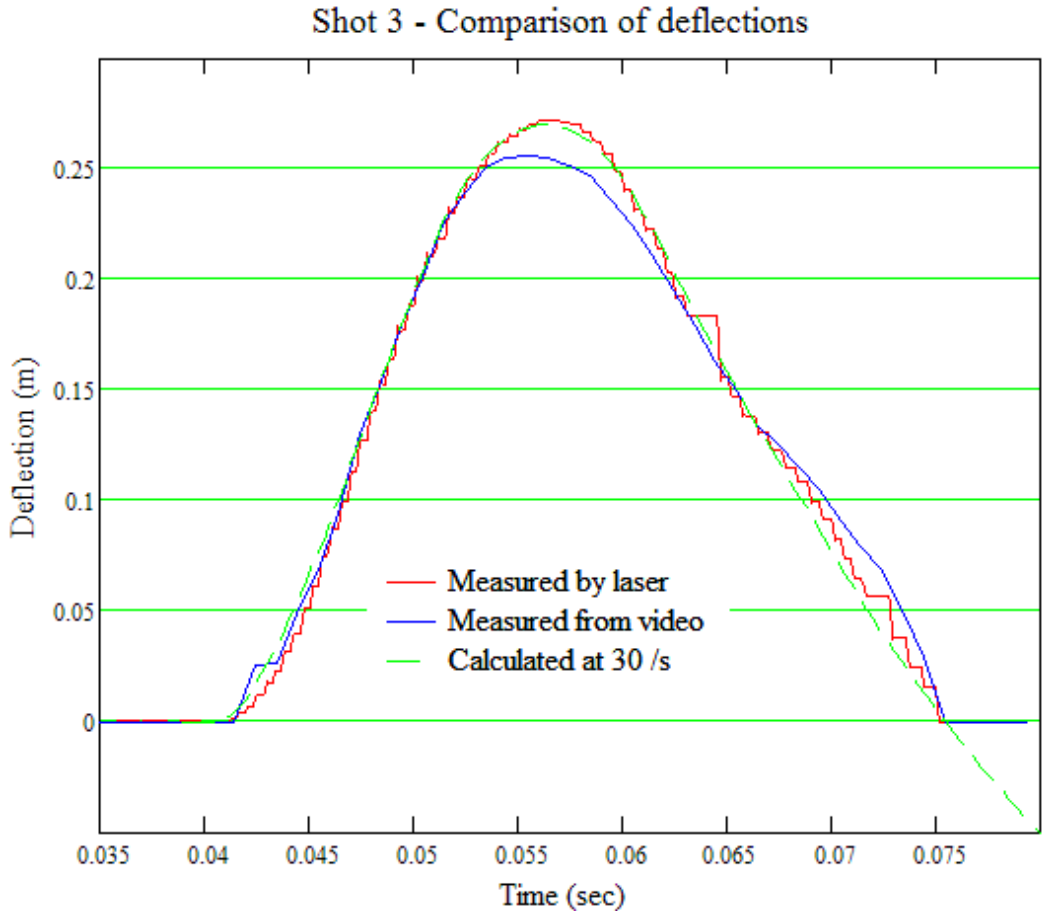

Figure 219. Deflections of Shot 3 for material at 20ºC and 30 /s

The measured deflection histories show good correlation on the rising curve and fair correlation on the falling curves with no adjustment. There is some divergence in the initial small deflections when the camera cannot be expected to be accurate, and near the peak deflection.

The calculated deflection history shows good correlation with the laser measurements throughout the rising and falling curves using material properties for 20ºC and 30 /s strain rate in PVB, with a 1.5 millisecond adjustment for agreement on the initial response time and a rebound material stiffness 45% of the initial PVB stiffness, giving a slack deflection of 100 millimetres. Material properties for 40 /s in PVB make 3% difference to the peak deflection, which corresponds to most of the difference on the two measured results, but results in an earlier rebound, which

reduces the correlation of the falling curve. The loading history extended to 70.5 milliseconds, and so effectively covers the whole analysis.

The deflection history of an analysis of Shot 4 with a resistance based on the material properties from the tensile material properties at 20ºC and 10 /s strain rate in PVB is shown in Fig. 220. The mean strain rate over the inwards deflection is shown in Table 73. The data from transducer No 24 only covers up to 52 milliseconds, and the lack of negative phase loading would distort the rebound analysis, so the analysis is based on transducer No 26, with the amplitude increased by 7.2% to match the positive impulse of transducer No 24.

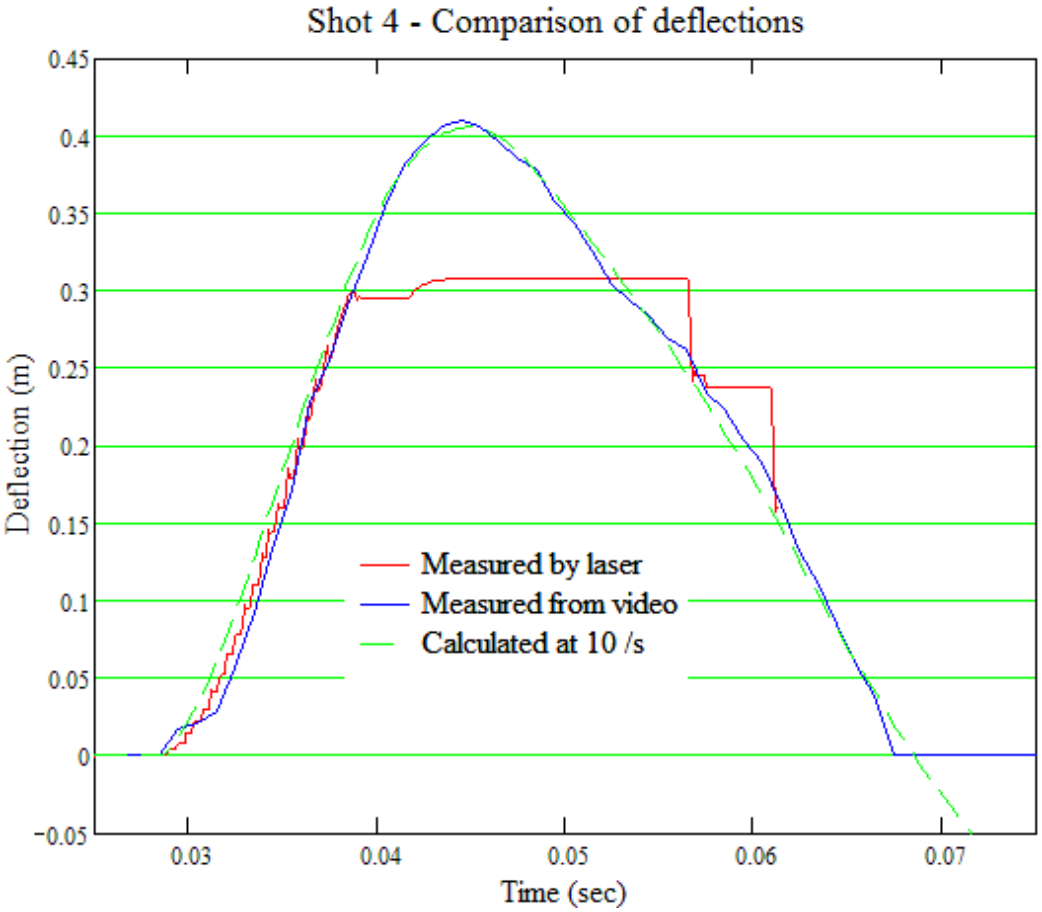

Figure 220. Deflections of Shot 4 for material at 20ºC and 10 /s

The measured deflection histories show good correlation on the rising curve with a 1 millisecond adjustment, until the laser 'pegged'. There were several points on the downwards curve where the laser was not blinded, and these correlate well with the video measurements. The peak deflection reading of the laser does not represent the maximum deflection of the glazing.

The calculated deflection history shows good correlation with the video measurements throughout the rising and falling curves using material properties for 20ºC and 10 /s strain rate in PVB, with a 1.5 millisecond adjustment for agreement on the initial response time and a rebound material stiffness 18% of the initial PVB stiffness, giving a slack deflection of 80 millimetres.

The deflection history of an analysis of Shot 5 with a resistance based on the material properties from the tensile material properties at 20ºC and 10 /s strain rate in PVB is shown in Fig. 221. The mean strain rate over the inwards deflection is shown in Table 73.

The PVB was reported to have torn in the middle during the subsequent rebounds [138], beyond the period for which the deflection measurements were available. Higher deflections on rebound are not uncommon, and are modelled in Section 10.5, but this does suggest that the PVB must have been close to failure at 33% of span.

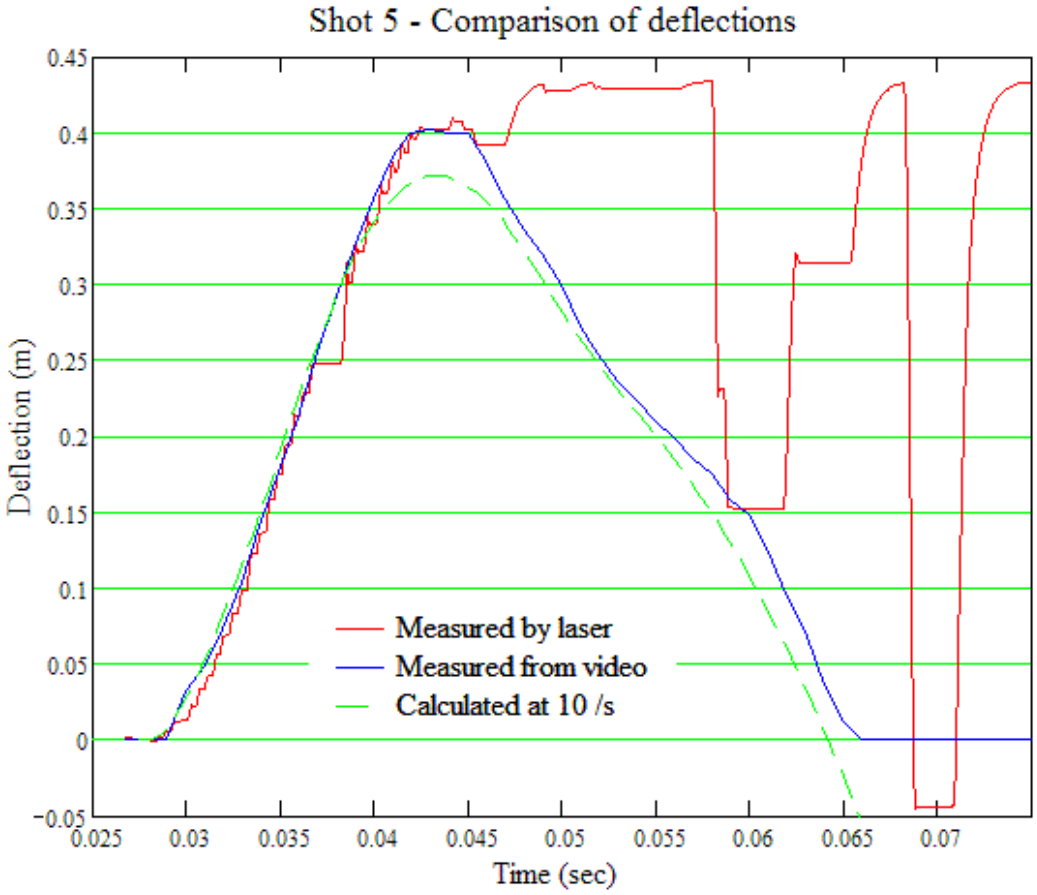

Figure 221. Deflections of Shot 5 for material at 20ºC and 10 /s

The measured deflection histories show good correlation on the rising curve with a 0.5 millisecond adjustment, until the laser was blinded shortly after the glass deflection peaked. There was one point on the downwards curve where the laser was not blinded, and this correlates well with the video measurements, and possibly one point in the rebound..

The calculated response is about 10% lower than the measured deflections. However, the discrepancy is more likely to be due to the measurement of the loading than a lower material stiffness, as the measured deflections are very close to those for Shot 4.

A 10% increase in the amplitude of the measured pressure history would give deflections close to those measured, and the Shot 4 loading gave a similar deflection with a 4% greater impulse, but a different blast history.

However, for the recorded blast loading a 30% reduction in the PVB stiffness would be required to reach this deflection, and the response would be slower, with a later peak, and the calculated rebound deflection consistently later, even with an elastic membrane rebound without slack.

The PVB was reported to have torn in the middle during the subsequent rebounds [138], beyond the period for which the deflection measurements were available. Higher deflections on rebound are not uncommon, and are modelled in Section 10.5, but this does suggest that the PVB must have been close to failure at 32% of span.

For the best fit analyses to the tests, shown in bold in Table 73, the ratio between the material strain rate and the mean membrane strain rate varies between 5.6 and 0.6, a variation of almost ten times. The mean value is 2.4, but this is unlikely to be significant from a small sample with diverse values.

The ratio was not expected to be unity, because there are a number of factors that should distort the relationship between the PVB material properties and the membrane response, including:

- The strain rate in the tensile tests was not uniform and constant, but varied locally in the straight section of the test sample with the "yield" transition into the lower stiffness phase in some parts of the sample before others.

- The strain distribution in the membrane was not uniform, but with the local strain rate sensitivity of a viscoelastic material will not be identical to the distribution in the finite element models shown in Fig. 193.

- The real deflected shape of the membrane will be intermediate between that for conservative forces used in the finite element analyses and that from follower forces, as the whole positive impulse is not applied while the deflections are still small.

- The stiffness of cracked laminated glass is expected to be greater than that of cured PVB, because of the stiffening effect of the attached glass fragments. These were expected to reduce the active length of PVB, increasing the strain in the active PVB between the fragments and hence the strain rate in this material.

Some diversity of the strain rate ratio could be expected due to the general variability of testing, and because the factors are likely to affect different cases differently. The final factor suggests that the values of the ratio should generally be greater than unity. However, the large variation observed suggests that there may be some other factors contributing to the variation in the strain rate ratio. One likely factor is that the tests may not have been undertaken at identical temperatures.

One feature pointing strongly at temperature variations to account for the differences is the difference of the measured deflection of Shot 1 from those of Shots 2 and 3, which were similar panels tested with similar blast loading, but which deflected only 85% as far.

From the viscoelasticity time adjustment term in Eqns. 25 & 45, using the coefficients from Ref. 88 given in Section 4.7.2, most of the factor of 9.3 difference in the strain rate ratio could be explained by a temperature range of only 4ºC in the testing, with Shots 1, 4 and 5 tested towards the upper end of the temperature range, and Shots 2 and 3 towards the lower end. Consideration of the bi-linear analyses suggest that PVB membranes may be a bit less sensitive than this, but temperature variations greater than this are very probable for a series of tests conducted over several days, but could only be confirmed if temperatures were recorded at the time of each test.

The analyses of the tests suggest that it is necessary to use a softer elastic Young's modulus than the initial Young's modulus of the loaded material to model the viscoelastic rebound of the cracked laminated glass. For deflections up to about 25% of the span, the best rebound models had a reduced stiffness that gave a minimal slack deflection. In practice, up to this limit a cubic elastic membrane curve could be used passing through the origin with no slack deflection and a Young's modulus adjusted for the cubic curve to pass through the deflection-resistance point at the maximum deflection.

For rebound from deflections above about 25% of the span, the analyses of the tests suggest that the recovery strain rate was faster than the viscoelastic recovery rate, resulting in the membrane becoming slack at significant deflections.

9.6 Analysis of membrane response of blast trials by BakerRisk

9.6.1 Shock tube blast tests

Twelve double glazing panels were tested for Permasteelisa [130] in the BakerRisk [129] shock tube at San Antinio, Texas, in August 2006. Three samples that were uncracked in testing have already been reported in Section 7.3.1 of this thesis, where the test conditions are described. The shock tube is shown in Fig. 222.

Of the remaining tests, two experienced partial or complete support failure at high loading levels because of the narrow "wet glazed" support detail used in accordance with normal American practice, and one involved partial cracking at lower loading levels. The remaining six tests experienced cracking of the glass and stretching of the PVB interlayer without damage to the PVB or to the supports. Temperatures measured immediately prior to each test ranged between 26ºC and 29ºC.

The test samples were all double glazing units with overall dimensions 2952 mm by 2157 mm, with a 25mm 'bite' on the supporting frame, giving a clear glazed area 2902 mm by 2107 mm. A typical panel after test is shown in Fig. 223.

Figure 222. Baker Risk shock tube at San Antonio

9.6.2 Pressure measurement

The loading from the shock tube is described in Section 7.3.1.

There was a generally triangular pressure distribution between 38.5 and 40 milliseconds long, followed by a further small positive pressure pulse, and a train of pressure fluctuations around atmospheric pressure. There is no significant negative phase impulse, just a series of short excursions into negative overpressure. For the cracked test samples, the time to peak response is significantly longer than the total blast loading to the first negative pressure, including the second pressure pulse, so the complete measured impulse is listed in Table 74, together with the sample makeups and the test conditions.

Figure 223. Typical cracked Panel 3 after test in the shock tube

The pressure histories are measured at three pressure transducers at the edges of the test panel. It is unclear how representative the second pressure pulse is of the pressure acting on the central part of the test panel, or whether it is representative of a side-to-side shock wave reflection against the sides of the shock tube. Typical pressure histories are shown in Fig. 224.

It was found that a significant pressure increase in the shock tube was required to achieve the desired impulse measurements for a test in which the panel cracked compared to the uncracked tests. This was illustrated by test 3, where the pressure was not adjusted after uncracked tests 1 and 2, resulting in an impulse to 40 ms only 90% of the intended triangular impulse, and 85% of the mean measured impulse from tests 1 & 2, as shown in Fig. 225.

This is consistent with the impulse measured around the face of the test sample being significantly reduced by the aeroelastic damping on the loaded face

Sample Makeup	Units	Test samples					
		3	9	4	10	5	8
Inner leaf plies	mm	10		10		8	
Inner leaf PVB interlayer	mm	1.52		1.52		2.28	
Inner leaf thickness	mm	21.52		21.52		18.28	
Inner leaf material		T*		HS*		HS*	
Cavity	mm	17.4		17.4		17.4	
Outer leaf	mm	10		10		10	
Outer leaf material		HS*		HS*		HS*	
Overall unit	mm	48.9		48.9		45.7	
Test Conditions							
Temperature at test	ºC	29	28	26	29	29	28
Specified peak pressure	kPa	59	62	59	62	59	48
Specified impulse	kPa.ms	1180	1241	1180	1241	1180	965
Specified blast duration	ms	40	40	40	40	40	40
Measured peak pressure	kPa	60	68	60	62	57	48
Measured impulse	kPa.ms	1090	1453	1223	1056	1134	1020
Measured duration	ms	57.5	100	58.7	56.3	59.0	59.1

* T is toughened glass, HS is heat strengthened glass

Table 74. Sample make-up and test conditions for cracked tests by BakerRisk

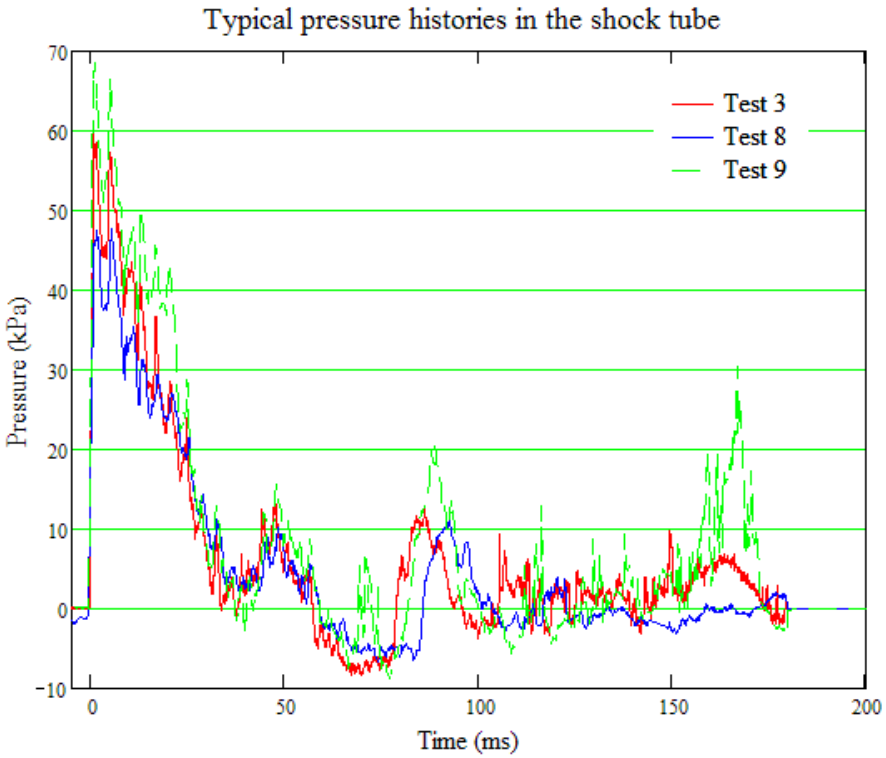

Figure 224. Typical pressure histories measured in the shock tube

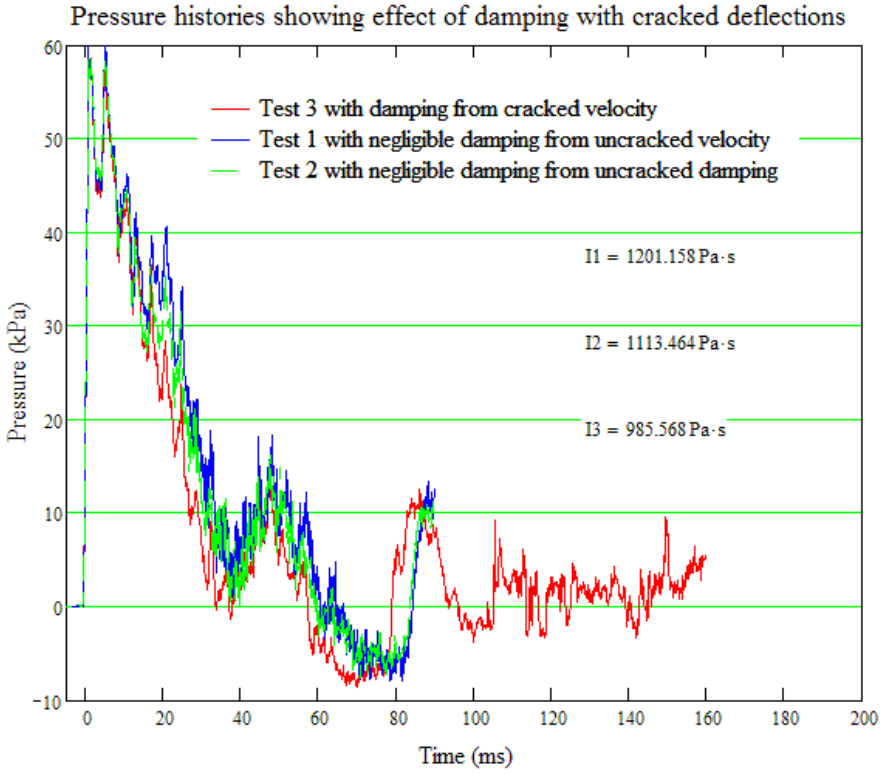

Figure 225. Pressure histories of cracked and uncracked tests showing aeroelastic damping effects for cracked tests

9.6.3 Deflection measurement

Deflection histories for each of the tests were measured at a position in the centre of each pane by a Baumer Electric laser distance measuring sensor, as described in Section 7.3.1. The sensor had a measurement range between 200 mm and 1000 mm and was positioned approximately 780 mm behind the rear of the glazing panels. The sensor was able to measure deflections up to about 580 mm before reaching the gauge measurement limit and 'pegging'. The sensor is shown on Fig 226.

Although the shock tube did not produce a flash to 'blind' the laser sensor, glass fragments spalling off the rear face did intermittently blind the sensor on some tests. However, true deflection readings can usually be identified between these events. The peak deflections measured and the strain rates derived from these are given in Table 75.

In addition to direct measurements of deflection, the glazing response was filmed by a high speed video camera mounted in the side wall of the test cubicle. No arrangements were made to eliminate parallax effects and there was not a calibrated scale on the far side of the test cubicle, although the plywood wall had a distinct grain pattern and the laser mount provided a reference line to assist in estimating deflections, as shown in Fig. 226. The frame supporting the perimeter of the test samples obscured the smaller deflections, but estimates of the maximum deflections were made from the video record for the later tests [129]. The maximum deflections

were sometimes obscured from the camera by the cloud of glass fragments generated by the test, and so were not easy to estimate and an approximate range was given.

Figure 226. Laser sensor and test cubicle, with panel 3 after test

Test	Laser sensor			High speed video	
	Deflection	ND deflection	Strain rate	Deflection	ND deflection
Test 3	>573mm*	N/A	2.2 /s	-	-
Test 9	>573mm*	N/A	2.2 /s	610-660mm	~0.300
Test 4	534 mm	0.253	2.0 /s	-	-
Test 10	510 mm	0.242	1.8 /s	<584 mm	-
Test 5	>560mm*	N/A	3.0 /s	-	-
Test 8	503 mm	0.239	1.8 /s	-	-

* Deflection limited by minimum range to sensor

Table 75. Measured maximum deflections from tests by BakerRisk, and associated strain rates

9.6.4 Analysis of tests

A two degree of freedom (2DOF) model was used to analyse the double glazing unit test samples, with the inner leaf and the outer leaf represented by separate degrees of

freedom, solved simultaneously using a differential solver in Mathcad [89] that can solve systems of differential equations.

The resistance of the inner leaf is formed from the combination of the resistance of the monolithic pane and the PVB membrane, as for the single glazed tests in Section 9.5. Typical resistance curves are shown in Fig. 227.

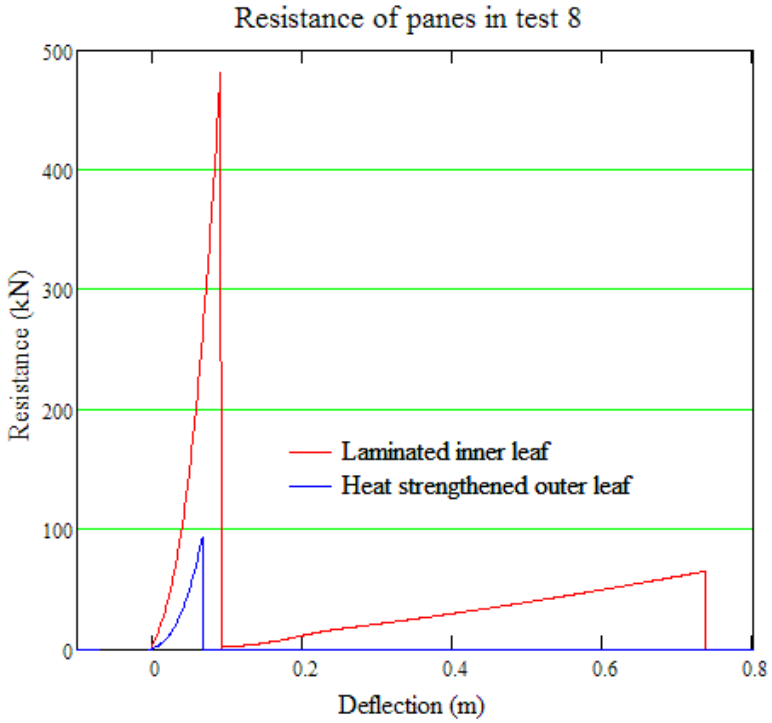

Figure 227. Typical resistances of panes for test 8

The very thick glass panes of strengthened glass result in a large resistance from the uncracked glazing. Allowing for the elevated temperature, the stiffness was taken as 80% of the fully composite stiffness. Because the breaking strength of individual glass panes may be significantly higher than the lower bound design values, particularly for new glass, the breaking strength of the individual panes was estimated from the effect on the deflection curves.

The membrane stiffnesses used were selected from the curves defined in Section 9.2.2 for the appropriate temperature listed in Table 74. Curves corresponding to different PVB strain rates were tried to see which gave the best correspondence with the measured deflections. Because none of the tests had shown any signs of PVB failure, not even the tests that failed at the supports, the failure deflection was set at 35% of span, greater than any of the deflections observed or estimated in the tests.

As for Section 9.5, a cubic elastic membrane resistance has been used for the rebound, with the stiffness relative to the initial PVB Young's modulus modified to chose a slack deflection on rebound on the basis of the observed effects on the rebound deflection history.

The resistance of the heat-strengthened outer leaf was calculated independently. Again cracking strengths greater than the lower bound design value were selected for

each test on the basis of the observed effect the outer glass breakage and fragment impact had on the deflection history of the inner leaf.

The blast loading was applied to the outer leaf, but load transfer between the leaves was calculated from the differential deflection of the two leaves by treating the air in the cavity of the sealed unit as an adiabatic gas spring. This is described in more detail in Chapter 10.

Passive aeroelastic damping based on constant atmospheric pressure was applied to the rear of the inner leaf in the test chamber. Aeroelastic damping based on the cavity pressure was applied to the cavity surfaces. This was calculated for pane velocities relative to the mean velocity of the cavity, so that it serves to damp the vibration of the cavity, rather than to damp the motion of the double glazed unit.

Active aeroelastic damping acts initially on the loaded face of the outer pane of the unit, in the shock tube. However, the measurements by the pressure transducers at the perimeter of the test units appear to have been reduced by aeroelastic damping already. If the sensors had been measuring the average pressure in front of the whole panel, the aeroelastic damping would already have been fully accounted for in any analysis that used this pressure history as loading. However, the pressure transducer mounts measured the pressure at the edges of the test units, which did not experience significant velocity and direct aeroelastic damping. Instead, they will have experienced a reduction in impulse due to a clearing effect from the centre of the test unit, where the reflected pressures will have been modified by the velocity of the reflecting surface.

This redistributed damping at the pressure transducers will mean that the aeroelastic damping will only be partially accounted for in the pressure measurements, so a proportion of the active aeroelastic damping on the loaded face has been used in the analyses, together with the passive damping on the rear face, as described later in Chapter 10. The proportion used in the analyses was chosen based on the effect on the deflection history.

When the deflection of the outer leaf in a model caused it to reach the cracking stress, the blast loading and active aeroelastic damping were taken to act on the inner leaf in place of the cavity pressure and damping. The debris of the outer leaf was taken to travel at the breaking velocity until it impacted the inner leaf, and then to ‘ride’ with the inner leaf until it was thrown clear by the rebound. This is described later in more detail in Chapter 10.

The qualitative effects on the deflection histories of the five independent variables considered in the analysis are described in Table 76.

Variable	Units	Qualitative effects on the inner leaf deflection history
Break strength of outer leaf	MPa	Break strength affected the velocity of the inner leaf when it cracked, and was critical for determining the velocity of the outer leaf debris and the time at which it impacted the inner leaf. The impact timing could significantly modify the shape of the deflection curve, particularly when it impacted near the peak deflection.
Break strength of inner leaf	MPa	The break strength of the glass affected the velocity at the start of the membrane resistance. This had a critical effect on the timing of the deflection and the amplitude of the peak. Even a single MPa difference had a visible effect, and a small increase could prevent the glass from cracking at all. This strength accounted for the conservatism of using the monolithic curve for laminated glass strength, and so tended to be higher than the outer leaf for the same glass type.
PVB strain rate	/s	Together with the temperature this identified the membrane stiffness in deflection. A higher stiffness slowed the velocities between cracking and maximum deflection, delaying the deflection curve and reducing the maximum amplitude.
Rebound stiffness factor	-	Reducing the stiffness on rebound from the loading elastic modulus reduced the deflection at which the membrane became slack. This gave a larger rebound reaction for a longer period, increasing the rebound velocity and reducing the rebound time, but did not affect the time and amplitude of the peak deflection.
Active damping factor	-	Reducing the active aeroelastic damping added during the analysis increased the velocities throughout the analysis. The effect prior to cracking was very small. During inwards deflection and initial rebound the effect was similar to, but not identical to, reducing the PVB strain rate and the rebound stiffness. Later in rebound the damping prevented continuous vibration.

Table 76. Effects of the variables on the deflection history of the inner leaf

9.6.5 Results of the analyses

The deflection history of an analysis of Test 3 with a resistance based on the tensile material properties at 29ºC and 10 /s strain rate in PVB reduced to 65% stiffness is shown in Fig. 228. The various parameters used in the analysis, the maximum deflection and the mean strain rate over the inwards deflection to peak are shown in Table 77.

Test No		3	9	4	10	5	8
Outer strength	MPa	130	172	155	153	145	127
Inner strength	MPa	200	230	200	223	190	198
Damping factor	%	30	30	62	57.1	70	32
Rebound stiffness	%	17	18	70	25.5	30	30
Slack deflection	mm	84	180	410	221	357	246
Material strain rate	/s	10*	12	10	10	20	10
Max deflection	mm	602	631	528	526	591	501
ND memb deflection	%	29.8	30.0	25.1	25.0	28.0	23.1
Mean strain rate	/s	1.6	2.0	2.0	1.5	2.8	1.9
Strain rate ratio		<6.2	6.0	5.0	6.7	7.1	5.3

* Stiffness reduced to 65% of that for 10 /s strain rate

Table 77. Strain rate comparison of analyses of BakerRisk tests

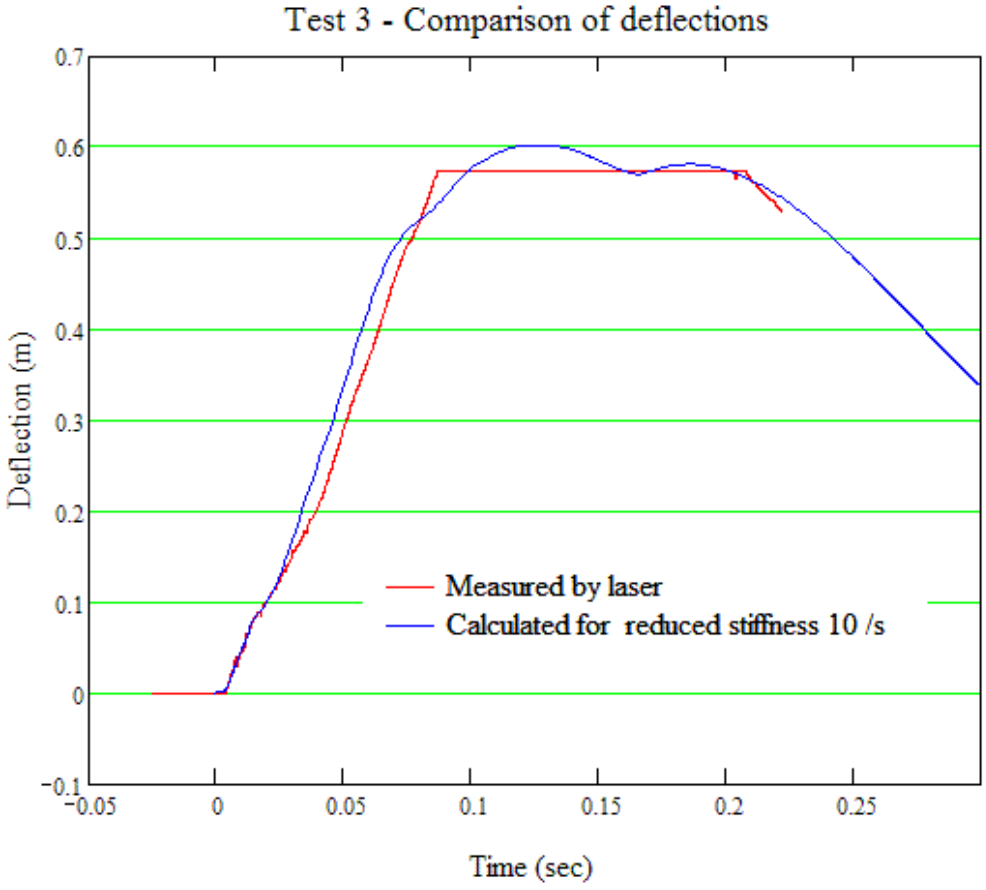

Figure 228. Deflections of Test 3 for material at 29ºC and 10 /s

For all curves that give a reasonable overall fit, the glass strength had to be sufficient to reduce the velocity at glass breakage to 2.75 m/s.

Even with no active damping at all, the 10 /s strain rate stiffness was too stiff and would substantially underestimate the deflection, although the match for the timing of the increasing deflection was best. Instead, the damping has been set to give a reasonable fit for rebound with a minimal rebound stiffness, and the resistance curve

has been scaled down to 65% of the 10 /s stiffness to give a reasonable fit for the maximum deflection, although this cannot be extrapolated to a particular strain rate.

The long period with the laser gauge "pegged" is explained by the timing of the impact from the fragments of the outer leaf, which keep the deflection above the cut-off for longer than would otherwise be expected. The dip and rise in velocity before the peak deflection are caused by the dip and pulse shown in the pressure curve in Figs. 224 and 225 between 60 and 100 milliseconds. There is no sign of such distortions in the measured response curve at the same time, which suggests that these fluctuations do not occur at these times in the central part of the shock tube. This would imply that these are side-to-side reflections shocking up near the corners of the shock tube.

The deflection history of an analysis of Test 9 with a resistance based on the tensile material properties interpolated to 28ºC from calculations for 26ºC and 29ºC is shown in Fig. 229. The various parameters used in the analysis, the maximum deflection and the mean strain rate over the inwards deflection to peak are shown in Table 77.

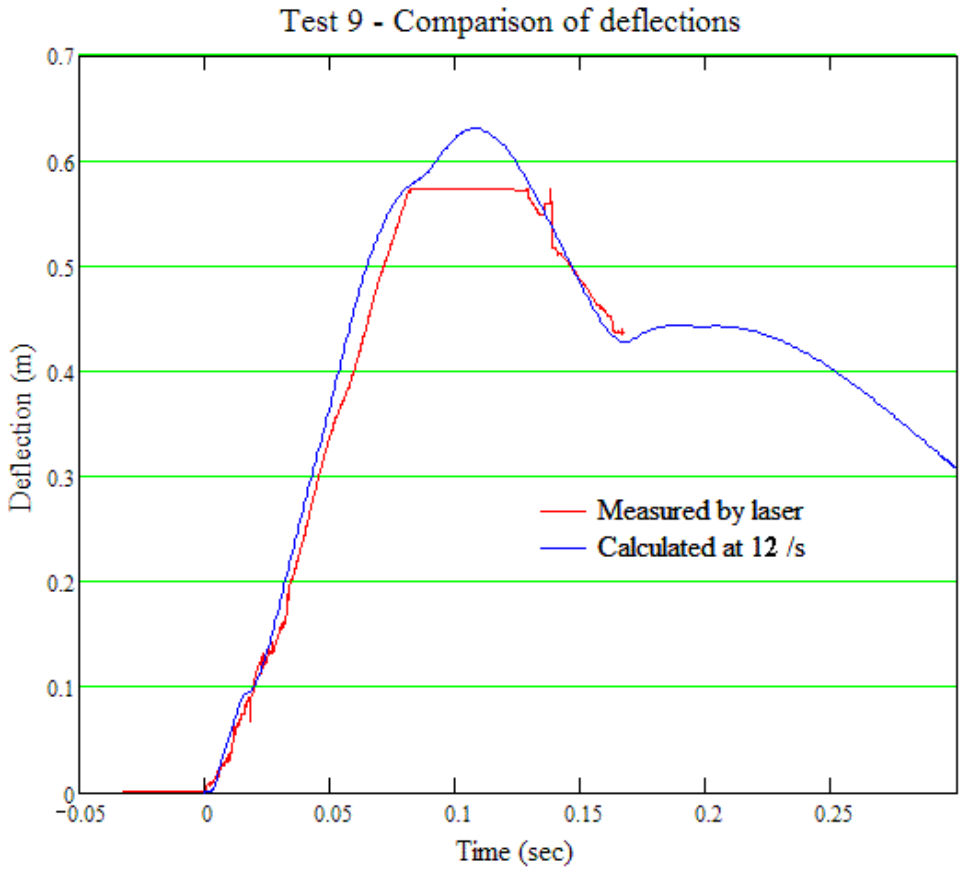

Figure 229. Deflections of Test 9 for material at 28ºC and 12 /s

The glass leaves appear to have been particularly strong for this test, both being at least 50 MPa above their design levels. The inner leaf velocity in the analysis drops to 0.8 m/s when it cracks to give a good fit to the deflection curve, and an increase of only 1 MPa would have prevented it from cracking. This high cracking strength is consistent with the measured deflections, as there is only a small deflection increase

over Test 3, which was of nominally the same construction, but deflected marginally less with a 33% greater impulse and only a 1ºC temperature difference.

The PVB stiffness was interpolated between those for 10 /s and 20 /s strain rates at 26ºC and at 29ºC to give the best fit for peak deflection, which is in the middle of the range estimated from the video record.

The eccentric tip of the deflection curve is caused by similar loading fluctuations over the 60-100 ms period similar to those described for Test 3, while the second, later peak is caused by the late loading pulse after 150 ms shown in Fig. 224, although the outer leaf debris is taken to impact around 200 ms.

The deflection history of an analysis of Test 4 with a resistance based on the the tensile material properties at 26ºC and 10 /s strain rate is shown in Fig. 230. The various parameters used in the analysis, the maximum deflection and the mean strain rate over the inwards deflection to peak are shown in Table 77.

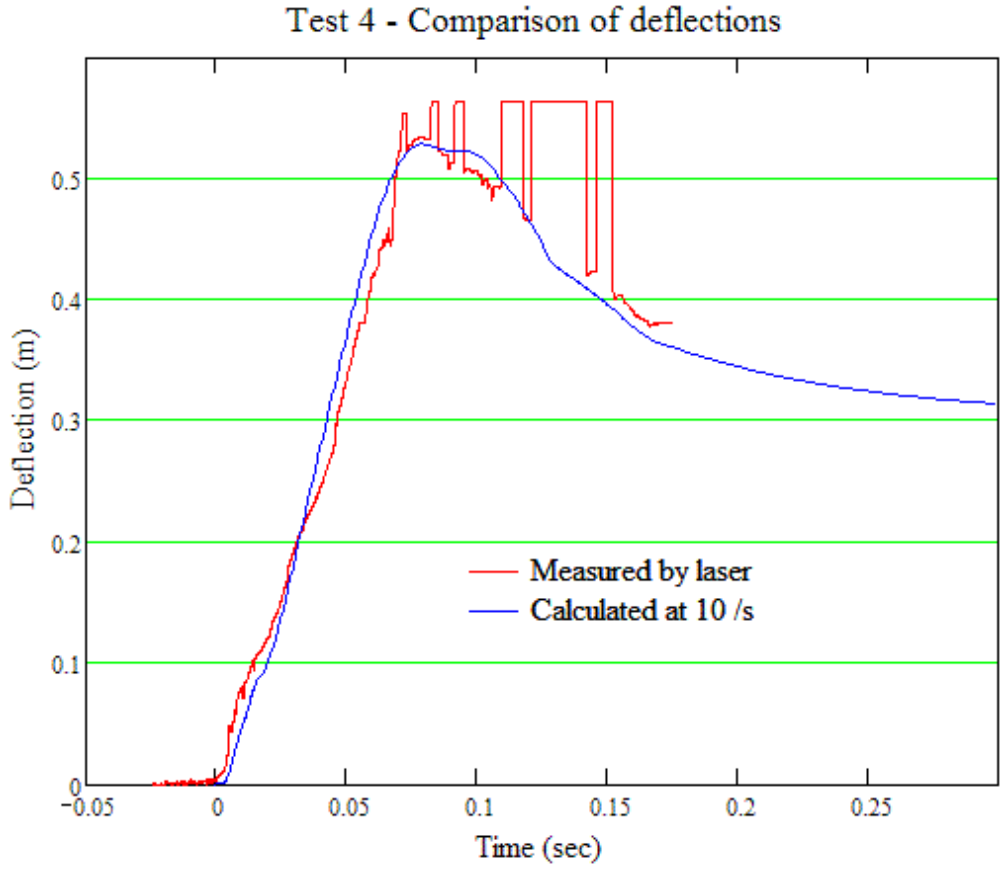

Figure 230. Deflections of Test 4 for material at 26ºC and 10 /s

For curves that give a reasonable overall fit, the glass strength had to be sufficient to reduce the velocity at glass breakage to 2.5 m/s.

A relatively high damping level and a high rebound stiffness with a large slack deflection were required to model the gentle rebound. In turn, these dictated the strain rate to give a reasonable curve and peak value, although the fine tuning was carried out by adjusting the damping for the best general fit.

In Test 4, the measured pressure pulse just before 100 ms that was commented on in previous tests causes the secondary bulge in the calculated deflection history just after the peak deflection. There is no evidence in the measured deflection history to suggest that such a pressure pulse actually acts on the laminated glass.

The debris from the inner leaf was taken to impact the inner leaf after the peak deflection, causing the first flattening kink in the rebound curve in Fig. 230 at about 120 ms.

The deflection history of an analysis of Test 10 with a resistance based on the tensile material properties at 29ºC and 10 /s strain rate is shown in Fig. 231. The various parameters used in the analysis, the maximum deflection and the mean strain rate over the inwards deflection to peak are shown in Table 77.

This test significantly underperformed its intended blast loading, but the reason for this is unknown.

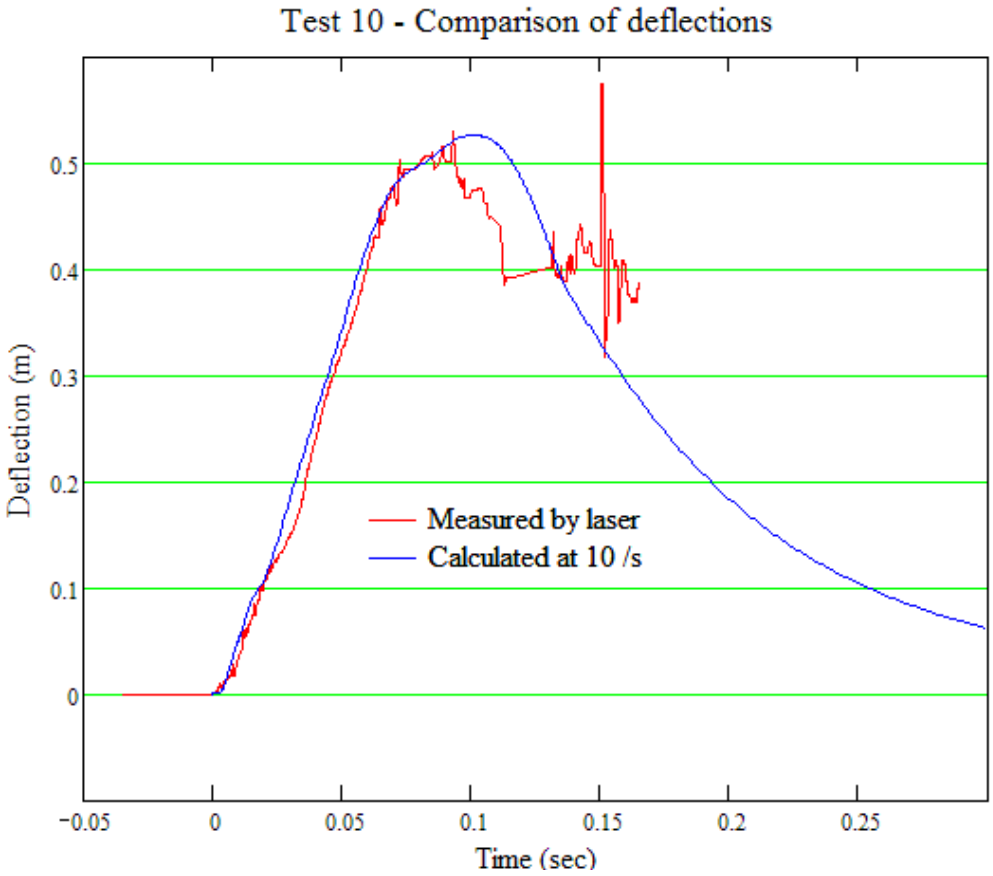

Figure 231. Deflections of Test 10 for material at 29ºC and 10 /s

The measured deflection data is difficult to follow at the peak, so there is some uncertainty as to the true peak deflection, and it is not possible to identify any points in the unloading curve from the data record with any confidence. It is unclear exactly with what the calculated curve should be compared. The modelling has concentrated on the rising curve.

The velocity of the inner leaf at cracking is 3.6 m/s in this model, but the analysis is particularly sensitive to the cracking strengths. Modification to the cracking strength of the inner leaf by as little as 0.5 MPa can make step changes to the maximum deflection of about 20mm, while either raising or lowering the cracking strength of the outer leaf causes the maximum deflection to reduce.

The deflection history of an analysis of Test 5 with a resistance based on the tensile material properties at 29ºC and 20 /s strain rate is shown in Fig. 232. The various parameters used in the analysis, the maximum deflection and the mean strain rate over the inwards deflection to peak are shown in Table 77.

The thinner, lighter construction compared to previous tests results in a faster response time and higher velocities and strain rate. For curves that give a reasonable overall fit, the glass strength had to be sufficient to reduce the velocity at glass breakage to 6.1 m/s.

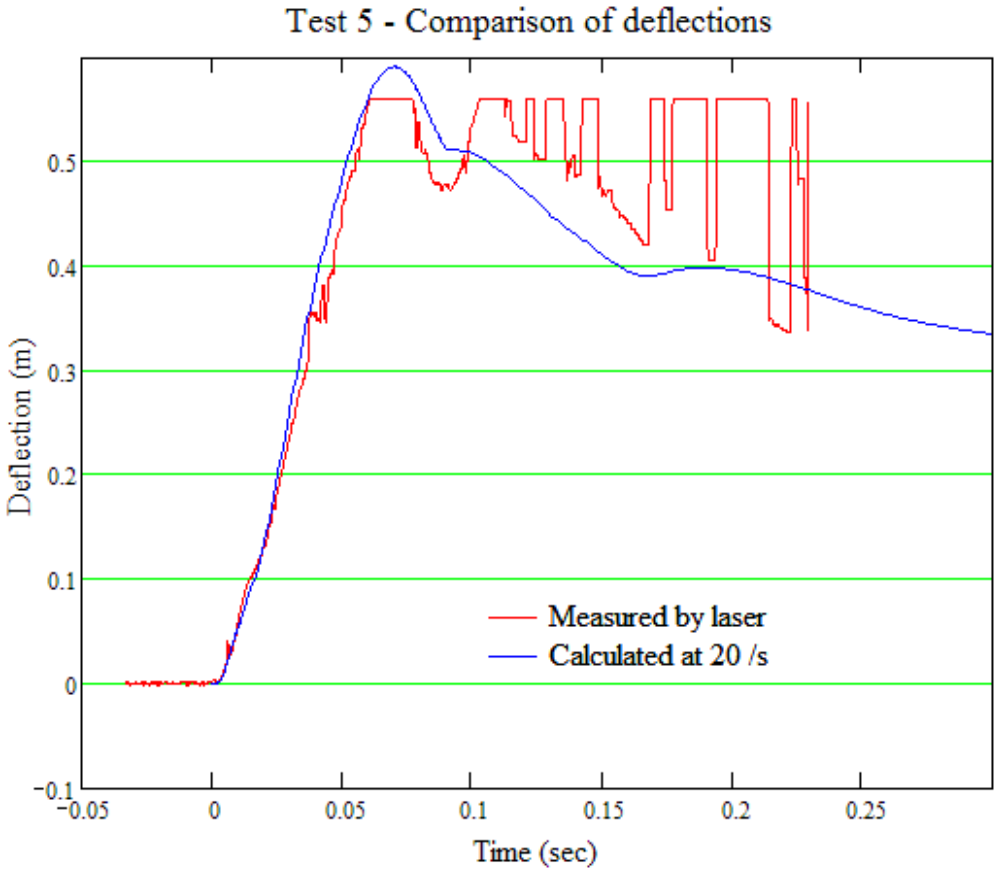

Figure 232. Deflections of Test 5 for material at 29ºC and 20 /s

The breaking stress of the outer leaf was selected to give a velocity to the debris that resulted in the debris impacting the inner leaf shortly after the first peak deflection. Even with the debris impact, it was not possible to reproduce the second deflection peak. This suggests that the secondary pressure vibrations recorded by the pressure transducers at the perimeter are different from those in the centre of the shock tube, which have most effect on the membrane deflection.

Without the second peak deflection, the rebound curve in the model can only follow the measurements in the most general way.

The deflection history of an analysis of Test 8 with a resistance based on the tensile material properties interpolated to 28ºC from calculations for 26ºC and 29ºC and 20 /s strain rate is shown in Fig. 233. The various parameters used in the analysis, the maximum deflection and the mean strain rate over the inwards deflection to peak are shown in Table 77.

For curves that give a reasonable overall fit, the glass strength had to be sufficient to reduce the velocity at glass breakage to 2.1 m/s.

The breaking stress of the outer leaf was chosen to give the debris a velocity that would result in impact with the inner leaf shortly after the peak deflection. In practice, there will never be a perfect match, as the model assumes that all the debris impacts simultaneously, while in reality there will be a more gradual impact over a finite time due to the range of velocity of the glass debris.

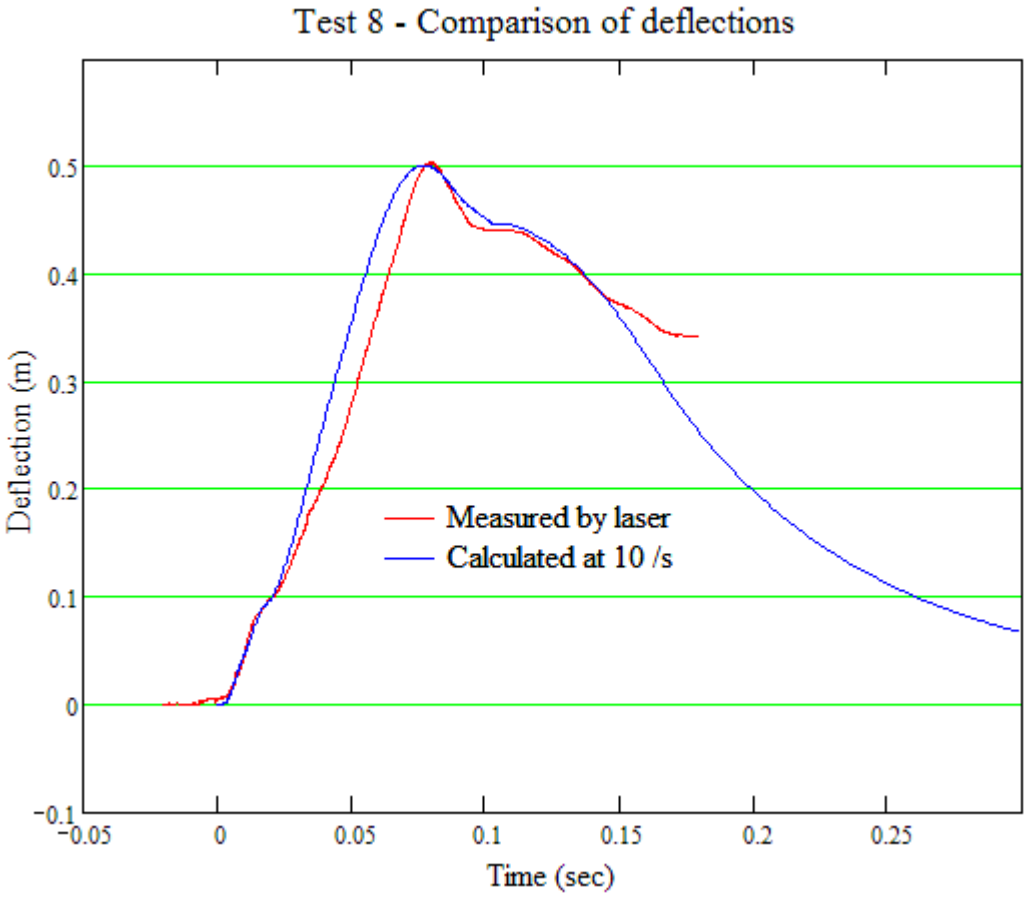

Figure 233. Deflections of Test 5 for material at 28ºC and 20 /s

In all of the shock tube analyses there was a tendency for the model deflection to increase slightly faster than that observed in the tests. A combination of breaking strengths, PVB stiffness and damping that eliminated this tenancy invariably resulted in a maximum deflection that was significantly lower than the observed maximum. In many cases the divergence occurs where the measured deflections experience a

temporary reduction in velocity early in the membrane deflection that is not observed in the analysis.

It may be possible that this temporary velocity reduction is a result of a temporary increase in the resistance of the PVB membrane due to a longer elastic phase and a later transition to a softer plastic phase, but this is not felt to be likely as the HOSDB results do not duplicate this. A more probable alternative is that there is a difference in the shape of the pressure history that acts on the glazing at the centre from the pressure history measured at the perimeter. A small trough and peak superimposed on the measured pressure history during the decay of the shock wave would explain this systematic discrepancy. Figs. 224 and 225 show that the measured curves are not smooth and this would not affect the overall impulse.

As has already been noted in reviewing the individual curves, there does appear to be a fluctuation in the measured pressure histories between 60 to 100 ms that does not appear to influence the response of the test units.

With the probable exception of Test 3, the strain rate ratios in Table 77 appear to be consistent with those for Shots 2 & 4 in Table 73. This would imply that these Shots were tested at around 20ºC and the other HOSDB shots were tested at higher temperatures. However, the reliability of the strain rate ratios in Table 77 is not high, so this implication is probably not warranted.

The tests at BakerRisk have shown the sensitivity of deflection history measurements to pressure measurements that do not closely match the pressure history on the glazing. Measurement from the surroundings of a flexible target may take partial account of the reduced reflection on the loaded face due to aeroelatic damping, but this introduces further uncertainty. Measurement immediately in front of the target would take full account, while measurement on a stiff measurement target, as for the HOSDB tests, takes no account, but gives confidence as to what should be included in the response calculations. The use of a variable proportion of the active aeroelastic damping, as in these models, provides extra variability that can induce a large element of uncertainty into the derivation of the strain rate ratio.

Tests of double glazed units and of laminated glazing with thick glass also makes identifying PVB stiffness and the corresponding strain rate more difficult, when a 5 MPa difference in breaking stress of the glass can have as much effect as doubling the PVB strain rate, and the breaking strengths are known to be highly variable.

For most of the tests analysed, a strain rate of 10 /s was used because it was the most suitable of the available data. This suggests that strain rate ratios of 5 to 7 represent a reasonable upper bound, and are consistent with the data from the HOSDB tests in Table 73, which showed an upper bound of 5.6.

However, fits as good or better than these might have been achieved with data for strain rates of 5 /s or 2 /s, if such data had been available. The large span, heavy glazing tested at San Antonio in 2006 was outside the range of experimentation anticipated when the PVB tests were undertaken in 2004. These tests do not give any reliable guidance to the lower bound that should be considered for the strain rate ratio.

9.7 Design properties of cracked laminated glass membranes

The maximum deflections in a number of tests equalled or exceeded 30% of the span without damage to the PVB interlayer, even with a softer interlayer at temperatures significantly above room temperature. This is significantly greater than the 16% deflection limit (200mm in 1250mm) assumed in HOSDB models [81] and adopted in other PVB material models [97, 100]. Tested deflections exceed some of those measured from quasi-static tests [93, 94] although they are still less than the 45% of span mean value of the static tests.

The largest deflections from successful tests define a possible lower bound for failure deflections. On the basis of data currently available, the use of a 90% confidence deflection limit of 27.8% of span from a statistical analysis of the quasi-static tests appears to be a reasonably conservative dynamic deflection limit for PVB.

The analyses show that the deflection histories of the laminated glass panes tested can be modelled with fair accuracy by using a resistance function after cracking derived from a PVB membrane, using a uniform bi-linear material model based on high strain rate test results of cured PVB.

For greatest accuracy, the PVB properties used should be based on a test strain rate modified from the average strain rate in the laminated glass membrane response by an adjustment factor, to allow for the various systematic distortions arising from the various simplifications and approximations in the analysis, and for the stiffening effect of the glass fragments that remain attached to the PVB.

Currently, the evidence for any particular adjustment factor is slight. There is a wide range of values from the HOSDB tests, from 0.6 to 5.6, possibly due to variations in the temperature at the time of testing. The data from the BakerRisk tests are clustered at the upper end, between 5.0 and 7.1. However, the reliability of these values is questionable because of the uncertainty caused by the variability of other parameters that substantially affect these analyses, and the lack of lower strain rate data that could have been more suitable. The most that can be said is that 7.1 appears to be a reasonable upper bound for the strain rate ratio to be applied to the average strain rate of a response to derive the PVB stiffness to be used, but that the most appropriate rate may be smaller, and that, on current data, the lower bound might have to be considered as 0.6.

The mean of the strain rate ratio values from the HOSDB and BakerRisk tests is 3.8. On the current information, this is the most appropriate ratio to use design. However, the use of this value should be considered provisional, until the results of a greater range of trials can be evaluated.

At deflections up to 25% of the span, the resistance during rebound at room temperature was consistent with an idealised elastic membrane with the stiffness reduced for the cubic curve to pass through the point of the maximum deflection and the corresponding loading resistance. At higher deflections, the rebound was faster than the viscoelastic material, leaving the membrane slack on rebound at a

significantly large deflection, which allowed a greater period of supercritical damping on rebound due to the aeroelastic damping used in all the SDOF analyses.

If design is undertaken using a maximum acceptable deflection up to about 30% of span, the use of an idealised elastic membrane for rebound will only marginally overstate the stiffness. The effect of this will be to model the rebound marginally early, and to marginally exaggerate the outwards velocity on rebound. This is considered an acceptable approximation in exchange for a simple and a consistent rule for the rebound stiffness, when the alternative calculations are likely to be equally uncertain.

9.8 Summary of cracked laminated glass membranes

Membrane theory [95] indicates that the resistance of an elastic membrane is proportional to the cube of the deflection. The closed form equation in the WINGARD manual [100] is consistent with the Timoshenko [38] solution for a square steel plate, but allows adjustment for Poisson's ratio and aspect ratio.

Finite element analysis of elastic membranes shows that analyses are consistent with this for deflections up to about 3% of the span, but deviate from the theoretical curve at larger deflections.

Membrane analyses using semi-loof thin shell elements show a stress and strain distribution that was increasingly inconsistent with the shape of the deformed panel as the aspect ratio increased, and a resistance that diverged from the analytical, being significantly stiffer for a square panel, and becoming much softer with increasing aspect ratio.

Membrane analyses using 3D solid elements showed a deviation from the analytical curve that initially became slightly stiffer after a deflection of about 3% of span, and later became slightly softer, so that it converged with the analytical curve, and then crossed it. For a square panel it crossed at a deflection of about 25% of span, increasing to about 45% of span for an aspect ratio of 4.0 for the recommended Co-rotational geometric non-linear formulation. However, Lagrangian and Eulerian non-linear formulations show similar trends, with only marginal differences in stiffness, and the trends up to 15% of span are consistent with FE results given in the WINGARD manual [100].

A choice was possible to use either conservative or follower forces in the analyses, although the dynamic response is expected to lie between. The decision to use an analysis with conservative loading will be most accurate for short duration loading and large panes, but will be less so for long duration loading and small panes. However, the slower response of the membrane compared to the uncracked glass plates suggests that this is more appropriate.

A non-dimensional deflection expressed as a proportion of the span was found to present the resistance of the membranes in a form that was insensitive to the membrane thickness. This is different from the non-dimensional deflection of the glass plates, that was expressed as a multiplier of the plate thickness.

Bilinear PVB material properties were defined for three temperatures at which instrumented blast tests were reported to have been undertaken, and membrane finite element analyses with the aspect ratios of the tested panels were undertaken for a range of material strain rates, using the Co-rotational non-linear formulation used to define the material properties in Chapter 8.

Membrane resistance curves, SDOF transformation factors and other coefficients were calculated from the deflections and reactions output from these finite element analyses to allow back-analysis of the trials by SDOF analysis.

To use the PVB bilinear material properties for design, it will be necessary to carry out this exercise for a wider range of aspect ratios at temperatures considered suitable for the design cases.

Blast and deflection data provided by HOSDB from five arena blast trials of 7.5mm thick laminated glass panes in June 2006 was used to provide a loading pressure history for an analysis of each test and measured deflection histories from laser measurement and high speed video for comparison.

Temperature data was not given for each blast trial, but the temperature was reported to have been around 20ºC for all the tests. Using bilinear PVB membrane stiffnesses for PVB at 20ºC and various strain rates, PVB strain rates were identified to give the best fit of the analysis to the deflection.

These PVB strain rates were then compared to the average strain rates in the laminated glass membranes of the tests, to try and identify a strain rate ratio that would account for:

- The strain rate not being uniform
- The strain distribution in the membrane not being uniform
- The membrane deflected shape and strains being based on conservative loadings
- The stiffening of the PVB by the glass fragments that remain attached after cracking.

The strain rate ratios calculated from the five tests varied between 0.6 and 5.6, but it was felt that some of this scatter was caused by differences between the actual and assumed temperature at the time of test.

Comparable 2DOF analyses were undertaken of six shock tube trials of large double glazing units conducted for Permasteelisa by BakerRisk at San Antonio. Although the temperatures were measured and recorded before each test, there is some uncertainty as to how accurately the recorded pressure histories represent the detail of the pressure history acting on the test units, including how much aeroelastic damping is already incorporated in the pressure measurements. Variable amounts of damping were used in the analyses, which added uncertainty to the estimation of PVB stiffness and strain rates.

In these tests of large panes of thick, high-strength laminated glass the cracking strength of the glass had a major influence on the deflection history, and the cracking strength of the monolithic outer leaf also had an influence. The cracking strengths are very variable, particularly in new glass, and the cracking strength of each pane had to be estimated separately from the deflection record. The variability of the glass strength and the approximate nature of the estimation of the strength added uncertainty to the estimation of PVB stiffness and strain rates.

The large, heavy windows resulted in long response times and average strain rates as low as 1.5 /s in the dynamic membranes. The PVB data only started at strain rates of 10 /s. Although reasonable deflection history fits were achieved with this data, giving

strain rate ratios between 5.0 and 7.1 for five of the tests, it is uncertain whether better fits with more consistent values for other variables could have been obtained with stiffnesses corresponding to lower PVB strain rates, which would have resulted in lower strain rate ratio values. Given the uncertainty of the strain rate values, these results can be considered to firm up the upper bound of the possible range of strain rate ratios, but cannot be taken as restricting the lower bound.

The mean of the strain rate ratios measured from both sets of tests was 3.8. Lacking more extensive and reliable data a ratio around 4 can be considered suitable for design, but this value should be considered as provisional, pending more extensive data.

A simplified cubic elastic membrane resistance curve was used for the unloading resistance of the membranes in all eleven analyses, shifted to allow a zone of deflection below which the membrane would go slack on rebound. In the analyses, the best fits for the rebound for maximum deflections up to about 25% of span generally occurred with small slack zones. For larger maximum deflections the slack zones were generally greater. However, it was concluded that, for limiting design deflections up to about 30% of span, a cubic curve through the point of maximum deflection on the PVB resistance curve and the origin, i.e. assuming no slack zone, would be a suitable approximate resistance model for unloading of a laminated glass membrane.

10 Application of laminated glass properties to design

10.1 Design objectives

The objectives for an analysis to be used in design are not the same as for the analyses of trials, when the objective was to model the response as closely as possible to the observed response, and to use this to identify material or model parameters.

Instead, the objective in an analysis for design is to use the known material and model parameters and knowledge of the behaviour of laminated glass, singly or as part of a double glazing unit, to estimate responses and forces for a chosen geometry and loading history, and identify whether these will fall within acceptance values that are sufficiently conservative as to reduce the risk of failure of the laminated glazing to an acceptable level.

For a design method to be practical, the analysis must be sufficiently straightforward to allow the design to be modified and the analysis iterated to identify a successful design. The single degree of freedom analysis of laminated glass will be suitable as a design method if the choice of temperature and strain rate can be resolved without the need for analysis at multiple temperatures and iteration of the strain rate to identify a design stiffness of the cracked laminated glass.

All the current methods of analysing laminated glass use a fixed design stiffness of cracked laminated glass, and temperature is not considered. In practice, the temperature of the PVB interlayer in laminated glass in the inner leaf of a double-glazed, blast-resistant window or façade will normally be fairly close to a normal room temperature of 23ºC, because of the insulation value of the cavity and the outer leaf, and the temperature control of the room behind the window. If the room is allowed to vary significantly from normal room temperatures it will be because the room is not occupied, in which case there will not normally be a requirement for blast protection.

With a few exceptions, such as when low emissivity films have been retrofitted to the inside face, there should only be a moderate variation of PVB temperature around this value as the external temperatures fluctuate. The temperature range to be considered for blast design should be a small proportion of the temperature range that must be considered for thermal movement of the outer leaf. However, suitable values are likely to vary with the climate; suitable limits in the United Kingdom may not be appropriate for the Middle East.

One method to resolve this would be to undertake design analysis at 23ºC, as the normal temperature to calculate deflections and reactions, but to chose a conservative deflection limit that would allow for the reduction in stiffness at an upper bound temperature for blast, and to apply a factor of safety on the reactions for design of attachments and fixings, that would allow for an increased stiffness at a lower bound temperature for blast. The deflection limit and factor of safety may be modified for different climates.

The appropriate temperature variations to consider for a reasonable level of risk have not been addressed in this thesis, and would require either a consensus judgement of specifiers and practitioners, or some very different research than that presented here.

In theory, strain rates for PVB material properties could be selected for design by iteration of the average analysis strain rate multiplied by a strain rate ratio between the PVB sample strain rate and the laminated glass strain rate until a consistent relationship is achieved. The mean strain rate ratio from ten tests in Chapter 9 is around 3.8, although various systematic errors in the tests or the test data contributed to the wide range in value between 0.6 and 7.1. This is an area where further trials would be beneficial in refining the strain rate ratio, but a provisional value of about 4.0 would be reasonable.

The laminated glass strain rate depends on the span of the glazing, the mass of glass and the thickness of the PVB, together with the load history and the stiffness of the PVB. An accurate strain rate would need to be calculate iteratively for each analysis, but the quality of the data currently available would make this an unnecessary refinement. Instead, the strain rate for panes with spans up to1.5m, interlayers 1.52mm thick, thickness up to 10 mm and blast loading to cause deflections of the order 25% of span could be analyses by assuming a laminated glass strain rate of the order 10 /s.

Combining these two, a provisional design PVB stiffness for such panes can reasonably be based on the material properties that correspond to test data for a PVB strain rate of 40 /s.

10.2 Resistance

As anticipated in Chapter 1, the resistance of laminated glass can be taken to comprise the combined resistances at various stages of damage to the laminated glass.

The non-linear resistance curve for monolithic glass was first presented by Moore [67], but was refined in Chapter 6. This can be used to define the resistance curve of the last ply to crack in a laminated glass pane.

The resistance curve of uncracked laminated glass was developed in Chapter 7. A formula for an equivalent monolithic pane was developed that will allow the data developed in Chapter 6 to be applied to uncracked laminated glass and partially cracked laminated glass with more than two glass plies.

The remaining uncertainty for a design based on the response at 23ºC is whether the laminated pane should be treated as fully composite. At 20ºC this would appear to be appropriate, while at 29ºC some reduction from the fully composite stiffness is required. There is currently no evidence between these temperatures. Currently, a fully composite stiffness will be used, but this may be modified if a reduction appears justified by further test results.

As shown in Chapter 4, the actual cracking strength of glass is variable, and there are a range of values that have been used as design strengths. In addition to the random variability of glass due to the distribution and size of Griffith flaws and the effects of aging on the flaws, the strength of glass is affected by the loading rate due to the 'static fatigue' effect of stress corrosion by atmospheric moisture at the crack tips. Although this leads to systematic differences in strength between blast loading rates and wind loading rates, this is not sufficiently sensitive to loading rates that any systematic variation in design strength need be considered for different blast loading strain rates.

The design strengths in Table 78 were defined by the Home Office Scientific Development Branch [81] in the UK and have also been used by the US Army Corps of Engineers [97]. They are based on a large body of blast trials of glazing [81, 96], and are also consistent with lower bound characteristic strengths from material tests of both new and weathered glass [40] and specified strengths of new glass [106-109], allowing for the difference in the blast and test loading rates.

The breaking strengths that gave the best fit in the back-analyses in Chapter 9 were all greater than the values in Table 78 for the corresponding glass type, which suggests that these design values are representative of the lower bound of real breaking strengths, and take account of the surface prestress in strengthened glass.

Glass Type	Design Cracking Strength	Typical surface pre-stress
	MPa	MPa
Annealed float glass	80	0
Heat strengthened glass	120	40
Toughened glass	180	100

Table 78. Design cracking strengths of glass

These breaking strengths can be used with the data from Chapter 6 to define a cracking deflection for monolithic panes equivalent to the uncracked or partially cracked multi-ply laminated glass. Studies described in Chapter 7 indicated that the stress in the laminated glass was lower than that in the equivalent monolithic pane, but that the degree of conservatism varied. Using the stress in the equivalent monolithic pane with the design strengths in Table 78 will result in a lower cracking deflection than would be obtained from a finite element analysis of the laminated glass, although this deflection will still be higher than for a monolithic glass pane of the same thickness as the laminated pane. The laminated glass resistance will be more conservative for deflection than a monolithic pane. The exception to this is the last glass ply to crack, which will be a monolithic plate in its own right, for which the data in Chapter 6 will apply directly.

Because of the different non-linear resistance curves, the deflection at first crack of the rear ply of slender panes with low aspect ratios and high cracking strengths tends to be greater than the deflections required to reach the subsequent cracking strengths. The other ply or plies would crack immediately the first crack occurred.

For less slender panes of weaker glass with high aspect ratios the second (or, when appropriate, sometimes even the third) crack may occur at higher deflections than the first crack, and the resistance curve of the glass will be stepped, as shown in Fig. 234 for 11.5mm laminated glass compared to 7.5mm laminated glass.

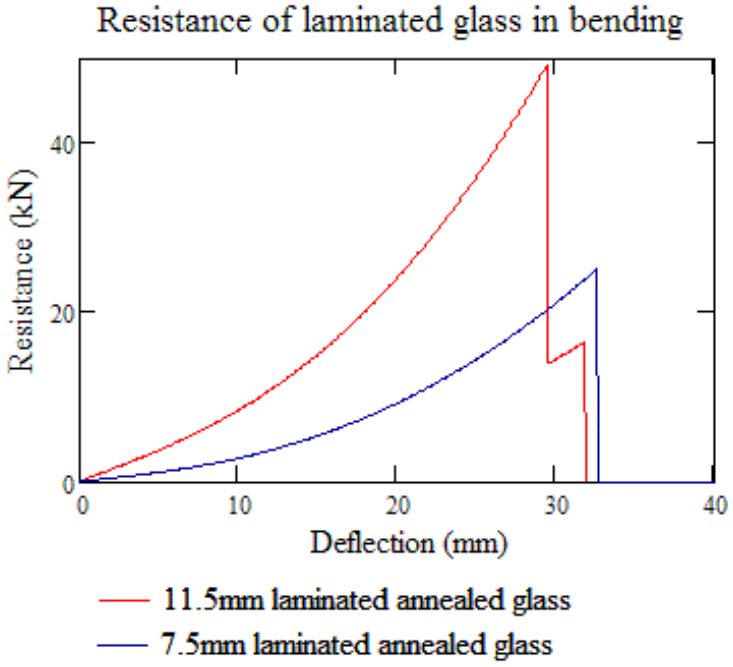

Figure 234. Typical glass flexural resistance of laminated glass panes

The resistance due to ‘elastic’ and ‘plastic’ stretching of the PVB membrane at various temperatures and strain rates has been developed in Chapters 8 and 9. The sensitivity to temperature and strain rate arises from the viscoelastic nature of PVB, but the sudden reduction in stiffness is non-linear viscoelasticity rather than true plasticity, as all of the elongation of the PVB is eventually recovered.

If, for design purpose, the design resistance of cracked laminated glass is based on the bare PVB material properties for a strain rate of 40 /s at a temperature of 23ºC, as proposed in Section 10.1, then the design resistance for initial deflection can be based on a bilinear material as defined in Table 79. The stress-strain curve for this material is shown in Fig. 235.

Property	Value
	MPa
Elastic modulus	214.2
Transition ‘yield’ stress	7.90
Hardening modulus	8.31

Table 79. Design values of PVB bilinear stiffness

The non-linear resistance curves for cracked laminated glass panes of various aspect ratios have been calculated using this bilinear material and are shown in Fig. 236. Resistance curves can be calculated from these for panels with specific spans and membrane thickness. These can be combined with the resistance up to final cracking to give a complete resistance function for laminated glass that will apply up until rupture of the PVB membrane, failure of the support anchorage or maximum deflection and rebound.

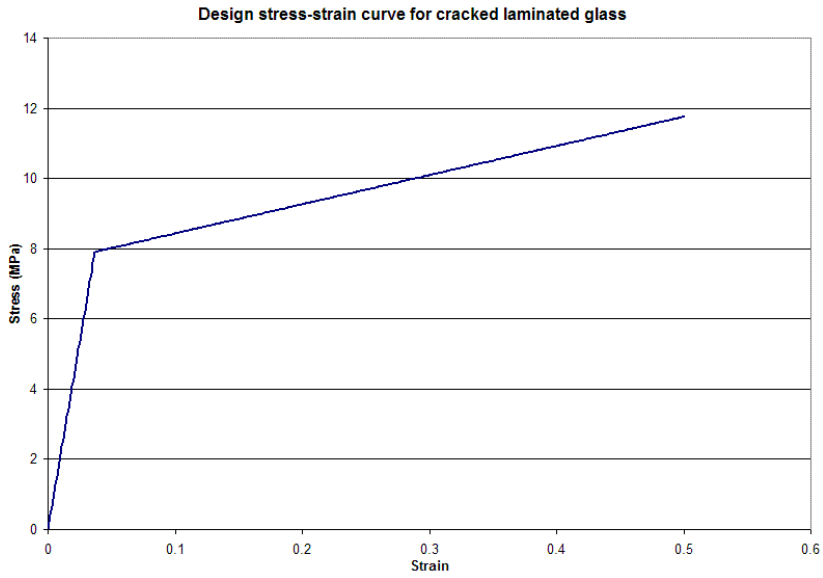

Figure 235. Design PVB bilinear material stiffness

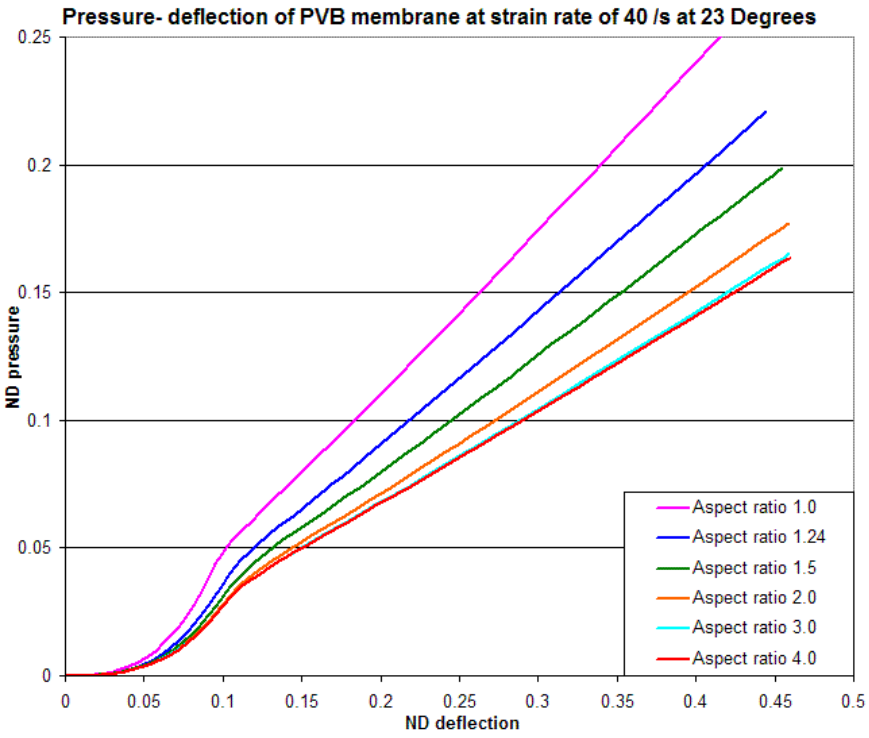

Figure 236. Design ND membrane resistance for cracked laminated glass

If the PVB or the support anchorage does not fail, then the cracked laminated glass will rebound. The viscoelastic nature of PVB indicates that the rebound resistance will not follow the path of the loading resistance. If PVB were an elastic-plastic material then the rebound would have had an elastic stiffness equal to the initial elastic stiffness, and the membrane resistance could have followed a displaced elastic curve down to a deflection at which the resistance would have become zero and the membrane would have become slack.

Back-analysis of the rebound from blast trials in Chapter 9 indicates that, for deflections up to about 30% of span at temperatures above 20ºC, the PVB will recover sufficiently quickly to maintain some resistance to sufficiently low deflections that it can reasonably be approximated by a cubic curve passing through the origin, representing an elastic membrane of a uniform (but reduced) material stiffness.

This approximation will tend to give an upper bound restoring force history on rebound, leading to a faster and larger rebound, with the least loss of rebound velocity to aeroelastic damping, compared to other rebound models that assume that the membrane becomes slack. However, it appears to give a rebound generally consistent with observed rebound response, and represents a straightforward rebound model that is suitable for incorporation in an analysis for design.

Typical rebound resistances are shown in Fig. 237. Because these are based on a simple cubic equation, the rebound resistance need not be pre-calculated, but can be calculated in the SDOF analysis when the maximum deflection has been found numerically.

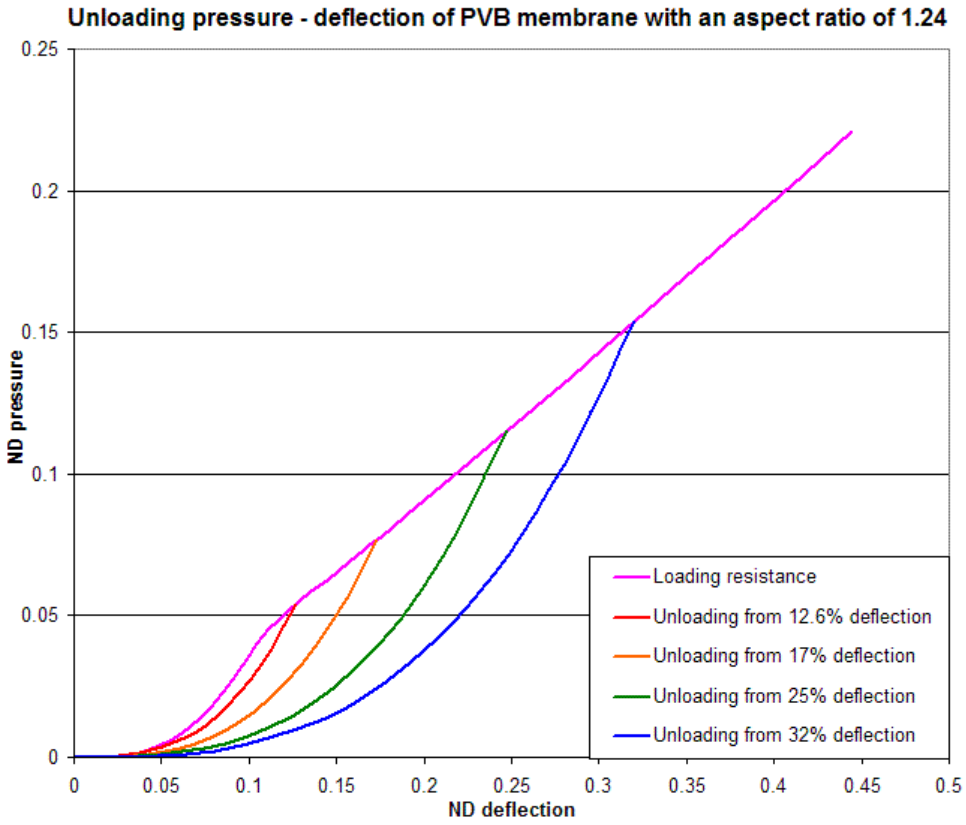

Figure 237. Typical design unloading resistances on rebound for a pane with an aspect ratio of 1.24

The most accurate resistance curve to use on re-loading once the rebounding laminated glass passes through its original position and deflects outwards is not known, but is expected to lie between the original and the unloading resistance curves. Use of the unloading curve will tend to give an upper bound outwards deflection, and may exaggerate the chance of failure on rebound.

In general, failure on rebound will not be critical for protection of building occupants from blast or glass fragments. However, for some applications, where it could lead to critical weaknesses in security or exposure of critical equipment to the weather it may be undesirable, so a design method that is conservative in predicting such failure may be desirable. Use of the rebound stiffness for outwards deflection of cracked laminated glass appears to be the most suitable model.

10.3 SDOF parameters

The transformation factors for SDOF analysis of laminated glass and the dynamic and distribution reaction coefficients can be calculated from the same finite element analyses that have been used to derive the resistance. Because the analyses are all non-linear and the deflected shapes and reaction distribution change with deflections, the factors and coefficients vary continuously with deflection, as well as showing abrupt steps when cracking causes abrupt changes.

For uncracked or partially cracked laminated glass, the equivalent monolithic panels from Chapter 7 have the same mix of membrane and bending in the resistance as the laminated glass, and so will have the same deflected shape. As a result, the transformation factors and coefficients in Chapter 6 can be calculated for the equivalent monolithic panes and applied to the laminated glass.

For design of cracked laminated glass, the transformation factors and reaction coefficients can be calculated from the analyses for the resistance curves in Fig. 236, using the methods described in Chapter 9. Typical transformation factors are shown in Fig. 238.

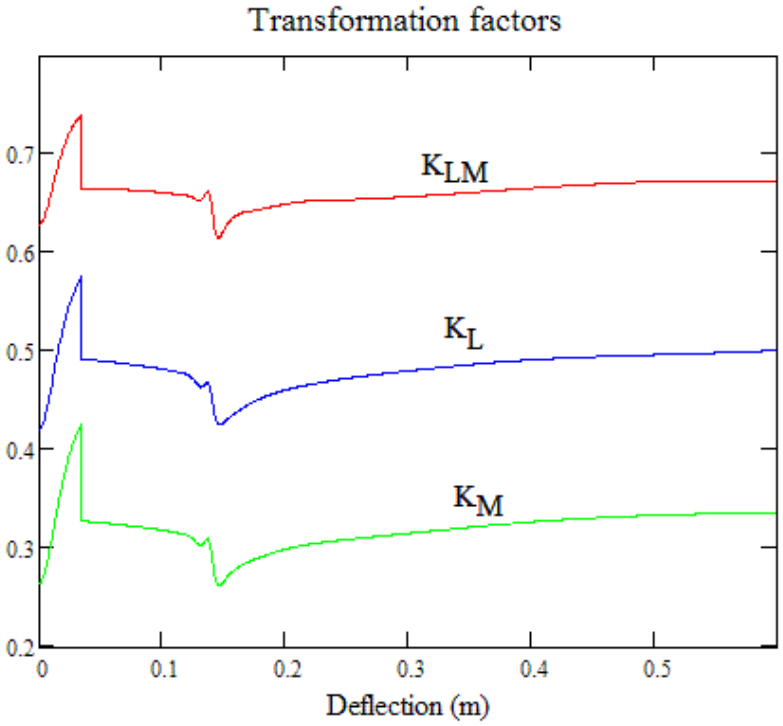

Figure 238. Design transformation factors for the HOSDB ‘large’ pane with an aspect ratio of 1.24

The transformation factors for uncracked laminated glass show a significant continuous change from the small deflection values with increasing deflection, and do vary significantly with aspect ratio. The transformation factors for cracked laminated glass are lower than the cracking values, so there is an abrupt drop on cracking. After cracking, the transformation factors vary only marginally except for a localised drop

and recovery as the quasi-plastic transition occurs first in the sides of the membrane and then in the centre.

The transformation factors are applied in the equation for acceleration and are double integrated over time to give the displacement. This smoothes out the effects of sharp changes and peak values, but the average values do affect the deflected shape and the maximum deflection. As the peak deflections vary with different blast loading, aspect ratio, span and glass and membrane thickness, the average transformation factors also vary. Although smoothed approximations could be substituted, they would introduce variable amounts of error into different analyses.

Transverse dynamic reaction coefficients are similarly a combination of those calculated for the equivalent monolithic panes for the uncracked and partially cracked panes using the data in Chapter 6 and those calculated for the PVB membrane as in Chapter 9. Typical transverse reaction coefficients are shown in Fig. 239.

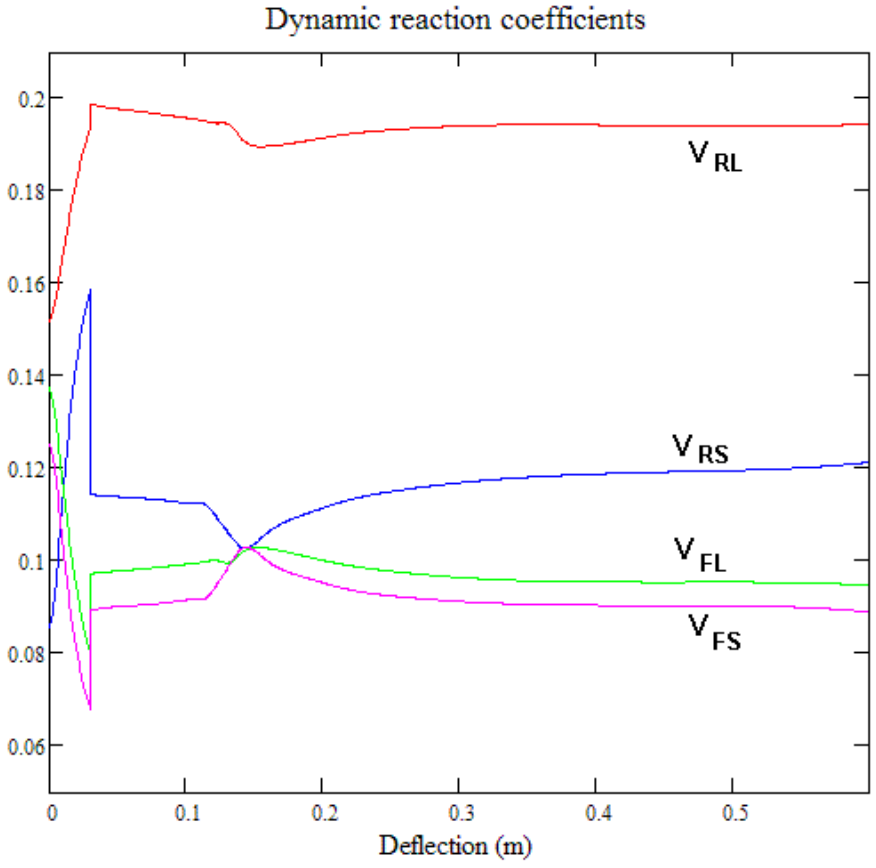

Figure 239. Design reaction coefficients for the HOSDB ‘large’ pane with an aspect ratio of 1.24

The reaction coefficients reflect the interplay of the loading and the resistance in the reactions as the centroids of inertia and reaction vary around the centroid of loading with the variations in the deflected shape and the distribution of internal forces. These variations occur rapidly in the uncracked glass and more gradually in the PVB membrane, with an abrupt transition on cracking.

Unlike the transformation factors, the reaction coefficients are applied directly to the calculation of reactions, and the variations directly affect the reaction history and the loading on fixings and supporting members.

In addition to transverse reactions, the membrane will generate in-plane reactions due to the membrane tension. These can be expressed in non-dimensional terms as:

$$S_{ND} = \frac{S}{E \cdot h \cdot b} \tag{64}$$

where S is the total in-plane tension at the long or short edge, E is the Young's modulus of PVB, h is the PVB membrane thickness and b is the span of the membrane. Typical design values for a membrane with a 1.24 aspect ratio, suitable for the HOSDB 'large' panel are shown in Fig. 240.

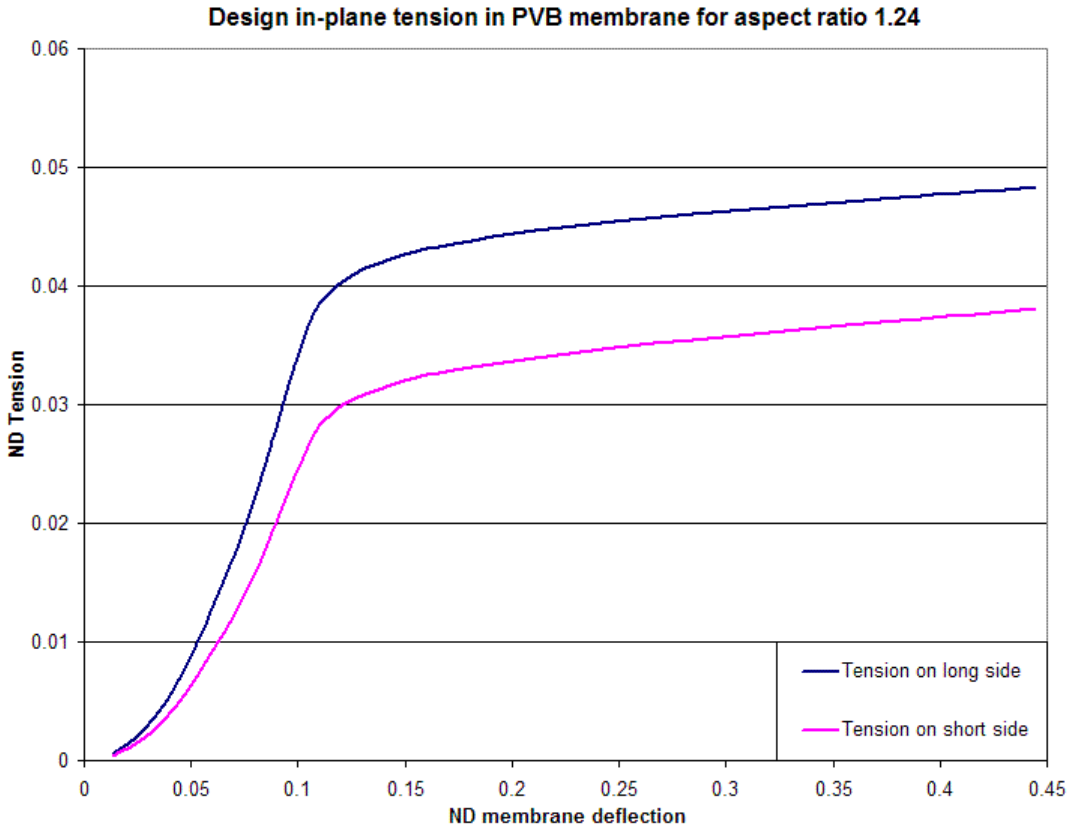

Figure 240. Design in-plane tension coefficients for the HOSDB 'large' pane with an aspect ratio of 1.24

After the transition stress is reached in the membrane, the change in in-plane force is a balance between strain hardening in the PVB material, increasing stresses in the diminishing elastic zones near the corners, and the geometric effects of increasing deflection that reduce the proportion of the tension acting in-plane. For the design material properties and an aspect ratio of 1.24 the total in-plane forces continue to increase with deflection. However, the peak in-plane forces may increase less, or even reduce.

The peak tensions and reactions for the laminated glass can be assessed by calculating the ratio of the peak to average value from the finite element analyses. The tension and reaction factors for the membrane stage with an aspect ratio of 1.24 are shown in Fig. 241. Before cracking occurs the reaction coefficients for the glass will apply, and the in-plane forces acting on the supports can be considered negligible.

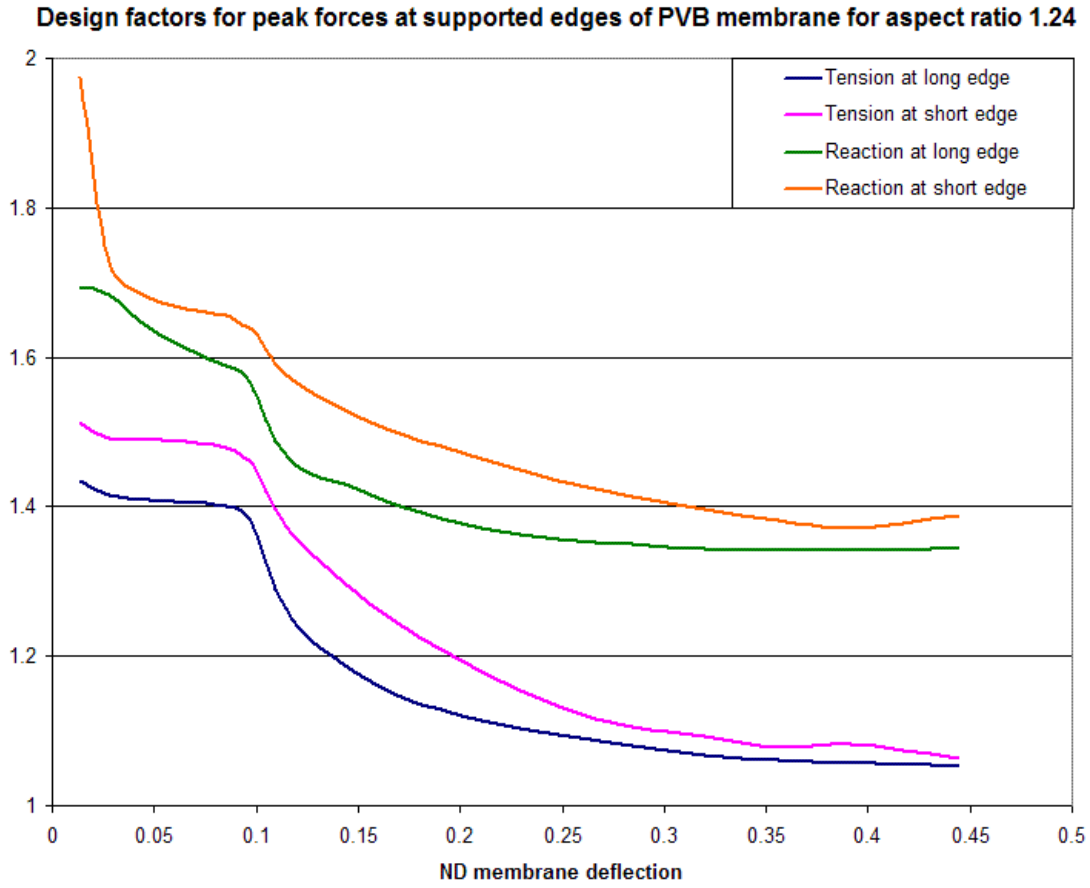

Figure 241. Design in-plane peak factors for the HOSDB ‘large’ pane after cracking with an aspect ratio of 1.24

The sharp reduction in the peak in-plane tension factors may result in the peak in-plane force reaching a maximum or a plateau value at a deflection substantially below the rebound or failure deflection.

10.4 The equivalent system SDOF equation of motion

As described in Chapter 3, the equation of motion of a real distributed mass system can be represented by an equivalent lumped system whose response to a dynamic load is obtained by solution of the following equation of motion:

$$\frac{d^2z}{dt^2} \cdot M_e + \frac{dz}{dt} C_e + R_e(z) = f_e(t) \tag{65}$$

in which z is displacement, t is time, M_e and C_e are the equivalent lumped mass and damping respectively, $R_e(z)$ is the equivalent lumped resistance function and $f_e(t)$ is the equivalent lumped loading history.

For transformation factors K_L and K_M as defined in Eqns. 11 and 12, the equation for the acceleration $\frac{d^2z}{dt^2}$ becomes:

$$\frac{d^2z}{dt^2} = \frac{K_L(f(t) - R(z)) - K_M \cdot C \cdot \frac{dz}{dt}}{K_M \cdot M} \tag{66}$$

Where M is the total actual mass of the pane, $R(z)$ is the resistance function of the pane, $f(t)$ is the loading history acting on the whole pane and C is the total damping acting on the whole pane. When the analysis defining the resistance is based on large deflection or membrane behaviour, the transformation factors will not be constants, but functions of deflection, so should be formally written as $K_L(z)$ and $K_M(z)$.

The design resistance and transformation factors for a particular rectangular pane have already been defined in Sections 10.2 and 10.3. The mass of the pane can be easily identified from the thicknesses and densities of the glass and PVB layers and the area of the pane. The loading history for a particular blast threat can be defined from the pressure history associated with the blast threat and the area of the pane.

The one parameter not yet defined is the damping. One form of viscous damping that will always be acting on a glass pane in air is aeroelastic damping. Some additional mechanical damping might be associated with energy absorption in the supports, but would be dependent on the support construction and is likely to be small for a firmly-supported pane.

Aeroelastic damping is a form of structure-medium interaction, similar to soil-structure interaction in ground shock, which is also known as radiated damping in seismic foundation analysis. It is a well-established phenomenon in wind vibration analysis [36], but has not been considered in blast analysis prior to the TPS analysis of glazing response [6] because it only has a significant effect on thin members of low mass and stiffness. The effect of aeroelastic damping on reinforced concrete blast walls is negligible.

The damping coefficient per unit area of the structure surface in structure-medium interaction is equal to the impedance of the surrounding medium, i.e. the product of the density and the pressure wave velocity in the material:

$$c = \rho \cdot U \tag{67}$$

where c is the damping coefficient per unit area, ρ is the air density, and U is the pressure wave velocity (sound speed). Air is a compressible material, so that the density and the wave velocity are functions of the pressure.

For the short time period concerned in blast response, the changes in air pressure can be considered as adiabatic. The relationship between pressure and density can be defined as:

$$\overline{P} \cdot \left(\frac{1}{\rho} \right)^{\gamma} = Const. \tag{68}$$

Where $\overline{P}$ is the total pressure, and γ is the adiabatic constant, which can be taken as 1.4 or 7/5 for air modelled as an ideal gas [22]. The same reference defines the pressure wave velocity as:

$$U = \left(\frac{\gamma \cdot \overline{P}}{\rho} \right)^{\frac{1}{2}} \tag{69}$$

On the unloaded face of the glass pane, assuming a large space whose volume will not be changed appreciably by the deflection of the glazing, the pressure can be taken as the atmospheric pressure P_A, for which the standard value at sea level is taken as 101.921 kPa. Air density at standard temperature and pressure ρ_A is taken as 1.225 kg/m^3.

Substituting Eqn. 69 into Eqn. 67, the atmospheric damping per unit area on this face is therefore:

$$c_A = (\gamma \cdot P_A \cdot \rho_A)^{\frac{1}{2}} = \left(1.4 \cdot 101.921 \cdot kPa \cdot 1.225 \cdot {kg}/{m^3} \right)^{\frac{1}{2}} = 418.1 \cdot \frac{{kg}/{s}}{m^2} \tag{70}$$

On the loaded face the pressure is a combination of the atmospheric pressure P_A, and the blast overpressure history $P(t)$. The damping per unit area on this face can be calculated as a damping coefficient history in terms of the blast loading by substituting Eqns. 68 and 69 into Eqn. 67:

$$c_P(t) = \left(1.4 \cdot (P(t) + P_A) \cdot \frac{6 \cdot P(t) + 7 \cdot P_A}{P(t) + 7 \cdot P_A} \cdot \rho_A \right)^{\frac{1}{2}} \tag{71}$$

The total damping coefficient C in Eqn. 66 becomes a function with time, equal to the sum of the damping acting on both faces:

$$C(t) = (c_A + c_p(t)) \cdot a \cdot b \tag{72}$$

where *a* and *b* are the length and breadth of the panel.

Starting from an initial deflection and velocity of zero before the arrival of the blast loading, the deflection history is calculated numerically by integration of the acceleration to give velocity and of velocity to give deflection over successive timesteps as described by Biggs [35]. This can be done by hand calculation or by using a dedicated program. The former is slow and repetitive, while most of the existing programs are written around SDOF analysis of reinforced concrete and cannot cater for non-linearity other than plasticity. However, complete flexibility of analysis is possible using either a spreadsheet or a differential equation solver in Mathcad [89] or other mathematical modelling software.

10.5 Worked examples to define design deflection limit for PVB Failure

In this section, the use of the foregoing concepts and analyses will be demonstrated by means of calculations aimed at producing a safe design of a laminated glass pane to resist blast threats. Two loading cases have been considered, based on a 100 kg TNT equivalent charge and a 500 kg TNT equivalent charge. These are typical of the design charge sizes considered for vehicle borne improvised explosives devices produced by terrorists.

The approach adopted is to determine the design deflection limit for PVB failure of an HOSDB 'large' pane of 7.5mm thick laminated glass, 1.25m wide and 1.55m high, giving an aspect ratio of 1.24. In addition to calculating the deflections for the laminated glass at a design temperature of 23ºC, the effect of an increase in temperature to 29ºC has also been evaluated, to assess the sensitivity of the deflection limit to increased temperature at the time of attack.

In the TPS analysis method [6], the limiting deflection for design was taken as 27.8% of the span, this being the 90% confidence deflection at maximum resistance calculated for seven low strain rate tests with 1.52mm thick PVB interlayers [93, 94], using the Student 't' distribution. This was probably a conservative estimate of this value, as the lower two of the seven deflections were associated with failure of the timber supports rather than of the PVB interlayer.

It was proposed that the majority of PVB failures occurred well below the limiting strain for bare PVB due to cutting of the PVB by the sharp edges of attached glass fragments at locations of high curvature, mostly at the middle of the long edges, but occasionally at the middle of the span. This was not considered to be strain rate sensitive, and so the limiting deflections of low strain rate tests were considered to be significant indicators of the deflection capacity at high strain rates.

A further factor that may make the slow strain rate deflections conservative for the design deflection under blast is the loading type. The water-bag pressure loading for the low strain rate tests will have acted as a follower force, while the blast impulse loading will make the blast response a conservative loading, or intermediate between the two. Follower forces tend to result in a rounder, fuller deflection with a steeper gradient at the edge of the membrane, and a sharper change in direction at the support, so the same support cutting resistance may be associated with larger midspan deflections under blast.

The measured deflections up to 30% and 32.8% of span without PVB failure reported in Chapter 9 indicate that 27.8% of span is indeed a lower bound value of the maximum deflection that can be achieved by laminated glass under blast.

In the TPS analysis, this deflection limit was used with back-analysis of the HOSDB fragility curves for laminated glass [81] to confirm a plastic yield stress of 8 MPa, very similar to that proposed in Table 79 and Fig. 236, but without the strain hardening.

With the design resistance calculated independently from measured PVB properties, the HOSDB 'High Hazard' fragility curve for 7.5mm laminated glass can be used to define worked examples to review the design deflection limit. The 'High Hazard' fragility curve is a lower bound line for failure from a substantial number of blast trials, listed in WinDAS [96]. The formal definition of 'High Hazard' is related to the presence and nature of glazing fragments behind the window [81], but for 7.5mm laminated glass, PVB failure or extensive support failure would be required to cause 'High Hazard' fragments.

The range for a 100 kg TNT equivalent charge was estimated as 31m from the 'High Hazard' fragility curve for 'large' 7.5mm laminated annealed glass panes in Ref. 81, as shown in Fig. 242. Similarly, the range for a 500 kg TNT equivalent charge was estimated as 64m. For laminated glass, this curve is the lower bound of failure for panels with enhanced fixing into the frame, but may cover failures other than failure of the PVB, and so may be more conservative than for PVB failure alone. The charge sizes and ranges on the fragility plot relate to reflected blast from a surface explosion without clearing, but the fragility curves are defined from measured pressure and impulses, and so allow for clearing and charge height in the trials.

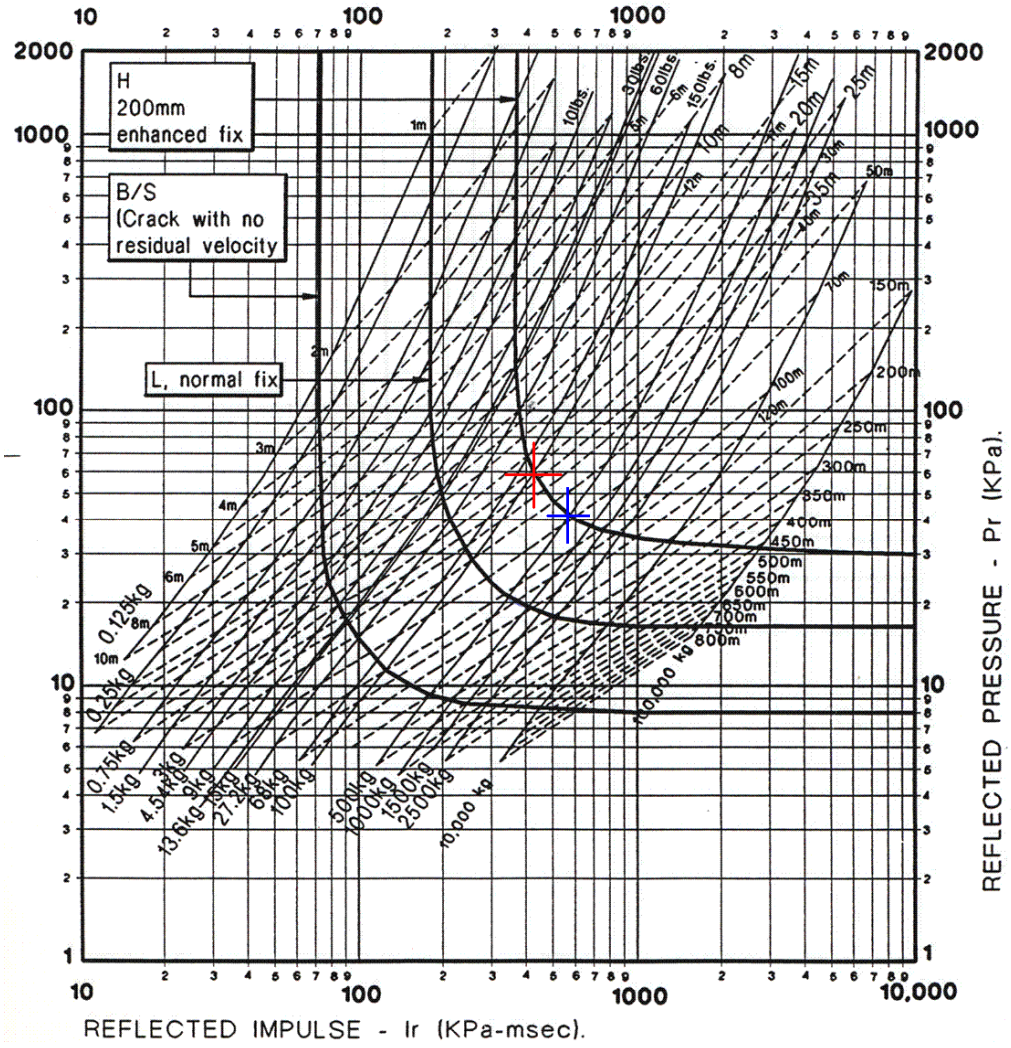

Figure 242. Fragility curves for 'large' 7.5mm laminated glass pane, showing cases used for examples

The positive phase loading for 100 kg TNT at 31m is a peak pressure of 58 kPa and an impulse of 420 kPa.ms [28]. It should be noted that the impulse is marginally lower and the pressure substantially lower than those observed for HOSDB tests 1-3 reported in Chapter 9 and listed in Table 71, so these tests were beyond the 'High Hazard' design curve, while the pressures and impulses for tests 4 and 5 were both about 50% higher without causing PVB failure. The fragility curve appears to be substantially conservative.

The positive phase loading for 500 kg TNT at 65m is a peak pressure of 42 kPa and an impulse of 583 kPa.ms [28].

Idealised pressure histories for these two cases incorporating positive and negative phases were modelled for this case using BlastX [139], consistent with Ref. 28 for positive pressure and impulse to within 3% (with the impulse high), and are shown in Fig. 243.

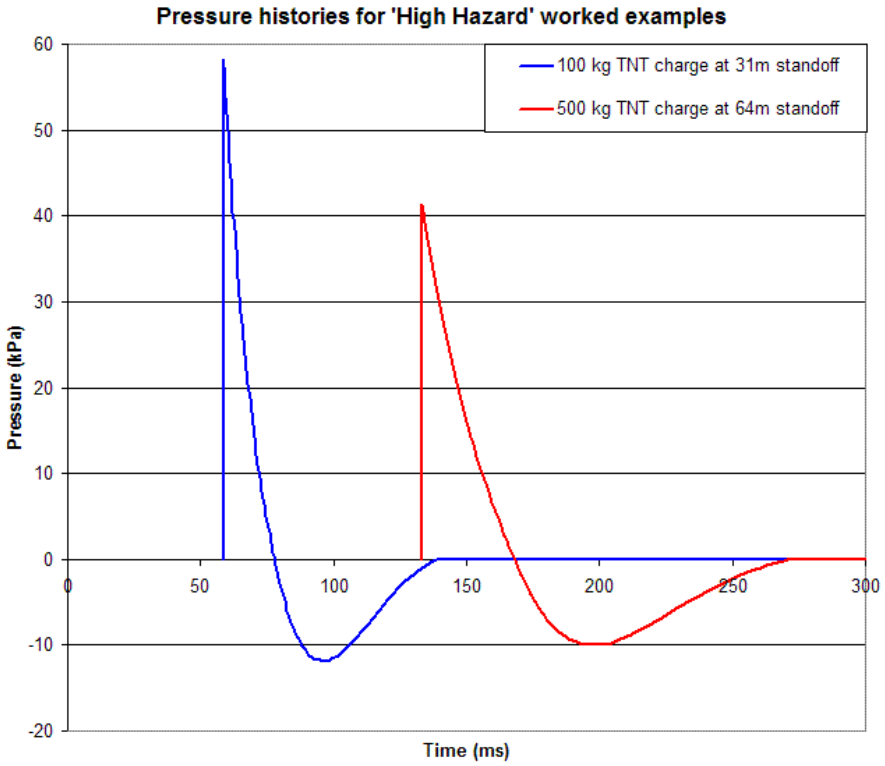

Figure 243. Idealised blast pressure histories for 'High Hazard' worked examples

A design resistance function was developed, using the design glass fracture strength of 80 MPa and the design membrane resistance for a panel with an aspect ratio of 1.24, using the data based on the stiffness in Fig. 235, as shown in Fig. 236. The full resistance curve is shown in Fig. 244. In addition, a resistance curve based on an analysis of the same panel with PVB properties for 29ºC (including 80% composite stiffness before cracking) has been included to assess the sensitivity of the deflections to elevated PVB temperatures.

SDOF analyses were run for the two example load cases in Fig. 243 with the design resistance in Fig. 244. In addition, to assess the sensitivity of the maximum

deflections to increased temperature, similar analyses were run with a resistance based on the membrane properties at 29ºC. The maximum inwards deflections are shown in Table 80.

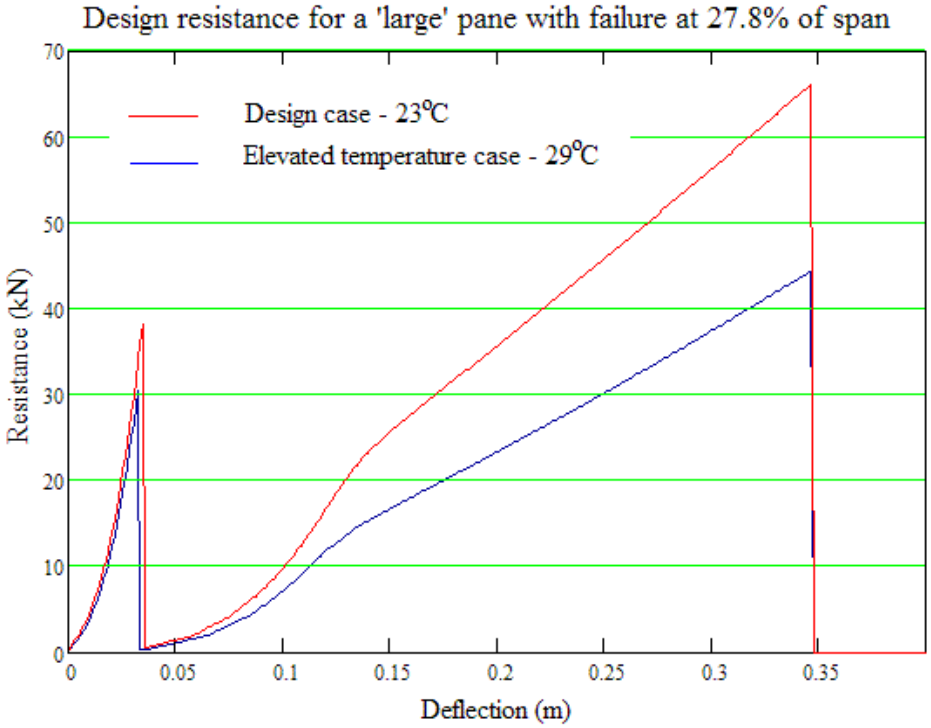

Figure 244. Design resistance curve for High Hazard examples

Load case	Property	Units	Temperature for properties		
			Design 23ºC	29ºC	% Increase
100 kg TNT at 31m	Max deflection	mm	268.3	309.7	15.4
	ND deflection	%	21.5	24.8	
	Rebound deflection	mm	-292.0	-325.4	11.4
	ND rebound	%	-23.4%	-26.0	
500 kg TNT at 64m	Max deflection	mm	309.0	374.3	21.1
	ND deflection	%	24.72	29.94	
	Rebound deflection	mm	-292.1	-364.3	24.7
	ND Rebound	%	-23.37	-29.14	

Table 80. Peak deflections for examples for design case and 29ºC

The examples show that a margin of 16-21% will need to be left in a chosen design deflection limit to allow for a temperature increase of up to 6ºC in the PVB interlayer, or alternatively that a lower confidence level will need to be accepted over the proportion of the time that the temperature in the PVB may be at a significantly elevated temperature. For example, a design limit of 23% of span could be used for the design case so that there is a 19% margin for temperature effects below 27.8% of span. Alternatively a limit of 27.8% of span could be used for design, allowing deflections up to 33% of span with a 21% margin for temperature.

There is no single correct answer to this question. A consensus will need to be developed as to where the limits to the confidence levels and acceptable risks lie. Further research on failure deflections of PVB membranes could significantly reduce the uncertainty, and might allow higher design limits, while still maintaining 90% confidence of survival at 29ºC.

There is a 15% difference between the inward deflections for the two different loading cases in the design case, and this increases with temperature. It is possible that this may reflect alternative failure mechanisms than PVB rupture with the 100 kg charge, such as failure of some support anchorages (e.g. solid gaskets in deep bites). The difference in the rebound deflections is much less, with the 100 kg charge causing a greater rebound than the initial deflection, while the rebound from the 500 kg charge is less than the inwards deflection. It is possible that partial PVB rupture on rebound under test for smaller charges may have influenced the fragility curve if the timing of the PVB failure could not be identified, although failure on rebound should not have increased the hazard.

The successive resistance curves used in the 100 kg case at 29ºC are shown in Fig. 245 with the sequence of the successive vibrations, and the deflection history for the same case is shown in Fig. 246.

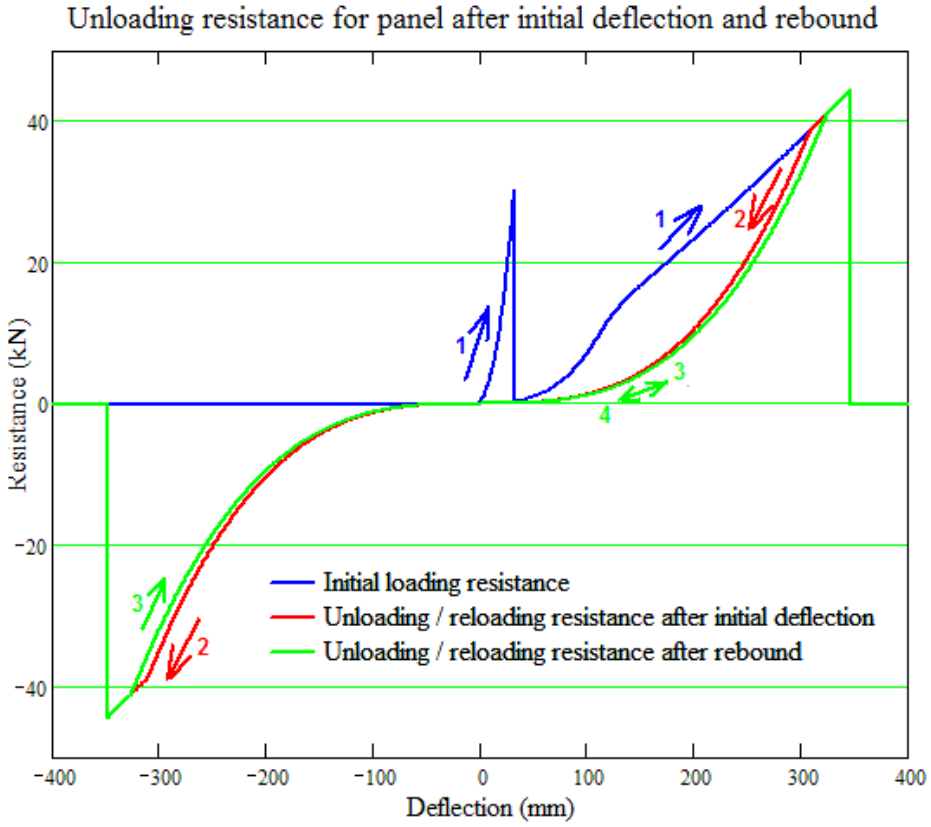

Figure 245. Resistance curves assumed on unloading and re-loading on reversal for 100 kg charge case at 29ºC

The initial stiffness from the uncracked glass is fairly high and the velocity is still rising during the low stiffness period immediately after the glass cracks, so the

aeroelastic damping has only a moderate damping effect on the initial maximum deflection.

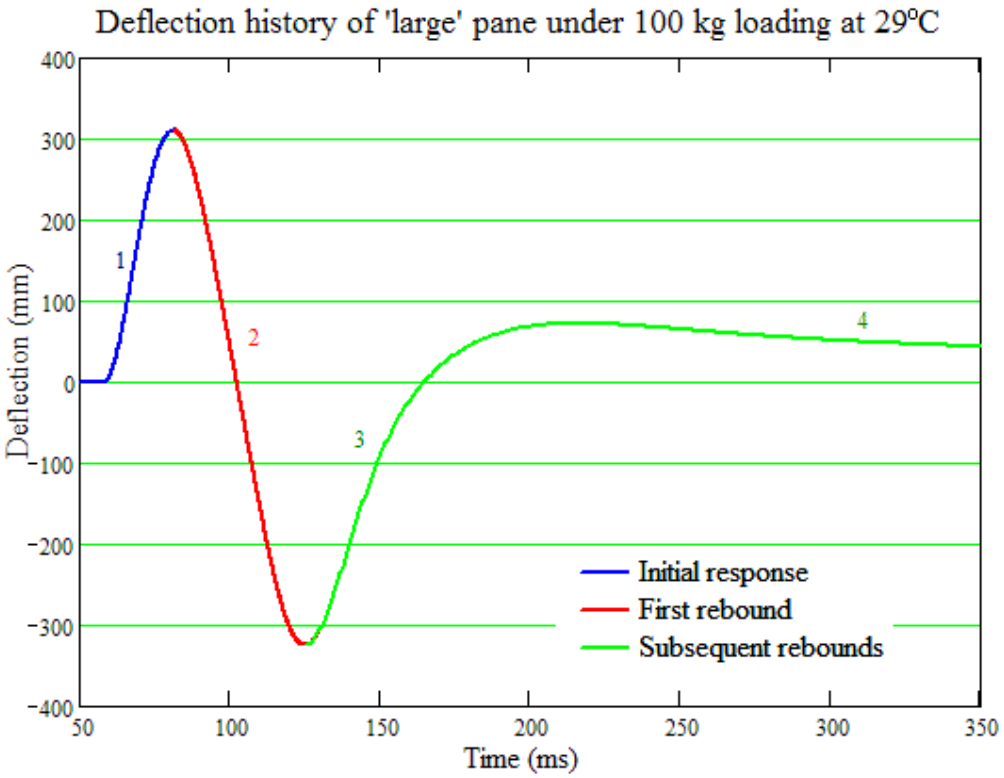

Figure 246. Deflection history for 'large' panel for 100 kg charge case at 29ºC

On rebound, the stiffness is low when membrane deflection is small, and the aeroelastic damping will briefly be supercritical as the membrane passes through zero deflection. However, at this time the negative phase loading in combination with the elastic rebound builds a rebound velocity as great as the peak inwards velocity, so the supercritical damping has little time to act.

On second rebound the resistance is softer so the supercritical damped zone is larger, and the little remaining negative phase loading opposes the elastic rebound, so the subsequent deflection is not critical, and the subsequent motion is all supercritically damped.

For the 500 kg charge case, the negative phase loading lasts longer and significantly slows the second rebound, so that the damping overcomes the velocity and the second rebound never crosses the initial position of the glazing.

The damped rebounds with only two or three peaks are representative of the motions of laminated glass tests observed on high speed video.

The foregoing has demonstrated that the definition of a design deflection limit can be achieved by the techniques presented here. Uncertainties remain about what is acceptable, but the principles used here can form the basis of a sound approach to safe design.

10.6 Worked examples to define the margin of safety for reactions

In this section, the design examples at 23ºC in Section 10.5 have been analysed for the design reactions and tensions, based on the same SDOF model, resistance and SDOF transformation factors, but applying the other parameters derived from the same finite element analyses, to calculate the maximum transverse reactions and in-plane tensions for the design cases. These are critical to the design of the anchorage and support of the laminated glass. In addition to PVB failure, failure of the anchorage is the other main form of failure of laminated glazing that could cause a 'High Hazard' outcome.

In addition, analyses based on PVB properties at 17ºC have been undertaken to evaluate the sensitivity of the reactions and tensions to reduced temperature, as the reactions and tension of the PVB membrane will be increased by a reduction in temperature from the design value of 23ºC.

Total reactions to inwards peak deflection are shown for analyses at 23ºC in Fig. 247. The initial peak values are an artefact of the assumption of the equivalent SDOF method that the initial deflected shape will be the static deflected shape under loading, even before the loading has been applied. Alternative modelling shows that the reaction starts at zero, and the initial peak reaction may be ignored in favour of the peak just before the glass cracks.

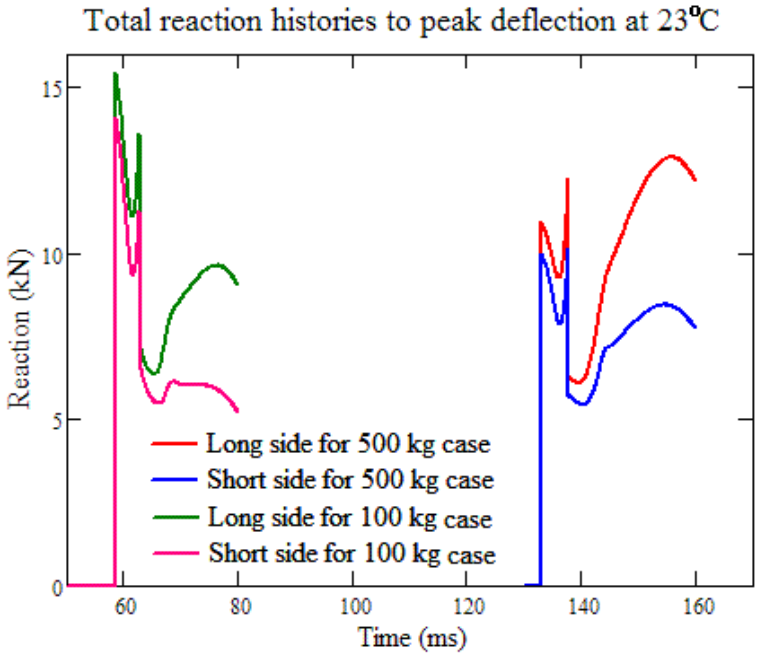

Figure 247. Reaction histories up to peak inwards deflection for analyses at 23ºC

Peak reactions and tensions based on this are presented in Table 81 for all of the analyses. The results show different sensitivity to temperature for the maximum transverse reactions and the maximum in-plane tension. The downwards changes in deflection for a 6º drop in temperature are consistent with the upwards changes in deflection for a 6º rise in temperature shown in Table 80.

Load case	Property	Units	Temperature for properties		
			Design 23ºC	17ºC	% Increase
100 kg TNT at 31m	Deflection	mm	269.4	227.2	-15.7
	Long side total reaction	kN	13.58	13.64	0.44
	Short side total reaction	kN	11.25	11.30	0.44
	Long side peak reaction	kN/m	15.62	15.69	0.45
	Short side peak reaction	kN/m	15.86	15.93	0.44
	Long side tension	kN	18.23	43.64	139
	Short side tension	kN	13.88	33.34	140
	Long side peak tension	kN/m	16.11	38.98	142
	Short side peak tension	kN/m	16.22	39.08	141
500 kg TNT at 64m	Deflection	mm	309.0	246.0	-20.4
	Long side total reaction	kN	12.93	16.17	25.1
	Short side total reaction	kN	10.40	10.60	1.92
	Long side peak reaction	kN/m	14.42	14.59	1.18
	Short side peak reaction	kN/m	14.62	14.79	1.16
	Long side tension	kN	18.50	43.87	137
	Short side tension	kN	14.16	33.66	138
	Long side peak tension	kN/m	16.20	38.98	141
	Short side peak tension	kN/m	16.27	39.08	140

Table 81. Maximum reaction and tension forces for a ‘large’ pane

Fig. 247 shows that the design maximum total reactions for the 100 kg case occur before the cracking of the glass. This is not sensitive to a reduction in temperature, and the increase in the membrane resistance has not been sufficient to overtake the cracking reactions, so the differences at 17ºC are negligible. The figure also shows that the design maximum total long side reaction for the 500 kg case occurs in the membrane, and the 25% increase in the reaction is a reflection of the increased stiffness of the membrane at 17ºC. For the short side reaction for the 500 kg case, the design maximum glass and membrane reactions are closer, and the overall maximum switches from the glass to the membrane with a reduction in temperature, with an intermediate increase in maximum reactions.

The maximum peak reactions are essentially unchanged, because they occur in the uncracked glass just before it cracks.

Contrasting the glass peak factors in Figs. 93 and 94 with the membrane peak factors in Fig. 241, the low and reducing peak factor in membranes at large deflections and the large and increasing peak factors in uncracked glass at large deflections makes it obvious why all the maximum peak reactions in Table 81 occur in the glass before it cracks, so the peak inwards reaction is not sensitive to the temperature. This has implications, for example, for the fixings for beads that can be used to secure laminated glazing into a frame.

The peak in-plane tension histories to maximum deflection for the 500 kg case at the design temperature of 23ºC and at a temperature of 17ºC are shown in Fig 248.

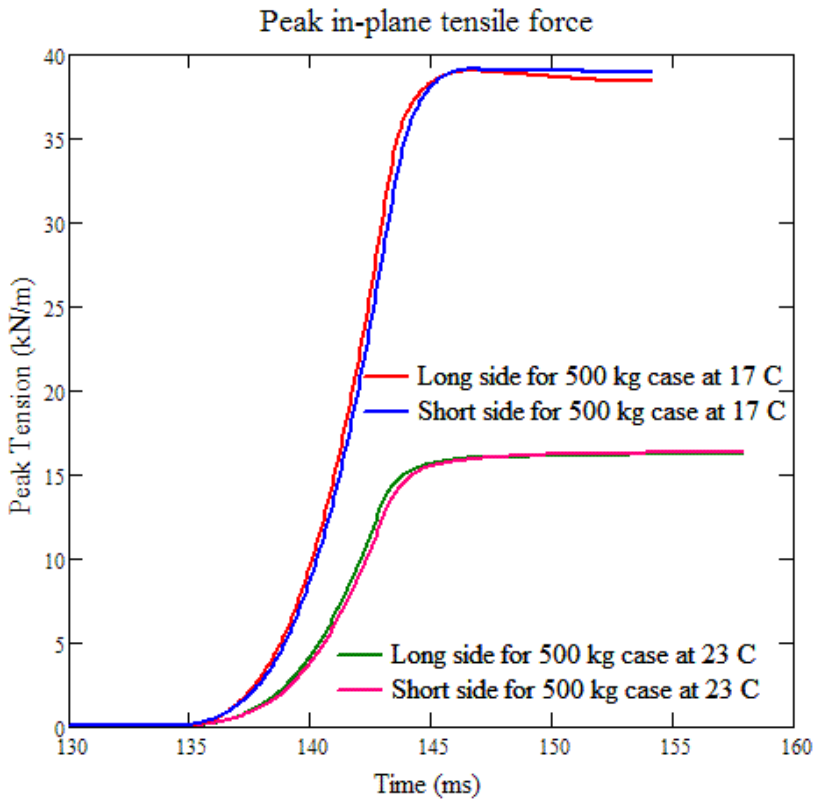

Figure 248. Peak in-plane tension to maximum deflection for the 500 kg TNT loadcase

Table 81 and Fig. 248 show that tensions increase by up to 2.4 times for a reduction in the PVB temperature of 6ºC from the proposed design value of 23ºC. At the reduced temperature the peak tension does not occur at the maximum deflection, but at a deflection of about 14% of the span, so the maximum peak values are the same for both load cases. In practice the flat plateau in the design case in Fig. 248 means that there will be very little variation in this tension also, even for substantial variations in aspect ratio.

In general blast resistant design, it has been good practice to allow a factor of safety against the ultimate capacity of fixings, typically of the order 1.5, to allow for possible reactions greater than the design values. These might arise from factors such as the greater maximum reactions that will occur if the glass does not crack until near its upper bound strength, the increasing membrane reactions and tensions if the loading on a pane is greater than calculated from the threat, and the uncertainty in the analysis. Although this would be sufficient to allow for the variability of the reactions with temperature, the results in Table 80 and Fig. 248 show that a larger margin of safety may need to be considered in designing to resist in-plane tension.

In typical glazing systems, two different mechanisms can contribute to the resistance against in-plane tension, sometimes acting in combination.

Even when the glass is cracked, radial tension in a laminated glass membrane causes a circumferential compression ring to form around the perimeter, provided the

perimeter is supported and restrained against buckling. This, together with some friction restraint, provides the anchorage in blast resistant glazing systems that use gaskets to support the glass. These have been proven in blast trials [81, 96] for large pane laminated glass test samples provided the bite of the glass and gasket in the frame was from 25mm up to 30mm.

In rectangular panels, the shear stiffness of the laminated glass is required to limit the inwards deflection of the mid-sides as the compressive anchor rings are formed. The shear stiffness of the cracked laminated glass is uncertain, but is substantially lower than for uncracked glass. The deep bite is required to prevent the cracked glass from pulling sufficiently out of the support to buckle.

It is likely that some of the HOSDB and COMBLAST tests of gasketed systems at Spadeadam took place at temperatures of 17ºC or below, so that a 30mm solid gasket 'bite' would have been adequate for tested panels. The 'bite' required to prevent pullout can be expected to increase with span and with aspect ratio.

When the glass is secured to the frame by structural silicone adhesive ('wet glazed', in American parlance) the shear strength of the silicone can be used to resist the in-plane tension force. However, structural silicone can deform grossly with a failure strain of nearly 3.0 [140, 141], so that an 8mm thick silicone joint can accommodate an edge pull-in of about 23 mm, which will allow substantial additional anchorage to be developed by the glass compression ring.

A structural silicone joint will have substantial additional strength beyond that of the silicone alone, although the extra margin will vary with span and aspect ratio. A structural silicone joint designed for a factor of safety of 1.5 on silicone strength alone is likely to have adequate reserves to resist the extra tension at 17ºC when the compression ring resistance is taken into account, although a higher factor of safety would be desirable for panes with large spans or high aspect ratios.

A recent development in anchoring glazing is glazing tapes, which are thin polymer tapes, only about 2mm thick, with high strength adhesives on both sides. These will not be flexible enough to mobilise a significant compression ring in the cracked glass before the tape fails, so the tape must be able to resist the whole of the in-plane tension. A factor of safety of at least 2.5 on design values may be required for these support systems to allow for temperature reduction.

10.7 Two degree of freedom analysis for double glazing

If the laminated glass is incorporated into a sealed cavity double glazing unit, the response of the unit may be analysed as a two degree of freedom model, with each pane modelled separately.

Good practice to control fragments is to use a laminated pane as the inner leaf. The outer leaf can be toughened, heat strengthened or even annealed, and for blast purposes need only be laminated if the blast is severe and an additional PVB interlayer is required. However, a laminated outer leaf will be more susceptible to environmental temperature variations than an inner leaf, as considered in this chapter.

The models for the two leaves can be identical to those for a single leaf of the same type, but load sharing between the leaves needs to be incorporated. The most effective way to model the sharing mechanism is to treat the sealed cavity volume as an adiabatic gas spring. The volume change in the cavity is equal to the volume swept by the inner leaf less the volume swept by the outer leaf. This can be calculated from the SDOF deflections of the two leaves and the average deflection factors, and this can be used to calculate a change in density, as there will be a fixed quantity of gas in the varying volume. The change in pressure P_C at timestep t is then related to this by Eqn. 68, and can be written in terms of the deflections of the two leaves z_o and z_i at that timestep:

$$P_C(z_o, z_i) = P_A\left(\left(\frac{D_C}{D_C - z_o \cdot Av(z_o) + z_i \cdot Av(z_i)}\right)^{\gamma} - 1\right) \tag{73}$$

Where P_A is the atmospheric pressure, D_C is the cavity depth and Av indicated the average deflection factor for the appropriate pane, e.g. as shown in Fig. 89.

The pressure change is applied as a loading to the rear of the outer leaf and the front of the inner leaf to redistribute the loading between the leaves. This tends to produce an oscillating cavity with alternating compression and rarefaction of the contained air.

Aeroelastic damping applies to the faces of the cavity, but the air in the cavity is moving at the mean of velocity of the two leaves. Damping of the cavity faces, based on the relative velocity of the surface to the cavity air, damps the cavity oscillations rather than the average deflection of the double glazing unit. The damping coefficient varies with the pressure in the cavity, but can be written in terms of the deflections of the two leaves by applying $P_C(z_o, z_i)$ from Eqn. 73 as the pressure history $P(t)$ in Eqn. 71, and can be incorporated into the acceleration equations of each leaf.

A schematic view of the double glazed model is shown in Fig. 249.

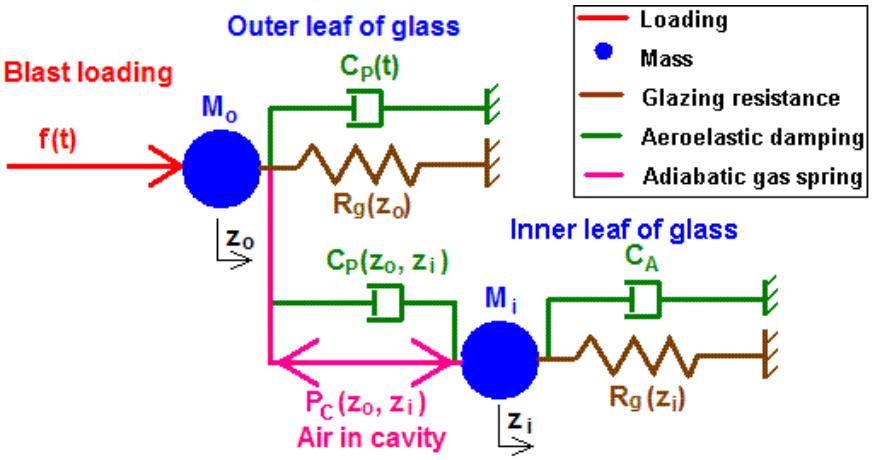

Figure 249. Schematic view of analytical model of a double glazed unit

In some cases with a thin outer leaf and a high initial blast pressure, the outer leaf deflects sufficiently quickly that it will close the cavity and impact the inner leaf before the cavity pressure can accelerate it to escape impact. By using equations for conservation of momentum and energy, separation velocities from a hard impact can be recalculated and input into the analysis.

When deflected sufficiently, the outer leaf will crack. If the outer leaf is not laminated, the glass will break up into fragments. At this point, the cavity pressure and damping are discontinued, and the blast loading and front face damping is taken to act on the inner leaf.

The fragments of the outer leaf are taken to continue at the velocity at which it cracked, and will eventually close the cavity and impact the inner leaf. A soft impact is assumed to produce a common velocity after the impact, in which momentum is conserved, but not energy. For convenience, the fragments are taken to impact simultaneously, although in practice the impacts will be spread over a finite time. The fragments will then 'ride' the inner leaf, with the outer leaf mass added to the inner leaf, but the resistance, loading and damping of the inner leaf alone used in the SDOF model of both leaves.

If the debris impacts the inner leaf before its deflection peaks, the inner leaf will field the debris and bring it to rest (provided it does not fail in turn). If the debris impacts the inner leaf just after the deflection has peaked, the added momentum may cause the glass to deflect outwards to form a second peak deflection. A later impact will turn the debris around, but only slow up the rebound of the inner leaf.

The debris will continue to ride the inner leaf until a maximum rebound velocity is reached, after which the fragments will be expelled at this velocity, while the inner leaf is decelerated by the resistance of the inner leaf, and any negative pressure from the blast load after this time. The inner leaf may be brought to rest and rebound back inwards, or may fail outwards.

10.8 Design Conclusion

The foregoing research into uncracked glass and PVB membranes can be combined into an analysis method for laminated glass that is suitable for design of single leaf or double glazed laminated glass systems.

Most blast resistant glazing will be used in double glazing units with an inner leaf of laminated glass, with the inner temperature conditioned to 23ºC. The temperature of the PVB interlayer in the inner leaf should be designed using material properties for this temperature.

However, there will be limited variation in the PVB temperature due to the external temperature. The design method needs to have margins of safety that will allow for the temperature sensitivity over a moderate range. A range of ± 6ºC has been considered.

Most window sized panes have a strain rate to failure under typical blast loading of the order 10/s. Combining this with the PVB to laminated glass strain-rate ratio of 3.8 indicates that PVB material properties at a strain rate of 40 /s would be appropriate for most design, although this value is tentative, and alternative values may need to be considered for large panes, thick glass and abnormal blast loads.

Analysis of worked examples indicates that a design limiting deflection will need a margin of safety of 16-22% to allow for the softening of PVB with temperature increase. A consensus will need to be developed on the appropriate risk levels, but design deflection limits in the range 23% to 28% of span may be appropriate.

Analysis of reaction and tension in the worked examples indicate that the peak perpendicular reactions will usually be dominated by the cracking reactions of the glass, which are not temperature sensitive. However, the peak in-plane tension at the supports can increase by a factor of 2.4 due to temperature reduction. Provision for this needs to be made in the design of the glazing supports.

11 Conclusions and further work

11.1 Conclusions

11.1.1 Single degree of freedom analysis

SDOF analysis for blast loading has been applied to glazing since the technique was first developed, though the use of small deflection formulae for resistance limited its early effectiveness.

The development of SDOF analysis for elastic-plastic analysis of reinforced concrete has resulted in some simplifications (e.g. the neglect of negative phase loading) which, although reasonable for an analysis of a plastic bending system, are inappropriate for an elastic-brittle system like glass or a membrane system like laminated glass.

The Equivalent SDOF method is a rational and consistent method of applying SDOF analysis to real distributed systems such as reinforced concrete beams, slabs and walls and glazed panels, based on sound principles. Provided that it is appropriately applied, it can give a good approximation of the structural response to blast, and with some reservations, the application of dynamic equilibrium can give a good approximation of the reactions acting on the supporting members and fixings.

Most applications of the Equivalent SDOF method to blast-loaded reinforced concrete structures has been based on two analyses published by the US Army Corps of Engineers in the 1950s [15, 16] and 1960s [17]. However, these analyses show some inconsistancies and incorporate a number approximations and mistakes that introduce significant errors into some of the SDOF parameters. Most of these appear to have arisen from over-simplifications used to minimise the amount of work required to produce the parameters by manual calculation.

Unfortunately, for over thirty years these analyses appear to have been treated as ‘received wisdom’, and have not been seriously challenged, although improved computing power and analysis methods have made a reappraisal steadily easier. Although some researchers have identified discrepancies [40], this has not resulted in reappraisal of the original parameters.

The alternative SDOF parameters presented in Chapter 5 for two-way spanning panels are based on the Equivalent SDOF method. Finite element analyses of the elastic stage, backed up by analytical formulae for deflection, are used to derive the deflected shape; the reactions and internal forces from the analyses are used to calculate the elastic SDOF parameters. Advanced yield line analyses combined with balanced finite element analyses are used to calculate the plastic SDOF parameters. A finite element analysis of edge moments in isolation provides a consistent way to calculate transitions and elastic shear for the elasto-plastic stage.

The revised parameters provide a more accurate interpretation of the Equivalent SDOF principles than existing published values. They could replace the corresponding values when manuals are revised, and the methods can be applied to other two-way spanning rectangular panels with free edges.

One reservation concerning the SDOF reactions is the high zero deflection dynamic reaction, which is an artefact of the assumption of a fixed deflected shape. Finite element analysis shows a much lower initial peak, arising from higher modes of vibration which are not modelled by SDOF. Another reservation is the fact that, even in the plastic stage, the finite element analyses show that there is an uneven distribution of shear at the supports with a higher peak value, although current design methods are based on uniform or near uniform distribution. Both of these aspects could be fruitful areas for further research.

11.1.2 Glass properties

With rare exceptions, the glass used in laminated glazing is soda lime silicate glass. The major ingredients of glass are mostly found from natural sources, and so there will be variations in the composition of glasses made of materials from different sources. The specification for soda lime silicate glass for glazing is fairly broad, to reflect the diverse sources of materials.

The elastic properties of soda lime silicate glass can vary with its composition. Sodium oxide reduces the Young's modulus as well as the melting point, and calcium oxide and some other optional ingredients increase the Young's modulus as well as reducing the sensitivity to moisture. The great majority of Young's Modulus values reported in the literature lie in the range that can be expected from the varied composition permitted in specifications. The most commonly reported design values of 70 GPa in Europe and 10 x 10^6 psi (69 GPa) in America are probably due to being 'rounded' numbers rather than to particular measurements. The European value appears to be closer to the mean of the reported values, and should be used in design when the source to be used is not known, or when there is no source-specific test data.

The Poisson's ratio appears to vary slightly, with a value below 0.22 with a high silica content, increasing to above 0.22 with an increasing proportion of other oxides. When the source is not known or there is no source-specific data then a value of 0.22 should be used in design. The design charts in Chapter 6 are all based on this value.

The density of glass will also vary slightly with composition, but there is less specific data on the variation. A value of 2490 kg/m^3 is near the mean of reported values and is recommended for design when there is no more specific data.

The cracking strength of glass is subject to two types of variability. The nature of cracking at Griffith flaws indicates that there will be a substantial random error in specific failures, although simple or sophisticated statistical distributions of strength can be developed, and factors like weathering that affect the distribution and strength of Griffith flaws can be accounted for.

The second form of variability is the loading rate sensitivity that reportedly results from the stress corrosion at the roots of the Griffith flaws by atmospheric water

vapour. This suggests that the results of test data measured at lower strain rates need to be modified for application to blast analysis.

The Weibull model of glass failure and the consequent statistical approach gives the most accurate measure of strength distribution. However, the method requires an analysis that gives the complete stress field at all the glass surfaces, which does not lend itself to simplified SDOF analysis, and the reliability of the application to blast design is reduced by the need to adjust for strain rate, which will not be uniform. Although the Weibull model will be a useful research tool, and awareness of it is useful to avoid false reasoning in other, simpler models, it is not appropriate for modelling glass failure in design.

Instead, a deterministic design breaking stress can be selected that can be taken as a characteristic value from a normal distribution of cracking strength. The HOSDB design strength of 80 MPa for annealed float glass is based on back-analysis from many blast trials, and is the most representative design stress. It can also be represented as a 90% confidence value for three second flexural loading tests on new or abraded glass, with a moderate dynamic increase factor to allow for the faster strain rate in blast loading.

Thermal strengthening of glass induces a compressive pre-stress in the surface layers where Griffith flaws cause cracking. The loading must overcome the pre-stress as well as the strength of the glass. The HOSBD design strength of 180 MPa for fully toughened glass is consistent with a typical surface pre-stress of 100 MPa in Europe, although the average in America may be closer to the minimum pre-stress of 70 MPa. Using the same reasoning, a design strength of 120 MPa should be used for heat strengthened glass with a specified pre-stress of 40 MPa.

11.1.3 SDOF analysis of glass to cracking

Analytical and experimental attempts to apply large-deflection theory to the analysis of glass in the 1960s and 1970s were limited to square panels. The large-deflection nonlinear finite element analysis by Moore [67] was the first that covered a range of aspect ratios, and was applied to blast SDOF analysis in the 1980s. However, only the resistance was based on the non-linear analyses, with the other SDOF parameters and a simplified reaction distribution based on small-deflection theory. The results were presented as non-dimensional charts, with non-dimensional deflection based on glass thickness.

The new large-deflection non-linear finite element analysis of monolithic glass panes described in Chapter 6 reproduced Moore's analysis with modern software, with the intent of modelling blast response. While confirming the general pattern of Moore's results, several differences were highlighted. The maximum stresses do move from the centre to the corner as the deflection increases, but there is a transition zone when the peak is intermediate, and the maximum stress does not move right to the corner, but to the edge about 4% of span from the corner. A very fine mesh is required in the corner to resolve this, and a graphical post-processor was used to identify this. This can affect the cracking deflection of slender glass leaves. Follower forces can also make a difference to the resistance of slender leaves at large deflections.

SDOF transformation factors and dynamic reaction coefficients were calculated from the same analyses as the resistance and maximum stresses. To comply with the principles of the Equivalent SDOF method, the incremental deflected shape was used by calculating the difference between deflected shapes at 99% and 100% loaded increments. The same finite element analysis was also used to evaluate the substantial variation in the reaction distribution as glass panes deflect.

A relationship between uncracked laminated glass panes and equivalent monolithic panes with modified properties was proposed in Chapter 7. This relationship is intended to match the mixture of flexural and membrane behaviour in the response, and hence in the resistance and the SDOF coefficients, so that the data from analyses of monolithic glass, presented in non-dimensional terms, can be applied to laminated glass.

The non-dimensional maximum stresses are not completely matched in this relationship, but it has been found to under-predict the cracking deflection of laminated glass. The degree of conservatism that this causes will vary with the deflection and cracking location, but is acceptable for design. For back-analysis of trials, the actual cracking strengths will need to be estimated from the deflection record, and will generally be higher than the lower bound design values, so the conservatism will merely increase the estimated cracking strengths of the laminated samples.

The deflection histories of uncracked laminated glass trials reported in Chapter 7 were generally consistent with the proposed relationship, and showed that, consistent with other sources, laminated glass can be taken as fully composite at temperatures up to 20ºC, but will be progressively less stiff at temperatures of 29ºC and above. At a temperature of 42ºC, one test showed that when there is little composite action left due to softening of the PVB interlayer and a substantial amount of additional damping occurs, presumably due to hysteresis damping in the PVB.

11.1.4 PVB properties

PVB is a nonlinear viscoelastic polymer. Viscoelasticity results in a time-dependent stiffness that will reduce gradually over time, and which reduces with increasing temperature. Benneson et al. [88] have reported linear viscoelastic material properties for PVB based on measurements over a range of velocities at small strains and small strain rates.

Preliminary tensile tests undertaken at Shrivenham demonstrated that PVB properties at high strains and high strain rates are substantially different, with two types of non-linearity. There is an abrupt reduction in stiffness, comparable to a plastic yield to a residual stiffness comparable to strain hardening, and a gradual stiffening of the hardening gradient at larger strains, similar to the non-linearity of soft rubber materials. The combination of these effects resulted in a material that was substantially softer than the small strain and small strain rate properties would suggest.

Although the abrupt softening transition was comparable in appearance to plasticity, the mechanism was different, as all of the deflections were seen to be recoverable,

over time. The stress at which the transition occurred increased with strain rate, and decreased with temperature, in step with linear viscoelasticity. However, the hardening stiffness operated in reverse relative to the elastic stiffness, increasing with temperature and reducing with stain rate, and the rubber-like stiffening was greater at high temperatures and low strain rates.

Various non-linear viscoelastic material models are being developed to model polymers in general and PVB in laminated glass in particular, for crash modelling in the automotive industry. However, the models currently available, even those reported in development finite element codes, are not yet capable of modelling the abrupt non-linearity in viscoelasticity observed in the tensile tests.

Instead, the response of PVB under tensile loading has been modelled by a bilinear elastic-plastic resistance, with the strain rate and temperature sensitivity approximated by variation of the model properties with temperature and average strain rate.

Extensive tensile testing of multiple samples of PVB was undertaken at Imperial College over a range of strain rates and temperatures to provide measured properties. Most of the test specimens were made from PVB that had been cured by the heat and pressure of the laminating process, but with the glass surfaces treated to avoid bonding. Sufficient tests of uncured PVB specimens were undertake to demonstrate that, contrary to expectations, the cured material is stiffer in tension than uncured PVB.

Back-analysis of the force-deflection measurements of test specimens was used to define bilinear material properties for strain rates between 10/s and 80/s and for temperatures between 5ºC and 35ºC, using a co-rotational non-linear formulation suitable for analysis of PVB membranes.

11.1.5 Behaviour of PVB membranes

Analytical solutions for elastic membranes use a cubic resistance curve, with a closed form solution for the cubic coefficient in terms of the elastic material properties and the aspect ratio. These can be presented as non-dimensional charts, but unlike glass plates, scaling the thickness by the span gives results that are not sensitive to the membrane slenderness. Finite element analyses are consistent with the analytical solutions only up to about 3% of the span.

Within LUSAS software there are a number of element types and non-linear formulations. Most analyses beyond 3% of span become first stiffer than the cubic curve, and then softer, but follow the same general trend. The co-rotational scheme that is reported as appropriate for large deflections and large rotations, used with eight-noded solid elements, can analyse membrane deflections up to around 45% of span. An exception to the general trend are models using semiloof shell elements, which show unrealistic stress distributions and resistance curves, demonstrating that they are not suitable for large deflection membrane analysis.

Co-rotational solid finite element models have been analysed for the aspect ratios of two sets of test panels, using bi-linear material properties for the temperatures at which the tests were reported to have occurred, and for a range of strain rates. As the

stresses near the edges of the membranes reached the transition stress, the membrane model 'yields' to the hardening gradient first at the edges and then over almost all of the membrane. The near cubic elastic membrane resistance transitions into a softer and more linear curve, in which the rising curve due to the material hardening is balanced against the geometric softening effect of increasing deflection in a yielding membrane.

SDOF transformation factors calculated from the same analyses showed a gradual drop in values in the elastic phases, a sharp drop with the onset of 'yield' at the edges, a recovery as the rest of the membrane 'yields'. Thereafter the transformation factors remain nearly constant. These variations are only over about 10% of the values of the transformation factors, which is less than the variations that typically occur before cracking. Dynamic reaction coefficients and other reaction parameters can also be derived from the same analyses.

These resistance curves and transformation factors have been used to back-analyse two sets of trials for which deflection histories had been recorded: 7.5mm thick laminated glass at around 20ºC in arena trials and thick double glazed units at 26ºC to 29ºC in shock tube trials. Fairly close fits to the measured deflection histories were obtained from SDOF and 2DOF analyses respectively, using pressure histories measured from the same tests. Alternative dynamic analyses were run based on the results of different finite element analyses to identify the material strain rate that gave the best fit between the measures and calculated deflection histories.

The ratio between the mean strain rate in the membrane derived from measured deflection histories and the material strain rate in the PVB that gave the best fit in the analysis was expected to be indicative of the stiffening effect of the glass fragments, as well as allowing for various simplifications and approximations. The mean value of this ratio was 3.8, but there was a wide spread of values, from 0.6 to 7.1. The limited number of tests and the wide diversity of the ratios indicate that little confidence should be placed in the mean value.

Some of the deflection results show a variation that suggests the temperature value used for some of the tests may have been inaccurate, while other results may have been biased to an upper bound value by the available PVB test data. In addition, the deflection histories are not very sensitive to changes in strain rates, and can be more sensitive to other parameters that are not accurately known, like the cracking strength of thick glass and the accuracy of the loading pressure history. In addition, the tests for which data was available may not have been representative of glazing as a whole. Back-analysis of as many further instrumented blast or shock tube tests as possible will be required to add to the data on strain rate ratios and to make the analysis more reliable.

The resistance functions that gave the best fit to the rebound response for maximum deflections up to about 25% of span was a cubic curve back to the origin, representing a softer elastic recovery, but suggesting that at the test temperatures the viscoelastic recovery rate was sufficiently fast to prevent the membrane becoming slack. At higher deflections the rebound response appeared to be more highly damped, suggesting a higher unloading stiffness followed by a significant period of slack membrane with no resistance and supercritical damping.

11.1.6 Design of laminated glass under blast loading

The blast resistance of panes of laminated glass can be analysed using the Equivalent SDOF method. The non-linear behaviour is different and more complex than the elastic-plastic analysis of reinforced concrete in bending, but can be evaluated by numerical analysis methods.

Blast resistant glazing is normally provided to reduce the risk of injury to and the fatality of people behind the glazing. The space behind the glazing will therefore normally be conditioned to room temperature, typically 23ºC. In modern buildings the thermal requirements will normally mandate double glazing. Blast protection will require the inner leaf to be laminated, with the cavity and outer leaf providing insulation to the inner leaf from the temperature fluctuations on the outside.

For most blast design scenarios, the temperature sensitive PVB interlayer will be held at or close to room temperature. It is recommended that the normal design of laminated glass under blast should be based on the properties at room temperature, but allowance needs to be made in the design process to accommodate moderate variations from this temperature. Where laminated glass is used to provide blast protection in other circumstances, modified design properties may need to be considered.

For the normal range of spans and glass thicknesses loaded close to failure the membrane strain rate is typically about 10/s. Combined with the mean strain rate ratio this suggests that design for typical blast resistant laminated glass can be based on PVB material properties with a strain rate of 40/s at 23ºC. This is a provisional conclusion, and could be modified in the light of further research.

Design resistance curves for laminated glass can be derived from the resistance data for uncracked glass and PVB membranes, with a single or multiple transitions depending on whether the whole of the laminated glass will crack immediately, or whether the initial cracking will be followed by cracking of the remaining plies at larger deflections. This can be calculated from the resistance curves and cracking deflections of models of intact and partially cracked laminated and monolithic glass configurations.

Design SDOF coefficient curves for the laminated glass are similar composites of the curves for uncracked glass and for the design PVB membrane, with transitions at the same design cracking deflections. There are two exceptions: concentrated corner reactions only occur in bending models before the last ply of glass cracks, while in-plane tension forces only become significant in PVB membranes, where the in-plane stiffness of the glazing becomes much less than the in-plane stiffness in the supports.

The use of a cubic elastic membrane model for rebound without a slack phase in design is consistent with the response for peak deflections up to about 25% of span, and will tend to be under-damped for larger peak deflections, giving upper-bound rebound deflections.

The response of the laminated glass under blast load can be calculated by double numerical integration of the acceleration defined in terms of the resistance curve and

transformation factor curves, together with the loading history, the mass and the damping.

One form of damping that will always be present for blast loading in air is aeroelastic damping, which is an interaction between the moving surface of the glass and the surrounding atmosphere. On both the front and rear surfaces the damping coefficient is equal to the impedance of the air, which will be constant on the rear face, and will vary with the pressure history on the loaded face. Aeroelastic damping has a negligible effect on thicker elements like reinforced concrete slabs, but has a significant effect on thinner elements like glass panes, and may have a dominant effect on membranes at small deflection, such as on rebound of a cracked laminated glass pane, where the low stiffness results in supercritical damping. The damped rebound response in analyses has strong similarities to the response observed in high speed video records of blast trials of laminated glass.

Analysis of 7.5mm laminated glass panels for threats from 100kg and 500kg TNT charges at the boundary of 'High Hazard' on HOSDB fragility curves shows design deflections at about 21.5% and 24.7% of span respectively. An increase of temperature by 6ºC gives an increase in deflection by 16 to 22% (i.e. up to 30% of span). This can be compared with the marginal survival in trials of laminated glazing at maximum deflections between 32% and 33% of span (at higher loading levels). Design deflection limits need to be selected not only to give a satisfactory confidence level of survival at room temperature, but to allow a suitable margin to trade-off confidence levels and probability of increased temperature.

Evaluation of the reactions from these analyses shows that the total reactions may peak just before the glass cracks, or may peak at maximum membrane deflection. A 6ºC reduction in temperature will increase the membrane resistance by 25% but not the cracking resistance. In some cases the maximum total reaction will switch from cracking to membrane, with a smaller rise in peak value. However, membrane reactions at large deflections are much more uniformly distributed than glazing reactions at cracking, so the peak reactions can normally be expected to occur before cracking, and to be insensitive to temperature.

Evaluation of in-plane tension force histories shows that the peak tensions rise to maximum or plateau values by deflections about 14% of span. However, a reduction of temperature by 6ºC can cause an increase in tension to 2.4 times the design tension. A substantial factor of safety needs to be built into the anchorage mechanisms to allow for this sensitivity to temperature, but both adhesive anchorage and the compressive ring resistance in the cracked laminated glass with compatible deflections can be taken into account.

Sealed double glazing units can be analysed as two independent degrees of freedom coupled by an adiabatic air spring that redistributes loading between the leaves, together with cavity damping and methods of modelling different types of impact between the leaves.

11.2 Recommendations for further work

11.2.1 Application of this research to design

The yield line and associated linear finite element analysis of reinforced concrete elements in Chapter 5 was only undertaken for rectangular panels with all four sides supported. Some existing manuals have also applied the previous, less accurate, analysis methods to panels with one edge free or two adjacent edges free. For the new analysis approach to become fully adopted, it will also be necessary to undertake the analyses to apply it to these cases.

The analyses in Chapter 6 have been undertaken for sufficient cases to populate the graphs, and to provide more accurate data for back-analysis of trial panels of a few aspect ratios, but this will still leave a fairly coarse interpolation for aspect ratios in between. Sufficient intermediate analyses can be undertaken and post-processed to fully populate an interpolation table for all the parameters over the full range of aspect ratios from 0.9 to 4.0 to allow cubic-spline interpolation. One aspect ratio less than 1.0 is desirable in the table to ensure that the gradient of the interpolation curve through the aspect ratio of 1.0 is correct. By transposing panels the table can then be used for the analysis of any panel with height to length ratios between 0.25 and 4.0.

The analyses in Chapter 9 were only undertaken for the full range of strain rates at particular aspect ratios and temperatures to match the circumstances for test panels to be back-analysed. Subsequent analyses were performed for one strain rate and temperature: the proposed design case of 40 /s and 23ºC over all the aspect ratios necessary to populate Fig. 236. Additional analyses for intermediate aspect ratios need to be completed and post-processed to populate an interpolation table for this design case. To cover larger, heavier panels, a similar data table also needs to be established for a lower strain rate.

Some additional analysis at 29ºC and 17ºC were undertaken for an aspect ratio of 1.24 and strain rate of 40 /s to evaluate the temperature sensitivity of the design failure criteria and factors of safety. This needs to be extended to other aspect ratios.

Other combinations of temperature and aspect ratio will need to be developed for a range of strain rates to back-analyse additional trials, but this analysis can be undertaken when new trials data has been obtained.

11.2.2 Further research that would improve this thesis

Additional tensile testing of PVB samples at intermediate temperatures and lower strain rates is desirable to provide a more complete PVB property database. Data at temperatures of 29ºC and 15ºC would allow better than linear interpolation of temperature effects. However, it might be easier to change the laboratory thermostat at the right time of year to reach these temperatures and dress appropriately, rather than to use local temperature adjustment. Additional test data at all temperatures and

at pull velocities of 0.5 m/s, and possibly at 0.25 m/s is desirable to avoid the need for extrapolation.

Compilation of additional arena blast and shock tube trials of laminated glass and double glazing with pressure history and deflection history records is desired to increase the data on glazing response. This can then undergo back-analysis to generate additional strain rate ratio data. Laser and high speed video technology appears to have reached the stage where collection of deflection history data from blast trials will become a regular feature. Single glazed laminated glass tests should give the best data, but are not common, and recording of the temperature at the time of the test is necessary to make best use of the data.

In addition to cracked laminated glass trials, instrumented blast tests of specimens that do not crack are desired, particularly in the temperature range 20ºC and 29ºC, to establish a threshold temperature below which fully composite action can be assumed, and the variation of stiffness above that temperature.

Investigation of the effect of PVB flexibility (that causes the reduced stiffness of the laminated glass at elevated temperature) on the maximum stress in the glass, and hence on the cracking deflection, is desirable. This is investigation is likely to be based on analysis, although uncracked glass tests at elevated temperatures may have a role.

Additional quasi-static testing of laminated glazing panels by water bag pressure loading is desirable, with measurement of deflected shapes and gradients by laser scanning and / or stereo photogrammetry. This could give much more extensive data than previous tests to assess failure criteria for laminated glass of various make-ups and thicknesses, and to provide improved confidence levels for failure deflections.

Investigation of anchorage mechanisms against in-plane membrane forces in cracked laminated glass, including the interaction of internal compression rings and adhesive anchorage which could also use quasi-static water bag pressure tests, would be useful.

11.2.3 Further research that would complement this thesis

Investigation into early reaction histories for elastic flexural members under blast loading could be used to find ways in which the early reaction could be modelled better in SDOF analysis.

Investigation into the shear distribution and resistance at supports of two-way spanning reinforced concrete members, including redistribution of reactions due to ductility in shear reinforcement would allow a more consistent application of shear failure criteria to two-way spanning panels, whether analysed by finite element or other methods.

Continued investigation into advanced non-linear viscoelastic material models for finite element analysis of PVB is desirable to identify models capable of reproducing the abrupt changes in stiffness observed in tests. However, such models are likely to still be more suitable for research than for routine design of glazing under blast loading.

12 References

1. BS 952-1:1995. "Glass for glazing – Part 1: Classification", British Standards Institution, London, 5th edition July 1995.

2. Road Research Laboratory note ARP/26/ARC "First interim report on blast tunnel tests with treated glass" Ministry of Home Security paper RC77, 1940.

3. Special Service Group, Explosion Protection. "Glazing Hazard Guide – Charts", Report SSG/EP/3/97, Security Facilities Executive, June 1997.

4. Williams J. "Lessons from the terrorist attack on HSBC Istanbul", at Building Security against a Threat of Terrorism, Joint CIBSE / ICE seminar, Marriott Hotel, London, 18 February 2004.

5. "HSBC launches fund for victims of Istanbul tragedy", HSBC press release 26 November 2006, on www.hsbc.com/hsbc/news-room/news/news-archive-2003, viewed 12/12/06

6. Morison C "Response of glazed facades to blast loading", MSc dissertation, U of Westminster, August 1999.

7. Rankine W J H. Phil. Trans. Roy. Soc., 1870, vol 160, pp277-288.

8. Hopkinson B. British Ordnance Board minute 13565, April 1915. (PRO volume Sup6/187)

9. Thomas W N. "The effects of impulsive forces on materials and structural members", The Civil Engineer at War. Vol. 3, ICE London, 1948.

10. Walley F. "The effect of explosions on structures", ICE Proceedings, Structures and Buildings, August 1994, Vol 104 Issue 3, pp 325-334.

11. Christopherson D G. "Structural defence", Ministry of Home Security, Research And Experiments Department, Paper R.C.450, 1945.

12. Walley F. "Memorandum on the design of bomb-resisting structures against he attack", Ministry of Works, March 1954.

13. Jarrett D E. "Derivation of british explosive safety distances", Annals of the New York Academy of Sciences, 1968, Vol 152, pp 18-35.

14. "Fundamentals of protective design (non-nuclear)" TM 5-855-1, Department of the Army, March 1965. (Reprint of former EM 1110-345-405, 1946).

15. “Design of structures to resist the effects of atomic weapons – principles of dynamic analysis and design”, EM 1110-345-415, US Army Corps of Engineers, March 1957

16. “Design of structures to resist the effects of atomic weapons – principles of structural elements subjected to dynamic loads”, EM 1110-345-416, US Army Corps of Engineers, March 1957

17. “Structures to resist the effects of accidental explosions”, Technical Manual TM5-1300, US Department of the Army, 1969

18. “Design of protective structures to resist the effects of nuclear weapons”, AFSWC TR-59-70, December 1959, 2nd Edition TDR-62-138 – US Air Force 1962.

19. Crawford R E et al. “Protection from non-nuclear weapons” AFWL RT-70-127 Air Force Weapons Laboratory, Kirtland AFB New Mexico 87117, 1970.

20. Crawford R E et al. “The air force manual for design and analysis of hardened structures”, AFWL-TR-74-102, Air Force Weapons Laboratory, Kirtland AFB New Mexico 87117, 1974.

21. “Fundamentals of protection of structures for conventional weapons” TM 5-855-1, US Army Corps of Engineers, Washington DC 20314-1000, 1986

22. Drake J L et al. “Protective construction design manual” ESL-TR-87-57, Air Force Engineering Services Lab, Tyndall Air Force Base, FL32403, November 1989

23. “Protective structures automated design system” v 1.0 (PSADS) (incorporating Army TM5-855-1, Air Force AFJAM32-1055, Navy NAVFAC P-1080 and DAHSCWEMAN-97) v 1.0, US Army Corps of Engineers, Washington DC 20314-1000, September 1998

24. “Structures to resist the effects of accidental explosions”, Technical Manual TM5-1300, US Department of the Army, November 1990

25. “Design of structures to resist nuclear weapon effects”. ASCE Manuals & Reports on Engineering Practice – No 42. American Society of Civil Engineers, New York, 1961.

26. “Design of structures to resist nuclear weapon effects”. ASCE Manuals & Reports on Engineering Practice – No 42, Revised Edition. American Society of Civil Engineers, New York, 1985.

27. Mays GC & Smith PD (Editors). “Blast effects on buildings”, Thomas Telford Publications, London 1995.

28. Kingery C N & Bulmash G. “Airblast parameters from TNT spherical air burst and hemispherical surface burst”; Technical report ARBRL-TR-

02555; US Army Research and Development Centre, Ballistic Research Laboratory, Aberdeen Proving Ground, Maryland; April 1984.

29. Building Research Station report HOPP 6, "The design of buildings against air attack", Ministry of Home Security paper RC 6, March 1939.

30. Fox E N. & Harris A J. "The design of buildings against air attack – Part II – mathematical analysis of the effect of blast on structures", Building Research Station report HOPP 18, Ministry of Home Security paper RC 23, June 1939.

31. Philip E B. "Blast and the ministry of home security research and experimental department, 1939-1945", Ministry of Home Security paper REN 585, 1945

32. Philip E B. "Effect of blast on rectangular panels of glass or other elastic material", Ministry of Home Security paper RC163, 8 January 1941.

33. Wise J A. "Rupture of glass by blast", National Defence Research Committee monthly report No ENT5e, Effects of Weapons on Targets, Vol 5. Office of Scientific Research and Development August 5 1945.

34. Newmark N M. "An engineering approach to blast resistant design", American Society of Civil Engineers Transactions, Paper No 2786, Vol 121 p45, 1956. (Noted as published "essentially as printed here" as proceedings –Separate No 506, October 1953.)

35. Biggs J M. "Introduction to structural dynamics", McGraw-Hill, New York, 1964.

36. Buchholdt H. "Structural dynamics for engineers", Thomas Telford, London, 1997.

37. Zobec M & De Bertoli L. "Blast theory manual*",* Permasteelisa, Vitorio Veneto, TV Italy, May 2005.

38. Timoshenko S P. "Theory of plates and shells", McGraw-Hill, New York & London, 1940.

39. Jones L L & Wood R H. "Yield line analysis of slabs", Thames & Hudson, Chatto & Windus, London, 1967.

40. Mayor R P & Flanders R. "Technical manual simplified computer model of air blast effects on building walls". US Department of State, Office of Diplomatic Security, Washington DC 20520, June1990

41. Donnell L H. "Beams, plates and shells", McGraw-Hill, New York, 1976. ISBN 0-07-017593-4.

42. Timoshenko S P & Goodier J N. "Theory of elasticity, 3rd edition", McGraw-Hill, New York & London 1970; ISBN 0-07-085805-5.

43. Ingerslev A. “Rectangular slabs”, Concrete & Construction Engineering, London, Vol 18, No 1, Jan 1923. (Abstract of a paper read at I Struct E, 14 Dec 1922)

44. Inaba S, Fujino S & Morinaga K. “Young’s modulus and compositional parameters of oxide glasses”, J. Am. Ceram. Soc. Vol 82 [12], pp3501-3507, 1999.

45. www.londoncrownglass.co.uk/History.html, viewed 11/12/06

46. McLellan G W & Shand E B. “Glass engineering handbook”, McGraw-Hill, New York, 3rd Edition, 1984.

47. www.specialistglass.co.uk/glass-history.asp, viewed 11/12/06

48. www.londoncrownglass.co.uk/Manufacturing.html, viewed 11/12/06

49. BS EN 572-4:1995. “Glass in building – Basic soda lime silicate glass products – Part 4: Drawn sheet glass”, British Standards Institution, London, 1995.

50. BS EN 572-5:1995. “Glass in building – Basic soda lime silicate glass products – Part 5: Patterned glass”, British Standards Institution, London, 1995.

51. BS EN 572-2:1995. “Glass in building – Basic soda lime silicate glass products – Part 2: Float glass”, British Standards Institution, London, 1995.

52. BS 6263-4:2005. “Glazing for buildings – Part 4: Code of practice for safety related to human impact”, British Standards Institution, London, 8th edition, October 2005.

53. Road Research Laboratory note No APR.12/SCR. “Preliminary note on the measurement of the fundamental frequency of vibration of glass window panes”, Ministry of Home Security paper RC 58, UK, November 1939.

54. Road Research Laboratory note No ARP 33/ARC. “Results of frequency measurements made on the test windows and roof lights for the Shoeburyness trial of 7th March 1940”. Ministry of Home Security paper RC 81, April 1940.

55. Road Research Laboratory note No ARP 35/ARC. “The measurement of the fundamental frequency of glass window panes”. Ministry of Home Security paper RC 87, April 1940.

56. Philip E B. “Blast tests on glass panes at Stewartsby, Jan-Feb 1942”. Ministry of Home Security paper REN 583, (No date, but believed to be 1945).

57. Road Research Laboratory note ARP/61/ARC. “High speed cine photographs of windows subjected to blast from an explosion” Ministry of Home Security paper RC 120, (No date, but believed to be 1941).

58. Road Research Laboratory note ARP/77/ARC. “Effects of repeated blasts from explosions on the strength of glass panes”, Ministry of Home Security paper RC 132, (No date, but believed to be 1941).

59. Philip E B. “Interim report on work connected with RC 163”, Ministry of Home Security paper REN 127. (No date, but believed to be 1942).

60. Philip E B. “Curves showing radius of blast damage to glass”, Ministry of Home Security paper REN 119, June 1942.

61. “The breakage of window panes by blast from bombs”, Ministry of Home Security RE 2/4 data sheet 8B6, Ministry of Home Security, July 1945.

62. “Miscellaneous approximate formulae for radii of various degrees of damage”, Ministry of Home Security RE 2/4 data sheet 8B7, Ministry of Home Security, August 1945.

63. Prichard D K. “Breakage of glass windows by explosions”, Journal of Occupational Accidents vol 3, pp69-95, Elsevier, 1981.

64. Bowles R & Sugarman B. “The strength and deflection characteristics of large rectangular glass panels under uniform pressure”, Glass Technology, Vol 3 pp 156-170, 1962.

65. Seaman L. “Response of windows to sonic booms”, Prepared by Stamford Research Institute for the Department of the Air Force SR1 Project ETU-5897, 1967.

66. Freynik H S. “The non-linear response of windows to random noise”, NASA technical note NASA TN D-2025, 1963.

67. Moore D M. “Proposed method for determining the glass thickness of rectangular glass solar collector panels subjected to uniform normal pressure loads”, JPL Publication 80-34, Jet Propulsion Laboratory, Pasadena, CA, October 1980.

68. Vallabhan C V G. “Iterative analysis of nonlinear glass plates”, Journal of Structural Engineering, Vol 109 No 2 pp489-502, ASCE, February 1983.

69. Al-Tayyib A J. “Geometrically nonlinear analysis of rectangular glass panels by the finite element method”, Dissertation presented to Texas Tech University, 1980.

70. Meyers G E. “User data package for blast resistant windows”. Technical Memo 51-86-13 Naval Facilities Engineering Command, Alexandria VA, June1986.

71. Meyers G E. BLASTOP version 1.4, US Department of Energy, 1994.

72. Norville H S & Minor J E. “Strength of weathered window glass”, American Ceramic Society Bullletin, 64 [11] pp 1467-70, 1985.

73. Minor J E & Resnik P L. “Failure strengths of laminated glass”, Journal of Structural Engineering Vol 116, No 4, pp1030-1039, ASCE April 1990

74. Linden M P, Minor J E & Vallabhan C V G. “Evaluation of laterally loaded laminated glass units by theory & experiment” (Supplemental Report No 1). Glass Research and Testing Laboratory, Texas Tech University, Lubbock, Texas, July 1984.

75. Behr R A, Minor J E, Linden M P & Vallabhan C V G. “Laminated glass units under uniform lateral pressure”, Journal of Structural Engineering Vol 111, No 5, pp1037-1050, ASCE May 1985.

76. Behr R A, Minor J E & Linden M P. “Load duration and interlayer thickness effects on laminated glass”, Journal of Structural Engineering, Vol 112, No 6, pp 1441-1453, ASCE June 1986.

77. Resnik P L & Minor J E. “Failure strengths of laminated glass units”. Glass Research and Testing Laboratory, Texas Tech University, Lubbock, Texas, October 1986.

78. Barnard B G. “A report on the preliminary evaluation of various glazing assemblies and protective measures to reduce injury and damage from flying glass resulting from bomb explosions”, Report 15/75, Home Office Scientific Advisory Branch, March 1978.

79. Barnard B G. “A report on the trials carried out with the Department of the Environment on various glazing assemblies subjected to bomb blast”, Working Note 32/75, Home Office Scientific Advisory Branch, November 1978.

80. Connell M. “Draft glazing hazard guide”, PSA reference UB 899/5/5MC, March 1992.

81. Special Services Group, Explosion Protection. “Glazing hazard guide – Charts”, Security Facilities Executive (now the Home Office Scientific Development Branch), Report SSG/EP/3/97; June 1997.

82. “Glazing standards for mod buildings subject to terrorist threat”, Defence Works functional standard design and maintenance guide 02, Defence Estates Organisation, Ministry of Defence May 1996.

83. “Counter terrorist protective security manual”, The Cabinet Office Security Division, London, April 2003.

84. Norville H S, King K W & Swofford J L. “Behaviour and strength of laminated glass”, Journal of Engineering Mechanics, ASCE, January 1998 pp 46-53.

85. Wei J, Shetty M S & Dharani L R. “Stress characteristics of a laminated architectural glazing subjected to blast loading”, Journal of Computers and Structures 84 pp 699-707, 2006.

86. Van Duser A, Jagota A & Bennison S J. “Analysis of glass/ polyvinyl butyral laminates subjected to uniform pressure”, Journal of Engineering Mechanics, ASCE April 1999, pp 435-442.

87. Ferry J D, “Viscoelastic properties of polymers”, ISBN 0471048941, Wiley, New York. 3rd Edition, 1980.

88. Benneson S J, Jacota A & Smith C A. “Fracture of glass/ poly(vinyl butyral) (Butacite®) laminates in biaxial flexure”, Journal of the American Ceramic Society 82 [7] pp 1761-70, 1999.

89. “Mathcad 8 user’s guide”, MathSoft inc., Cambridge, MA, 1998.

90. Chia C Y. “Nonlinear analysis of plates”, McGraw-Hill, New York, 1980; ISBN 0-07-010746-7

91. Aalami B & Williams D G. “Thin plate design for transverse loading”, Crosby Lockwood Staples, London 1975; ISBN 0 258 96991 1

92. Fullermann M. “Zugversuche an verklebten Glasmustern”, Prufberricht-Nr.: 970826, Schmidlin AG, Aesch Switzerland, 26 August 1997.

93. Ellis B R. “Static testing of glazing for Property Services Agency”. Client report TCR 28/91, Building Research Establishment, June 1991.

94. Ellis B R & Beak M. “Static testing of glazing phase II”. Client report GIO 451, Building Research Establishment, July 1992.

95. Mansfield E H. “The bending and stretching of plates 2nd Edition”, Cambridge University Press, Cambridge, 1989. ISBN 0-521-33304-0.

96. Window design and analysis software (WinDAS) version 2.5, US Army Engineer Research & Development Centre, Vicksburg MS 39180-6199, July 2001.

97. Window fragment hazard level analysis (HAZL) version 1.2, US Army Engineer Research & Development Centre, Vicksburg MS 39180-6199, July 2004.

98. Norville H S & Conrath E J. “Considerations for blast-resistant glazing design”, Journal of Architectural Engineering, 1 September 2001, Vol 7 (3), P80-86.

99. “Standard practice for determining the load resistance of glass in buildings”, E1300-96, ASTM, Philadelphia, PA, 1996.

100. Applied Research Associates Inc. “Window glazing analysis response & design – WINGARD – Technical manual”, ARA-TR-05-16462-2, US General Services Administration, Washington DC, July 2005.

101. Du Bois P A, Kolling S & Fassnacht W, “Modelling of safety glass for crash simulation” Computational Material Science, 28 pp675-683, Elsevier 2003.

102. Du Bois P A, Kolling S, Koesters M & Frank T. “Material behaviour of polymers under impact loading”, International Journal of Impact Engineering 32 pp 725-740, Elsevier 2006.

103. Mullerschon H, Dangel A, Karjan N, Hummel & Wurst A, “Modelling of plastics for crash simulation of fuel tanks”, LS-DYNA Anwenderforum, Bamberg 2004.

104. Spingler G. “Numerical modelling of polymer materials for crash applications”, Benchmark, NAFEMS, E Kilbride, January / April 2006.

105. Bansal N P & Doremus R H. “Handbook of glass properties”, Academic Press Inc, New York, 1986.

106. BS EN 572-1:2004. “Glass in building – Basic soda lime silicate glass products – Part 1: Definitions and general physical and mechanical properties”, British Standards Institution, London, 2004.

107. BS EN 1863-1:2000. “Glass in building – Heat strengthened soda lime silicate glass – Part 1: Definition and description”, British Standards Institution, London, 2000.

108. BS EN 12150-1: 2000. “Glass in building –Thermally toughened soda lime silicate safety glass – Part 1: Definition and description”, British Standards Institution, London, 2000.

109. BS EN 14179-1: 2005. “Glass in building – Heat soaked thermally toughened soda lime silicate safety glass – Part 1: Definition and description”, British Standards Institution, London, 2005.

110. Griffith A A. “The phenomena of rupture and flow in solids”, Philosophical Transactions of the Royal Society of London Series A, Containing Papers of a Mathematical or Physical Character, Vol 221, pp 163-198, London 1921.

111. Meier M. “Griffith flaws in brittle materials”, Notes for experiments, Department of Chemical Engineering & Material Science, University of California, Davis CA, Sept 2004. On www.matsci.ucdavis.edu/matsciLT /other/files/Griffith flaws.pdf viewed 29/1/07

112. Joffé A. “The physics of crystals”, McGraw-Hill Book Co, New York, 1928.

113. J Zarzycki. “Glasses and the vitreous state”, English Edition, Cambridge University Press, 1991.

114. Andrade E N da C & Tsien L C. Proceedings of the Royal Society A159, pp. 346-354, London 1937.

115. Ernsberger F M. “Detection of strength impairing flaws in glass”, Proceedings of the Royal Society A257 pp.213-223, London 1960.

116. Beckett N E. “The Nature and properties of glass”, in “Glass in Architecture and Decoration, New Edition”, ed McGrath R & Frost A C. The Architectural Press, London 1961.

117. Ward S P. “Blast effects on glazing”, MSc Project Dissertation, Royal Military College of Science, Cranfield University, Shrivenham, November 1994.

118. www.saflex.com/pages/about/physicalprop.asp, viewed 11/12/06

119. Warren G & Millea M. “Measured shear properties of polyvinyl butyral laminate”, NCEL Technical Note N-1780, Naval Civil Engineering Laboratory, Port Hueneme, CA, January 1988.

120. Bennison S J. e-mail to De Luca O, (Permasteelisa) 24 July 2002

121. Morison C M. “Recent developments in single degree of freedom analysis of walls and windows”, 11th International Symposium on the Interaction of the Effects of Munitions with Structures, Manheim, Germany, May 2003.

122. Morison C M. “Dynamic response of walls and slabs by single degree of freedom analysis – a critical review and revision”, Journal of Impact Engineering, Vol 32(8) pp 1214-1247, Elsevier, August 2006.

123. Morison C M. “A review of the single degree of freedom method for dynamic response of reinforced concrete structures”, 12th International Symposium on the Interaction of the Effects of Munitions with Structures. Not presented at New Orleans, USA, September 2005, but incorporated on ‘Proceedings’ CD.

124. “LUSAS user manuals, Version 13”, Finite Element Analysis Ltd, Kingston on Thames, KT1 1HN, 2002.

125. Microsoft Office Excel 97/2003, Microsoft Corporation, Seattle,WA, 1985-2003.

126. Johansen K W. “Yield line theory”, William Clowes & Sons, London 1962 (Translation of doctoral thesis presented at the Danmarks Teksniske Højskole 1943.)

127. Vallabhan C V G, Das Y C, Magdi M, Asik M, Bailey J R. “Analysis of laminated glass units”, Journal of Structural Engineering, Volume 119(5), pp1572-1585, ASCE, New York, May 1993.

128. Wei J & Dharani L R. “Fracture mechanics of laminated glass subjected to blast loading”, Theoretical and applied fracture mechanics 44 (2), pp157-167, Elsevier 2005.

129. Lowak M J & Montoya J R, “Blast performance testing of windows”, Project No. 01-1539-001-06, Baker Engineering and Risk Consultants Inc, San Antonio TX, 23 October 2006.

130. Morison C M. “Testing of glass panels for the ******* ***** building, **”, Report 109757/REP/0001, TPS Consult, Croydon, September 2006. (Details redacted for commercial confidentiality)

131. Morison C M. “Permasteelisa blast resistant façade – Bomb blast testing”, Report 108906/REP/0002, TPS Consult, Croydon, January 2006.

132. “GSA security criteria, Final working version”, Public Buildings Service, General Services Administration, Washington DC, 8 October 1997.

133. “Glass in building – Explosion resistant security glazing – Test and classification for arena air blast loading”, DIS 16933, International Standards Organisation, draft dated 4 May 2004.

134. Morison C M. “High rate of strain testing of PVB and cracked laminated glass samples”, Report 108906/REP/0001, TPS Consult, Croydon, May 2005.

135. BS EN ISO 527-3: 1996. “Plastics – Determination of tensile properties – Part 3: Test conditions for films and sheets” (with corrections), British Standards Institution, London, August 2001.

136. BS EN ISO 527-1: 1996. “Plastics – Determination of tensile properties – Part 1: General principals”, British Standards Institution, London, 1996.

137. Sheldon R. HOSDB Test data in e-mail Robert Sheldon / Colin Morison, 20 December 2006.

138. Sheldon R, e-mail Robert Sheldon / Colin Morison, 22 December 2006.

139. BlastX program, incorporated in “Protective structures automated design system” v 1.0 (PSADS) (incorporating Army TM5-855-1, Air Force AFJAM32-1055, Navy NAVFAC P-1080 and DAHSCWEMAN-97) v 1.0, US Army Corps of Engineers, Washington DC 20314-1000, September 1998.

140. Fumagalli P, “H shaped DC 993 Material samples”, Mechanical testing report No ME03/312A99, CSI SpA, Milan, 1 March 2000.

141. Hautekeer J-P, Monga F, Giesecke A, O,Brien W, “The use of silicone sealants in protective glazing applications”, Glass Processing Days 2001, Proceedings of 7th international glass conference in Tampere, Finland, June 2001.

Appendix A

Paper presented at the 11th International Symposium on the Interaction of the Effects of Munitions with Structures, Manheim, Germany in May 2003

RECENT DEVELOPMENTS IN SINGLE DEGREE OF FREEDOM ANALYSIS OF WALLS AND WINDOWS

Colin Morison
TPS Consult Ltd, UK

1. Abstract

Recent analyses indicate that there is substantial inaccuracy in the historic tables of the elastic single degree of freedom (SDOF) transformation factors and reaction coefficients. Although alternative sources for a few transformation factors have been found, the use of these does not appear to have been developed to any extent. Indeed, the original 1950s data was still being incorporated in authoritative manuals as recently as 1998.

In this paper both linear Finite Element (FE) analysis and classic algebraic formulae give transformation factors that are in good agreement with those found in the alternative sources, but not with the 1950s values. The accuracy of the reaction coefficients from algebraic formulae is limited by slow convergence and arithmetical limits. Numerical analysis appears to be the most reliable means to derive all the SDOF parameters and, in this paper, linear FE analysis has been used to produce revised tables of coefficients for pinned and fixed edged reinforced concrete slabs.

The linear formulae and linear FE analysis are only accurate for elastic deflections up to about half of the panel thickness. This is appropriate for the analysis of thick concrete slabs and walls, but not for the analysis of thin panels such as window glass or steel plates.

Although data from non-linear FE has previously been used in deriving resistance functions and failure criteria for windows subjected to blast, the approach has not been extended to derive the SDOF parameters for dynamic analysis: small deflection values continue to be applied.

This paper reports on a new non-linear FE analysis that has been used to evaluate stiffness and stress data for simply-supported glass panes with large deflections, and to assess the variation in SDOF parameters due to non-linearly. Results show that the SDOF parameters for thin plates change significantly with large deflection.

Sensitivity studies investigating the effects of slenderness and of more realistic support conditions are also reported.

2. Introduction

The single degree of freedom (SDOF) method is the most common method used for analysing the dynamic flexural response of a structural member to a transient loading

such as blast. It is a method simple enough for manual calculation or for design charts and easily converted to computer analysis.

The method works by converting the distributed mass *M*, damping *C*, resistance *R* and loading *F* of the flexural model to those of an idealised equivalent concentrated resistance, mass, damper system with only one degree of freedom, *x*, and then explicitly solving Newton's equation of motion for the response:

$$M_e \cdot \frac{d^2x}{dt^2} + C_e \cdot \frac{dx}{dt} + R_e(x) = F_e(t)$$

to calculate a response history *x(t)* for the idealised system, which will also be the response of a selected point of the distributed system and to which the overall response of the member is related.

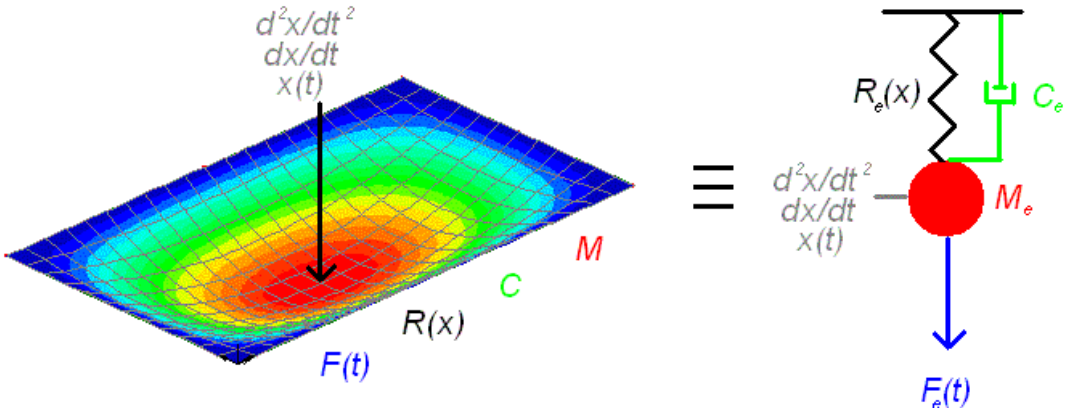

Figure 1 – Distributed system and equivalent concentrated system

The key to the method is the calculation of SDOF transformation factors to be applied to the member properties to derive the equivalent concentrated properties. The derivation of the formulae to be used is presented in a number of textbooks, such as those by Biggs (1) and by Buchholdt (2). With suitable transformation factors, the response of the equivalent system will be equal to the response of the selected point on the member in both amplitude and timing.

In both references, the mass transformation factor K_M and the loading transformation factor K_L are defined by energy methods as functions of the deflected shape. Biggs reasons that the transformation factor for the resistance K_R, linear or non-linear, must be equal to K_L. Buchholdt demonstrates that the damping transformation factor K_C is equal to K_M. The acceleration of the single degree of freedom and of the selected point on the member (eg the centre point) can therefore be written as:

$$\frac{d^2x}{dt^2} = \frac{F(t) - R(x) - K_{LM} \cdot C \cdot \frac{dx}{dt}}{K_{LM} \cdot M} \qquad \text{where } K_{LM} \text{ is } K_M/K_L$$

and this can be used to calculate the response *x(t)*. For single pulse loading, such as blast, normal levels of structural damping are rarely significant to the maximum response and are difficult to assess, so damping is often ignored.

The accuracy of the method depends upon the deflected shape used to calculate the coefficients. Best accuracy will be obtained with a deflected shape close to the dynamic deflected shape that can be expected for the member and loading. In practice, results accurate to within a few percent have been obtained from transformation factors based upon the incremental deflected shape under a static load of the same distribution. As the elastic, elasto-plastic and plastic deflected shapes of members are different, the SDOF coefficients vary with the deformation state of the member. Alternatively, the mode shape of the fundamental mode of free vibration has also been used as the deflected shape for linear systems.

The SDOF method also includes coefficients to calculate a reaction history from factored combinations of the internal resistance and the applied load:

$$V(t) = V_R \cdot R(x(t)) + V_F \cdot F(t) \qquad \text{Where } V_R \text{ and } V_F \text{ are coefficients}$$

These coefficients are derived from an equilibrium calculation of all of the external and internal forces, including the momentum forces, on the basis that the acceleration distribution is proportional to the deflection distribution.

The derivation of SDOF transformation factors and reaction coefficients for beams or one-way spanning slabs, with various support conditions and loads, is straightforward and forms part of many structural dynamics courses. The derivation of factors and coefficients for two-way spanning members, however, is more complex.

For plates and shells in plastic bending, yield line theory can be used to derive simple plastic mechanisms and the associated deflected shapes and transformation factors. However, even the static deflected shape of a two-way spanning plate or shell is difficult to derive for the calculation of transformation factors, and the combination of deflected shape, bending moment distribution and reaction distribution required to calculate elastic reaction coefficients is sufficiently complex that up to now only one set of results appears to have been derived and published.

3. Current SDOF parameters for slabs, walls and windows

Biggs provides tables of parameters for simply-supported two-way slabs in the elastic and plastic ranges, and for fully fixed two-way slabs in the elastic, elasto-plastic and plastic ranges. He gives as his source a 1957 US Army Corps of Engineers (US ACE) Engineering Manual: EM 1110-345-415 “Design of Structures to Resist the Effects of Atomic Weapons”.

Although this publication has been long since superseded, these tables have been incorporated in all subsequent US ACE manuals for resistance of the effects of atomic and conventional weapons up to the current publication, PSADS (3), in 1998. In addition to the tables referenced by Biggs, tables for slabs with some edges fixed and for a fixed slab with one unsupported edge are included. The tables cover slabs with aspect ratios λ, the ratio of the slab sides, between square (1:1) and 1:2 or 2:1.

These tables have found their way into other Manuals (4), other textbooks, and SDOF software. (5)

Apart from one digit (which may be a typographical error), the elastic transformation factors and reaction factors appear to be unaltered from 1964 to 1998, and the slabs with 4 edges supported have elasto-plastic factors equal to the same elastic factors for the simply supported slab.

Biggs includes the elastic and elasto-plastic spring constants in the same tables as the SDOF factors. Although these are given separately in PSADS these are also unchanged, except that the three significant figure fixed edge elastic spring constants have been rounded to two significant figures.

This gives the appearance of a solid and consistent body of data, which has been the established basis of SDOF analysis for over 40 years. Slabs and walls with λ greater than 2:1 have been designed as one-way spanning, and slabs and walls with λ between 2:1 and 1:2 have been designed to the two-way slab data. However, this approach seems to be all based upon one set of calculations in the 1950s, presumably undertaken effectively by hand.

Details of the elastic analysis used in this historic work and the assumptions that underlie it are difficult to find. Biggs indicates that the elastic factors were based upon approximations to the classical plate theory for deflections, but gives no indication of the Poisson's ratio assumed for the analysis. PSADS indicates that the equations for the spring constants are based on elastic uniform plate theory, and that the coefficients given are for a Poisson's ratio v of 0.15. The adjustment for v of 0.3 is also given. However, the SDOF coefficients are listed for a v of 0.3. This suggests that the data is not quite as consistent as it might at first appear.

There are also contradictory transformation factors in the literature and in use. In the US ACE Manual TM 5-1300 (6) the K_{LM} transformation factor for a square slab is given as 0.63, rather than 0.67 in refs (1), (3) and (4), and is assumed to interpolate linearly to the one-way transformation factor at an aspect ratio of 2, rather than the two-way factor in refs (1), (3) and (4).

Mayor and Flanders (7), in deriving transformation factors for walls with openings for use in the computer program BLAST for the US Department of Transportation, also calculated them for walls without openings, and for aspect ratios λ between square and 2:1. A fairly coarse finite element (FE) analysis was used to calculate the transformation factors for simply supported walls, but the K_L factor was also checked using the first 30 terms in the classic Navier equation for plate deflection. The alternative results for simply supported slabs and walls are compared in Table 1.

Source	SDOF transfo-rmation factors	Aspect Ratio μ					
		1.0	0.9	0.8	0.7	0.6	0.5
Biggs, and refs, (3) & (4)	K_L	0.46	0.47	0.49	0.51	0.53	0.55
	K_M	0.31	0.33	0.35	0.37	0.39	0.41
	K_{LM}	0.67	0.70	0.71	0.73	0.74	0.75
TM 5-1300	K_{LM}	0.63	0.63	0.67	0.70	0.74	0.79
Mayor & Flanders	$K_{L\ (Analysis)}$	0.419	0.419	0.420	0.423	0.427	0.435
	$K_{L\ (Numerical)}$	0.416	0.416	0.417	0.419	0.423	0.431

	K_M (Numerical)	0.257	0.257	0.258	0.260	0.264	0.271
	K_{LM} (from numerical)	0.618	0.618	0.619	0.621	0.624	0.629

Table 1 – SDOF Transformation Factors for simply supported slabs and walls.

These show a substantial difference between alternative sources.

TM5-1300 only considers reactions in the plastic flexural mode, which it assumes are dependent only on the resistance. Mayor and Flanders do not calculate reactions. The only published source of reaction coefficients in the elastic flexural mode are therefore the original US ACE figures, even though the analysis upon which they are based appears to be open to challenge.

The classical elastic plate theories, by Navier and others, are equations for small deflections, of the order of 0.5 times the plate thickness, because they ignore the membrane effects that become increasingly significant with increasing deflections. This is appropriate for the original application of the SDOF method (i.e. thick reinforced concrete slabs and walls) where plastic response will take over at deflections of only a few percent of the wall thickness. However, the classical elastic theories are unsatisfactory for thinner members such as steel plates or glass panes, where the elastic deflection of two-way members can be many times the thickness. They are particularly unsatisfactory for elastic-brittle glass panes where the error in the elastic response is not diluted by a subsequent long plastic response.

The results of non-linear FE analysis of glass panels by Moore at the Jet Propulsion Laboratory, California, as reported by Meyers (8), have been used to substitute non-linear resistance functions for the elastic spring constants, and non-linear failure criteria, for aspect ratios λ between square and 4:1 in analysis of glass panes under blast loading. This approach was incorporated in TM 5-1300 in 1990, and has been widely adopted for analysis of windows. However, it is still generally used with the Biggs or TM 5-1300 transformation factors rather than factors based on the non-linear deflected shapes, for lack of any better information.

Although information on elastic distribution of reactions along the edge of a simply supported pane is included in TM 5-1300, it is based on a simplified small deflection static distribution of reaction applied to a maximum dynamic reaction assumed to be equal to the resistance, with no contribution from the applied loading.

4. Small deflection analysis

In this paper three types of small deflection analysis have been undertaken to calculate spring constants, SDOF transformation factors and reaction coefficients for simply supported plates. Two analyses are based on classical elastic plate formulae described by Timoshenko and Wowinowsky-Krieger (9), the Navier and Levy formulae, dating from 1820 and 1899 respectively. The third is based on a linear elastic finite element analysis.

4.1 Analysis using the Navier formulae

The Navier formulae for a uniformly loaded plate are based on the exact solution for the double Fourier deflected shape of a rectangular slab under a two dimensional sine wave shaped load distribution, together with the bending, torsion and reaction distributions derived from this. This exact solution can be extended to apply to any loading distribution of *n* by *m* half sine waves. A uniformly distributed load can be represented as a series of sine wave loads with *n* and *m* independently increasing from 1 to infinity, with amplitudes of each coefficient a function of *n* and *m*. The deflection *w* of a uniformly loaded rectangular plate of size *a* by *b* at any point *(x,y)* can therefore be given by an infinite double Fourier series in *m*, *n*, *x* and *y*, for odd values of *m* and *n*:

$$w = \frac{16a^4 p_0}{\pi^6 D} \cdot \sum_m \sum_n \frac{\sin\frac{m\pi x}{a} \sin\frac{n\pi y}{b}}{mn(m^2 + \frac{a^2}{b^2} \cdot n^2)}$$

where p_0 is the pressure and $D = \frac{E \cdot I}{(1-\nu^2)}$

As the value of the terms decrease with increasing *n* and *m*, the series is convergent and a finite number of terms can be used to obtain results to a chosen accuracy. Using Mathcad (11) to undertake the calculations, including a numerical integration across the surface of the plate, the spring stiffness and transformation factors have been calculated. For m and n up to 11, the first 36 terms will give at least 3 significant figure accuracy for $\lambda=a/b$ between ¼ and 4, and 4 significant figures between ½ and 2. These are consistent with the K_L values produced by Mayor and Flanders from a similar calculation with 30 terms, and have a comparable relationship with their FE terms. They differ substantially from the values in refs (1), (3) and (4), being lower and less sensitive to aspect ratio.

Similar calculations have been undertaken to derive the moment across the centrelines, the reactions along the sides, and the location of the centroids of the deflection, moment and reactions for a quarter span. However, the reactions in particular are sensitive to the accuracy of the loading series close to the supports, and so require very large numbers of terms to converge. With *m* and *n* up to 401, giving 40,000 terms of the series, the sum of the reactions is still 0.2% less than the loading, indicating an accuracy less than 3 significant figures, Convergence is very slow as the last 30,000 terms only halve the error of 0.4% for 10,000 terms.

The reaction coefficients are calculated from simultaneous equations using the above values, and this can amplify or reduce the error in some circumstances. The comparison of the sum of the dynamic reaction coefficients with the static reaction gives an error of 0.1% for each side of a square panel relative to the static reactions and up to 0.4% for the short side reactions with an aspect ratio λ of 2:1. Sensitivity studies show that this error derives mainly from the reaction and reaction centroid calculations. Even with the enormous number of terms used, the coefficients are only reliable to about 2 significant figures. However, the values calculated are substantially different from those in refs (1), (3) and (4), with higher force terms and lower resistance terms.

Fourier series, rather flatter than the single half sine wave assumed by TM5-1300, give the formulae for the reactions along each side. The reverse reaction at the corners

is numerically equal to the torsion from the two adjacent sides, which are equal at the points of right angle corners.

Clearly, the Navier method, requiring thousands of terms for reasonable accuracy of some coefficients is not a candidate for the method used by the US Army Corps of Engineers for manual calculations in the 1950s. The fundamental free vibration mode shape is equal to the first term of the Navier deflection formula, which would give lower transformation factors that are independent of λ. This is also clearly not the basis of the manual calculations.

4.2 Analysis using the Levy formulae

The Levy formulae were developed to converge faster than the Navier formulae. It is based on calculating the deviations from the one-way deflected shape using an infinite single Fourier series containing a number of hyperbolic terms. The one-way-spanning deflected shape can be kept separate or can be expressed as a term in the single Fourier series:

$$w = \frac{4 \cdot p_0 \cdot a^4}{\pi^5 \cdot D} \cdot \sum_{m=1}^{\infty} \frac{1}{m^5} \cdot \left[\begin{array}{l} 1 - \left[\dfrac{\dfrac{m \cdot \pi \cdot b}{2 \cdot a} \cdot \tanh\left(\dfrac{m \cdot \pi \cdot b}{2 \cdot a} \right) + 2}{2 \cdot \cosh\left(\dfrac{m \cdot \pi \cdot b}{2 \cdot a} \right)} \cdot \cosh\left(\dfrac{m \cdot \pi}{a} \cdot y \right) \right] \ldots \\ + \dfrac{\dfrac{m \cdot \pi \cdot b}{2 \cdot a}}{2 \cdot \cosh\left(\dfrac{m \cdot \pi \cdot b}{2 \cdot a} \right)} \cdot \dfrac{2 \cdot y}{b} \cdot \sinh\left(\dfrac{m \cdot \pi}{a} \cdot y \right) \end{array} \right] \cdot \sin\left(\frac{m \cdot \pi}{a} \cdot x \right)$$

for a panel from *+b/2 to –b/2* and from *a* to *0*, where the 1 inside the square bracket covers the one-way span deflected shape.

The spring stiffness has been calculated in Mathcad to three significant figures using 4 terms of this series. However the higher terms are required mostly for the accuracy of the one-way span, as with this element extracted from the series and the exact deflection for the midspan substituted, a spring stiffness to three significant figures was calculated for aspect ratios $\lambda=a/b$ between square and 2:1 with only one term of the series.

The series expression was found the more practical for calculation of the transformation functions, but even with this, 4 terms of the Levy formula were sufficient to give the same accuracy as 36 terms of the Navier formula.

The full analysis of the reaction coefficients has not been undertaken using this approach because the total reactions for aspect ratios λ of ¼ to 4 can only be calculated for the first 7 terms in Mathcad. For higher terms, an intermediate value in the hyperbolic equation is greater than 10^{37}, causing an overflow error message. For 7 terms the error in the static loading is 0.16%, which is similar to the accuracy given by 40,000 terms of the Navier series. For aspect ratios λ between ½ and 2 up to 10

terms of the series can be used before overflow occurs in Mathcad, and the error reduces to 0.05%. This would give an improvement in accuracy over the Navier series as well as a massive reduction in calculation effort. However without implementing the algorithm in higher precision calculations, the accuracy is limited to three significant figures by the large numbers generated by the hyperbolic functions in the formula.

Although the Levy formulae could have been used to produce the US Army Corps of Engineers tables by hand calculations in the 1950s there is no indication that they were. The discrepancy between the SDOF transformation values in the different methods cannot be explained by any variation in the number of terms used in the Levy series. Using fewer terms in the series or using fewer points in a numerical integration over the surface would result in a lower value of K_L or K_M, and the tables in refs (1), (3) and (4) give higher values.

4.3 Analysis using linear FEA

Linear FE analysis was undertaken using thin shell, 8 noded, semi-loof elements in the LUSAS general FE program (10). Quarter panel models were analysed between two supported edges and two lines of symmetry. In linear analysis, panels were analysed with aspect ratios λ between 1 and 0.5, directly corresponding to the aspect ratios in the tables in refs (1), (3) and (4), although small deflection non-linear calculations also covered λ between 1 and 4. A uniform mesh of square elements was used with a minimum of 10 elements in each direction, increasing to 20 by 10 for the 0.5 aspect ratio and 10 by 40 for the aspect ratio of 4.

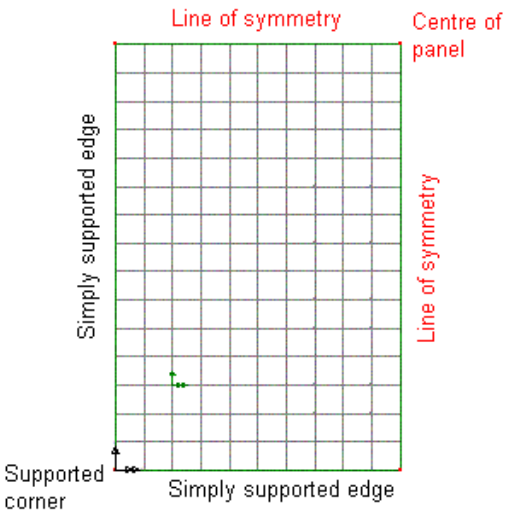

Figure 2 – Typical regular mesh quarter panel model, for λ of 1.5

Numerical output from the FE analyses was exported to Excel for post processing. Deflections and back surface principal tensile stresses were analysed for all nodes, and reaction forces and moments at all supports, which include the nodes on the boundaries modelling the axes of symmetry.

Edge conditions of simple support were analysed for Poisson's ratios v of 0.15, 0.22 and 0.3, corresponding to reinforced concrete, glass and steel. Full moment fixity but

no in-plane edge restraint was also analysed for reinforced concrete, corresponding to the results in refs (1), (3) and (4).

The spring constant was calculated from the maximum deflection at the centre point of the panel, and the transformation factors were calculated using all the node deflections and the trapezoidal rule for numerical integration. The maximum stress at mid-span was used to calculate a coefficient for the maximum pure elastic resistance, although this is not equivalent to the plastic or elasto-plastic transition resistances presented in refs (1), (3) and (4). The reactions and moments around the perimeter of the model and the deflections of the whole model were used to calculate parameters for the reaction coefficients, with a Mathcad "Add-in" to Excel used to solve the simultaneous equations.

For 6 significant figure data exported from LUSAS, the static reactions are within the rounding error of the applied loads, and all the combined dynamic coefficients are likewise within 1.34 in 10^{-6} of the static reactions on each side. However, this close equilibrium does not take account of the discretization error of the element mesh. Changing the mesh of a square panel from 10 elements by 10 to 20 by 20 affected the fifth significant figure of some results, as did the secondary effects in a small amplitude non-linear analysis. The results are considered reliable to 4 significant figures.

4.4 Conclusions from small deflection analysis

The three forms of analysis used give results that are consistent with each other to at least 3 significant figures. The results calculated by FE analysis have a greater accuracy as well as covering a greater range of cases. The results presented in Table 2 are for a simply supported slab with Poisson's ratio ν of 0.15 and are appropriate for the analysis of reinforced concrete walls and slabs.

Aspect ratio	Spring Constant	Elastic Resistance	Transformation Factors			Reaction Coefficients			
			K_L	K_M	K_{LM}	V_{SF}	V_{SR}	V_{LF}	V_{LR}
1	251.9	11.74	0.418	0.262	0.627	0.137	0.113	0.137	0.113
0.9	229.3	11.43	0.418	0.263	0.628	0.133	0.097	0.140	0.130
0.8	212.2	11.35	0.420	0.264	0.627	0.128	0.081	0.142	0.149
0.7	200.9	11.53	0.422	0.266	0.629	0.122	0.064	0.143	0.171
0.6	196.7	12.13	0.427	0.270	0.632	0.115	0.046	0.143	0.196
0.5	202.0	13.41	0.435	0.278	0.639	0.106	0.029	0.142	0.222

Table 2 – Simply supported analysis for ν of 0.15

Except for one value, the spring constants agree with the US ACE tables to three significant figures. The fully elastic resistance is between 49% and 64% of the fully plastic resistance, which appears reasonable. However, the transformation factors are significantly lower and less sensitive to changes in aspect ratio than those from refs (1), (3) and (4). The reaction coefficients also are significantly different, with higher force coefficients and lower resistance coefficients than refs (1), (3) and (4), although the static ratio between the long and short side reactions is similar.

There is agreement with the K_{LM} value in TM 5-1300 of 0.63 for a square panel, to 2 significant figures. However, the interpolation to a one-way span at a 2:1 aspect ratio is clearly not supported; it would have been more accurate to keep the K_{LM} value constant.

The results agree to within 0.25% with the analytical calculations of Mayor and Flanders. Their FE analyses were apparently performed with a coarser mesh of 4 noded elements, so the difference between the results is likely to have arisen from discretization error in their analysis. However, the trend in the results is consistent.

It is recommended in SDOF calculations that the values in Table 2 be used for the elastic stages of simply-supported reinforced concrete slabs and walls in lieu of the tables in Biggs, PSADS or TM5-1300. The same figures should also be used for the elasto-plastic stages of SDOF calculations of walls and slabs with initial edge fixity.

Aspect ratio	Spring Constant	Elastic Resistance	Transformation Factors			Reaction Coefficients			
			K_L	K_M	K_{LM}	V_{SF}	V_{SR}	V_{LF}	V_{LR}
1	808.6	24.51	0.308	0.183	0.593	0.134	0.116	0.134	0.116
0.9	741.3	23.55	0.309	0.183	0.594	0.132	0.095	0.136	0.137
0.8	701.8	23.66	0.311	0.185	0.596	0.128	0.074	0.137	0.161
0.7	693.4	24.72	0.317	0.190	0.600	0.123	0.054	0.138	0.185
0.6	723.3	27.37	0.328	0.199	0.608	0.117	0.034	0.138	0.211
0.5	807.3	32.52	0.347	0.216	0.624	0.107	0.018	0.138	0.236

Table 3 – Analysis with moment fixity on all edges, for v of 0.15

The results presented in Table 3 for a fully fixed edged slab also show a similar spring stiffness to the Biggs tables, consistent within 2 significant figures, but generally not to 3 significant figures. The transformation factors and reaction coefficients differ from refs (1), (3) and (4), with the pattern of differences similar to that for the simply supported analysis. It is recommended that these values should be used for fixed or continuous concrete slabs and walls in lieu of the fully fixed tables in Biggs, PSADS or TM5-1300.

Similar results can be calculated for other support conditions.

For the original application of the SDOF method, these discrepancies are not of great significance. For thick slabs and walls subject to severe blast or shock loads, a design with a high plasticity ratio is expected and the elastic stage could be omitted with errors of only a few percent. A discrepancy of 15% in the elastic transformation factors would result in a change to the overall response of well under 1 percent, and this is small compared to other approximations and uncertainties. If this were the only application for the SDOF method, the significance of the discrepancies identified would be small. However, over the years the published data has been employed for a much wider range of applications.

Even for concrete walls there are many applications where the acceptable plastic rotations have to be reduced for other reasons, such as to prevent damage to Electromagnetic Pulse or Electromagnetic Emission shields supported by the structure, or to maintain continuous operation through and after an explosive event without the need of subsequent closure for structural repairs. For such a design, the discrepancy in elastic SDOF properties will be of greater significance, as much because of the change in the natural period of vibration that results and the change in the reactions as for the change in the maximum response.

The alternative analyses undertaken show that the spring constant varies with Poisson's ratio, as noted in PSADS, while the transformation factors are unaltered. The reaction coefficients are affected by the value of Poisson's ratio, but in a more complex way, with a greater reaction contribution with increased aspect ratio for square panels, but a reduced reaction contribution for an aspect ratio of 0.5.

Small deflection analysis of this type is likely to be inappropriate for the elastic response of other types of structure such as steel plates or glass window panes, where the slender members can deflect to many times their own thickness before the elastic limit is exceeded. Applying tables of small deflection SDOF parameters would be misleading for these materials where large deflection theory should be applied.

5. Large deflection analysis of windows

Non-linear plate and shell theories do exist, but they are generally limited to moderate deflections by the assumption that the bending deflected shape can be used, and additional stiffness due to the membrane stresses can be grafted on. Formulae from these theories can predict the static behaviour of square panels, but they can have problems with panels of high aspect ratio. They will not be useful in evaluating large deflection SDOF parameters that will be sensitive to the changes in deflected shape induced by the membrane effects.

This leaves non-linear numerical analysis as the only suitable tool for investigating large deflection SDOF analysis of elements that can undergo large elastic deflections, such as glass panes and steel plates.

A series of non-linear FE analyses of simply supported glass panes was undertaken using thin shell, 8 noded, semiloof elements in the LUSAS general FE program. Quarter panel models were analysed between two supported edges and two lines of symmetry.

The analyses were used to cover the same range as that analysed by Moore and incorporated in TM5-1300, for aspect ratios λ from 1 to 4, and for non-dimensional loading L given by:

$$L = p \cdot \frac{12 \cdot (1 - \nu^2)}{E} \cdot \left(\frac{b}{t} \right)^4 \qquad [10<L<100{,}000]$$

where p is the applied pressure, b the shorter span and t the thickness. A small deflection non-linear analysis with L = 1 or 5 was included for comparison with linear

analysis, and where convergence could be achieved an analysis at L=200,000 was also included. In the non-linear analyses successive load increments were analysed at factors of 1, 2 and 5 times successive powers, to provide near equal spacing of data on a logarithmic scale.

For the models analysed the span b was set at 1m, and t was generally chosen as 3.57383mm, so that for normal glass properties of E= 70 MPa and ν= 0.22 the non-dimensional load L is equal to the pressure p. This gives a slenderness t/b of approximately 1:280, corresponding to a 6mm pane over a span of 1.67m, which is at the slender end of practical glazing.

The elements and loading type selected produced follower forces in a non-linear analysis, as is appropriate for a true pressure loading on a surface with large deflection. However, a fully Eulerian solution was not available in LUSAS where the follower forces are in equilibrium for the deformed shape of that increment. Instead, an "Incremental Lagrangian" solution was used, where the follower forces are based on the deformed shape of the previously converged increment. To minimise the difference, intermediate loading steps were set in the calculation with a loading equal to 99% of that of the load steps that were post-processed.

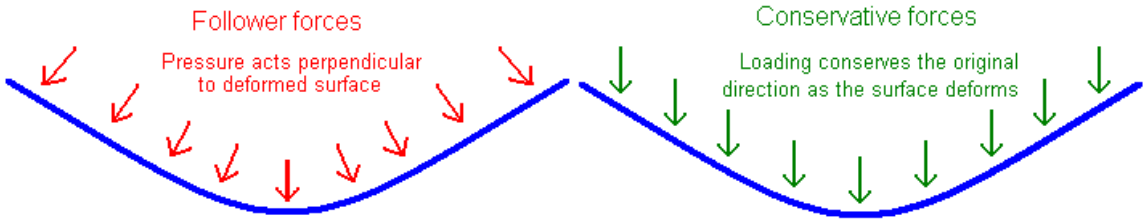

Figure 3 – Large deflected shapes contrasting follower forces and conservative forces

5.1 Non-linear deflection and maximum stress

Numerical output from each significant load increment was exported to Excel for post processing. This was similar to the data for the small deflection analyses, except that the deflections in all 3 axes was used, not just in the loaded directions.

Charts of non-dimensional centre deflection: $$d = \frac{x}{t} = \frac{x}{d} \cdot \frac{b}{t}$$

and non-dimensional stress: $$f = \sigma \cdot \frac{12 \cdot (1 - \nu^2)}{E} \cdot \left(\frac{b}{t}\right)^2$$ (where σ is the actual stress)

plotted against L are shown as Figures 4 and 5. These directly correspond to the charts after Moore in TM5-1300, and are the non-linear equivalents of the spring stiffness and elastic resistance calculated for the linear analysis.

The initial analysis was undertaken with the same uniform mesh as the static analysis. However, sensitivity analysis showed that mesh refinement was required to produce a consistent value of stress in the corner of the panel, due to the high local stress gradient in the anticlastic surface close to the corner. To analyse the stresses a refined

mesh was used, with three times as many elements along a side, and with a grading to make the largest elements 4 times the size of the smallest elements at the corner. This makes the largest elements in the centre of the panel about half the size of the uniform grid in each direction, and the smallest elements in the corner about 1/8 of the size.

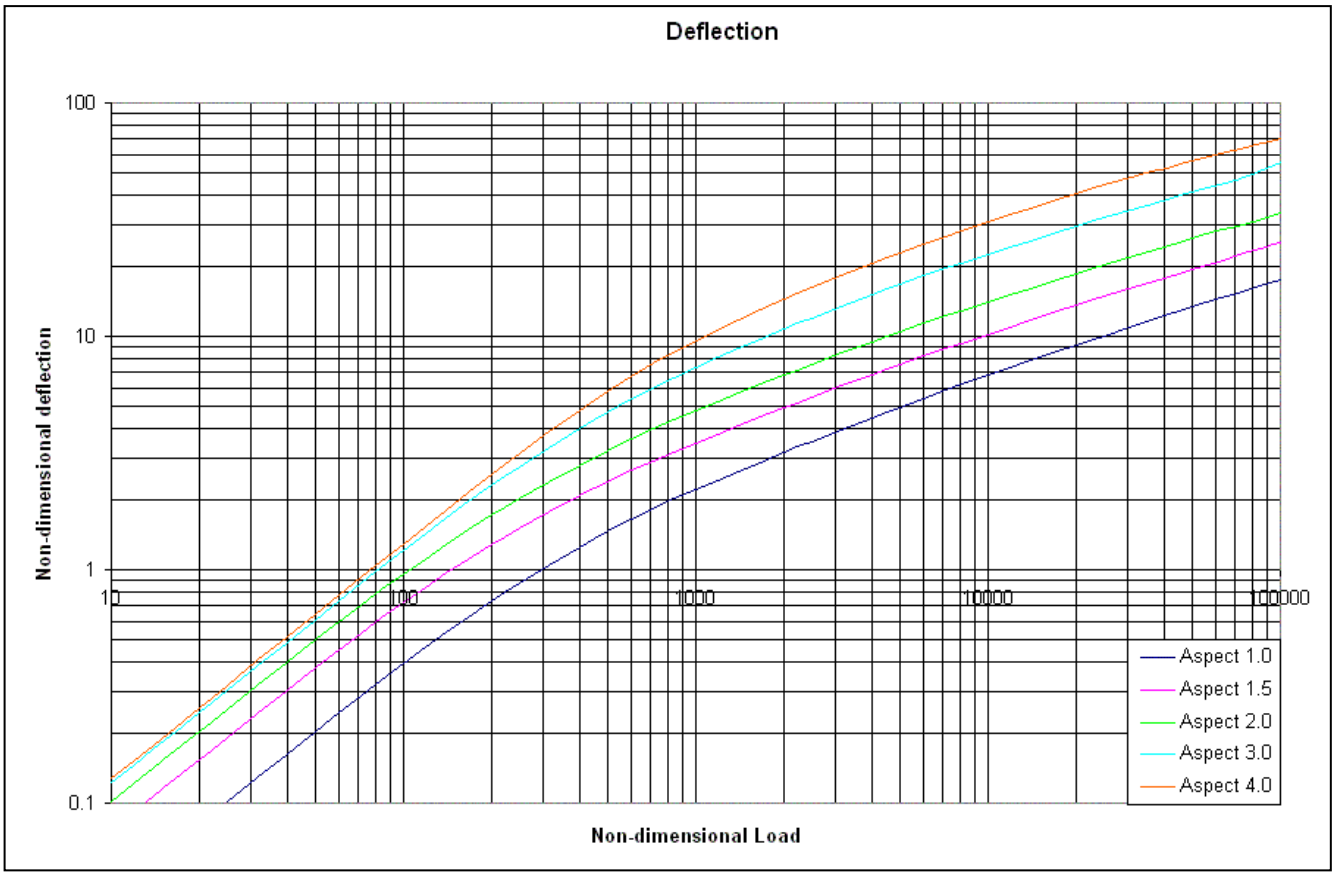

Figure 4 – Deflections of simply supported glass panes

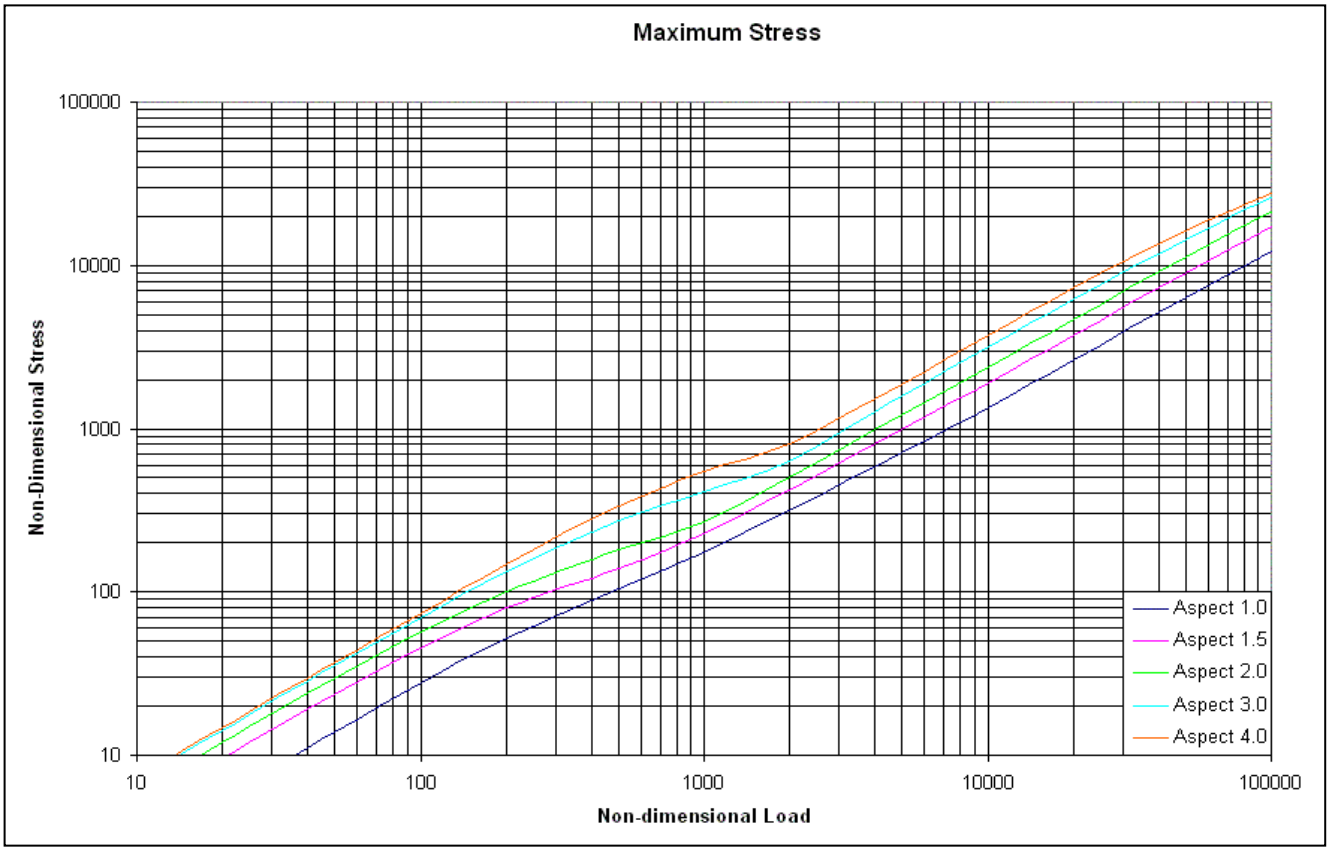

Figure 5 – Maximum stress in simply supported glass panes

The sensitivity analysis shows that, for λ=1 and L=100,000, halving the size of the uniform grid will increase the deflection by about 0.64%, and that the introduction of the refined mesh illustrated in Figure 6 adds only a further 0.08%.

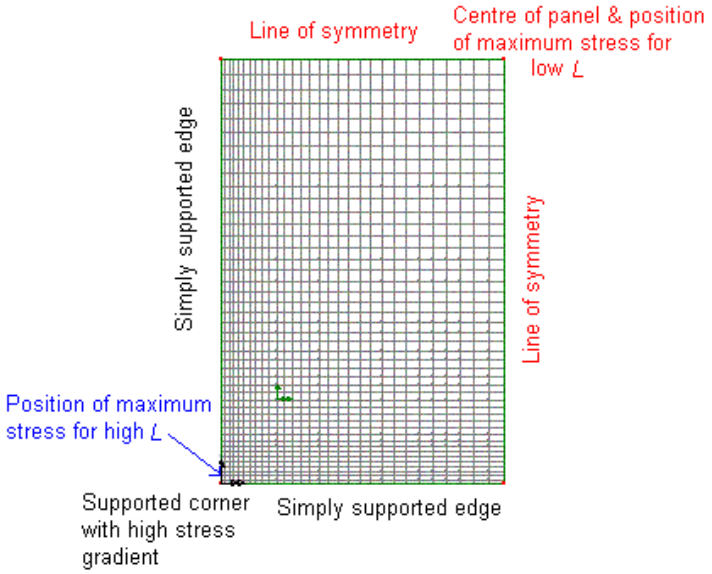

Figure 6 - Typical refined mesh quarter panel model, for λ of 1.5

For the same case, a first level of mesh refinement with 50% more elements than the uniform grid, and the corner elements about ¼ of the uniform mesh size results in a substantial reduction in the maximum stress. However, doubling the number of elements to give corner elements $\frac{1}{8}$ of the uniform mesh, as illustrated in Figure 6, results in a further 12% reduction. This demonstrates an unacceptable error in the coarser refined mesh. In contrast increasing the gradation of the refined mesh further to reduce the mesh in the corner to about $\frac{1}{11}$ of the uniform mesh size decreases the maximum stress by only 0.6%, demonstrating that the error in the second level of refinement is acceptably small.

The results of these analyses are similar, but not identical, to the charts in TM 5-1300 after Moore. The deflections at the lower loaded end are identical, but the maximum deflections at the upper end of the scale are about 8% lower for the square panel, and about 10% for λ of 4. Although mesh refinement from this analysis would reduce the discrepancy, the effects are small and diminishing, unlikely to make more than 1% total difference.

The source of the remaining 7% discrepancy is unclear at present, but might be explained by detailed differences in the FE models. For example, if Moore were concerned with the effect of acceleration forces rather than pressure forces, he would not have included follower forces in his model. An analysis for λ=1 and L=100,000, using "Total Lagrangian" non-linear control which creates conservative rather than follower forces, shows a 3% increase in deflection. However the maximum stress also increases by 12.5% for this analysis.

The maximum stresses in the centre of the pane are indistinguishable from Moore's, but maximum stresses found away from the centre are significantly higher than given by Moore for the corner. The introduction of the refined mesh reduces the maximum stress for λ=1 and L=100,000 from almost double Moore's value to 1.31 times, or 1.46 times with conservative forces from "Total Lagrangian" control.

However, for high values of L the maximum stress does not occur at the corner node, as assumed by Moore and as shown by coarser mesh FE analysis, but on the supported edge about 1.4% of the span from the corner.

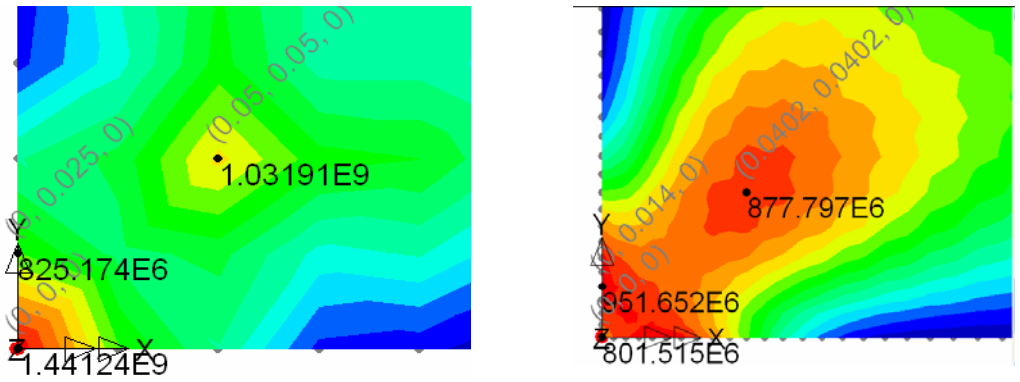

Regular Mesh Refined Mesh

Figure 7. – Corner stresses in Regular and Refined meshes, μ=1, L=100,000

Unlike the 8-noded shell element, mesh refinement for 4-noded shell elements converges towards the true maximum stress from lower bound values. For λ=1 and L=100,000 a 4 noded analysis with conservative forces will match Moore's corner stress with a 24 x 24 element mesh. However, the maximum stress is 13.5% higher.

If the mesh is refined, the corner stress first rises and then starts to drop, but the maximum stress continues to rise. Although the corner stress for a 30 x 30 graduated mesh with conservative forces is only 1% higher than for the 24 x 24 mesh, the maximum stress is 29% greater, 88.4% of the maximum stress of the refined 8-noded analysis with conservative forces and 99.5% of the maximum stress of the refined 8-noded analysis with follower forces.

As 4-noded elements are significantly less accurate than 8-noded elements with the same mesh density, it is probable that most of the remaining discrepancy lies in the 4-noded element analysis.

It appears likely that Moore's analysis was based on a mesh of 4-noded elements, and it is possible that the plateau of the corner stresses seen here may have convinced Moore that the mesh that he had used was sufficiently refined. However, consideration of nodes away from the corner could have increased the maximum stresses by more than 30%. Moore's analysis may have significantly exaggerated the deflection of glass panes before the failure stress was reached.

It is considered that the use of 8-noded elements, mesh refinement and testing for maximum stress throughout the model has resulted in a significant improvement in

accuracy for this analysis over that reported to have been undertaken by Moore, and the use of follower forces is considered to have produced a more appropriate model for blast pressure loading.

Figure 8 – Deflection-Stress plot of simply supported glass panes

For SDOF analysis the deflection curve can be used to define a non-linear resistance function for a glass pane. Plotting the deflection against the stress, as Figure 8, allows the cracking deflection of the glass to be found.

5.2 Non-linear transformation factors

The SDOF transformation factors were calculated for each loadstep. The deflections of the nodes around the uniformly sized elements were weighted in accordance with the trapezoidal rule for numerical integration and K_L and K_M were calculated.

Above a loading of L=1000 a further weighting was included in the calculation. As the deflection increases the slope of the element becomes significant, and the projected surface perpendicular to the overall direction of loading reduces. For the calculation of K_L for higher loading, the nodes' weightings were adjusted by the projected areas of the associated elements. A linear approximation was used based upon the relative X and Y axis displacements of adjacent nodes nearer the lines of symmetry, and with symmetry nodes weighted as unity. Below L=1000, where this modification affected the 4th or 5th significant figure, this weighting was ignored. At L=100,000 it affects the 2nd or 3rd significant figure.

As the mass of the elements is not altered by their inclination, this weighting was not applied to the calculation of K_M. As a result, the incorporation of this additional weighting in K_L affects the 2nd or 3rd significant figure of K_{LM} for high loading levels.

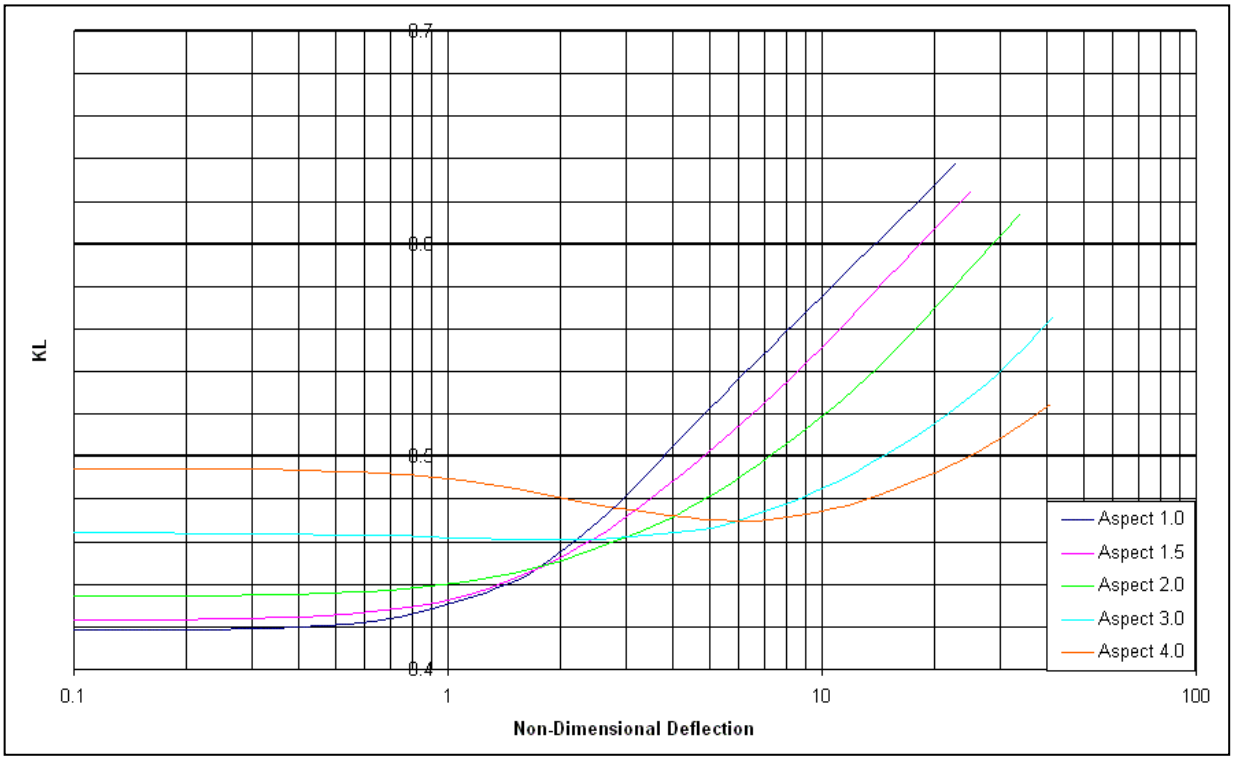

Figure 9a Load transformation factors for simply supported glass panes

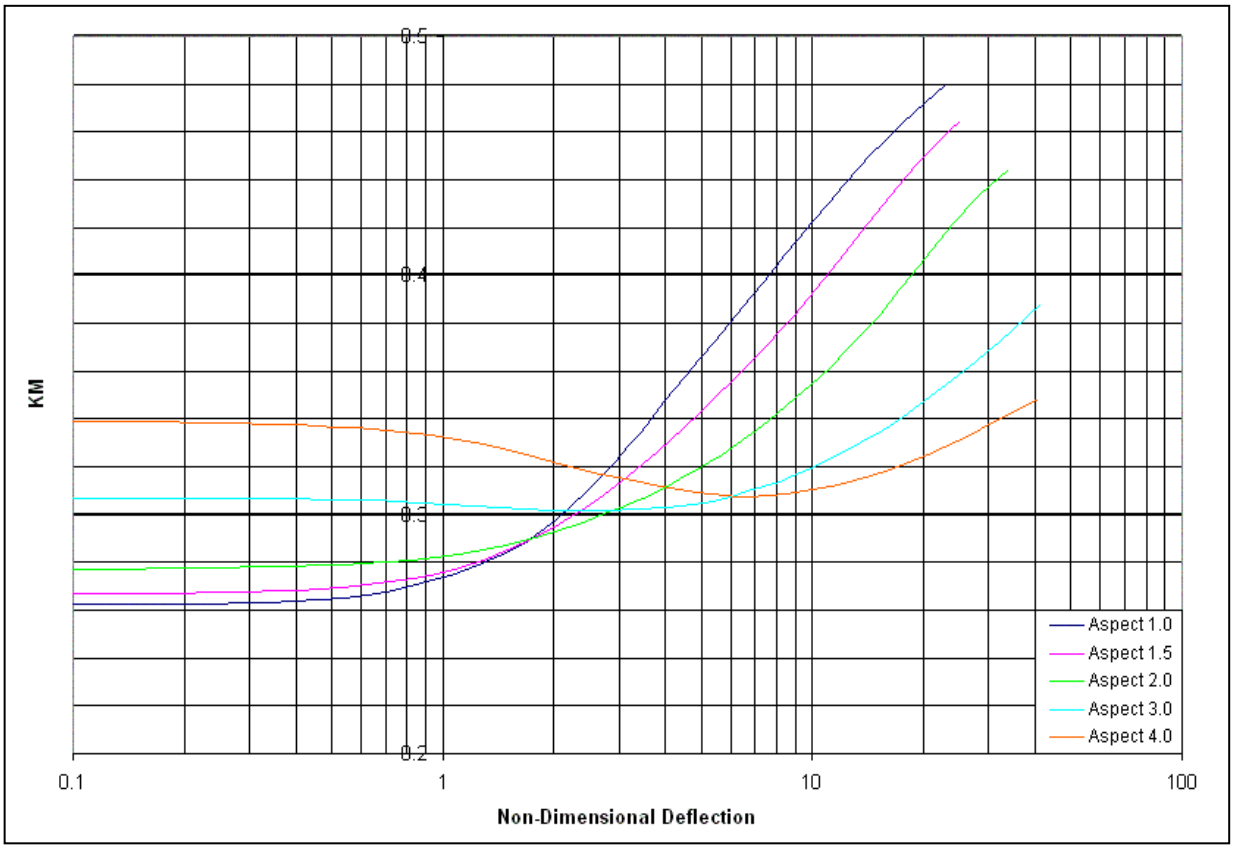

Figure 9b Mass transformation factors for simply supported glass panes

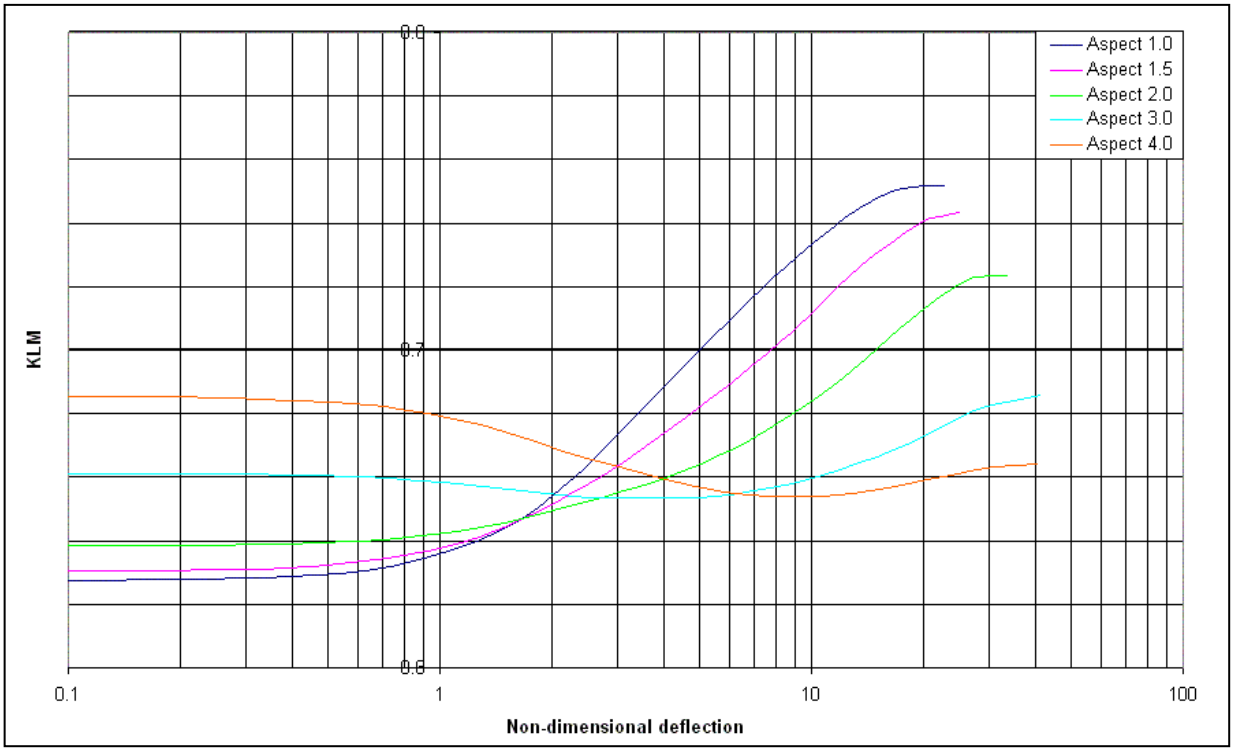

Figure 9c – Load-Mass transformation factors for simply supported glass panes

As can be seen from Figure 9 the membrane effect is negligible for deflections less than half the glass thickness t, and small for deflections up to t. However, for greater deflections the change in the K_{LM} factor is substantial, particularly for low aspect ratios where the membrane effect is at its strongest.

5.3 Non-linear reaction coefficients

For large deflections, the terms used in the differential equations to calculate the reaction coefficients change significantly from the small deflection case, and secondary effects that are zero in a linear analysis and negligible in a small deflection non-linear calculation can substantially influence the results. These have been included simply and locally in each element by the FE analysis and produce an overall effect on the equilibrium state reached. However, in the post-processing it has been necessary to identify the overall effect from the local effects at each node to incorporate them into the two parallel simultaneous equilibrium calculations for force and resistance coefficients.

Secondary effects that have been incorporated into the post-processing calculations for the non-linear analyses include:

- The horizontal movement of the centroid of acceleration and damping forces due to horizontal deflection of elements and edge pull-in. (for L=1000 or more)

- The level of the deformed pane at the centroid, about which moments are taken.

- The horizontal components of applied pressure due to the follower forces, and the levels at which they act.

- The internal resistance due to the membrane forces acting at different levels in opposition, and the net force (balancing the horizontal pressures) and the level at which it acts.

- The modified lines of action of the reactions as the edge of the pane pulls in.

A number of these have been only approximated in the calculations with linear or first order solutions that do not fully account for the effects within the curved 8-noded elements. In addition, there will be other minor effects that have not been covered in the post-processing. All of these will contribute to error in the terms in the simultaneous equations. These incorporate the calculations based on small differences between relatively large numbers, so the reaction coefficients are prone to be inaccurate, particularly at large deflections when the secondary effects are at their greatest.

This has been monitored by calculating the ratio between the relevant dynamic reaction coefficients and the static reaction on the long and short sides and overall. Results have only been included in the output if the dynamic to static ratios are within 2% of unity. This has excluded some results for L=50,000 and 100,000, when the aspect ratios are high.

The general pattern is for the short side coefficients to be upper bound and the long sides to be lower bound, with the balance resulting in a smaller, lower bound error overall. The nature of the secondary effects, the greater error amplification in the simultaneous equations and the sharp changes in trends on graphs when errors increase all indicate that force coefficients appear to contribute most of the error.

However, high deflection coincides with high resistance, and is associated with blast loading at a time after the blast peak has passed. Conversely, the peak loading occurs when deflection is small and the post-processing error is orders of magnitude smaller. Both of these indicate that in practice the errors in calculation of reactions arising from error in the coefficients in Figures 10 and 11 will be significantly less than 2%.

However, high deflection coincides with high resistance, and is associated with blast loading at a time after the blast peak has passed. Conversely, the peak loading occurs when deflection is small and the post-processing error is orders of magnitude smaller. Both of these indicate that in practice the errors in calculation of reactions arising from error in the coefficients in Figures 10 and 11 will be significantly less than 2%.

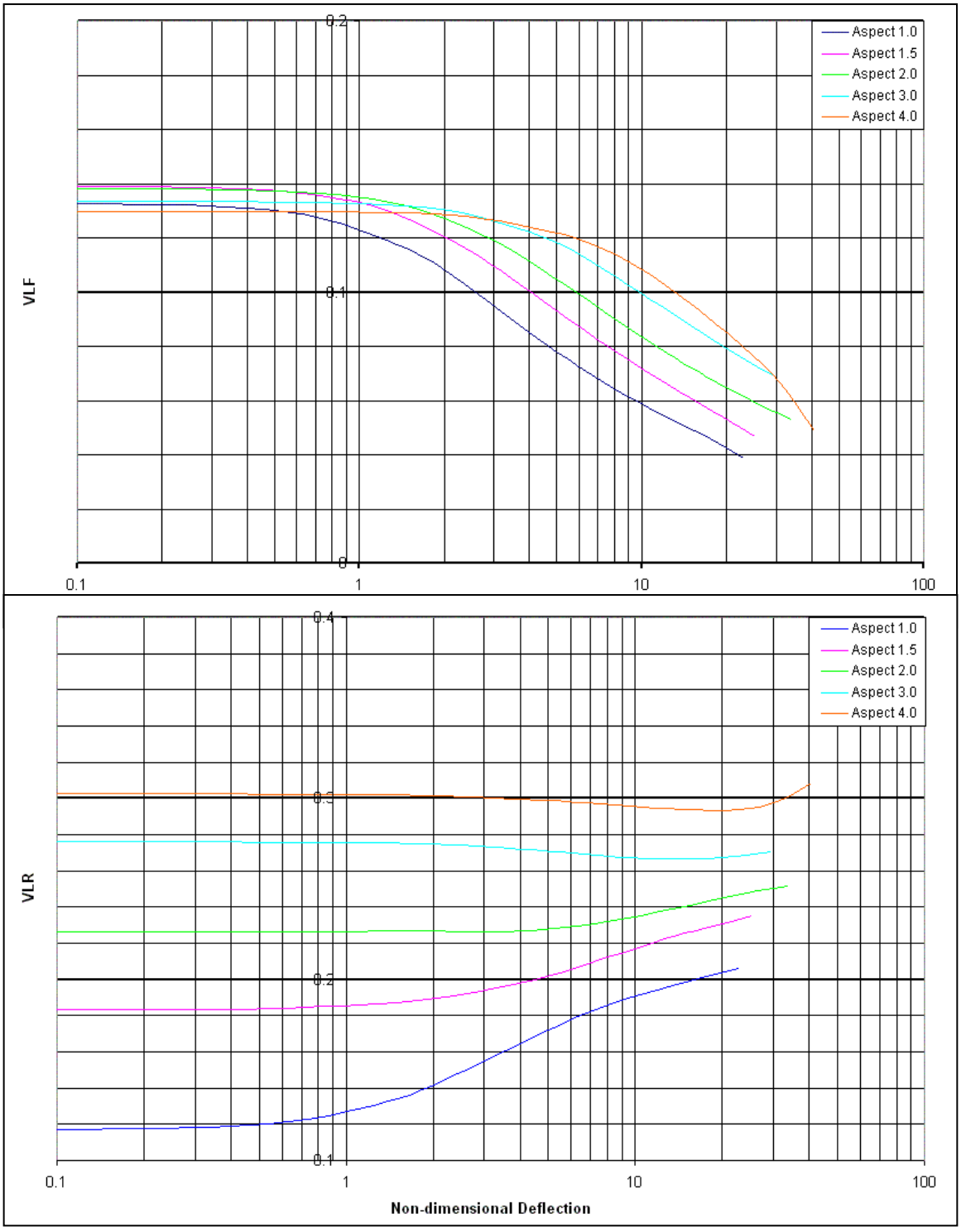

Figure 10 – Reaction coefficients for the long side of simply supported glass panes

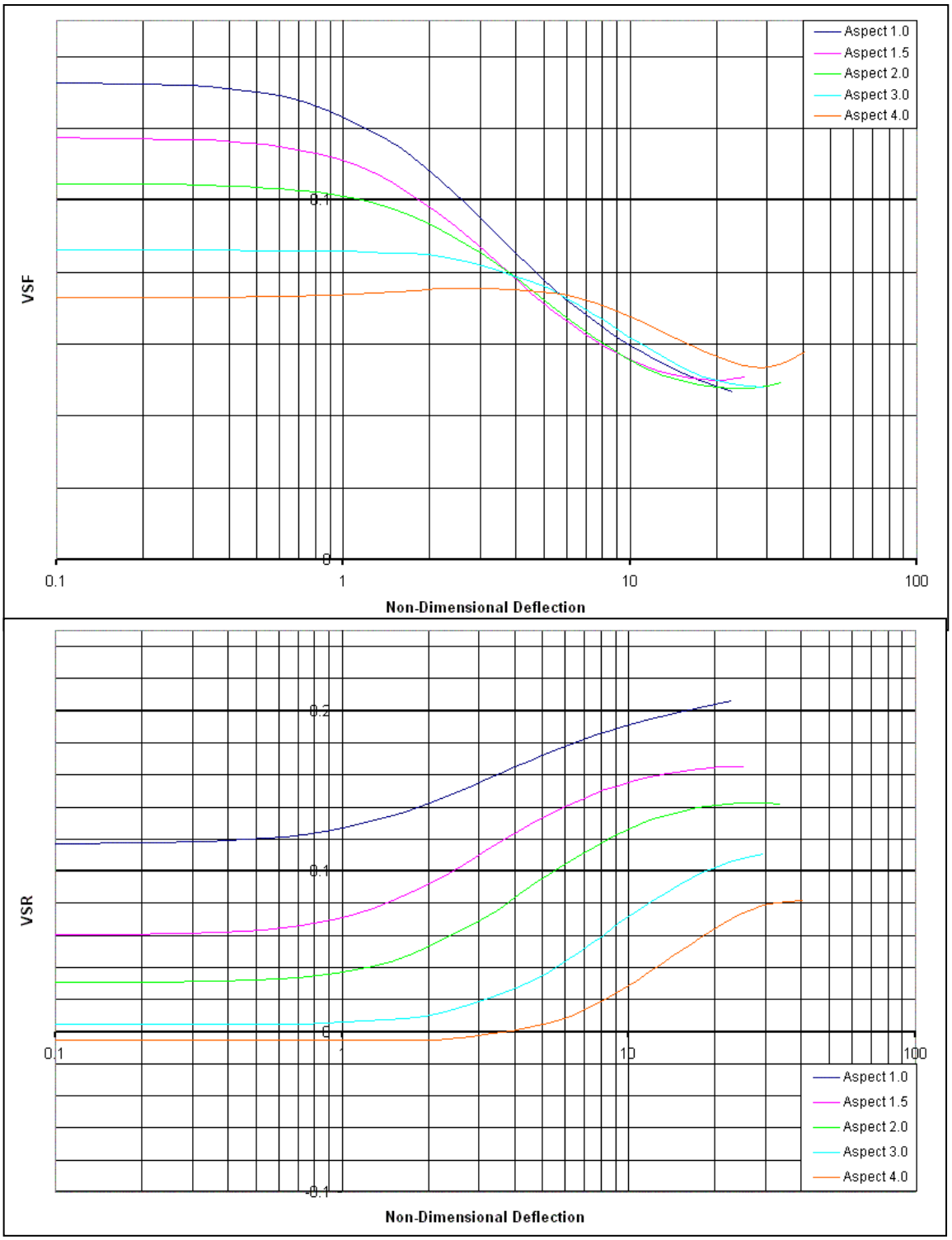

Figure 11 – Reaction coefficients for the short side of simply supported glass panes

5.4 Distribution of reaction

The distribution of the reaction along the edges of the glass pane also varies significantly with deflection. The SDOF reaction calculation assumes that the force and resistance components of reaction both have the same distribution along the sides

as the static loading, and that reverse reaction at the corners is distributed evenly between the two sides.

The local reverse reaction at the corners is evaluated as a point load by classical small deflection formulae and linear FEA, although this is in fact an artifact of the assumptions. If shear stiffness or a less than perfect simple support were included, it would be seen that the reverse reaction is distributed over a small but finite width. The refined mesh analysis showed that for large deflections the reverse reaction is a local distributed effect even with the simplified assumptions.

The distributed reaction between the corners has to balance the reverse corner reaction as well as the applied load. However, the shape of the distribution varies substantially with the deflection. For small deflections the reaction distribution peaks at the centre, but is a little flatter than the half sine wave assumed in TM 5-1300 part 6 for glazing reactions, with a peak of 1.72 times the mean reaction.

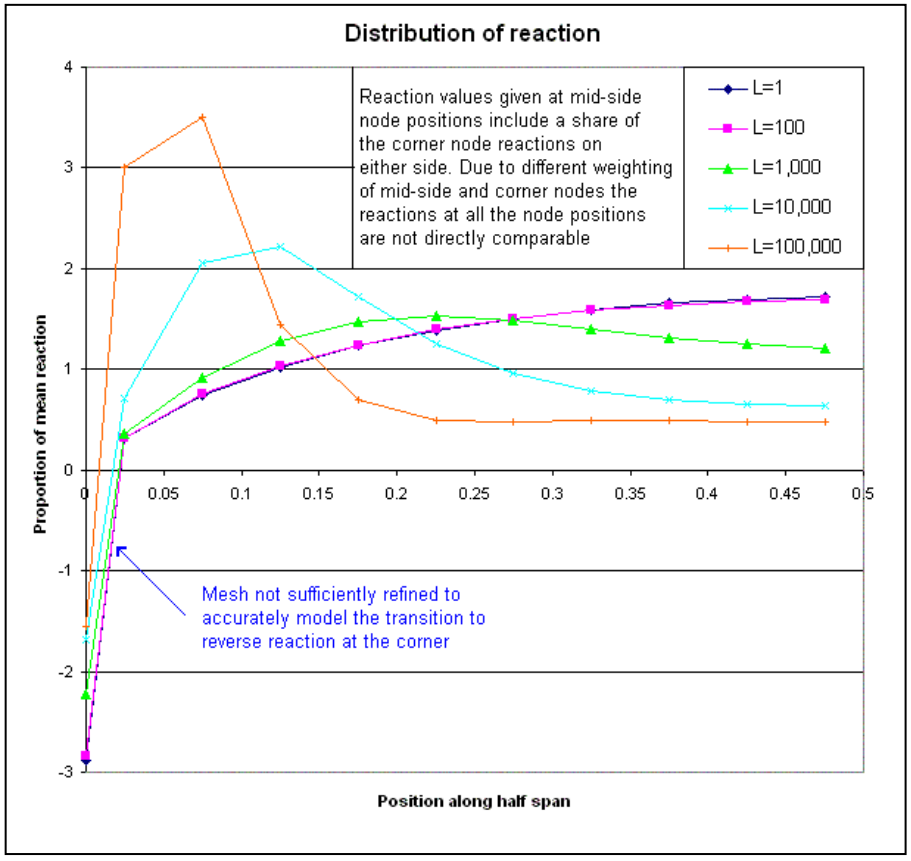

Figure 12 – Relative reaction distributions for varying load on a pane with λ=1

As illustrated by Figure 12, for a load L=1000, corresponding to a deflection of just over twice the pane thickness, the maximum reaction has moved from the centre of the span to beyond the quarter point, with a maximum value of 1.53 times the mean reaction. For greater deflections the peak reaction becomes higher and closer to the support.

6. Sensitivity studies of SDOF large deflection parameters

A number of studies have been carried out to assess the sensitivity of the analyses to some of the assumptions, to see how well the idealised model is likely to represent more realistic cases.

6.1 Sensitivity to slenderness of the pane

As described above, the main analysis was undertaken on models with a slenderness ratio of 1:280. Although this represents about the practical limit of slenderness for window construction, individual glass laminae in laminated glass could be more slender, and most blast resistant glazing will be significantly less slender.

The non-dimensional loading formulae defined by Moore and used in this paper contains a fourth power slenderness term, while the stress contains a second power term and the deflection a single power term. This pattern should give relationships independent of slenderness for pure bending, but not for pure membrane behaviour, so the response of panes of different slenderness could be expected to diverge at high deflections when membrane behaviour is significant.

Analyses were undertaken for aspect ratios λ of 1, 2 and 4 for panes of relative thickness of ½, 2 and 5, and compared with the original analyses to study the sensitivity to different slenderness of the glass. The divergence of deflection shown in Figure 13 and similar downwards divergences of maximum stresses and K_{LM} demonstrate that the non-linear deflection is not independent of slenderness.

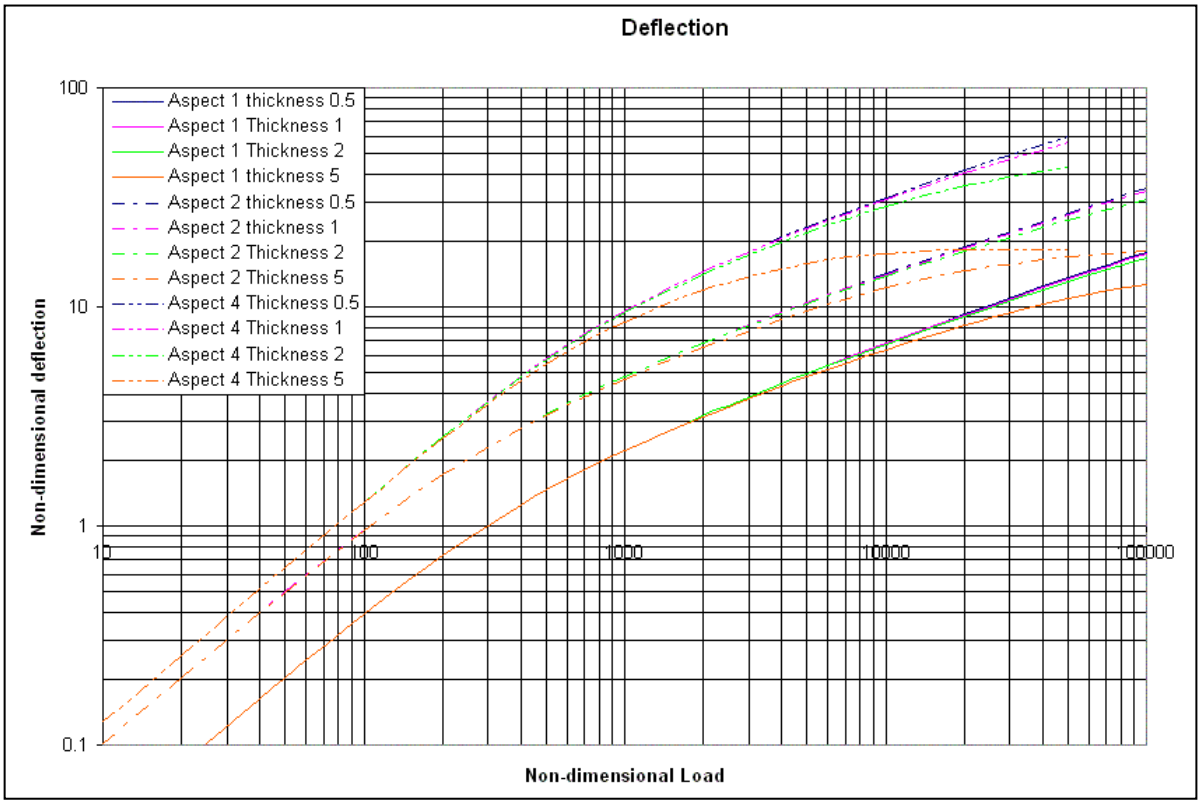

Figure 13 – Variation in deflection of glass panes with slenderness

However, the effect of this sensitivity to slenderness will not be very significant for practical applications. The reduction in deflection is not noticeable until non-dimensional deflections of about 4 for 5x thickness and about 10 for 2x thickness, corresponding to 20 times unit thickness. Even for toughened (fully tempered) glass strengths, slender windows will rarely reach this level before failing, and the non-dimensional failure stresses will reduce by the square of the reducing slenderness, so the actual failure deflection will decrease with increasing thickness.

Practical problems with glass should be confined to the parts of the original 1:280 slenderness curves where the divergence is not significant, and so the original curve can be used for all analyses of solid glass. Separate consideration may be required for Polycarbonate glazing.

Greater error could actually occur in assessing very slender laminated glass plies. However, the breaking deflection of these under blast loading tends to be lower than the breaking deflection of the intact laminated glass, so the error introduced by using the original slenderness curve is unlikely to have any practical significance.

6.2 Sensitivity to lack of rigidity in the transverse support

The perfect condition of a simple support is a tool to simplify analysis, but the condition is never achievable in practice. Glazing is mounted in a frame using gaskets or a gap- filling adhesive such as silicone rubber, which is not perfectly rigid. In addition, there is likely to be some give in even a hole-in-the-wall window frame between the mounting for the glass and the connections to the supporting wall.

The stiffness of the support can vary between a stiff, blast-enhanced frame using substantial areas of structural silicone to support the glass, to a light aluminium frame with finned neoprene gaskets or even UPVC domestic window frames with thin neoprene gaskets. Analyses were undertaken for aspect ratios λ of 1, 2 and 4 with different linear spring stiffnesses at the supports to assess the effect that this has on the glazing response and SDOF parameters.

A non-dimensional stiffness parameter for the support was chosen that set unity as the stiffness of support that, for a rigid body, would be equal to the small deflection spring stiffness for the pane. The stiffness per m of the supports was set to give a proportion of the unit flexibility, e.g. for 1% flexibility a stiffness 100 times that of the pane was modelled as distributed equally around the supported perimeter. Values of 0.01% to 1% were considered to cover the likely range between stiff and soft supports.

With the exception of maximum stress, the differences are negligible for all parameters for flexibilities less than 1%. For 1% support flexibility the deflections increase generally by 1-3% depending on aspect ratio until higher deflections are reached, when greater increases occur, as shown in Figure 8. The curves for 0.01% support flexibility have been omitted from Figure 8 for clarity.

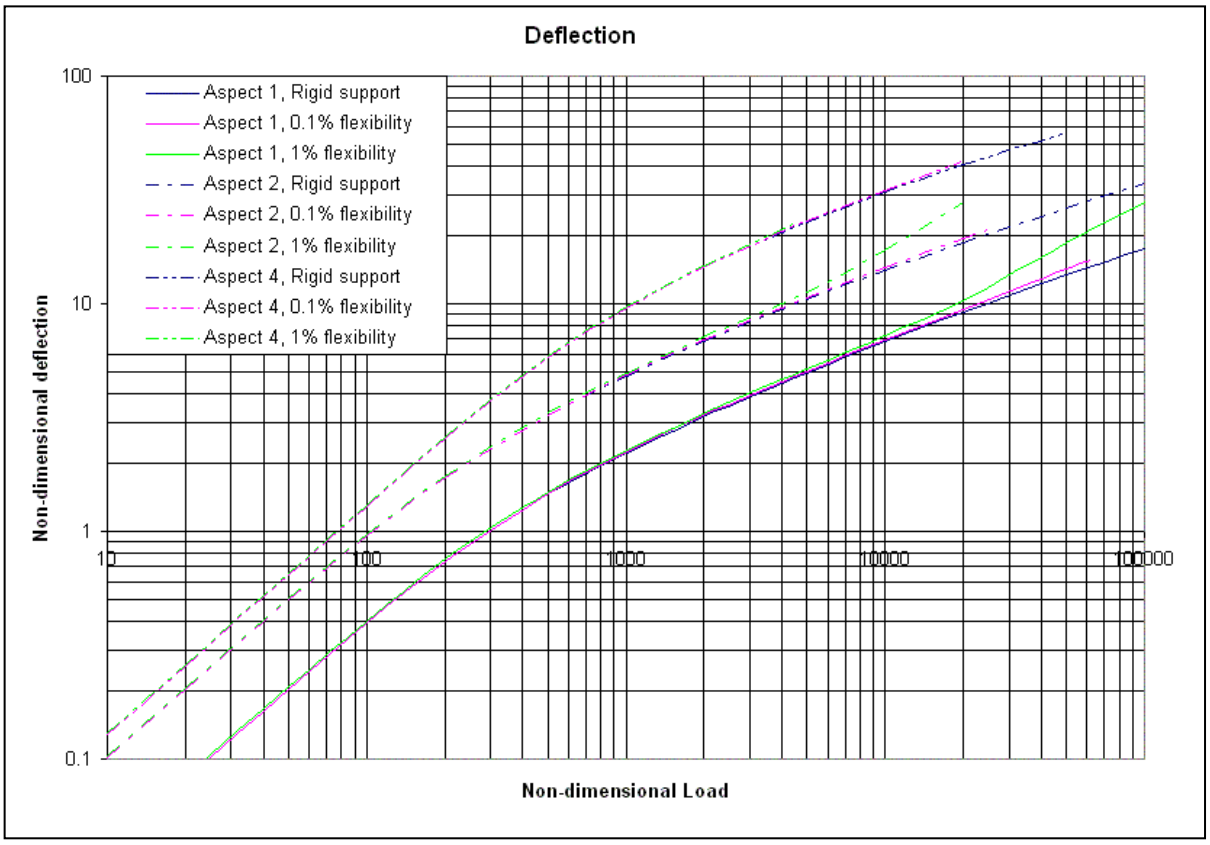

Figure 14 – Variation in deflection of glass panes with transverse support flexibility

K_L and K_M are both increased for all deflections and a support flexibility of 1%, such that K_{LM} increases only about 0.2% at small deflection and no more than 0.5% generally when plotted against non-dimensional load. If plotted against non-dimensional deflection, allowance would have to be made for the increase in deflection in Figure 14. Similarly, changes in the reaction coefficients occur only in the third decimal place if plotted against load.

The effect on the maximum stresses is complex. For all of the cases assessed, the flexibility of the support allows a lifting of the corner and a significant reduction of the torsion stress not only at the corner, but also in the area near the corner where the maximum membrane stresses are enhanced by a lesser level of torsion. This will have little effect on the bending stress that controls the maximum stress at lower loads, and can reduce the maximum stress at higher loading; however, in the middle either a lower bending and membrane combination may control, or, in some cases a membrane stress enhanced to compensate for the loss of torsion stiffness may control. Figure 15 illustrates the effect on the maximum, corner and centre stresses for an aspect ratio λ of 1. Note that the figure is based on the regular mesh analysis that produces an exaggerated torsion stress at the corner, but this highlights the influence of the support flexibility more strongly.

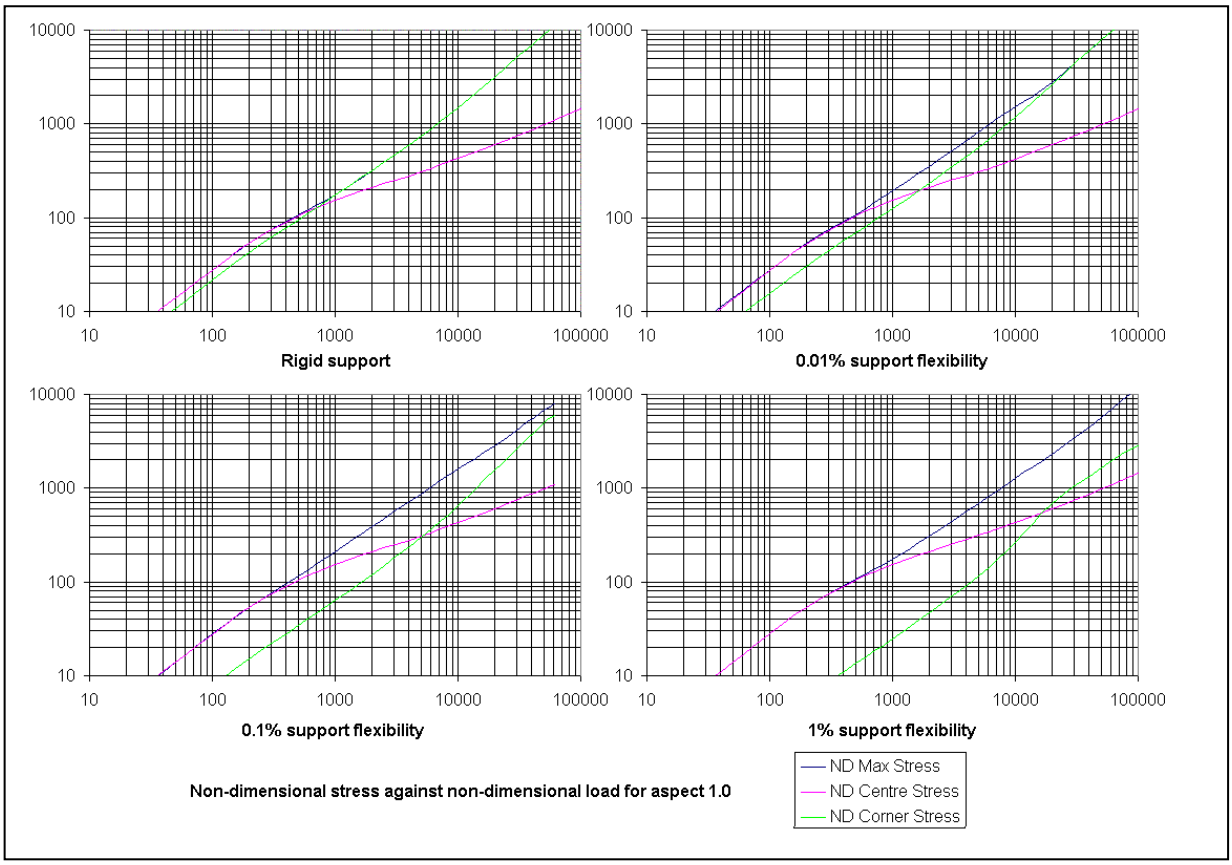

Figure 15 – variation of stresses with support flexibility for a glass pane with λ=1

The interaction of the different stresses at different locations leads to complex changes as the support flexibility changes. In the middle zone around L=500 to 10,000 there are increases in maximum stress up to 20% for stiffer supports, but reductions of about 10% for softer supports. In the higher zone there are reductions up to about 25% for stiffer supports, but less reduction for softer supports except for low aspect ratios, where the reductions can increase to about 40%.

Most windows expected to resist blast will have stiffer supports from at least solid neoprene gaskets, and will be of a slenderness to break in the middle zone. The increased stress means that the deflection at breaking may be lower than expected from Figure 8. Conventional windows with narrow or finned gaskets will have softer support flexibility. Annealed glass is likely to fail in the middle zone, but toughened glass could survive into the higher zone. The reduced stress means that the deflection at breakage may be higher than expected, but the degree of enhancement will vary from case to case.

6.3 Sensitivity to in-plane and rotational stiffness in the support

Just as the rigid lateral support of a simple support is not achievable in practice, neither is the complete lack of in-plane and rotational restraint assumed in the idealised support.

The degree of support will depend on the stiffness of the frame and the glass support mechanism. The non-dimensional unit stiffness per m width for in-plane restraint has been taken as the plane-stress one way axial stiffness of the glass pane $= E \cdot \frac{t}{b}$

For an "enhanced support" of 25mm double sided silicone bite, the high-rate-of-strain stiffness is approximately 1% of the axial stiffness of a 1:280 slender pane, provided the stiffness of the frame is high. However, an enhanced support will normally be supporting laminated glass, and most usually a double glazed unit or single glazing of substantially lower slenderness. For these the glazing stiffness will be significantly less, and the support restraint proportionally less.

For gasketed glazing systems there will be a non-linear in-plane resistance with a "plastic" stage when the static friction of the gaskets has been overcome. The in-plane resistance of such systems will depend upon the pressure of the gaskets on the glass, but will be substantially lower than for silicone supports.

Analyses were undertaken for aspect ratios λ of 1, 2 and 4 with in-plane stiffnesses from 0.01% to 1% to cover the likely range of support stiffnesses.

The non-dimensional unit stiffness per m width for rotational restraint has been taken as the rotational stiffness of the one-way span

$$= \frac{24 \cdot E \cdot I}{(1-\nu^2) \cdot b^2} \qquad \text{which for a solid glass pane} \quad = \frac{2 \cdot E \cdot b}{(1-\nu^2)} \cdot \left(\frac{t}{b}\right)^3$$

Most real rotational restraints are likely to be significantly non-linear over the degree of support rotation compatible with large deflection. Stiffest are likely to be wide single sided silicone bonding and silicone "enhanced supports" for blast. Flexing of the frame, cover plates, thermal breaks etc. are likely to contribute significantly to the rotational stiffness value, not just the immediate glass support.

Analyses were undertaken for aspect ratios λ of 1, 2 and 4 with rotational stiffnesses from 0.1% to 10% to cover the likely range of support stiffnesses. A 10% stiffness will result in support moments of the order of 20% of midspan moments. A 0.1% rotational stiffness gives results that are nor significantly different from the unrestrained cases, so these have been omitted from Figure 16 for clarity

The effect of greater in-plane restraint is to reduce deflections, but the amount is very sensitive to the aspect ratio, as shown in Figure 16. The maximum stresses undergo comparable reductions. Plotted against the deflections, the value of K_{LM} diverges downwards only at high deflections for λ =1 and 2, but for λ = 4, it diverges upwards from deflections as low as 1x thickness. The force reaction coefficients experience minor changes at high deflections, but for high aspect ratios and high deflections there is a substantial transfer of resistance reaction from the short span to the long span, with changes of up to 0.04 to the coefficients.

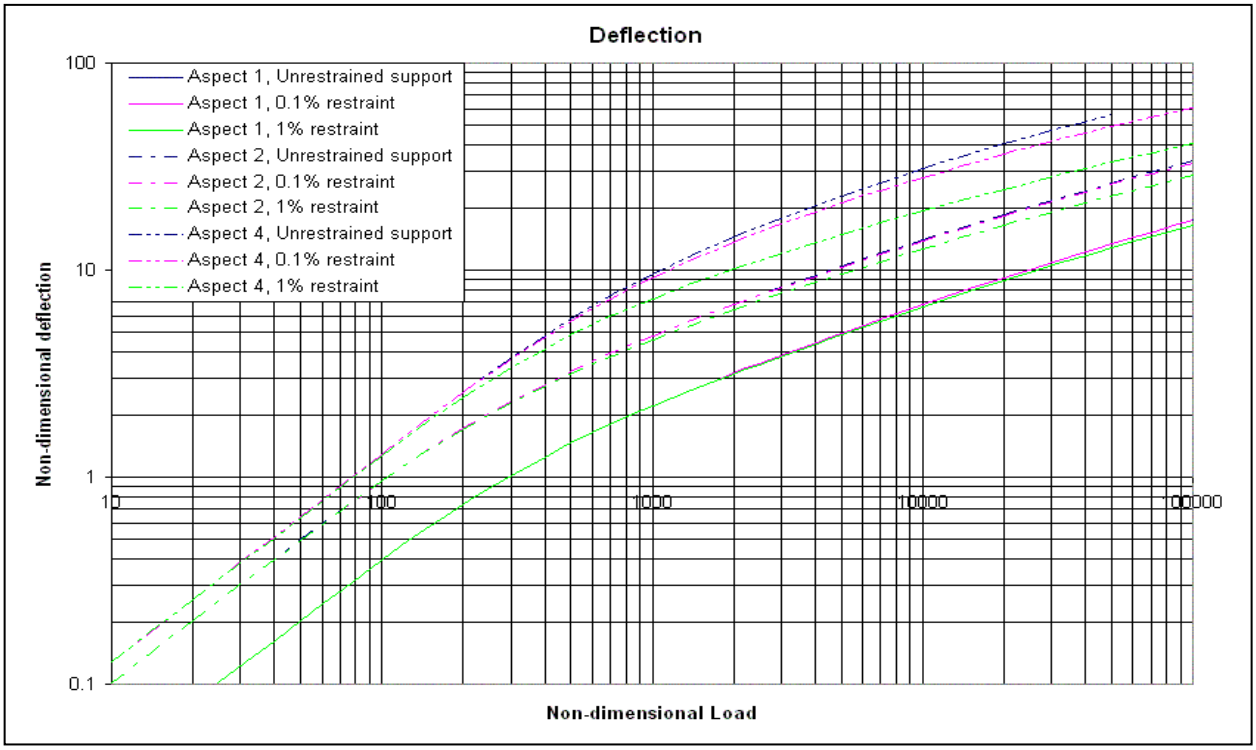

Figure 16 – Variation in glass pane deflection with in-plane restraint

The effect of substantial rotational constraint is also significantly to decrease deflection, particularly at high aspect ratios, but the effect is very different as the decrease is greatest at low loading, and reduces as loading increases, as shown in Figure 17.

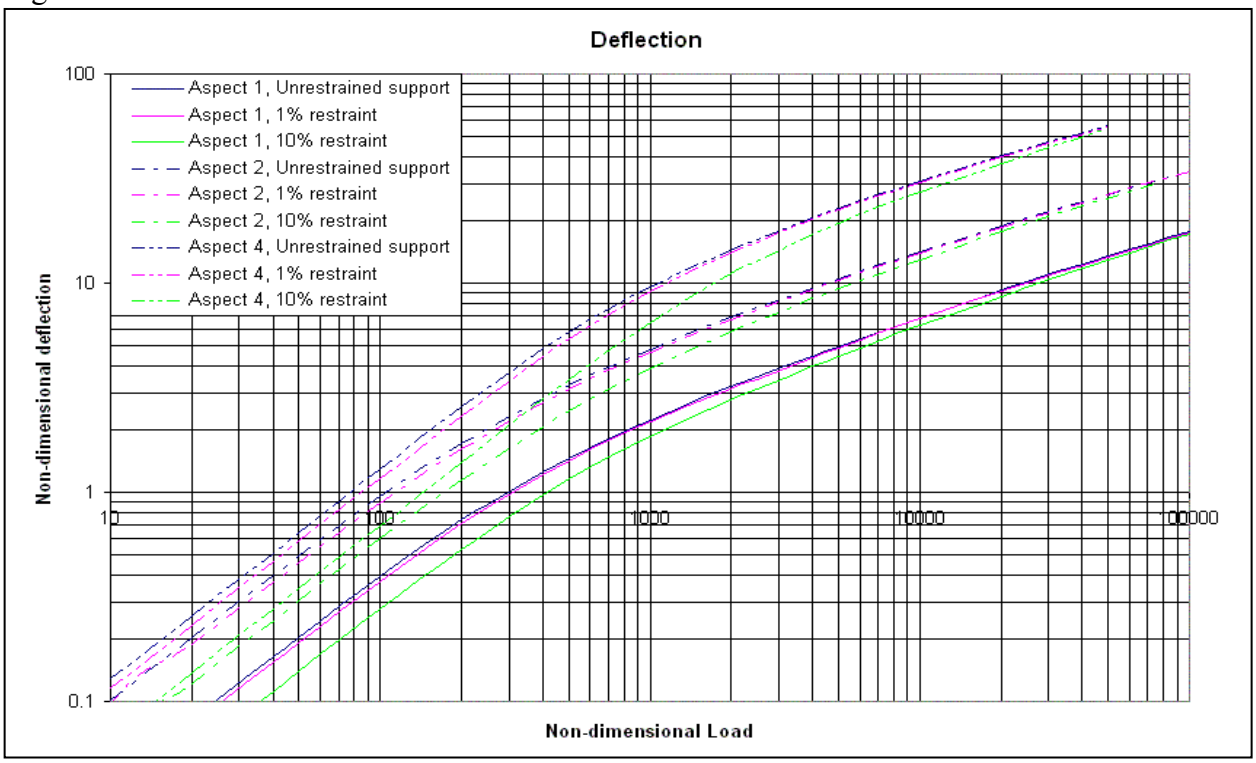

Figure 17 - Variation in glass pane deflection with rotational restraint

Stresses show a similar pattern of reduction at low load levels. K_{LM} values show a near uniform reduction of the order 0.01, except for small deflections at $\lambda = 4$, which shows a comparable increase, with a change-over point at a deflection of 2x thickness. The reaction coefficients undergo somewhat smaller changes, with the greatest at low deflections and low aspect ratio, as the pane becomes partially fixed in bending.

In practice high in-plane restraint and high rotational restraint are often combined in the same mounts, using silicone adhesive and either a deep rebate for an "enhanced support" for blast resistance, or a wide single sided joint for architectural reasons. However, the unit stiffnesses are both sensitive to slenderness, and restraint levels will reduce as the glass thicknesses increase. The likelihood of a very slender glass pane very strongly mounted is low in practice, but if it occurred there would be a significant shift of many of the design parameters. A typical change in deflections for such cases is shown in Figure 18, assuming 1% in-plane and 10 % rotational constraint.

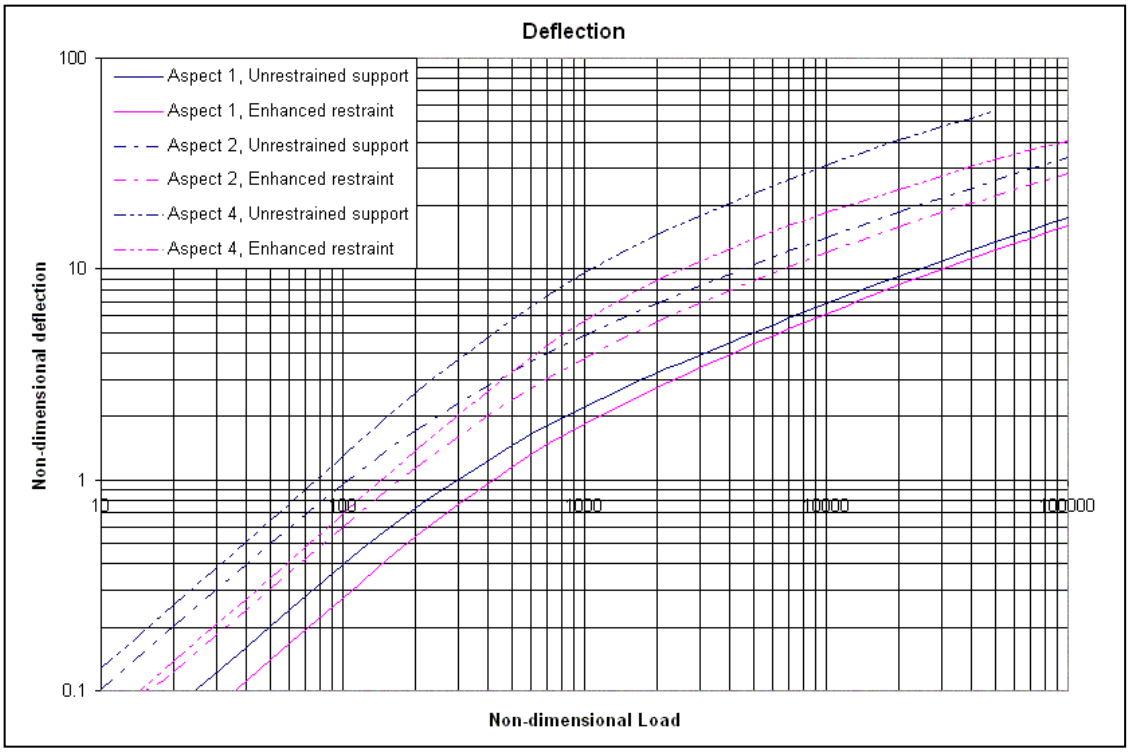

Figure 18 – Variation in deflections for 1:280 slenderness glass panes in enhanced supports

The stresses also reduce, so that cracking deflections plotted against stresses are within 10% of Figure 8, higher for the upper part of the curves for all λ, and lower for the lower part of the curve for $\lambda = 1$, with no significant change for $\lambda = 2$ or 4.

The change to K_{LM} is fairly uniform with deflection, but varies with λ, from a reduction of 0.013 for $\lambda = 1$ and of 0.008 for $\lambda = 2$ to an initial increase of 0.012 for $\lambda = 4$, becoming 0.003 for deflections between 4 and 10 times thickness, and then 0.007 for large deflections.

Changes to reaction coefficients depend on deflection and aspect ratio. One general trends is a reduction in force coefficients at low deflections, reversing for high deflections, generally around 2x thickness. There is an increase in the long side reaction coefficients for $\lambda = 2$ and 4, but neutral to reduction for $\lambda = 1$. There are substantial reductions to the short side reaction coefficients for $\lambda = 2$ and 4 at large deflections, but smaller changes for $\lambda = 1$.

For a slender pane in a highly restraining frame the dynamic response and reaction history are likely to be significantly changed, and an alternative analysis may be desirable. However for most double glazing and blast designed glazing in blast enhanced frames the restraints will be substantially less significant, and a design based on a simply supported analysis will still be a reasonable approximation.

7. Comparison of SDOF and dynamic transient analysis

A number of SDOF analyses of a simply supported pane have been undertaken in Mathcad, and compared with a non-linear transient dynamic FE analysis undertaken on LUSAS.

The example used has been chosen as convenient for analysis rather than representative of any real case. For comparable analyses, the following parameters have been used throughout the exercise:

Young's modulus E	70×10^9 Pa
Poisson's Ratio ν	0.22
Cracking Stress	Ignored – assumed for the analysis not to crack.
Density	2490 kg/m^3
Pane thickness t	12mm
Short span b	1.679m
Long span a	3.358m
Aspect ratio λ	2.0
Slenderness	~1:140
Support conditions	Simply-supported
Peak pressure P	30 kPa
Impulse I	300 kPa.ms
Triangular load duration t_r	20 ms
Damping C	Taken as aeroelastic damping for atmospheric pressure on both sides (enhanced damping on loaded face during loading ignored to simplify transient FEA).

The cases analysed were:

- Non-linear transient FE analysis, using the regular mesh model, Incremental Lagrangian non-linear control, an implicit Newmark time integration scheme and a transient pressure loading defined as a variation curve with time. Newmark integration gives unconditionally stable time integration without numerical dissipation of higher modes of vibration.

- SDOF using linear resistance and transformation factors and reaction parameters from the table for a simply supported slab from Biggs
- SDOF using non-linear resistance after Moore and factors and parameters from Biggs
- SDOF using non-linear resistance from Figure 4 and small deflection parameters from linear analysis (similar to Table 2 with ν of 0.22)
- SDOF using non-linear resistance from Figure 4 and non-linear parameters from Figures 9, 10 and 11, for unit thickness based on a slenderness of 1:280.
- SDOF using non-linear resistance for thickness=2 from Figure 13 and corresponding non-linear parameters for a slenderness of 1:140

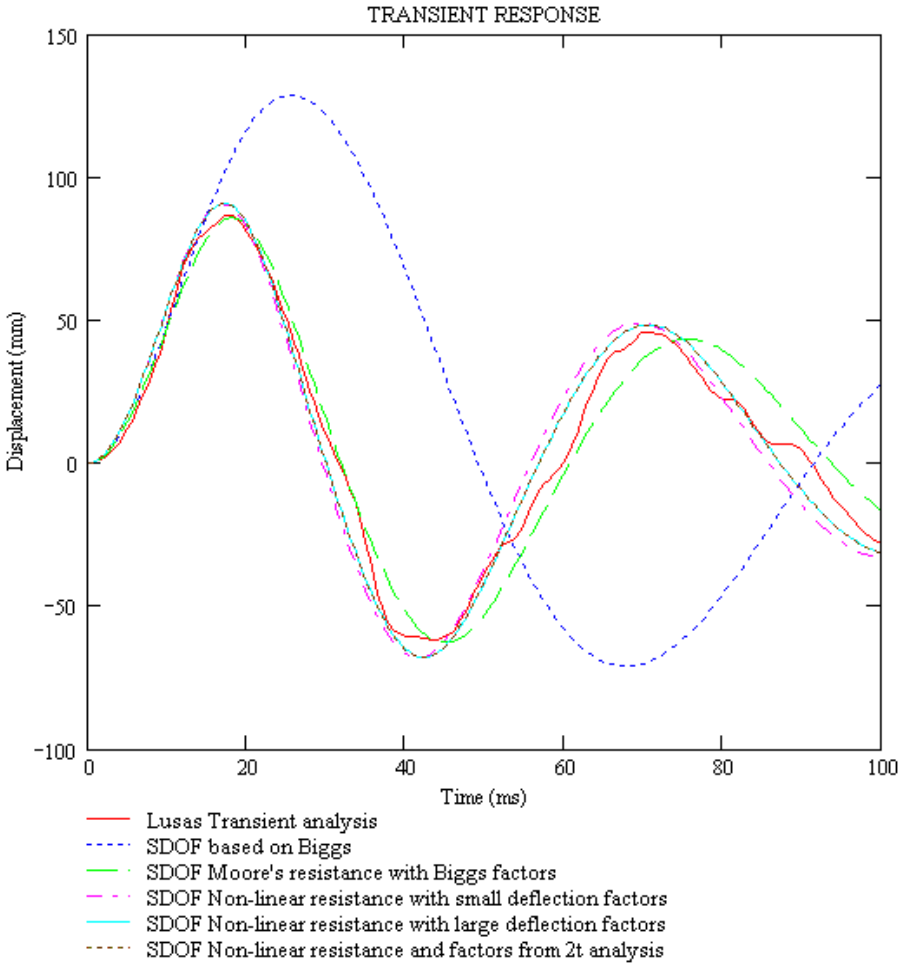

Figure 13 – Midspan deflection history of the pane in cases analysed

In the response of this example using the linear analysis in Biggs, it can be seen that the linear stiffness calculated from small deflection theory gives (seriously) incorrect predictions of amplitude and timing of the response for large deflections, of the order 10 times thickness.

With Moore's non-linear resistance the fit is much closer for the initial pulse, but over several cycles it can be seen that the response time is a bit longer than for the transient analysis, an indication that the effective mass is too high, and/or the non-linear stiffness is too low. For maximum deflections of the order 7 times thickness most of the cumulative delay will come from a K_{LM} that is too high.

Using the slightly different non-linear resistance curve from Figure 4 and the small deflection K_{LM} the timing of the initial pulse is good, although the amplitude is a little high. Over several several cycles the SDOF results tend to lead the transient FE results a little, indicating that the K_{LM} is a little too low.

The analyses with the non-linear resistance curves and large-deflection variable K_{LM} produce responses that are indistinguishable from each other, with a difference in peak deflection of 0.025%. This confirms the conclusion in 6.1 that the data based on the unit thickness in figures 4, 5 and 9 to 11 may generally be used to analyse glass panes of any slenderness. For this example these analyses appear to give the best fit to the transient dynamic response. After several cycles the timing of the peaks is identical within a 0.5ms timestep over 70ms. The variation between the peaks appears to arise mostly from the higher order vibration included in the transient FE analysis, together with a small difference in amplitude.

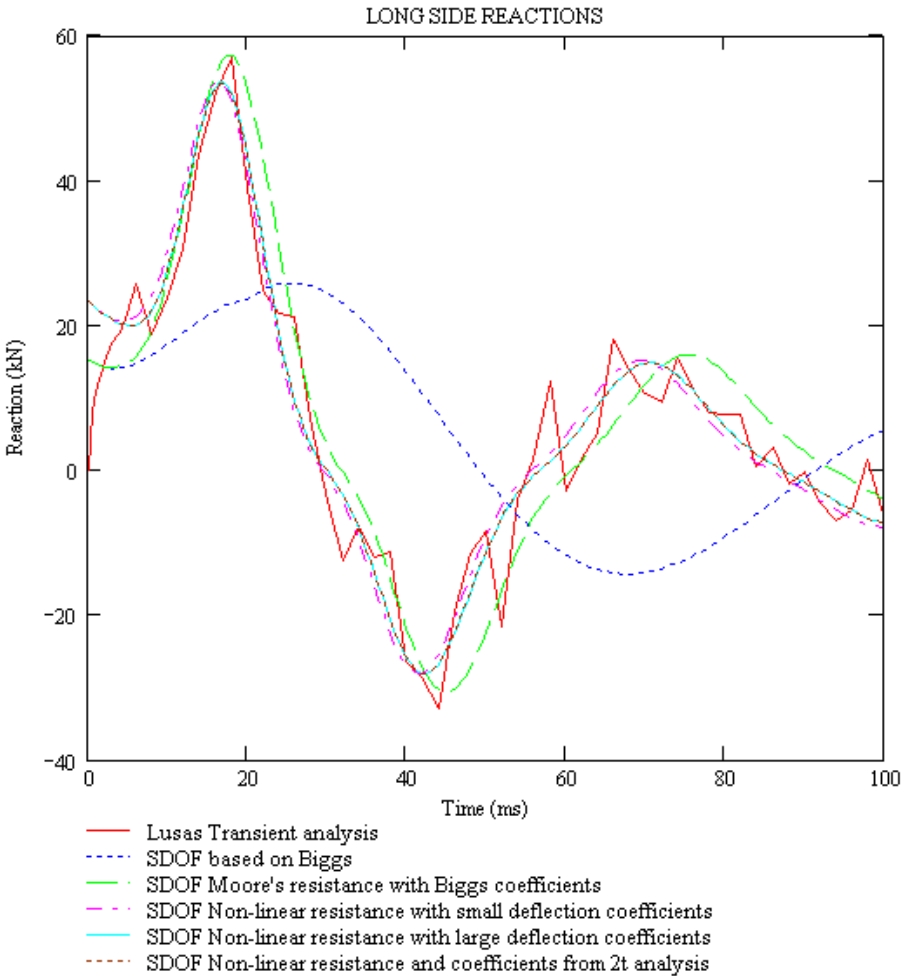

Figure 14 – Reaction history on the long side of the pane in the cases analysed

The maximum deflection is about 4.5% greater than the transient dynamic response, and 6% at the second positive peak. This could arise in part from the higher order vibrations that distort the peak of the fundamental transient FE response, and makes the SDOF analysis slightly conservative. The peak response using Moore's stiffness and the original K_{LM} is 1.8% low for the maximum response, and is still only 5% low at the second positive peak. However using these values in design would be unconservative.

This suggests that, although the ratio of the equivalent mass to resistance in the large deflection SDOF analysis is a close fit to the FE analysis, the product of them is still a little low. This appears to arise from the fundamental approximation of using the static deflection as the basis of the dynamic SDOF analysis, as mesh refinement of the static FE analysis would tend to marginally reduce the stiffness.

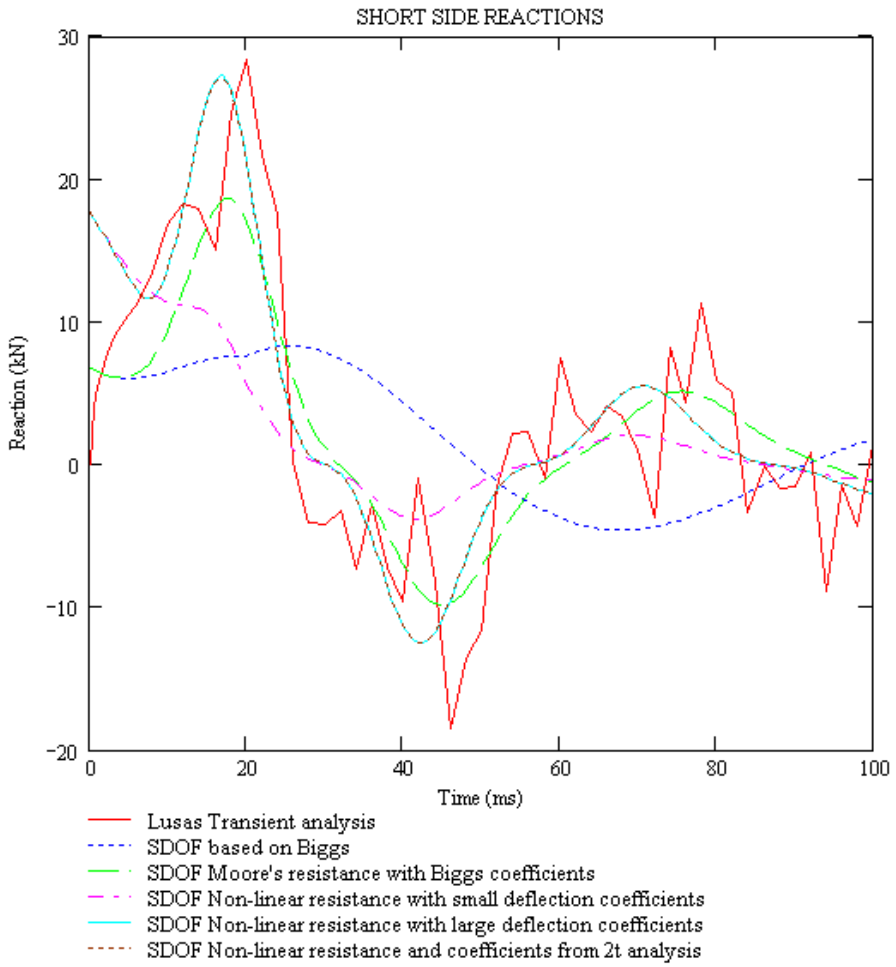

Figure 15 - Reaction history on the short side of the pane in the cases analysed

The reaction histories highlight the "ringing" of higher frequency responses in the transient FE analysis. One of the fundamental assumptions in the SDOF approach is that the higher frequency response of the real glass panes is sufficiently low as to be negligible, as by its very nature the SDOF analysis can only consider the fundamental mode of response. It is expected that in a real window the higher frequency effects would be substantially reduced by hysteresis (structural) damping, particularly in the

glass supports, but no damping of this type has been included in this transient FE analysis.

The case using Moore's non-linear resistance and the coefficients from Biggs gives the closest amplitude match to the peak long side reactions from the transient FE analysis. However, this means that the case is exaggerating the reaction to be expected from the fundamental mode. The current analyses give a good fit for the peak reactions on the long side and a close fit for the timing. The requirement for the non-linear analysis is demonstrated by the reaction on the short side, where the change from force to resistance coefficient with increasing deflection gives the only reasonable estimate of the peak reaction.

The comparison of SDOF and transient FE analyses demonstrates that, for analysis of glass panes, the peak reactions based on resistance coefficients derived from equilibrium calculations are sound. The use of reactions based on the total resistance as in TM5-1300 will be very conservative.

However, the comparison also illustrates one of the fallacies of the reaction coefficient approach. The high initial reaction due to the force coefficients and the initial blast pressure is not a real condition, as it takes much of the initial response time for the glass pane to change from the true initial state of uniform acceleration with no significant reaction to a flexural response.

For the example given, with the response time longer than the positive phase loading, the applied load does not contribute to the peak reaction. It is reasonable to expect that in another case with a longer duration loading, where a substantial part of the blast pressure remains at the time of peak response, that the force coefficients may realistically give an appropriate contribution to the total peak reaction. However the high initial reaction and initial falling arm of the reaction history can be ignored for the analysis of glass panes.

8. Conclusions

- The SDOF transformation factors and reaction coefficients for elastic response of slabs in general use almost all contain a substantial degree of inaccuracy.

- This is not of great significance for the analysis of thick reinforced concrete slabs and walls that are expected to experience high plasticity ratios while resisting high blast loads.

- However, it is of significance for thinner slabs and walls under moderate blast loads where the plasticity ratio is less, or for slabs and walls where the response is limited to the elastic or elastoplastic regions.

- This paper provides alternative values of elastic transformation factors and reaction coefficients for concrete slabs and walls that accurately reflect the static deflected shape and equilibrium.

- These values, based on small deflection theory are not suitable for the analysis of thin plates such as glass panes and steel plates, which will experience large deflections in the elastic region.

- Large deflection analysis of glass panes in this paper has shown elastic non-linear deflection and stress response similar to but not identical to the analysis after Moore in TM 5-1300.

- The analysis after Moore may over-estimate the cracking deflection and resistance of some glass panes by presenting corner stresses rather than the maximum stresses from throughout the model.

- This analysis shows that transformation factors and reaction coefficients also vary substantially over large deflections, and that these variable values should be used in SDOF analyses of glass panes under blast loading, with the non-linear resistance and cracking deflection derived from the deflection and stress response.

- Although the charts developed in this analysis are not truly independent of slenderness, for practical purposes all slenderness of glass panes can be analysed using the same charts based on a slenderness ratio of 1:280.

- Transverse flexibility of supports only affects the stiffness of the glass panes significantly for high flexibility, at large deflections and affects lower aspect ratios more. Transformation factors and reaction coefficients are not significantly affected once the modified stiffness is accounted for.

- Transverse flexibility of supports affects the cracking deflection even for low flexibility. In practice blast resistant glass in stiff supports is likely to crack at lower deflections, and lighter glazing in softer supports is likely to crack at higher deflections than the simply supported analysis would indicate.

- Rotational and in-plane restraint is generally only of great significance for slender glazing mounted in blast enhanced silicone rubber supports, or for single sided silicone supports with a significant silicone width. The effect is sensitive to slenderness; so thicker glass or double-glazing will be substantially less affected.

- For enhanced restraint of slender glazing the non-linear resistance is enhanced in all cases, but the cracking deflection is increased by no more than 10%, with many cases unaffected, dependant on aspect ratio and deflection.

- Changes to the transformation factor are significant, but vary with the aspect ratio, and changes to the reaction coefficients vary with aspect ratio and deflection.

9. References

1. Biggs JM. *Introduction to Structural Dynamics.* McGraw-Hill, New York 1964

2. Buchholdt H. *Structural Dynamics for Engineers*. Thomas Telford, London, 1997

3. *Protective Structures Automated Design System v 1.0 (PSADS)* incorporating Army TM5-855-1, Air Force AFJAM32-1055, Navy NAVFAC P-1080 and DAHSCWEMAN-97. US Army Corps of Engineers, Washington DC 20314-1000, September 1998

4. Drake JL et al. *Protective Construction Design Manual* ESL-TR-87-57, Air Force Engineering Services Lab, Tyndall Air Force Base, FL32403, November 1989

5. *SPAnW, Version DAHS CWE 1.1.1.0, June 1997*, Incorporated in PSADS, ref 3, September 1998

6. Technical Manual TM5-1300, *Structures to Resist the Effects of Accidental Explosions*. US Department of the Army, November 1990

7. Mayor RP & Flanders R. *Technical Manual Simplified Computer Model of Air Blast Effects on Building Walls.* US Department of Transportation, Safety and Security Division, Cambridge MA 02142, June1990

8. Meyers GE. Tech Memo 51-86-13, *User Data Package for Blast Resistant Windows*. Naval Facilities Engineering Command, Alexandria VA, June1986

9. S P Timoshenko & S Woinowsky-Krieger; *Theory of Plates and Shells, 2nd Edition.* McGraw-Hill, New York 1959

10. *LUSAS User Manuals, version 13*. Finite Element Analysis Ltd, Kingston Upon Thames KT1 1HN, 2002

11. *Mathcad 2001i Users Guide with Reference Manual*. Mathsoft Engineering and Education Inc, Cambridge MA 02142, 2001

Appendix B

Paper prepared for the 12th International Symposium on the Interaction of the Effects of Munitions with Structures, New Orleans, USA, September 2005.

This paper was not presented owing to the cancellation of the Symposium as a result of Hurricane Katrina, but was published in the Proceedings.

A review of the Single Degree of Freedom method for dynamic response of reinforced concrete structures

Colin Morison BSc MSc NRA CEng MICE

TPS Consult, Croydon, UK.

Synopsis of Paper

The single degree of freedom (SDOF) analysis method is an approximate method for non-linear analysis of distributed structural members, based on equivalent energy of assumed deflected shapes. The deflected shape most usually considered is the static deflected shape under the same load distribution.

Over almost 50 years, reliance has been placed on tabulated stiffness, transformation and dynamic reaction factors calculated in the 1950s and 1960s to derive an equivalent SDOF model and analyze the response of a wide variety of structural members. These factors are still in current use.

The source calculations and assumptions for the factors in these tables are reviewed, and a number of approximations, simplifications, omissions and errors are identified in the factors for both one-way spanning and two-way spanning structural members.

Alternative calculations have been undertaken for a range of tabulated data, using advanced yield line and numerical analysis methods with modern computing power. Alternative tables are proposed that more accurately reflect the response based on the static deflected shapes for the elastic, elastic-plastic and plastic ranges of deformation.

One systematic artifact of the SDOF analysis of response to blast or shock loading has been a high initial dynamic reaction at the arrival of the loading wave. The significance of this is reviewed and possible future approaches are discussed.

Nomenclature

A	Short span dimension of panel
B	Long span dimension of panel
d	Deflection
E	Young's Modulus
F, F(t), F_e	Total load history on distributed or lumped system
f	Distributed load
I	Second moment of area per unit width of panel
ke	Elastic spring stiffness or spring constant
ke_{SS}, ke_{fixed}	Elastic spring stiffness for simply-supported and fixed edge panels
K_L	Loading transformation factor
K_M	Mass transformation factor
K_{LM}	Load-Mass transformation factor = K_M/K_L
M, M_e	Total mass of distributed or lumped system
M_F, M_S	Moment resistance (at fixed supports and in spans)
m	Isotropic moment resistance per unit length, distributed mass
m_F, m_{FA}, m_{FB}	Moment resistance per unit length at fixed edges (any, short and long)
m_{SA}, m_{SB}	Moment resistance per unit length in spans (short and long)
R, R(t) R_e	Resistance history of distributed or lumped system
R_m, Re, Ru	Maximum resistance in a given strain range (any, elastic, plastic)
t	Time
V, V(t)	Dynamic reaction (or support shear) history = $V_F.F+V_R.R$
V_A	Total reaction history on short edge = $V_{FA}.F+V_{RA}.R$
V_B	Total reaction history on long edge = $V_{FB}.F+V_{RB}.R$
V_F, V_{FA}, V_{FB}	Load reaction coefficient (end, short and long edges)
V_R, V_{RA}, V_{RB}	Resistance reaction coefficient (end, short and long edges)
V_{PA}, V_{PB}	Peak reaction history per unit length on short and long edges
X, x, y	Position on span or panel
λ	Aspect ratio = A/B
λ`	Aspect ratio of affine isotropic panel
ϕ	Shape function of member deflection

1. Introduction

Design of defense structures to resist blast effects developed throughout the 20th century, and particularly since the Second World War. More recently, the use of bombs by terrorist organizations has greatly increased the range of structures that may be subjected to blast effects. Analysis of the response of flexural members under transient dynamic loading up to and beyond the elastic limit is a key part of the design of blast resistant structures.

Analytical solutions for the forced vibration of structural members with distributed mass and load become very involved for cases more complicated than simply supported beams, so approximate methods of analysis have normally been employed.

Until the advent of non-linear transient dynamic finite element (FE) analysis in the 1980s, almost all analysis has been based on Single Degree of Freedom (SDOF) methods. Even with powerful FE methods available, SDOF analysis is still very widely used as a cost-effective approach requiring relatively simple input data. Even where the complexity of the structure justifies a FE analysis, SDOF analysis will often be used for preliminary calculations or as a check on the FE response.

Because of the military basis of the threats, the development of SDOF methods can be traced largely through the substantial numbers of military design manuals written or commissioned by the US armed forces. References here are to manuals published by the US Army Corps of Engineers (USACE). As well as collaborating on some of these manuals, the US Naval Facilities Engineering Command and the US Air Force Weapons Laboratory published other design manuals independently, but these have not been referenced in this paper.

These manuals incorporate two main SDOF approaches, the Modal method, and the Equivalent SDOF method. Both work by treating the response of one point of the distributed member as being typical of the whole response, and equating the response at that point to that of an idealized lump mass-spring system that only has a single displacement variable. The modal method appeared as early as 1946 [1], but was less versatile than the Equivalent SDOF method, and had been more or less superseded by the 1970s. It is not considered further in this paper.

Although the Equivalent SDOF method is also used in other fields of dynamic analysis, such as for assessing sway of buildings under seismic excitation, this paper only reviews the application of the method for analysis of one and two way spanning reinforced concrete structural members in flexure, subject to blast or shock loading.

2. The theoretical basis

The Equivalent SDOF method was first widely disseminated for blast analysis in the 1957 USACE manual "Design of Structures to resist the Effects of Atomic Weapons". EM 1110-345-415 "Principals of Dynamic Analysis and Design [2] contains a detailed description of the method. Text books [3,4] and other manuals up to the current day [5] have contained similar descriptions of the method in greater or lesser detail, but the principals have not changed.

2.1 Dynamic deflection

Before analyzing the response of a structural element with distributed mass and loading, the mass, resistance and loading are replaced in Newton's Equation of Motion with the equivalent values for a lumped mass-spring system.

Newton's differential equation of motion for the lumped system,

$$M_e \cdot \frac{d^2x}{dt^2} + R_e(x) = F_e(t) \qquad \{1\}$$

can then be solved by a range of different techniques, from charts based on solutions for idealized resistance functions and loadings, to direct step-by-step numerical integration of the differential equation with interpolation of piecewise resistance functions and loading histories.

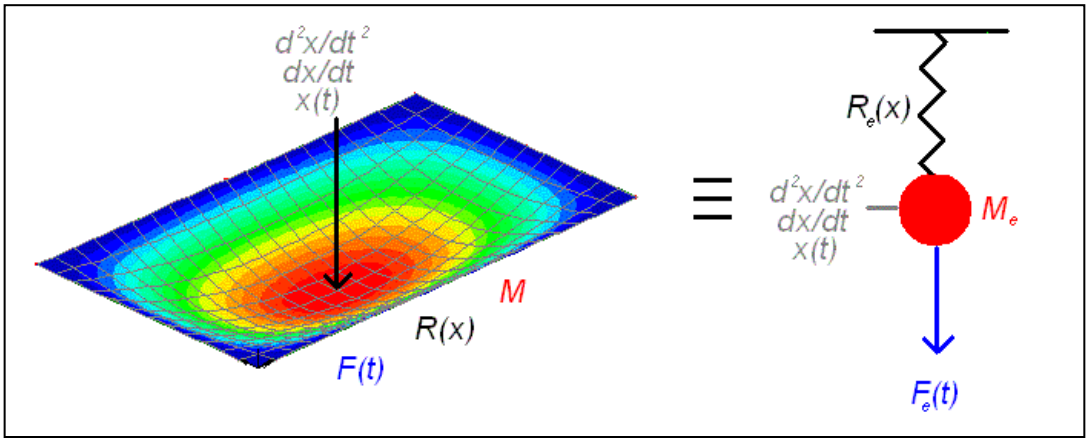

Figure 1. Distributed flexural member and equivalent lumped model

The equivalence of the terms is based upon energy, with the equivalent mass having equal kinetic energy, the equivalent resistance having equal internal strain energy and the equivalent loading having equal external work to the distributed system. The energy equations can be used to derive formulae for transformation factors to convert the total distributed mass, loading and resistance into the equivalent lumped values.

These transformation factors are functions of the distribution of mass and loading over the member, and of the incremental shape function of the deflected member. The

shape function is defined as the deflected shape at all points of the element, divided by the deflection at a chosen reference point, usually at midspan or at the point of maximum deflection. The incremental deflected shape function for a small additional deflection at the current deflection must be used to account for non-linearity. The basic formulae for the transformation factors hold for any deflected shape and mass or load distribution.

Loading factor $$K_L = \frac{F_e(t)}{F(t)} = \frac{\int_0^L f(x)\cdot\phi(x)dx}{\int_0^L f(x)dx} \; or = \frac{\oint_{Area} f(x,y)\cdot\phi(x,y)dxdy}{\oint_{Area} f(x,y)dxdy} \qquad \{2\}$$

Mass factor $$K_M = \frac{M_e}{M} = \frac{\int_0^L m(x)\cdot\phi(x)^2 dx}{\int_0^L m(x)dx} \; or = \frac{\oint_{Area} m(x,y)\cdot\phi(x,y)^2 dxdy}{\oint_{Area} m(x,y)dxdy} \qquad \{3\}$$

The resistance factor has been shown to be equal to the loading factor K_L, with the resistance defined as a loading with the same distribution in space as the applied loading.

In practice, the ratio of the mass factor to loading factor, the load-mass factor K_{LM}, is the single transformation factor required to define an equivalent equation of motion for a structural member loaded by most transient loadings.

For any particular case of mass and loading distribution, if the incremental deflected shape used to calculate the transformation factors is the exact dynamic deflected shape over time, then the response of the equivalent SDOF system will exactly match the response of the chosen reference point on the structural element, in both amplitude and time. In practice, the deflected shape varies with time, and cannot be known accurately without a prior dynamic analysis of the distributed structural element, which would defeat the purpose of using a SDOF analysis.

However, the Equivalent SDOF method can be used as an approximate method of analysis if a deflected shape is assumed, with the accuracy of the approximation depending upon the particular deflected shape assumed. Any deflected shape consistent with the kinematic constraints of the supports may be assumed.

Two deflected shapes generally shown to give a reasonably accurate approximation are the mode shape of the fundamental mode of free vibration, and the static deflected shape under the same distribution of load as occurs in the blast loading. The mode shapes are difficult to derive for all but the simplest cases, and only apply to the elastic response, so the static deflected shape is the most common approximation used. It is relatively straightforward to derive and has been shown to give dynamic responses accurate to within a few percent for the cases assessed.

For analysis of non-linear elasto-plastic flexural members, different incremental deflected shapes are used for different strain ranges, from fully elastic, through

elastic-plastic (where plastic hinges have formed at the supports but not in the span) to fully plastic (where sufficient hinges have formed to produce a plastic mechanism). This gives rise to different transformation factors at different strain ranges, with corresponding changes in stiffness and strength.

2.2 Dynamic Reactions

The reactions from the lumped SDOF analysis do not give the dynamic reactions of the distributed element. However, the Equivalent SDOF method has a systematic way of calculating the reactions using dynamic equilibrium.

If the structural member is divided into sections such that there is no shear force across the internal division lines, then the loads, the resistance moments, the reactions and the inertia forces acting on each section will be in dynamic equilibrium. The only forces on sections that are not pre-defined for a given time and deflection are the inertia forces. However, although the value of the inertia forces cannot be pre-defined, the centre of action of the inertia on each section can be calculated from the mass distribution and the acceleration distribution. The acceleration distribution is assumed the same as the incremental deflected shape, which will be correct if the shape function does not vary with time.

For a point of zero shear at X, Distance of the centre from the support is given by:

$$\overline{X}_{inertia} = \frac{\int_0^X m(x) \cdot \phi(x) \cdot x dx}{\int_0^X m(x) \cdot \phi(x) dx} \qquad \{4\}$$

If the rotational equilibrium of each section is calculated about the centre of action of the inertia forces, the value of the inertia forces will be eliminated from the equation and the reaction history can be defined as a factored combination of the loading history and the resistance history. The resistance will have been pre-defined in terms of deflection, but the SDOF calculation will give the deflection history, which can be used to define the reaction history:

$$V(t) = V_F \cdot F(t) + V_R \cdot R(d(t)) \qquad \{5\}$$

The factors are dependent on the spatial distribution of the loading, but not on the temporal distribution. As a result, the two dynamic reaction factors for any support are always equal to the static reaction coefficient, i.e. $V_F+V_R = V_{Static}$, as F = R for a static case.

3. Implementation for one-way spanning members

3.1 Historic implementation

The next section of "Design of Structures to resist the Effects of Atomic Weapons", EM 1110-345-416 "Structural Elements Subjected to Dynamic Loads" [6], contained extensive tables of resistance formulae, SDOF transformation factors and SDOF reaction coefficients for a range of structures, as well as example calculations for their derivation.

This manual included tables for one-way spanning slabs and beams with three support conditions and appropriate strain ranges arising from yield conditions:

- Simply supported (elastic & plastic ranges)
- Fixed ended (elastic, elastic-plastic & plastic ranges)
- Propped cantilever (elastic, elastic-plastic & plastic ranges)

Three loading distributions were included:

- Uniformly distributed
- Single concentrated load at mid-span
- Two equal concentrated loads at third points

For concentrated load cases, the alternative options of distributed mass and mass lumped with the loads were both addressed.

3.2 Subsequent developments

A modified version of the propped cantilever table was published in 1964 by Biggs [3] incorporating elastic shear terms in the reactions, although as discussed below it does not fully resolve the problem.

The one-way spanning coefficients have not been revised since, and are still mostly in current use [5,7].

Cantilever spans in elastic and plastic ranges for concentrated loads at the tip and for distributed loads are included in more recent manuals.

At the start of the 1990s, dissatisfaction was being expressed by Krauthammer et al. with the accuracy of the dynamic deflections and reactions calculated from the tabulated parameters, particularly for non-symmetric cases with complicated boundary conditions [8]. However, the focus was on development of alternative methodology, rather than on the accuracy of the published tables.

3.3 Re-evaluation of tables

Evaluation of historic implementation and developments has identified four areas where the theory has been incorrectly applied in deriving these tables, mostly for the propped-cantilever table. In addition, there appears to be at least one calculation error in the tables.

- All reactions in the tables are based on the centre of inertia being at the centre of the incremental deflected shape of the sections. This is correct only for uniformly distributed mass. The tabulated reaction coefficients are incorrect for beams supporting concentrated mass.

- In propped-cantilevers, the maximum deflection is not at the centre of the span. The elastic stiffness and shape functions in the propped-cantilever table have been based on reference positions at the point of maximum deflection, even though this is inconsistent with the elastic-plastic and plastic parameters based on the mid-point. A consistent reference point must be used for all strain ranges. In practice a reference point at mid-span is the most practical.

- The total force diagram should be used to identify the point of zero shear for dynamic equilibrium calculations. For symmetrical spans, the total and incremental force diagrams are the same, but this is not true for propped cantilevers. The reaction coefficients in the elastic-plastic and plastic ranges are not the same as for the simply supported case. The addition of the elastic shear term corrects the static equilibrium, but not the dynamic equilibrium for third-point loads or distributed loads, where the total shear is not zero at mid-span.

- The point of zero shear in the elastic-plastic range is also the point of maximum bending moment, and will determine where the span plastic hinge forms on transition to the plastic range. This in turn will influence the deflected shape, and hence the plastic resistance and all of the plastic SDOF coefficients. In the propped-cantilever tables this has been applied inconsistently. The third-point resistance is based upon a hinge at a third point, but the other resistances and all of the plastic SDOF parameters are based on a mid-point hinge. In practice only the central point load produces a plastic hinge at mid-span, so all the other cases are incorrect.

- For third-point loads and distributed mass on a simply supported span, the values of K_M and K_{LM} and the reaction coefficients are incorrect, although the shape function in Biggs and the value of K_L are correct. This appears to be the result of incorrect calculations.

4 New calculations for one-way spans

New calculations have been undertaken for all of the one-way cases normally tabulated. The results are listed in tables 1 to 4.

These calculations have been produced on Mathcad [9], using elastic deflected shapes derived from Roark's Formulas for Stress & Strain [10]. Symbolic solutions of calculus were generally used to produce values as ratios of integers, before converting to decimal values for tabulation.

The solution for a propped-cantilever carrying a uniformly distributed load is particularly complicated, as the point of zero shear in the elastic-plastic range varies with deflection. As a result, the elastic-plastic reaction coefficients of force and resistance, and even of elastic shear are not constant, and vary with the loading and resistance. In practice these variations are small for values of force and resistance around the elastic resistance or greater, but are significant at lower values. To be in the elastic-plastic range the resistance must exceed the elastic resistance, so the reaction is not sensitive to variation in resistance. However the influence of loading and elastic shear on the reaction may vary significantly with lower values of loading. The full equation is given with table 4, as well as tabulated values that will be reasonably accurate for higher values of loading.

The location of the plastic hinge in the span of a propped-cantilever carrying a uniformly distributed load will depend on the ratio of the resistance moments at the support and in the span. The full equations for the SDOF parameters are given with table 4, as well as values tabulated for the most common case with equal moment resistance.

The propped cantilever model gives mid-point deflections, not maximum deflections. For the case with uniformly distributed load, the plastic deflection can be used to calculate the support rotation for the fixed support. However, the location of the span hinge will be required to calculate the greater rotation of the pinned support.

Table 1. SDOF factors for simply supported one-way spans

Loading distribution	Strain range	Mass distribution	Load factor K_L	Mass factor K_M	Load-mass factor K_{LM}	Maximum Resistance R_m	Spring constant k	Dynamic Reaction V
Single point load at mid-spam	Elastic	Uniform	1.0	0.49	0.49	4 M_S/L	48 EI/L^3	0.78R-0.28F
		Concentrated		1.0	1.0			0.5R
	Plastic	Uniform	1.0	0.333	0.333	4 M_S/L	0	0.750R-0.250F
		Concentrated		1.0	1.0			0.5R
Two point loads at third-points	Elastic	Uniform	0.87	0.502	0.577	6 M_S/L	65.4 EI/L^3	0.474R+0.026F
		Concentrated		0.76	0.87			0.5R
	Plastic	Uniform	1.0	0.56	0.56	6 M_S/L	0	0.522R-0.022F
		Concentrated		1.0	1.0			0.5R
Uniformly distributed load	Elastic	Uniform	0.640	0.504	0.787	8 M_S/L	348 $EI/5L^3$	0.393R+0.107F
	Plastic	Uniform	0.500	0.333	0.667	8 M_S/L	0	0.38R+0.12F

Table 2. SDOF factors for cantilevered one-way spans

Loading distribution	Strain range	Mass distribution	Load factor K_L	Mass factor K_M	Load-mass factor K_{LM}	Maximum Resistance R_m	Spring constant k	Dynamic Reaction V
Single point load at free end	Elastic	Uniform	1.0	0.236	0.236	M_F/L	$3EI/L^3$	1.737R-0.737F
		Concentrated		1.0	1.0			1.0 R
	Plastic	Uniform	1.0	0.333	0.333	M_F/L	0	1.500R-0.500F
		Concentrated		1.0	1.0			1.0 R
Uniformly distributed load	Elastic	Uniform	0.400	0.257	0.642	2 M_F/L	$8EI/L^3$	0.692R+0.308F
	Plastic	Uniform	0.500	0.333	0.667	2 M_F/L	0	0.750R+0.250F

Table 3. SDOF factors for fixed-ended one-way spans

Loading distribution	Strain range	Mass distribution	Load factor K_L	Mass factor K_M	Load-mass factor K_{LM}	Maximum Resistance R_m	Spring constant k	Dynamic Reaction V
Single point load at mid-span	Elastic	Uniform	1.0	0.37	0.37	$8\ M_F/L$	$192\ EI/L^3$	0.71R-0.14F
		Concentrated		1.0	1.0			0.5R
	Elastic-plastic*	Uniform	1.0	0.49	0.49	$4\ (M_F + M_S)/L$	$48\ EI/L^3$	0.78R-0.28F
		Concentrated		1.0	1.0			0.5R
	Plastic	Uniform	1.0	0.33	0.33	$4\ (M_F + M_S)/L$	0	0.75R-0.25F
		Concentrated		1.0	1.0			0.5R
Uniformly distributed load	Elastic	Uniform	0.53	0.41	0.77	$12\ M_F\ /L$	$384\ EI/L^3$	0.36R+0.14F
	Elastic-plastic	Uniform	0.640	0.504	0.787	$8(M_F + M_S)/L$	$348\ EI/5L^3$	0.393R+0.107F
	Plastic	Uniform	0.500	0.333	0.667	$(M_F + M_S)/L$	0	0.38R+0.12F

For M_F = ultimate moment capacity at support and M_S = ultimate moment capacity at mid-span.

* Note that the elastic-plastic strain range will only occur if $M_F > M_S$. If they are equal the transition will be direct from elastic to plastic

Table 4. SDOF Factors for propped-cantilever one-way spans

Loading distribution	Strain range	Mass distribution	Load factor K_L	Mass factor K_M	Load-mass factor K_{LM}	Maximum Resistance R_m	Spring constant k	Dynamic Reaction V1	Dynamic Reaction V2
Single point load at mid-span	Elastic	Uniform	1.0	0.445	0.445	16 M_F /3L	109.7 EI/L^3	0.495R-0.182F	0.971R-0.284F
		Concentrated		1.0	1.0			0.375R	0.625R
	Elastic-plastic	Uniform	1.0	0.49	0.49	2 (M_F +2 M_S)/L	48 EI/L^3	0.78R-0.28F-Mps/L	0.78R-0.28F+Mps/L
		Concentrated		1.0	1.0			0.5R-Mps/L	0.5R+Mps/L
	Plastic	Uniform	1.0	0.33	0.33	2 (M_F +2 M_S)/L	0	0.75R-0.25F-Mps/L	0.75R-0.25F+Mps/L
		Concentrated		1.0	1.0			0.5R-Mps/L	0.5R+Mps/L
Two point loads at third-points	Elastic	Uniform	1.067	0.767	0.719	6 M_F /L	172.8 EI/L^3	0.513R-0.179F	0.621R+0.046F
		Concentrated		1.169	1.096			0.333R	0.632R+0.034F
	Elastic-plastic	Uniform	0.87	0.502	0.577	2 (M_F +3 M_S)/L	65.4 EI/L^3	0.681R-0.181F-Mps/L	0.381R+0.119F+Mps/L
		Concentrated		0.76	0.87			0.5R-Mps/L	0.5R+Mps/L
	Plastic	Uniform	1.0	0.56	0.56	2 (M_F +3 M_S)/L	0	0.750R-0.250F-Mps/L	0.375R+0.125F+Mps/L
		Concentrated		1.111	1.111			0.5R-Mps/L	0.5R+Mps/L
Uniformly distributed load	Elastic	Uniform	0.600	0.483	0.804	8 M_F /L	192 EI/L^3	0.292R+0.083F	0.459R+0.166F
	Elastic-plastic	Uniform	0.640	0.504	0.787	(3.479 M_F + 8.178 M_S)/L **	348EI/5L^3	0.387R+0.098F -Mps/L #	0.387R+0.114F +Mps/L #
	Plastic	Uniform	0.589*	0.462*	0.785*	(3.479 M_F + 8.178 M_S)/L **	0	0.311R+0.104F*	0.439R+0.146F*

Approximate value for F~R~10 M_F/L or greater. For general elastic-plastic case where M_F/L=Re/8:

$$V1=(\frac{R}{2}-\frac{\mathrm{Re}}{8})\cdot\frac{3072(\frac{R}{\mathrm{Re}})^3+336(\frac{R}{\mathrm{Re}})^2-24\frac{R}{\mathrm{Re}}-3}{3904(\frac{R}{\mathrm{Re}})^3+528(\frac{R}{\mathrm{Re}})^2-36\frac{R}{\mathrm{Re}}-5}+(\frac{F}{2}-\frac{\mathrm{Re}}{8})\cdot\frac{832(\frac{F}{\mathrm{Re}})^3+192(\frac{F}{\mathrm{Re}})^2-12\frac{F}{\mathrm{Re}}-2}{3094(\frac{F}{\mathrm{Re}})^3+528(\frac{F}{\mathrm{Re}})^2-36\frac{F}{\mathrm{Re}}-5}$$

$$V2=(\frac{R}{2}+\frac{\mathrm{Re}}{8})\cdot\frac{3072(\frac{R}{\mathrm{Re}})^3-336(\frac{R}{\mathrm{Re}})^2-24\frac{R}{\mathrm{Re}}+3}{3904(\frac{R}{\mathrm{Re}})^3-528(\frac{R}{\mathrm{Re}})^2-36\frac{R}{\mathrm{Re}}+5}+(\frac{F}{2}+\frac{\mathrm{Re}}{8})\cdot\frac{832(\frac{F}{\mathrm{Re}})^3-192(\frac{F}{\mathrm{Re}})^2-12\frac{F}{\mathrm{Re}}+2}{3094(\frac{F}{\mathrm{Re}})^3-528(\frac{F}{\mathrm{Re}})^2-36\frac{F}{\mathrm{Re}}+5}$$

* Values vary. Values given are for $M_S = M_F$ only. For the general plastic case, where $N = M_S / M_F$:

$$K_L=1-\frac{1-2N+\sqrt{(1-2N)^2-2}}{4} \qquad K_M=\frac{4}{3}K_L^{\,2} \qquad K_{LM}=\frac{4}{3}K_L \qquad V1=(\frac{3}{8}R+\frac{1}{8}F)\cdot(-2N+\sqrt{(1+2N)^2-1}) \qquad V2=(\frac{3}{8}R+\frac{1}{8}F)\cdot(2+2N-\sqrt{(1+2N)^2-1})$$

** Linear approximation. For the general plastic case where $N = M_S / M_F$: $$Ru=\frac{M_F}{L}\frac{2}{(2N+1)-\sqrt{(2N+1)^2-1}}$$

5. Implementation for two-way spanning members

5.1 Historic implementation and evaluation

EM 1110-345-416 "Structural Elements Subjected to Dynamic Loads" [6] contains tables for a simply supported rectangular slab with uniform loading in elastic and plastic strain ranges, and tables for rectangular slabs fixed at all edges, long edges and short edges only, in the elastic, elastic-plastic and plastic strain ranges.

Although these are tabulated for six aspect ratios between 1 and 0.5, in practice only the fully pinned and fully fixed cases for an aspect ratio of 1 were calculated, and the parameters were extrapolated between these cases and one-way spanning parameters at an aspect ratio of zero.

5.1.1 Plastic analysis

The plastic deflected shapes were based on simple yield line patterns. The interpolation process used results in a fixed yield line angle of 45° in the spans. The reactions are based on dynamic equilibrium calculations assuming that there is zero shear across the span yield lines. Review by the author [11] of the plastic calculations showed a number of sources of inaccuracy:

- A 45º yield-line approximation is justified in static analysis because it only affects the resistance. This has a stationary value at the critical angle, so a moderate error in yield-line position will only cause a small error in the resistance. The SDOF parameters are not stationary, so the errors due to the approximation will be larger in these, as is illustrated in Table 5.

Parameters for simply supported plastic panel of aspect ratio of 0.5	Stationary node point	45 degree node point	Difference
Resistance coefficient, Ru/*m*	28.21	28.80	1.83%
Load factor, K_L	0.391	0.417	6.45%
Mass factor, K_M	0.225	0.250	11.2%
Load-mass factor, K_{LM}	0.574	0.600	4.49%
Load reaction coefficient, short edge, V_{FA}	0.054	0.042	-23.2%
Resistance reaction coefficient, short edge, V_{RA}	0.109	0.083	-23.2%
Load reaction coefficient, long edge, V_{FB}	0.098	0.104	6.45%
Resistance reaction coefficient, long edge, V_{RB}	0.239	0.271	13.2%

Table 5. Plastic parameters for alternative yield-line models

- The equilibrium method of yield line solution requires the use of nodal forces to represent shears and twists across yield lines [12], so the assumption of no shear transfer is not universally correct. A constraint such as 45º yield-line

angles will require non-zero nodal forces for equilibrium. Neglecting these forces in the dynamic equilibrium calculations leads to larger errors in the reaction coefficients, as shown in Table 5.

- A 1951 American Concrete Institute document is cited for the resistance coefficients used in the tables. These values are not consistent with the 45º assumptions and give more upper bound, i.e. less accurate, results, as shown in Table 6.

Resistance coefficient of simply supported isotropic panel	Stationary Node Point	45 degree node point		EM 1110-345-416[9] (table 6.2A)	
Aspect ratio λ	Ru/*m*	Ru/*m*	Difference	Ru/*m*	Difference
1.0	24.0	24.0	0%	24.0	0%
0.9	24.10	24.13	0.12%	24.22	0.50%
0.8	24.44	24.55	0.45%	24.88	1.80%
0.7	25.13	25.34	0.84%	26.0	3.46%
0.6	26.31	26.67	1.37%	27.5	4.52%
0.5	28.28	28.80	1.83%	30.0	6.08%

Table 6. Plastic resistance coefficients from alternative models

- The plastic resistance is defined in terms of different span and support resistances, implying that the analysis can be applied to an orthotropic slab. In yield line theory, yield line angles are modified by orthotropy. The Affinity Theorem is used to convert the orthotropic panel to an isotropic affine panel with a modified aspect ratio [12]. If the yield-line angles in the affine panel are solved assuming a 45º angle, the yield-line angles in the real orthotropic panel cannot be 45º.

- A particular case of orthotropic slabs is fixity on two opposite sides only. If the reinforcement were otherwise isotropic, the Affinity Theorem would change 45º yield line angles to approximately 35º or 55º, depending on which edges are fixed. The interpolation used for long or short edges fixed assumes an unchanged 45º angle, and is not consistent with yield-line theory.

5.1.2 Elastic analysis

The elastic and elastic-plastic analyses are based on a very crude approximation of two-way spanning deflected shape, using triangular and trapezoidal panels as for the yield-line calculations, but with one-way spanning deflected shapes, so as to allow extrapolation from the square case to the one-way spanning. This gives rise to a number of sources of inaccuracy:

- The assumed deflected shape is substantially different from the deflected shape of a slab under static uniformly distributed load, as can be seen in Figure 2. This introduces significant errors even for the symmetrical square panel, as shown in Table 7.

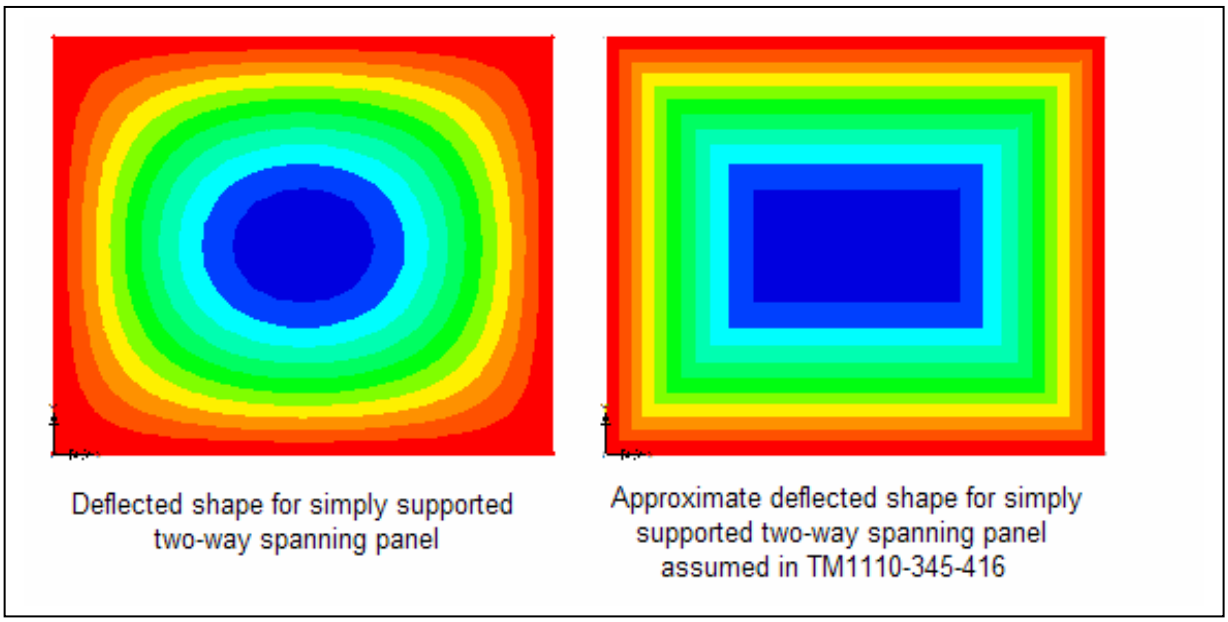

Figure 2. Comparison of typical true and approximate elastic deflected shapes

Parameters for simply supported elastic panel of aspect ratio 1.0, using Poisson's ratio of 0.3	Navier solution after Timeshenko	EM 1110-345-416 (table 6.2A)	Difference
Spring constant coefficient $ke/(A^2/EI)$	270.5	271	0.18%
Load factor, K_L	0.418	0.45	7.66%
Mass factor, K_M	0.262	0.31	18.3%
Load-mass factor, K_{LM}	0.627	0.68	8.45%
Load reaction coefficient, short edge, V_{FA}	0.128	0.07	-45.3%
Resistance reaction coefficient, short edge, V_{RA}	0.122	0.18	+47.5%
Load reaction coefficient, long edge, V_{FB}	0.128	0.07	-45.3%
Resistance reaction coefficient, long edge, V_{RB}	0.122	0.18	+47.5%

Table 7. Elastic parameters for alternative deflected shapes

- The mixing of one-way deflected shapes for simple and pinned supports for the panels with fixity on two edges implies a deflected shape which does not even meet at the joins, and is therefore not kinematically compatible.

- There is no justification for the assumption that 45° lines in an elastic panel represent lines of zero shear except in symmetrical square panels. Ignoring any shear transfer will introduce substantial errors in the reactions.

- The spring constants are based on coefficients given by Timoshenko [13] for a Poisson's ratio of 0.3, suitable for steel plates, but twice the customary value for reinforced concrete. These have been used unaltered, which introduces additional inaccuracy, as a simple adjustment in the formula can be made for Poisson's ratio.

- The reference to Timeshenko's "Theory of Plates and Shells" to calculate spring constants is rather ironic as the book contains all the formulae required for a proper elastic deflected shape and stress calculation for different aspect ratios.

- In employing the simply-supported elastic model to represent the incremental elasto-plastic stage, no provision is made to allow for the elastic shear in the supports. Even though the panels are symmetrical in two axes, unequal fixity will give rise to an elastic shear transfer from the pinned edges to the fixed edges that will modify the reactions. This omission leads to inaccurate distribution of reactions for panels with unequal fixity.

Numerical accuracy is suspect in the original tables. Using rounded values of K_L and K_M to calculate K_{LM} results in rounding errors and inconsistent trends in K_{LM} from what is supposed to be a smooth interpolation. This helps to conceal a typographical error where a value of K_M repeats that of the line above, and is used to calculate an incorrect K_{LM}. There are also rounding mistakes where the same ratio has sometimes been rounded down where it has been correctly rounded up elsewhere, and cases where some of the few calculated values of K_L and K_M for square panels have been incorrectly rounded to try to equalize the interpolation steps.

5.2 Biggs 'Introduction to Structural Dynamics'

In 1964, Biggs [3] included tables extracted from EM-1110-345-416 in his seminal textbook, although for two-way spans he considered only the simply supported and fully fixed cases. He stated that the factors given were based upon approximations to the classical plate theory for deflections in the elastic range and yield line theory in the plastic range, which in the light of foregoing comments may rather overstate their provenance.

Biggs did make two improvements to the two-way tables:

- the elastic spring constant, corresponds to an aspect ratio of 0.15 rather than 0.3, as appropriate for reinforced concrete, although this is not stated in the text or tables.

- the elastic resistance of the fully fixed panels was recalculated.

Biggs also tidied up the inconsistent elastic/ elastic-plastic value of K_L for a square panel, giving a consistent, if not completely accurate, value of 0.46. However, other errors in the two-way tables that he included from EM-1110-345-416 are not corrected.

5.3 SDOF COEFFICIENTS IN TM 5-1300

In 1969, USACE published TM 5-1300, "Structures to Resist the Effects of Accidental Explosions" [14], a manual for safety in storing and processing explosives

and munitions. This makes extensive use of SDOF analysis for structural response to external and internal explosions.

5.3.1 Plastic Analysis

There are extensive charts, tables and formulae defining hinge or yield-line location, resistance, and static shears for plastic analysis of uniformly loaded one-way spans and a variety of two-way spans. These include panels with one or two edges unsupported, so long as opposed supports have symmetric support fixity. The single chart for load-mass factor against yield line location covers all these cases.

This data is based upon the equilibrium method of yield-line analysis for the classical yield-line pattern, with the interior "sagging" yield-lines extending to the corners of the panels, and the nodes free to find the stationary position, as described by Jones and Wood [12]. The data incorporates the Affinity Theorem, and works equally for isotropic and orthotropic panels. As such, it represents a major step forward from the approximations of EM 1110-345-416.

Even so, there are three areas of concern about the analysis used:

- An arbitrary modification of stress is used to reduce the resistance from the "classic" yield-line values by between 11% and 17% to account for corner stiffness. This adjustment is at least 50% greater than can be justified by advanced yield-line models, and fails to adjust the deflected shape and transformation factors.

- The equilibrium equations do not include nodal force terms, and will reach an incorrect equilibrium where these are non-zero, such as where diagonal yield lines reach free edges.

- TM5-1300 does not provide formulae for calculating the dynamic reactions. It uses a static plastic resistance as a generally conservative approximation for shear design, but does not allow calculation of a reaction history on a support. This makes it impractical for calculating successive degrees of freedom.

5.3.2 Elastic Analysis

Charts and tables are provided to derive the elastic and elastic-plastic stiffness and resistance, to build up a multi-stage resistance curve. A table is provided to give transformation factors for uniformly loaded elastic and elastic-plastic cases, both one-way and two-way spanning.

This table gives values of K_{LM} only, for a range of support conditions and support fixity. For square panels supported uniformly on four sides, the values are superior to those produced by EM 1110-345-416, being accurate within the 2 decimal places given for all sides simply-supported, and within 3% for all sides fixed. This implies more realistic two-way spanning shape functions.

However, outside these two values, the table is based on linear interpolation, mostly between one-way spanning values assumed at aspect ratios of 0.5 or 2, irrespective of the support conditions.

For the panels supported on all four edges this is interpolated to the square panel with an aspect ratio of unity. This is less accurate than the linear interpolation between aspect ratios of zero and unity in EM 1110-345-416, as the true transformation factors are actually less sensitive to aspect ratio than a linear interpolation. It would actually be considerably more accurate to apply the K_{LM} value for the square panel as a constant value between aspect ratios of 2 and 0.5 than to use the table in TM5-1300.

The situation is even worse for panels with one edge free. No two-way spanning case has been analyzed, and interpolation goes linearly from the one-way span at an aspect ratio of 0.5 to a cantilever at an aspect ratio of 2. There appears to have been no consideration that a two-way pattern might exist between these extremes with a K_{LM} value lower than either, or that the cut-off limit of 2 is wholly inappropriate for a panel with a free edge, when this is actually around the point of maximum two-way action.

The interpolation between simply-supported and fully fixed is again linear and is based solely on the number of fixed edges, taking no account of the distribution, or whether the long or the short edges are fixed. The true variation of K_{LM} with edge fixity is far more complex than assumed, with unequal fixity modifying the shape function.

TM5-1300 contains no data for calculating elastic reactions. The only recommendation is that, if the member does not go fully plastic, the elastic or elasto-plastic resistance at peak deflection is calculated, and then distributed between the supports in proportion to the static plastic reactions to approximate maximum elastic reactions.

5.3.3 1990 revision

Some additional data was incorporated in the 1990 revision of TM5-1300:

- Plastic resistance and shear data was added for asymmetric support fixity, but the K_{LM} chart is still limited to symmetric fixity by the text of the manual.

- Elastic resistance data for asymmetric support fixity is included, and the original K_{LM} table can be taken to apply, although this merely stretches further the already unreasonable interpolation.

- Cases with concentrated loads from EM 1110-345-416 have been included in the one-way span tables. These are often used to analyze supporting members, but the usefulness is somewhat reduced by the inability to generate a reaction history for the supported members.

5.4 SDOF coefficients in "Blast" computer program

In 1990 Mayor & Flanders adapted a SDOF computer model for the US Department of Transportation, sponsored by the US Department of State Office of Diplomatic Security, to predict failure of building walls subjected to blast pressure loading from conventional explosives.

The plastic analysis used, attributed to an earlier work by Wood (see reference12), treats the position of the simple yield lines as a variable to be optimized to give the minimum resistance. The resistance that this produces with no openings is compared favourably with those from Biggs. The K_L and K_M values used in the program are based on the deflected shape that this produces, but are not listed in the Technical Manual [15].

A finite element (FE) program was used to calculate the elastic deflected shapes, and derive values of K_L and K_M. The K_L values were checked using the first 30 terms of the Navier equations from Timeshenko [13]. Although a coarse FE mesh was used, coefficients were consistent within 1%, but differed from EM 1110-345-416 and Biggs values by up to 34%.

These discrepancies do not appear to have been followed up at the time.

5.5 Protective Structures Automated Design System (PSADS) 1998

This current document [5] supersedes a 1986 edition of TM5-855-1, whose SDOF approach was based on EM1110-345-416. It continues the use of this approach, except that the plastic resistances of panels with fixed supports are reduced by an arbitrary 10% to allow for the upper bound nature of simple yield line analysis. Some, but not all, of the improvements by Biggs have been incorporated in the tables of SDOF coefficients. An additional two-way spanning table has been added, for a panel with one free edge and three fixed edges, based upon the 45° internal yield line assumption, covering aspect ratios from 0.5 to 2.0.

However, PSADS does hedge its bets by including the TM5-1300 SDOF data as an Appendix. It leaves it to the user to find the conflicts between the data and to decide which to follow, although the supporting programs appear to be based on the values in the main text.

PSADS has sufficiently lost contact with the source of its data that EM 1110-345-416 is not referenced. The resistance and SDOF coefficients have been split and are presented in separate tables. The SDOF tables are headed as being for a Poisson's ratio of 0.3, although the worked examples in EM 1110-345-416 demonstrate that all of the coefficients in that table are independent of Poisson's ratio. Only the values of elastic spring stiffness in the other table are sensitive to Poisson's ratio. These are based on a value of 0.15.

Although PSADS does allow calculation of dynamic reactions, it has adopted the use of the quasi-static reaction for shear calculations from TM5-1300 because of the artificially high initial reactions that can be produced by the simplified assumptions of a SDOF analysis.

6 New analysis for two-way spans

Given the discrepancies found between the previously published values for the equivalent SDOF parameters, new analyses have been undertaken for elastic, elastic-plastic and plastic ranges for two-way spanning members supported on four sides, corresponding to the tables in EM 1110-345-416.

6.1 Plastic analysis

A range of five different symmetrical yield line patterns have been analysed over a range of aspect ratios and support fixities using the energy method.

- Classic yield-lines extending to corners – 1 variable
- Floating corner levers – 4 variables
- Anchored corner levers – 3 variables
- Floating circular corner fans – 3 variables
- Anchored circular corner fans – 2 variables

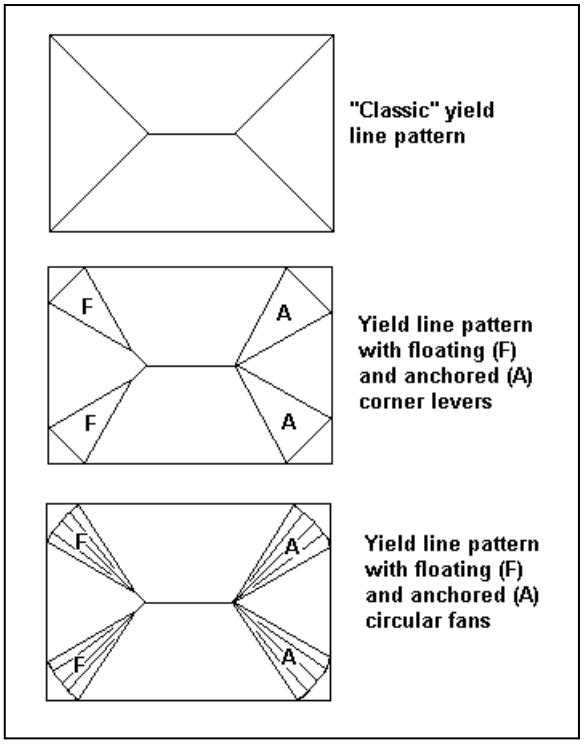

Figure 3. Alternative yield line patterns

For each case, equations to calculate the stationary value of the variables were derived by differentiating the work equation with respect to each independent variable. The non-linear equations were solved simultaneously in Mathcad for selected values of

aspect ratio and support fixity by numerical methods, except for the classic case where the single quadratic equation was solved analytically.

Except for nearly square, symmetrically supported panels, the corner levers proved to be the patterns giving the least upper-bound resistance. For consistency, the calculations presented have therefore been based on corner levers throughout, using floating corner levers where the optimal mechanism is valid and anchored corner levers where it is not. The results of this analysis are given in tables 8-11.

Most members designed to resist blast loading are doubly reinforced, even when some of the supports are modeled as simply supported. This affects the yield line patterns at the corner levers, and has been taken into account in the energy equations used. As a result the simply supported corner levers are very small, and the resistance and deflected shape are indistinguishable from the classic case.

Where singly reinforced members are taken to resist blast, the properties can be calculated by applying the Affinity Theorem for orthotropic members to the values for the fully fixed model, as shown in figure 4.

The rigid components of the classic or corner-lever yield-line model were then modeled in a balanced FE analysis, with the yield line moments applied as well as the loading, nodal connections and one support to restrain the mechanism. This confirmed the equilibrium of the geometry and loading, with a negligible reaction on the extra support, due to discretisation error and reducing with mesh refinement. It also confirmed the presence and amplitude of non-zero nodal forces for anchored corner levers, and provided information on peak reactions, which are far from uniformly distributed even after plastic hinges have formed.

The dynamic reactions were calculated from the equilibrium of the different surfaces, initially ignoring nodal forces. The reactions from the corner lever and the rigid corner were divided between the sides to maintain equilibrium. Where the corner levers were anchored, the differences in reaction between the equilibrium calculations and the FE calculations were used to correct the dynamic reactions for the nodal forces.

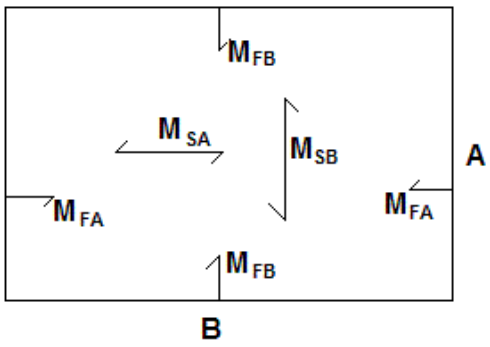

For analysis of Orthotropic Panels with λ = A/B

For simply supported panels with both faces reinforced and corners held:

Use Table 4 with $\lambda' = \lambda \cdot \sqrt{\frac{m_{SB}}{m_{SA}}}$ and take $m = \sqrt{m_{SB} \cdot m_{SA}}$

For fully fixed panels (or any panels with corner moments of resistance equal to the support moment of resistance in the same direction):

Use Table 5 with $\lambda' = \lambda \cdot \sqrt{\frac{m_{SB} + m_{FB}}{m_{SA} + m_{FA}}}$ and take $m = \frac{\sqrt{(m_{SB} + m_{FB}) \cdot (m_{SA} + m_{FA})}}{2}$

For panels with the long edges fixed and both faces reinforced (m_{FA}=m_{SA}) at corners

Use Table 6 with $\lambda' = \lambda \cdot \sqrt{\frac{m_{SB} + m_{FB}}{2 \cdot m_{SA}}}$ and take $m = \sqrt{\frac{(m_{SB} + m_{FB}) \cdot m_{SA}}{2}}$

For panels with the short edges fixed and both faces reinforced (m_{FB} = m_{SB}) at corners

Use Table 7 with $\lambda' = \lambda \cdot \sqrt{\frac{2 \cdot m_{SB}}{m_{SA} + m_{FA}}}$ and take $m = \sqrt{\frac{m_{SB} \cdot (m_{SA} + m_{FA})}{2}}$

Figure 4. Use of the Affinity Theorem for the analysis of orthotropic panels

Aspect Ratio	Resis-tance	Transformation Factors			Dynamic Reactions			
		Load Factor	Mass Factor	Load-mass Factor	Short Side Total	Short Side Peak	Long Side Total	Long Side Peak
λ	Ru	K_L	K_M	K_{LM}	V_A	V_{PA}	V_B	V_{PB}
1	24.00*m*	0.333	0.167	0.500	0.083F+0.167R	1.718 V_A/A	0.083F+0.167R	1.718 V_B/B
0.9	24.10*m*	0.342	0.176	0.513	0.079F+0.158R	1.729 V_A/A	0.086F+0.178R	1.724 V_B/B
0.8	24.44*m*	0.352	0.186	0.527	0.074F+0.148R	1.731 V_A/A	0.088F+0.190R	1.704 V_B/B
0.7	25.13*m*	0.364	0.197	0.542	0.068F+0.136R	1.735 V_A/A	0.091F+0.205R	1.676 V_B/B
0.6	26.31*m*	0.376	0.210	0.558	0.062F+0.123R	1.743 V_A/A	0.094F+0.221R	1.629 V_B/B
0.5	28.28*m*	0.391	0.225	0.574	0.054F+0.109R	1.755 V_A/A	0.098F+0.239R	1.548 V_B/B

Table 8. Dynamic coefficients for uniformly loaded, simply supported, isotropic, plastic panel

Aspect Ratio	Resis-tance	Transformation Factors			Dynamic Reactions			
		Load Factor	Mass Factor	Load-mass Factor	Short Side Total	Short Side Peak	Long Side Total	Long Side Peak
λ	Ru	K_L	K_M	K_{LM}	V_A	V_{PA}	V_B	V_{PB}
1	44.00*m*	0.318	0.160	0.502	0.091F+0.159R	0.132F/B+0.269R/B	0.091F+0.159R	0.132F/B+0.269R/B
0.9	44.20*m*	0.327	0.168	0.514	0.086F+0.147R	0.140F/B+0.284R/B	0.096F+0.171R	0.138F/B+0.285R/B
0.8	44.88*m*	0.338	0.178	0.526	0.080F+0.135R	0.148F/B+0.299R/B	0.101F+0.184R	0.142F/B+0.300R/B
0.7	46.22*m*	0.350	0.189	0.540	0.073F+0.121R	0.158F/B+0.317R/B	0.106F+0.200R	0.147F/B+0.320R/B
0.6	48.55*m*	0.364	0.202	0.555	0.066F+0.106R	0.168F/B+0.337R/B	0.110F+0.218R	0.150F/B+0.340R/B
0.5	52.44*m*	0.379	0.217	0.571	0.057F+0.090R	0.183F/B+0.366R/B	0.115F+0.238R	0.150F/B+0.356R/B

Table 9. Dynamic coefficients for uniformly loaded, isotropic, plastic panel, fixed on all sides

Aspect Ratio	Resis-tance	Transformation Factors			Dynamic Reactions			
		Load Factor	Mass Factor	Load-mass Factor	Short Side Total	Short Side Peak	Long Side Total	Long Side Peak
λ	Ru	K_L	K_M	K_{LM}	V_A	V_{PA}	V_B	V_{PB}
1	34.07*m*	0.355	0.190	0.537	0.036F+0.138R	0.120F/B+0.240R/B	0.134F+0.192R	0.147F/B+0.312R/B
0.9	35.09*m*	0.364	0.199	0.548	0.031F+0.127R	0.126F/B+0.251R/B	0.137F+0.205R	0.149F/B+0.325R/B
0.8	36.58*m*	0.374	0.209	0.559	0.027F+0.115R	0.132F/B+0.261R/B	0.139F+0.219R	0.152F/B+0.340R/B
0.7	38.72*m*	0.385	0.220	0.571	0.023F+0.103R	0.137F/B+0.270R/B	0.140F+0.234R	0.152F/B+0.352R/B
0.6	41.82*m*	0.397	0.232	0.584	0.018F+0.090R	0.145F/B+0.282R/B	0.141F+0.241R	0.151F/B+0.363R/B
0.5	46.47*m*	0.410	0.245	0.596	0.014F+0.076R	0.153F/B+0.296R/B	0.141F+0.268R	0.151F/B+0.374R/B

Table 10. Dynamic coefficients for uniformly loaded, isotropic, plastic panels, fixed on long sides only

Aspect Ratio	Resis-tance	Transformation Factors			Dynamic Reactions			
		Load Factor	Mass Factor	Load-mass Factor	Short Side Total	Short Side Peak	Long Side Total	Long Side Peak
λ	Ru	K_L	K_M	K_{LM}	V_A	V_{PA}	V_B	V_{PB}
1	34.07*m*	0.355	0.190	0.537	0.134F+0.192R	0.147F/A+0.312R/A	0.036F+0.138R	0.120F/A+0.240R/A
0.9	33.32*m*	0.345	0.181	0.525	0.132F+0.179R	0.144F/A+0.301R/A	0.040F+0.149R	0.115F/A+0.231R/A
0.8	32.80*m*	0.335	0.172	0.512	0.127F+0.165R	0.141F/A+0.288R/A	0.046F+0.162R	0.109F/A+0.217R/A
0.7	32.64*m*	0.329	0.166	0.504	0.121F+0.150R	0.191F/B+0.384R/B	0.052F+0.177R	0.146F/R+0.293R/B
0.6	32.99*m*	0.342	0.179	0.522	0.113F+0.133R	0.212F/B+0.416R/B	0.059F+0.195R	0.154F/B+0.315R/B
0.5	34.16*m*	0.358	0.194	0.541	0.103F+0.114R	0.236F/B+0.473R/B	0.067F+0.216R	0.159F/B+0.339R/B

Table 11. Dynamic coefficients for uniformly loaded isotropic plastic panels, fixed on short sides only

6.2 Elastic analysis

The response in the elastic and elastic-plastic ranges was calculated by a FE analysis of a quarter panel, using a moderately fine mesh of 8 noded shell elements. The simply supported deflections were checked against both the Navier and Levy solutions in Timeshenko, and the stresses and reactions against the Navier solution, matching to greater accuracy than is presented in table 12. With a suitable mesh the FE approach proved to be as accurate, and is easier to adapt for different support conditions, as given in tables 13-15.

A spreadsheet was used to post process the deflections, stresses and reactions from each case to establish the stiffness and SDOF parameters. Numerical integration from the FE output was used to calculate the transformation factors.

An alternative approach was used to calculate the dynamic reactions of symmetrical panels, still in accordance with the principles in EM1110-345-415, but without the need to make dubious assumptions.

Lines of zero shear were taken at the lines of symmetry, isolating the quarter panel used for the FE analysis. Deflection output was used to calculate the centre of the inertia forces in both axes. The centre of loading is calculated from the corner coordinates, the moments due to resistance are calculated from the reaction moments at the symmetry edges and supports (where fixed), and the centre of the reaction is calculated on each side from the reactions. By calculating equilibrium of resistance and forces taken about the centre of the inertia forces in two axes, four linear simultaneous equations are derived which are solved to give the total dynamic reaction coefficients presented in Tables 12 to15.

The elastic properties in Tables 12 to 15 are only applicable to panels with isotropic stiffness. However, orthotropic strength is permitted, provided hogging of the supports is not so much stronger than sagging of the spans that yield will occur in the spans before the supports have yielded. The elastic resistances have been written in terms consistent with orthotropic strength.

The elasto-plastic range for panels with some edges fixed has traditionally been analyzed by applying the simply-supported elastic stiffness and transformation factors, as the incremental deflection is the same. However, the reaction coefficients should be based on the total resistance, so the effect of the support moments must still be considered after they have reached the moment capacity. Similarly, the resistance at which the transition is taken to occur must be considered.

A consistent basis for both has been provided by analyzing a quadrant of a simply supported elastic panel with unit moment per unit length upon either edge. By equating midspan deflections of the elastic panel with edge fixity and the simply-supported panel combined with a unit bending moment on the fixed edge or edges, the value for the elastic resistance of the panels with support fixity has been calculated, as presented in Tables 13 and 15.

Aspect Ratio	Ultimate resistance	Elastic Stiffness Coefficient	Transformation Factors			Dynamic Reactions			
			Load Factor	Mass Factor	Load-mass Factor	Short Side Total	Short Side Peak	Long Side Total	Long Side Peak
λ	Re = Ru	$ke / (EI/A^2)$	K_L	K_M	K_{LM}	V_A	V_{PA}	V_B	V_{PB}
1	24.00*m*	251.8	0.419	0.262	0.626	0.136F+0.114R	1.752 V_A/A	0.136F+0.114R	1.752 V_B/B
0.9	24.10*m*	229.3	0.419	0.263	0.627	0.133F+0.098R	1.796 V_A/A	0.139F+0.130R	1.703 V_B/B
0.8	24.44*m*	212.2	0.420	0.264	0.628	0.128F+0.081R	1.839 V_A/A	0.142F+0.149R	1.644 V_B/B
0.7	25.13*m*	200.9	0.423	0.266	0.629	0.122F+0.064R	1.877 V_A/A	0.143F+0.171R	1.574 V_B/B
0.6	26.31*m*	196.7	0.427	0.270	0.632	0.115F+0.046R	1.908 V_A/A	0.143F+0.196R	1.493 V_B/B
0.5	28.28*m*	202.0	0.435	0.278	0.639	0.106F+0.029R	1.929 V_A/A	0.142F+0.223R	1.402 V_B/B

Table 12. Dynamic coefficients for uniformly loaded, simply supported, isotropic, elastic panels

Aspect Ratio	Elastic resistance	Elastic Stiffness Coefficient	Transformation Factors			Dynamic Reactions			
			Load Factor	Mass Factor	Load-mass Factor	Short Side Total	Short Side Peak	Long Side Total	Long Side Peak
λ	Re	$ke /(EI/A^2)$	K_L	K_M	K_{LM}	V_A	V_{PA}	V_B	V_{PB}
1	12.93 m_{FA} +12.93 m_{FB}	808.5	0.308	0.182	0.593	0.134F+0.116R	1.763 V_A/A	0.134F+0.116R	1.763 V_B/B
0.9	11.40 m_{FA} +14.53 m_{FB}	741.2	0.308	0.183	0.594	0.132F+0.095R	1.797 V_A/A	0.136F+0.137R	1.718 V_B/B
0.8	9.76 m_{FA} +16.37 m_{FB}	701.8	0.311	0.185	0.596	0.128F+0.074R	1.822 V_A/A	0.137F+0.161R	1.657 V_B/B
0.7	8.05 m_{FA} +18.56 m_{FB}	693.4	0.317	0.190	0.600	0.123F+0.054R	1.836 V_A/A	0.138F+0.185R	1.579 V_B/B
0.6	6.29 m_{FA} +21.28 m_{FB}	723.3	0.328	0.199	0.608	0.117F+0.034R	1.840 V_A/A	0.138F+0.211R	1.485 V_B/B
0.5	4.50 m_{FA} +24.95 m_{FB}	807.3	0.347	0.216	0.624	0.107F+0.018R	1.837 V_A/A	0.139F+0.236R	1.378 V_B/B

Table 13. Dynamic coefficients for uniformly loaded, isotropic, elastic panels fixed on all sides

Aspect Ratio	Elastic resistance	Elastic Stiffness Coefficient	Transformation Factors			Dynamic Reactions			
			Load Factor	Mass Factor	Load-mass Factor	Short Side Total	Short Side Peak	Long Side Total	Long Side Peak
λ	Re	$ke / (EI/A^2)$	K_L	K_M	K_{LM}	V_A	V_{PA}	V_B	V_{PB}
1	16.86 m_{FB}	533.6	0.359	0.220	0.611	0.090F+0.013R	3.111V_A/A	0.187F+0.209R	1.304V_B/B
0.9	17.44 m_{FB}	539.9	0.361	0.221	0.613	0.088F+0.003R	3.178V_A/A	0.188F+0.220R	1.283V_B/B
0.8	18.37 m_{FB}	560.6	0.365	0.225	0.617	0.086F-0.005R	3.212 V_A/A	0.187F+0.232R	1.256 V_B/B
0.7	19.80 m_{FB}	600.6	0.372	0.232	0.623	0.082F-0.012R	3.215 V_A/A	0.185F+0.244R	1.223 V_B/B
0.6	21.95 m_{FB}	669.3	0.383	0.243	0.633	0.077F-0.017R	3.190 V_A/A	0.182F+0.258R	1.184 V_B/B
0.5	25.20 m_{FB}	783.1	0.401	0.261	0.651	0.070F-0.020R	3.145 V_A/A	0.177F+0.272R	1.141 V_B/B

Table 14. Dynamic coefficients for uniformly loaded, isotropic, elastic panels, fixed on long sides only

Aspect Ratio	Elastic resistance	Elastic Stiffness	Transformation Factors			Dynamic Reactions			
			Load Factor	Mass Factor	Load-mass Factor	Short Side Total	Short Side Peak	Long Side Total	Long Side Peak
λ	Re	$ke / (EI/A^2)$	K_L	K_M	K_{LM}	V_A	V_{PA}	V_B	V_{PB}
1	16.86 m_{FA}	533.6	0.359	0.220	0.611	0.187F+0.209R	1.304 V_A/A	0.090F+0.013R	3.111 V_B/B
0.9	16.55 m_{FA}	437.3	0.359	0.219	0.610	0.184F+0.197R	1.323 V_A/A	0.093F+0.026R	3.000 V_B/B
0.8	16.52 m_{FA}	361.0	0.359	0.219	0.610	0.179F+0.183R	1.341 V_A/A	0.094F+0.044R	2.839 V_B/B
0.7	16.94 m_{FA}	303.3	0.362	0.221	0.611	0.172F+0.164R	1.357 V_A/A	0.096F+0.068R	2.623 V_B/B
0.6	18.05 m_{FA}	263.5	0.366	0.225	0.613	0.162F+0.141R	1.370 V_A/A	0.098F+0.100R	2.358 V_B/B
0.5	20.31 m_{FA}	242.5	0.376	0.233	0.619	0.149F+0.111R	1.381 V_A/A	0.100F+0.139R	2.061 V_B/B

Table 15. Dynamic coefficients for uniformly loaded, isotropic, elastic panels, fixed on short sides only

The edge moment reactions also indicate the elastic shear transfers due to a uniform edge moment, as assumed for the elasto-plastic stage.

The total transfers are equal and opposite, increasing the reaction of the fixed sides, and reducing the reactions of the free side. The amplitude of the reaction transfer depends only upon the resistance moment at the supports, and the aspect ratio, as shown in Table 16. With fixity on all sides and isotropic support moment capacity, the transfers cancel out. However, for orthotropic support moment capacity there will be a net reaction transfer proportional to the difference in support moment capacity in the two directions.

The distribution of elastic shear is not the same as that from loading, being greatest at the corners and least in midspan. The changes to peak elasto-plastic reactions at the centre of the sides are given in Table 17 for fixity on long or short sides, and for isotropic fixity on all sides. For orthotropic support moment capacity the net changes can be calculated by summing the effects of the long side and short side fixity.

It should be noted that the values given in tables 16 and 17 are for initial (positive) deformation. For rebound, the direction of the support bending moments will be reversed, so the sign of the transfer factors should be reversed when applied to the scalar value of the support moment capacity.

Even this loading model is somewhat artificial, as in real, non-linear, panels the full plastic support moment would only actually be generated at a larger deflection and a larger resistance, and this approach ignores the corner effects in the final yield-line mechanism. The calculated elastic resistance lies between the true resistance with full support moments and the onset of plasticity calculated from the elastic analyses, as shown in Figure 5.

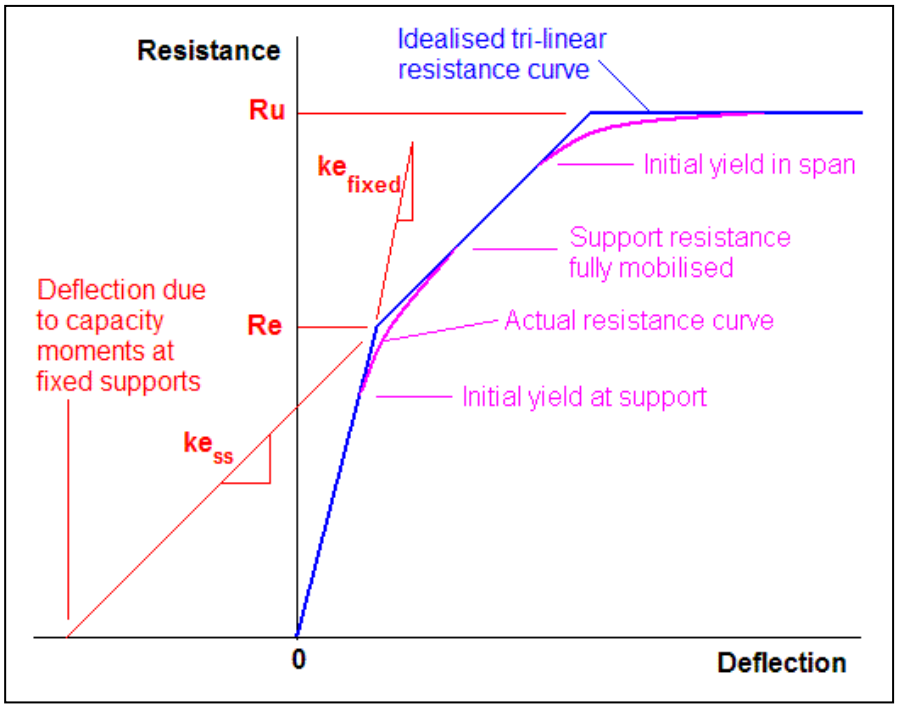

Figure 5. Construction of idealised tri-linear resistance curve

Aspect Ratio	Magnitude of transfer		Sign of adjustment to total reactions for elastic shear due to fixity on edges of panel		
λ				Short Side Total	Long Side Total
1	3.14 m_F		Fixed Edges	V_A	V_B
0.9	3.11 m_F				
0.8	3.06 m_F		Long	**Subtract**	**Add**
0.7	2.99 m_F				
0.6	2.91 m_F		Short	**Add**	**Subtract**
0.5	2.80 m_F				

Table 16. Total shear transfer for simply supported, elastic shears, when used for elasto-plastic range of panels with opposite edges fixed

Aspect Ratio	Isotropic panel with all edges fixed		Panel with long edges fixed		Panel with short edges fixed	
	Short Side peak	Long Side peak	Short Side peak	Long Side peak	Short Side peak	Long Side peak
λ	Add to V_{PA}	Add to V_{PB}	Add to V_{PA}	Add to V_{PB}	Add to V_{PA}	Add to V_{PB}
1	-0.668 m_F/B	-0.668 m_F/B	-0.971 m_{FB}/B	+0.303 m_{FB}/B	+0.303 m_{FA}/B	-0.971 m_{FA}/B
0.9	-0.706 m_F/B	-0.622 m_F/B	-1.075 m_{FB}/B	+0.231 m_{FB}/B	+0.369 m_{FA}/B	-0.853 m_{FA}/B
0.8	-0.739 m_F/B	-0.562 m_F/B	-1.174 m_{FB}/B	+0.149 m_{FB}/B	+0.435 m_{FA}/B	-0.711 m_{FA}/B
0.7	-0.765 m_F/B	-0.485 m_F/B	-1.260 m_{FB}/B	+0.062 m_{FB}/B	+0.495 m_{FA}/B	-0.547 m_{FA}/B
0.6	-0.784 m_F/B	-0.389 m_F/B	-1.327 m_{FB}/B	-0.023 m_{FB}/B	+0.544 m_{FA}/B	-0.367 m_{FA}/B
0.5	-0.795 m_F/B	-0.277 m_F/B	-1.372 m_{FB}/B	-0.089 m_{FB}/B	+0.577 m_{FA}/B	-0.188 m_{FA}/B

Table 17. Adjustment for simply supported, peak elastic shears, when used for elasto-plastic range of panels with opposite edges fixed

6.3 Limitations of the analysis

The two-way spanning calculations are based upon a yield-line criterion suitable for reinforced concrete, a Poisson's ratio of 0.15, elastic small deflection theory and thin shell finite element formulations. These limit the application of the tabulated data.

Steel plates, with a Von Mises yield criterion, will be weaker near fixed supports, so the tables will overstate the resistance of plates with fixed edges. Even for the simply supported tables, the higher Poisson's ratio for steel or glass will alter the elastic stiffness and dynamic reactions.

The small deflection elastic analyses are accurate only up to deflections of about half the member thickness. Beyond this point tensile membrane effects will modify not only the stiffness, but also all of the SDOF parameters. This is no handicap for reinforced concrete sections, which should be plastic well before this, but makes these tables inappropriate for thinner steel plates or glass panes.

Thin shell finite elements do not incorporate shear deflection. The deflected shapes and stress distributions in the elastic and elastic-plastic ranges will not be accurate for very deep sections in which a significant part if the deflection is shear deflection. If flexural cracking occurs before shear cracking then the tables may still be accurate for deep sections after cracking.

These limitations of the analysis are important, and need to remain associated with the tables, if these are not to be applied inappropriately.

One of the remaining limitations for any flexural analysis of reinforced concrete is the appropriate flexural stiffness to use for a material whose strength is predicated on a cracked section, but where the location, strength and pre-existing condition of potential cracks at the time of detonation are all unknown quantities. I can offer no easy solutions to this conundrum.

The practice in PSADS and TM5-1300 of using a value of EI averaged between the uncracked and the cracked and un-stiffened section stiffness throughout the initial elastic analysis is a reasonable, but essentially arbitrary, assumption. For normal levels of reinforcement, this is around 55% of the uncracked stiffness. The variability and uncertainty in real cracked reinforced concrete makes the detailed calculation of the reinforcement stiffness spurious. Lacking more specific data, this arbitrary assumption is no worse than any other, so long as it is recognized for what it is.

A value of 50% of uncracked stiffness could as easily be used without loss of any real accuracy. However, if the elastic stiffness is likely to have a significant influence on critical results it might be wise to bound the stiffness by considering 25% and 75% of elastic stiffness also.

7. Potential for further development

7.1 Extension of the two-way analysis

The elastic and plastic analysis methods can readily be extended to rectangular panels with one or two free edges. In the elastic dynamic reaction analysis a free edge can be used as a line of zero shear.

It is much more difficult to extend the analyses to panels with asymmetric fixity at supports. Plastic analysis is still possible, but the larger number of independent variables in the energy equation will greatly increase the complexity. Resistance and transformation factors can be calculated for elastic models, but without lines of symmetry, the calculation of dynamic reactions will no longer be accurate. Consideration of the propped-cantilever case suggests that the lines of zero shear will move in the elastic-plastic range, and that the incremental deflected shape in the plastic range will vary with the support to span moment capacity ratios.

7.2 Reaction distribution and shear

The use of FE analyses has enabled the distribution of reaction onto supports to be calculated for all strain ranges. The general assumption of a uniform or near uniform distribution, particularly in the plastic range, has been shown not to be correct for rigid supports.

Shear resistance has historically been based on data from one-way spans where the applied stresses are uniform along the support, but little or no peak factor has been taken into account in the applied when applying this.

For blast, shear has been treated as a brittle failure, with no ductility, and conservative values of shear resistance have been used, without Dynamic Increase Factors, to reduce the probability of a shear failure.

In practice, when shear reinforcement contributes to the shear resistance, ductility of this shear reinforcement as shear cracks form will allow redistribution of the shear stresses. A resistance relating the shear capacity to the mean shear stress is reasonable. However, where blast is resisted by two-way members without shear reinforcement, the shear failure would be brittle, and shear capacity should more realistically be related to the peak shear stress.

With information available on peak reactions, and hence peak shear stresses, a more detailed consideration of shear should be developed.

7.3 Use of dynamic reactions

TM5-1300 and PSADS both propose the use of a quasi-static plastic resistance rather than the dynamic reaction for analysis of maximum shear in reinforced concrete members, because the initial peak dynamic reactions (arising from the force component of the dynamic reaction) can be exaggerated by a factor as high as 5. However this limit is no help in obtaining a reaction history to use as a loading history on the support. It is desirable to find better alternatives.

From the one-way spanning tables, it can be seen that this generally only concerns distributed loading cases. For concentrated mass the reactions have little or no force component, and for typical support structures the distributed mass will be small compared to the concentrated mass, which will minimize the initial negative reactions using a weighted combination.

The peak initial reactions are partially, but not wholly, an artifact of the simplifying assumptions for SDOF analysis.

7.3.1 Early shape functions

One such assumption is that the loaded member follows a uniform elastic deflected shape from the onset of loading, even before significant deformation has occurred. A more realistic assumption is that at the first instance of loading all the points of mass are accelerated uniformly, with the supports causing distortion only when the member starts to move. This would give an early reaction with no force component, similar to those for lumped masses.

As deformation starts, FE transient analyses show the early deflected shape to be "dished", with a flat middle and steep edges, consistent with a transition from a uniform acceleration model to the elastic deflected shape model. However even if this transient shape function could be modeled accurately, it could not be used to calculate the reaction history by dynamic equilibrium. The assumption that the centre if the inertial forces can be taken at the centre of the deflected shape for uniform mass is based on the acceleration distribution being the same as the deflection distribution. However this will only be accurate when the shape function is invariant with time, which is clearly not the case in the initial response.

Some transition of the shape function may give a better early reaction history, but the transitional relationship depends on more than just the interim deflected shape, and will need to be based on actual test data.

7.3.2 Finite element modeling

Transient FE models also show an early spike of reaction, although it rises from an initial zero value, so this is not purely an artifact of the SDOF method. The amplitude of the spike gets larger relative to the reaction at peak response as the duration of the loading is reduced, and the rise time of the spike is sensitive to the timesteps and the

mesh density. However as the duration of the loading is reduced, the free vibration in higher modes of vibration comes to dominate the later reactions, which makes comparison with SDOF analysis impractical. The Raleigh damping typically available for this sort of analysis is of little use, as it will give variable damping through the higher modes, up to supercritical damping in the highest modes, which in turn distorts the later reactions.

An alternative FE approach for linear systems is to use modal analysis, and then applying the Duhamel Integral to calculate a transient response to a pulse loading. By superposition of pulse loads, a transient response to any shape of forcing function may be found. The SDOF response and reactions for a uniformly distributed triangular shock pulse can be closely modeled by setting the damping of the fundamental frequency to zero, or to a normal level of structural damping, while setting the damping in all higher modes to critical or high sub-critical damping.

The response part of the SDOF reactions is accurately modeled by the free (or lightly damped) vibration in the fundamental mode, as shown in figure 6 for the reactions of a simply supported beam with a natural period of 50ms, loaded by a triangular pulse with peak load of 100 kN and duration 0.5ms.

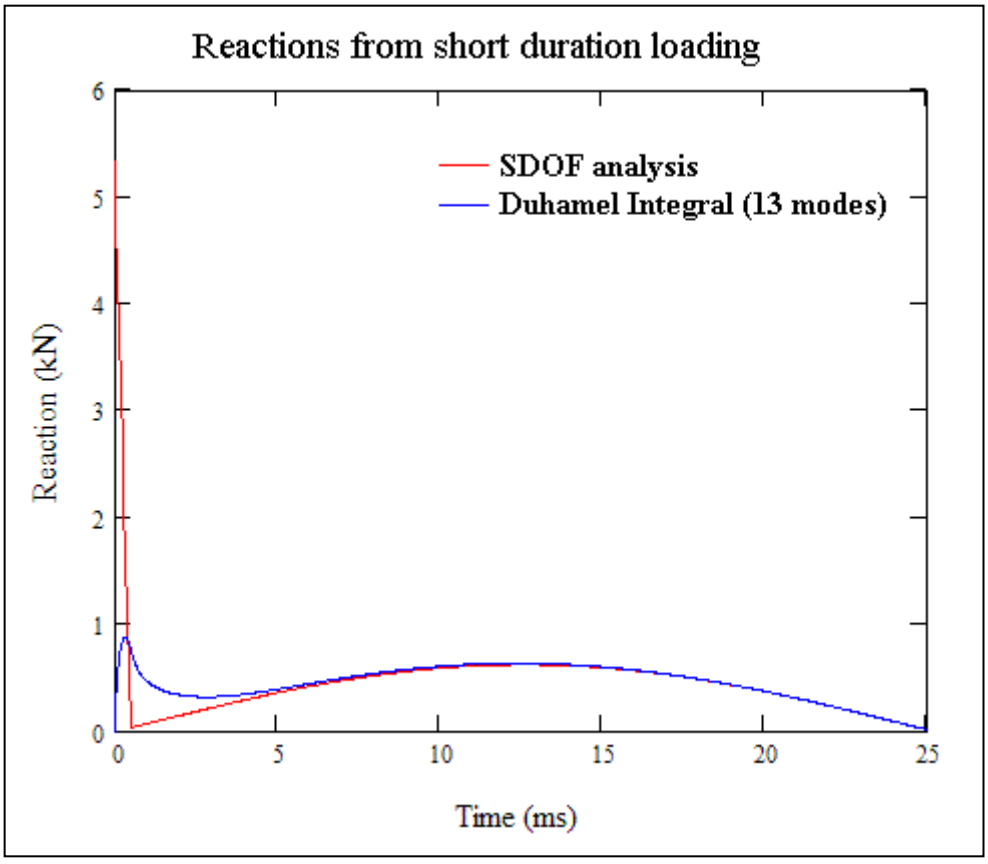

Figure 6. Similar reactions at time of maximum deflection

Although the multi-frequency forced vibration does produce a separate initial peak, the shape and amplitude are different from the SDOF calculation. As the number of critically damped symmetric modes are increased, additional responses are added at the start of the pulse that increase the peak value, and reduce the rise time to peak

response, as shown in figure 7 for the same analysis. However there appear to be diminishing returns, as the gain from modes 8 to 13 is little more than from modes 6 and 7. Even from a very large number of modes the peak reaction is expected to be much lower than the SDOF initial peak. However the amplitude and timing of the peak is likely to be sensitive to the damping assumed for higher modes.

In real life, the higher modes will not all be critically damped, but damping is substantially greater for higher modes. Reduced damping in mode 2, to 30% for example will widen the upper part of the initial reaction pulse after the peak, but will shorten the tail of the pulse, and add a ripple to the subsequent reaction history, without significantly increasing the height of the initial peak. High but sub-critical damping of the higher modes will tend to increase the peak response and make it earlier. However so long as the damping is significant, it will have eliminated the higher frequency vibrations before the peak deflection of the fundamental mode.

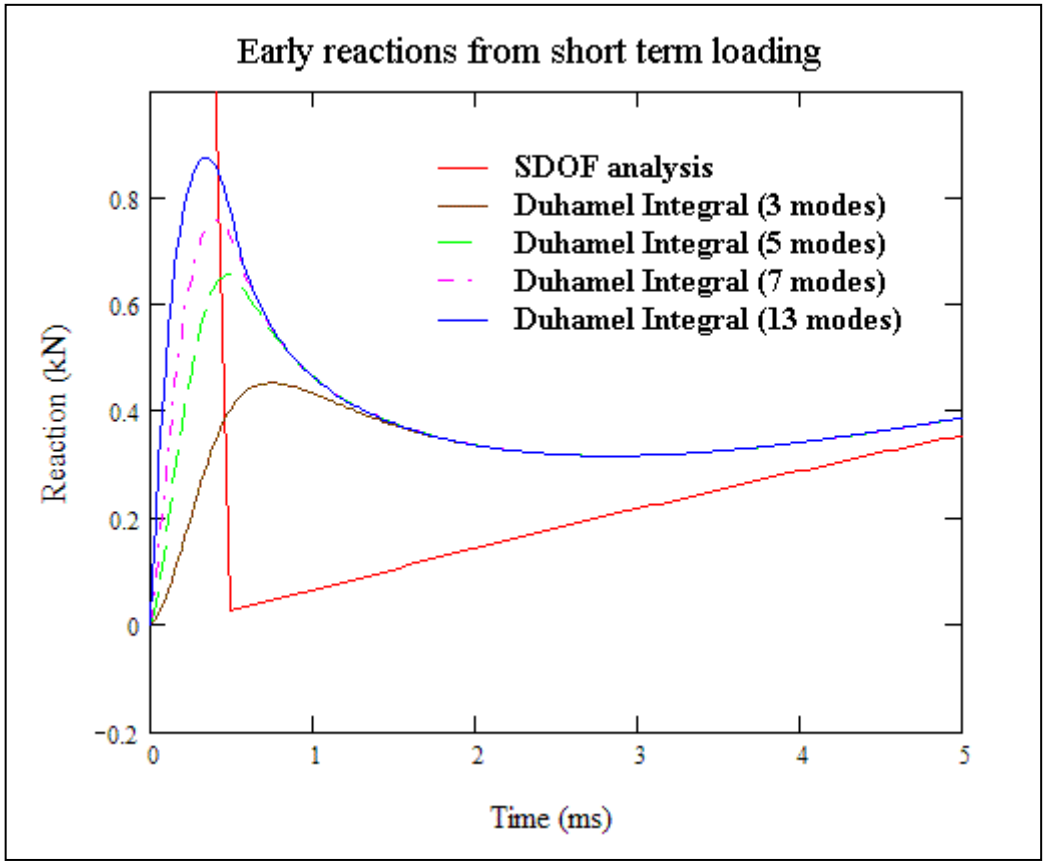

Figure 7. Variation in initial peak reaction with the number of modes considered

7.3.3 Shear distribution and Direct Shear

The distribution of the shear force along the span is of as much interest as the distribution in time. For each mode, the shear is greatest at the support, and reverses at the first peak deflection. Superposition will only give constructive interference from all modes to the first peak of the highest mode considered. For the 13 symmetrical modes considered, this occurs only 2% of the span from the supports. As a result, at the time of the initial reaction peak the shears will be high only in the immediate

vicinity of the support, and they will drop off sharply to a low value over most of the span. This is consistent with the early deflected shapes observed in transient FE analyses.

As the shear stress will be so local to the supports, the initial reaction peak could not cause a conventional flexural-shear failure. Instead a much steeper crack and concrete compression line would have to be considered, as when there is a dominant concentrated load close to the support. There is an enhanced concrete shear capacity for this steeper failure mechanism. There is already a name for a recognized blast phenomenon that involves early shear failure at steep angles with enhanced resistance: Direct Shear.

Direct Shear has been investigated in the 1980s [16] and is covered in PSADS and TM5-1300 design recommendations. However, the shear stress in the manuals is based on the quasi-static plastic resistance calculation, which is unrelated to the initial peak reaction and may or may not be conservative. The allowable Direct Shear capacity is based on the upper limit permitted for static shear stresses, which are usually derived from static test data, although they can be related to the concrete crushing capacity in strut-&-tie shear models. Alternatively, diagonal reinforcement can be provided to resist the shear force in tension.

This suggests that conventional flexural shear calculations could justifiably be based on the maximum reactions excluding the initial spike, either at the peak elastic deflection or at the onset of full plastic rotation. Unless the loading is higher than the resistance at this time, this will be less conservative than the plastic resistance approach. However, more cases will need to be examined to ensure that this can always be used with confidence.

Further research will be needed to identify actual values of the initial reaction spike over a range of loading durations, member configurations and strain ranges. This could be used to identify reasonable numbers of modes and modal damping to model the reaction spike with the FE Duhamel Integral, and to identify an interaction equation between the uniform acceleration and flexural SDOF models that will calculate a suitably truncated initial reaction spike. In turn, these could be used to calculate the Direct Shear force, and to calculate loading histories for supporting members.

8 Conclusions

The equivalent SDOF method of analysis is based on sound principals, and is still a useful tool for analyzing structural response to blast.

The tables prepared by the pioneers of the method are flawed by some incorrect application of principles, some inappropriate simplifications to reduce computational effort, and some simple errors. Nevertheless, they have server the blast community well for decades. However, the uncritical treatment of these tables as “received wisdom”, often in isolation from their context, has served neither the pioneers nor the blast community well.

The alternative tables presented in this paper have been produced with the advantage of modern calculation methods and computer power, and could, with review, serve as the basis for an updated treatment of SDOF analysis in the manuals.

It is important that the data tables remain accompanied by a statement of the limitations of the analysis on which they are based, to limit the risks of inappropriate application.

The treatment of shear in previous analyses has been rather simplistic. The current analysis offers the opportunity to refine the method, and to differentiate between average and peak shear stresses and the resistance of different forms of construction. However, additional research and development would be required to substantiate any proposals.

The very large initial reaction spike calculated by SDOF analysis for distributed loads is mostly, but not entirely, an artifact of the design assumptions of applying the elastic factors in the early stages of the blast loading. However, a transition from a more realistic initial model to the elastic case cannot be calculated from SDOF principals, and would have to be based on a pragmatic interaction derived from trials data.

Alternative forms of analysis can model the early reactions better, but will still require factors to be calibrated against trials data.

Consideration of alternative analyses can help in an understanding of the distinction between Direct Shear and normal flexural shear, and the forces that should be applied to each mechanism.

References

1. *Fundamentals of Protective Design (Non-nuclear)* TM 5-855-1, Washington DC: Department of the Army, March 1965. (Reprint of former document 1110-345-405, 1946.)

2. *Design of Structures to Resist the Effects of Atomic Weapons – Principals of Dynamic Analysis and Design*, EM 1110-345-415, Washington DC: US Army Corps of Engineers, March 1957.

3. Biggs JM. *Introduction to Structural Dynamics.* New York: McGraw-Hill, 1964.

4. Buchholdt H. *Structural Dynamics for Engineers*. London: Thomas Telford, 1997.

5. *Protective Structures Automated Design System v 1.0 (PSADS)* incorporating Army TM5-855-1, Air Force AFJAM32-1055, Navy NAVFAC P-1080 and DAHSCWEMAN-97. Washington DC : US Army Corps of Engineers, September 1998.

6. *Design of Structures to Resist the Effects of Atomic Weapons – Principals of Structural Elements Subjected to Dynamic Loads*, EM 1110-345-416, Washington DC: US Army Corps of Engineers, March 1957.

7. *Structures to Resist the Effects of Accidental Explosions,* Technical Manual TM5-1300, Washington DC: US Department of the Army, November 1990.

8. Krauthammer T, Shahriar S & Shanaa HM. Response of Reinforced Concrete Elements to Severe Impulsive Loading. J. Struct. Engrg., ASCE, Vol 116, No 4, pp1061-1079, 1990.

9. *Mathcad 12*: Mathsoft Engineering & Education Inc. Cambridge MA 02142, USA 2005

10. Young WC. *Roark's Formulas for Stress and Strain, 6th Edition.* New York: McGraw-Hill 1989.

11. Morison CM. *Dynamic Response of Walls and Slabs by Single Degree of Freedom Analysis – A Critical Review and Revision.* Intl. J. Imp. Engrg., Elsevier, Awaiting publication. doi:10.1016/j.ijimpeng.2004.11.008 (on line via Science Direct).

12. Jones LL & Wood RH. *Yield-line analysis of slabs*. London : Thames & Hudson, Chatto & Windus, 1967.

13. Timoshenko SP. *Theory of Plates and Shells.* New York : McGraw-Hill, 1940.

14. *Structures to Resist the Effects of Accidental Explosions,* Technical Manual TM5-1300, Washington DC: US Department of the Army, 1969.

15. Mayor RP & Flanders R. *Technical Manual, Simplified Computer Model of Air Blast Effects on Building Walls.* Washington DC: US Department of State, Office of Diplomatic Security, June1990.

16. Krauthammer T, Bazeos N & Holmquist TJ. *Modified SDOF Analysis of RC Box-Type Structures*. J. Struct. Engrg., ASCE, Vol 112, No 4, pp726-744, 1986

Appendix C

Paper published in the International Journal of Impact Engineering, August 2006

Available on-line from February 2005

Available online at www.sciencedirect.com
SCIENCE DIRECT®
ELSEVIER
International Journal of Impact Engineering 32 (2006) 1214–1247
INTERNATIONAL JOURNAL OF IMPACT ENGINEERING
www.elsevier.com/locate/ijimpeng

Dynamic response of walls and slabs by single-degree-of-freedom analysis—a critical review and revision

Colin M. Morison*

TPS Consult, Centre Tower, Whitgift Centre, Croydon, Surrey, CR9 0AU, UK

Received 20 April 2004; received in revised form 18 November 2004; accepted 20 November 2004
Available online 25 February 2005

Abstract

Single-degree-of-freedom (SDOF) methods for dynamic analysis of reinforced concrete flexural members subjected to blast or ground-shock loading are reviewed. It is concluded that the Equivalent single-degree-of-freedom method is an appropriate approximate method of analysis, but that the widely published parameters in common usage for two-way spanning members such as slabs and walls are inaccurate by up to almost 50% for some coefficients, due to inappropriate assumptions and approximations being used in their original derivation. Revised values of SDOF parameters are presented for two-way spanning members, based on modern finite element and yield-line calculations.
© 2005 Elsevier Ltd. All rights reserved.

Keywords: Dynamic analysis; Walls; Slabs; Blast; Ground-shock; Single degree of freedom

1. Introduction

Design techniques for structures to resist blast and ground shock loadings have been developed over the second half of the 20th century primarily due to the threat to reinforced concrete bunkers from large military explosives charges, (either conventional or nuclear), delivered from long

*Tel.: +44(0)20 8256 4047; fax: +44(0)20 8256 4082.
E-mail address: morison.colin@tpsconsult.co.uk.

0734-743X/$ - see front matter © 2005 Elsevier Ltd. All rights reserved.
doi:10.1016/j.ijimpeng.2004.11.008

Nomenclature

A, A short span dimension of panel
B, B long span dimension of panel
E Young's modulus
F, $F(t)$ total load history on panel
I second moment of area per unit width of panel
ke elastic spring stiffness or spring constant
ke_{ss}, ke_{fixed} elastic spring stiffness for simply supported and fixed edge panels
K_L loading transformation factor
K_M mass transformation factor
K_{LM} load–mass transformation factor $= K_M/K_L$
λ aspect ratio $= A/B$
λ' aspect ratio of affine isotropic panel
m isotropic moment resistance per unit length
m_F, m_{FA}, m_{FB} moment resistance per unit length at fixed edges (any, short and long)
m_{SA}, m_{SB} moment resistance per unit length in spans (short and long)
P maximum load in a triangular load history
R, $R(t)$ resistance history of panel
Re elastic resistance limit
r_u, Ru ultimate (plastic) resistance
T duration of triangular load history, thickness of slab
T_N fundamental period of vibration
t_m time of maximum deflection
V_{FA}, V_{FB} load reaction coefficient (short and long edges)
V_{RA}, V_{RB} resistance reaction coefficient (short and long edges)
V_A total reaction history on short edge $= V_{FA} \times F + V_{RA} \times R$
V_B total reaction history on long edge $= V_{FB} \times F + V_{RB} \times R$
V_{PA}, V_{PB} peak reaction history per unit length on short and long edges
X_E elastic deflection limit
X_m maximum deflection

ranges by aircraft and missiles. However, the methods developed have wider application, for example, in designing against accidental explosions of petrochemicals or high explosives, and in designing conventional structures that may be threatened by terrorist attack.

Analysis of the response of flexural members under transient dynamic loading up to and beyond the elastic limit has always been a key part of such design. Analytical solutions for the forced vibration of structural members with distributed mass and load become very involved for cases more complicated than simply supported beams, so approximate methods of analysis have always been employed.

Until the advent of non-linear transient dynamic finite element (FE) analysis in the 1980s, these have been based on single-degree-of-freedom (SDOF) methods. Even with powerful FE

methods available, SDOF analysis is still very widely used as a cost-effective approach requiring limited input data. Even where the complexity of the structure justifies an FE analysis, SDOF analysis will often be used for preliminary calculations or as a check on the FE response.

Because of the military basis of the threats, the development of SDOF methods can be traced largely through the substantial numbers of military design manuals written or commissioned by the US armed forces. Written in-house or by consultants, these were principally published by the US Army Corps of Engineers (USACE) and the US Air Force Weapons Laboratory (USAFWL). The US Naval Facilities Engineering Command also published design manuals, but these are not referenced in this paper.

These manuals present two main SDOF approaches, the Modal method, and the Equivalent SDOF method. Both work by treating the response of one point of the distributed member as being typical of the whole response, and equating the response at that point to that of an idealised lump mass-spring system that only has a single displacement variable.

2. The modal single-degree-of-freedom method

The Modal SDOF method appeared first, in a 1946 US Manual, ''Fundamentals of Protective Design (Non-Nuclear)'' EM 1110-345-405, re-issued in 1965 as TM5-855-1 [1], and not superseded until 1986.

The Modal method assumes that the elastic forced response of a member will be approximated by the first mode for free vibration. The natural period of the SDOF model is taken to be the period of the first mode of free vibration of the element with distributed mass. Non-dimensional charts have been created by rigorous analysis of Newton's equation of motion of a lumped mass–spring system for an idealised elastic-pure plastic resistance function and a range of idealised loading functions, most notably a triangular load history with zero rise time. From a chart like Fig. 1, the maximum deflection can be calculated, and other charts can be used to calculate the time of maximum deflection.

The method requires that formulae are available for the member types analysed to evaluate the ultimate resistance and elastic limit of the idealised elastic-pure plastic resistance curve, and the natural period of the fundamental mode of vibration. In EM 1110-345-405/TM5-855-1 the only flexural member covered was the simply supported beam. As this would give the largest deflection this was considered to be conservative for all other types of flexural element.

The Modal method had an influential proponent in N M Newmark, who produced design methods using this technique [2], and developed solutions for additional element types. Contained in the 1959 ''Design of Protective Structures to Resist the Effects of Nuclear Weapons'', AFSWC TR-59-70 [3] and the 1961 ASCE manual ''Design of Structures to Resist Nuclear Weapon Effects'' [4] 14 modal period formulae were listed, together with corresponding stiffness and strength formulae. Some of these were for axial modes in columns and arches, while reinforced concrete formulae are based on experimental work, allowing for concrete cracking, rather than analytical solutions.

However, this was about the high point of acceptance of this method. By 1970 USAFWL manuals [5] had adopted the Equivalent SDOF method instead, and the 1985 edition of the ASCE

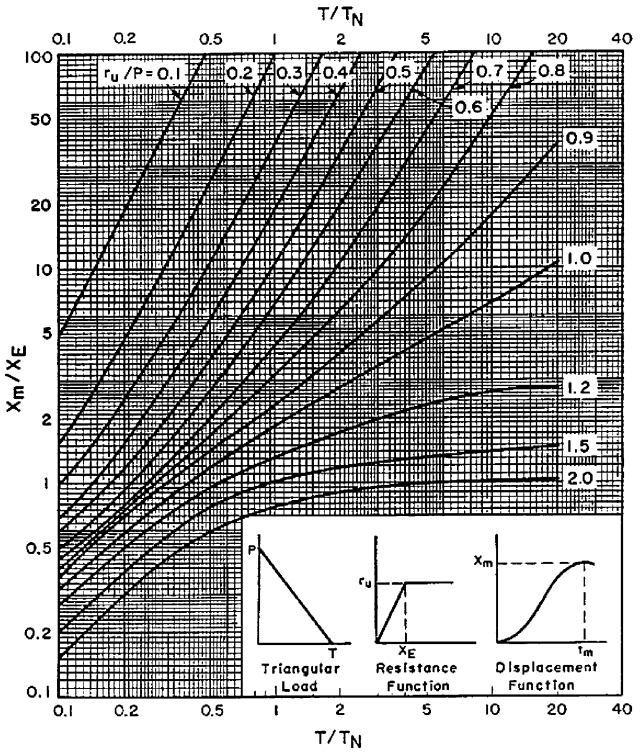

Fig. 1. Typical chart to calculate maximum response X_m (from TM5-1300 [19]).

manual "Design of Structures to Resist Nuclear Weapon Effects" [6] referenced Equivalent SDOF parameters from a 1974 USAFWL manual [7].

There were two main weaknesses to the modal SDOF method that led to it falling out of favour. One was its lack of versatility, because it can only be used with charts of idealised SDOF systems, and cannot be used in numerical solutions of general SDOF systems with more complex loading histories and resistance functions.

The other main weakness was the inadequate treatment of reaction forces. The modal method only accounts for a forcing function distributed spatially with the same shape as the vibration mode shape. Although this part of a distributed load dominates the displacement, it can be less than 25% of the total uniformly distributed load (UDL) on a two-way spanning member. The rest of the loading will make a major contribution to the reaction, but is ignored in the analysis, so the SDOF reaction may be a serious underestimate of the reactions at the member supports.

A later text [6] suggests, as a refinement, that the missing load from a UDL could be taken as acting directly onto the supports when calculating reactions. However, no means of quantifying this load and how it is distributed to the different supports was suggested. The lack of reliable reaction calculations from the Modal SDOF method precluded suitable dynamic shear designs for reinforced concrete members.

3. The equivalent SDOF method

The equivalent SDOF method appeared later than the Modal method. The method and an extensive range of parameters derived using the method were first widely published in 1957, in two parts of the USACE manual ''Design of Structures to resist the Effects of Atomic Weapons'', EM 1110-345-415 ''Principals of Dynamic Analysis and Design [8], and EM 1110-345-416 ''Structural Elements Subjected to Dynamic Loads'' [9]. Much of the analytical work in these volumes is attributed to the firm of Amman and Whitney of New York. Methods in a 1952 document, ''Interim Design Manual for Protective Construction'', by Amman and Whitney are cited as the principal basis for the approximations introduced into the analysis of the two-way spanning elements.

3.1. The theoretical basis

EM 1110-345-415 [8] contains a presentation of the theoretical basis of the Equivalent SDOF method. Before analysing the response of a structural element with distributed mass and loading, the mass, resistance and loading are replaced in Newton's equation of motion with the equivalent values for a lumped mass–spring system. The equivalence is based upon energy, with the equivalent mass having equal kinetic energy, the equivalent resistance having equal internal strain energy and the equivalent loading having equal external work to the distributed system. Although not included at this time, equivalent damping can also be calculated by equating virtual work, e.g. as presented by Buchholt [10].

The transformation factors that are applied to the distributed values to calculate the equivalent lumped values are a function of the distribution of mass and loading over the element, and the shape function of the deflected element. The shape function is defined as the deflected shape at all points of the element, divided by the deflection at a chosen reference point, usually at midspan or at the point of maximum deflection. The basic equations for the transformation factors hold for any deflected shape and mass or load distribution.

The resistance factor has been shown to be equal to the loading factor K_L, with the resistance defined as a loading with the same distribution in space as the applied loading. The damping factor has also been shown to be equal to the mass factor K_M when the damping distribution is the same as the mass distribution. In practice, the ratio of the mass factor to load factor, the load–mass factor K_{LM}, is the single transformation factor required to define an equivalent equation of motion for a structural member loaded by most transient loadings.

For any particular case of mass and loading distribution, if the deflected shape used to calculate the transformation factors is the exact dynamic deflected shape over time, then the response of the equivalent SDOF system will exactly match the response of the chosen reference point on the structural element, in both amplitude and time. In practice the deflected shape varies with time and cannot be accurately known without a prior dynamic analysis of the distributed structural element, which would defeat the purpose of using a SDOF analysis.

However, the equivalent SDOF method can be used as an approximate method of analysis if a deflected shape is assumed, with the accuracy of the approximation depending upon the particular deflected shape. Any deflected shape consistent with the kinematic constraints of the supports may be assumed. Two deflected shapes generally shown to give a reasonably accurate approximation

are the mode shape of the fundamental mode of free vibration, and the static deflected shape under the same distribution of load as occurs in the blast loading. The mode shapes are difficult to derive for all but the simplest cases, and only apply to the elastic response, so the static deflected shape is the most common approximation used. It is relatively straightforward to derive and has been shown to give dynamic responses accurate to within a few percent for most cases.

Different incremental deflected shapes may be used for different stages of deformation of elastic–plastic structural members, from fully elastic, through elasto-plastic (where plastic hinges have formed at the support but not in the span) to fully plastic (where sufficient hinges have formed to produce a plastic mechanism). This gives rise to different transformation factors at different stages of response, with corresponding changes in stiffness and strength.

As with the Modal SDOF method, the reactions from the lumped SDOF analysis do not give the dynamic reactions of the distributed element. However, the equivalent SDOF method has a systematic way of calculating the reactions using dynamic equilibrium.

If the structural element is divided into sections such that there is no shear force across the internal division lines, then the loads, the resistance moments, the reactions and the inertia forces acting on each section will be in dynamic equilibrium. The inertia forces are taken to act at the centroid of the volume swept by the incremental deflection. If this point is identified and moments taken about it, then separate reaction coefficients can be calculated for loading and resistance. These dynamic reaction coefficients are consistent with the static case, as the sum of the dynamic coefficients so calculated at a support will always equal the static reaction coefficient for that support. The dynamic reaction history is given by the combination of loading and resistance histories, as indicated in Table 1.

The equivalent lumped system can be analysed as a SDOF system by a number of different methods:

(a) The natural period of the equivalent system can be calculated, and then the same idealised charts as used in the Modal SDOF method may be used to quickly derive the amplitude and time of peak response.
(b) For a wholly or mostly elastic response, the dynamic load factor (DLF) method calculates the static load as a factor of the initial dynamic load P to give the same elastic deflection. A chart

Table 1
Plastic parameters for alternative yield-line models

Parameters for simply supported plastic panel of aspect ratio of 0.5	Stationary node point	45° node point	Difference (%)
Resistance coefficient, Ru/m	28.21	28.80	1.83
Load factor, K_L	0.391	0.417	6.45
Mass factor, K_M	0.225	0.250	11.2
Load–mass factor, K_{LM}	0.574	0.600	4.49
Load reaction coefficient, short edge, V_{FS}	0.054	0.042	−23.2
Resistance reaction coefficient, short edge, V_{RS}	0.109	0.083	−23.2
Load reaction coefficient, long edge, V_{FL}	0.098	0.104	6.45
Resistance reaction coefficient, long edge, V_{RL}	0.239	0.271	13.2

of DLF against T/T_N can also produce the amplitude and time of peak response, but requires a shorter, simpler iterative calculation than the elastic–plastic chart.

(c) For a purely impulsive loading of short duration compared to the natural period, the K_{LM} factor may be used to calculate the equivalent mass to be used in calculating the initial velocity and the kinetic energy, which can then be equated to the internal work under any shape of resistance curve to find the maximum displacement.

(d) The equation of motion of the equivalent system may be solved rigorously by algebra for the chosen resistance function and loading function to give a complete response history. From this, a reaction history may be calculated to find the maximum reaction. This option was often attractive before the advent of computers, so that a more complicated but still analytical loading history such as a specific bilinear load curve could be applied.

(e) The equation of motion of the equivalent system may be solved numerically in a step-by-step calculation. This can allow complete flexibility in the resistance and loading functions and incorporation of damping forces. This will allow a SDOF analysis to cater for factors such as:
- Explicit analysis of the tri-linear resistance of fixed supports, including the rebound loop.
- Strain hardening effects.
- Non-linear resistance of thin plates incorporating elastic membrane effects.
- Loading curves including the negative phase of blast.
- The effects of multiple reflections on blast loading, e.g. from internal explosions.
- Damping terms due to structure–medium interaction.
- Multiple degrees of freedom with the reaction history from one acting as loading history for the next.

EM 1110-345-416 proposes the use of step-by-step numerical solution for the final analysis if the loading or resistance curves have had to be simplified or approximated to use one if the other methods for choosing a structural thickness and strength. However, the method of step-by-step solution is not presented in Ref. [9]. A very cogent presentation of the technique is given by Biggs in his 1964 ''Introduction to Structural Dynamics'' [11].

3.2. Factors and coefficients derived in EM 1110-345-416

EM 1110-345-416 [9] presents 6 sets of tables of equivalent SDOF data and parameters, for:

- Beams and one-way slabs.
- Two-way slabs.
- Flat slabs.
- Tee beams.
- Elastic deep beams.
- Trusses.

The last three have fallen out of use, and flat slabs are rarely used for blast resistant structures, but the first two sets of tables are widely copied and used. A substantial part of the document describes the methods by which the data and parameters in the tables have been derived, including sample computations. In this paper, only the one-way and two-way spans will be considered.

3.2.1. Beams and one-way slabs

The one-way spans are based upon the deflected shape for the beam under a static load with the same distribution as the dynamic loads. The equations in the sample computations are presented in the calculations without derivation or reference, but they are well known and can be obtained from references or derived from first principles. Analytical integration is used to calculate the transformation factors and equilibrium of the half span is used to calculate the reaction coefficients. The stiffnesses come from the formulae for maximum deflection, and the maximum resistances from the bending moment diagrams.

The calculations for simply supported and fully fixed spans are not controversial. Similar derivations can be found in dynamics text books [10,11], and form a normal part of many courses in structural dynamics.

The calculations for propped cantilevers on the other hand contain a number of errors:

– The stiffness and transformation factors for the different stages use as reference points the point of maximum incremental deflection for each stage, even though these differ between the stages.
– The plastic analysis assumes a symmetric failure mechanism, based on the incremental bending moment diagram rather than the overall bending moment diagram, although that will not normally be the case. As well as the inaccuracy that this introduces for a uniform section, this assumption eliminates the variation in parameters that should occur as the support moment resistance varies from the span moment resistance.
– The application of a simply supported span to model the elasto-plastic stage neglects the elastic shear arising from the support moment when calculating the reactions.

3.2.2. Plastic analysis of two-way spans

Although the tables for two-way slabs published in EM 1110-345-416 cover four different edge support cases and six aspect ratios (λ) for slabs with uniformly distributed loads, in fact only two yield-line calculations for two-way spans were analysed; simply supported and fully fixed cases for square slabs. All the other plastic cases were derived by assuming linear interpolation between fixities, and between the square cases at an aspect ratio of 1 and the previously described one-way spanning cases at an aspect ratio of zero. This is consistent with an assumed internal yield line angle of 45°, which is a common approximation in static application of yield-line theory, e.g. as expounded by Jones and Wood [12].

However, if the assumptions underlying this analysis are examined in detail, a number of flaws can be identified in the reasoning and interpretation:

(a) The 45° yield-line approximation is justified in static analysis because it only affects the resistance. This has a stationary value at the critical angle, so a moderate error in yield-line position will only cause a small error in the resistance. The SDOF parameters are not stationary, so the errors due to the approximation will be larger in these, as is illustrated in Table 1.
(b) The shear coefficient calculation assumes that there is no shear transfer across the internal yield lines. The equilibrium method of yield line solution requires the use of nodal forces to represent shears and twists across yield lines, so the assumption of no shear transfer is not universally correct. Nodal force theory provides for zero forces at an internal 3-line node only

if the node is unrestrained and free to find its stationary position [12]. A constraint such as 45° yield-line angles will require non-zero nodal forces for equilibrium. Neglecting these forces in the dynamic equilibrium calculations leads to larger errors in the reaction coefficients, as shown in Table 1.

(c) Resistance for the non-square panels has not been calculated from the 45° assumption or by interpolation. Instead, a 1951 American Concrete Institute document is cited for the resistance formulae used in the tables. These values are not consistent with the 45° assumption and give more upper bound, i.e. less accurate, results, as shown in Table 2.

(d) The plastic resistance is defined in terms of different span and support resistances, implying that the analysis can be applied to an orthotropic slab. In yield line theory, yield line angles are modified by orthotropy. The Affinity Theorem is used to convert the orthotropic panel to an isotropic affine panel with a modified aspect ratio [12]. If the yield-line angles in the affine panel are solved assuming a 45° angle, the yield-line angles in the real orthotropic panel cannot be 45°. Even in static analysis the 45° approximation is only directly applicable to isotropic panels.

(e) A particular case of orthotropic slabs is fixity on two opposite sides only. If the reinforcement were otherwise isotropic, Affinity Theorem would change 45° yield line angles to 35° or 55°, depending on which edges are fixed. The interpolation used for long or short edges fixed assumes an unchanged 45° angle, and is not consistent with yield-line theory.

3.2.3. *Elastic analysis of two-way spans*

As for the plastic analysis, the elastic two-way analysis is based on only two cases, simply supported and fully fixed for the square panel, and linear interpolation to the one-way case at an aspect ratio of zero. A number of flaws can be identified in the reasoning and interpretation for the elastic analysis also:

(a) There is no theoretical justification given for the interpolation with aspect ratio in elastic models, and no check has been provided of its accuracy.

(b) The shape functions used for the elastic analyses are based upon a very crude approximation. The 45° lines assumed for the plastic analysis are taken as predicted lines of failure, and the

Table 2
Plastic resistance coefficients from alternative models for simply supported isotropic panels

Aspect ratio, λ	Stationary node point, Ru/m	45° Node point		EM 1110-345-416[9] (table 6.2A)	
		Ru/m	Difference (%)	Ru/m	Difference (%)
1.0	24.0	24.0	0	24.0	0
0.9	24.10	24.13	0.12	24.22	0.50
0.8	24.44	24.55	0.45	24.88	1.80
0.7	25.13	25.34	0.84	26.0	3.46
0.6	26.31	26.67	1.37	27.5	4.52
0.5	28.28	28.80	1.83	30.0	6.08

one-way spanning deflected shape appropriate to the support fixity is applied to the triangular and trapezoidal panels between the lines. This assumed deflected shape is substantially different from the deflected shape of a slab under static uniformly distributed load, as can be seen in Fig. 2. This introduces significant errors even for the symmetrical square panel, as shown in Table 3.

(c) The mixing of one-way deflected shapes for simple and pinned supports for the panels with fixity on two edges implies a deflected shape which does not even meet at the joins, and is therefore not kinematically compatible.

(d) There is no justification for assuming that 45° lines in an elastic panel represent lines of zero shear, except in symmetrical square panels. Ignoring any shear transfer will introduce substantial errors in the reactions.

(e) The maximum deflection figures are based on coefficients given by Timoshenko [13] for a Poisson's ratio of 0.3, suitable for steel plates, but twice the customary value for reinforced concrete. These have been used unaltered, which introduces additional inaccuracy, as a simple adjustment in the formula can be made for Poisson's ratio. The reference is rather ironic as Timeshenko's "Theory of Plates and Shells" contains all the formulae required for a proper elastic deflected shape and stress calculation for different aspect ratios, as used for Table 3, not just for maximum deflection.

(f) In employing the simply supported elastic model to represent the incremental elasto-plastic stage, no provision is made to allow for the elastic shear in the supports. Even though the panels are symmetrical in two axes, unequal fixity will give rise to an elastic shear transfer from the pinned edges to the fixed edges that will modify the reactions.

3.2.4. *Accuracy of tabulated data*

Numerical accuracy does not appear to have been a priority in preparing the tables in Ref. [9]. Values of K_L and K_M calculated as fractions have been rounded to two decimal places, and the rounded values have been used to calculate K_{LM}. For the square plastic plates where K_L is 1/3 and K_M is 1/6 this gives 0.51 in the table rather than 0.50. The tabulated values of K_{LM} have irregular steps in most tables, and even one reversal of sequence locally solely due to rounding error, even though the calculation is entirely based on linear interpolation. This makes less obvious the case where a value of K_M has been incorrectly entered, which results in an out-of-sequence value of K_{LM}. There are other rounding inconsistencies in K_{LM} values, where the same ratio has been correctly rounded up in two tables, but has been rounded down in two others.

Liberties also appear to have been taken with the numerical accuracy at some points in the tables in favour of providing convenient increments between interpolated values expressed only to two decimal places. The calculated value of 7/15 (0.4667) has been given as 0.45 in the square simply supported elastic table and 0.46 in the elasto-plastic tables, and the calculated value of 1/5 has been given as 0.21 for K_M of the elastic fixed edge slab. This appears to have been done to try to even up the numerical steps in the table as the aspect ratio changes, although it introduces a systematic error into some of the few calculated values.

EM 1110-345-416 acknowledges the approximate nature of the derivation of the SDOF parameters for two-way spans, but states that the approximate nature of the methods of design and analysis, and of the basic data used therein, do not warrant the development of exact relationships for determining the behaviour of two-way slabs subjected to impulsive load.

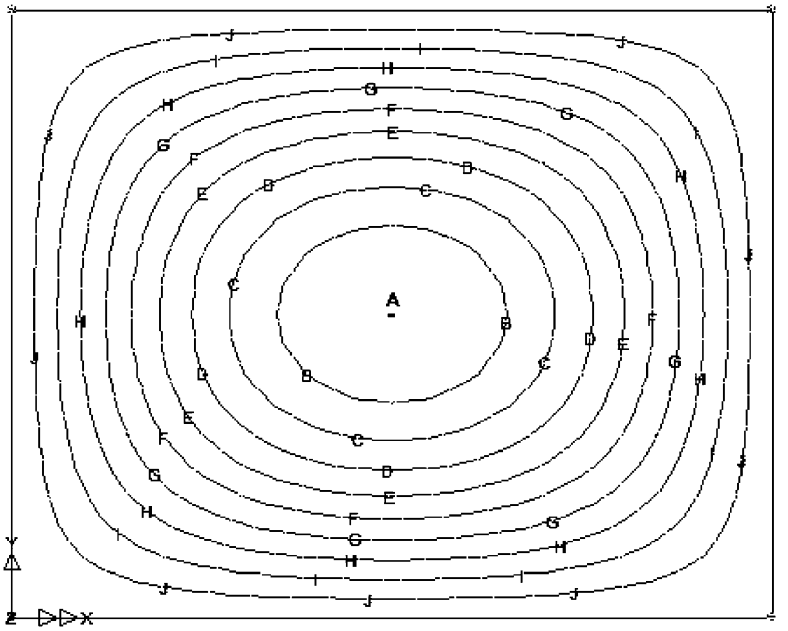

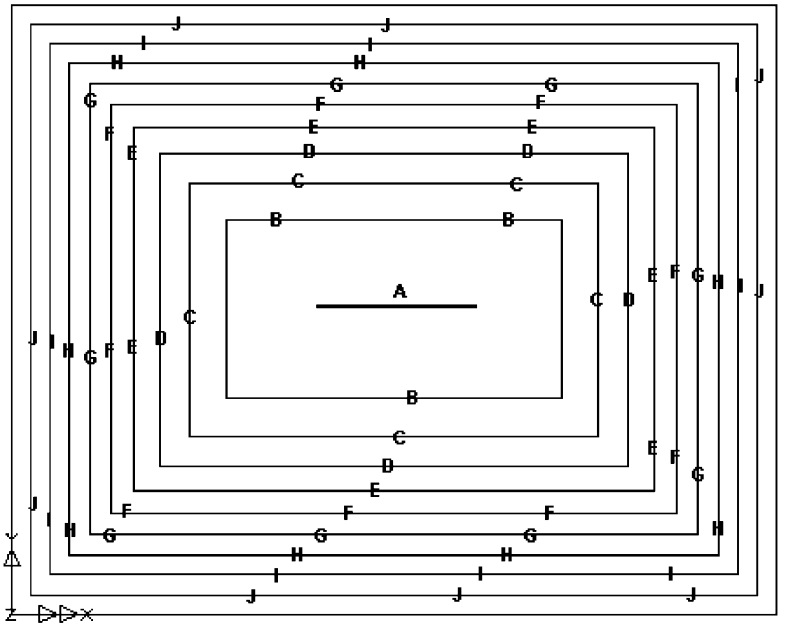

Fig. 2. Comparison of typical true and approximate deflected shapes.

Table 3
Elastic parameters for alternative deflected shapes

Parameters for simply supported elastic panel of aspect ratio 1.0, using Poisson's ratio of 0.3	Navier solution after Timeshenko	EM 1110-345-416 (table 6.2A)	Difference (%)
Spring constant coefficient $ke/(A^2/EI)$	270.5	271	0.18
Load factor, K_L	0.418	0.45	7.66
Mass factor, K_M	0.262	0.31	18.3
Load–mass factor, K_{LM}	0.627	0.68	8.45
Load reaction coefficient, short edge, V_{FS}	0.128	0.07	−45.3
Resistance reaction coefficient, short edge, V_{RS}	0.122	0.18	+47.5
Load reaction coefficient, long edge, V_{FL}	0.128	0.07	−45.3
Resistance reaction coefficient, long edge, V_{RL}	0.122	0.18	+47.5

However, it is likely that the authors had no clear understanding of the degree of inaccuracy introduced by their approximations and mistakes, as all of the appended comparisons with more exact methods were for one-way spans.

3.3. Development of tables from EM 1110-345-416

The tables from EM 1110-345-416 have been copied in textbooks, manuals and computer programs in the 1960s [11], 1970s [5,7], 1980s [14,15] and 1990s [16,17]. However the methodology, approximations and limitations behind the actual values in the tables have not been copied with the tables, and have generally been forgotten.

3.3.1. Biggs 'Introduction to Structural Dynamics'

Biggs [11] included tables extracted from EM-1110-345-416. He states for the two-way and flat slabs that the factors given were based upon approximations to the classical plate theory for deflections in the elastic range and yield line theory in the plastic range, which in the light of foregoing comments may rather overstate their provenance.

He employs them in the context of a well-presented methodology for step-by-step numerical solutions for SDOF problems of reinforced concrete slabs, as well as idealised methods, but does not limit the applicability to reinforced concrete or high plasticity, the original context for the approximations and simplifications.

Biggs did make three improvements to the tables. One was to modify the elastic spring constant, to correspond to an aspect ratio of 0.15 rather than 0.3, although this is not stated in the text or tables. Another was to include elastic shear terms for the support moment in the elasto-plastic stage of the propped cantilever one-way spans, although the terms that he used relate only to the resistance. The third was to re-calculate the elastic resistance of the fully fixed panels.

Biggs also tidied up the inconsistent elastic/elastoplastic value of K_L for a square panel, giving a consistent, if not completely accurate, value of 0.46. However, other errors in the tables that he included from EM-1110-345-416 are not corrected.

3.3.2. Military manuals by USACE and USAFWL

The changes introduced by Biggs have generally been adopted by subsequent military manuals. However, Biggs did not include two-way panels with non-uniform fixity, and the lack of elastic shear for these panels has not been addressed in the manuals that do include them.

Some of the numerical errors and inconsistencies noted in the tables in EM 1110-345-416 have been corrected in some of the manuals, but not in a consistent or progressive way. For example PSADS [16] has corrected a rounding error in one table, but has not corrected the same error in a different table. At the same time it has not corrected the inconsistency modified by Biggs over 20 years earlier.

The earlier military manuals reference EM 1110-345 or the 1960s reprint, TM 5-856. However, by the time PSADS [16] was published in 1998, there is no reference to an explanation of the table values. This leads to misunderstandings. In PSADS the resistance and spring stiffness have been tabulated separately from the SDOF parameters, and the spring stiffness has been adjusted for a Poisson's ratio of 0.15. However, the SDOF parameters are tabulated as being for a Poisson's ratio of 0.30, even though Poisson's ratio was not used in their derivation, but was associated only with the original spring stiffness calculation.

In addition to the tables from EM 1110-345-416, the later manuals, PCDM[15] and PSADS, include additional tables for fixed panels with one or two free edges. However, the source for the values in these tables and the method of derivation are not stated.

These various references have been used in the design of most reinforced concrete silos, Command, Control and Communication facilities and military hardened buildings in NATO and the West built in the last 45 years. The tables have also been applied to a wide range of other blast and dynamics problems, such as petrochemical control facilities, steel plate structures on oil production platforms and window glass, generally without consideration whether the assumptions and approximations on which they are based are valid and relevant.

Over the last 20 years, transient dynamic finite element analysis has taken over for the final design of some of the more complex structures, which introduces an alternative set of approximations. Even then, SDOF calculations have generally been used for preliminary and check calculations.

3.4. SDOF coefficients in TM 5-1300

In 1969, USACE published TM 5-1300, "Structures to Resist the Effects of Accidental Explosions" [18], a manual for safety in storing and processing explosives and munitions. This makes extensive use of SDOF analysis for structural response to external and internal explosions.

3.4.1. Plastic analysis

There are extensive charts, tables and formulae defining hinge or yield-line location, resistance, and static shears for plastic analysis of uniformly loaded one-way spans and a variety of two-way spans. These include panels with one or two edges unsupported, so long as opposed supports have symmetric support fixity. The single chart for load–mass factor against yield line location covers all these cases.

This data is based upon the equilibrium method of yield-line analysis for the classical yield-line pattern, with the interior "sagging" yield-lines extending to the corners of the panels, and the

nodes free to find the stationary position, as described by Jones and Wood [12]. The data incorporates the Affinity Theorem, and works equally for isotropic and orthotropic panels. As such, it represents a major step forward from the approximations of EM 1110-345-416.

Even so, there are three areas of concern about the analysis used:

(a) A reduction in the positive and negative moment capacity is taken in the corners, resulting in a reduction of resistance from the "classic" yield-line values of between 11% and 17% depending on aspect ratio. This is justified on the basis of the high stiffness of the corner. However, the adjustment is basically arbitrary in amplitude, and does not give the change in the deformed shape that would arise from advanced yield-line methods for accounting for the corner stiffness, such as corner levers and fans. The reduction in resistance chosen is at least 50% greater than can be justified by any advanced yield-line method, and the approach will not correctly model changes in dynamic coefficients.
(b) Nodal force theory indicates that there are non-zero nodal forces where yield lines meet a free edge at any angle other than a right angle [12]. These do not appear to be accounted for in the equilibrium equations for panels with one or two free edges, so the analysis of these panels is incorrect for some aspect ratios.
(c) TM5-1300 does not provide formulae for calculating the dynamic reactions. It acknowledges that the support shears or reactions are a function of the applied loading and the dynamic resistance, but states that for short duration blast loads the load can reasonably be neglected, and the maximum reactions calculated from the ultimate resistance distributed between the supports as for a static case. This will be conservative provided the applied loading has dropped below the ultimate resistance before the panel goes into plastic deformation. This may not be conservative for longer duration loading such as the explosion of an explosives store at a distance, and does not provide a reaction history that can be used for a dynamic analysis of the support.

3.4.2. Elastic analysis

Charts and tables are provided to derive the elastic and elasto-plastic stiffness and resistance, to build up a multi-stage resistance curve. A table is provided to give transformation factors for uniformly loaded elastic and elasto-plastic cases, both one-way and two-way spanning.

This table gives values of K_{LM} only, for a range of support conditions and support fixity. Where two-way spanning values have actually been calculated, for square panels supported on four sides, the values are superior to those produced by EM 1110-345-416, being accurate within the 2 decimal places given for all sides simply supported, and within 3% for all sides fixed. This implies more realistic two-way spanning shape functions.

However, outside these two figures the table is based on linear interpolation, mostly between one-way spanning values assumed at inappropriate values of aspect ratio. The elastic charts indicate that maximum bending moments and deflections generally do not converge to the one-way spanning values until the aspect ratio drops to 0.3 or 0.25 (or rises to 3 or 4). The transformation factors are based on the whole deflected shape, and the ends will always have some influence even when the centre is spanning one-way, so they will converge to the one-way spanning value more slowly. Nevertheless, in TM5-1300 the K_{LM} values have been taken as equal to the one-way spanning values for aspect ratios of 0.5 or 2, irrespective of the support conditions.

For the panels supported on all four edges this is interpolated to the square panel with an aspect ratio of unity. This is less accurate than the linear interpolation between aspect ratios of zero and unity in EM 1110-345-416, as the true transformation factors are actually less sensitive to aspect ratio than a linear interpolation. It would be considerably more accurate to apply the K_{LM} value for the square panel as a constant value between aspect ratios of 2 and 0.5 than to use the table in TM5-1300.

The situation is even worse for panels with one edge free. No two-way spanning case has been analysed, and interpolation goes linearly from the one-way span at an aspect ratio of 0.5 to a cantilever at an aspect ratio of 2. There appears to have been no consideration that a two-way pattern might exist between these extremes with a K_{LM} value lower than either, or that the cut-off limit of 2 is wholly inappropriate for a panel with a free edge, when this is actually around the point of maximum two-way action.

The interpolation between simply supported and fully fixed is again linear and is based solely on the number of fixed edges, taking no account of the distribution, or whether the long or the short edges are fixed. The true variation of K_{LM} with edge fixity is far more complex than assumed.

TM5-1300 contains no data for calculating elastic reactions. The only recommendation is that, if the member does not go fully plastic, the elastic or elasto-plastic resistance at peak deflection is calculated, and then distributed between the supports in proportion to the static plastic reactions to approximate maximum elastic reactions.

3.4.3. Application

TM 5-1300 mostly uses the SDOF approach to calculate the natural period, and then employs idealised charts to calculate the peak response and timing. The limitation of this approach is illustrated by the fact that over 200 charts are provided to cover the bilinear triangular loading history for an internal explosion sufficiently to allow interpolation to the final answer, because there are two additional loading variables compared to the linear triangular loading history for an external explosion, which can be covered by a single chart, Fig. 1.

The more accurate and consistent approach to the plastic stage, and the more accurate shape function used to calculate the transformation factors of square elastic and elasto-plastic panels are significant improvements over EM 1110-345-416. However, the inaccurate and essentially arbitrary interpolation to one-way spans means that most elastic SDOF calculations based on transformation factors in TM 5-1300 will have significant errors. The decision to ignore the calculation of reaction coefficients tends to result in conservative simplification for very simple structures, but restricts the possibilities that can be analysed for structures that are slightly more complex without resorting to a complex finite element analysis.

The TM 5-1300 approach to SDOF was retained in the 1990 update of the document [19], which is still current, but has not been adopted for other applications. Some additional data was incorporated in 1990:

- Plastic resistance and shear data was added for asymmetric support fixity, but the KLM chart is still limited to symmetric fixity by the text of the manual.
- Elastic resistance data for asymmetric support fixity is included, and the original KLM table can be taken to apply, although this merely stretches further the already unreasonable interpolation.
- Cases with concentrated loads from EM 1110-345-416 have been included in the one-way span

tables. These are often used to analyse supporting members, but the usefulness is somewhat reduced by the inability to generate a reaction history for the supported members.

TM 5-1300 has been the basis for the design and analysis of most reinforced concrete explosives stores and process buildings built (or upgraded) in NATO countries since 1969, either directly or by reference, e.g. in Explosives Storage and Transportation Committee (ESTC) leaflets and various MOD Explosives Regulations in the UK. It is also commonly used more widely than high explosives facilities, e.g. for inhabited buildings in petrochemical facilities.

3.5. SDOF coefficients in "BLAST" computer program

In 1990 Mayor & Flanders adapted a SDOF computer model for the US Department of Transportation, sponsored by the US Department of State Office of Diplomatic Security, to predict failure of building walls subjected to blast pressure loading from conventional explosives. They produced a Technical Manual [20] containing the theoretical development and reference material.

The Technical Manual describes the approach used for the derivation of stiffness, resistance, K_L and K_M to be applied in the program to reinforced concrete walls both without openings and with symmetrical openings. The plastic analysis used, attributed to an earlier work by Wood (see Ref. [12]), treats the position of the simple yield lines as a variable to be optimised to give the minimum resistance. The resistance that this produces with no openings is compared favourably with those from Biggs and the ASCE manual [4]. K_L and K_M calculations are then based on the deflected shape that this produces, but are not presented in the Technical Manual.

To derive elastic stiffness and transformation factors for walls that can contain openings, the authors employed linear elastic FE analyses. An 8×8 panel of 4-noded plate elements was used to model $\frac{1}{4}$ of the wall panel with either simple or fixed supports all round. The stiffness for the panels without openings were shown to be within 1% of the factors tabulated by Biggs for aspect ratios between 1 and 0.5. Values of K_L and K_M were calculated by numerical integration using the nodal deflections from the FE analysis. A check was undertaken for the values of K_L for the simply supported panels without openings by using a computer program to calculate the value integrated from the first 30 terms of the Navier solution given by Timoshenko [13]. The numerical and analytical values were shown to be in agreement with each other to within 1% for aspect ratios between 1 and 0.5, but are up to 22% lower than the values from EM 1110-345-416 and Biggs, with the greater discrepancy being with the interpolated values for aspect ratio of 0.5. The discrepancy is even greater for K_M, with the numerical values up to 34% less.

Although K_{LM} values are not given in the Technical Manual, they can be calculated from the K_L and K_M numerical values from the finite element analysis. Although the values are consistent within 2–5% with the values in TM 5-1300 for square panels, they are 21% lower than the values for an aspect ratio of 0.5. They are also up to 15% lower than the values given in EM 1110-345-416.

3.6. Other SDOF research

Considerable research was undertaken in the 1980s into single-degree-of-freedom methods, for example by Krauthammer et al. [21,22]. The earlier work reported applies enhanced resistance

from compressive and tensile membrane behaviour to one-way spans, and develops a parallel SDOF analysis to assess direct shear response. The later work develops a general SDOF approach to one-way spanning members by using numerical methods to produce variable SDOF parameters.

Reference to published SDOF parameters was to the tables for one-way spans in Biggs [11]. However, one of the reasons given for proposing the variable SDOF parameters was that "it has been shown that the traditional approach is unreliable for non-symmetric cases with complicated boundary conditions." It is interesting to speculate how much this unreliability may be owed to the errors in the propped cantilever calculations in EM1110-345-416 noted in Section 3.2.1.

Although the developments reported may provide an improved approach to one-way spans, they are not readily extended to the more complex two-way spanning cases, and the experimental data against which they are assessed all comes from one-way spanning tests, or tests on two-way spans with an aspect ratio of 4, treated as one-way spanning.

As the traditional SDOF approach still forms a major part of the response analysis in current military manuals, there appears to be a strong case for deriving revised SDOF parameters for two-way spanning members to apply the equivalent SDOF method more accurately.

4. New values for the Equivalent SDOF method

Given the discrepancies found between the previously published values for the Equivalent SDOF parameters, new analyses have been undertaken for both the elastic and plastic phases for two-way spanning members. Appendix A contains a comparison of typical analyses using the new parameters derived below with those from PSADS (after EM1110-345-416) and TM5-1300. For an analysis in the linear elastic range, comparison is also made with a transient finite element analysis.

4.1. Plastic yield line analysis

This has been undertaken in two stages. Firstly the work equations for a number of yield line configurations have been solved to give stationary positions, using the mathematical calculation program Mathcad to apply methods and geometries described by Jones and Wood [12]. Then the yield line mechanism has been modelled for quarter panels using the FE program Lusas and post-processed in Excel spreadsheets, to confirm the equilibrium of the solution, to confirm nodal forces and to gain additional information on reactions.

The work equation has been defined from the equations for external work and internal plastic stress for five different symmetrical geometries of yield-lines, shown in Fig. 3, with different numbers of independent variables defining the node positions:

– Classic yield-line extending to corners—1 variable.
– Floating corner levers—4 variables.
– Anchored corner levers—3 variables.
– Floating circular corner fans—3 variables.
– Anchored circular corner fans—2 variables.

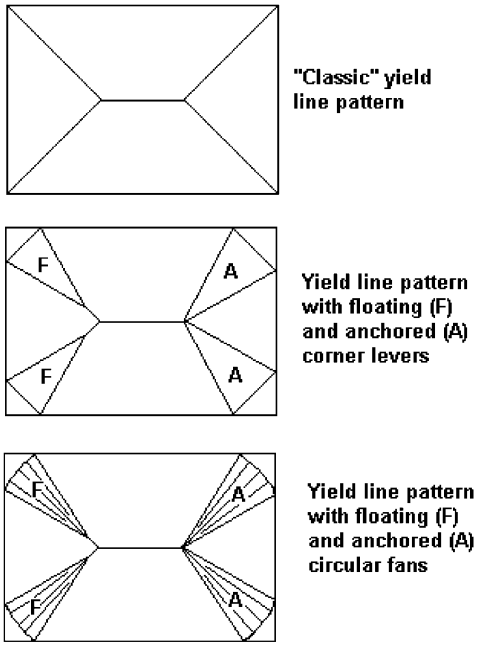

Fig. 3. Alternative yield line patterns.

For each case, equations to calculate the stationary value of the variables are derived by differentiating the work equation with respect to each independent variable. The non-linear equations were solved simultaneously for selected values of aspect ratio and support fixity by numerical methods (except for the classic case where the single quadratic equation was solved analytically). The stationary node positions can then be applied to the work equation to calculate the resistance and to the deflected shape of the components between the yield-lines to calculate the transformation factor of the panel and dynamic reaction coefficients of the components, assuming no shear transfers.

For the advanced yield-line geometries, the corner levers or fans and the rigid corner components of the panel distribute reaction on both long and short sides. The distribution of these reactions can be determined from a balanced FE analysis, where the separate components are modelled with both transverse loading calculated from the resistance and unit sagging and hogging moments on the yield-lines. The components are connected with the minimum number of joints to form an articulated mechanism, and converted to a structure by a single dummy support at the centre. The equilibrium of the yield-line pattern and resistance is demonstrated by the residual reaction on the dummy support being negligible.

To model the edge moments and to minimise the averaging length for peak reactions, a 4-noded (linear) irregular shell element was used with dummy beams at the edges. Typically, the quarter panel was modelled with 50–80 elements to a side. For such analyses, residual values of the order 10^{-6} of the transverse loading were found, caused by discretisation error in representing a continuous system as discrete finite elements, reducing by a factor of 3–4 when the mesh size was halved.

For floating corner levers or fans, the zero shear transfer claimed for internal three-line nodes by Nodal Force theory for the equilibrium method of yield-line analysis [12] was confirmed by the joint forces being of the same order as the residual reaction, and reducing by a similar factor when the mesh was refined. For anchored corner levers or fans, one of the variables is eliminated as the three-line nodes combine, being replaced by a five-line node with a geometrical constraint. The non-zero shear transfer for such nodes claimed by Nodal Force theory was also vindicated by joint forces of the order 100 times the residual reaction in the FE analysis, which only changed in the 3rd significant figure when the mesh was refined.

For the floating corner levers and fans, the total static reactions from each component in the FE model are consistent, within the discretisation error, with those calculated from the geometry. However, they are distributed onto the long and short sides in accordance with equilibrium and the elastic deformation within the components between yield-lines. This distribution has been applied to the force and resistance components of the dynamic reaction, and coefficients have been summed along each edge to give the total dynamic reactions.

For the anchored corner levers and fans, the shear or twist transfer represented by the nodal forces in the joint modifies the static reactions in the panels. As these forces are part of the resistance, the difference between the two static reaction calculations has been used to modify the resistance coefficients of the dynamic reaction before summing along each edge to give dynamic reactions that allow for the nodal forces.

The FE analysis also gives the distribution of reaction along the edge of the components, which allows the peak reactions to be identified at mid-side. These have been calculated from the greatest average reaction along one element edge, but because of slight ripples in the reaction values from the FE model these tend to be upper bound, and the maximum value may be found a few elements off the centreline.

The FE analysis demonstrated that the yield-line solutions are upper bound, as expected. The bending moments in the components do exceed the yield-line moments in some locations, most notably at the tips of the rigid component, demonstrating that there is not a matching lower bound solution. This is the norm even for more complex geometries such as cosh fans, which are currently the least upper bound fan solutions known, and require several additional variables to define.

With the introduction of corner levers and fans, some of the hogging yield-lines cross the interior of the panel corners. The yield-line moment capacity on these yield-lines will depend on the reverse reinforcement in the structural component, rather than on the edge fixity. As most panels designed to resist blast are reinforced equally on both sides to resist rebound and to provide adequate compressive resistance at large plastic hinge rotations, the panels have been calculated as isotropic panels with equal reverse moment in the corners, and the corners taken as held down, even when edges are simply supported.

With hogging moment capacity in the circular fans, no valid mechanisms are possible for either floating or anchored fans in a simply supported panel. The square panel reverts to the classic pattern with zero fan angle, and the other aspect ratios give an invalid mechanism with negative fan angles for equilibrium.

With hogging moment capacity and simple supports, valid anchored corner lever mechanisms were found, but the corner levers were so narrow that there was no difference in resistance and SDOF parameters from the classic mechanism. The results from the classic yield line analysis for simply supported panels are given in Table 4.

Table 4
Dynamic coefficients for uniformly loaded, simply supported, isotropic, plastic panel

Aspect ratio, λ	Resistance, Ru	Transformation factors			Dynamic reactions			
		Load factor, K_L	Mass factor, K_M	Load–mass factor, K_{LM}	Short side total, V_A	Short side peak, V_{PA}	Long side total, V_B	Long side peak, V_{PB}
1	24.00m	0.333	0.167	0.500	$0.083F+0.167R$	$1.718V_A/A$	$0.083F+0.167R$	$1.718V_B/B$
0.9	24.10m	0.342	0.176	0.513	$0.079F+0.158R$	$1.729V_A/A$	$0.086F+0.178R$	$1.724V_B/B$
0.8	24.44m	0.352	0.186	0.527	$0.074F+0.148R$	$1.731V_A/A$	$0.088F+0.190R$	$1.704V_B/B$
0.7	25.13m	0.364	0.197	0.542	$0.068F+0.136R$	$1.735V_A/A$	$0.091F+0.205R$	$1.676V_B/B$
0.6	26.31m	0.376	0.210	0.558	$0.062F+0.123R$	$1.743V_A/A$	$0.094F+0.221R$	$1.629V_B/B$
0.5	28.28m	0.391	0.225	0.574	$0.054F+0.109R$	$1.755V_A/A$	$0.098F+0.239R$	$1.548V_B/B$

Table 5
Dynamic coefficients for uniformly loaded, isotropic, plastic panel, fixed on all sides

Aspect ratio, λ	Resistance, Ru	Transformation factors			Dynamic reactions			
		Load factor, K_L	Mass factor, K_M	Load–mass factor, K_{LM}	Short side total, V_A	Short side peak, V_{PA}	Long side total, V_B	Long side peak, V_{PB}
1	44.00m	0.318	0.160	0.502	$0.091F+0.159R$	$0.132F/B+0.269R/B$	$0.091F+0.159R$	$0.132F/B+0.269R/B$
0.9	44.20m	0.327	0.168	0.514	$0.086F+0.147R$	$0.140F/B+0.284R/B$	$0.096F+0.171R$	$0.138F/B+0.285R/B$
0.8	44.88m	0.338	0.178	0.526	$0.080F+0.135R$	$0.148F/B+0.299R/B$	$0.101F+0.184R$	$0.142F/B+0.300R/B$
0.7	46.22m	0.350	0.189	0.540	$0.073F+0.121R$	$0.158F/B+0.317R/B$	$0.106F+0.200R$	$0.147F/B+0.320R/B$
0.6	48.55m	0.364	0.202	0.555	$0.066F+0.106R$	$0.168F/B+0.337R/B$	$0.110F+0.218R$	$0.150F/B+0.340R/B$
0.5	52.44m	0.379	0.217	0.571	$0.057F+0.090R$	$0.183F/B+0.366R/B$	$0.115F+0.238R$	$0.150F/B+0.356R/B$

For panels fixed on all sides, full sized corner levers or fans are developed, extending up to 15% of the span length from each corner, and varying in size and orientation with aspect ratio. Textbooks suggest circular or hyperbolic fans produce less upper bound solutions than corner levers by giving examples for square panels. However, this analysis has demonstrated this to be the case only for nearly square panels. For aspect ratios as high as 0.8, corner levers are less upper bound than circular fans, as the ability to vary the two sides of the corner lever independently is more critical than the curvature of the fan. The values given in Table 5 are for corner levers throughout, ignoring the slightly lower resistance and slightly higher K_{LM} of the nearly square panels with circular fans, to permit smooth interpolation within the table. Although the transition in resistance in a table using a mixture of yield-line geometries would be smooth, the transition in K_{LM} would be stepped.

Most of the cases tabulated come from floating corner levers, which are marginally less upper bound than anchored corner levers. Only for an aspect ratio of 0.5 did this give an invalid mechanism and leave the anchored corner lever as the valid mechanism.

The fully fixed panel requires no difference between edge and corner lever resistance, and so can serve as the affined slab for any slab that is simply supported and singly reinforced in one or both directions. Such slabs may be designed by applying the Affinity Theorem to the data in Table 5, as shown in Fig. 4.

Panels fixed on the long sides only and panels fixed on the short sides only are part of a continuum and could have been presented as panels fixed on opposite sides for aspect ratios between 2 and 0.5. Unlike the uniform fully fixed or simply supported panels, the transition between horizontal and vertical orientation of the yield-line pattern does not occur with an aspect ratio of unity, but with the short edges fixed and an aspect ratio of $1/\sqrt{2}$ (0.707). With reverse reinforcement in the corners even in the simply supported directions, the fans or corner levers are about half the size of the fully fixed case, and the corner levers are less upper bound than circular fans by a significant margin in all cases.

Valid mechanisms and smaller resistances are found for floating corner levers around the transition point, with short sides fixed and aspect ratios from 0.8 to 0.5 in Table 6. With short sides fixed and aspect ratios from 0.9 to 1.0 in Table 6 and for all panels with long sides fixed in Table 7, the floating corner levers are invalid and anchored corner levers have been used.

Although Tables 4–7 have all been presented for isotropic panels, they may also be utilised to analyse orthotropic panels by applying the Affinity Theorem, as shown in Fig. 4.

4.2. Elastic finite element analysis

The elastic phases of the SDOF response have been analysed in Lusas using unit loading on models of quarter panels in linear elastic analyses, with the results post-processed in Excel. The models used 8-noded (quadratic) square thin shell elements, varying between 20×20 and 20×10 regular element grids with the aspect ratio varying between unity and 0.5. The quadratic elements give better deflection and stress accuracy than double the density of linear elements, but the peak reactions have to be averaged over 3 nodes, as the side and corner nodes have different weighting.

The post-processing calculates the elastic spring stiffness from the maximum deflection and the transformation factors by numerical integration of the deflections at all nodes, using the trapezium rule. These have been checked to better than 5 significant figures for the simply

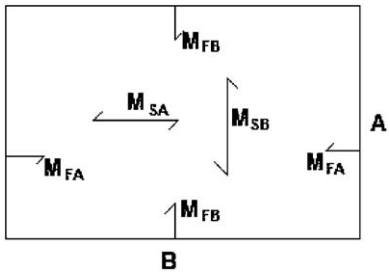

For analysis of Orthotropic Panels with = A/B

For simply supported panels with both faces reinforced and corners held:

Use Table 4 with $\lambda' = \lambda \cdot \sqrt{\frac{m_{SB}}{m_{SA}}}$ and take $m = \sqrt{m_{SB} \cdot m_{SA}}$

For fully fixed panels (or any panels with corner moments of resistance equal to the support moment of resistance in the same direction):

Use Table 5 with $\lambda' = \lambda \cdot \sqrt{\frac{m_{SB} + m_{FB}}{m_{SA} + m_{FA}}}$ and take $m = \frac{\sqrt{(m_{SB} + m_{FB}) \cdot (m_{SA} + m_{FA})}}{2}$

For panels with the long edges fixed and both faces reinforced (m_{FA}=m_{SA}) at corners

Use Table 6 with $\lambda' = \lambda \cdot \sqrt{\frac{m_{SB} + m_{FB}}{2\ m_{SA}}}$ and take $m = \sqrt{\frac{(m_{SB} + m_{FB}) \cdot m_{SA}}{2}}$

For panels with the short edges fixed and both faces reinforced ($m_{FB} = m_{SB}$) at corners

Use Table 7 with $\lambda' = \lambda \cdot \sqrt{\frac{2 \cdot m_{SB}}{m_{SA} + m_{FA}}}$ and take $m = \sqrt{\frac{m_{SB} \cdot (m_{SA} + m_{FA})}{2}}$

Fig. 4. Use of the Affinity Theorem for the analysis of orthotropic panels.

supported case in Table 8 against analytical values calculated using both the Navier and Levy solutions in Timeshenko [13]. However, the Navier solution needs tens of thousands of terms to converge the reaction distribution to better than 3 significant figures, and the Levy solution can only achieve similar accuracy in reactions from 7 to 10 terms before large interim values in the calculations cause overflow errors in Mathcad. The FE approach was therefore considered more practical and accurate for calculating dynamic reactions, as well as being more versatile for different support conditions, as shown in Tables 9–11.

The approach adopted to calculate the dynamic reactions for elastic panels is different from that used in EM 1110-345-416 or in the plastic analysis, although consistent with the principles in EM 1110-345-415. In symmetrical panels with all edges supported, lines of symmetry have been taken as lines of zero shear, isolating a quarter panel. Deflection output is used to calculate the centroid of the inertia forces in both axes. The centre of loading is calculated from the corner coordinates, the moments due to resistance are calculated from the reaction moments at the symmetry edges and supports (where fixed), and the centre of the reaction is calculated on each side from the reactions. By calculating equilibrium of forces and resistance about the centroid of

Table 6
Dynamic coefficients for uniformly loaded, isotropic, plastic panels, fixed on long sides only

Aspect ratio, λ	Resistance, Ru	Transformation factors			Dynamic reactions			
		Load factor, K_L	Mass factor, K_M	Load–mass factor, K_{LM}	Short side total, V_A	Short side peak, V_{PA}	Long side total, V_B	Long side peak, V_{PB}
1	34.07m	0.355	0.190	0.537	$0.036F+0.138R$	$0.120F/B+0.240R/B$	$0.134F+0.192R$	$0.147F/B+0.312R/B$
0.9	35.09m	0.364	0.199	0.548	$0.031F+0.127R$	$0.126F/B+0.251R/B$	$0.137F+0.205R$	$0.149F/B+0.325R/B$
0.8	36.58m	0.374	0.209	0.559	$0.027F+0.115R$	$0.132F/B+0.261R/B$	$0.139F+0.219R$	$0.152F/B+0.340R/B$
0.7	38.72m	0.385	0.220	0.571	$0.023F+0.103R$	$0.137F/B+0.270R/B$	$0.140F+0.234R$	$0.152F/B+0.352R/B$
0.6	41.82m	0.397	0.232	0.584	$0.018F+0.090R$	$0.145F/B+0.282R/B$	$0.141F+0.241R$	$0.151F/B+0.363R/B$
0.5	46.47m	0.410	0.245	0.596	$0.014F+0.076R$	$0.153F/B+0.296R/B$	$0.141F+0.268R$	$0.151F/B+0.374R/B$

Table 7
Dynamic coefficients for uniformly loaded isotropic plastic panels, fixed on short sides only

Aspect ratio, λ	Resistance, Ru	Transformation factors			Dynamic reactions			
		Load factor, K_L	Mass factor, K_M	Load–mass factor, K_{LM}	Short side total, V_A	Short side peak, V_{PA}	Long side total, V_B	Long side peak, V_{PB}
1	34.07m	0.355	0.190	0.537	$0.134F+0.192R$	$0.147F/A+0.312R/A$	$0.036F+0.138R$	$0.120F/A+0.240R/A$
0.9	33.32m	0.345	0.181	0.525	$0.132F+0.179R$	$0.144F/A+0.301R/A$	$0.040F+0.149R$	$0.115F/A+0.231R/A$
0.8	32.80m	0.335	0.172	0.512	$0.127F+0.165R$	$0.141F/A+0.288R/A$	$0.046F+0.162R$	$0.109F/A+0.217R/A$
0.7	32.64m	0.329	0.166	0.504	$0.121F+0.150R$	$0.191F/B+0.384R/B$	$0.052F+0.177R$	$0.146F/B+0.293R/B$
0.6	32.99m	0.342	0.179	0.522	$0.113F+0.133R$	$0.212F/B+0.416R/B$	$0.059F+0.195R$	$0.154F/B+0.315R/B$
0.5	34.16m	0.358	0.194	0.541	$0.103F+0.114R$	$0.236F/B+0.473R/B$	$0.067F+0.216R$	$0.159F/B+0.339R/B$

Table 8
Dynamic coefficients for uniformly loaded, simply supported, isotropic, elastic panels

Aspect ratio, λ	Ultimate resistance, Re = Ru	Elastic stiffness coefficient, $ke/(EI/A^2)$	Transformation factors			Dynamic reactions			
			Load factor, K_L	Mass factor, K_M	Load–mass factor, K_{LM}	Short side total, V_A	Short side peak, V_{PA}	Long side total, V_B	Long side peak, V_{PB}
1	$24.00m$	251.8	0.419	0.262	0.626	$0.136F+0.114R$	$1.752\ V_A/A$	$0.136F+0.114R$	$1.752\ V_B/B$
0.9	$24.10m$	229.3	0.419	0.263	0.627	$0.133F+0.098R$	$1.796\ V_A/A$	$0.139F+0.130R$	$1.703\ V_B/B$
0.8	$24.44m$	212.2	0.420	0.264	0.628	$0.128F+0.081R$	$1.839\ V_A/A$	$0.142F+0.149R$	$1.644\ V_B/B$
0.7	$25.13m$	200.9	0.423	0.266	0.629	$0.122F+0.064R$	$1.877\ V_A/A$	$0.143F+0.171R$	$1.574\ V_B/B$
0.6	$26.31m$	196.7	0.427	0.270	0.632	$0.115F+0.046R$	$1.908\ V_A/A$	$0.143F+0.196R$	$1.493\ V_B/B$
0.5	$28.28m$	202.0	0.435	0.278	0.639	$0.106F+0.029R$	$1.929\ V_A/A$	$0.142F+0.223R$	$1.402\ V_B/B$

Table 9
Dynamic coefficients for uniformly loaded, isotropic, elastic panels fixed on all sides

Aspect ratio, λ	Elastic resistance, Re	Elastic stiffness coefficient, $ke/(EI/A^2)$	Transformation factors			Dynamic reactions			
			Load factor, K_L	Mass factor, K_M	Load–mass factor, K_{LM}	Short side total, V_A	Short side peak, V_{PA}	Long side total, V_B	Long side peak, V_{PB}
1	$12.93m_{FA}+12.93m_{FB}$	808.5	0.308	0.182	0.593	$0.134F+0.116R$	$1.763V_A/A$	$0.134F+0.116R$	$1.763V_B/B$
0.9	$11.40m_{FA}+14.53m_{FB}$	741.2	0.308	0.183	0.594	$0.132F+0.095R$	$1.797V_A/A$	$0.136F+0.137R$	$1.718V_B/B$
0.8	$9.76m_{FA}+16.37m_{FB}$	701.8	0.311	0.185	0.596	$0.128F+0.074R$	$1.822V_A/A$	$0.137F+0.161R$	$1.657V_B/B$
0.7	$8.05m_{FA}+18.56m_{FB}$	693.4	0.317	0.190	0.600	$0.123F+0.054R$	$1.836V_A/A$	$0.138F+0.185R$	$1.579V_B/B$
0.6	$6.29m_{FA}+21.28m_{FB}$	723.3	0.328	0.199	0.608	$0.117F+0.034R$	$1.840V_A/A$	$0.138F+0.211R$	$1.485V_B/B$
0.5	$4.50m_{FA}+24.95m_{FB}$	807.3	0.347	0.216	0.624	$0.107F+0.018R$	$1.837V_A/A$	$0.139F+0.236R$	$1.378V_B/B$

Table 10
Dynamic coefficients for uniformly loaded, isotropic, elastic panels, fixed on long sides only

Aspect ratio, λ	Elastic resistance, Re	Elastic stiffness coefficient, $ke/(EI/A^2)$	Transformation factors			Dynamic reactions			
			Load factor, K_L	Mass factor, K_M	Load–mass factor, K_{LM}	Short side total, V_A	Short side peak, V_{PA}	Long side total, V_B	Long side peak, V_{PB}
1	$16.86m_{FB}$	533.6	0.359	0.220	0.611	$0.090F+0.013R$	$3.111V_A/A$	$0.187F+0.209R$	$1.304V_B/B$
0.9	$17.44m_{FB}$	539.9	0.361	0.221	0.613	$0.088F+0.003R$	$3.178V_A/A$	$0.188F+0.220R$	$1.283V_B/B$
0.8	$18.37m_{FB}$	560.6	0.365	0.225	0.617	$0.086F–0.005R$	$3.212V_A/A$	$0.187F+0.232R$	$1.256V_B/B$
0.7	$19.80m_{FB}$	600.6	0.372	0.232	0.623	$0.082F–0.012R$	$3.215V_A/A$	$0.185F+0.244R$	$1.223V_B/B$
0.6	$21.95m_{FB}$	669.3	0.383	0.243	0.633	$0.077F–0.017R$	$3.190V_A/A$	$0.182F+0.258R$	$1.184V_B/B$
0.5	$25.20m_{FB}$	783.1	0.401	0.261	0.651	$0.070F–0.020R$	$3.145V_A/A$	$0.177F+0.272R$	$1.141V_B/B$

Table 11
Dynamic coefficients for uniformly loaded, isotropic, elastic panels, fixed on short sides only

Aspect ratio, λ	Elastic resistance, Re	Elastic stiffness, $ke/(EI/A^2)$	Transformation factors			Dynamic reactions			
			Load factor, K_L	Mass factor, K_M	Load–mass factor, K_{LM}	Short side total, V_A	Short side peak, V_{PA}	Long side total, V_B	Long side peak, V_{PB}
1	$16.86m_{FA}$	533.6	0.359	0.220	0.611	$0.187F+0.209R$	$1.304V_A/A$	$0.090F+0.013R$	$3.111V_B/B$
0.9	$16.55m_{FA}$	437.3	0.359	0.219	0.610	$0.184F+0.197R$	$1.323V_A/A$	$0.093F+0.026R$	$3.000V_B/B$
0.8	$16.52m_{FA}$	361.0	0.359	0.219	0.610	$0.179F+0.183R$	$1.341V_A/A$	$0.094F+0.044R$	$2.839V_B/B$
0.7	$16.94m_{FA}$	303.3	0.362	0.221	0.611	$0.172F+0.164R$	$1.357V_A/A$	$0.096F+0.068R$	$2.623V_B/B$
0.6	$18.05m_{FA}$	263.5	0.366	0.225	0.613	$0.162F+0.141R$	$1.370V_A/A$	$0.098F+0.100R$	$2.358V_B/B$
0.5	$20.31m_{FA}$	242.5	0.376	0.233	0.619	$0.149F+0.111R$	$1.381V_A/A$	$0.100F+0.139R$	$2.061V_B/B$

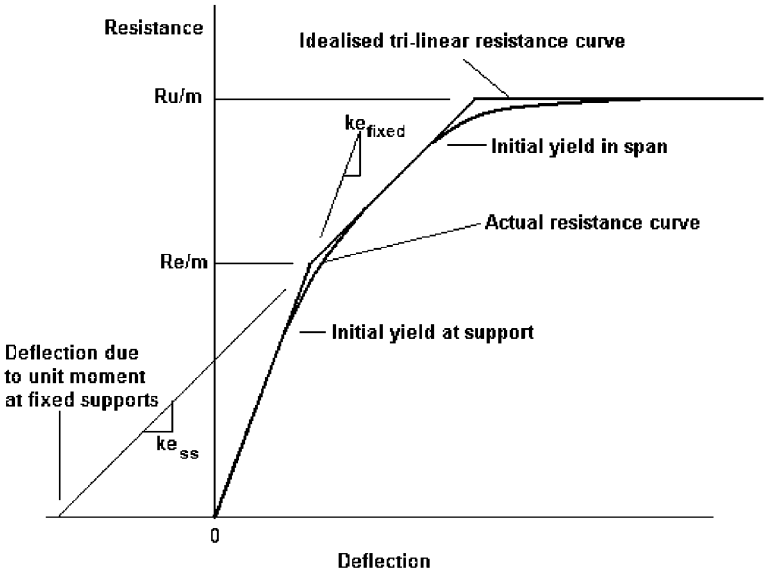

Fig. 5. Construction of idealised tri-linear resistance curve.

the inertia forces in two axes, four linear simultaneous equations are derived which are solved to give the total dynamic reaction coefficients presented in Tables 8–11.

The peak reaction at the middle of each side has been calculated from the mean of corner and mid-side node reactions on the side of the element adjacent to the panel centreline on each supported side. The different weighting on the nodes in the quadratic element composition means that individual nodal reactions are not indicative of the distributed peak value. The peaks are expressed as a factor applied to the mean reaction on each side.

The elasto-plastic phase for panels with some edges fixed has traditionally been analysed by applying the simply supported elastic stiffness and transformation factors, as the incremental deflection is the same. However, the reaction coefficients should be based on the total resistance not the incremental resistance, so the effect of the support moments must still be considered after they have reached the moment capacity. Similarly, the resistance at which the transition is taken to occur must be considered. EM 1110-345-416 ignored the first, and bases the second on the long side moments for the 45° sectors.

A consistent basis for both is now provided by analysing a quadrant of a simply supported elastic panel with unit moment per unit length upon either edge. Because of the need to apply moment loading, this analysis followed the practice used for the plastic FE analyses rather than for the other elastic FE analyses. By equating midspan deflections for the elastic panel with edge fixity and for the simply supported panel combined with a unit bending moment on the fixed edge or edges, the value for the elastic resistance of the panels with support fixity has been calculated, as presented in Tables 9–11. This loading model is somewhat artificial, as in real, non-linear, panels the full plastic support moment would only actually be generated at a larger deflection and a larger resistance, and this approach ignores the corner effects in the final yield-line mechanism. The elastic resistance lies between the true resistance with full support moments and the onset of plasticity calculated from the elastic analyses, as shown in Fig. 5.

Table 12
Shear transfer for simply supported, total elastic shears, when used for elasto-plastic phase of panels with opposite edges fixed

Aspect ratio, λ	Magnitude of transfer
1	$3.14m_F$
0.9	$3.11m_F$
0.8	$3.06m_F$
0.7	$2.99m_F$
0.6	$2.91m_F$
0.5	$2.80m_F$

Sign of adjustment to total reactions for elastic shear due to fixity on edges of panel

Fixed edges	Short side total, V_A	Long side total, V_B
Long	Subtract	Add
Short	Add	Subtract

The elastic properties in Tables 8–11 are only applicable to panels with isotropic stiffness. However, orthotropic strength is permitted, provided hogging of the supports is not so much stronger than sagging of the spans that yield will occur in the spans before the supports have yielded. The elastic resistances in Tables 8–11 have been written in terms consistent with orthotropic strength.

It should be noted that a single elastic resistance is given for each fully fixed panel in Table 9 that corresponds to all supports yielded, to give a tri-linear resistance function. An alternative quadri-linear resistance function could be modelled with an intermediate phase based on the elastic panel with short ends fixed and unit plastic moment on the long edge, with two transition points. The values of elastic resistance in EM 1110-345-416 are written in terms of the moment capacity of the long side only, but do not form an obvious pattern, with the values high for square panels and low for more elongated panels compared to this systematic approach applied to isotropic panel strength. The alternative values proposed by Biggs are closer, but still too high for square panels. They still appear to be based on long side plasticity only.

The reactions from the analyses with edge moment loading also indicate the elastic reaction transfers due to a uniform edge moment, as assumed for the elasto-plastic stage. The total transfers are equal and opposite, increasing the reaction of the fixed sides, and reducing the reactions of the free side. The amplitude of the reaction transfer depends only upon the resistance moment at the supports, and the aspect ratio, as shown in Table 12. With fixity on all sides and isotropic support moment capacity the transfers cancel out, but for orthotropic support moment capacity there will be a net reaction transfer proportional to the difference in support moment capacity in the two directions.

The reaction distribution due to support moments is different from that due to loading, being least at the centre and greatest at the corner, and differs along the fixed and simply supported edges, so that there is always a change to the peak reaction due to support fixity in the elasto-plastic stage, even when the changes in the total reactions cancel out. The changes to peak elasto-plastic reactions at the centre of the edges are given in Table 13 for fixity on long or short

Table 13
Adjustment for simply supported, peak elastic shears, when used for elasto-plastic phase of panels with opposite edges fixed

Aspect ratio, λ	Isotropic panel with all edges fixed		Panel with long edges fixed		Panel with short edges fixed	
	Short side peak	Long side peak	Short side peak	Long side peak	Short side peak	Long side peak
	Add to V_{PA}	Add to V_{PB}	Add to V_{PA}	Add to V_{PB}	Add to V_{PA}	Add to V_{PB}
1	$-0.668m_F/B$	$-0.668m_F/B$	$-0.971m_{FB}/B$	$+0.303m_{FB}/B$	$+0.303m_{FA}/B$	$-0.971m_{FA}/B$
0.9	$-0.706m_F/B$	$-0.622m_F/B$	$-1.075m_{FB}/B$	$+0.231m_{FB}/B$	$+0.369m_{FA}/B$	$-0.853m_{FA}/B$
0.8	$-0.739m_F/B$	$-0.562m_F/B$	$-1.174m_{FB}/B$	$+0.149m_{FB}/B$	$+0.435m_{FA}/B$	$-0.711m_{FA}/B$
0.7	$-0.765m_F/B$	$-0.485m_F/B$	$-1.260m_{FB}/B$	$+0.062m_{FB}/B$	$+0.495m_{FA}/B$	$-0.547m_{FA}/B$
0.6	$-0.784m_F/B$	$-0.389m_F/B$	$-1.327m_{FB}/B$	$-0.023m_{FB}/B$	$+0.544m_{FA}/B$	$-0.367m_{FA}/B$
0.5	$-0.795m_F/B$	$-0.277m_F/B$	$-1.372m_{FB}/B$	$-0.089m_{FB}/B$	$+0.577m_{FA}/B$	$-0.188m_{FA}/B$

sides, and for isotropic fixity on all sides. For orthotropic support moment capacity the net changes can be calculated by summing the effects of the long-side and short-side fixity.

It should be noted that the values given in Tables 12 and 13 are for initial (positive) deformation. For rebound, the direction of the support bending moments will be reversed, so the sign of the transfer factors should be reversed when applied to the scalar value of the support moment capacity.

4.3. Limitations in application

The calculations are based upon a yield-line criterion suitable for reinforced concrete, a Poisson's ratio of 0.15, elastic small deflection theory and thin shell finite element formulations. These limit the application of the tabulated data.

In a simply supported steel plate and in the centre of clamped plates, the bending is hogging in both directions, and the Von Mises failure criterion will fit reasonably well with yield-line yield criteria. However, at clamped supports and at corners outside the line of contraflection, the bending will be hogging in one direction and sagging in the other. Von Mises moment capacities could be as little as 70% of the uniaxial bending capacity. The ultimate resistance values in the tables will significantly overstate the moment resistance of clamped steel plates.

In elastic analyses, the dynamic support coefficients and the peak reaction coefficients vary with Poisson's ratio, although the transformation factors do not. Even if the spring stiffness is modified for different Poisson's ratio, the reactions in the tables will not be accurate for other materials such as glass or steel.

The elastic analyses are reasonably accurate up to a limiting deflection of about half the thickness, as has previously been demonstrated by the author for simply supported glass [23]. Beyond this point tensile membrane effects will modify not only the stiffness, but also all of the SDOF parameters. This is not a significant constraint on thick concrete walls, where for a slenderness of 0.1 a deflection of half the thickness corresponds to a support rotation of 6°. For slender glazing there is guidance in TM5-1300 Part 6 [19] and in the author's paper on the subject [23]. However, application of the tables in this paper to slender steel plates is likely to lead to significant inaccuracy.

Thin shell FE models do not consider out-of-plane shear deflection, which will reduce the stiffness and modify the deflected shape and hence the elastic SDOF parameters of squat reinforced concrete members, with a slenderness significantly greater than 0.1. The effect of shear deflection will vary with the slenderness of the member, and the support fixity.

Separate SDOF models for direct shear failure were developed in the 1980s. Research [21] indicates that these can be decoupled from the flexural and flexural shear model considered here. For squat reinforced concrete members, either design rules and reinforcement detailing should be used that eliminate the risk of direct shear failure, or a direct shear SDOF analysis may have to be undertaken in addition to the flexural analysis.

4.4. Potential for further development

All of the methods used for these analyses may be applied to analyse panels with one or two adjacent free edges, provided that support fixity on opposite supported sides is symmetric. For calculation of elastic reaction coefficients, the free edges can be used as lines of zero shear.

The methods may also be applied to panels supported on three or four sides with asymmetric support fixity, except that half or whole panels must be used where there is no longer symmetry, and additional independent variables will be required in the yield-line analyses where the opposite corners are not identical. Although the methods will be the same, the solutions will be significantly more demanding. Without lines of symmetry to serve as lines of zero shear, the exact calculation of elastic dynamic reactions will not be possible. However, a reasonably accurate approximation is possible by using a slender thick shell model of the panel and calculating the line of zero shear numerically. The nodes in the parts of the model either side of the line can then be used for the reaction calculations.

One area in which the tri-linear, static deflected shape, SDOF model has been observed to produce significant errors is at the very early stages of a blast or shock response. The assumption of the initial deflected shape as the elastic static deflected shape implies that when the loading arrives the panel ''knows'' that it will deform in this way. This assumption can give very large initial reactions by applying the elastic force coefficients to the peak of the shock wave loading. However, these reactions are not real, but are an artefact of the assumptions. A more realistic model at time zero is a uniform acceleration model, in which the restraint of the supports is not yet significant. This will give a K_{LM} value of unity, with the reaction being based entirely on the resistance, with no loading term. Transient FE modelling [23] suggests that the deflected shape undergoes transition from this to the elastic shape through a ''tray'' shape with curvature at the edges but with uniform acceleration in the centre. Significant improvements could be made in the early reaction history together with smaller improvements in the deflection history if an initial transition into the elastic deflected shape were applied. Further research would be required to identify parameters for the transition time.

The elastic distribution of reaction along supports of yield line FE models is very different from the uniform distribution assumed in most military manuals when calculating shear capacity. The peak factor in many cases is greater than the load partial safety factor. Although the conventional wisdom is that shear should be treated as a brittle failure, in practice where shear resistance is provided by the interaction of concrete and shear links working as struts and ties, there will be significant ductility when links yield, and this will allow redistribution of the reaction away from

the peak value. The current practice of applying the mean reaction with a factor of safety still appears reasonable in practice. However, if a member is to be designed to resist the blast shear without links there is a strong case that the design shear stress should be based upon the peak reaction. This is an area where further research might be required.

5. Conclusions

The principals of the Equivalent SDOF method described in EM1110-345-415 are sound, and are well proven for one-way spanning members. However the application to two-way spanning members in EM1110-345-416 was flawed by some of the assumptions and approximations used to minimise the effort in calculating the values. Errors in some coefficients have been found approaching 50%.

The adoption as "received wisdom" of many of the values from EM1110-345-416 in design manuals down to the present time shows the danger of uncritical adoption of any historic data, and the need for periodic review of even the most basic data and assumptions.

The separation of the tabulated data from the information on how it was generated and limitations of applicability was begun early by Biggs, and has continued to the present. However, it creates a serious risk that the data will be applied wrongly or out of context. To avoid repeating this it is suggested that Section 4.3 of this paper should always be copied with Tables 4–13.

TM5-1300 offered improvements in SDOF parameters for plastic analysis, if not for most elastic cases, but the failure to consider reaction histories resulted in a partial implementation with limited applicability outside its immediate context, which was not suitable for implementation in modern computer-based applications.

Mayor & Flanders used computer methods to produce new SDOF parameters, but these were for application inside a "black box" implementation, and the discrepancy between these and the current published parameters did not appear to be generally realised at the time.

The new analyses described in this paper build upon major developments in yield-line theory, numerical methods, software tools and calculating power since the original Equivalent SDOF calculations were undertaken, and the tabulated results provide a more accurate and consistent implementation for two-way spanning members of the equivalent SDOF method described in EM1110-345-415.

The authors of EM1110-345-416 did not consider further refinement justified, because of the approximate nature of the other data used in the calculation of the structural response. The use of this argument to justify the systematic errors is at the least questionable. In addition, various developments since then have produced refinement of much of the other data, with improved test data and numerical analysis providing better prediction of blast and ground shock loading, incorporation of structure–medium interaction into the analysis providing better structural response, and more consistent materials with better data on material properties providing some improvement in prediction of material failure. Refinement of the SDOF parameters is not simply desirable, but is necessary to bring the expected errors from the analysis in line with the reduced uncertainty from other causes.

It is recommended that Tables 4–13 are used to replace the Tables derived from EM1110-345-416, and the calculations in TM5-1300 for panels supported on four edges. Calculations on the

same basis can be used to provide similar tables for panels with one or two free edges, to replace those in TM5-1300 and PSADS.

Acknowledgements

I would like to acknowledge the encouragement of my colleagues at TPS Consult and of Dr. P Smith, my supervisor at Cranfield University, in the preparation of this paper.

Appendix A. —typical calculations

Comparative calculations of dynamic response have been undertaken using PSADS (after EM1110-345-416), TM5-1300 and the new data presented in this paper.

The panel analysed is shown in Fig. A.1.

Assuming a depth to vertical reinforcement of 50 mm and to horizontal reinforcement of 75 mm, properties common to all the analyses are:

–Second moment of inertia (after TM5-1300)	$I = 6.533 \times 10^9\,\mathrm{mm}^4/\mathrm{m}$
–Concrete Young's Modulus	$E = 30\,\mathrm{kN/mm}^2$
–Mass	$M = 38400\,\mathrm{kg}$
–Vertical bending moment in span	$M_{SB} = 699\,\mathrm{kNm/m}$
–Horizontal bending moments	$M_{SA} = M_{FA} = 657.5\,\mathrm{kNm/m}$

The PSADS properties are all as EM1110-345-416, except that the stiffnesses have been adjusted for a Poisson's ratio of 0.15, and the plastic resistance Ru has been reduced by 10% to allow for corner fans in yield line mechanisms.

The elastic and elasto-plastic properties are all based on an aspect ratio A/B of 0.5. The plastic properties from PSADS are also based on an aspect ratio of 0.5, but the plastic TM5-1300 properties are based on a panel with four-sided support (Figs. 3–17) and an affine aspect ratio of 1.458, giving a hinge position x of 3.188 m from the side. The plastic properties from the new

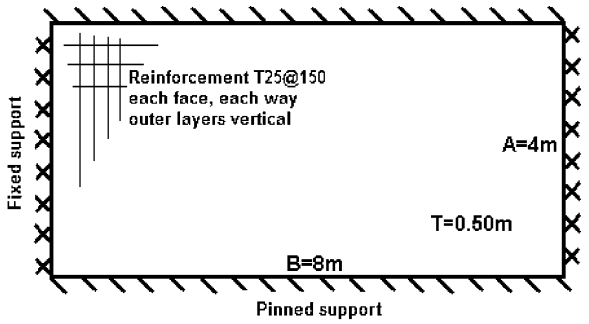

Fig. A.1. Reinforced concrete panel analysed.

Table A.1
Properties for SDOF analyses

Property	PSADS	TM5-1300	New analysis
ke_{fixed}	240 EI/BA^3	EI/0.0005277(1−ν^2)B^4	242.5 EI/BA^3
	91.87 MPa/m	92.76 MPa/m	92.81 Mpa/m
Re	7.4(M_{FA} + 2.43M_{SB})	M_{FA}A/0.02977B	20.31M_{FA}
	17435 kN	11043 kN	13354 kN
Xe	5.93 mm	3.72 mm	4.50 mm
ke_{ss}	201 EI/BA^3	EI/0.000633(1−ν^2)B^4	202.0 EI/BA^3
	76.94 MPa/m	77.33 MPa/m	77.31 MPa/m
Ru	10.8(M_{FA} + M_{SA} + 1.50 M_{SB})	5(M_{SA} + M_{FA})AB/x^2	33.97 m
	25526 kN	20697 kN	23029 kN
Xep	9.22 mm	7.62 mm	7.23 mm
K_{LMe}	0.73	0.78	0.619
K_{Lmep}	0.75	0.79	0.639
K_{LMp}	0.59	0.544	0.538
V_{Ae}	0.05F + 0.08R	—	0.149F + 0.111R
V_{Aep}	0.04F + 0.09R	—	0.142F + 0.223R–2.80M_{FA}
V_{Ap}	0.04F + 0.08R	1237 kN/m × (5/6 A)	0.104F + 0.117R
V_{Be}	0.09F + 0.28R	—	0.100F + 0.139R
V_{Bep}	0.09F + 0.28R	—	0.106F + 0.029R + 2.80M_{FA}
V_{Bp}	0.11F + 0.27R	897 kN/m × (B−x/3)	0.066F + 0.213R

Table A.2
Results of mainly plastic SDOF analyses

Result	PSADS	TM5-1300	New analysis
Deflection X_m	52.8 mm	102.0 mm	83.7 mm
Time of Defln t_m	21.9 ms	30.1 ms	26.3 ms
Span ductility X_m/X_{ep}	5.73	13.4	9.96
Support ductility X_m/X_e	8.90	27.4	18.6
Support rotation	0.756°	1.46°	1.20°
Short reaction V_A	3429 kN	4124 kN	5867 kN
Long reaction V_B	10,005 kN	6224 kN	7154 kN
Distributed react V_{DA}	857 kN/m	1237 kN/m	1467 kN/m
Distributed react V_{DB}	1251 kN/m	897 kN/m	894 kN/m
Mid-span react V_{PA}	857 kN/m	1237 kN/m	2173 kN/m
Mid-span react V_{PB}	1251 kN/m	897 kN/m	1562 kN/m

analysis are based on a panel with the short sides fixed (Table 7) with an affine aspect ratio of 0.516 and an affine bending moment m' of 678 kNm/m.

Properties from the different design methods are summarised in Table A.1.

For a mainly plastic response the panel has been analysed for the application of a triangular blast loading with a peak pressure of 1000 kPa and duration of 40 ms, giving an impulse of 20 kPa s. Numerical analyses with a structural damping of 3% of critical were undertaken. The results are summarised in Table A.2.

Table A.3
Results of mainly elastic SDOF analyses

Result	PSADS	TM5-1300	New analysis	FEA
Deflection X_m	4.25 mm	4.193 mm	4.297 mm	4.808 mm
Time of Defln t_m	8.8 ms	9.05 ms	8.1 ms	8.4 ms
Support ductility X_m/X_e	0.717	1.127	0.956	—
Short reaction V_A	1228 kN	2433 kN	2101 kN	2273 kN
Long reaction V_B	3907 kN	3672 kN	2203 kN	2768 kN
Distributed react V_{DA}	307 kN/m	730 kN/m	539 kN/m	568 kN/m
Distributed react V_{DB}	488 kN/m	529 kN/m	282 kN/m	346 kN/m
Mid-span react V_{PA}	307 kN/m	730 kN/m	739 kN/m	994 kN/m
Mid-span react V_{PB}	488 kN/m	529 kN/m	580 kN/m	850 kN/m

The predominant factor in the different deflections is the plastic resistance Ru, but the SDOF reaction coefficients and the assumptions on how it is distributed have a major effect on the reactions.

For a mainly elastic response the same panel has also been analysed for the application of a triangular blast loading with a peak pressure of 250 kPa and duration of 20 ms, giving an impulse of 2.5 kPa s. In addition to the numerical SDOF analyses, a linear elastic transient dynamic finite element model was analysed using a thickness and density selected to give the same I and M. The analyses were all undamped to make the SDOF analyses comparable to the FE analysis. The results are summarised in Table A.3.

The time of peak deflection in the New Analysis is slightly early due to the inaccuracy of using the flexural shape from the start of the analysis. In the other SDOF analyses, the high K_{LM} values results in later peaks in spite of this effect. In the FE analysis the higher modes of vibration contribute significantly to the peak reactions, and marginally to the peak displacement.

References

[1] Fundamentals of protective design (Non-nuclear) TM 5-855-1. Washington, DC: Department of the Army; March 1965. (Reprint of former document 1110-345-405, 1946.)
[2] Newmark NM. An engineering approach to blast resistant design, American Society of Civil Engineers Transactions, Paper No. 2786, vol. 121, 1956. p. 45.
[3] Design of protective structures to resist the effects of nuclear weapons, AFSWC TR-59-70, December 1959. 2nd ed. TDR-62-138. Washington, DC: US Air Force; 1962.
[4] Design of structures to resist Nuclear weapon effects. ASCE manuals & reports on engineering practice—No. 42. New York: American Society of Civil Engineers; 1961.
[5] Crawford RE, et al. Protection from non-nuclear weapons AFWL RT-70-127 Kirtland AFB. New Mexico: Air Force Weapons Laboratory; 1970.
[6] Design of structures to resist nuclear weapon effects. ASCE manuals & reports on engineering practice—No. 42. revised ed. New York: American Society of Civil Engineers; 1985.
[7] Crawford RE, et al. The air force manual for design and analysis of hardened structures, AFWL-TR-74-102, Kirtland AFB. New Mexico: Air Force Weapons Laboratory; 1974.

[8] Design of structures to resist the effects of atomic weapons—principals of dynamic analysis and design, EM 1110-345-415. Washington, DC: US Army Corps of Engineers; March 1957.
[9] Design of structures to resist the effects of atomic weapons—principals of structural elements subjected to dynamic loads, EM 1110-345-416, Washington, DC: US Army Corps of Engineers; March 1957.
[10] Buchholdt H. Structural dynamics for engineers. London: Thomas Telford; 1997.
[11] Biggs JM. Introduction to structural dynamics. New York: McGraw-Hill; 1964.
[12] Jones LL, Wood RH. Yield-line analysis of slabs. London: Thames & Hudson, Chatto & Windus; 1967.
[13] Timoshenko SP. Theory of plates and shells. New York: McGraw-Hill; 1940.
[14] Fundamentals of protection of structures for conventional weapons TM 5-855-1. Washington, DC: US Army Corps of Engineers; 1986.
[15] Drake JL, et al. Protective construction design manual ESL-TR-87-57, Tyndall Air Force Base. Florida: Air Force Engineering Services Lab.; 1989.
[16] Protective structures automated design system v 1.0 (PSADS) incorporating army TM5-855-1, Air Force AFJAM32-1055, Navy NAVFAC P-1080 and DAHSCWEMAN-97. Washington, DC: US Army Corps of Engineers; September 1998.
[17] SPAnW, Version DAHS CWE 1.1.1.0, June 1997, Incorporated in PSADS, Ref 16, September 1998.
[18] Structures to resist the effects of accidental explosions. Technical manual TM5-1300. Washington, DC: US Department of the Army; 1969.
[19] Structures to resist the effects of accidental explosions. Technical manual TM5-1300. Washington, DC: US Department of the Army; 1990.
[20] Mayor RP, Flanders R. Technical manual, simplified computer model of air blast effects on building walls. Washington, DC: US Department of State, Office of Diplomatic Security; 1990.
[21] Krauthammer T, Bazeos N, Holmquist TJ. Modified SDOF analysis of RC box-type structures. J. Struct. Eng., ASCE 1986;112(4):726–44.
[22] Krauthammer T, Shahriar S, Shanaa HM. Response of reinforced concrete elements to severe impulsive loading. J. Struct. Eng., ASCE 1990;116(4):1061–79.
[23] Morison CM. Recent developments in the single degree of freedom analysis of walls and windows. Proceedings of 11th international symposium on interaction of the effects of munitions with structures, Manheim, Germany, May 2003.